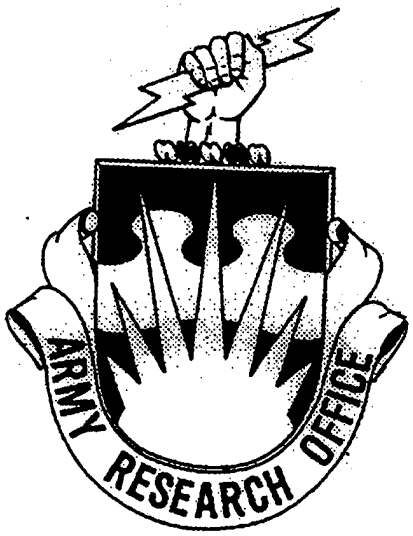

ARO & AFOSR CONTRACTOR'S MEETING

in

CHEMICAL PROPULSION

June 3 – 6, 1996
Virginia Beach, Virginia

19960726 022

Hosted by
The Department of Physics
Hampton Universtiy

DISCLAIMER NOTICE

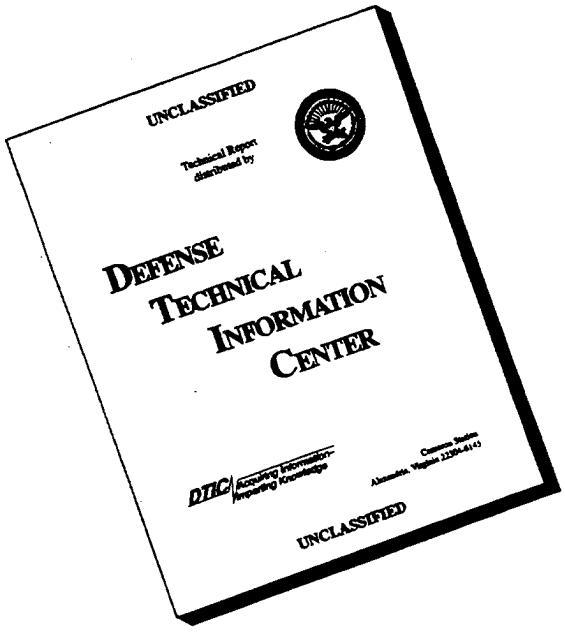

THIS DOCUMENT IS BEST QUALITY AVAILABLE. THE COPY FURNISHED TO DTIC CONTAINED A SIGNIFICANT NUMBER OF PAGES WHICH DO NOT REPRODUCE LEGIBLY.

AFOSR-TR-96

0356

REPORT DOCUMENTATION PAGE

Public reporting burden for this collection of information is estimated to average 1 hour per response, including the t
gathering and maintaining the data needed, and completing and reviewing the collection of information. Send comm
collection of information, including suggestions for reducing this burden, to Washington Headquarters Services, Direc
Davis Highway, Suite 1204, Arlington, VA 22202-4302, and to the Office of Management and Budget, Paperwork Reduc
(0704-0188), Washington, DC 20503.

1. AGENCY USE ONLY (Leave blank)	2. REPORT DATE	3. REPORT TYPE AND DATES COVERED
	20 June 1996	Technical - 1 Jun 95 - 31 May 96

4. TITLE AND SUBTITLE
(U) ARO and AFOSR Contractors Meeting in Chemical Propulsion

5. FUNDING NUMBERS
PE - 61102A
61102F

6. AUTHOR(S)
David M. Mann, Mitat A. Birkan, and Julian M. Tishkoff

7. PERFORMING ORGANIZATION NAME(S) AND ADDRESS(ES)
Air Force Office of Scientific Research
Bolling AFB DC 20332-0001

Army Research Office
Research Triangle Park NC 27709-2211

8. PERFORMING ORGANIZATION REPORT NUMBER

9. SPONSORING/MONITORING AGENCY NAME(S) AND ADDRESS(ES)
Air Force Office of Scientific Research
Bolling AFB DC 20332-0001

Army Research Office
Research Triangle Park NC 27709-2211

NA

10. SPONSORING/MONITORING AGENCY REPORT NUMBER

11. SUPPLEMENTARY NOTES

12a. DISTRIBUTION/AVAILABILITY STATEMENT
Approved for public release; distribution is unlimited

12b. DISTRIBUTION CODE

13. ABSTRACT *(Maximum 200 words)*

Abstracts are given for research in chemical propulsion supported by the Air Force Office of Scientific Research and the Army Research Office

14. SUBJECT TERMS
Flames, Propulsion, Gas Turbines, Chemical Rockets, Diesel Engines, Scramjets, Soot, Sprays, Turbulence, Diagnostics

15. NUMBER OF PAGES
280

16. PRICE CODE

17. SECURITY CLASSIFICATION OF REPORT	18. SECURITY CLASSIFICATION OF THIS PAGE	19. SECURITY CLASSIFICATION OF ABSTRACT	20. LIMITATION OF ABSTRACT
Unclassified	Unclassified	Unclassified	UL

DTIC QUALITY INSPECTED 1

CORRECTION

Page 49A by mistake moved to page 127. Please ignore page 127 and accept the attached correction to the "Table of Contents". We apologize for this error.

CORRECTION TO THE TABLE OF CONTENTS

NONSTEADY COMBUSTION MECHANISMS OF ADVANCED SOLID PROPELLANTS
M.C. Branch.....50

CHEMICAL MECHANISMS AT THE BURNING SURFACE
T.B. Brill.....56

NONLINEAR, ROTATIONAL-ACOUSTIC PROCESSES IN A SOLID ROCKET MOTOR
D.R. Kassoy.....60

INVESTIGATION OF ACTIVE CONTROL OF COMBUSTION INSTABILITIES IN CHEMICAL ROCKETS
B.T. Zinn, et al.....64

MODELING AND ACTIVE CONTROL OF NONLINEAR UNSTEADY MOTION IN COMBUSTION CHAMBERS
F.E.C. Culick.....68

HOLOGRAPHIC TECHNIQUE FOR MEASUREMENT AND VISUALIZATION IN LIQUID PROPELLANT ATOMIZATION
D. Poulikakos.....72

MECHANISMS CONTROLLING SOOT FORMATION IN DIFFUSION FLAMES
M.B. Colket, et al.....76

SOOT EVOLUTION AND CONTROL
R. A. Dbbins.....80

MODELING STUDY TO EVALUATE THE IONIC MECHANISM OF SOOT FORMATION
H.F. Calcote.....84

SOOT, TEMPERATURE AND OH MEASUREMENTS IN AN UNSTEADY COUNTER-FLOW DIFFUSION FLOW
W. Roberts.....88

TRANSPORT PHENOMENA AND INTERFACIAL KINETICS IN MULTIPHASE COMBUSTION SYSTEMS
D.E. Rosner.....92

IGNITION IN CONVECTIVE-DIFFUSIVE SYSTEM
C.K. Law.....96

FLAMELET SURFACE DENSITY AND BURNING RATE INTEGRAL IN PREMIXED FLAME
F.C. Gouldin.....100

ADVANCED SUPERCRITICAL FUELS
T. Edwards, et al.....104

FUELS COMBUSTION RESEARCH
I. Glassman, et al.....108

THEORETICAL AND COMPUTATIONAL STUDIES OF NUCLEATION IN SUPERCRITICAL FUELS
P.G. Debenedetti.....112

HIGH PRESSURE PREIGNITION CHEMISTRY OF HYDROCARBONS AND HYDROCARBON MIXTURES
N.P. Cernansky, et al.....116

ADVANCED DIESEL INJECTION STRATEGIES
F.V. Bracco.....120

FUEL INJECTION AND MIXING STUDIES FOR SCRAMJETS AND RAMJETS
P. Wu, et al.....123

ARO/AFOSR CONTRACTORS MEETING

IN

CHEMICAL PROPULSION

Sheraton Oceanfront Hotel
Virginia Beach VA
3-6 June 1996

MONDAY, 3 JUNE 1996

7:30 - 8:30	Continental Breakfast
8:30 - 8:35	Welcome - Dr. Calvin Lowe, Vice President for Research, Hampton University
8:35-8:40	Opening Remarks - B Tabibi, Hampton University
8:40-9:00	Air Force Office of Scientific Research - M A Birkan

Liquid Propulsion
Moderator: D Talley, Phillips Laboratory

9:00-9:30	Supercritical Droplet Behavior D G Talley, Phillips Laboratory
9:30-9:50	Fundamentals of Acoustic Instabilities in Liquid-Propellant Rockets F A Williams, University of California
9:50-10:10	Modeling Primary Atomization Processes S D Heister, Purdue University
10:10-10:30	Liquid-Propellant Droplet Dynamics and Combustion in Supercritical Forced-Convective Environment V Yang, Penn State
10:30-11:00	BREAK

11:00-11:20	Contributions of Shear Coaxial Injectors to Liquid Rocket Motor Combustion Instabilities M M Micci, Penn State
11:20-11:40	Combustion Instability Phenomenon of Importance to Liquid Propellant Rocket Engines R J Santoro, Penn State
11:40-12:00	Droplet Collision in Liquid Propellant Combustion C K Law, Princeton University
12:00-12:30	DISCUSSION
12:30-2:00	LUNCH BREAK

Plumes
Moderator: D. Weaver

2:00-2:30	Combustion and Plumes D Weaver, Phillips Laboratory
2:30-2:50	Development of a Collisional Radiative Emission Model for Strongly Nonequilibrium Flows D Levin, IDA
2:50-3:10	Energy Transfer Processes in the Production of Excited States in Reacting Rocket Flows J W Rich and V V Subramaniam, Ohio State University
3:10-3:30	BREAK
3:30-3:50	Modeling Nonequilibrium Radiation in High Altitude Plumes I D Boyd, Cornell University
3:50-4:10	Combustion Kinetics of HEDMs and Metallic Fuels A Fontijn, RPI
4:10-4:40	DISCUSSION
4:40-5:00	BREAK

Solid Propulsion
Moderator: J. Levine, Phillips Laboratory

5:00-5:20 Nonsteady Combustion Mechanisms of Advanced Solid Propellants (URI)
M. Branch, University of Colorado; M. Beckstead, Brigham Young University; M. Smooke, Yale University; V. Yang, Penn State University

5:20-5:240 Chemical Mechanisms at the Burning Surface
T. B. Bril, University of Delaware

5:40-6:00 Nonlinear Acoustic Processes in Solid Rocket Engines
D. R. Kassoy, University of Colorado

6:00-6:30 DISCUSSION

6:30-8:30 RECEPTION DINNER

Active Control of Instabilities
Moderator: J Levine

8:30-8:50 Modeling and Active Control of Nonlinear Unsteady Motions in Combustion Chambers
F. E. C Culick, California Institute of Technology

8:50-9:10 Investigation of Active Control of Combustion Instabilities in Liquid Propellant Rocket Motors
B. T. Zinn, Georgia Tech

9:10-10:00 DISCUSSION

TUESDAY, 4 JUNE 1996

7:30-8:30 Continental Breakfast

10:00-12:30 **BASIC RESEARCH NEEDS FOR CHEMICAL ROCKET PROPULSION FOR SPACE APPLICATIONS**
Moderator: D. Talley

- Technological Needs in the Next Century
- What needs to be done to achieve breakthroughs?
- What is the role of basic research? Do we need it?

If you are interested in sharing your ideas, please call Dr. Douglas Talley at (805) 275-6174.

TUESDAY, 4 JUNE 1996 (Parallel Session)

7:30 - 8:15	Continental Breakfast
8:15 - 8:20	Opening Remarks - Bagher Tabibi, Hampton University
8:20 - 8:40	Army Research Office Overview - David Mann
8:40 - 9:00	Air Force Office of Scientific Research Overview - Julian Tishkoff

TOPIC: Combustion Chemistry

Session Chairman: Milt Linevsky, National Science Foundation

9:00 - 9:30	Mechanisms Controlling Soot Formation in Diffusion Flames Meredith B. Colket, United Technologies Research Center
9:30 - 10:00	Soot Evolution and Control R. A. Dobbins, Brown University
10:00 - 10:30	Evaluation of the Ionic Mechanism of Soot Formation H. F. Calcote, AeroChem Research Laboratories, Inc.
10:30 - 10:50	BREAK
10:50 - 11:20	Soot, Temperature, and OH Measurements in an Unsteady Counter-Flow Diffusion Flame William L. Roberts, North Carolina State University
11:20 - 11:50	Transport Phenomena and Interfacial Kinetics in Multiphase Combustion Systems Daniel E. Rosner, Yale University
11:50 - 1:00	LUNCH

Session Chairman: Dan Fant, South Carolina Energy Research and Development Center

1:00 - 1:30	Ignition and Extinction in Convective-Diffusive Systems C. K. Law, Princeton University
1:30 - 2:00	Flamelet Surface Density and Burning Rate Integral In Premixed Combustion F. C. Gouldin Cornell University

TOPIC: High Pressure Phenomena

2:00 - 2:30	Supercritical Fuels Tim Edwards, WL/POSF and W. M. Roquemore, WL/POSC
2:30 - 3:00	Fuels Combustion Research Irvin Glassman, Princeton University
3:00 - 3:30	BREAK
3:30 - 4:00	Theoretical and Computational Studies of Nucleation in Supercritical Fuels Pablo Debenedetti, Princeton University
4:00 - 4:30	High Pressure Preignition Chemistry of Hydrocarbons and Hydrocarbon Mixtures Nicholas Cernansky, Drexel University
7:30 - 9:30	Supercritical Fuels Workshop - Dr. Tim Edwards, WL/POSF

WEDNESDAY, 5 JUNE

7:30 - 8:15	Continental Breakfast
8:15 - 8:30	Announcements

TOPIC: Sprays

Session Chairman: W. M. Roquemore, WL/POSC

8:30 - 9:00	Advanced Diesel Injection Strategies Fediano V. Bracco, Princeton University
9:00 - 9:30	Ramjet Research Abdollah Nejad, WL/POPT
9:30 - 10:00	Nonlinear Distortion and Disintegration of Liquid Sheets for Pressure Atomization Systems William A. Sirignano, University of California, Irvine
10:00 - 10:30	BREAK

10:30 - 11:00	Computational Investigations of Atomization Gretar Tryggvason, University of Michigan
11:00 - 11:30	The Effect of Turbulence on Droplet Drag, Dispersion, Vaporization, and Secondary Breakup in Diesel Fuel Sprays Domenic A. Santavicca, Pennsylvania State University
11:30 - 12:00	Secondary Atomization and Turbulence Interactions of Drops G. M. Faeth, University of Michigan
12:00 - 1:30	LUNCH
Session Chairman:	Edward Mularz, Army Research Laboratory Vehicle Propulsion Directorate
1:30 - 2:00	The Evaporation of Liquid Droplets in Highly Turbulent Gas Streams Richard D. Gould, North Carolina State University
2:00 - 2:30	Particle Dispersion in Turbulent Sprays Ian Kennedy and Wolfgang Kollmann, University of California, Davis
2:30 - 3:00	Application of Parallel Processing to the Investigation of Supercritical Droplet Evaportion and Combustion Using Molecular Dynamics M. M. Micci and Lyle N. Long, Pennsylvania State University
3:00 - 3:30	BREAK
3:30 - 4:00	Fluorescent Diagnostics and Fundamental Droplet Processes Lynn Melton, University of Texas at Dallas and Michael Winter, United Technologies Research Center

TOPIC: Gas Turbine Engines

4:00 - 4:30	Intelligent Turbine Engines B. T. Zinn, Georgia Institute of Technology
4:30 - 5:00	A Multidisciplinary Research Proposal for MEMS-Based Smart Gas Turbine Engines Mehran Mehregany, Case Western Reserve University
7:30 - 9:00	BUSINESS SESSIONS - Contractors and Grantees Only
	Army Research Office - Dr. Mann
	Air Force Office of Scientific Research - Dr. Tishkoff

THURSDAY, 6 JUNE

7:30 - 8:15	Continental Breakfast
8:15 - 8:30	Announcements

Topic: Diesel Engines

Session Chairman: Ernest Schwarz, US Army Tank Automotive Command

8:30 - 9:00	Engine Research Center: Advanced Diesel Engine Research David Foster, University of Wisconsin
9:00 - 9:30	Collaborative Research in Diesel Engine Combustion David E. Klett, NorthCarolina A&T University
9:30 - 10:00	Engineering Model Development for Diesel Performance and Emissions A. M. Mellor, Vanderbilt University
10:00 - 10:30	BREAK
10:30 - 11:00	Analysis of Advanced Direct-Injection Diesel Engine Development Strategies K. T. Rhee, Rutgers University

Topic: Diagnostics

11:00 - 11:30	Advanced Diagnostics for Reacting Flows R. K. Hanson, Stanford University
11:30 - 12:00	Resonant Holographic Interferometry, and Innovative Technique for Combustion Diagnostics Peter A. DeBarber, MetroLaser
12:00 - 1:30	LUNCH

Session Chairman: David Mann, Army Research Office

1:30 - 2:00	Nonlinear Optical Spectroscopy of Multicomponent Droplets Richard K. Chang, Yale University
2:00 - 2:30	Nonlinear Laser Diagnostics for Combustion and Plasma Processes David Huestis, Gregory Faris, and Jay Jeffries, SRI International
2:30 - 3:00	Rapid Concentration Measurements by Picosecond Time-Resolved Laser-Induced Fluorescence Galen B. King and Normand M. Laurendeau, Purdue University
3:00 - 3:30	BREAK

3:30 - 5:45	WORKSHOP - Modeling Combustion Turbulence-Chemistry Interactions
7:00 - 9:30	WORKSHOP - Modeling Turbulence-Chemistry Interactions (Continued) - Application to Hydrocarbon-Fueled Scramjets

TABLE OF CONTENTS

SUPERCRITICAL DROPLET BEHAVIOR
D.G. Talley....1

FUNDAMENTALS OF ACOUSTIC INSTABILITIES IN LIQUID-PROPELLANT ROCKETS
F.A. Williams....5

MODELING LIQUID JET ATOMIZATION PROCESSES
S.D. Heister....9

LIQUID-PROPELLANT DROPLET DYNAMICS AND COMBUSTIONS IN SUPERCRITICAL FORCED-CONVECTIVE ENVIRONMENTS
V. Yang....13

CONTRIBUTIONS OFSHEAR COAXIAL INJECTORS TO LIQUID ROCKET MOTOR COMBUSTION INSTABILITIES
M.M. Micci....17

HIGH PRESSURE COMBUSTION STUDIES UNDER COMBUSTION-DRIVEN OSCILLATORY FLOW CONDITIONS
R.J. Santoro, et al....21

DROPLET COLLISION IN LIQUID PROPELLANT COMBUSTION
C.K. Law....25

COMBUSTION AND PLUMES
D.P. Weaver, et al....29

DEVELOPMENT OF A COLLISIONAL RADIATIVE EMISSION MODEL FOR STRONGLY NON-EQUILIBRIUM FLOWS
D.A. Levin....33

ENERGY TRANSFER PROCESSES IN THE PRODUCTION OF EXCITED STATES IN REACTING ROCKET FLOWS
J.W. Rich, et al....39

MODELING NONEQUILIBRIUM RADIATION IN HIGH ALTITUDE PLUMES
I.D. Boyd....43

KINETICS OF PLUME RADIATION, AND OF HEDMs AND METALLIC FUELS COMBUSTION
A. Fontijn....47

NONSTEADY COMBUSTION MECHANISMS OF ADVANCED SOLID PROPELLANTS
M.C. Branch....51

CHEMICAL MECHANISMS AT THE BURNING SURFACE
T.B. Brill....57

NONLINEAR, ROTATIONAL-ACOUSTIC PROCESSES IN A SOLID ROCKET MOTOR
D.R. Kassoy....61

INVESTIGATION OF ACTIVE CONTROL OF COMBUSTION INSTABILITIES IN CHEMICAL ROCKETS
B.T. Zinn, et al....65

MODELING AND ACTIVE CONTROL OF NONLINEAR UNSTEADY MOTIONS IN COMBUSTION CHAMBERS
F.E.C. Culick....69

HOLOGRAPHIC TECHNIQUE FOR MEASUREMENTS AND VISUALIZATION IN LIQUID PROPELLANT ATOMIZATION
D. Poulikakos....73

MECHANISMS CONTROLLING SOOT FORMATION IN DIFFUSION FLAMES
M.B. Colket, et al....77

SOOT EVOLUTION AND CONTROL
R.A. Dobbins....81

MODELING STUDY TO EVALUATE THE IONIC MECHANISM OF SOOT FORMATION
H.F. Calcote....85

SOOT, TEMPERATURE AND OH MEASUREMENTS IN AN UNSTEADY COUNTER-FLOW DIFFUSION FLAME
W. Roberts....89

TRANSPORT PHENOMENA AND INTERFACIAL KINETICS IN MULTIPHASE COMBUSTION SYSTEMS
D.E. Rosner....93

IGNITION IN CONVECTIVE-DIFFUSIVE SYSTEMS
C.K. Law....97

FLAMELET SURFACE DENSITY AND BURNING RATE INTEGRAL IN PREMIXED FLAMES
F.C. Gouldin....101

ADVANCED SUPERCRITICAL FUELS
T. Edwards, et al....105

FUELS COMBUSTION RESEARCH
I. Glassman, et al....109

THEORETICAL AND COMPUTATIONAL STUDIES OF NUCLEATION IN SUPERCRITICAL FUELS
P.G. Debenedetti....113

HIGH PRESSURE PREIGNITION CHEMISTRY OF HYDROCARBONS AND HYDROCARBON MIXTURES
N.P. Cernansky, et al....117

ADVANCED DIESEL INJECTION STRATEGIES
F.V. Bracco....121

FUEL INJECTION AND MIXING STUDIES FOR SCRAMJETS AND RAMJETS
P. Wu, et al....124

NONLINEAR DISTORTION AND DISINTEGRATION OF LIQUID SHEETS FOR PRESSURE ATOMIZATION SYSTEM
W.A. Sirignano....128

COMPUTATIONAL INVESTIGATION OF ATOMIZATION
G. Tryggvason....132

THE EFFECT OF TURBULENCE ON DROPLET DRAG, DISPERSION, VAPORIZATION AND SECONDARY BREAKUP IN DIESEL FUEL SPRAYS
D.A. Santavicca....136

SECONDARY BREAKUP AND TURBULENCE INTERACTIONS OF DROPS
G.M. Faeth....140

THE EVAPORATION OF LIQUID DROPLETS IN HIGHLY TURBULENT GAS STREAMS
R.D. Gould....144

PARTICLE DISPERSION IN A TURBULENT SHEAR FLOW
I.M. Kennedy, et al....148

APPLICATION OF PARALLEL PROCESSING TO THE INVESTIGATION OF SUPERCRITICAL DROPLET EVAPORATION AND COMBUSTION USING MOLECULAR DYNAMICS
M.M. Micci, et al....152

FLOURESCENT DIAGNOSTICS AND FUNDAMENTAL DROPLET PROCESSES
L.A. Melton, et al....156

INTELLIGENT TURBINE ENGINES
B.T. Zinn, et al....160

A MULTIDISCIPLINARY RESEARCH PROPOSAL FOR MEMS-BASED SMART GAS TURBINE ENGINES
M. Mehregany, et al....164

ENGINE RESEARCH CENTER: ADVANCED DIESEL ENGINE RESEARCH
M. Corradini, et al....168

ENGINEERING MODEL DEVELOPMENT FOR DIESEL PERFORMANCE AND EMISSIONS
A.M. Mellor, et al....172

ANALYSIS OF ADVANCED DIRECT-INJECTION DIESEL ENGINE DEVELOPMENT STRATEGIES
K.T. Rhee....176

ADVANCED DIAGNOSTICS FOR REACTING FLOWS
R.K. Hanson....180

RESONANT HOLOGRAPHIC INTERFEROMETRY: AN INNOVATIVE COMBUSTION DIAGNOSTICS
P.A. DeBarber....184

NONLINEAR SPECTROSCOPY OF MULTICOMPONENT DROPLETS
R.K. Chang....188

NONLINEAR DIAGNOSTICS FOR COMBUSTION AND PLASMA PROCESSES
D.L. Huestis, et al....192

RAPID CONCENTRATION MEASUREMENTS BY PICOSECOND TIME-RESOLVED LASER-INDUCED FLUORESCENCE
G.B. King, et al....196

RESEARCH ON SUPERSONIC REACTING FLOWS
C.T. Bowman, et al....201

TURBULENCE-CHEMISTRY MODELS IN HIGHLY STRAINED NON-PREMIXED FLAMES
S.M. Correa, et al....205

HIGH RESOLUTION MEASUREMENTS OF SUPERSONIC MIXING AND COMBUSTION IN COFLOWING TURBULENT JETS
W.J.A. Dahm, et al....209

CHEMICAL REACTIONS IN TURBULENT MIXING FLOWS
P.E. Dimotakis, et al....213

STUDIES ON HIGH PRESSURE AND UNSTEADY FLAME PHENOMENA
C.K. Law....217

TWO- AND THREE-DIMENSIONAL MEASUREMENTS IN FLAMES
M.B. Long....221

MODELING MIXING AND REACTION IN TURBULENT COMBUSTION
S.B. Pope....225

AFOSR SPONSORED RESEARCH IN AIRBREATHING COMBUSTION
J.M. Tishkoff....229

AFOSR SPONSORED RESEARCH IN PROPULSION DIAGNOSTICS
J.M. Tishkoff....231

COMPRESSIBLE TURBULENT REACTING FLOWS
F.A. Williams, et al....232

SPACE AND ROCKET PROPULSION - GRANTEES AND CONTRACTORS....236

SPACE AND ROCKET PROPULSION - INVITEES....239

AIRBREATHING COMBUSTION INVITEES....256

SUPERCRITICAL DROPLET BEHAVIOR

AFOSR Task 2308AP

Principle Investigator: D.G. Talley
Fundamental Technologies Division
Propulsion Directorate
OLAC Phillips Laboratory
Edwards AFB, CA 93524-7660

Summary/Overview:

The fundamental behavior of transcritical droplets and jets/sprays is studied. Droplets are produced in an improved pressure vessel/drop generator arrangement whereby gases used to facilitate drop generation are stripped away in a stagnation flow while the droplets fall through the stagnation plane into the test gas. The results are visualized using shadowgraphy and planar Raman imaging. Jets which under subcritical conditions would otherwise fall into a wind induced breakup regime are also studied as they transition to a supercritical state. Breakup and mixing mechanisms are shown to change significantly as this occurs. The composition of the ambient gas is also shown to have a significant effect. Simple simulations of these processes have also been further pursued using miscible liquid/liquid combinations at ambient pressure, where the miscibility destroys the surface tension in a manner similar to transcritical fluids.

Authors: R.D. Woodward and D.G. Talley

Background and Objectives

Reducing the cost of future Air Force rocket and air breathing propulsion systems requires an improved understanding of combustion fundamentals. In large rocket engines, for example, an error of even a fraction of a percent in predicted combustion efficiency can magnify into a change in payload capability worth millions of dollars per launch. Saving the necessity for even one engine test during engine development can be worth many hundreds of thousands of dollars. Needs exist to better understand and predict mechanisms leading to combustion performance, chamber wall and injector faceplate heat transfer, and combustion instabilities. This is particularly true in high pressure systems which exceed the critical pressure of the propellants. In many cases the fuel or oxidant (liquid oxygen in rocket propulsion systems) is injected at supercritical pressures but initially at a subcritical temperature. The propellant then undergoes a transition to a supercritical state as it is heated and burned in the combustion chamber—the so-called transcritical process. Compared with the analogous subcritical case, transcritical and supercritical injection and combustion remains poorly understood. Factors contributing to this include vanishing of the surface tension as a supercritical state is approached, vanishing enthalpy of vaporization, anomalous property behavior in the vicinity of the critical point, and increased solubility of the gas phase in the liquid phase and the impact of this on the critical properties of the resulting mixture. Accordingly, the objective of this work is to understand the impact of these factors on the mechanisms leading to atomization, vaporization, and mixing of transcritical fluids.

Supercritical Droplet Generator

Past work demonstrated the feasibility of generating monodisperse cryogenic droplets at elevated pressures and performing planar Raman imaging of the oxygen concentration fields. However, experimental control was found to be lacking. A new pressure vessel with enhanced optical access has been designed and fabricated in which control is facilitated by forming cryogenic droplets in downward flowing chilled helium, and then letting them fall through a stagnation plane, which strips away the helium, into warm upward flowing test gas. Assembly of the new vessel is currently in progress and should be complete by the time of the meeting.

Transcritical Jet Studies

Studies of transcritical jets were performed as described fully in [1]. The results are summarized in Fig. 1. Injection of LN2 into GN2 is given in Figs 1a-c for reduced pressures Pr of .83, 1.03, and 2.03, corresponding to subcritical, near critical, and supercritical nitrogen. The pressure in Fig. 1d is the same as in 1c, except that the ambient gas is a mixture of GN2 and GHe. The jet mass flow rate for all images was 0.068 g/s, corresponding to Reynolds numbers of 4090 (a) , 4010 (b), and 3350 (c,d).

The subcritical jet in Fig. 1(a)(1-4) has a sharp gas/liquid interface throughout. The Weber and Ohnesorge numbers in Fig 1a were 3.6 and .002, respectively, corresponding to a wind induced regime, and the liquid to gas density ratio is about 25. The relatively low speed jet does not exhibit much breakup, although disturbances are evident on the surface of the jet. Symmetric disturbances generally dominated closer to the injector and helical instabilities dominated further downstream.

The near critical jet in Fig. 1b behaves much differently. Unlike Fig 1a, the jet is initially very smooth until aerodynamic disturbances cause unstable wave growth. The sheet-like fan of liquid originating presumably from an imperfection in the injector orifice is not present in Fig 1a, suggesting very little surface tension is present to pull the fan back in Fig. 1b, corresponding to very large if not infinite Ohnesorge and Weber numbers. No droplet like structures are observed further downstream. Instead, stringy structures are observed that may exhibit some interfacial behavior but which mix in a manner more like that of a turbulent jet.

The supercritical jet in Fig. 1c is very similar to Fig 1b, except that aerodynamic instabilities occur earlier and more vigorously as expected in the higher density ambient. The jet in Fig 1d is at the same pressure as in Fig. 1c, except that here the ambient gas is a mixture of 3.9 parts N2 to one part He by mass. The addition of helium has obviously caused a reappearance of liquid like structures. This is due to helium dissolving into the liquid nitrogen and thereby raising the critical pressure of the mixture to at least more than twice that of the pure phase. However, the jet does break up more readily than the subcritical case, due to the higher density ambient and perhaps because the resulting blobs are beginning to undergo transcritical vaporization as they heat up, vaporize, and locally increase the nitrogen concentration.

Raman Images

Sample Raman images of supercritical jets corresponding to Figs. 1c and 1d are shown in Figs. 2a and 2b, respectively. Features corresponding to jet- and liquid-like structures can be discerned but with less spatial resolution than the shadowgraph images. The shadow at the left center of Fig. 2a is caused by a window imperfection. The shadow is quickly dissipated on the opposite side of the jet due to scattering of the laser light in the jets. The laser sheet boundary shown at the top of the image indicates Raman scattering from the gaseous nitrogen. In the future, this effect will be used to quantify the composition of the mixture in the near vicinity of the droplets and jets.

Miscible Fluid Simulations

Miscible liquid/liquid experiments have been performed at atmospheric pressure to study the effects of vanishing surface tension expected in transcritical fluids on particle breakup regimes [2,3]. Previous work was performed with glucose/water mixtures where the viscosity ratio was varied by predissolving small amounts of water into the glucose. Further experiments have been performed with pentane/petroleum oil mixtures. The breakup regimes mapped thus far are shown in Figs. 3 and 4. It is evident that viscosity ratio and Reynolds number alone are not sufficient to characterize the breakup regimes. It is speculated that the diffusion rate of the less viscous fluid into the more viscous fluid, and the subsequent degree to which viscosity is lowered, must also play a role. The appropriate dimensionless number in this case may be a Schmidt number.

Conclusions

The breakup and mixing behavior of jets at constant Reynolds number changes significantly as the critical pressure is approached and exceeded, due to increases in Weber and Ohnesorge numbers approaching infinity. The effect is strongly dependent on the ambient gas composition. In addition, the diffusion rate of the less viscous fluid into the more viscous fluid also appears to be a controlling parameter, at least in cases where surface tension has vanished.

References

1. Woodward, R.D., and Talley, D.G., "Raman Imaging of Transcritical Cryogenic Propellants," 34th Aerospace Sciences Metting & Exhibit, paper AIAA 96-0468, 15-18 January, 1996.
2. Mitts, C., Poulikakos, D., and Talley, D.G., "A Fundamental Study of Supercritical Droplet Deformation and Breakup through a Miscible Fluid Analog," 32nd AIAA/ASME/SAE/ASEE Joint Propulsion Conference and Exhibit, paper AIAA 96-2858, 1-3 July 1996.
3. Mitts, C., Poulikakos, D., and Talley, D.G., "The Characterization of Supercritical Droplet Deformation and Breakup Through a Miscible Fluid Analog," 9th Annual Conference on Liquid Atomization and Spray Systems, 19-22 May 1996.

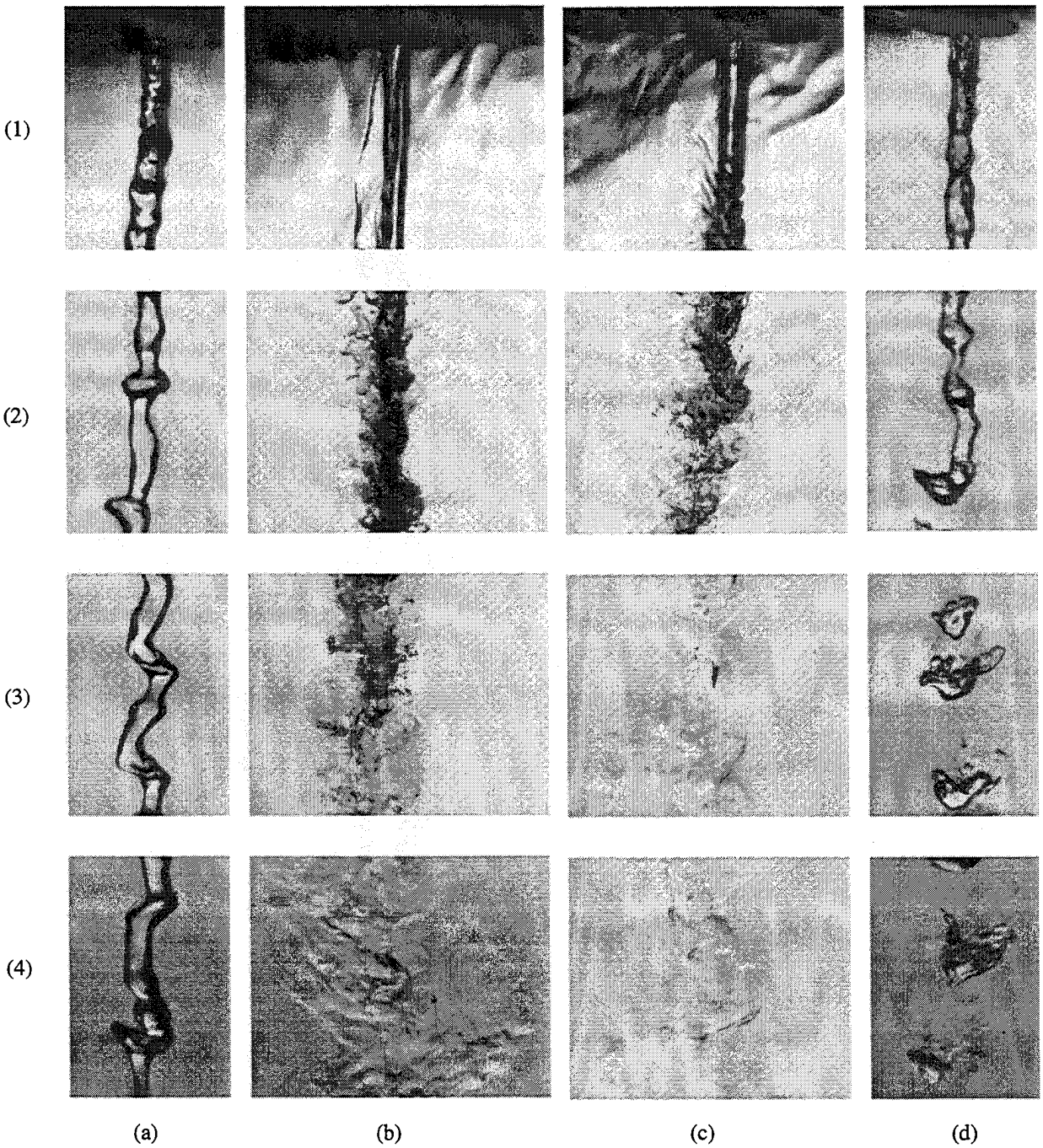

Fig. 1. Shadowgraph images of liquid nitrogen jets issuing into a pressurized chamber. Injection diameter is 0.25 mm (0.010").

(a) into subcritical nitrogen: 28 atm, P/Pcrit = 0.83
(b) into near-critical nitrogen: 35 atm, P/Pcrit = 1.03
(c) into supercritical nitrogen: 69 atm, P/Pcrit = 2.03
(d) into a mixture of nitrogen and helium at 69 atm, mixture ratio (N2/He) of 3.9

Images recorded at the following locations downstream of the injector exit:
(1) 0.0 to 1.9 mm, (2) 7.4 to 9.5 mm, (3) 15.0 to 17.1 mm, (4) 22.6 to 24.7 mm

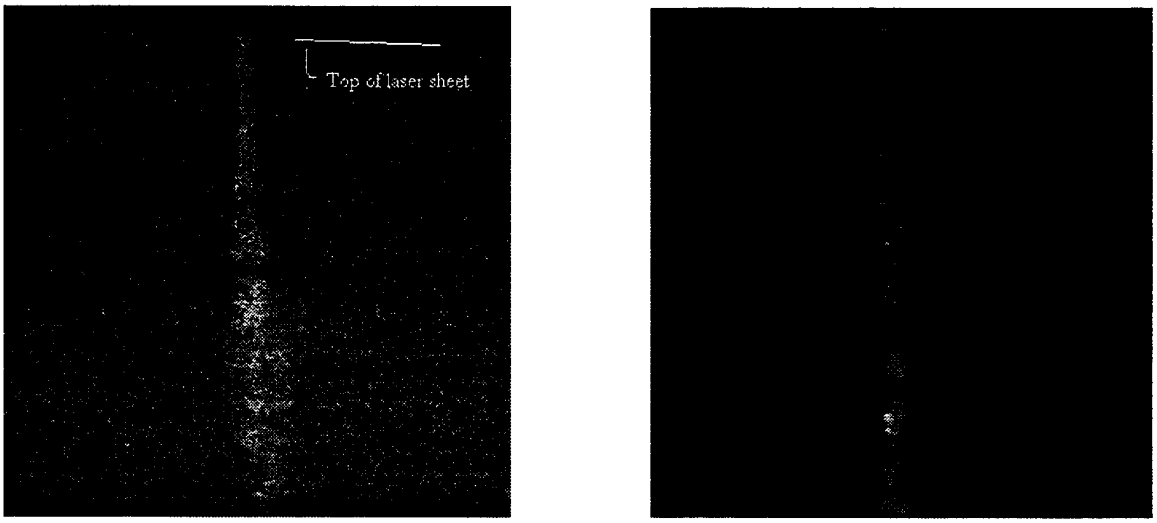

(a) (b)

Figure 2. Raman images of LN2 jet at 69 atm (Pr=2.03) into (a) GN2 and (b) GN2 and He mixture.

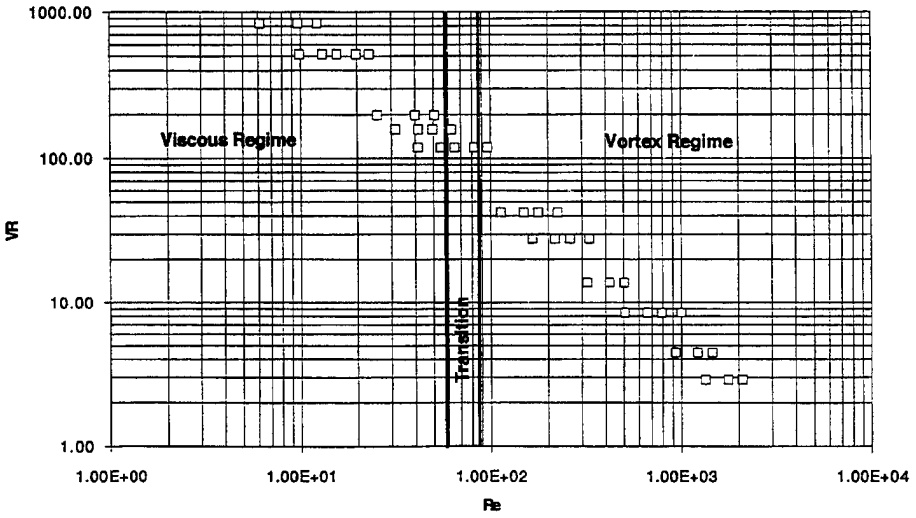

Figure 3. Breakup regimes for petroleum oil into pentane.

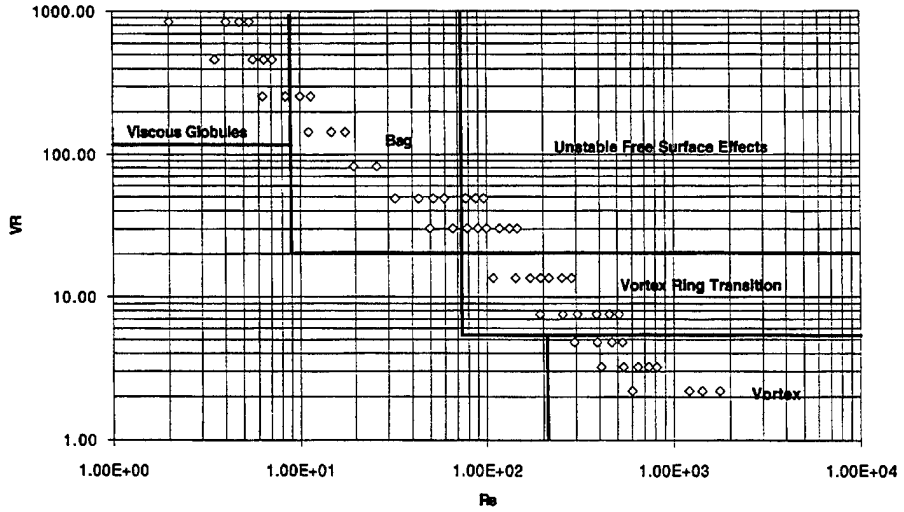

Figure 4. Breakup regimes for sucrose solutions in water

FUNDAMENTALS OF ACOUSTIC INSTABILITIES IN LIQUID-PROPELLANT ROCKETS

(AFOSR Grant No. F49620-94-1-0166)

Principal Investigator : F. A. Williams

Department of Applied Mechanics and Engineering Sciences
University of California at San Diego
La Jolla, CA 92093-0411

Summary/Overview

The objective of this research was to improve understanding of the mechanisms by which flow, mixing and combustion processes are coupled to acoustic fields in liquid-propellant rocket motors. Particular attention was focused on analyses of amplification mechanisms coupled with finite-rate chemical reactions by use of numerical and analytical methods. A theoretical explanation of empirical correlation of instability boundaries for engine-test results for LOX/RP-1 rockets was developed on the basis of amplification by finite-rate chemical reactions in strained mixing layers. In addition, a new numerical computation of nonlinear amplification mechanisms in LOX/GH_2 combustion suggested a possible explanation of threshold phenomena found in liquid-propellant rockets.

Technical Discussion

The research on interaction of acoustic instability with turbulence, which was described in a previous summary, has now been completed and the final citations for the publication is available [1]. The present summary concerns ongoing research on nonlinear acoustic amplification mechanisms with finite-rate chemistry in droplet flames and theoretical explanation of empirical correlation of engine-test results through theoretical work on acoustic amplification mechanisms by finite-rate chemistry. These latter topics are discussed below.

Theoretical Explanation of Acoustic Instability Boundaries

It has been know for some time that the most severe instabilities in liquid rockets are acoustic, that is, sound waves may be amplified by interactions with combustion processes to an intensity high enough to damage the engine. However, the acoustic instability mechanisms have been poorly understood, so that as a design guideline engineers had to rely on empirical methodologies based on previous engine-test results to estimate where the boundaries of acoustic instability lie. Good understanding of the mechanisms by which such empirical relations emerge could help in the design of stable liquid rocket engines without excessive trial and error. One such empirical result is the Hewitt stability correlation. Figure 1 shows the correlation for rocket engines using LOX/RP-1 propellant combinations and like-on-like impinging-jet injectors, in terms of the highest sustainable acoustic frequency and the injection parameter d_o/U_i, where d_o is the orifice diameter of the injector and U_i is the injection velocity.

Here, we are concerned with identification of the instability mechanism that is responsible for the emergence of the Hewitt correlation. In the first attempt to identify the main acoustic instability mechanisms, the response characteristics of various combustion processes have been analyzed to calculate their amplitude and phase relationships with the imposed acoustic waves. Among these processes, the dominant amplification effect is found to be associated with near-extinction diffusion flamelets because the dominant nonlinear term in combustion processes arises from the finite-rate chemical reaction. The time-dependent characteristics of near-extinction flamelets have been analyzed for the strained diffusion flame model by employing activation-energy asymptotics to predict the linear response of the burning rate [2, 3]. These near-extinction strained diffusion flames are expected to be encountered most often between impinging spray fans of fuel and oxidizer. The high sensitivity near extinction can be seen from the well-known S-curve behavior; Fig. 2, obtained from a calculation

performed in a counterflow diffusion flame [2], shows a typical result of the steady reaction-sheet response as a function of the Damköhler number Da. It is clear from Fig. 2 that, for the same fractional variation of Damköhler number, $\delta Da/Da$, shown by vertical bars, the near-extinction flame experiences a much larger reaction-sheet displacement, and the flame-temperature variation, as marked by horizontal bars, also is much larger. In addition, the flame responses are expected to diminish as the acoustic frequency becomes greater than the strain rate, since accumulation of the unsteady effect coming from the imposed acoustic oscillations gives rise to the response delay and attenuation effects. More detailed results on the flame responses with acoustic waves are discussed in our previous works [2, 3, 4].

In liquid-propellant rocket chambers, the rate of strain decays in the axial direction. Consequently, flamelets near extinction may be expected to be encountered more often in the near-injector region and the dominant amplification effect is considered to be coming from these flamelets near the injectors. This is consistent with observations in engine tests, indicating that stability is often achieved by moving the flame zone away from the injector assembly. The effects of finite-rate chemistry are also consistent with the temperature-ramping test, a stability-rating method in which the fuel is gradually heated until instability begins to disappear. As the temperature of the reactants increases, equilibrium chemistry becomes more prevailing, and the consequent reduction of the amplification contributions results in stable operation of the rocket engine.

The strain rates for these flamelets can be approximated as U_i/d_o, which is the strain rate at the impact point of the two jets and also is the reciprocal of the injection parameter [5]. Since the strain rate in impinging-jet flows tends to be spatially uniform, the value of U_i/d_o represents the strain rate for flamelets in a relatively wide region near the injector. However, the strain rate is expected to fluctuate about U_i/d_o because of turbulence. As the strain rate U_i/d_o is increased by increasing U_i or by decreasing d_o, the chance to encounter near-extinction flamelets also increases, thereby resulting in a larger amplification rate. This instability tendency is consistent with the Hewitt correlation in that instability appears by decreasing the injection parameter, *i.e.* increasing the strain rate. In addition, the existence of a high-frequency cutoff is suggested because the flame response rapidly decreases with increasing acoustic frequency. A substantial increase of the flame response is seen in our previous analysis if the nondimensional acoustic frequency ω is smaller than a value that is typically less than unity. Therefore, the cutoff frequency should be linearly proportional to the strain rate U_i/d_o, which is again consistent with the Hewitt correlation. Although it is of course necessary to balance amplification against attenuation, and many different phenomena arise, it is interesting that this one particular phenomenon exhibits all of the right functional dependences [5].

Nonlinear Acoustic Response of LOX/GH_2 Flames

In the previous year's summary, some of the results on the linear acoustic responses of subcritical LOX/GH_2 droplet flames, obtained by activation-energy asymptotics, were reported. That analysis has now been extended to include the effects of detailed H_2–O_2 chemistry and nonlinear acoustic perturbations. Since the pressure is well below the critical pressure of oxygen, the characteristic time for droplet regression is much greater than the characteristic diffusion time, so that the quasisteady droplet combustion model is still valid, and acoustic pressure oscillations can be superposed on the quasisteady droplet flames. Also, spatial variations of the acoustic wave are not considered because the characteristic length of acoustic waves is much larger than that of droplet flames.

First, the steady-state characteristics of the droplet flames are calculated for various pressures by using an inverse numerical method, in which the flame structures are calculated as a function of the maximum temperature instead of the droplet diameter. Since the flame structure is a single-valued function in the parameter space of the maximum temperature, the inverse numerical method enable us to calculate the flame structure even beyond extinction conditions, where the conventional flame codes fail to converge because of intrinsic flame instability. Therefore, the inverse numerical method provides the flame structures near extinction, with a greater accuracy, where the flame response is expected to be the greatest. Initial results of the steady numerical analysis are shown in Fig. 3, where variations of the maximum flame temperature with the droplet diameter are shown for various subcritical pressures. The extinction droplet diameter is seen to increase with decreasing chamber pressure, and extinction

can be achieved for a droplet flame by sufficiently reducing the chamber pressure. Therefore, the numerical results imply that, for a droplet flame with a given diameter, finite-rate chemistry is more important for low pressures, while equilibrium chemistry prevails for high pressures.

Nonlinear response to the imposed acoustic pressure oscillation $P' = P_a \sin(2\pi t/\tau)$, with the acoustic period $\tau = 10^{-3}$s, is considered for a droplet flame of 2.5μm-LOX-diameter at the mean pressure $P_m = 10$ atm. The burning-rate fluctuation is nondimensionalized as

$$Q = \int_0^\tau \left(\frac{h}{h_m} - 1\right) \sin\left(\frac{2\pi t}{\tau}\right) dt$$

where h is the instantaneous rate of heat release and h_m the mean rate of heat release. The variation of Q with the normalized acoustic amplitude P_a/P_m is shown in Fig. 4. The characteristics of the heat-release response are seen to be extremely nonlinear in that the increase of Q with increasing P_a becomes greater as P_a increases and in that the value of Q becomes zero beyond a critical value of the acoustic pressure amplitude P_e. These behaviors can be easily explained from the steady flame structure shown in Fig. 3. Since higher flame sensitivity comes from the effect of finite-rate chemistry, a greater nonlinear heat-release response occurs when the instantaneous pressure is near the minimum. As the acoustic amplitude increases, the flame becomes closer to extinction during the passage of the minimum pressure. Consequently, the increase of Q is faster than the increase of P_a. If P_a is greater than a critical value, which is about 4.9 atm for this calculation, then the chemical reaction during the minimum pressure is too weak to support the flame, so that the flame becomes extinguished and the flame response vanishes.

This type of nonlinear flame response is viewed as a possible mechanism to produce the threshold phenomena discussed in our previous work [6], in which acoustic instabilities can be trigerred only by acoustic perturbations with amplitudes greater than a critical perturbation amplitude. To show this possibility, three different damping response lines, each corresponding to strong, weak and intermediate damping, are drawn as dashed lines in Fig. 4. Stationary amplitudes of acoustic waves can be found from some of the intersections of the amplification and damping lines, at which the effects of damping and amplification can balance each other. First considering the case of strong damping, the situation marked stable in Fig. 4, the only intersection occurs at $P_a = 0$, so that any acoustic perturbations will be attenuated and the system is stable. For the case of weak damping, there are intersections at $P_a = P_e$ and at $P_a = 0$, and only the intersection at $P_a = P_e$ is stable. Therefore, all acoustic disturbance will eventually converge to $P_a = P_e$, and the system is always unstable. The third case corresponds to intermediate damping, in which two stable intersections at $P_a = P_e$ and $P_a = 0$ are separated by an unstable one at $P_a = P_t$. If an initial amplitude of disturbance is greater than P_t, the acoustic amplitude will converge to P_e. Otherwise, the disturbances will be attenuated. Consequently, the system is metastable and exhibits threshold behavior. Our previous analysis has demonstrated that such a metastable acoustic system can exhibit bimodal distributions for the amplitude of acoustic waves. It is also worthy of note that, though the nonlinear response shown in Fig. 4 is calculated from a droplet-flame model, such response behaviors are expected from any type of flame configurations exhibiting usual high sensitivity near extinction.

References

[1] Kim, J. S., "Effects of Turbulence on Linear Acoustic Instability: Spatial Inhomogeneity," *Liquid Propellant Rocket Combustion Instability* (V. Yang Ed.), *Progress in Astronautics and Aeronautics* **169**, 431-454, AIAA, Washington DC, (1995).

[2] Kim, J. S., and Williams, F. A., "Contribution of Strained Diffusion Flames to Acoustic Pressure Response," *Combustion and Flame*, **98**, 279-299 (1994).

[3] Im, H. G., Law, C. K., Kim, J. S., and Williams, F. A., "Response of Counterflow Diffusion Flames to Oscillating Strain Rates," *Combustion and Flame*, **100**, 21-30 (1995).

[4] Sohn, C. H., Chung, S. H., Kim, J. S., and Williams, F. A., "Acoustic Response of Droplet Flames to Pressure Oscillations," *AIAA Journal*, (1996) IN REVIEW.

[5] Kim, J. S. and Williams, F. A., " Boundaries of Acoustic Instability in Liquid-Propellant Rocket Engines: A Theoretical Explanation of an Empirical Correlation," *Journal of Propulsion and Power*, (1996) IN PRESS.

[6] P. Clavin, J. S. Kim and F. A. Williams, Turbulence-Induced Noise Effects on High-Frequency Combustion Instabilities, *Combustion Science and Technology*, **96**, 61-84 (1994).

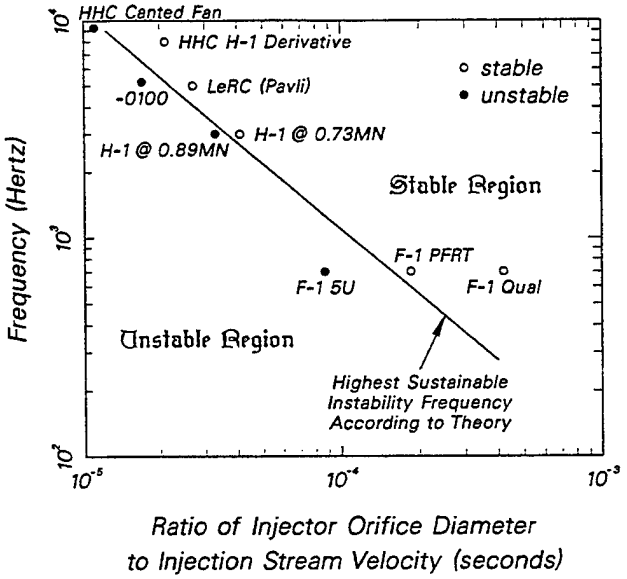

Figure 1. The Hewitt stability correlation for rocket engines using LOX/PR-1 and like-on-like injectors.

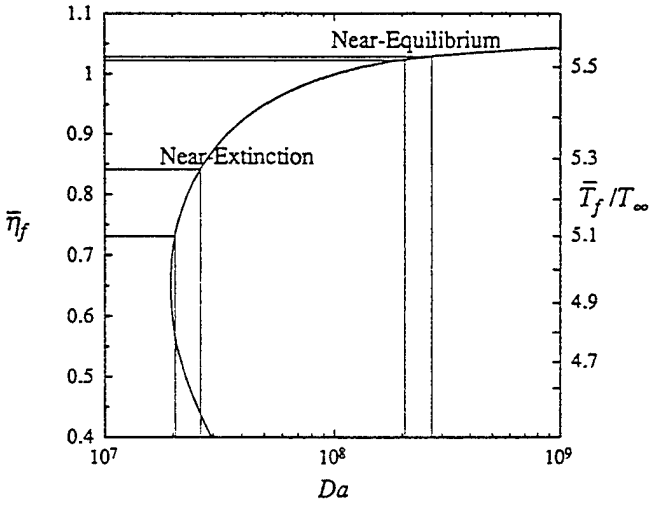

Figure 2. Steady reaction-sheet location and flame temperature as a function of the Damköhler number, showing the high sensitivity of the flame response near extinction.

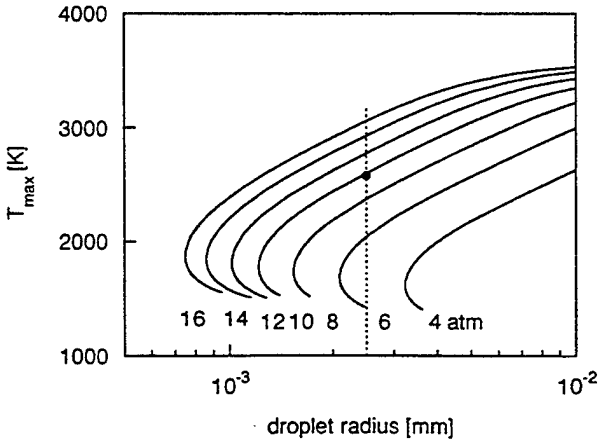

Figure 3. Variation of the maximum temperature with the droplet diameter for LOX/GH_2 droplet flames at various pressures.

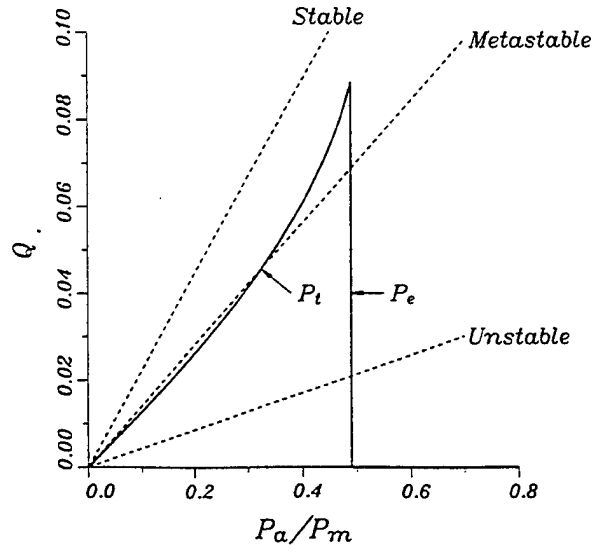

Figure 4. Variation of the nonlinear heat-release response with the normalized acoustic-pressure amplitude. Interaction with intermediate damping exhibits metastable characteristics.

MODELING LIQUID JET ATOMIZATION PROCESSES

AFOSR Contract No. F49620-94-1-0151

Principal Investigator: Stephen D. Heister

School of Aeronautics and Astronautics
Purdue University, W. Lafayette, IN 47907

Summary/Overview

This research program is focused on enhancing the understanding of jet atomization processes and their contribution to combustion instabilities in liquid rocket engines. During the past year, progress has been made in understanding the role of the atomization process in tangential-mode instabilities in the F-1 engine. In addition, the nonlinear response of a droplet to an imposed acoustic perturbation has been studied. Two new models have been developed during the past year. The first model involves a fully-coupled gas/liquid simulation of an injection process under unsteady chamber conditions. The second model involves a zonal approach to a fully viscous simulation, wherein boundary layers are treated via an integral formulation and boundary elements are used at the viscous/inviscid interface. Results from both models are discussed below.

Technical Discussion

During the past year, research has focused on a series of unsteady simulations involving both jets and droplets. In addition, new models have been developed to address coupling of gas and liquid phases during jet injection, and to include viscous effects in the liquid. The following sections summarize progress made in these areas.

Simulation of F-1 Engine Tangential-Mode Instability

Through the recent development of a 2-D simulation of a liquid column responding to an imposed crossflow, we have been able to construct simulations pertinent to tangential-mode acoustic instabilities in liquid rocket engines. As a result, efforts have been focused to analyze both stable and unstable injector designs from the F-1 engine test program[1]. As one might expect, the response of the column grows dramatically when the acoustic frequency (ω_g) is near that of the column natural frequency (ω). From a linear analysis[2], one can show that $\omega^2 = 6\sigma/((\rho + \rho_g)a^3)$, where σ is surface tension, ρ and ρ_g are liquid and gas densities, and a is the orifice radius. Figure 1 details the column response over a large range of frequencies for a Weber number of 0.1 and a gas/liquid density ratio of 0.01. Here, the Weber number is defined, $We = \rho_g U^2 a/\sigma$ where U is the peak velocity in the acoustic wave. This figure notes heightened response near the conditions $\omega_g/\omega = 0.5$, 1.0, and 2.0 which correspond to sub-harmonic, primary harmonic, and a 2nd harmonic of the column natural frequency.

Using the model, a simulation was conducted of a highly-unstable F-1 injector configuration (the Double Row Cluster, DRC), as well as the final, stable configuration demonstrated in Flight Rating Tests (FRT). The DRC design exhibited a 1T instability at 454 Hz which led to chamber pressure oscillations of the order of 400% of the mean. The most prominent difference between these two injectors is the fuel orifice size (3.57 mm radius on FRT vs. 1.4 mm radius on DRC). The combination of the acoustic frequency in the chamber and the natural frequency of the DRC fuel colum leads to conditions very near the resonant freqency noted in Fig. 1. In fact, we calculate that $\omega_g/\omega = 1.7$ for the DRC, while the FRT design has $\omega_g/\omega = 7.0$, a value far from the high response region in Fig. 1.

To assess the impact of the fuel orifice design differences between the two injectors, we have completed a simulation for both designs at a fixed Weber number of 0.1. Results of the column shapes at various times are shown in Fig. 2 for both designs. This figure shows that the unstable DRC design undergoes violent oscillations, whereas the stable FRT design is relatively unaffected by the imposed oscillation. Clearly, the large deformations of the DRC design will have substantial effect on the jet impingement region - a critical

design feature for this impinging element injector. For this reason, we believe that the sensitivity of the DRC design to transverse acoustic energy may be a major contributer to the instability of this injector design.

Nonlinear Droplet Response to Acoustic Excitation

A model analagous to the liquid column has been developed for the axisymmetric flow around a deforming droplet. In this case, the natural frequency (second mode) of excitation is given by the classic result due to Lamb[3]:

$$\omega^2 = \frac{24\sigma}{(3\rho + 2\rho_g)a^3} \tag{1}$$

A series of simulations at a constant gas/liquid density ratio of 0.001, and at $We = 0.58$ have been conducted to determine the frequency response of the droplet. Figure 3 presents a result of this calculation, where response is inferred from the overall aspect ratio (in either prolate or oblate form) of the droplet under maximum deformation conditons. The droplet response is much more complex than that of the liquid column in that 4th-mode coupling is present in many cases. Sharp peaks are realized at several higher-order harmonics. The region $0.9 < \omega_g/\omega < 1$ is characterized by actual fragmentations of the droplet.

Figure 4 highlights the droplet breakup modes identified using this model. At lower We values, small "nipples" are pinched from the main body of fluid. As We grows, dumbell-shaped structures are encountered, followed by "doughnut-shaped" structures. At the very high We values, the droplet flattens to a disk, and small rings are shed from the periphery. This behavior has been noted by several experimentalists by exposing droplets to shock waves, thereby causing a large dynamic pressure about the drop. Breakup times decrease dramatically as We is increased.

Liquid Jet Simulations

During the past year, we have run further validations of existing liquid jet models, and have developed new, more capable models to address more of the physics relevent to atomization processes. Recently, we ran a simulation using our finite-length jet code[4] in order to compare results with experimental images recorded by Moses[5] here at Purdue. Results of this comparison are shown in Fig. 5. The agreement between the BEM simulation and the experimental measurements are very good; "recoil" waves generated as a result of the pinching process are resolved within the calculation, as is the relative spacing of main and satellite droplets.

A fully-coupled, nonlinear simulation of a liquid jet issuing into a quiescent gas has been developed to assess unsteady chamber effects on the atomization process. Researchers have speculated that the unsteady chamber conditions existing during combustion instabilities could impact the atomization process, thereby amplifying (or damping) the instability. While several calculations have been made using our model, a single highlight will be discussed here. Figure 6 illustrates the influence of chamber gas density on the behavior of the jet at fixed inflow (i.e. Weber number) conditions. The gas density effect is measured through the input gas/liquid density ratio, ϵ. Mushroom-capped structures appear at high ϵ values due to the substantial momentum required to displace the "heavy" gas in the chamber. Such conditions exist in high pressure combustion devices such as LREs.

BEM for Viscous Flows

Substantial progress has also been made in the development of a model capable of addressing liquid-phase viscous contributions to the atomization process. Unfortunately, we were forced to abandon the Dual Reciprocity Method for which we presented some preliminary results last year. This method gave fine solutions for steady flows, but for unsteady flows the resulting matrices turn out to be ill-conditioned, making numerical inversion processes inaccurate. For this reason, we have adopted a zonal scheme in which the viscous region is treated separately via an integral method formulation. Full unsteady simulations are possible using this methodology within the framework of the BEM code which is used to solve for properties within the inner, inviscid region. Results will be presented at the upcoming meeting.

References

1. Oefelein, J. C. and Yang, V., "Comprehensive Review of Liquid-Propellant Combustion Instabilities in F-1 Engines," *Journal of Propulsion and Power*, Vol. 9, No. 5, 1993, pp. 657-677.

2. Heister, S. D., Rutz, M., and Hilbing, J., "Effect of Acoustic Perturbations on Liquid Jet Atomization", AIAA 95-2425, 31st AIAA Joint Propulsion Conference, San Diego, CA, 1995.

3. Lamb, H., *Hydrodynamics, 6th Ed.*, Dover Publications, 1982.

4. Hilbing, J. H., Heister, S. D., and Spangler, C. A., "A Boundary Element Method for Atomization of a Finite Liquid Jet", *Atomization and Sprays*, V 5, No. 6, pp 621-638, 1995.

5. Moses, M. P., Collicott, S. H., and Heister, S. D., "Visualization of Liquid Jet Breakup and Droplet Formation", 7th International Symposium on Flow Visualization, Seattle, WA, 1995.

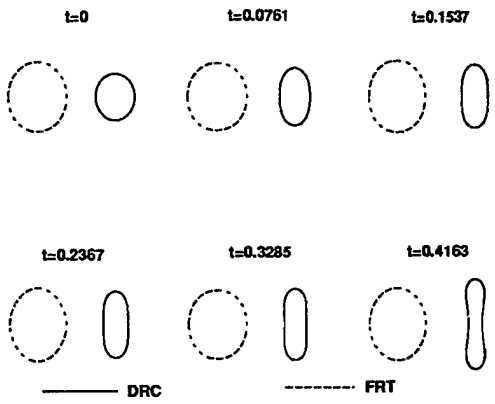

Figure 2: Simulation of Fuel-Jet Response in the Unstable Double-Row Cluster (DRC) and Stable Flight Rating Tests (FRT) F-1 Engine Injectors (times are measured in seconds from start of disturbance)

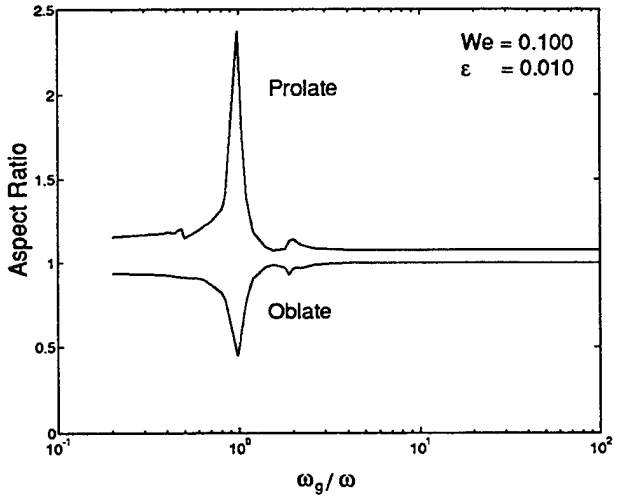

Figure 1: Nonlinear Frequency Response of Liquid Column; Maximum (Prolate) and Minimum (Oblate) Aspect Ratios Obtained During Oscillation

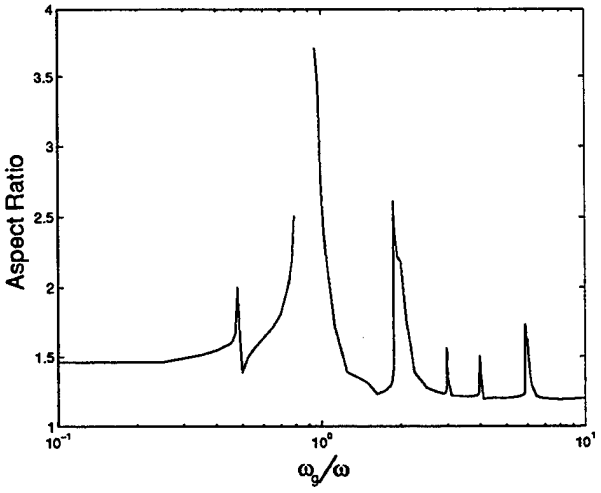

Figure 3: Nonlinear Frequency Response of Liquid Droplet, Gas/Liquid Density Ratio = 0.001, Weber number=0.58

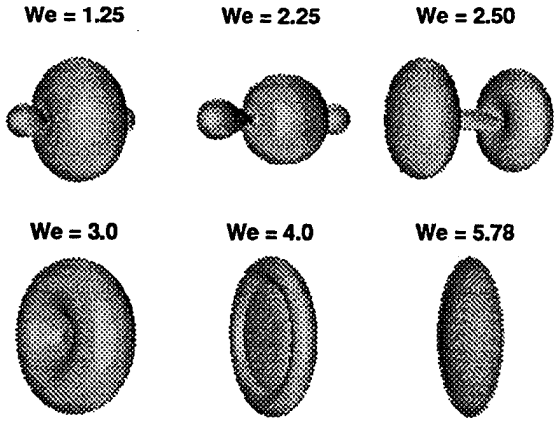

Figure 4: Droplet Breakup Modes Encountered Under Acoustic Excitation at the Drop's Natural Frequency

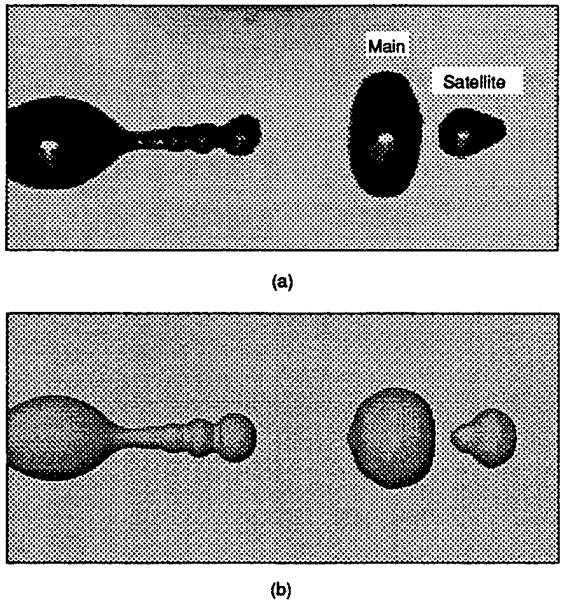

Figure 5: Jet Profile Comparison Near the Pinch Location, (a) Experiment of Moses, (b) BEM Result, We=17.6, Bo=0.0109, $k = 0.447$.

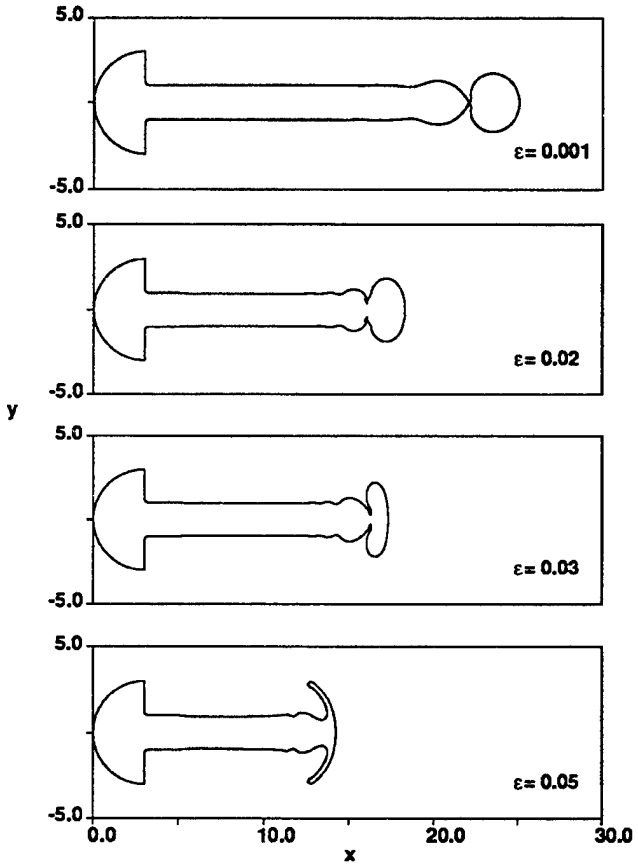

Figure 6: Effect of Gas Density on Initial Liquid Jet Behavior, $We = 17.6$

LIQUID-PROPELLANT DROPLET DYNAMICS AND COMBUSTION IN SUPERCRITICAL FORCED-CONVECTIVE ENVIRONMENTS

(AFOSR Grant No. F49620-95-1-0193)

Vigor Yang
Department of Mechanical Engineering
The Pennsylvania State University
University Park, PA 16802

SUMMARY/OVERVIEW

A focused research program is conducted to investigate the dynamic behavior of liquid-propellant droplets in supercritical forced-convective environments. The purpose is to establish a solid theoretical basis for enhancing the understanding of liquid-propellant droplet vaporization, combustion, and dynamics at supercritical conditions, with emphasis placed on the effect of forced convection. A variety of liquid propellants and propellant simulants, including hydrocarbon and cryogenic fluids, at both steady and oscillatory conditions are treated systematically. The formulation is based on the full conservation equations for both gas and liquid phases, and accommodates variable properties and finite-rate chemical kinetics. Full account is taken of thermodynamic non-idealities and transport anomalies at high pressures, as well as liquid-vapor phase equilibria for multi-component mixtures. Because the model allows solutions from first principles, a systematic examination of droplet behavior over wide ranges of temperature and pressure is made possible. Results not only enhance the basic understanding of the problem, but also serve as a basis for establishing droplet vaporization and combustion correlations for the study of liquid rocket engine combustion, performance, and stability.

TECHNICAL DISCUSSION

Liquid-droplet vaporization and combustion in supercritical environments have long been matters of serious practical concern in combustion technology, mainly due to the necessity of developing high-pressure combustion devices such as liquid-propellant rocket engines, diesel engines and liquid propellant guns. Although several studies have been devoted to this problem, a number of fundamental issues regarding the attainability of critical conditions and droplet gasification and burning mechanisms at high pressures remain unresolved. Most of the existing theories are based on certain assumptions and empirical correlations that are extrapolated from atmospherical conditions, with their validity for high-pressure applications subject to clarification. Furthermore, no unified analysis of the entire droplet history, in particular the transition from the subcritical to supercritical state, was conducted. Almost all of the models for supercritical combustion have assumed *a priori* that the droplet reaches its critical state instantaneously upon introduction into a supercritical environment. Neither initial heatup transients nor nonuniformities of liquid-phase properties are considered. In addition, the treatment of transport properties and thermodynamics nonidealities is overly simplified to yield complete information. Recent reviews of this subject are given in Refs. 1-4.

The physical model treated here is an isolated liquid-propellant droplet (or an array of droplets) when suddenly confronted with a supercritical fluid flow. The initial temperature of the droplet is subcritical. As the droplet is heated by the ambient gas, its temperature increases and finally exceeds the critical point. Several important aspects must be noted during this process. First, when the droplet surface approaches its thermodynamic critical state, the difference in density between gas and liquid phases becomes smaller. The characteristic times of the transport processes near the droplet surface in both phases have the same order of magnitude. Therefore, the transient effects in the gas phase are as important as those in the liquid phase, and the quasi-steady condition may never be reached during the lifetime of the droplet. Second, the latent heat of

vaporization decreases to zero at the critical point. Conventional low-pressure models may erroneously predict the vaporization rate if the variation of latent heat with pressure is not properly taken into account. In addition, if the droplet is moving, the behavior of liquid deformation and breakup may be altered considerably due to the diminished value of surface tension. Third, at high pressures, effects of thermodynamic non-idealities and property variations play decisive roles in determining transport properties and interfacial thermodynamic relationships. The solubility of the ambient gas in the liquid phase increases with pressure, and the classical Raoult's law for ideal mixtures is not applicable for phase-equilibrium analysis. One must develop a more comprehensive model for vapor-liquid interface conditions in terms of fugacity. Finally, when the droplet exceeds its critical state, it essentially becomes a "puff" of dense fluid. The entire field becomes a continuous medium, and no distinct interfacial boundary can be identified.

The primary purpose of this research project is to establish a theoretical framework within which various issues of supercritical droplet vaporization and combustion can be addressed systematically. Specific tasks conducted during the past year include: (1) investigation of supercritical droplet vaporization and combustion in steady convective environments, and (2) study of dynamic responses of droplet vaporization and combustion to ambient flow oscillations. The progress made to date for these tasks is given below.

1. Supercritical Droplet Vaporization and Combustion in Steady Convective Environments

A comprehensive theoretical analysis has been established to investigate droplet vaporization and combustion in forced convective environments at supercritical conditions. Both hydrocarbon and cryogenic propellant droplets are considered over a pressure range from one to 400 atm. Specific processes treated in this task are:

1. complete time history of droplet gasification, including the transition from the subcritical to supercritical state;
2. ignition and flame development;
3. droplet dynamics, including deformation, stripping, and shattering; and
4. interphase transport between droplet and surrounding flow.

Figure 1 shows the time evolution of the critical surfaces at under various flow conditions at p=100 atm. Owing to the difference between mass and thermal diffusivity, the surface which attains the critical mixing temperature usually regresses faster than that with the critical mixing composition. The dynamic deformation of the droplet is substantially enhanced by increasing the momentum carried by the ambient flow. The effect of pressure on the evolution of the critical surfaces is illustrated in Fig. 2. In addition to enhanced droplet deformation, entrainment of gasified oxygen into the recirculating eddies in the wake region is augmented with increasing pressure. At p=400 atm, the isocomposition skirt even exhibits oscillatory motion. The gaseous oxygen entrapped by the recirculating flow tends to move forward and drives the skirt to expand in the cross steam direction. The convective flow, on the other hand, suppresses this lateral expansion and forces the skirt to bend and stretch downstream. As a result, more oxygen is trapped into the recirculating eddies, leading to another locomotion. Detailed discussions of this phenomenon are given in Refs. 5 and 6.

2. Dynamic Responses of Droplet Vaporization and Combustion to Ambient Flow Oscillations

The dynamic responses of supercritical droplet vaporization and combustion to ambient flow oscillations have been examined [7-8]. The analysis extends the droplet combustion model established for steady environments, and accommodates periodic pressure and velocity fluctuations in the ambiance. The oscillatory characteristics of droplet gasification and burning mechanisms are studied in detail over a broad range of pressure. Results indicate that the droplet response functions (both pressure- and velocity-coupled responses) increase progressively with pressure

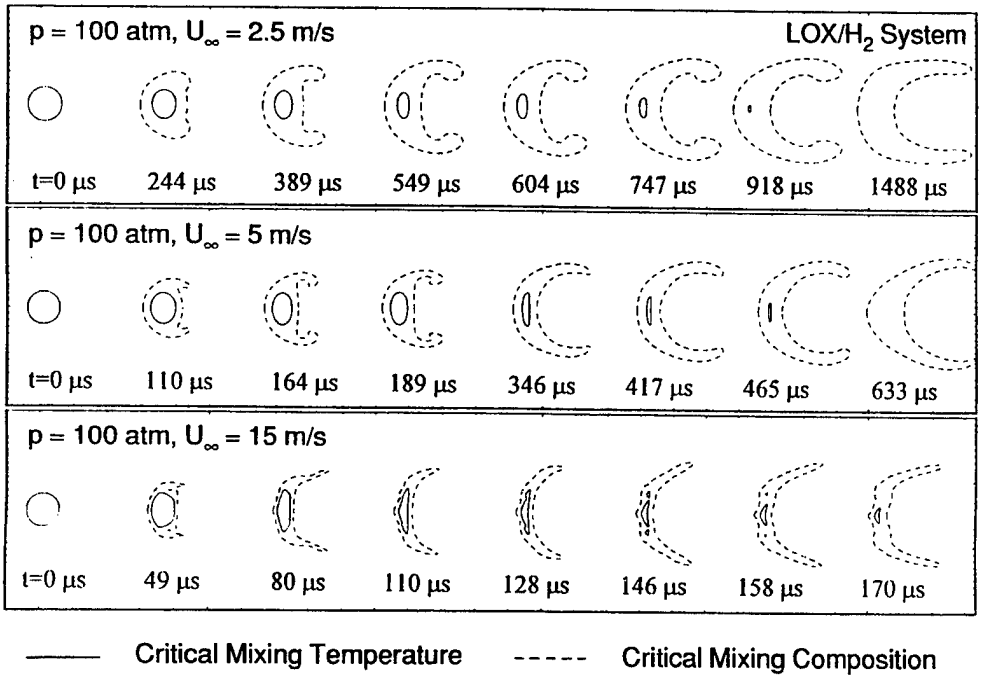

FIGURE 1. Effect of Ambient Velocity on Evolution of Droplet Surface, *LOX / H2* System at p = 100 atm.

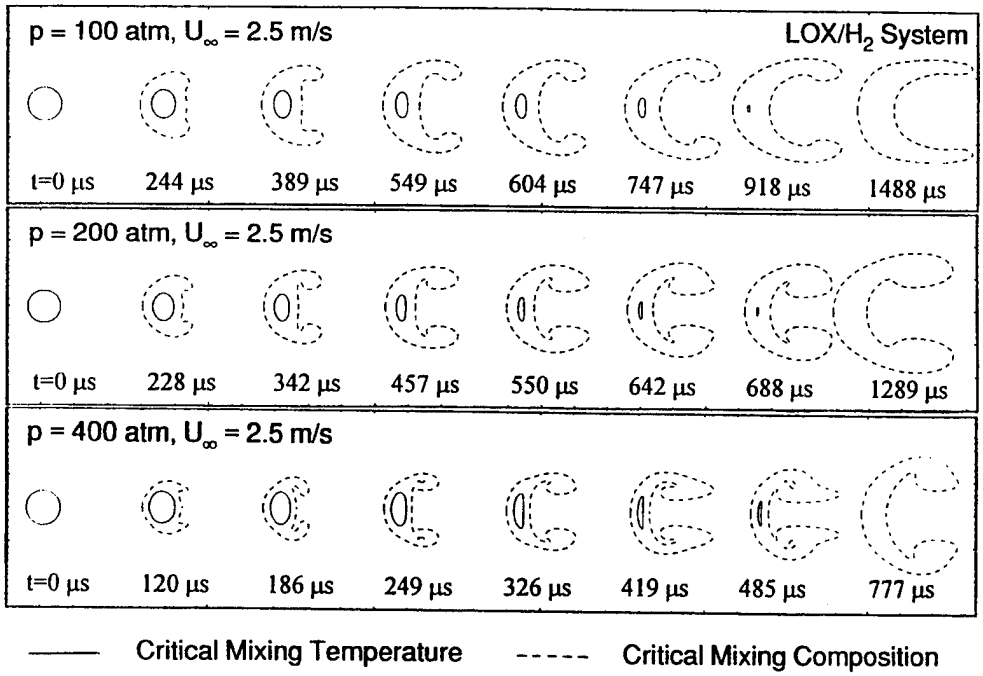

FIGURE 2. Effect of Ambient Pressure on Evolution of Droplet Critical Surface, *LOX / H2* System at $U\infty$ = 2.5 *m/s*.

due to reduced thermal inertial at high pressures. Furthermore, a rapid amplification of droplet vaporization/combustion response occurs when the droplet surface reaches its critical mixing point. This phenomenon may be attributed to the strong sensitivities of latent heat of vaporization and fluid transport properties to small perturbations near the critical point.

In addition to basic investigation into the thermophysical processes involved, correlations of droplet response functions are established in terms of droplet and oscillatory flow properties. This information can be effectively used in liquid rocket engine combustion instability analysis.

REFERENCES

[1] Hsieh, K.C., Shuen, J.S., and Yang, V. (1991). Droplet Vaporization in High Pressure Environment. I: Near Critical Conditions. *Combustion Science and Technology*, 76, 111.

[2] Shuen, J.S., Yang, V., and Hsiao, G.C. (1992). Combustion of Liquid-Fuel Droplets at Supercritical Conditions. *Combustion and Flame,* 89, 299.

[3] Yang, V., Lin, N.N., and Shuen, J.S. (1994). Vaporization of Liquid Oxygen (LOX) Droplets in Supercritical Hydrogen Environments. *Combustion Science and Technology*, 97, 247.

[4] Lafon, P., Yang, V., and Habiballah, M. (1996). Supercritical Vaporization of Liquid Oxygen Droplets in Hydrogen and Water Environments. Submitted to *Journal of Fluid Mechanics.*

[5] Yang, V., Hsiao, G.C., and Shuen J.S. (1996). Droplet Behavior at Supercritical Conditions. *Recent Advances in Spray Combustion,* AIAA Progress in Astronautics and Aeronautics Series, Vol. 166, 1996.

[6] Hsiao, G.C., Yang, V., and Shuen, J.S. (1996). Gasification of Liquid Oxygen Droplets in Supercritical Hydrogen Streams. Submitted to *Journal of Fluid Mechanics.*

[7] Hsiao, G.C., Yang, V., and Shuen, J.S. (1995). Pressure-Coupled Vaporization Response of Liquid Hyddrocarbon Droplets at High Pressures. Submitted to *Journal of Propulsion and Power.*

[8] Lafon, P., Yang, V., and Habiballah, M. (1995). Pressure-Coupled Vaporization and Combustion Responses of Liquid Oxygne (LOX) Droplets in Supercritical Hydorgen Environments. AIAA Paper 95-2432, also submitted to *Journal of Propulsion and Power.*

CONTRIBUTIONS OF SHEAR COAXIAL INJECTORS TO LIQUID ROCKET MOTOR COMBUSTION INSTABILITIES

AFOSR Grant No. F49620-95-1-0184

Michael M. Micci

Department of Aerospace Engineering
The Pennsylvania State University
University Park, PA 16802

SUMMARY/OVERVIEW:

The determining factors for the combustion stability of liquid rocket motors using coaxial injectors are still unknown by the propulsion community. Experiments over the past year have focused on our hot-fire combustion chamber utilizing liquid oxygen and gaseous hydrogen with one full-size SSME preburner element at full scale LOX flow rates and oxidizer to fuel mixture ratios between 2.2 and 5.6. LOX droplet sizes and velocities were measured with an Aerometrics Phase Doppler Particle Analyzer (PDPA) for chamber pressures between 300 and 800 psia and the first ever measurements of LOX droplet sizes above the critical pressure of pure oxygen were obtained. Droplet sizes were found to decrease while the droplet velocity increased with increasing gas/liquid velocity ratio and increasing chamber pressure resulted in decreased droplet size. A one-dimensional acoustic chamber analysis is being formulated in conjunction with ONERA for use with upcoming modulated chamber experiments.

TECHNICAL DISCUSSION:

Hot-Fire Experiment. The subscale combustion chamber was dimensioned after the preburner of the Space Shuttle Main Engine because of the capability of the test facility to match the flow rates of a single injector element within the preburner. Facility limitations do impose a maximum chamber pressure of approximately 8.0 MPa, which results in chamber Mach numbers an order of magnitude less than the SSME preburner. Nevertheless, similar mass flow rates per unit area were addressed in the chamber design. The chamber, as illustrated in Fig. 1, is modular in design, allowing for simple variation of the chamber length, location of optical access, injector design and throat diameter. The individual chamber segments include the injector segment, window segment, igniter segment, blank segment and nozzle segment. With all segments in place the interior length of the combustion chamber measures 25.7 cm. The chamber is mounted together with a hydraulic press and sealed between segments with standard polymer O-rings. The chamber is designed to operate for 4 seconds at steady state chamber pressures up to 10 MPa.

Injector faceplates of several existing and proposed liquid propellant rocket engines were reviewed to ascertain the local grouping of injector elements around a single element. Although combustion chambers are

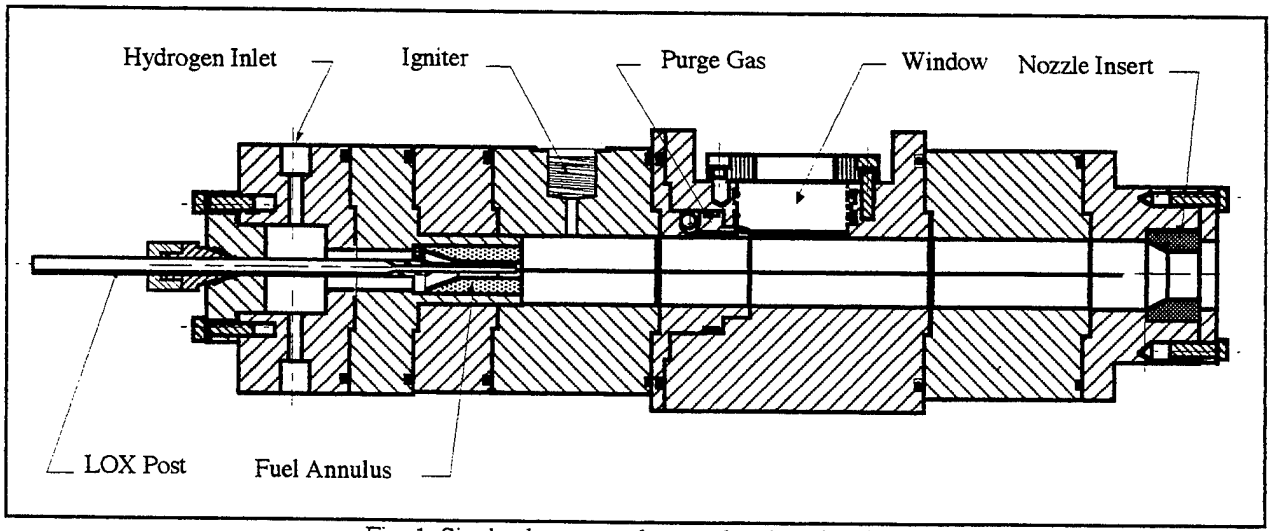

Fig. 1 Single element rocket combustion chamber.

generally cylindrical in design, the immediate boundary of a single injector element was found to be more accurately represented by a hexagon formed by six adjacent injector elements. This distribution of injector elements is illustrated in Fig. 2. Based on this consideration and the requirement of flat windows for laser based diagnostic devices, a hexagon enclosing a 2.82 cm circle was selected for the chamber interior cross-section. With the six sided polygon flat windows can be mounted onto the chamber at opposite sides or at an inclination of 60° to the principal axes of the windows. Detail of the window segment is provided in Fig. 3. The segment is intended for droplet size and velocity measurements within the liquid oxygen spray using a phase Doppler interferometric device. Since the optimal orientation of the instrument optics is 30° for this technique, the velocity measurement is limited to one component with the present chamber window locations. Light collection at the 60° orientation of the windows is being evaluated for future tests involving two component velocity measurements. To reduce or eliminate contaminants from collecting on the windows during engine testing, a purge gas section was incorporated into the design of the window segment. Eight small holes inject nitrogen gas across the inner surface of the windows within the window recess region. Preliminary tests with the window segment located at the chamber midsection verified adequate window purging with nitrogen flow rates less than 10% of the total propellant flow rate. Measurements of the chamber inner surface temperature and the steady and oscillating components of chamber pressure are made in this segment.

The injector segment is separated into two concentric brass sections. The forward section contains a threaded insert which forms the outer diameter of the fuel annulus and may be replaced between tests without complete chamber disassembly. The rear section provides the coupling of the injector to the propellant feed system. In addition, fuel plenum pressure, both the steady and oscillating components, as well as fuel injection temperature are measured in the rear section. Pressure and temperature of the liquid oxygen are measured in the liquid supply line at the entrance to the LOX post. The baseline dimensions of the injector were modeled after the injector element of the SSME preburner. Additional fuel annuli were fabricated for the first series of tests in which the effect of gas-to-liquid velocity ratio, density ratio and mixture ratio on injector performance were to be examined.

The nozzle segment houses a water cooled nozzle throat insert that is sized for a specific propellant mass flow rate and chamber pressure. A stainless steel flange retains the insert within the nozzle segment while serving a second function as a pressure relief mechanism. During instances of excessive chamber pressures, the nozzle flange is designed to break away from its fasteners allowing for nozzle removal and rapid chamber depressurization. Propellant ignition is accomplished with a gaseous oxygen/gaseous hydrogen torch igniter. Both gases are introduced into a small combustion chamber attached to the side of the igniter segment and ignited by a high voltage, electrical discharge. The resulting flame is drawn into the main chamber to ignite the main propellant.

For the hot-fire experiments conducted to date, mixture ratios ranged from 2.17 to 5.61, which resulted in velocity ratios between 10.4 and 30.1, however the majority of the tests were conducted with a mixture ratio of approximately 4.25. The mixture ratio was varied by varying the gaseous hydrogen flow rate with the LOX flow rate being held constant at 0.113 kg/s. Chamber pressures ranged from 300 to 800 psia. Care was taken to avoid conditions which resulted in cavitation of the LOX before or during injection.

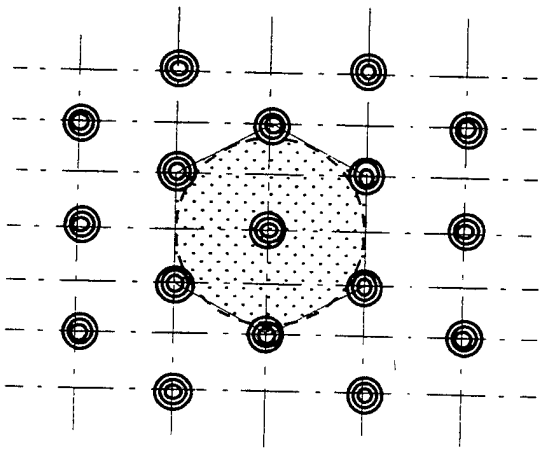

Fig. 2 Illustration of element distribution on injector faceplate.

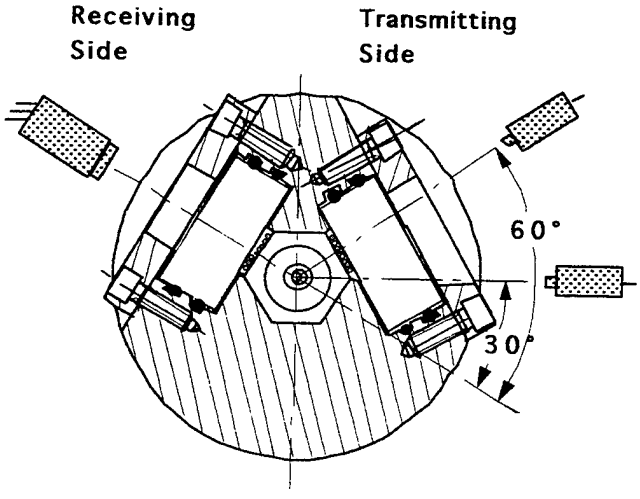

Fig. 3 Detail of window cross-section depicting phase Doppler interferometry orientations.

Experimental Results. Figure 4(a) shows the arithmetic mean diameter plotted versus the velocity ratio. For these tests the mixture ratio varied from 3.45 to 4.98. Chamber pressures ranged from 306 to 606 psia. All measurements were taken along the axis at a distance of 11.4 cm downstream of the injector face. A dramatic increase in the arithmetic mean diameter can be seen as the velocity ratio drops below a value of 12. This is the same effect one would observe as the hydrogen temperature dropped in a hydrogen temperature ramping test. Figure 4(b) shows the droplet velocity as a function of the velocity ratio for the same tests. It can be seen that the droplet velocity increases linearly with the velocity ratio, starting with a value of the droplet velocity approximately equal to the LOX injection velocity of 30 m/s.

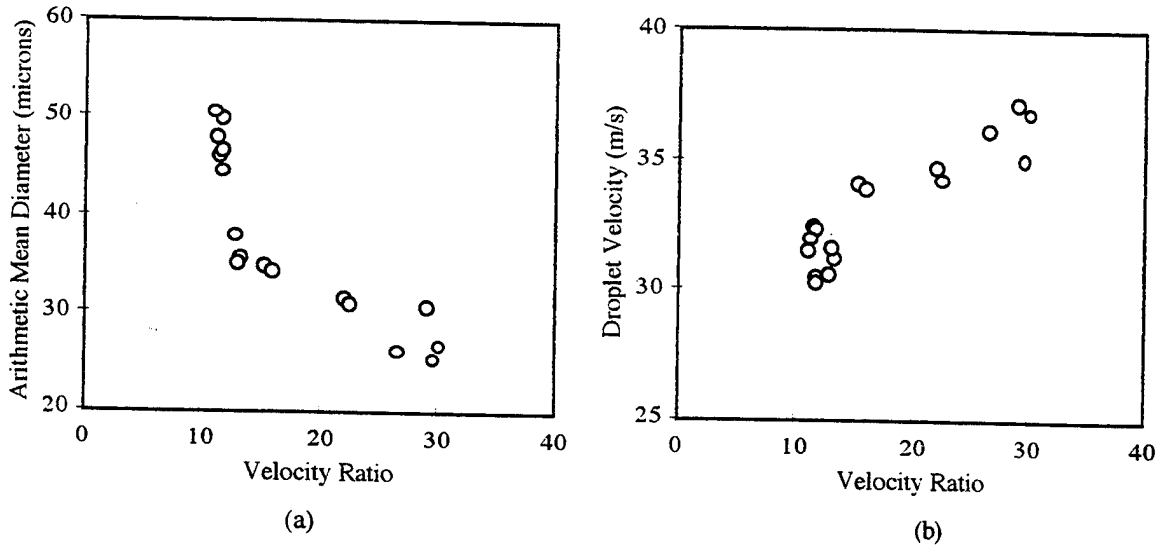

Fig. 4 Effect of gas/liquid velocity ratio on (a) droplet arithmetic mean diameter and (b) droplet axial velocity (chamber pressures from 420 to 500 psia).

Figure 5 shows the arithmetic mean diameter as a function of the chamber pressure with the velocity ratio held between 10.9 and 13.9. For these tests the mixture ratio varied from 3.3 to 4.8. Measurements were taken approximately 12 cm downstream from the injector face and 4 mm off axis. Increasing pressure decreases the arithmetic mean diameter and measurements were still being obtained at 800 psig, 80 psi above the critical pressure of pure oxygen. These constitute the first ever PDPA droplet measurements for LOX above its critical pressure, indicating the existence of drops at least slightly above the critical pressure perhaps due to dissolved water. Future experiments will attempt to operate at increased pressures.

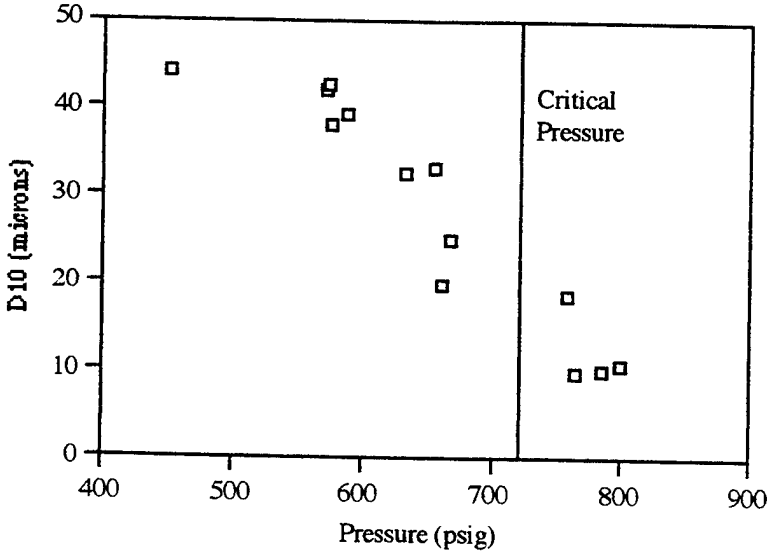

Fig. 5 Arithmetic mean diameter as a function of chamber pressure showing decrease of droplet size with increasing pressure and existence of droplets past the critical pressure of pure oxygen (P_C = 720 psig).

Based on the sensitivity of the arithmetic mean diameter to both velocity ratio and chamber pressure, the arithmetic mean diameter is plotted in Fig. 6(a) as a function of the gas/liquid momentum ratio for the tests plotted in Fig. 4. The momentum ratio used in Fig. 6 is defined as:

$$\frac{\rho_g U_g^2}{\rho_l U_l^2} \tag{1}$$

Fig. 6(a) depicts a good correlation between the measured size data and the momentum ratio as well as a significant rise in arithmetic mean diameter at momentum ratios below approximately 0.5. Fig. 6(b) shows the c* efficiency plotted versus the momentum ratio for the tests performed between 400 and 500 psia. The remaining tests could not be considered due to nozzle erosion. As can be seen in Fig. 6(b), the consequence of a lower momentum ratio is a reduction in the combustion efficiency of the subscale rocket combustion chamber.

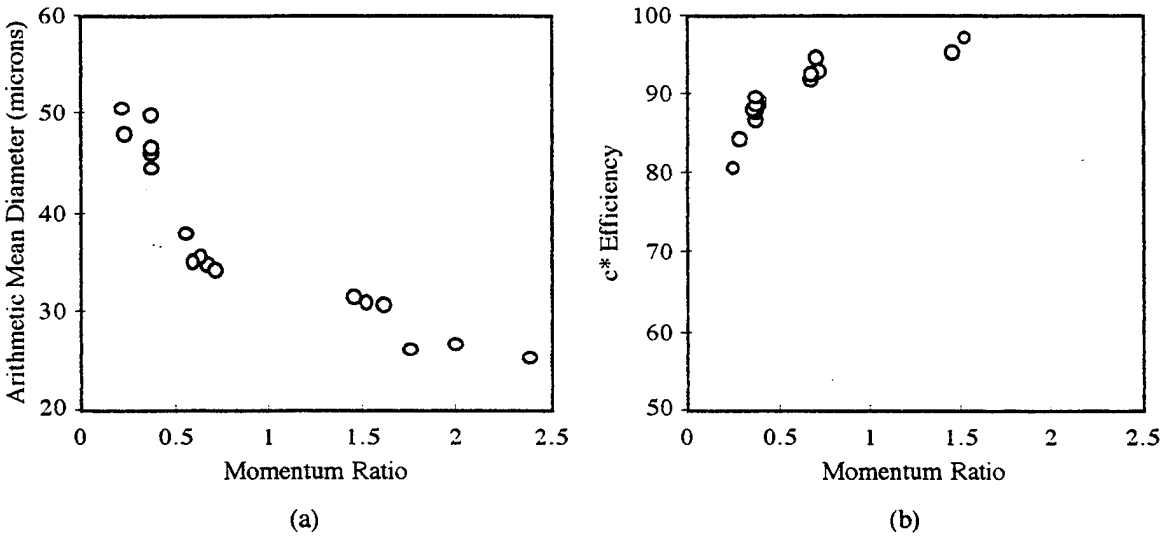

Fig. 6 Examination of gas/liquid momentum ratio on (a) droplet arithmetic mean diameter and (b) c* efficiency (velocity ratios from 11.1 to 30.1).

Radial scans made at several pressures all showed the largest droplets along the axis of the spray with the drop size decreasing as one moved away from the axis. The large droplets along the axis are remnants of the liquid core while moving away from the axis the liquid comes under the shearing effect of the gas resulting in smaller droplets. The droplet velocity was found to increase linearly with radial distance, moving from the slow moving liquid core to the high velocity gas stream.

Analysis. The operation of an experimental subscale liquid propellant rocket chamber where the flow is predominantly one-dimensional offers both experimental and analytical simplifications. By making unsteady pressure and velocity (by means of magnetic velocimetry[1]) measurements at various locations within a modulated motor, one is able to obtain with an appropriate analyses the complex (real and imaginary) components of the liquid propellant evaporation/combustion response as a function of location within the chamber. Such an analysis has been under development over the past year in conjunction with Mohammed Habiballah of ONERA. The governing equations for the two-phase flow are one-dimensional versions of those originally derived by Sutton et al[2], but assuming one droplet size group and neglecting viscosity and diffusion effects. The simultaneous gas and liquid phase equations for mass, momentum, energy and species are solved numerically for small sinusoidal perturbations (acoustics). Both the droplet evaporation and viscous drag are modeled. This analysis will be used for comparison with experimental results to be obtained starting Summer 1996 with a modulated LOX/GH_2 hot-fire combustion chamber.

References

1. Wilson, J. R. and Micci, M. M., "Direct Measurement of High Frequency, Solid Propellant, Pressure-Coupled Admittances," Journal of Propulsion and Power, Vol. 3, No. 4, July-August 1987, pp. 296-302.
2. Sutton, R. D., Hines, W. S. and Combs, L. P., "Development and Application of a Comprehensive Analysis of Liquid-Rocket Combustion", AIAA Journal, Vol. 10, No. 2, Feb. 1972, pp. 194-203.

HIGH PRESSURE COMBUSTION STUDIES UNDER COMBUSTION-DRIVEN OSCILLATORY FLOW CONDITIONS

AFOSR Grant No. F49620-94-1-0235

Principal Investigators: R.J. Santoro and W.E. Anderson

Propulsion Engineering Research Center
and
Department of Mechanical Engineering
The Pennsylvania State University
University Park, PA 16802

SUMMARY/OVERVIEW:

The performance, heat transfer, and combustion stability characteristics exhibited by rocket engine combustors are dictated by the injector design. Studies of impinging jet, swirl coaxial, shear coaxial, and pintle injectors used for liquid-liquid, liquid-gas, and gas-gas propellant injection comprise a comprehensive research effort undertaken at Penn State to develop a detailed understanding of common injector element types through experimentation and analysis. The present research is specifically focused on identifying the physical processes that play a dominant role in combustion instability in liquid-fueled rocket engines. The results of this research will provide understanding of these key processes, a quantitative basis for the development of advanced combustor design analysis models, and design guidelines for impinging jet injectors that promote high combustion efficiency and stable combustion.

TECHNICAL DISCUSSION:

Introduction and Background

Combustion instability is the limiting factor in achieving high combustion efficiency in liquid fuel-based rocket engines. Most liquid fuel-based combustors use impinging jet injectors. Previously, we showed the importance of the atomization process in determining the combustion stability characteristics of rocket engine combustors that use impinging jet injectors. Effects of jet flow condition, orifice diameter, orifice length-to-diameter ratio, impingement angle, pre-impingement length, fabrication procedure, and jet velocity at steady and oscillating, and atmospheric- and high-pressure ambient conditions were investigated and documented [1,2]. A key element of the study was the use of a proven empirical correlation [3,4], used in industry to predict the stability characteristics of injector/combustor configurations, to define the parameters of the experimental study, to aid in the interpretation of the experimental results, and to verify mechanistic models of combustion stability.

From the earlier studies, three important observations related to the basis of the stability correlation were made: (1) as the stability parameter (the ratio of the orifice diameter to the injection velocity, d_o/U_j) is increased, which leads to increased stability margin, the spray drop size distribution becomes more polydisperse; (2) as the stability parameter is increased, the mean drop size is increased; and (3) the frequency with which ligaments are shed off the sheet leading edge has a functional dependence on the stability parameter, d_o/U_j, similar to that of the maximum predicted instability frequency [4]. The earlier results also showed that the process of ligament shedding was synchronized with the arrival of "impact waves" at the leading edge of the sheet. The impact waves are formed near the point of impingement, and have a characteristic length that is linearly dependent on jet diameter, but apparently independent of jet velocity, impingement angle, or ambient pressure. Near inception, the impact waves have a wavelength that is close to the jet diameter. The waves travel downstream at a speed that is near the injection speed of the liquid jet. Their wavelength increases linearly with distance from the impingement point [5]. Periodic atomization occurs when the ligaments disintegrate into drops. It will be shown that the similarity between the ligament shedding frequency and the combustion instability frequency is significant.

Presently under this contract, both analytical and experimental studies are underway to provide a more definitive description of the primary mechanism by which combustion instability limits the ability to achieve high performance liquid fueled rocket engines. The following sections provide a brief description of results in four areas of recent concentration: development of an atomization model for impinging jets; analysis of the cold-flow atomization data using a combustion response model; experimentation with impinging jets to define the process of impact wave formation and ligament production; and initial testing with a windowed instability chamber.

Model of High-Speed, Turbulent Impinging Jet Atomization

An atomization model should be able to account for the evident phenomena present for impinging jet injectors, which are fan formation and the appearance of impact waves; fan fragmentation into ligaments and other large structures; and disintegration of the large structures into small drops which represent the quasi-equilibrated end state of atomization. A three-step model which can predict the drop size distribution and the atomization frequency has been developed [6].

The initial fragmentation process of the fan into ligaments is periodic and the ligament shedding frequency is controlled by the impact waves. The diameter of the ligaments is dependent on the thickness of the fan at breakup, the distance between the impact waves, and the angle away from the plane containing the jet axes. The mean fan thickness at breakup is dependent on the geometry of the impinging jets and the axial distance from the impingement point to the point of incipient fan breakup. The average size of the ligaments, d_{lig}, that are shed off the leading edge of the liquid fan can be determined from the apparent wavelength of the impact waves, λ, and the thickness, h_b, of the sheet at the point where the sheet breaks up, i.e.,

$$d_{lig} = \sqrt{4\lambda h_b / \pi} \tag{1}$$

where, for impinging jets with an impingement angle θ, h_b can be written as

$$h_b = \frac{d_o^2 \sin^3\theta}{4x_b(1-\cos\phi\cos\theta)^2} = \frac{d_o^2}{4x_b} f(\theta) \tag{2}$$

Correlations were developed from cold-flow data [5] to account for the dependence of λ on x_b, and for the dependence of x_b on jet conditions (in terms of the jet Weber number, We_j) and ambient density (in terms of density ratio, s):

$$\frac{\lambda}{d_o} = 0.687 + 0.1019\frac{x_b}{d_o} \tag{3}$$

$$\frac{x_b}{d_o} = 13.56(We_j s^2)^{-0.102} \tag{4}$$

The above equations can be combined to yield an equation for the average diameter of a ligament shed off the liquid fan. At the centerline of the fan, $\phi = 0$, the ligament diameter is:

$$\left.\frac{d_{lig}}{d_o}\right|_{cl} \approx 0.22\sqrt{\frac{f(\theta)}{\pi}\left\{\left(We_j s^2\right)^{0.102} + 2\right\}} \tag{5}$$

The next step in the process is the disintegration of the ligaments into drops. Instead of attempting to develop a physical model of this process, the approach here is to develop a correlation for d_d/d_{lig} that relies on a combination of Eqn (5) and existing correlations for drop size. The drop size correlations are used to calculate the mean drop size that would exist at the conditions that produced the correlation given by Eqn (5). The ligament Weber number based on gas density, $We_{g,lig}$, is used as the correlating parameter. The correlations used to generate the mean drop size are those obtained by Dombrowski and Hooper [7] for the Sauter mean diameter (d_{32}) of a spray formed by impinging water jets at ambient air pressures ranging from 0.01 to 2.2 MPa. The ambient conditions under which the correlation of Eqn (5) was obtained ranged from 0.1 MPa to 1.05 MPa. Calculated values of d_d/d_{lig} are plotted against $We_{g,lig}$ in Fig. 1. The calculated points in Fig. 1 correspond to flow conditions that were used in the generation of Eqn (4). It is seen from Fig. 1 that a good correlation of d_d/d_{lig} vs. $We_{g,lig}$ can be obtained over a range of ambient pressures from 0.1 to 1.05 MPa; this result and the fact that d_d/d_{lig} is dependent on $s^{-0.136}$, which is consistent with other studies of the effect of ambient gas density on drop size, provides confidence in the use of an impact wave-based model of impinging jet atomization.

Combustion Response Analysis

An analysis of the combustion response of a heptane spray to ambient acoustic oscillations was performed to quantitatively evaluate the role of spray condition in the combustion instability mechanism. The response function, R, which is essentially a measure of the amplification of an acoustic wave due to periodic heating, is:

$$R = \frac{\int_0^{t_{drop}} m'p'dt}{\int_0^{t_{drop}} (p')^2 dt} \tag{6}$$

In Eqn (6) t_{drop} is the drop lifetime, m' is the unsteady component of the vaporization rate, and p' is the unsteady component of the ambient pressure. In the present implementation of the combustion response analysis, an open loop response is calculated. Theoretically, a value of R of at least $(\gamma+1)/2\gamma(\sim 0.9)$ is required to drive a longitudinal instability for the case of concentrated combustion at the pressure antinode of a closed chamber, where γ is the specific heat ratio of the gas. A standing pressure wave in a two-dimensional chamber was considered in the analysis, and the maximum amplitude of the pressure oscillation was set at 0.1 times the mean chamber pressure.

The vaporization of heptane drops burning in an oxygen environment at a mean chamber pressure of 1.72 MPa was calculated. Combustion was assumed to occur immediately after vaporization. The initial conditions for

the analysis (drop size distribution, mean drop size, atomization frequency) were obtained from results from previous experiments and the atomization model described above. The results of the analysis indicated that the drop size distribution and the atomization frequency are highly coupled, and together determine the combustion stability characteristics. The drop size distribution essentially determines the spectral range over which pressure oscillations can grow efficiently, whereas periodic atomization causes large variations in the magnitude of the combustion response. It was also confirmed that increased spray polydispersity attenuates the response of combustion to acoustic oscillations. Figure 2 shows the results from parametric studies that indicate that the peak calculated values of R are far above the theoretical limit for driving an instability when the effects of temporally-dependent atomization are included. The effects of periodic atomization on response magnitude were most evident when the atomization frequency was within a factor of ten times the oscillation frequency.

Atomization Mechanism Studies

A more precise knowledge of the impact wave formation process is required to engineer design strategies for high-performing, stable rocket injectors. A new experimental technique has been developed to investigate the process of impact wave formation on sheets formed by impinging jets, and the process through which these waves cause the sheet to break into ligaments. In the experiment, perturbations are imposed on the jets prior to their impingement. The perturbations are generated by piezoelectric drivers located upstream of each nozzle orifice. The frequency and amplitude of the perturbations imposed on the jets can be controlled by the signal input to the piezoelectric drivers. Both sinuous (anti-symmetric) and dilatational (symmetric) disturbances on the sheet can be generated by adjusting the phase angle between the signal to the individual drivers. Both linear and nonlinear instabilities can be generated by adjusting the signal amplitude.

Figure 3 shows the periodic breakup of the sheet formed by impinging jets with imposed perturbations. It is seen that a coherent breakup process can be realized by introducing perturbations on the jets prior to impingement. In this case, symmetric disturbances are generated by running the drivers in phase with each other. Future experiments will focus on providing a comprehensive map of the behavior of the sheet, including the most amplified modes and the stability limits. This knowledge of how the sheet responds to input disturbances at the impingement point can lead to upstream control strategies that will result in the optimal combination of performance and stability.

Windowed Instability Chamber Tests

The primary focus of ongoing research is on the measurement of impinging jet injector spray combustion phenomena at representative rocket engine combustor conditions and under simulated combustion instability conditions. Initial tests with a windowed instability chamber (WIC) have commenced. The variable-length rectangular combustor, with a cross section 0.23 m wide and 0.10 m deep, is comprised of the study element (the impinging jets), a device for generating pressure oscillations in the chamber, a variable exhaust nozzle, and an injector faceplate that incorporates a diffusion flame burner to provide hot gas that surrounds the spray field of the study element. The combustor design allows for substitution of different types of injector elements. Complete optical access to the combustion zone is allowed by quartz windows. Figure 4 is a plot of flow parameters measured during one of the initial tests. Figure 5 shows the WIC installment and a close-up view of ethanol spray combustion through an oval window. The next test series will focus on the acquisition of drop size data at three different stability conditions - stable, marginal, and unstable - as predicted by the empirical stability correlation. Work is also underway to develop a control element with which to modulate combustion and simulate transverse modes of combustion instability.

---

[1] Ryan, H.M., Anderson, W.E., Pal, S., and Santoro, R.J., "Atomization Characteristics of Impinging Liquid Jets," *Journal of Propulsion and Power*, 1995, Vol. 11, No.1, pp. 135-145.
[2] Anderson, W.E., Ryan, H.M., and Santoro, R.J., "Impinging Jet Injector Atomization," Chapter 7 in *Liquid Rocket Combustion Instability*, AIAA Progress in Astronautics and Aeronautics, 1995.
[3] Anderson, W.E., Ryan, H.M., and Santoro, R.J., "Combustion Instability of Importance to Liquid Bi-Propellant Engines," 28th JANNAF Combustion Subcommittee Meeting, San Antonio, TX, Oct. 28 - Nov. 1, 1991.
[4] Anderson, W.E., Ryan, H.M., Santoro, R.J., and Hewitt, R.A., "Combustion Instability Mechanisms in Liquid Rocket Engines Using Impinging Jet Injectors," AIAA Paper No. 95-2357, 31st AIAA/ASME/SAE/ASEE Joint Propulsion Conference and Exhibit, San Diego, CA, July 10-12, 1995.
[5] Anderson, W.E., Berthoumieu, P., Huang, C., Lecourt, R., Yatsuyanagi, N., and Zhu, N., "Atomization of Impinging Liquid Jets," Chapter 3 in Proceedings of the Second International Symposium on Liquid Rocket Propulsion, ONERA-Chatillon, FRANCE, June 19-21, 1995.
[6] Anderson, W.E., Ryan, H.M., and Santoro, R.J., "A Model for Impinging Jet Atomization," 32nd JANNAF Combustion Subcommittee Meeting, Propulsion Engineering Research Center Seventh Annual Symposium, October 23-27, 1995, Marshall Space Flight Center, AL.
[7] Dombrowski, N., and Hooper, P.C., "The Performance Characteristics of an Impinging Jet Atomizer in Atmospheres of High Ambient Density," *Fuel*, 1962, pp. 323-334.

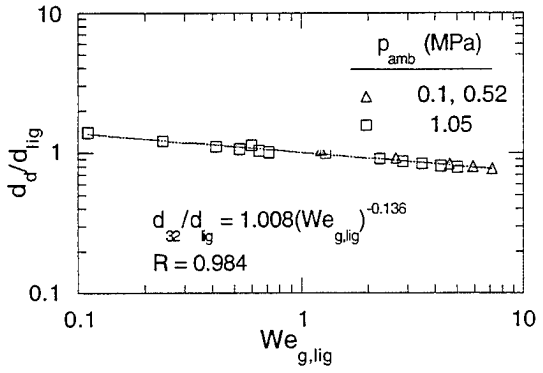

Fig. 1. Correlation of non-dimensional drop size, d_d/d_{lig} with Weber number based on ligament diameter and gas properties, $We_{g,lig}$.

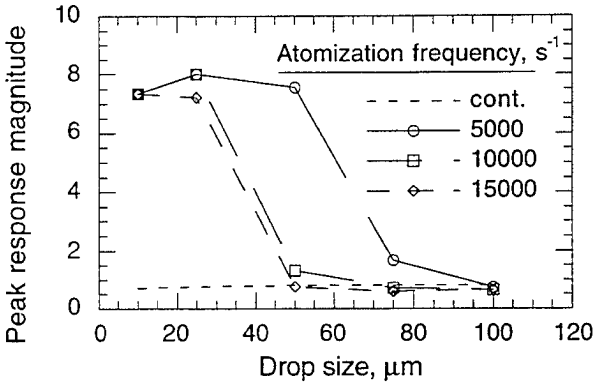

Fig. 2. Combustion response magnitude of heptane drops to ambient acoustic oscillations. Destabilizing effects of periodic atomization are shown.

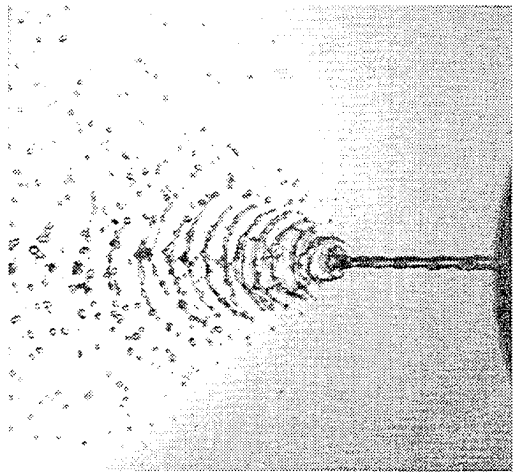

Fig. 3. Sheet formed by two impinging jets. Coherent periodic structures are created by imposing $2500s^{-1}$ disturbances on the jets prior to impingement.

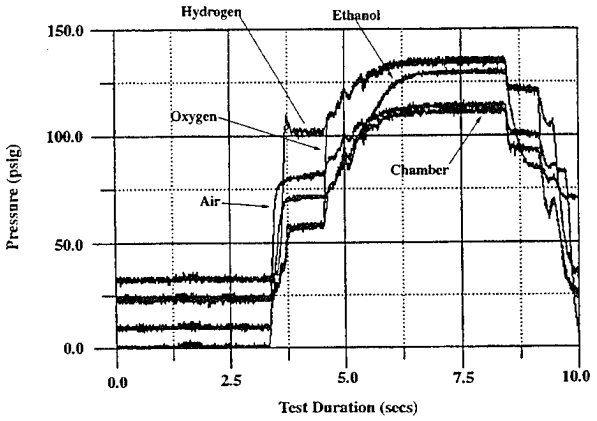

Fig. 4. Traces of chamber pressure and propellant injection pressures. Ignition of air/hydrogen occurs at 3.25s. Ethanol ignition occurs at 4.25s.

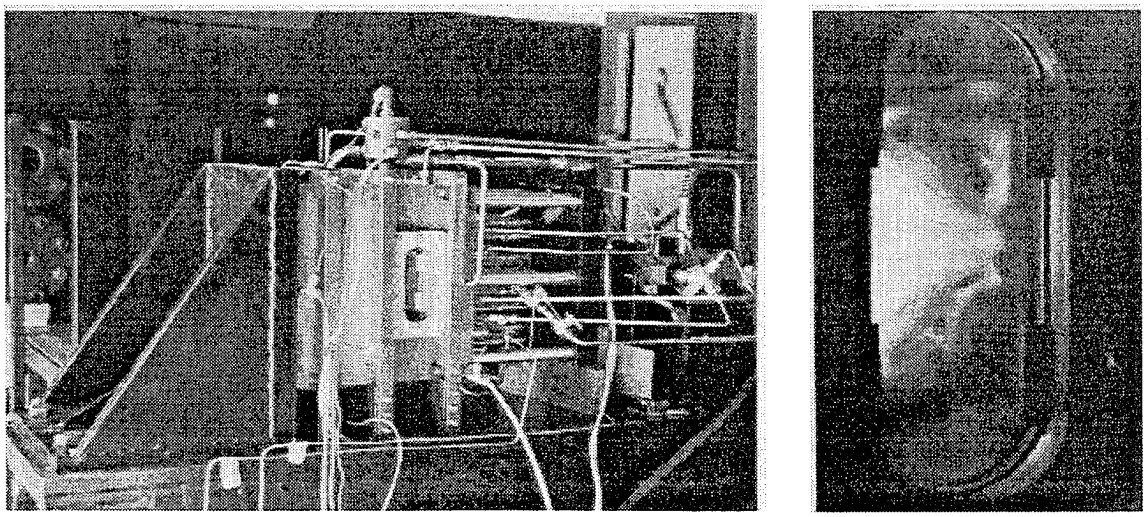

Fig. 5. Setup of chamber at the Cryogenic Combustion Laboratory with a close-up view of the combusting ethanol spray. Impinging jets are used to produce the spray. Chamber interior dimensions are 0.23m (width), 0.22m (axial length) and 0.10m (depth).

DROPLET COLLISION IN LIQUID PROPELLANT COMBUSTION

(AFOSR GRANT No. F49620-95-1-0377)

Principal Investigator: Chung K. Law

Princeton University
Princeton, NJ 08544

SUMMARY/OVERVIEW

Droplet collision is of relevance to spray combustion, intimately influencing the spray characteristics in the dense spray region. The present study aims to gain fundamental understanding on the mechanisms governing the observed phenomena of permanent coalescence, bouncing, and separation upon collision. Specific issues of interest include the extent of droplet deformation, the dynamics of inter-droplet flow, the relative importance of the gas resistance force as compared to the collisional inertia, and the relevant rheological properties of the gases and liquids. A computational code has been developed and additional experiments performed to gain fundamental understanding on the dynamics of the inter-droplet flow and evolution of the droplet contour during the collision and bouncing event.

TECHNICAL DISCUSSIONS

Our previous experimental results indicated that the collisional dynamics of droplets is mechanistically similar for different liquids when the influence of the environment gas properties are taken into account. Specifically, there are generally five collision outcome regimes, representing (I) coalescence with small droplet deformation, (II) bouncing, (III) coalescence with large droplet deformation, (IV) separation after near head-on coalescence, and (V) separation after off-center coalescence, as shown in Figure 1. Here We and B are the collision Weber number and nondimensional impact parameter. Regimes I to IV occur for near head-on collisions with increasing We, while Regime V is characteristic of large values of We and B. The crucial factors responsible for the transitions between Regimes (I), (II) and (III) and the appearance of Regime (II) are the properties of the liquid and the gas. As the droplets collide, they become deformed due to the pressure buildup in the gas film between them. This deformation absorbs the kinetic energy of collision, therefore reduces the ability for inter-droplet gas film to be squeezed out in order to effect coalescence. For the liquid with low surface tension or gas with high density and viscosity, the significant loss of droplet kinetic energy and high pressure buildup inside the gap can prevent contact of the droplet surfaces and result in bouncing. Conversely, high liquid surface tension or low gas density and viscosity can enhance coalescence and decrease the domain of Regime (II).

In the present study we use a recently developed numerical method of "front tracking" to study the droplet head-on bouncing collision. We were able to accurately simulate the detailed droplet bouncing collision process. The evolution of the gas gap configuration was evaluated, and it was found that the minimum gap size is the controlling factor for the transition between bouncing and coalescence outcomes. Finally the droplet collision time was shown to be related to the droplet oscillation time.

When the droplets approach each other and gas is being squeezed out from the gap between the droplet surfaces, relatively high pressure is built up there, causing flattening of the droplets and conversion of the droplet kinetic energy into surface tension energy. The kinetic energy is also partly dissipated through the internal motion within the droplet and gas flow. Figure 2(a) shows the half inter-droplet gap shape during water droplet collision in 14.6 atmosphere argon with Weber number 2.25 at different time t until the droplet reaches the maximum surface deformation, here t is the time normalized by the droplet oscillation period based on inviscid and small amplitude considerations. We plot the half gap width h, where h represents the droplet interface position. Note that as the two droplet surfaces approach each other, high pressure is built up in the direction

of the lines of centers, causing indentations on the surfaces of the droplets in this region. It is seen that at t=0.20, the center region is slightly dented toward the liquid phase, and the minimum clearance takes the form of a ring at the edge of the flattened droplet surface. As the droplets surface approaches the maximum deformation, the indentation in the center increases, while the minimum clearance ring expands with increasing flattening of the droplet surface. After the droplets reach their maximum deformation at t=0.63, most of the initial droplet kinetic energy is transformed into surface tension energy. At this stage, the droplets start to contract because of the surface tension force, while the high gas pressure inside the gap pushes the droplets away. This is clearly shown in Figure 2(b), which shows the gap evolution at $t \geq 0.63$ after the maximum deformation is reached. As the droplets bounce away, the size of the minimum clearance ring gradually decreases and the gap thickness increases.

One interesting phenomena observed from the gap evolution is the droplet surface deformation in the center region during collision. It is seen that the center indentation develops gradually until t=0.63. As the droplets bounce away, the indentation remains until the very end as shown in Figure 2(b). However, at t=1.30, the high pressure within the liquid causes the indented surface to rapidly buckle outward. This causes the minimum clearance position to switch from the ring to the center, and the minimum gap size temporary decreases and then increases again at times t=1.30, 1.31 and 1.32.

The characteristics of gap evolution for water droplet collision discussed above are also observed for other liquids. Figure 3 plots the center clearance h(0) and minimum gap clearance h_m as function of time t for water and tetradecane droplet collision in 14.6 atmosphere argon and nitrogen with Weber numbers 2.25 and 7.42 respectively. It shows that $h(0)>h_m$ during most of the collision time as the minimum clearance ring stays away from the center. At the final collision stage, the center indentation buckles out and the minimum gap recovers its position to the center, implying that h_m equals to h(0).

The study of the gas gap evolution brings a critical question about what mechanism controls the collision outcome of coalescence and bouncing. It is the gas pressure buildup which retards the droplet inter-surface movement and pushes the droplet away in the bouncing collision. Coalescence occurs when the gap size reaches the molecular interaction range, while bouncing occurs when the minimum gap is still larger than the molecular interaction range. Recognizing that as the droplet kinetic energy increases, the collision outcome changes from coalescence to bouncing, and then back to coalescence again, we would like to check the variation of the gap size as the droplet kinetic energy changes. Figure 4 plots the minimum gap size during the whole collision process, say $h_{m,m}$, as a function of Weber number for heptane, decane, and dodecane in 14.6 atmosphere argon. It is seen that $h_{m,m}$ initially increases but then decreases as We increases. In other words, with small relative velocity the droplets can approach toward each other and coalesce readily, since the gas pressure buildup between the droplet surfaces is small. This is verified by the small deformation in regime I. As the droplet kinetic energy increases, the gas pressure built up inside the gap also increases which results in the large flattening of the surface and high gas resistance. The droplets can only approach each other until a minimum interface distance which is larger than the molecular force range and then bounce away (regime II). With further increase of the kinetic energy, the droplets can overcome the gas forces and the minimum gap size is in the range of molecular force, and results in coalescence again (regime III). Therefore we conclude that it is the non-monotonic variation of the minimum gap width that causes the non-monotonic transition between the collision outcomes of coalescence and bouncing.

One intriguing observation in the present investigation is that the droplet collision time, represented as τ, is close to the droplet oscillation time. Figure 5 shows the experimental and the numerical prediction of τ for water droplets in 14.6 atmosphere argon. It is seen that the numerical predications agree well with the experimental results. Because of viscous dissipation and large deformation, τ is larger than unity in the measured We range and decreases as We increases. During the droplet bouncing collision, the droplet surface movement is similar to that of oscillation, therefore the droplet collision time is mainly controlled by the oscillation time.

MAJOR PUBLICATIONS

[1] "Regimes of coalescence and separation in droplet collision," by J. Qian and C. K. Law, J. Fluid Mech. under revision (1996).
[2] "Bouncing and deformation in droplet collision," by J. Qian, G. Tryggvason and C. K. Law, submitted (1996).

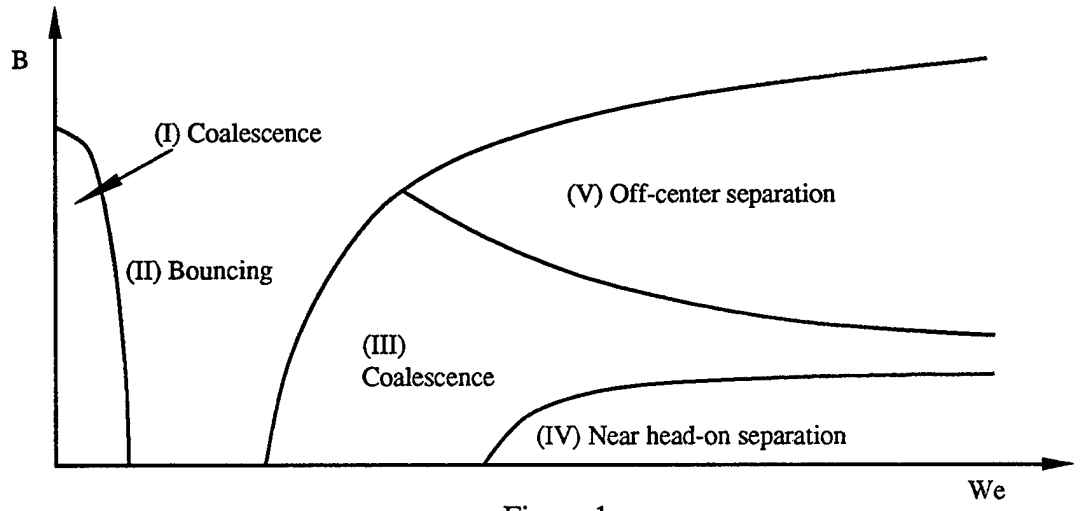

Figure 1

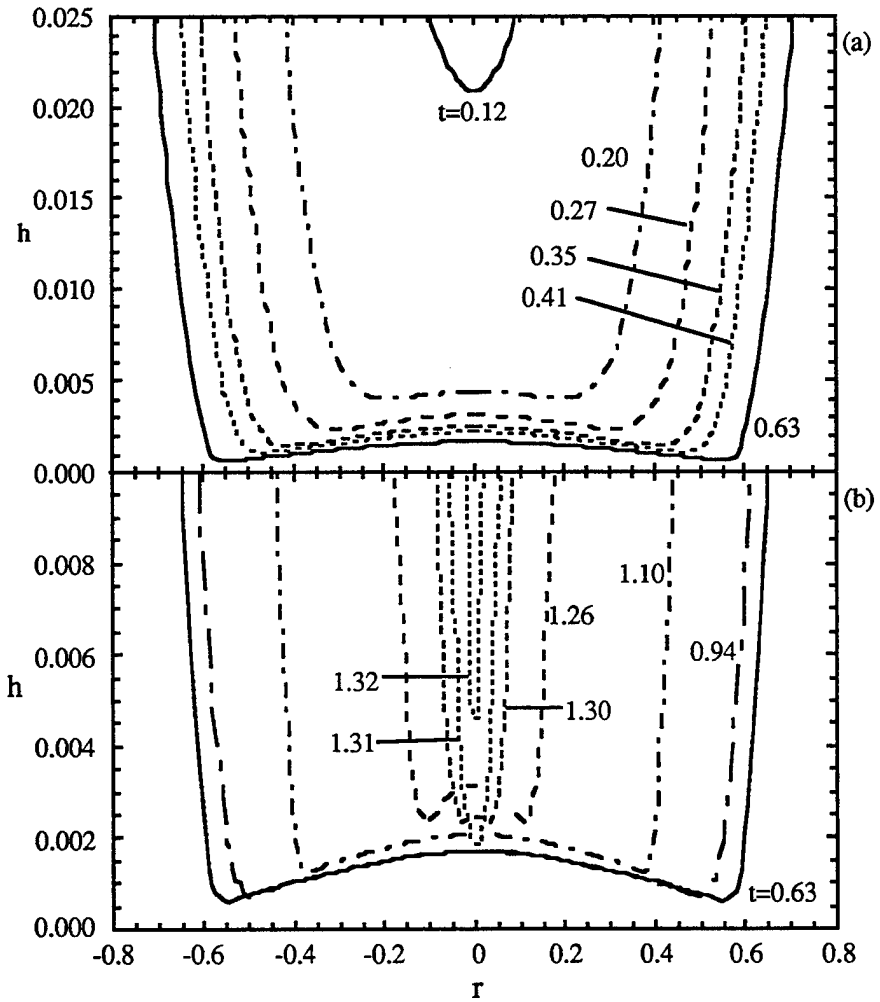

Figure 2

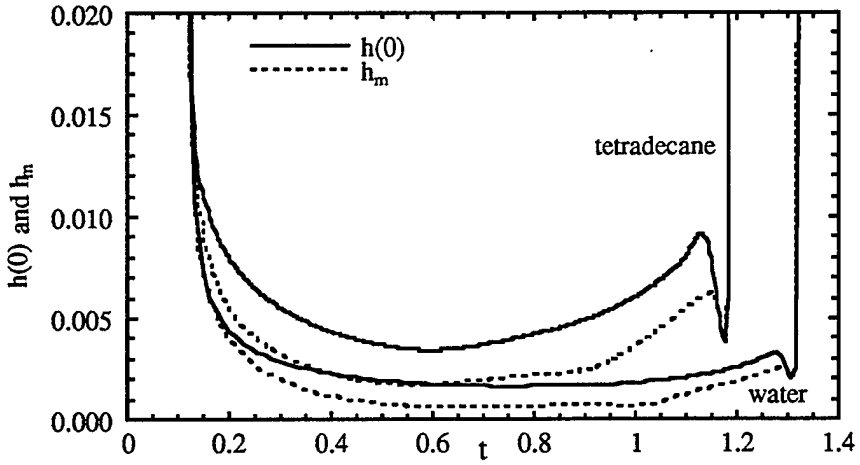

Figure 3

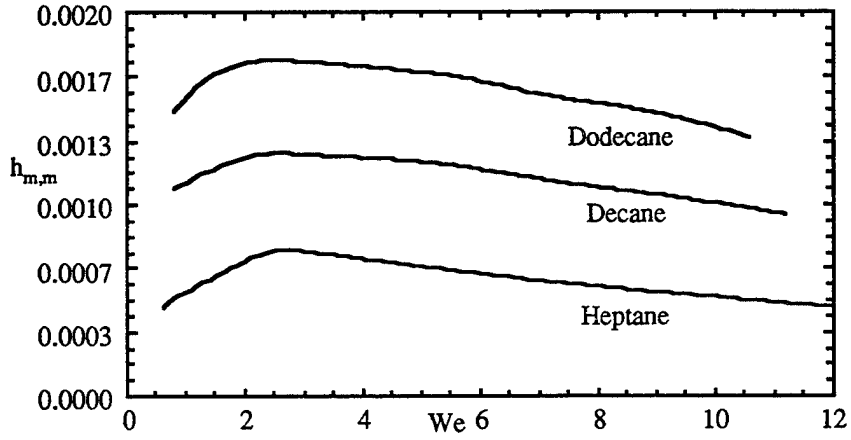

Figure 4

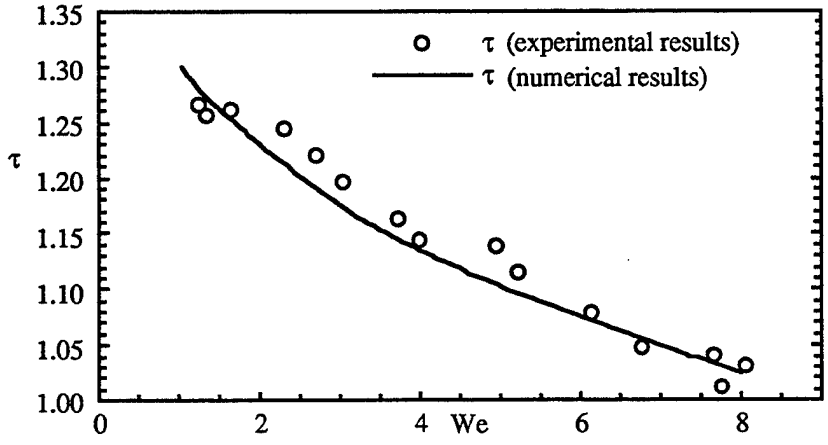

Figure 5

Combustion and Plumes

(AFOSR Grant Contract No. 2308 M1)

Principle Investigators: D. P. Weaver, D. H. Campbell, I. J. Wysong, G. L. Vaghjiani, A. Alfano, D. Wadsworth, and A. Ketsdever

Phillips Laboratory, OLAC PL/RKFA
Rocket Propulsion Directorate
10 Saturn Blvd.
Edwards AFB, Ca. 93524-7660

SUMMARY/OVERVIEW:

In this program, research is performed in the areas of rocket exhaust plume physics and rocket propellant combustion. Experimental measurements, theoretical modeling, and computational investigations are all performed. Laser diagnostic techniques are used in both plume and combustion areas to map basic properties, such as temperature and density, of gases in various combusting and non-combusting environments. Chemical kinetic measurements are also carried out to determine the specific reaction pathways and kinetic rates for specific reactions of interest. Results of these investigations are used to help in the design of future rocket propellants and to further our understanding of the chemical and collisional processes in rocket exhaust plumes that give rise to emissions in the infrared, visible and ultraviolet spectral regions so that better predictions of these emissions can be used in designing ballistic missile detector systems. Typical results obtained in several of the research areas are detailed below.

TECHNICAL DISCUSSION:

An investigation of the relationship between strained ring hydrocarbon molecular structure and decomposition mechanism is underway, and is partially directed toward controlling the sooting tendency of quadricyclane in combustion applications. The initial step of the quadricyclane pyrolysis mechanism yields norbornadiene. Norbornadiene then produces a mixture of acetylene, cyclopentadiene, toluene, and cycloheptatriene. A detailed sooting study on quadricyclane is not available but some generalities from the extensive research on soot should apply to this pyrolysis mechanism: a) acetylene has been shown to be important in sustaining soot growth after the precursor molecules (polynuclear aromatic hydrocarbons, PAH) are depleted in premixed flames; b) two free radical mechanisms also explain the role of acetylene in PAH growth; and c) aromatics and dienes show an increased propensity toward sooting when compared to aliphatics. Our approach is to suppress the norbornadiene reactions which directly produce acetylene, cyclopentadiene, and toluene by providing

detailed gas phase pyrolysis/combustion mechanisms and the associated kinetics for selected substituted and heterosubstituted quadricyclanes. The selection is based upon the expectation of a quadricyclane pyrolysis mechanism which either a) has a dominant single reaction channel for the substituted norbornadiene following the initial quadricyclane to norbornadiene isomerization or b) leads directly to cycloheptatrienes , their heterosubstituted analogs or rearrangement products without the intermediate formation of a norbornadiene. Substituted quadricyclanes which exhibit these mechanistic patterns should be less likely to form soot than unsubstituted quadricyclane.

Published synthetic routes to 3-oxaquadricyclane were evaluated during the year and the 3 step procedure shown below was attempted. Typical yields for step 1 have been in excess of 94%. Currently 11 grams of the Diels-Alder adduct I are on hand. The sodium amalgam (Na/Hg) for step 2 is not commecially available and its preparation and use have also been perfected. Step 2 has been carried out and scale-up is in progress. A photochemical reactor needed to convert the oxanorbornadiene (II) to 3-oxaquadricyclane (III) in step 3 has also been assembled.

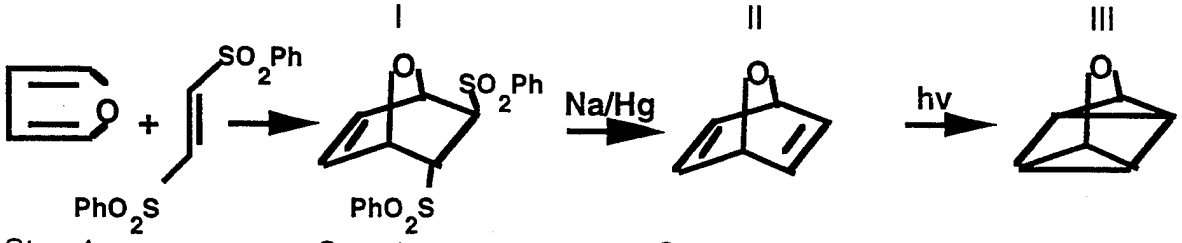

A flow reactor with diagnostics to verify the expected pyrolysis mechanism in Eq. 2 and to establish the reaction kinetics has also been prepared.

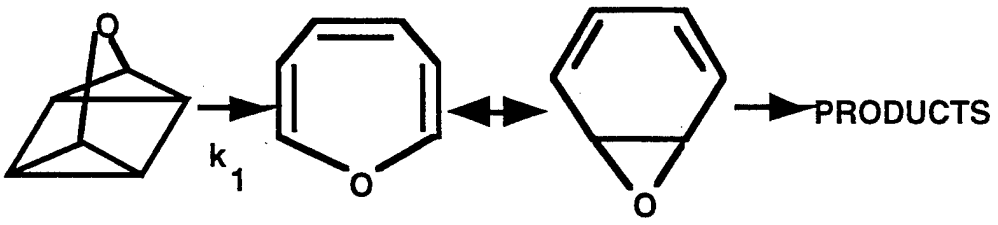

IV Eq. 2

Preliminary estimates for k_1 based upon substituted 3-oxaquadricyclanes suggest conversion to the oxepin (IV) in < 10 us at 700 C. A pump-probe scheme to generate the transient oxepin intermediate via sensitized pulsed ir laser pyrolysis and to optically follow its growth and disappearance is under construction. The uv absorbing oxepin intermediate will be followed by a 10 MHz train of 200 ps pulses at 335 nm which is produced by a fast pulsed, frequency doubled laser diode. Few spectroscopic reports have appeared which utilize laser diodes in a time-resolved mode.

During the current year, validation of the pump-probe diode laser system and scale-up of the 3-oxaquadricyclane synthesis is being completed. The low temperature pyrolysis kinetics of 3-oxaquadricyclane is also being measured. These tasks will serve as the basis for establishing the operational limits of the pulsed laser diode absorption instrument on an actual combustion intermediate (oxepin): stability, dynamic range, reliability/convenience of operation, and potential for system encapsulation/miniaturization/simplification.

Significant progress was made during the year in development of our 3-D direct simulation Monte Carlo capability. Results illustrating this progress from our application of the DSMC technique to the AF/BMDO Skipper satellite program and the first time simulation of a 3D realistic plasma reactor including ions, neutrals, and static fields performed jointly with Intel Corporation will be presented.

The direct simulation Monte Carlo (DSMC) computational technique is the preferred method of flowfield prediction for high altitude rocket exhaust plumes. A series of computations are being conducted using the DSMC technique to evaluate this technique's ability to predict accurate flowfield parameters, internal energy state populations, and chemical species reaction processes. Typical of our results this year are simulations of the potential contamination flowfield surrounding the BMDO Skipper satellite. Shortly before launch of this satellite, concerns developed as to the impact of such contamination on sensitive UV optial sensors arising from outgassing of adhesives used to attach solar panels to the satellite. Results simulating the expanding contaminate flowfield helped mission planners asses the potential impact on the optical sensor surfaces. Additionally, simulations of several plasma etch reactor flowfields using the DSMC technique were performed for both industry and government reactors. Typical early results are shown in figure 1 below showing a comercial etch reactor flow of SIO_4.

Number Density of SiH_4

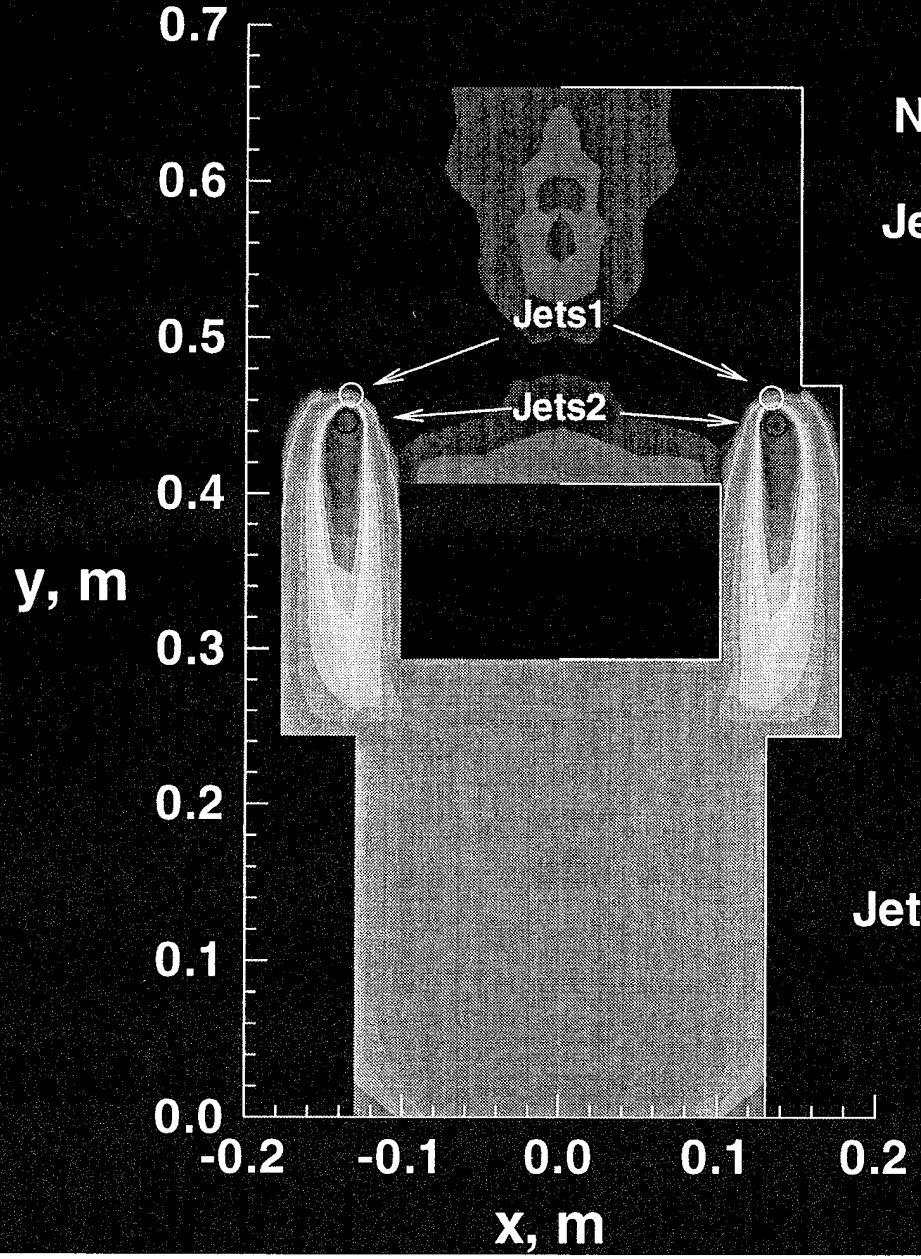

No. of Particles From Jets

Jet2 (SiH_4) = 50.0 E21/s

Jet2 Velocity = 300 m/s

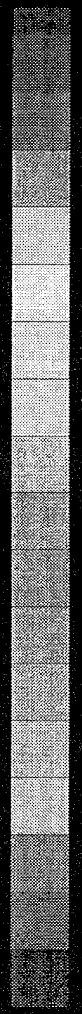

n/ m^3

2.0E22
1.0E22
9.0E21
8.0E21
7.0E21
6.0E21
5.0E21
4.0E21
3.0E21
2.0E21
1.0E21
9.0E20
8.0E20
7.0E20
6.0E20
4.0E20
3.0E20
2.0E20
1.0E20

DEVELOPMENT OF A COLLISIONAL RADIATIVE EMISSION MODEL FOR STRONGLY NON-EQUILIBRIUM FLOWS

AFOSR Grant Contract No.

Principal Investigator:

Deborah A. Levin

Institute for Defense Analyses
Science and Technology Division
Alexandria VA, 22311-1772

SUMMARY/OVERVIEW:

This aim of this research is to characterize the passive and active signatures of high-altitude hypersonic vehicles for space-based surveillance. These signatures consist of emissions from molecules created in the diffuse body shock, plume shock, and outgassing of space materials. A collisional radiative emission model for strongly non-equilibrium flows is under development. The Direct Simulation Monte Carlo (DSMC) formalism is being modified to include state-specific, electronically excited species reactions. As part of this task vibrational and rotational-level state specific collisional cross sections for the DSMC modeling are being provided.

TECHNICAL DISCUSSION:

An important aspect of the Signature Control Initiative is the radiation modeling of the hypersonic shock structure at sufficiently high altitudes such that thermo-chemical non-equilibrium conditions exist. The important contributions to the signature include the hardbody-plume shock, outgassing, and persistence phenomena. The operational, detection requirements are multi-spectral and cover the ultraviolet (UV) through the long wave IR (LWIR). From the phenomenology point of view, the selection of the UV has the benefit of providing the most information about specific mechanisms.

An extensive program has been funded under the Strategic Defense Initiative Organization (now the Ballistic Missile Defense Organization, BMDO) to study the phenomenology of high-altitude ultraviolet signatures. Some fairly expensive space programs have been funded, but do not provide the necessary diagnostics and measurements to model UV radiation from first principals. The most successful, however, of these programs has been the Bow Shock UltraViolet Flight experiments[1,2,3] funded by the Innovative Science and Technology Office of BMDO. These relatively

simple and inexpensive sounding rocket flights provide the only in-situ, flight measurements of the important components of the hypersonic shocklayer structure. The research community received a number of surprises from the ultraviolet spectra and radiometric measurements of NO, OH, CO, and O made during these flights. Perhaps the key one being that the pre-flight *predicted* NO (γ,β) band radiance was about five orders of magnitude lower than observed.[4,5] This surprise initiated a large amount of research to correct the discrepancy. An overwhelming simplification of the results of that research is that the contribution and interpretation of multiple shocklayer temperatures is now better understood. In addition, the development and use of an overlay approach[6] has enabled the use of different vibrational-dissociative coupling models[7] and evaluation of the importance of different excitation mechanisms.

Nevertheless, a complete understanding of the mechanisms that populate excited electronic states through neutral and electron collisions remains elusive. State-specific mechanisms and rates are highly uncertain. The modeling of vibrational-energy coupling and quenching processes in conjunction with the fluid flow modeling has not been applied to non-continuum approaches. These gaps in our research base preclude a predictive spectral radiance capability for altitudes above 70 km. Depending on the speed and shape of the vehicle, the gap between models and data grows as effects due to surface materials, distinct excited state temperatures, and photon scattering processes become important.

The goal of this research is to develope an approach to address the non-equilibrium radiation modeling deficiencies. It is based on a joint effort between the Direct Simulation Monte Carlo (DSMC) hypersonic flow modeling technique of Prof. Iain Boyd[8] and the non-equilibrium ultraviolet radiation modeling work of myself.[9] The present treatment is reviewed and the key elements of an improved radiation model are explained below.

The radiation model that has been developed is based on the work of Park[10] and later extensions.[11] The original model of Park was developed for fluid flow conditions much closer to thermochemical non-equilibrium, as is experienced in aero-braking applications. The radiation calculation proceeds with the calculation of the distribution of atomic or molecular states for the radiating species of interest, followed by the computation of the spectral radiance and absorption. The tangent slab approximation is used to compute the optically thin and thick radiance along a chosen line-of-sight. The present systems include NO, N_2, N_2^+, CN, CO, C_2, OH, N, and O. The radiation and flow calculations

are uncoupled. Moreover, the influence of the radiation field on the excited state populations is ignored.

The excited state processes included in the original model were those primarily due to electron impact excitation. The degree of ionization, however, for non-aero-braking applications, such as those discussed here, is much lower. Hence neutral collisional excitation has been incorporated in the modeling in a sufficiently general fashion to include both neutral and electron excitation processes. These processes may be summarized as follows,

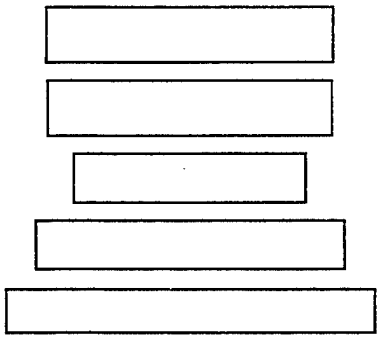

(1a)

(1b)

(1c)

(1d)

(1e)

The processes represent neutral collisional (species M) excitation from electronic level i to j, electron collisional excitation, spontaneous emission, electron-collisional ionization, and neutral collisional dissociation, respectively. Equations 1 (a) - (e) can be further generalized so that N_i represents a specific *vibronic* state of a molecular system, such as OH.[6] With the assumption of detailed balancing and steady state[9] the master set of equations can be cast in the following matrix form,

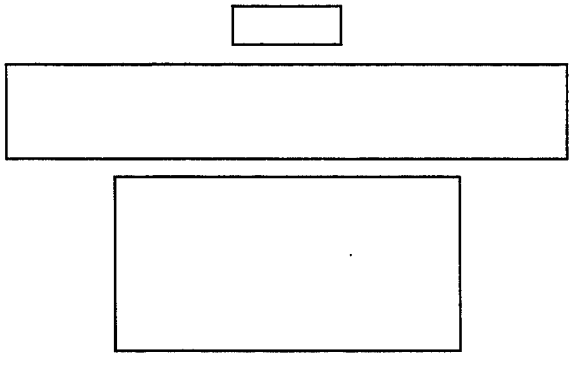

(2a)

(2b)

(2c)

where

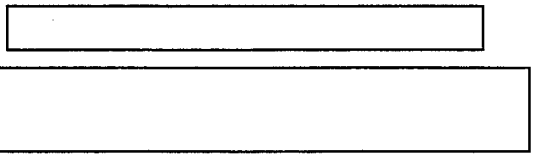

(2d)

(2e)

The subscript E denotes the equilibrium concentration, the square brackets denotes concentration, T_v is the vibrational temperature, T is the heavy particle translational temperature, and m is the number of states. Depending on the radiative lifetime of the state and the number density, the steady state assumption is valid up to fairly high altitudes in many, but not all, cases.[9]

Additional key assumptions exists in the use of Eqs. (2a - e) to solve for the excited state distributions. Foremost, it is assumed that the vibrational, rotational, and translational temperatures of the molecular ground and excited electronic states are identical. Secondly, it is also assumed these temperatures are the same as that of the majority, or bulk, constituents in the flow, e.g., N_2. Comparisons of recent modeling calculations of OH(X $\rightarrow$ A) with in-flight spectra at 110 km have shown that this assumption is invalid.[6] The vibrational temperature was found to be 7,000 K; yet, the bulk vibrational temperature is only 2,000 K. Clearly the continuum-based notion of temperature is unsatisfactory. The correction of this deficiency requires a particle-based formalism.

In collaboration with Prof. Boyd, Cornell University, the specific post-collisional distribution of the translational, rotational, and vibrational energies for the electronically excited state will be obtained with DSMC. The OH data will be used as a calibration of this proposed method, which would be sufficiently general to apply to other molecular systems of interest. The multi-temperature distribution of the OH(A) states will be used in the generalized OH spectroscopic model of Levin and Laux[12] to compute high-wavelength-resolution spectra. This model has been validated with high-resolution ground based spectra and for space-rarefied conditions.

Collisional cross sections will be obtained from the existing literature and from research funded in the Chemical Mechanisms and Chemistry/Flow Field Coupling portions of this initiative. It is also anticipated that we will perform our own trajectory calculations[13] to match the pre-collisional flow energy conditions. Relevant semi-empirical potential energy surfaces for water dissociation may be provided by researchers at Philips Laboratory, Edwards, Air Force Base, Mr. David Weaver, point of contact.

The development of a DSMC radiation model will address a second important deficiency mentioned earlier. For optically thick media the magnitude of the radiation field effects the excited state populations. This is especially evident in the resonance atomic-line transitions, but is observed in other optical transitions as well. Under such conditions the form of Eqs. (2d and e) is modified such that the Einstein A coefficients are multiplied by a factor proportional to the intensity of the radiation field.

[1] P. W. Erdman, E. C. Zipf, P. Espy, C. Howlett, D. A. Levin, R. Loda, R. J. Collins, and G. V. Candler, "Flight Measurements of Low Velocity Bow Shock Ultraviolet Radiation," *Journal of Thermophysics and Heat Transfer*, **7**, 37 (1993).

[2] P. W. Erdman, E. C. Zipf, P. Espy, C. Howlett, C. T. Christou, D. A. Levin, , R. J. Collins, and G. V. Candler, "In-situ Measurements of UV Plume Radiation from the Bow Shock Ultraviolet 2 Rocket Flight," *Journal of Thermophysics and Heat Transfer*, **7**, 704 (1993).

[3] P. W. Erdman, E. C. Zipf, P. Espy, C. Howlett, D. Levin, R. Collins, and G. Candler, "Measurements of Ultraviolet Radiation from a 5 km/sec Bow Shock," *Journal of Thermophysics and Heat Transfer,* **8**, 441 (1994).

[4] D. A. Levin, G. V. Candler, R. J. Collins, P. W. Erdman, E. Zipf, P. Espy, and C. Howlett, "Comparison of Theory with Experiment for the Bow Shock Ultraviolet Rocket Flight," *Journal of Thermophysics and Heat Transfer*, **7**, 30 (1993).

[5] D. Levin, G. Candler, R. Collins, P. Erdman, E. Zipf, and C. Howlett, "Examination of Theory for the Bow Shock Ultraviolet Rocket Experiments - I," *Journal of Thermophysics and Heat Transfer,* **8**, 447 (1994).

[6] D. Levin, R. Collins, G. Candler, and P. Erdman, "Examination of OH Ultraviolet Radiation from Shock-Heated Air," *AIAA Paper No. 95-0708*, January 1995, presented at the 33rd Aerospace Sciences Meeting.

[7] I. Boyd, G. Candler, and D. Levin, "Dissociation Modeling in Low Density Hypersonic Flows of Air," accepted for publication in *Physics of Fluids.*

[8] Haas, B. L. and Boyd, I. D., "Models for Direct Monte Carlo Simulation of Coupled Vibration-Dissociation," *Physics of Fluids A,* Vol. 5, 1993, pp. 478-489.

[9] D. Levin, M. Braunstein, G. Candler, R. Collins, and G. Smith, "Examination of Theory for Bow Shock Ultraviolet Rocket Experiments - II," *Journal of Thermophysics and Heat Transfer,* **8**, 453 (1994).

[10] Park, C., "Calculation of Nonequilibrium Radiation in the Flight Regimes of Aero-Assisted Orbital Transfer Vehicles," *Thermal Design of Aero-Assisted Orbital Transfer Vehicles*, Ed. H. F. Nelson, Progress in Astronautics and Aeronautics, **96**, 1985.

[11] Moreau, S., Laux, C., Chapman, D., and MacCormack R., "A more accurate Nonequilibrium Air Radiation Code: NEQAIR Second Generation," *AIAA Paper No. 92-2968*, July, 1992.

[12] Levin, D. A., Laux, C., O, and Kruger, C. H., "A general model for the spectral calculation of OH radiation in the ultraviolet," *AIAA Paper No. 95-1990*, 26th AIAA Plasmadynamics and Lasers Conference, San Diego, June 19-22, 1995.

[13] Hase, W. L., QCPE 3 (1983), 453.

ENERGY TRANSFER PROCESSES IN THE PRODUCTION OF EXCITED STATES IN REACTING ROCKET FLOWS

AFOSR Grant Contract No.

Principal Investigators: J. William Rich and Vish V. Subramaniam

Dept. of Mechanical Engineering
The Ohio State University
206 W. 18th Ave.
Columbus, OH 43210-1107

SUMMARY/OVERVIEW:

An experimental and analytical program of research into the aerothermodynamic environments and processes creating ultraviolet radiation from high altitude rocket plumes is being conducted. Laser-excited flowing gas and liquid absorption cells are used to create thermodynamic environments in extreme vibrational and electronic mode disequilibrium. We investigate mechanisms and measure specific state-resolved rates of key vibration-to-vibration, vibration-to-translation/rotation, and vibration-to-electronic mode energy transfer processes in CO, NO, and selected additional species. In addition, coupling of these modes to free electrons is studied. Emphasis is placed on processes controlling CO 4th Positive, CO Cameron, NO Beta, and NO Gamma band ultraviolet radiation in rocket exhaust expansions. In the analytic portions of the program, semiclassical rate theories are being developed to predict these high-vibrational-quantum-state energy transfer processes, and are being incorporated into gas dynamic models of the rocket nozzle flows. The results of these studies are applied to accurate prediction of visible and ultraviolet radiation signals from rockets.

TECHNICAL DISCUSSION:

Fig. 1 shows a schematic of a typical experimental setup of a laser-pumped flowing absorption cell of the type currently being used at OSU. Radiation from a CO gas laser (1) is used to excite a vibrational mode of a gas in the absorption cell (4). In experiments to date, the vibrational modes of NO and CO have been excited by this means. The gas in the cell may be the single diatomic species, or a mixture of the absorbing species and various energy transfer or reaction partners. Gas densities can be varied over a large range, from .01 atm to > 10 atm. The translational-rotational temperature of the gas mixture is controlled by varying the gas density, by addition of vibrationally inactive diluents (argon, helium), by varying the laser power, and by varying the gas flow velocity through the cell. This temperature can be varied from cryogenic levels, O[100 K], to above 1,000 K. The pump laser can be pulsed, with a rise time to steady-state power of < 0.1 msec, permitting time-dependent energy transfer and chemical kinetic studies. It is also possible to maintain vibrational mode disequilibrium with a non-flowing, static cell configuration. Recently, we have successfully created extreme vibrational mode

disequilibrium in *cryogenic liquid* CO/Ar mixtures in such cells, and observed evidence of strong vibrational-to-electronic mode energy transfer, CO ($X\ ^1\Sigma \Rightarrow a\ ^3\Pi$).

A major advantage of this type of experiment is that it is possible to study thermally nonequilibrium gases in a controlled environment, with a limited number of possible energy transfer channels. Fig.2 shows typical results of such experiments using a flowing mixture of NO/Ar in the cell of Fig. 1. The pump laser radiation prepares a certain amount of NO in its v = 1 vibrational quantum state; the laser is repetitively pulsed, using the mechanical chopper (6 in Fig.1), with a duty cycle which allows reaching steady-state nonequilibrium conditions, when the laser pulse is on, and complete relaxation to equilibrium, when the pulse is off. The time-dependent infrared and visible/ultraviolet radiation is analyzed using the monochromators, detectors, etc., shown in Fig.1. Fig 2 shows the infrared radiation emitted from selected states of the NO, subsequent to the laser pump excitation of v = 1. Also shown are the incident pump laser pulse itself, and the residual laser pump pulse after transmission through the cell. Finally, the total ultraviolet signal, which is created entirely by NO Beta and Gamma band radiation, is also displayed. The total time evolution during a single pulse is shown on the top part of the figure, and the rise portion of the emission signals to steady state is shown on a more highly resolved time scale on the lower part of the figure. The data show that the vibrational level populations rise sequentially with quantum number, after the preparation of level v = 1. The levels shown, v = 3,5,9, and 12, and the increasing time delays for each level, are evident.

What is being observed is the diffusion upward in vibrational quantum space of energy, by means of inelastic vibration-to-vibration energy transfer collisions, followed by collision-induced energy transfer into excited electronic states, the NO A and B states, with subsequent ultraviolet radiation. From such data, it is possible to infer the specific rates of the inelastic energy exchange processes among these excited states, using master equation kinetic analyses. Detailed inference of the energy transfer paths and rates by these means will be presented, and the use of a recently acquired step-scan Fourier transform spectrometer for much greater quantum state and time resolution experiments of this type will be discussed. Recent related results in CO will also be presented.

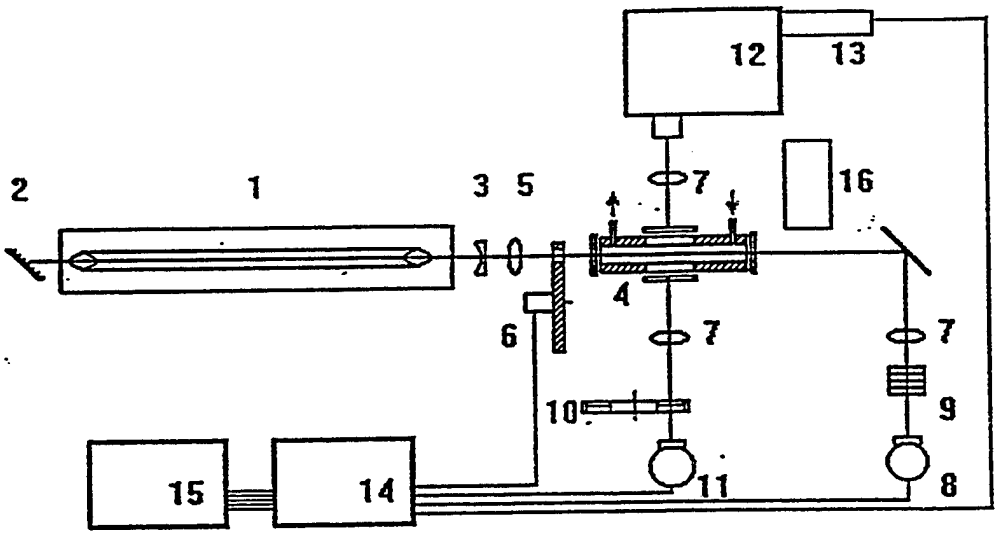

The experimental setup. (1) CO laser; (2) grating; (3) output coupler; (4) absorption cell; (5) focusing lens; (6) chopper; (7) collection optics; (8) HgCdTe detector; (9) filters; (10) filter wheel with IR filters; (11) InSb detector; (12) monochromator; (13) photomultiplier; (14) digitizing oscilloscope; (15) computer

Fig. 1 Laser-Excited Flowing Gas Optical Absorption Cell

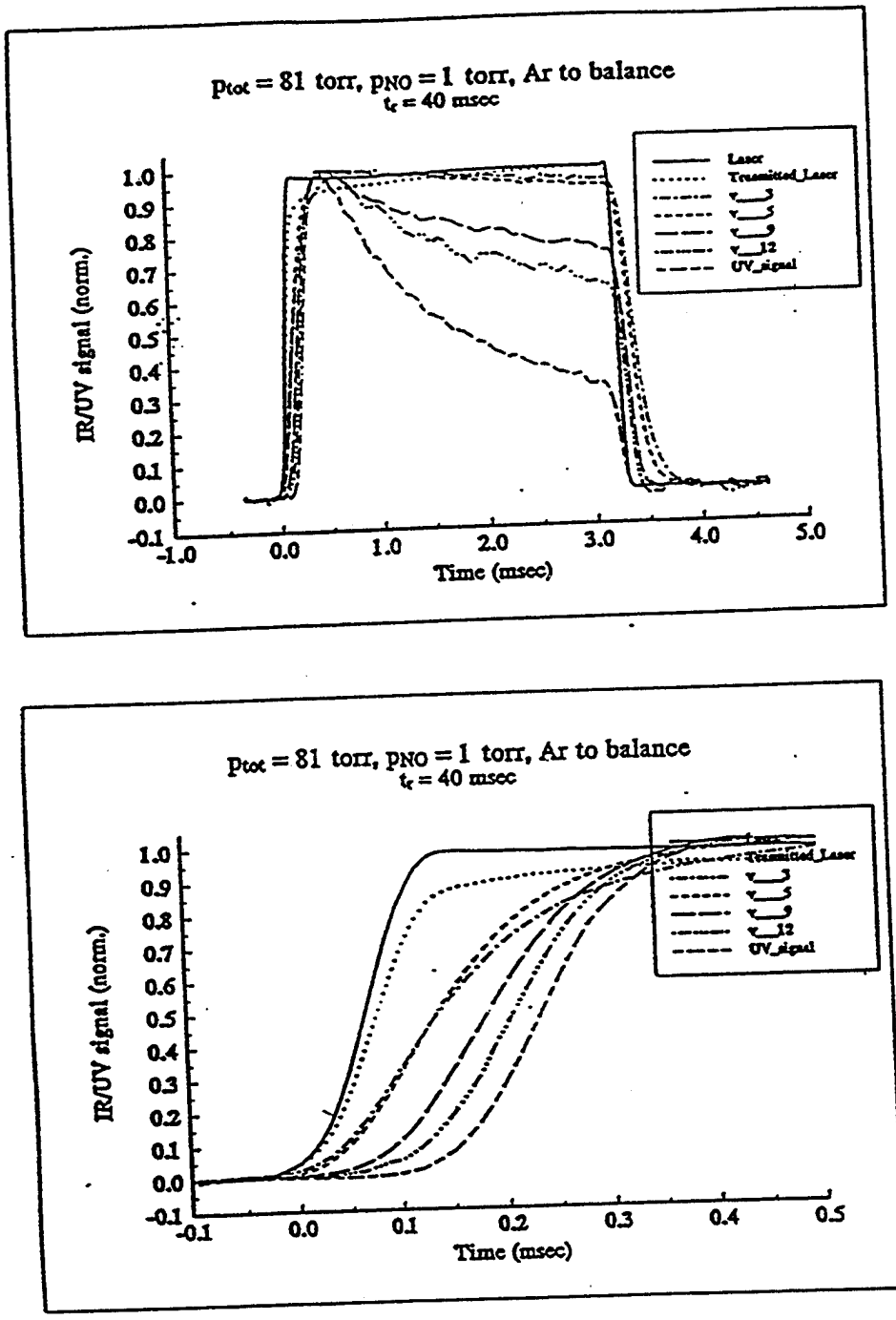

Fig. 2 Time-dependent IR and UV Emission from Selected States in Nonequilibrium Optically-Excited NO. P_{NO}= 1.0 Torr

MODELING NONEQUILIBRIUM RADIATION IN HIGH ALTITUDE PLUMES

(AFOSR Grant Contract No. F49620-96-1-0091)

Iain D. Boyd

School of Mechanical and Aerospace Engineering
Cornell University, Ithaca, NY 14853.

SUMMARY/OVERVIEW:

The work concerns development of sophisticated numerical techniques to simulate radiative emission in high altitude plumes under conditions of strong thermochemical nonequilibrium. The primary applications are plumes from high altitude missiles, and from spacecraft control thrusters. The numerical method employed is the direct simulation Monte Carlo method (DSMC). The DSMC technique is being advanced through development of new electronic excitation models and development of new schemes for effective simulation of charged species.

TECHNICAL DISCUSSION

Introduction

There is a strong requirement for prediction of radiative emission from high altitude plumes at altitudes above 50 km. The detection and tracking of high altitude missiles is a matter of national security. Radiative emissions generated by the high temperature core of missile plumes, and by interaction of the plume with the ambient atmosphere provides an excellent method for successfully achieving these objectives. In terms of satellite surveillance, there is a requirement for characterization of emissions caused by the interaction of spacecraft propulsion systems with the energetic ambient atmosphere at altitudes up to 1000 km.

The modeling of high altitude plumes presents several technical difficulties. At high altitude, the ambient density is naturally low so that interaction between plume and free stream occurs under high Knudsen number, nonequilibrium conditions. The energy exchanged between plume and free stream is extremely high promoting relaxation of the internal modes, chemical reactions, and radiative emission. To understand the problems associated with simulating such physics it is appropriate to review the two Bow Shock Ultra Violet flight experiments (BSUV) that were flown under funding from SDIO. These two flights measured ultraviolet radiative emission in front of a blunt body during hypersonic entry into the atmosphere at high altitudes. The results and conclusions are directly relevant to the problem under consideration here.

BSUV-1 flew in 1990 over the altitude range of 40 to 70 km at a velocity of 3.5 km/sec. Preflight predictions were obtained using computational fluid dynamics (CFD) and a nonequilibrium radiation code, NEQAIR [1]. It was found initially that the calculations underpredicted the radiative emission by several orders of magnitude and that agreement grew worse as the altitude increased. After much effort at improving the NEQAIR code, satisfactory agreement with all data was achieved [2].

BSUV-2 flew in 1991 over the altitude range of 60 to 90 km at a velocity of 5.1 km/sec. Relative to BSUV-1, the increases in both altitude and velocity greatly increased the degree of nonequilibrium in the flow. While the CFD preflight predictions agreed with the emission data at lower altitudes, at 88 km the calculated results were too low by a factor of 200. Use of the direct simulation Monte Carlo (DSMC) technique for fluid mechanics and chemistry, and the

NEQAIR code for radiation, gave an improvement by a factor of about 3, still leaving a very unsatisfactory margin of error. Careful scrutiny of the modeling of vibration-dissociation coupling under the very strong degree of thermal nonequilibrium experienced by BSUV-2 at 88 km revealed that traditional CFD and DSMC chemistry models were inaccurate [3]. Using a more detailed model led to significant improvements in calculation of both NO and O emission. This study is a major breakthrough in understanding nonequilibrium thermochemical processes.

Several lessons can be learned from the BSUV studies. Clearly, as the degree of nonequilibrium increases in these flows, the continuum assumptions for fluid mechanics, chemistry, and eventually radiation will fail. It is now well established that the appropriate numerical technique for simulation of gas flows in such strong states of kinetic nonequilibrium is the direct simulation Monte Carlo method (DSMC) [4]. However, in its present level of development, this technique is far from being able to predict all the relevant phenomena associated with high altitude plumes. The primary aim of this research is to develop a new radiation model for the DSMC technique based on the continuum nonequilibrium radiation code, NEQAIR.

Current State-of-the-Art for Modeling Nonequilibrium Radiation

As stated above, the most appropriate numerical technique for simulating flows in a state of strong thermochemical nonequilibrium is the direct simulation Monte Carlo method (DSMC) [4]. In this scheme, particle trajectories are followed and collisions computed in the flow domain of interest. In this manner, a direct simulation of nonequilibrium energy distributions and subsequent nonequilibrium kinetic rates is performed at the molecular level. In order to accurately calculate radiative emission, it is important that all collision mechanisms leading to change in the internal energy of the gas are modeled in sufficient detail.

A model for rotational relaxation has been developed for the DSMC technique by detailed study of nitrogen shock waves [5]. This model has been extended to include quantized energy levels [6], and has been modified for various gases including hydrogen [7] and iodine [8]. The model uses an overall rotational relaxation time, and there is a requirement to include more detailed state-specific rate coefficients.

A model for vibrational relaxation has been developed for the DSMC technique for quantized energy levels [9,10]. A number of more detailed state-specific models are available in the literature [e.g. 11,12] and many should be usable in a straightforward manner by the DSMC technique.

The Vibrationally-Favored-Dissociation model (VFD) [13] is a DSMC chemistry model that includes the coupling between the rate of dissociation and the state of the vibrational energy mode. Specifically, the rate of dissociation is reduced when the vibrational temperature is lower than the translational value. The model has been successfully verified against experimental data under relatively high pressure flow conditions [14]. However, this approach has been shown to be inaccurate when the degree of thermal nonequilibrium is very great such as the high altitude BSUV-2 flight conditions. New approaches are currently under investigation to address this problem directly [15].

In the previous BSUV studies, radiative emission was determined from the flow field solution in a decoupled manner. It has been shown that this approach gives results consistent with coupled radiation simulations under conditions where the degree of nonequilibrium is not too great [16]. However, many of the flows of interest in high altitude plume signature characterization require the development of accurate radiation models for the DSMC technique that are directly coupled to the flow field solution as it progresses. Existing DSMC radiation models [17] are rather simplistic in nature, and omit many of the key emission mechanisms.

It is also the intention to model emission generated by the interaction of spacecraft control thruster plumes and the ambient atmosphere at altitudes above 200 km. Under these conditions, the role of charged species is significant. Ions such as O+ existing in the ambient environment

may readily undergo charge exchange collisions with neutral molecules from the control thruster plume. Subsequently, the plume ions may become electronically excited and radiate in the visible region. In order to include these effects in the DSMC technique there is a requirement for a physically accurate yet simple scheme for simulating electrons. The main issue here is that when electric fields are neglected, the electrons tend to diffuse over unphysically large distances due to their very small mass. The charge exchange cross sections may be taken from experimental studies such as those conducted by the group of Dr. Edmond Murad at Hanscom AFB.

Research Program

This research aims at the development of models and algorithms for the DSMC technique to enable accurate simulation of radiative emission coupled to flows in a state of strong thermochemical nonequilibrium found in high altitude plumes. This involves three main tasks which are described below.

(1) Electronic Excitation

The strength of the DSMC technique is that it provides a framework for simulating detailed collision phenomena. However, the method is only as good as the collision models it employs. For simulation of nonequilibrium radiation, there is a large advantage in basing a new DSMC model on the existing knowledge contained in the continuum radiation code NEQAIR. Many of the physical coefficients required by a number of important emission mechanisms have been verified over the years in this code by comparison with experimental data. The main task here involves the conversion of temperature dependent rate coefficients used in NEQAIR to collision probability models for DSMC that depend on the energy of each individual collision. This is essentially the approach that has been taken previously in development of DSMC models for rotational, vibrational, and chemical collision mechanisms. In this task we are interacting informally with Dr. Deborah Levin of the Institute for Defense Analyses who has several years experience in developing the NEQAIR code.

(2) Electrons

Electrons occur naturally in the atmosphere at high altitude, and are produced collisionally in the energetic flows of interest here. In many cases, the excitation cross-sections associated with electron collisions are significantly larger than heavy-particle events. It is therefore important to simulate the role of these species with particular accuracy. Unfortunately, including electrons in the DSMC technique presents technical difficulties due to their very small mass. If plasma effects are neglected, then simply including the electrons as an additional species requires the simulation time-step to be reduced by about 2 orders of magnitude due to their large diffusion velocities. Even with modern supercomputers, this increase in numerical cost is unworkable. Alternative strategies are being explored that involve the use of simple plasma physics models for ambi-polar diffusion. This represents a more physically realistic approach to the electron motion than pure diffusion. The ambi-polar approximation constrains the distance through which the electron may move due to the attractive pull of neighboring ions.

(3) Numerical Implementation

The new models for electronic excitation and electrons are being implemented in the parallelized DSMC code developed at Cornell University that is called MONACO. This code performs efficiently on a range of computer platforms including the IBM SP-2 parallel computer. The parallel nature of the MONACO implementation requires special attention to be paid to the implementation of new numerical models. In particular, the ambi-polar diffusion model for electron motion is complicated by the use of unstructured grids in MONACO.

These models and algorithms are being developed in DSMC codes at Cornell University. They are being written in modular form for use by others such as Mr. David Weaver of Phillips Laboratory, Edwards Air Force Base.

References

[1] Park, C., "Calculation of Nonequilibrium Radiation in the Flight Regimes of the Aero-Assisted Orbital Transfer Vehicles," *Progress in Astronautics and Aeronautics*, Vol. 96, AIAA, New York, 1985.

[2] Levin, D.A., et al., "Comparison of Theory and Experiment for the Bow Shock Ultraviolet Rocket Flight," J. Thermophysics, Vol. 7, 1993, p. 30.

[3] Boyd, I.D., Candler, G.V., and Levin, D.A., "Dissociation Modeling in Low Density Hypersonic Flows of Air," Phys. Fluids, July 1995.

[4] Bird, G.A., *Molecular Gas Dynamics and the Direct Simulation of Gas Flows*, Oxford University Press, 1994.

[5] Boyd, I.D., "Temperature-Dependence of Rotational Relaxation in Shock-Waves of Nitrogen," Journal of Fluid Mechanics, Vol. 246, 1993, pp. 343-360.

[6] Boyd, I.D., "Relaxation of Discrete Rotational Energy Distributions Using a Monte Carlo Method," Physics of Fluids A, Vol. 5, 1993, pp. 2278-2286.

[7] Boyd, I.D., Beattie, D.R., and Cappelli, M.A., "Numerical and Experimental Investigations of Low-Density Supersonic Jets of Hydrogen," J. Fluid Mech., Vol. 280, 1994, pp. 41-67.

[8] Boyd, I.D., Pham-Van-Diep, G.C., and Muntz, E.P., "Monte Carlo Computation of Nonequilibrium Flow in a Hypersonic Iodine Windtunnel," AIAA J., Vol. 32, 1994, pp. 964-970.

[9] Boyd, I.D., "Analysis of Vibrational-Translational Energy Transfer Using the Direct Simulation Monte Carlo Method," Phys. Fluids A, Vol. 3 (7), 1991, pp. 1785-1791.

[10] Bergemann, F. and Boyd, I.D., "New Discrete Vibrational Energy Method for the Direct Simulation Monte Carlo Method," *Rarefied Gas Dynamics*, Progress in Astronautics and Aeronautics, Vol. 158, 1994, pp. 174-183.

[11] Kunc, J.A., "Vibration-Translation Exchange in Diatom-Diatom Collisions," Journal of Physics B, Vol. 24, 1991, pp. 3741-3761.

[12] Adamovich, I.V., et al., "Vibrational Relaxation and Dissociation of Diatomic Gasses Behind Strong Shock Waves," AIAA Journal, July 1995.

[13] Haas, B.L. and Boyd, I.D., "Models for Direct Monte Carlo Simulation of Coupled Vibration-Dissociation," Physics of Fluids A, Vol. 5, 1993, pp. 478-489.

[14] Boyd, I.D., "Analysis of Vibration-Dissociation-Recombination Processes Behind Strong Shock Waves of Nitrogen," Physics of Fluids A, Vol. 4 (1), 1992, pp. 178-185.

[15] Boyd, I.D., "Monte Carlo Evaluation of Threshold Line Models for Dissociation," International Symposium on Shock Waves, Pasadena, California, July 1995.

[16] Boyd, I.D. and Whiting, E.E., "Decoupled Predictions of Radiative Heating in Air Using a Particle Simulation Method," Paper 92-2971, July 1992.

[17] Bird, G.A., "Nonequilibrium Radiation During Re-enty at 10 km/s," AIAA Paper 87-1543, June 1987.

KINETICS OF PLUME RADIATION, AND OF HEDMs AND METALLIC FUELS COMBUSTION

AFOSR Grants No. F49620-95-1-0258 AND F49620-95-1-0473

Principal Investigator: Arthur Fontijn

High-Temperature Reaction Kinetics Laboratory
The Isermann Department of Chemical Engineering
Rensselaer Polytechnic Institute
Troy, NY 12180-3590

SUMMARY

The development of uv plume radiation codes requires data on the kinetics of chemiluminescent emissions of individual reactions as a function of pressure and temperature. A method has been developed and demonstrated that allows providing such information, for reactions involving precursor reactants which are best produced photochemically. It is an adaptation of one of our high-temperature reactor techniques for studies of combustion reactions in isolation. The investigations concentrate on CO emissions in the VUV. In other work, with the reactors in their normal configuration, boron oxide kinetics is measured.

TECHNICAL DISCUSSION

Plume Radiation

The goal of this work is to provide kinetic information to help develop plume uv-radiation codes. To this end individual combustion reactions involved in chemiluminescence from C/H/O compound reactions are studied. In later work this may be extended to include nitrogeneous or metallic species. In particular, we are concentrating on emission of the CO Fourth Positive Band System, CO 4+ for short, i.e. the $A^1\Pi$ - $X^1\Sigma$ system of CO, Fig. 1.

In the laboratory this emission had been studied mainly from O-atom reactions with C_2H_2 and C_3O_2.[1-4] The main mechanism has been identified as formation of C_2O, followed by

$$C_2O + O \rightarrow CO(^3) + CO \quad (1),$$

$$CO(^3) + M \rightarrow CO\,(A^1\Pi) + M \quad (2),$$

The occurence of reaction (2) is indicated by the observation that the intensity of the CO 4+ emission increases with pressure over the 1-13 mbar range.[1] It is also consistent with the observation that this radiation appears later in time than the $CO(^3)$ emissions,[3] and with the anomalies observed within the CO 4+ system emissions[4].

One problem with this scheme is that the maximum energy available from the O + C_2H_2 reaction (C_3O_2 is not a reactant encountered in combustion systems) is 9.8 eV,

corresponding to the 10th vibrational level of $CO(A^1\Pi)$, while emission from levels with up to 0.3 eV more excitation energy has been observed. This can be explained by energy transfer processes or collisions at the tail end of the Boltzman distribution, but other mechanisms should be considered for plume radiation.

It has been established[5] that

$$C_2(X^1\Sigma, a^3\Pi) + O_2 \rightarrow 2\,CO \qquad (3),$$

which is 10.84 and 10.92 eV exothermic, for $(X^1\Sigma)$ and $(a^3\Pi)$ respectively, leads to both $CO(^3)$ and $A^1\Pi$ emissions. (These two states of C_2 are so close together, 0.08 eV, that in kinetic systems one can not normally distinguish their reactions). However, the pressure-dependence of these emissions has not been investigated. If $CO(A^1\Pi)$ can form directly in this system, rather than via a $CO(^3)$ intermediate, reaction (3) would be a more likely candidate for the high-altitude, i.e. low pressure, VUV plume emission. A major goal for the present work is to establish the influence of pressure on the CO 4+ intensity from reaction (3).

The established way for producing C_2 is by multi-photon photolysis of C_2H_2 or C_2H_4.[6] This requires the use of a different type of apparatus than the microwave discharge flow tubes used for the measurements of the pressure dependence of the O + C_2H_2 reaction.[1] A design like our HTP (high-temperature photochemistry) apparatus is required for the photolysis experiments. In such reactors the O atoms are produced in the center of the observed reaction zone and diffuse out. The observation zone is geometrically restricted and an increase in pressure will cause an increased amount of the reaction events to be observed, which would falsify pressure dependence observations. To eliminate this problem the arrangement shown in Fig. 2 has been used. We alternately study the reaction of interest, O + C_2H_2 in these first experiments, and the reaction O + NO $\rightarrow$ NO_2 + hν, which at pressures above about 0.1 mbar is known to be pressure independent.[7] The intensity ratio I(CO 4+)/I (NO_2) then gives the true pressure-dependence, which is shown in Fig. 3 and agrees with the earlier flow tube observations. In these experiments the O atoms were produced by photolysis of SO_2 at 193 nm.

Hence, we are now ready to study the pressure dependence of the emissions from reaction (3). However, we are first attempting to see if the negative pressure dependence of some of the $CO(^3)$ emissions from O + C_2H_2, predicted by reaction (2), can be demonstrated.

Boron Oxide Kinetics

Measurements have been made in the 300-1200 K range on

$$BO + CO_2 \rightleftarrows BO_2 + CO \qquad \Delta H = -1.6 \text{ kJ mol}^{-1} \qquad (4),$$

in both directions, in an HTFFR (high-temperature fast-flow reactor). Apart from a possible indication of a slow addition reaction between BO and CO_2 at room temperature, no reaction could be observed, i.e. the reactions shown have rate coefficients less than 1×10^{-15} cm^3 $molecule^{-1}s^{-1}$. This is significant as these are important reactions in the current B/O/H/C homogeneous reaction model,[8] which also

8. R.A. Yetter, H. Rabitz, F.L. Dryer, R.C. Brown, and C.E. Kolb, "Kinetics of High-Temperature B/O/H/C Chemistry", Combust. Flame 83, 43 (1991).

9. R.C. Brown, C.E. Kolb, S.Y. Cho, R.A. Yetter, F.L. Dryer, and H. Rabitz, "Kinetic Model for Hydrocarbon-Assisted Particulate Boron Combustion", Int. J. Chem. Kin. 26, 319 (1994).

10. C.T. Stanton, N.L. Garland, and H.H. Nelson, "Temperature Dependence of the Kinetics of the Reaction BO + O_2", J. Phys. Chem. 95, 8741 (1991).

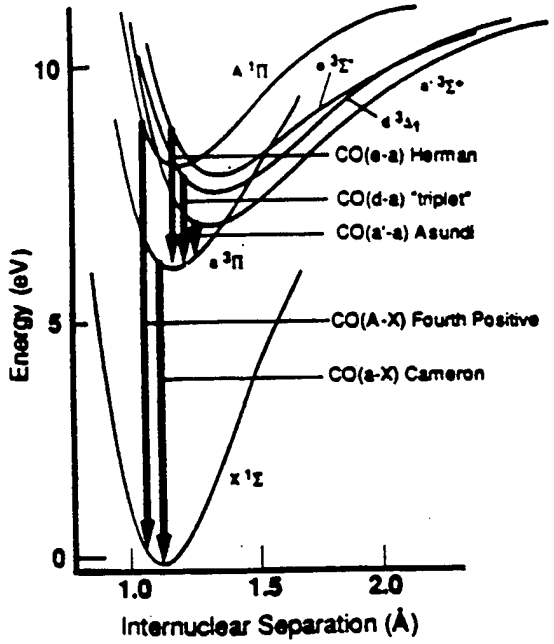

Fig. 1: CO Potential Curves and Transitions. From a presentation by W.L. Dimpfl

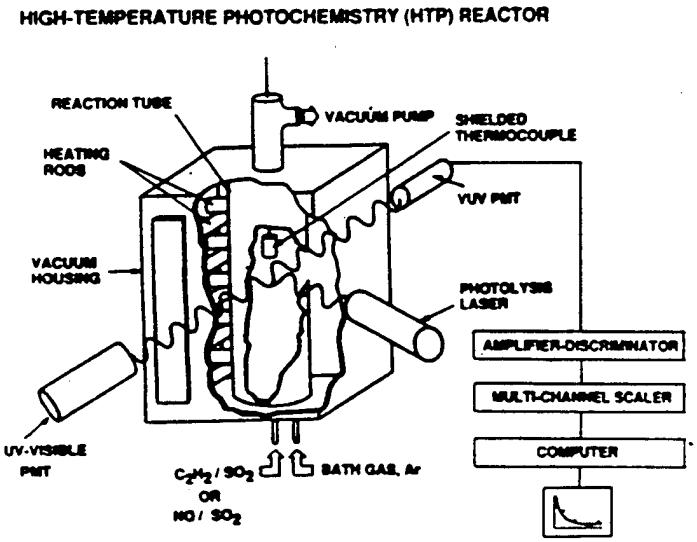

Fig. 2: The HTP reactor, as configured for chemiluminescence observations

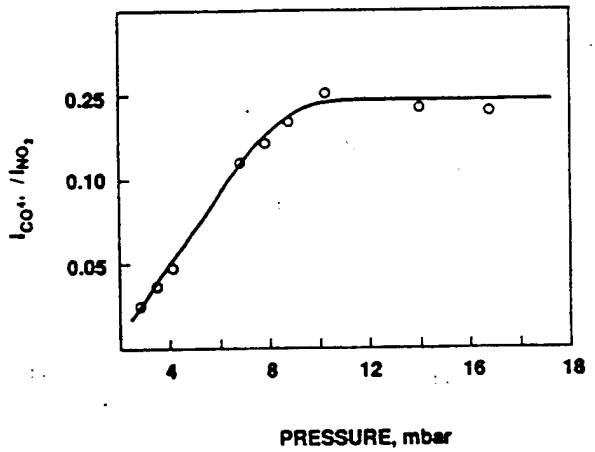

Fig. 3: Pressure dependence of the CO 4+ radiation from the O + C_2H_2 reaction

represents a subset[9] of the reactions in models of heterogeneous combustion. The present measurements show that rate coefficient values estimated there[8] are more than two orders of magnitude too high.

Other BO reactions, studied in an HTFFR, e.g.,

$$BO + O_2 \rightarrow BO_2 + O \qquad (5),$$

showed large scatter, probably attributable to BO wall-induced dimerization. We therefore have repeated the study of the BO + CO_2 and O_2 reactions in an HTP reactor, where wall reactions can not interfere. This confirmed the absence of a measurable BO + CO_2 reaction and yielded agreement with previous measurements[10] of reaction (5). The combined measurements for the latter give k(300-1000 K) = 7.9×10^{-12} exp(161 K/T) cm^3 $molecule^{-1}s^{-1}$.

Equilibrium calculations show that, if BO + CO_2 is too slow for measurement, BO_2 + CO must be too. However, as a further check on reactions (4), and the reliability of an HTFFR for BO_2 reactions, we plan to study another important reaction of the B/O/H/C model[8] for which no measurements exist:

$$BO_2 + H_2 \rightarrow HBO_2 + H \qquad (6)$$

References

1. A. Fontijn and S.E. Johnson, "Mechanism of CO Fourth Positive VUV Chemiluminescence in the Atomic Oxygen Reaction with Acetylene. Production of $C(^3P,^1D)$", J. Chem. Phys. 59, 6193 (1973).

2. K.H. Becker and K.D. Bayes, "CO Chemiluminescence from Flames", J. Chem. Phys. 48, 653 (1968).

3. W. Bauer, K.H. Becker, and R. Meuser, "Laser-Induced Fluorescence Studies on C_2O and CH Radicals", Ber. Bunsenges. Phys. Chem. 89, 340 (1985).

4. K.D. Bayes, "Spectroscopic Study of the Chemiluminescent Reaction O + CCO", J. Chem. Phys. 52, 1093 (1970).

5. H. Reisler and C. Wittig, "Electronic Luminescence Resulting From Infrared Multiphoton Excitation", *Photoselective Chemistry, Part 1*, J. Jortner, R.D. Levine, and S.A. Rice, Eds., (Wiley, New York, 1981), p. 679.

6. V.M. Donnely and L. Pasternack, "Reactions of $C_2(a\ ^3\Pi_u)$ with CH_4, C_2H_2, C_2H_4, C_2H_6 and O_2 Using Multiphoton UV Excimer Laser Photolysis, Chem. Phys. 39, 427 (1979).

7. A. Fontijn, C.B. Meyer, and H.I. Schiff, "Absolute Quantum Yield Measurements of the NO-O Reaction and its Use as a Standard for Chemiluminescent Reactions", J. Chem. Phys. 40, 64 (1964).

8. R.A. Yetter, H. Rabitz, F.L. Dryer, R.C. Brown, and C.E. Kolb, "Kinetics of High-Temperature B/O/H/C Chemistry", Combust. Flame 83, 43 (1991).

NONSTEADY COMBUSTION MECHANISMS OF ADVANCED SOLID PROPELLANTS

AFOSR Grant No. DOD-F49620-93-0430

M.C. Branch, University of Colorado
M.W. Beckstead, Brigham Young University
T.A. Litzinger, Pennsylvania State University
M.D. Smooke, Yale University
V.H. Yang, Pennsylvania State University

SUMMARY/OVERVIEW

This report describes progress during the third year of a collaborative research program combining the expertise of individuals from several universities to develop a new ability to predict the propulsion performance of solid rocket motors. The focus of the research on nonsteady behavior is unique and the overall project is not possible at any one of the institutions participating in this coordinated research. The individual tasks which we are studying will pursue solid propellant decomposition under unsteady conditions, nonsteady aspects of gas phase flame structure measurements, numerical modeling of multidimensional flame structure, propellant/flame interactions, and overall nonsteady propellant combustion characteristics in realistic rocket motor environments. Our goal is to develop general models of fundamental mechanisms of combustion instability that can be applied to a variety of new energetic materials.

TECHNICAL DISCUSSION

Condensed Phase Propellant Decomposition Processes (Litzinger)

A microprobe sampling and mass spectrometric analysis technique (MPMS) has been developed and is being used to measure decomposition products of solid propellants for comparison to modeling studies. The objective of MPMS studies is to determine the chemical mechanisms for solid propellant combustion with an initial emphasis on the decomposition of HMX and on the gas phase reactions of the products of its decomposition for steady and unsteady conditions. A triple quadrupole mass spectrometer (TQMS) and quartz microprobes are used to obtain quantitative species profiles above the surface of the sample during CO_2 laser induced decomposition or during laser assisted deflagration of the sample. Gas phase temperature profiles are measured with micro-thermocouples no larger than 75 micron. The results of the studies provide the boundary conditions at the interface between the condensed and gas phases which is critical for modeling. In addition they provide gas phase species and temperature profiles over a range of experimental conditions that will be used to test the models as described in the following section of this abstract.

Over the last year experiments under steady-state conditions have been performed with HMX at

two heat fluxes, 100 and 300 W/cm^2, under atmospheric pressure in argon. In these experiments both species and temperature profiles were obtained. For both heat fluxes, the species identified at the surface were H_2O, CH_2O, HCN, NO_2 NO, N_2O, N_2 and CO. No CO_2 was observed at the surface. Results of the experiments show that increasing heat flux increased the burning rate from 0.9 to 1.2 mm/s and also increased the CN flame stand-off distance from 2.7 to 4.8 mm. The results of the studies will provide key information for the modeling of propellant combustion. It will provide the boundary conditions at the interface between the condensed and gas phases which is critical for modeling. In addition, it will provide gas phase species and temperature profiles over a range of experimental conditions that will be used to test the models. Finally, the results will give insight into the key chemical reactions to be studied in the flame experiments.

Gas Phase Flame Processes (Branch)

The development of detailed models of solid propellant combustion requires detailed information on the gas-phase chemistry occurring above the propellant surface. In particular, systems which need study are flames of carbon monoxide and hydrocarbons burning with nitrogen oxides. Since both premixed and diffusion flame chemistries exist above the propellant surface, premixed and diffusion flames involving these reactants need to be studied. In the past decade, several experimental studies have been made of premixed flames consisting of these reactants. More recently, counterflow diffusion flames consisting of these reactants have been studied as well. In the present work, several premixed and counterflow diffusion flames have been modeled using a common, 275-reaction mechanism.

Solid propellant combustion models require gas-phase chemical kinetic mechanisms which are as small as possible. Therefore, for each premixed flame system studied, sensitivity and rate generation analyses have been used to identify which reactions in the detailed mechanism are critical to each system. Based on these analyses, and comparisons with the experimental data, reduced mechanisms, consisting of only the essential chemical reactions for each flame system, have been developed. These reduced mechanisms have been combined into a comprehensive, reduced mechanism consisting of 42 reactions. In general, this reduced mechanism models the flames' chemistry as accurately as the full mechanism does.

The full and reduced mechanisms have also been used to model methane-nitrous oxide and carbon monoxide-nitrous counterflow diffusion flames. From comparisons with the experimental data, it is determined that, in general, the full mechanism and the reduced mechanism model the diffusion flame chemistry as accurately as they modeled the premixed flame chemistry. Also, in the diffusion flames, there is reasonable agreement between the modeling results using the full and reduced mechanisms.

RDX Monopropellant Model (Beckstead)

The one-dimensional RDX monopropellant model has been refined and compared to available experimental data. Using values of the pertinent properties that are available from the literature the model calculates burn rate (as a function of pressure and initial temperature), surface temperature (as a function of pressure) and melt layer thickness (as a function of pressure) all well within the scatter of the experimental data. Calculated species profiles agree well with both

laser and non-laser assisted experimental measurements. The major weaknesses of the model lie in the evaporation-condensation rate calculations, vapor pressure correlations and the condensed phase reaction mechanism. The model calculates accurate surface temperature data only when using sublimation pressure data rather than vapor pressure data. From sensitivity analysis, the calculated surface temperature is dependent primarily on the RDX sublimation or vapor pressure (using the sublimation pressure gives results in better agreement with the data), and the calculated melt layer thickness is a strong function of liquid thermal conductivity. The thermal conductivity of a liquid is generally greater than that of the solid and because no RDX liquid thermal conductivity data could be found in the literature, the thermal conductivity of RDX liquid was estimated to be ~2.5 times the measured solid value (1.045E-3 cal/cm-s-K). The model was also able to match experimental laser assisted temperature and species data by mimicking the two dimensionality of the experiment. The calculation indicates that the laser induces a dark zone which is strongly dependent upon H_2CN formation from the two-phase surface region. Typical results are shown in Figure 1. The most significant discrepancies in the calculated species concentrations occur for NO, which the model predicts to be ~28% versus the experimental data of ~20%, and for NO_2, which is predicted to be ~5% versus the experimental data of ~15%. Further work on the gas phase mechanism is needed to resolve these discrepancies.

HMX Monopropellant Model (Smooke)

During the past year our research has focused on the development of a computational model which is applicable to the study of HMX combustion. The three-tiered model allows for solid, liquid and gaseous phases of HMX. The resulting nonlinear two-point boundary value problem is solved by Newton's method with adaptive gridding. In our model the burning rate is computed as a eigenvalue which removes the uncertainty associated with employing evaporation and condensation rate laws in its evaluation. We have applied the model to the study of both laser-assisted and self-deflagration of HMX monopropellants and we have compared the results with the experimental measurements of Tim Parr (Figure 2). The burning rates have been computed over a wide range of pressures and they compare well with experimental results from one to ninety atmospheres. The burning rate is found to be proportional to the pressure raised to the 0.82 power (Figure 3). Sensitivity of the burning rate to initial propellant temperature was calculated and found to be extremely low which is in agreement with past theoretical predictions and experimental data. Results for self-deflagration studies do not indicate a two-zone flame. Laser-assisted studies illustrate a distinct primary and secondary flame separated by a dark zone, the length of which is dependent upon the incident laser flux intensity.

Propellant Combustion and Chamber Dynamics (Yang)

Results obtained from the preceding tasks provide a concrete basis for understanding the detailed combustion mechanism of solid propellants in an isolated environment. To extend these fundamental investigations to practical motor design issues, it is important to study the propellant burning behavior under conditions representative of realistic rocket motor environments. Most previous research on motor interior ballistics was either focused on cold-flow simulation or based on simplified approaches with propellant burning rates modeled by empirical formulas. Very little is known about detailed physico-chemical processes near the propellant surface which dictate the burning characteristics. The purpose of this task is to remedy these technical and

scientific deficiencies by treating the intricate interactions between local flow motions and chemical reactions at scales sufficient for resolving the rapid variations of flow properties in the near field. Both steady and oscillatory conditions are considered. The work mainly addresses two issues: how the motor internal flow is established by propellant burning, and how the local flowfield affects propellant burning (Figure 4).

The model appears to be the first and most complete of its kind to date, providing comprehensive information about propellant combustion and motor chamber dynamics. The instantaneous burning rate of propellant is calculated as part of the solution from first principles. Figure 2 shows typical result of heat-release fluctuations near the head end of the chamber. The problem investigated involves a two-dimensional chamber loaded with composite propellant subject to periodically forced oscillations at the chamber exit. This result can be effectively used to identify the key mechanism responsible for driving combustion instabilities in rocket motors. In particular, the effects of spatial distribution and temporal evolution of the heat-release process, as well as their mutual coupling with local flow motions, on motor stability can be clearly examined.

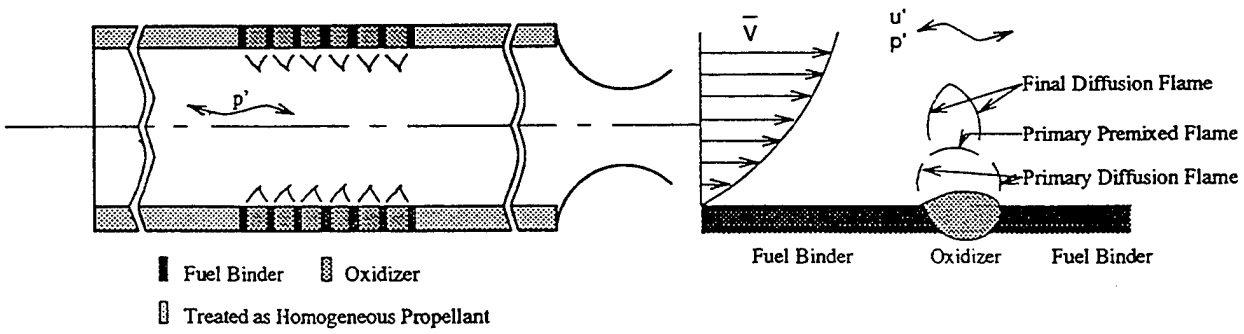

Figure1 Schematic Diagram of a Solid-Propellant Rocket Motor

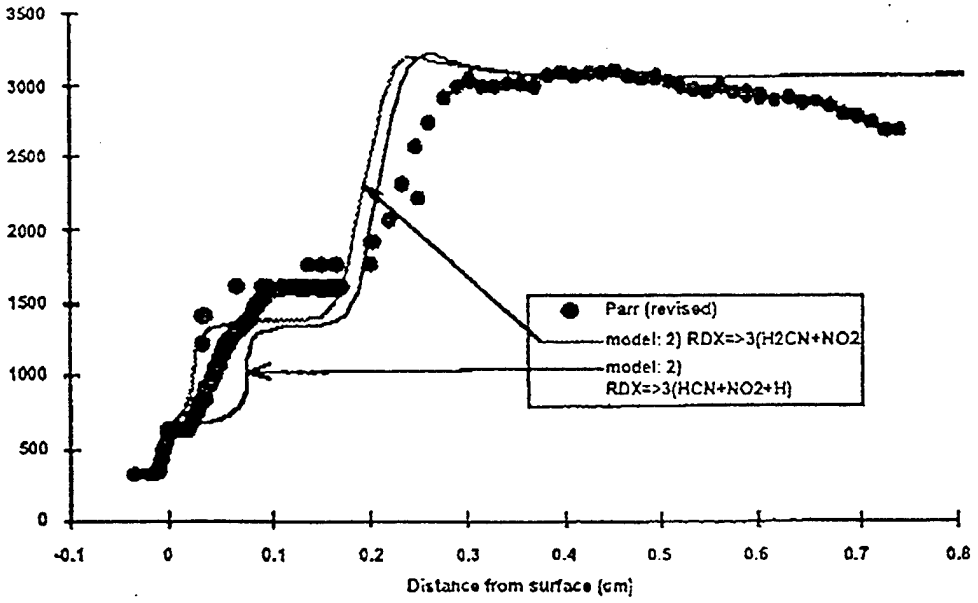

Figure 2. Measured and predicted temperature profile in laser assisted deflagration of RDX at 1 atm.

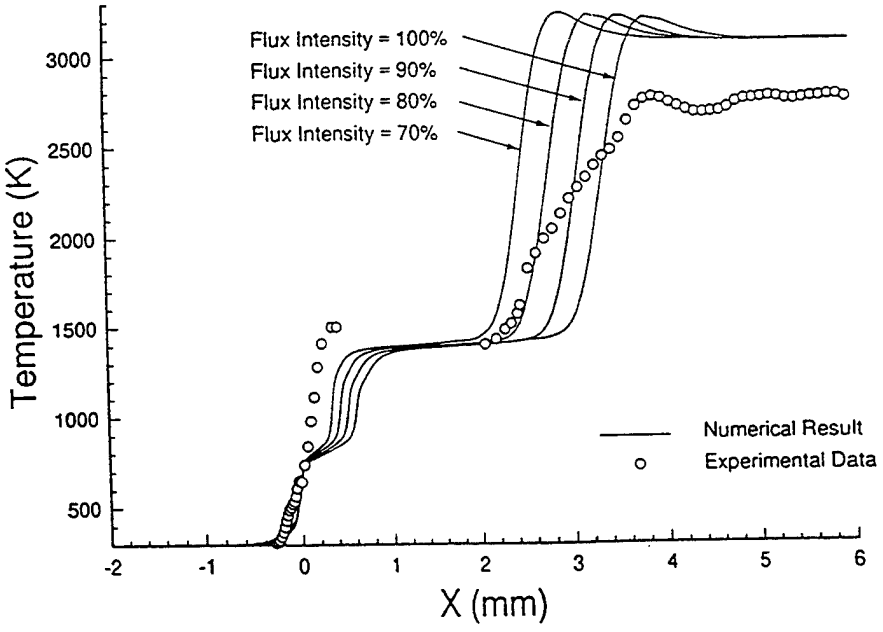

Figure 3. Measured and predicted temperature profile in laser assisted deflagration of HMX at 1 atm.

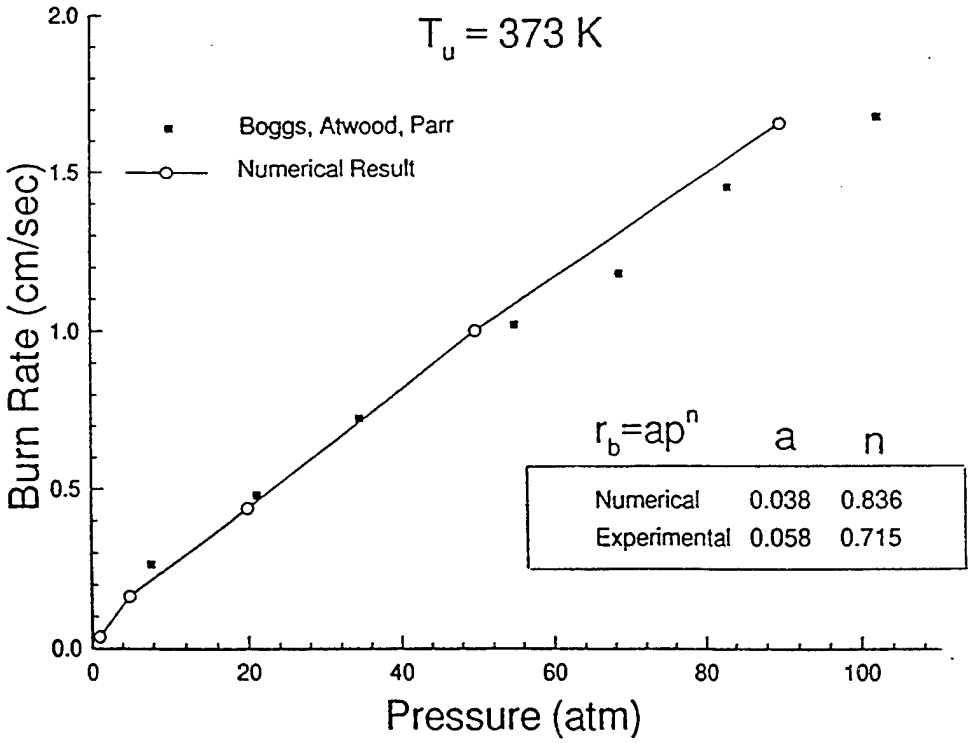

Figure 4. Measured and predicted burn rate of HMX as a function of pressure.

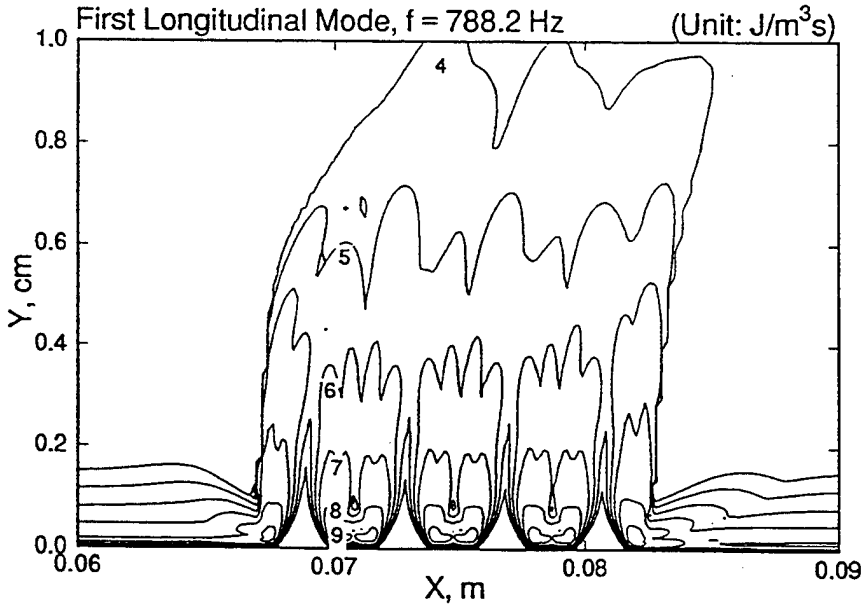

Figure 5. Amplitude of Fluctuating Heat Release Rate near the Head End of the Chamber

CHEMICAL MECHANISMS AT THE BURNING SURFACE

AFOSR Grant No. F49620-94-1-0053 and
F49620-96-1-0086

Principal Investigator: Thomas B. Brill

Department of Chemistry
University of Delaware
Newark, DE 19716

SUMMARY/OVERVIEW

Determination of the rates and pathways of pyrolysis of the main ingredients of solid rocket propellant components is needed to define the chemistry of the surface reaction zone during steady and non-steady combustion. To obtain this information we use spectroscopically-instrumented, high-rate, pyrolysis techniques to simulate the heating rate and temperature at the surface during steady combustion. The focus this year has been on "non-energetic" binders about which little is known. Polyethyleneglycol (PEG) and polymethylmethacrylate (PMMA) have been characterized this year to add to our study of hydroxyl-terminated polybutadiene (HTPB) which was completed in the summer of 1995.

TECHNICAL DISCUSSION

By comparison with the energetic components of propellants, the pyrolysis chemistry of binders is largely unknown under combustion-like conditions. In addition to being binders, HTPB and PMMA are potential fuels for hybrid rockets. The rate of formation of the dominant individual volatile products as well as the global gas evolution rates are useful information for combustion modeling because they give the species and mass flow rates from the surface into the flame zone. In addition to the kinetics, some understanding about the thermochemistry of the condensed phase has been a valuable bonus of the T-jump/FTIR method.

Figure 1 shows the control voltage traces of the Pt filament on which the film of polymer was cast. By heating at 2000°C/s and subtracting these voltages from the filament under the same conditions without sample, an indication of the endothermicity or exothermicity of the decomposition process is gained. Figure 1 reveals that HTPB is mildly exothermic upon decomposition [1,2], whereas PEG [3,4] and PMMA [5] are endothermic. This observation of the exothermicity of HTPB has been important in analytical modeling of hydrid rockets [6].

To identify the products and to determine the kinetics of formation of products from flash-heated polymer films in near-real time, the rapid-scan FTIR spectra must first be deconvoluted into the spectra of the individual products. This has been achieved by the use of elaborate chemometric schemes employing non-negative least squares and quadratic programming methods [1-5]. Table 1 summarizes the identified and temporally-quantified products from HTPB, PEG, and PMMA. An number of important features emerge.

In terms of product identities, PMMA is unusually simple. It liberates only the monomer (methymethacrylate) and CO_2. PEG liberates primarily oligomers with various end groups. HTPB liberates a wide variety of products, many of which result from secondary reactions. The temperature and pressure dependence of each of these products was determined in this work [1-5].

In terms of kinetics, it is apparent for HTPB and PMMA that two main mechanisms operate in the 380-600°C range to release the individual products. Figure 2 compares the global Arrhenius data for HTPB, PMMA and PEG. HTPB decomposes faster than PEG and PMMA. In the lower temperature range, the values of the activation energy (E_a) are reflective of bulk phase decomposition reactions, i.e. $E_a \simeq 30$-75 kcal/mol. A few exceptions obviously exist. On the other hand, in the higher temperature range, $E_a \simeq 6$-25 kcal/mol, which is more reflective of desorption and evaporation control. Again, a few exceptions obviously exist. It is perhaps most informative to compare the global kinetics data which were obtained by combining the kinetics of evolution of the individual products. At 2 atm Ar, PMMA and HTPB clearly show the pressure of competing mechanisms which switch in the 490±30°C range. PEG also changes behavior in about this range at 2 atm Ar, but the values of E_a suggest that desorption is important in controlling the gaseous products over the entire range of temperatures studied. Further studies of PEG indicate that the desorption of oligomers from the parent polymer is the controlling process in the 370-440°C range. However, a large quantity of residue forms simultaneously which has higher Mw and more cross-linking. Thus, pyrolysis of PEG at 470-550°C reflects both the parent polymer and the residue reactions.

An increase in the pressure from 2 atm to 11 atm Ar has unexpected effects. In the case of PMMA and PEG, the desorption process is suppressed which is intuitively expected. For HTPB, on the other hand, an increase in the pressure causes the desorption rates to be emphasized, which is not expected. Various models of the kinetics of vaporization of polymers have been derived and two equations are needed because of the opposite effect of pressure on the kinetics of gas evolution.

1. Arisawa, H. and Brill, T. B. (1996) Flash Pyrolysis of Hydroxyl-terminated Polybutadiene (HTPB) I: Analysis and Implications of the Gaseous Products, Combust. Flame, in press.

2. Arisawa, H. and Brill, T. B. (1996) Flash Pyrolysis of Hydroxyl-terminated Polybutadiene (HTPB) II: Implications of the Kinetics to the Combustion of Organic Polymers, Combust. Flame in press.

3. Arisawa, H. and Brill, T. B. (1996) Flash Pyrolysis of Polyethyleneglycol I: Chemometric Resolution of FTIR spectra of the Volatile Products at 370-550°C, Combust. Flame, submitted.

4. Arisawa, H. and Brill, T. B. (1996) Flash Pyrolysis of Polyethyleneglocol II: Kinetics Determined by T-jump/FTIR Spectroscopy, Combust. Flame, submitted.

5. Arisawa, H. and Brill, T. B. (1996) Kinetics and Mechanisms of Flash Pyrolysis of Polymethlmethacrylate (PMMA), Combust. Flame, submitted.

6. Farmer, R. C. SECA, Inc., Hunstville, AL, personal communication, 1995.

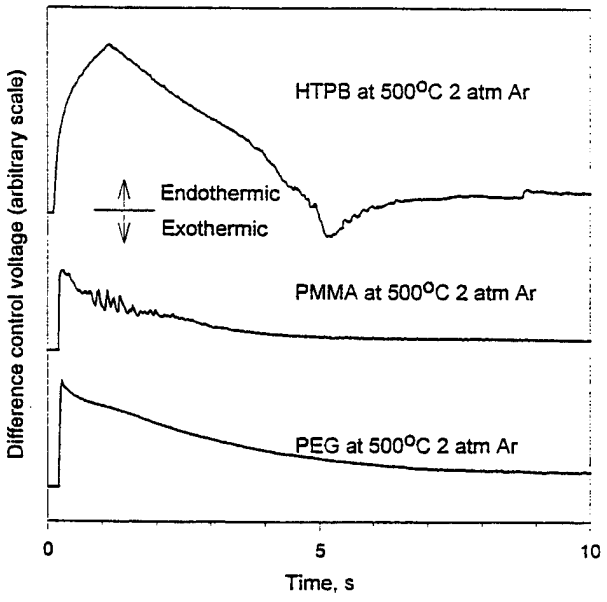

Figure 1. The control voltage traces for HTPB, PMMA and PEG showing the exothermic valley for HTPB, but only endothermic behavior of PEG and PMMA.

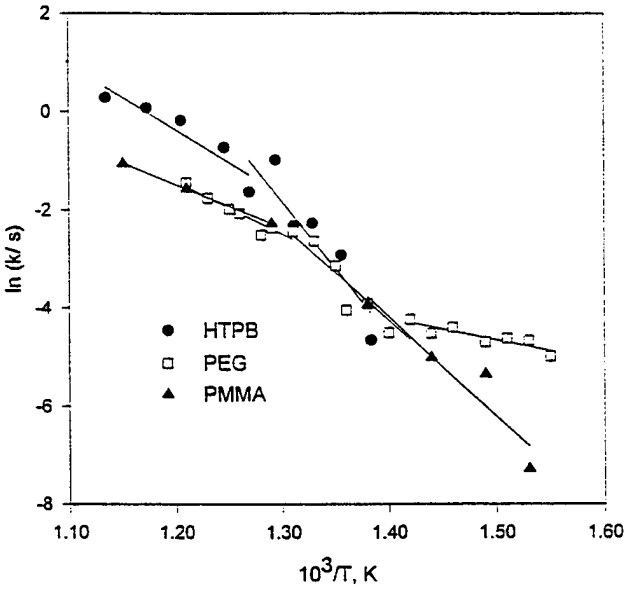

Figure 2. The global Arrhenius plots for HTPB, PEG and PMMA at 2 atm Ar. The slope break is apparent in the mid-temperature range.

Table 1

Arrhenius Parameters for Flash Pyrolysis of Polymers

Product	P, atm	E_a, kcal/mol	ln(A/s)	E_a, kcal/mol	ln(A/s)
PMMA-2000		T≈380-460°C		T≈500-600°C	
methyl-methacrylate	2	43±5	26±3	16±1	8.4±0.5
CO_2	2	46±1[a]	27±1[a]	19±0.4	9.8±0.2
methyl-methacrylate	11	49±9	29±6	28±2	15±1
CO_2	11	45±3[a]	26±2[a]	30±2	17±1
global	2	45±4	27±3	17±1	8.6±0.5
global	11	53±7	33±5	27±3	15±2
PEG-2090		T≈370-440°C		T≈370-550°C	
monoether oligomers	2	---	---	27	15
ethyleneglycol	2	---	---	31	18
diether oligomers	2	10	6	---	---
diethylene glycol	2	18	10	---	---
ethyl vinyl ether	2	---	---	24	14
global	2	7±8	1±6	22±4[b]	12±3[b]
global	11	---	---	52±0.3[c]	32±0.2[c]
HTPB-2500		T≈450-515°C		T≈515-600°C	
butadiene	2	75	48	16	9
4-vinyl-cyclohexane	2	76	49	6	3
t-butadiene-oligomers	2	67	41	12	7
ethylene	2	57	36	20	11
cyclopentene	2	13	8	13	8
1,5-hexadiene	2	38	22	38	22
butadiene	11	16	9	16	9
4-vinyl-cyclohexane	11	6	3	6	3
t-butadiene-oligomers	11	12	6	12	6
ethylene	11	17	9	17	9
cyclopentene	11	-8.5	-6.4	-27	-18
1,5-hexadiene	11	15	8	15	8
global	2	51	31	18	11
global	11	12	7	12	7

[a]T=420-500°C; [b]T=470-550°C; [c]T=400-550°C

NONLINEAR, ROTATIONAL-ACOUSTIC PROCESSES IN A SOLID ROCKET MOTOR

AFOSR Grant F 49620-94-1-0042

Principal Investigator: D. R. Kassoy

Center for Combustion Research
Mechanical Engineering Department
University of Colorado
Boulder, CO 80309

SUMMARY/OVERVIEW:

Numerical and analytical modeling methods are used to predict the transient flow dynamics in a solid rocket motor chamber model. Prescribed time-dependent sidewall mass addition is used to simulate irregular burning rates that characterize motor instabilities. The flow field consists of co-existing, equal magnitude acoustic (irrotational) and vorticity (rotational) fields present across the entire diameter of the cylindrical chamber. Numerical flow data is analyzed using turbulent flow techniques to capture the impact of the intense, transient vorticity dynamics. The numerical methods are evaluated for impact of artificial diffusion on the solutions. Finally, nonaxisymmetric boundary forcing is used to establish asymmetric, three-dimensional flow in a model chamber. Results of an asymptotic analysis show that such a flow is confined to limited spatial regions.

AUTHORS: D. R. Kassoy, T. Y. Chang, P. Staab, and A. M. Hegab

OBJECTIVES:

1. Describe the initiation and evolution of unsteady vorticity in a model of a solid rocket motor chamber: a low Mach number internal flow sustained by sidewall mass addition into a cylinder with transients driven by a time dependent injection velocity that mimics propellant burning rate variation, including the effect of non-axisymmetric boundary conditions.

2. Demonstrate that vorticity is created on the sidewall by an inviscid interaction between axail acoustic waves (axial acoustic pressure gradient) and the distributed injected fluid, and is then convected into the cylinder by the radial component of th injected velocity field.

3. Show that weakly nonlinear axial convection and radial diffustion (due to viscosity) affect the time and spatial dependence of the vorticity distribution.

4. Develop solutions from an initial-boundary value analysis based on the complete equations of motion for a compressible fluid (like a direct numerical simulation based on the Navier Stokes Equations).

5. Find the amplitude of the shear stress on the wall.

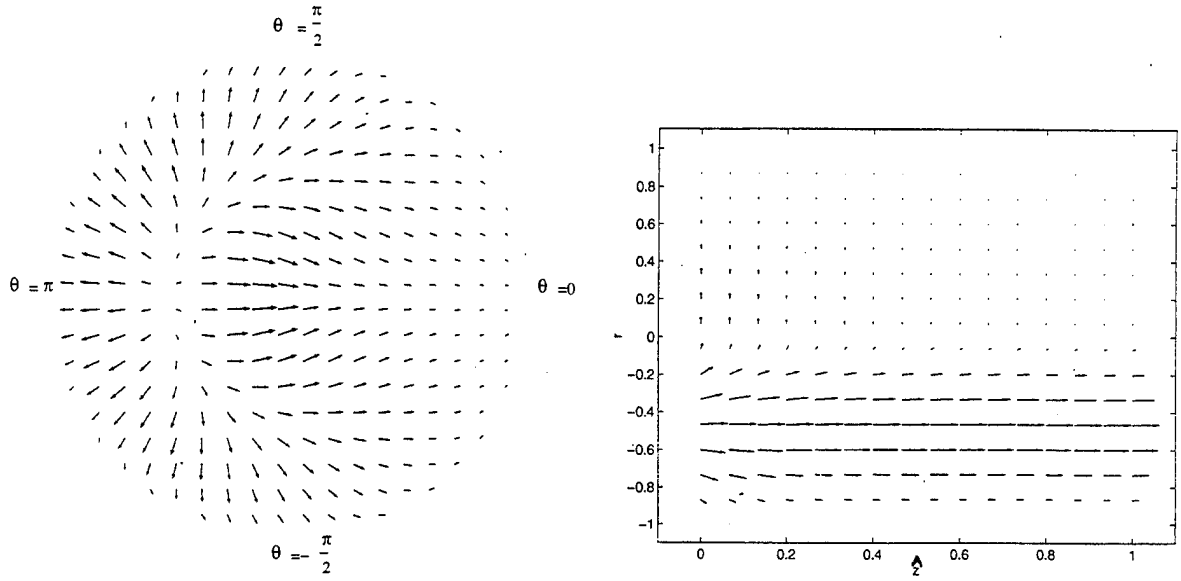

Figure 1: The figure on the left is a velocity vector diagram in a cylinder cross section close to the endwall, where the condition $V_z = 16r^2(1-r)^2 \sin^2(\frac{\theta}{2})$ is imposed. The figure on the right shows a vector diagram on a plane defined by the diameter between $\theta = 0$ and $\theta = \pi$, for the same endwall condition.

I. Most studies of rocket motor flow dynamics are focused on the behavior and impact of axial acoustic disturbances. In principle, azimuthally dependent, time varying burning rates could be the source of non-axisymmetric acoustic disturbances that initiate three dimensional motor chamber flow transients. Sabnis et. al (1989) develop a three-dimensional numerical solution to a turbulent flow model, driven by an imposed non-axisymmetric pressure disturbance on a cross section of a long, narrow cylinder. The results show that the nonaxisymmetric portion of the flow is found only within two diameters from the cross section on which the pressure disturbance is imposed.

Staab and Kassoy (1996), model non-axisymmetric unsteady flow in a cylindrical solid-rocket chamber with uniform sidewall mass injection and a non-axisymmetric endwall condition on the axial velocity. Asymptotic analysis, similar to that of Zhao et al. (1995) and Zhao (1994) is used for solution development.

The flow at a few multiples of the radius downstream from the closed endwall is always characterized by axisymmetric properties. A three-dimensional flow transition layer exists between the downstream axisymmetric regime and the endwall. The unsteady components of the radial and azimuthal velocities vanish at the edge of the layer as does all r and θ dependence of the axial velocity and pressure. The basic result is in excellent agreement with that described by Sabnis et. al., (1989). The results in Figure 1 show the three dimensional character of the flow in the cross sectional plane, and on a plane that cuts the cylinder in the axial direction along a diameter. Figure 1–left shows that the flow is symmetric across a line between $\theta = 0$ and $\theta = \pi$, also there is flow from the left to right side of the cylinder. The source of the flow is located at the position of the maximum of the endwall condition. Figure 2–right, shows that there is flow across the centerline from the bottom to the top. Near the line $\hat{z} = 1$, only an axial velocity is present because non-axisymmetric effects decay rapidly.

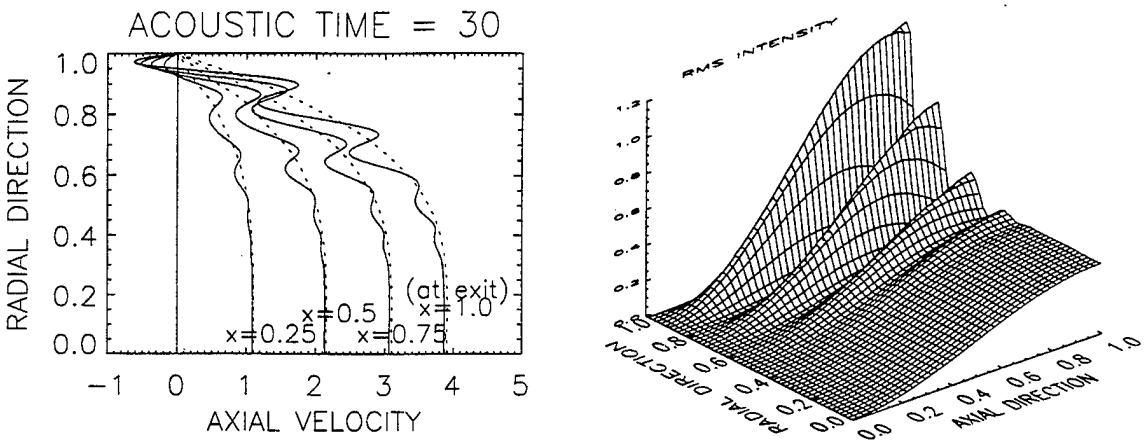

Figure 2: The figure on the left shows a radial profile of axial velocity at four different axial locations. The dotted lines are mean velocity and the solid lines are instantaneous velocity. The figure on the right shows the RMS axial velocity fluctuation intensity defined as $[< (u'_p + u'_v)(u'_p + u'_v) >]^{1/2} = [< u'_p u'_p > +2 < u'_p u'_v > + < u'_v u'_v >]^{1/2}$, where u'_p is the pure acoustic fluctuation velocity, u'_v is the pure rotational fluctuation velocity, and $<>$ denotes the time averaging.

II. High Reynolds number flow inside a long narrow circular cylinder with transient sidewall injection can have turbulent characteristics. Beddini (1986), Beddini and Roberts (1988), and Sabnis et al. (1989) provide numerical solutions for turbulent flow models. In this regard, it is interesting to employ turbulence statistical methods to analyze numerical results obtained from the compressible, axisymmetric time-dependent Navier-Stokes equations. Both mean and instantaneous velocity fields are computed in addition to the fluctuation intensity. The left side of Figure 2 shows a comparison of the radial profiles of the mean and instantaneous axial velocity at four different axial locations after thirty acoustic times scales (based on the cylinder length) have elapsed. The instantaneous velocity differs considerably from the mean velocity. For instance, one finds reverse flow near the wall. The configuration shown suggests the existence of a large scale circulation in the instantaneous flow field. The spatial fluctuations shown on the left side in Figure 2 are due to the interaction of axial acoustic waves with the fluid injected from the sidewall. Transient vorticity is generated at the sidewall due to the interaction. The magnitude of the fluctuation is larger at the downstream locations. The shear of the instantaneous flow field near the wall is much larger than the shear of the mean flow, which may be an important parameter for combustion processes near the sidewall.

The right side of Figure 2 shows the fluctuation intensity of the axial velocity as a function of radial and axial location. The axial fluctuation intensity can be decomposed into three parts: pure acoustics, acoustic-rotational interaction, and pure rotational. The ramp-like surface near $r = 0$ shows the contribution from the pure acoustics alone. Contributions from the interaction effect and the pure rotational effect, of similar magnitude, are responsible for the corrugated surface.

III. Analytical solutions for the acoustic component of the transient flow in a model rocket motor chamber are composed of a forced response to boundary driven disturbances and an eigenfunction response, Zhao (1994). Numerical solutions to quite similar initial-boundary value problems appear to include only the forced component (Vuillot and Avalon

(1991), Smith et al. (1993), Kirkkopru et al. (1996), for example). Careful analysis of our own numerical work indicates that additional frequencies are present briefly, but are damped out over a few acoustic time periods. The damping mechanism, whether from real or numerical viscosity, or accumulated nonlinear effects has not been definitively identified. This issue has been addressed for a simple model problem; axial acoustic waves in an impermeable cylinder wall, with an oscillating piston at one end and a pressure node at the other. The large acoustic Reynolds number flow for a high aspect ratio cylinder is described in terms of an inviscid acoustic core and a thin, traditional viscous, acoustic boundary layer adjacent to the sidewall. The analytical solution for the acoustic field includes both a nonresonant forced mode and eigenfunctions. A weakly nonlinear analysis shows that no damping of eigenfunctions occurs from convective or axial viscous effects. Numerical solutions to the planar, linear acoustic wave equation, and to the one and two-dimensional Euler equations are nearly identical to the analytical results. This confirms that nonlinear convective terms are not a source of eigenfunction damping, and that the MacCormack code employed for solution development of the Euler equations has little numerical viscosity. In contrast, considerable eigenfunction damping occurs in high Reynolds (Re) solutions to the two-dimensional, parabolized Navier-Stokes equations. The characteristic damping time increases with increasing values of Re, while the thickness of the acoustic boundary layers decrease. However, the latter are thicker than those in the analytical theory and grow in an unphysical way with increasing computation time. These results suggest that transverse viscous effects are responsible for eigenfunction damping, and that accumulated numerical diffusion will overwhelm the real physics of the flow when sufficient time has elapsed. These concepts are being used to reevaluate the numerical methods in Kirkkopru et al. (1996) for the study of sidewall injected flows. There, real viscous effects are more important because a mean shear flow exits.

REFERENCES

1. Beddini, R. A. 1986, *AIAA J.*, **24**, 1766-1773.
2. Beddini, R. A. and Roberts, T. A. 1988, *AIAA J.*, **26**, 917-923.
3. Kirkkopru, K., Kassoy, D. R., and Zhao, Q. 1996, accepted for publication in *J. Prop. Power.*
4. Sabnis, J. S., Gibeling, H. J., and McDonald, H. 1989, *J. Prop. Power*, **5**, 657-664.
5. Smith, T. M., Roach, R. L., and Flandro, G. A. 1993, *31st Aerospace Sciences Meeting,* AIAA 93-0012.
6. Staab, P., Kassoy, D. R., 1996, in preparation.
7. Vuillot, F. and Avalon, G. 1991, *J. Prop. Power*, **7**, 231-239.
8. Zhao, Q. 1994, *Ph.D. Thesis*, Dept. of Mechanical Engineering, Univ. of Colorado at Boulder.
9. Zhao, Q., Kassoy, D. R., Kirkkopru, 1995, submitted, *J. Fluid Mech.*.

INVESTIGATION OF ACTIVE CONTROL OF COMBUSTION INSTABILITIES IN CHEMICAL ROCKETS

AFOSR Grant No. F49620-93-1-0177

Principal Investigators

Dr. Ben T. Zinn, David S. Lewis Jr. Chair and Regents' Professor
Mr. Brady R. Daniel, Senior Research Engineer
Dr. Yedidia Neumeier, Research Engineer

School of Aerospace Engineering
Georgia Institute of Technology
Atlanta, GA 30332

Summary/Overview

This program investigates active control of detrimental combustion instabilities in chemical rockets. The investigated active control system (ACS) identifies the characteristics of the unstable combustor modes in real time, provides each mode with a gain and a phase delay, and sends a control signal to a fuel injector actuator that modulates the injection rate of a secondary fuel stream into the combustor, thus generating combustion process heat release oscillations that damp the instability. To damp the instability, the generated heat release oscillations must be out of phase with the unstable combustor pressure oscillations. To generate such heat release rate oscillations, the frequency response of the fuel injector actuator must be known. The latter has been determined in open loop control tests, incorporated into the ACS controller and used in closed loop control of combustion instabilities in the developed rocket motor. This study has demonstrated that the developed ACS effectively damps large amplitude instabilities within periods of the order of 40 milliseconds, which is considerably faster than any known ACS. This study showed that the damping is optimized when the secondary combustion heat release and combustor pressure oscillations are 180 degrees out of phase. Finally, the open loop studies showed that the effectiveness of the ACS actuator strongly depends upon the design of the primary injection system and location of the secondary fuel injection.

Technical Discussion

This program consists of parallel theoretical and experimental investigations whose goal is to develop the fundamental knowledge needed for active control of combustion instabilities in chemical rockets. Such instabilities are generally driven by a periodic combustion process whose oscillations are in phase with the combustor pressure oscillations, in agreement with Rayleigh's criterion. The operation of a rocket motor becomes unstable if the driving provided by the combustion process is larger than the damping inherently present within the system due to, for example, viscous dissipation and nozzle wave transmission/reflection processes. The processes responsible for the establishment of a periodic combustion process generally involve complex interactions between the combustion process, flow and acoustic oscillations within the combustor, which depend upon the rocket motor design and operating conditions. Since the onset of combustion instabilities generally results in system and/or mission failure, engineers have been searching for decades for effective approaches for stabilizing combustors of chemical rockets and other propulsion systems. To date, passive approaches have been primarily used to damp combustion instabilities with limited success. The present study investigates whether a practical

active control system for stabilizing rocket motors, which utilizes recently developed electronics, computers, sensors and actuators, can be developed.

Rayleigh's criterion indicates that acoustic oscillations are driven or suppressed when heat is added in or out of phase with the local combustor pressure oscillations, respectively. This suggests that combustion instability oscillations could be damped if effective means for generating heat addition oscillations out of phase with the combustor pressure oscillations could be developed. Active control of combustion instabilities investigated to date[1] utilized a time domain control approach and focused on the damping of combustion instabilities consisting of the fundamental longitudinal mode or, at most, a combination of low frequency longitudinal modes. Moreover, the application of these methods required apriori knowledge of the characteristics of the unstable modes. In reality, the characteristics of the instability are not known in advance, and they often change with time in response to changes in rocket motor operating conditions.

The ACS investigated under this program overcomes the limitations of other ACS. It consists of a pressure transducer, an observer, a controller and an actuator. The pressure transducer monitors the combustor's performance by continuously measuring its pressure. The measured pressure is transmitted to the observer, where it is analyzed to determine, in virtually real time, the frequencies, amplitudes and phases of the unstable combustor modes. These data are sent to the controller where appropriate phase shift and gain are added to each mode. The modified modes are then synthesized into a control signal, which is sent to an actuator consisting of a fuel injector capable of modulating the injection rate of a secondary fuel stream into the combustor. The novel features of this ACS are: 1. the application of Rayleigh's criterion to guide the operation of the ACS, 2. the observer's algorithm that determines the characteristics of the unstable combustor modes in real time, 3. the controller that provides each mode with an appropriate phase shift and a gain that generates combustion process heat release oscillations out of phase with the unstable combustor pressure modes oscillations, thus damping the instability, and 4. the actuator that can generate large amplitude fuel injection rate oscillations over a wide frequency range.

The feasibility and performance of the developed active control method were initially investigated theoretically assuming that the flow in the combustor can be modeled by the one dimensional, nonlinear, Euler equations. The driving of the instability by the combustion process was modeled by means of a simple linear feedback between the pressure and combustion process heat addition oscillations. The unstable combustor model was then "equipped" with the developed ACS and the resulting system of equations was solved to investigate the effectiveness of the ACS. Numerical simulations showed that the developed ACS can rapidly damp various combustion instabilities including, for example, combustor acoustic mode oscillations with amplitudes equaling twenty five percent of the mean combustor pressure, which were damped out within a few milliseconds of "activating" the controller.

Continued theoretical studies led to the development of a heuristic model of an unstable combustor. It includes a phenomenological mixing model that accounts for the mixing of the reactants with the hot combustion products and the mixing of the secondary, control, fuel stream with the combustor gases. Once a combustible mixture is formed, its reaction and heat release rates are controlled by Arrhenius type kinetics. These efforts also improved the numerical representation of the injector face and nozzle boundary conditions, and modified Roe's Rieman scheme to properly account for the presence of sources (e.g., heat addition) in the model conservation equations.

The experimental efforts developed a small scale, actively controlled, gas rocket motor, which was used to investigate the open loop performance of the ACS and closed loop control of combustion instabilities. It consists of a primary reactants feed system, a combustor section with windows for combustion process visualizations and optical diagnostics, and an ACS. During testing, the combustor is cooled in a running water bath. The combustor has a large length-to-diameter ratio to prevent the excitation of transverse and three dimensional instabilities. The

1. Gutmark, E., Wilson, K. J., Parr, T. P. and Schadow, K. C., Feedback Control of Multi-Mode Combustion Instability, AIAA Paper 92-0778, 30th Aerospace Sciences Jan. 1992, Reno, Nevada.

combustor length can be changed to permit investigation of active control of axial instabilities having different frequencies.

Open loop control studies were conducted to: 1. determine whether the fuel injector actuator can excite combustion process heat release and pressure oscillations with amplitudes capable of destructively interfering with the processes that drive combustion instabilities, and 2. determine the frequency dependence of the phase and amplitude of the driven combustion process heat release oscillations. The first objective was met earlier under this program. The second objective was pursued by developing two different approaches for measuring the frequency dependence of the secondary combustion process response. The first approach used a short combustor whose fundamental mode frequency was above the upper limit of the investigated frequency range. The pressure excited in this combustor under different, open loop, excitation conditions was related to the combustion process response using analytical expressions derived from a linear model of the combustor behavior. The second approach determined the combustion process response from global CH radicals radiation from the combustion zone. Figure 1 compares the two combustion process responses, which were determined using different approaches in different combustors, and it shows that the two are in excellent agreement. This excellent agreement between the measured combustion process responses strongly suggests that the secondary combustion process response is not strongly dependent upon the combustor's acoustics.

The phase and gain data presented in Fig. 1 were incorporated into the ACS controller and used to determine the phase and gain that must be added to each unstable combustor mode to generate heat release oscillations out of phase with the unstable combustor modes. Subsequent tests, using the measured open loop results, showed that the developed ACS effectively damps large amplitude combustion instabilities. The combustor pressure, actuator control signal and observed frequency measured in a typical test before and after activation of the ACS are described in Fig. 2. In this test, the ACS was set to damp (i.e., control) the dominant mode only. The development of a large amplitude instability was "monitored" by the observer before activating the

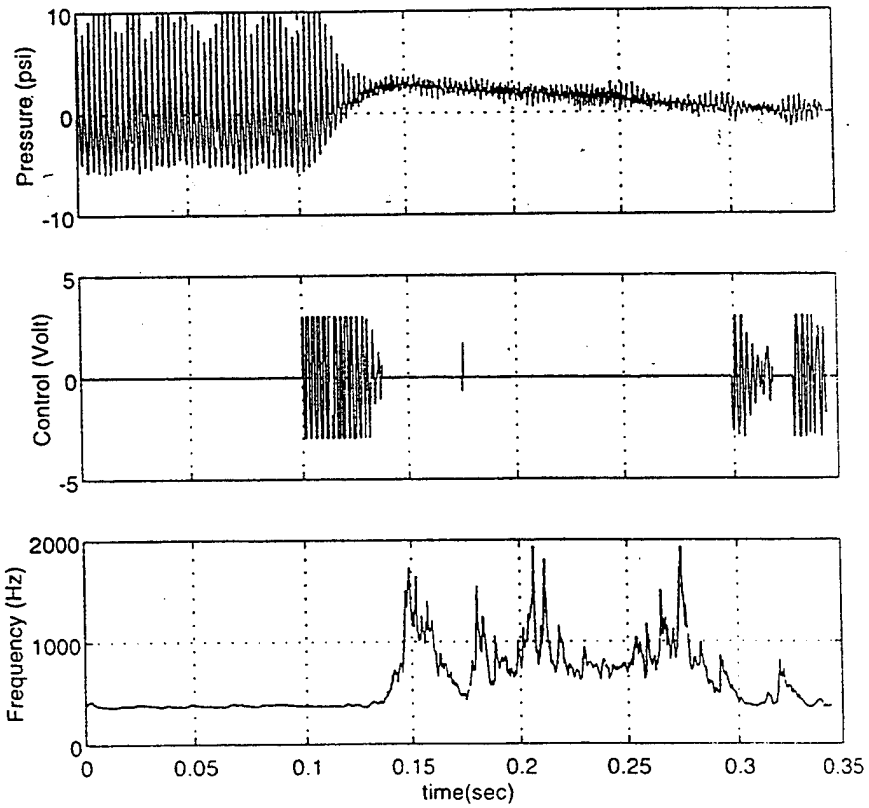

Figure 1. Time dependence of the pressure, control signal and observed frequency before and after the activation of a closed loop control of the instability in a gas rocket

control system at t=0.1 seconds to determine the frequency of the most unstable mode. Subsequently, the ACS was activated whenever the difference between the observed frequency and that of the "most" dominant mode (i.e., 370 Hz.) was smaller than a certain specified (small) number. The ACS was activated by changing the value of the gain assigned by the actuator's control signal from zero to a gain value provided in Fig. 1 at the 370 Hz., which was the frequency of the dominant mode of the instability, see Fig. 2. This required the controller to "remember" the frequency of the dominant mode before activating the ACS and to respond only when this mode became dominant, thus leaving other modes uncontrolled.

Figure 2-a shows that the ACS effectively damped the instability in 40 milliseconds, indicating that it could damp rocket instabilities before they would seriously damage the engine and/or cause mission failure. FFT analysis of the combustor pressure oscillations before and after the activation of the ACS showed that the amplitude of the dominant mode was reduced by 26 dB., which exceeds the performance of ACS investigated elsewhere. Figure 2-b describes the time dependence of the control signal to the actuator, which is proportional to the magnitude of the control signal gain. Figures 2-b,c show that the control signal goes to zero whenever the 370 Hz. dominant mode is damped by the ACS. When this occurs, the observer identifies the 740 Hz. harmonic as the dominant mode and stops controlling the 370 Hz. mode, see Fig. 2-b. Consequently, the unstable 370 Hz. mode starts growing again. When its amplitude exceeds that of other unstable modes (e.g., the 740 Hz. mode), the observer identifies this mode again as the dominant mode and turns on the actuator. This sequence of events continuously repeats itself, resulting in effective damping of the dominant 370 Hz. mode (and instability!), while not destabilzing other modes of the combustor.

The results of this program provide fundamental information needed for developing practical and effective ACS for unstable chemical rockets and related propulsion systems.

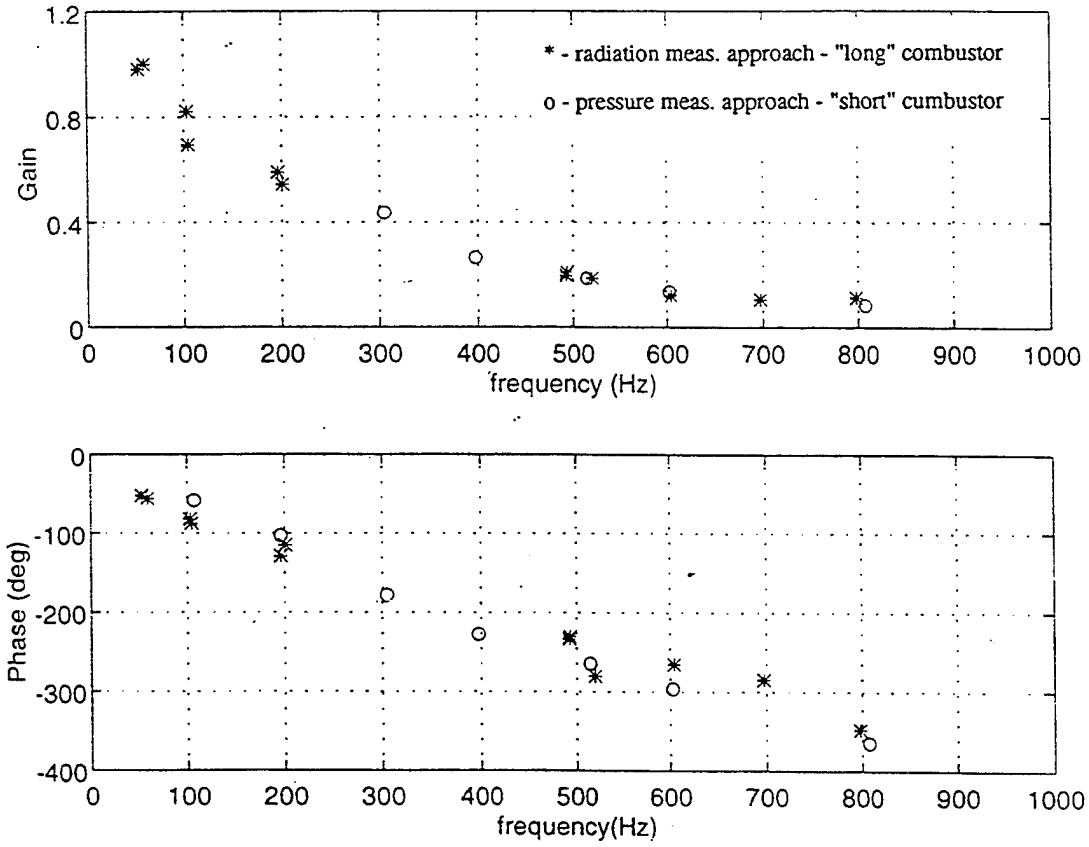

Figure 2. Comparisons of the frequency dependence of the amplitude and phase of the heat release oscillations produced by the fuel injector actuator obtained using pressure data measured in the short combustor and direct CH radiation measurements in the long combustor.

MODELING AND ACTIVE CONTROL OF NONLINEAR UNSTEADY MOTIONS IN COMBUSTION CHAMBERS

AFOSR Grant Contract No. F49620-95-1-0272

Principal Investigator: F. E. C. Culick

207 Guggenheim Bldg., M/S 205-45

California Institute of Technology

Pasadena, CA 91125

Summary

This program began 1 April 1995, comprising chiefly analysis concerned with fundamental problems arising with unsteady motions in combustion chambers. Particular emphasis is placed on matters relating to possible active control of combustion systems. We believe that considerable progress is required in order to reach a level of basic understanding sufficient to explain observed behavior and to provide the foundation for more rational design and application of active control. The main subjects addressed are linear and nonlinear acoustics; oscillations in the presence of noise; modeling nonlinear combustion processes; and active control of combustion systems in which significant nonlinearities and time lags exist. The last item really comprises problems of combustion and fluid mechanics particularly significant when control is to be exercised. During the past year we have carried out some tests with a dump combustor illustrating a tactic of nonlinear control of oscillations based on hysteretic behavior previously observed in the combustor. We have shown how the region of stable combustion can be extended to lower equivalence ratios by injecting a small number of discrete pulses of secondary fuel in the recirculation zone.

Technical Discussion

Control of a combustion system poses special circumstances not arising in most other situations, for at least four reasons: (1) when a combustion system is controlled, the parameters defining its state (e.g. the distribution of energy release) normally change and there are usually significant parametric uncertainties; (2) control must be exerted on a system containing substantial internal noise, a fundamental difference from the usual situations treated by control theory, in which only external disturbances and sensor noise are accounted for; (3) particularly in problems of combustion instabilities, the required bandwidth of the control system may be much greater than those in

conventional applications; and (4) because flow is involved, the system may contain significant time lags, a feature common in problems of process control but not often an important feature of mechanical systems. Moreover, the unsteady motions in a combustion system are 'self-excited' due to the internal energy release, so instabilities reach limiting amplitudes only due to the action of one or more nonlinear processes. Thus, these systems are intrinsically nonlinear, but the extent of the influence of that property on practical use of active control is presently unknown.

How actuation is to be accomplished with an active control system poses very special problems for a combustion system. Following the successful practice in active control of noise by making use of destructive interference, most laboratory demonstrations of active control of combustion systems have used loudspeakers as actuators. A few have used actuation of the fuel supply, which seems the most likely strategy for applications to large scale operational systems having high densities of energy release. In the program followed here, both types of actuation are accommodated, but for practical purposes we assume the second form thereby linking intimately the problems of modeling combustion processes and of designing a control law.

The work covered by this program is largely theoretical, with appeal to experimental results available from other research programs at Caltech and other organizations. During the past year, the experimental effort has grown, for reasons given below. The foundation for the analysis is essentially a form of Galerkin's method, expansion in normal modes of the pressure field in the chamber, an approach effectively used for many years by the Principal Investigator and his colleagues, for analyzing linear and nonlinear combustion instabilities in propulsion systems. The methods used rely heavily on recent developments in the theory of nonlinear systems, involving particularly the application of a continuation method and bifurcation theory to computations of nonlinear acoustics. In the current program, an essential extension is the inclusion both of nonlinear combustion processes and of random processes to approximate more closely the actual behavior in combustion chambers. That extension requires investigation of nonlinear stochastic differential equations. It is within that general context that the subject of active control will be investigated.

The methods and procedures forming the basis of the proposed work have been described recently in several papers (Culick et al. 1991; Culick and Yang 1992; Culick 1994; Jahnke and Culick 1994 and most recently in a Ph.D. thesis, Burnley 1996). A formulation of the general problem of unsteady motions in a combustion chamber has been constructed in such a form as to accommodate linear and nonlinear behavior in any practical geometry with any of the sorts of reactants commonly used.

Theoretical/analytical work has been progressing in roughly three principal directions: (1) influences of nonlinear combustion responses on combustion

instabilities; (2) influences of noise on combustion instabilities; (3) and some aspects of active control of instabilities.

1) Influences of Nonlinear Combustion Response on Combustion Instabilities

A significant problem, particularly for solid and liquid propellant rockets consists in determining the conditions under which a linearly stable motor is nonlinearly unstable, i.e. a sufficiently large pulse will evolve into a stable limit cycle. Work spread over more than fifteen years has established the conclusion that this kind of "triggering" cannot be explained as a consequence of nonlinear gasdynamics. Previous numerical analysis (Levine and Baum) had suggested that nonlinear 'velocity-coupled' combustion contains pulsed instabilities. During the past year, Burnley (1996) has shown that velocity coupling, with a threshold velocity, may act together with nonlinear gasdynamics to give nonlinear instabilities.

2) Influences of Noise in Combustion Instabilities

Culick et al (1991) first published some results for combustion instabilities with stochastic sources. The approach, based on a Monte Carlo method has been extended to be applicable to any geometry, accounting for many modes, and has been applied to the case of nonlinear velocity coupled instability. A few results have been obtained for some influences of noise on pulsed instabilities.

3) Active Control of Unsteady Motions in Combustion Chambers

Our work in this subject is motivated by our belief that the motions in a combustor necessarily involve time delays and nonlinear behavior. An unstable linear system with time delay is known in classical control theory to be nearly uncontrollable except in narrow ranges of parameters characterizing the system. This suggests that successful demonstrations of controlled instabilities in combustions may in fact involve nonlinear behavior not accommodated in existing analyses or interpretations of data. This possibility is being pursued, to date only in the initial stages. We are also engaged in some separate analyses applying robust control and application of adaptive control.

During the past year we have also succeeded in demonstrating experimentally what we believe is the first clearly nonlinear control strategy (Knoop, Culick and Zukoski, 1996). The idea is based on the hysteresis discovered twenty years ago in work at Caltech on a dump combustor supported by AFOSR fulnding. The 'boundary' for stability of oscillations, determined by changing the equivalence ratio ϕ the reactants, is not sharp as one would find for true linear instabilities. On the contrary, when ϕ is increased from low values, oscillations occur at a value ϕ_1 larger than the value ϕ_2 at which the

oscillations cease when the equivalence ratio is reduced. In the range $\phi_2 < \phi < \phi_1$ a hysteresis loop exists. The lower branch contains nearly quiescent states and the upper branch consists of stable limit cycles. We have shown that injecting pulses of secondary fuel in the recirculation zone, or in the upstream shear layer, will cause the transition from the upper to the lower branch, thereby stabilizing the system. The lower branch is stable unless sufficiently large pulses are injected, a clear case of 'triggered' instabilities.

References

Burnley, V. (1996) "Nonlinear Combustion Instabilities and Stochastic Sources," Ph.D. Thesis, Department of Aeronautics, California Institute of Technology.

Culick, F. E. C. (1994) "Some Recent Results for Nonlinear Acoustics in Combustion Chambers," *AIAA Journal*, Vol. 32, No. 1, pp. 146-169.

Culick, F. E. C. and Yang, V. (1992) "Prediction of the Stability of Unsteady Motions in Solid Propellant Rocket Motors," Chapter 18 in *Nonsteady Burning and Combustion Stability of Solid Propellants*, Progress in Astronautics and Aeronautics (L. de Luca, E. W. Price, and M. Summerfield, Eds.).

Culick, F. E. C., Paparizos, L., Sterling, J. D., and Burnley, V. (1991) "Combustion Noise and Combustion Instabilities in Propulsion Systems," *Proceedings of the AGARD Conference on Combat Aircraft Noise*, AGARD CP 512.

Jahnke, C. C. and Culick, F. E. C. (1994) "Application of Dynamical Systems Theory to Nonlinear Combustion Instabilities," *J. Propulsion and Power*, Vol. 10, No. 4, July-August 1994.

Kim, J. S. and Williams, F. A. (1994) "Effects of Nonhomogeneities on the Eigenmodes of Acoustic Pressure in Liquid-Propellant Rocket Engines," submitted for publication.

Knoop, P., Culick, F. E. C. and Zukoski, E. E. (1996) "Extension of the Stability of Motions in a Combustion Chamber by Nonlinear Active Control Based on Hysteresis," submitted for publication to *Combustion Science and Technology*.

Zinn, B. T., Daniel, B. R., and Neumeier, Y. (1994) "Investigation of Active Control of Combustion Instabilities in Chemical Rockets" School of Aerospace Engineering, Georgia Institute of Technology, AFOSR.

4/26/96

HOLOGRAPHIC TECHNIQUES FOR MEASUREMENTS AND VISUALIZATION IN LIQUID PROPELLANT ATOMIZATION

AFOSR Grant No. F49620-95-1-0323

Principal Investigator : Prof. Dimos Poulikakos

Department of Mechanical Engineering
University of Illinois at Chicago
842 W. Taylor St.
Chicago, IL 60607-7022

SUMMARY

This research project aims at the development and automation of non-intrusive holographic techniques for measurements and visualization of liquid atomization processes relevant to rocket propulsion, including atomization in a high pressure and temperature environment. The specific application, which will be investigated simultaneously with developing and testing various aspects of the techniques, is impinging jet atomization under high pressure, reaching transcritical and supercritical conditions. During the first year of the research, a considerable amount of the effort was dedicated to the design and construction of the facility for the high pressure and temperature experiments. The construction of the high pressure facility is completed. Major components designed and fabricated include a high temperature and pressure chamber and an integrated liquid nitrogen impinging spray injector. The chamber has been designed to safely withstand up to twice the critical pressure of liquid nitrogen at the high temperature condition of 500K. In addition, by employing an already available facility, a series of experiments was performed on impinging jet atomization in a high temperature environment at atmospheric and moderate pressures. Finally, progress was made in the development of the image processing software for droplet size analysis and velocity measurements that will aid the automation of the technique.

TECHNICAL DISCUSSION

1. High Pressure Facility

Figure 1 is the schematic of the just fabricated high temperature high pressure chamber assembled with the impinging jet injector for the study of transcritical cryogenic impinging jet sprays. The cylindrical chamber is made out of 304 stainless steel. It has a 6 inch inner diameter and it is 10 inches tall. Four rectangular window openings of 1.6 inches in width by 5.0 inches in

length with round corners are positioned at four sides of the chamber. A 1.5 inch thick clear fused quartz glass window is installed in each of the four window openings to provide optical access from different directions. The self sealing method has been applied in the windows. To this end, the high pressure in the chamber is utilized as the sole force to hold the windows uniformly against the graphite gaskets on the sitting area of the window covers. Therefore, the windows are able to sustain the high pressure with the least stress concentration. Both O-ring and graphite gasket sealing methods are applied to seal the chamber. A K-type thermocouple is inserted from a hole of bottom cover into the center of the chamber to monitor the temperature. The high temperature inside the chamber is generated by four 600 watt, evenly distributed electric cartridge heaters. A well insulated ceramic cylindrical sleeve is used inside the chamber to confine the heat. The ceramic sleeve, which also has four quartz glass window openings for the optical measurements, is 7 inch long and 4 inches in inner diameter. In addition to providing quickly a more uniform temperature distribution in the impinging jet region, the insulation sleeve protects the quartz glass windows installed on the high pressure chamber from thermal shock, by preventing the splashing of the spray on these windows.

The impinging jet sprays are generated by the injector assembly inserted from the center hole on the top cover. Liquid nitrogen will be first stored in a 300 cc bottle. The bottle is connected to the injector and the nozzle by a cryogenic solenoid valve. When the liquid nitrogen stored in the bottle is pressurized by gas nitrogen to a desired pressure, the solenoid valve is activated and opened. The working fluid is ejected through the nozzle and forms the impinging jet spray. A thermocouple is placed near the nozzle in the injector to monitor the exit temperature of liquid nitrogen that forms the spray. The impinging jet nozzle is designed to be interchangeable so that the impinging angle can be varied from 40 to 90 degrees, and the jet orifice diameter from 1.0 to 1.5 mm.

2. *Image Processing Software*

Software for automatic processing of reconstructed holographic images is being developed for measurements in the spray. The software package applies both user defined threshold values and various edge detector techniques to identify effectively the droplets from the background noise. Different filtering algorithms and a special 'region growing' method are then utilized to eliminate the background noise without losing the droplet characteristics. The image is then processed automatically for droplet features such as area, centroid, orientation eccentricity et. al.. In addition, droplet velocity can be determined. When a pair of spray images, separated by a certain time interval is given, a droplet matching method has been developed to identify the positions of the same droplet in the two images. Vectors are drawn to indicate the positions. In the near future these vectors will be utilized for the automatic calculation of velocities.

3. Preliminary Results on High Temperature Atomization at Atmospheric Pressure

By employing an already available low and moderate pressure facility [1], a series of experiments was performed during the past year (while the high pressure facility was under construction) on impinging jet atomization in a high temperature environment at atmospheric pressure. Representative results are shown in Figs. 2-4. The terminology "top" and "bottom" regions indicates the regions near the impingement point and further downstream, respectively.

The experimental data for the top region of an ethanol spray at 25°C and the bottom region of a water spray at 250°C are compared to various distribution functions [2] in Figures 2a and 2b respectively. The deviation of the distribution functions from the experimental data in Figure 2a was largest for the cases examined, while the results of Figure 2b were typical. The universal root-normal distribution provided the best fit to the data over all cases examined. The deviation of the data from the distribution functions was greatest between a volume fraction of 0.75 and 0.95 for each of the cases. This phenomenon is potentially explained by the bimodal characteristics of impinging jet sprays that Heidmann et al. [3] first observed. Despite the slight deviation, the universal root-normal distribution still adequately represented the characteristics of the drop size distributions.

Figure 3 is a plot of the Sauter mean diameter and the mass median diameter in the upper and lower regions for ethanol. Each data point is a representative diameter taken from a sample size of at least 5,500 droplets. Both the Sauter and mass median diameters decrease with increasing temperature until it is well beyond the boiling point of each fluid. At a temperature of approximately 80°C beyond the boiling point of ethanol, both the Sauter mean diameter and the mass mean diameter for the upper region increase with temperature. This is attributed to the fact that at this point, the mean diameters are affected to a greater degree by evaporation and complete dissappearance of the smaller dropets, than the size decrease of the larger droplets. Therefore, while individual droplet sizes are steadily decreasing with temperature, the representative diameters increase over a short temperature span as a result of the disappearance of the smaller droplets. Eventually, the representative diameters begin decreasing with temperature again. The counter-intuitive trend of representative diameters increasing with increasing temperature illustrates the importance of presenting both a representative diameter and a size distribution parameter when analyzing sprays.

The velocity of a droplet was determined as the ratio of the absolute displacement of the centroid divided by the time interval between exposures. Figure 4 is the velocity vector field, for the dense region of an ethanol spray at 251°C. The velocity distribution indicates that the average velocity of the particles near the centerline of the spray is approximately equal to the mean velocity of the jets. As the azimuthal angle increases, the average velocity of the droplets decreases until an angle of 80° and beyond, where the average particle velocity is approximately half that of the mean

jet velocity. In addition, the direction of the droplet velocities tends to correspond to the azimuthal angle.

References

1. Y. Shen, C. Mitts and D. Poulikakos, "A Holographic Investigation on the Effect of Elevated Ambient Temperature on the Atomization Characteristics of Impinging Jet Sprays," *Atomization and Sprays,* to appear in 1996.
2. A. H. Lefebvre, Atomization and Sprays, Hemisphere Publishing Corporation, N.Y., 1989.
3. M. F. Heidmann and H. H. Foster, Effect of Impingement Angle on Drop-Size Distribution and Spray Pattern of Two Impinging Water Jets, National Aeronautics and Space Administration Rept., TN D-872, 1961.

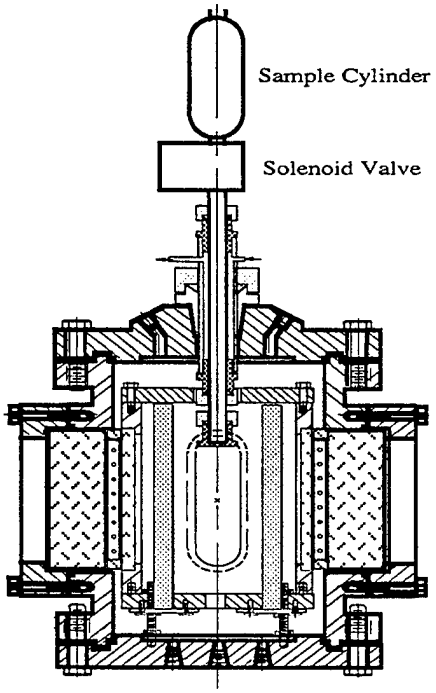

Figure 1 High Temperature High Pressure Chamber

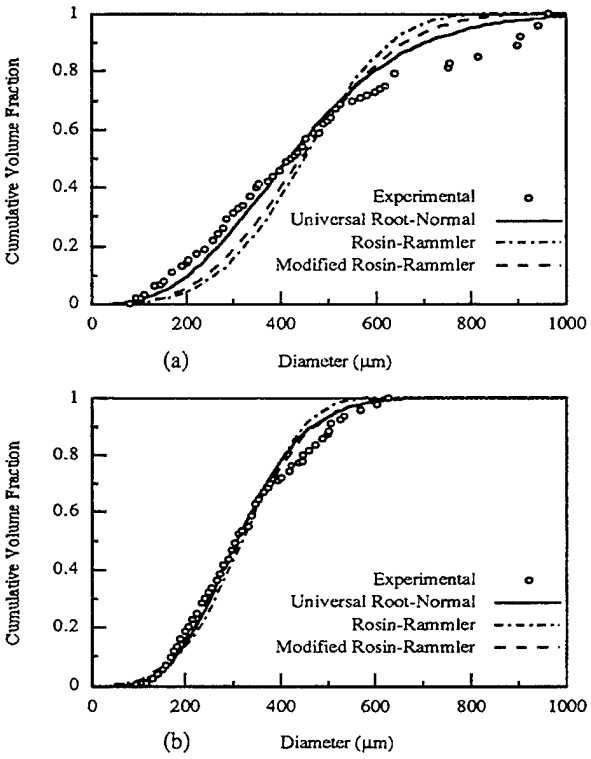

Figure 2 Comparison of experimental cumulative volume distribution with various distribution function for (a) the top region of an ethanol spray at 25°C and (b) the bottom region of a water spray at 250°C, D=0.8mm, θ=90°, V=12.5m/s.

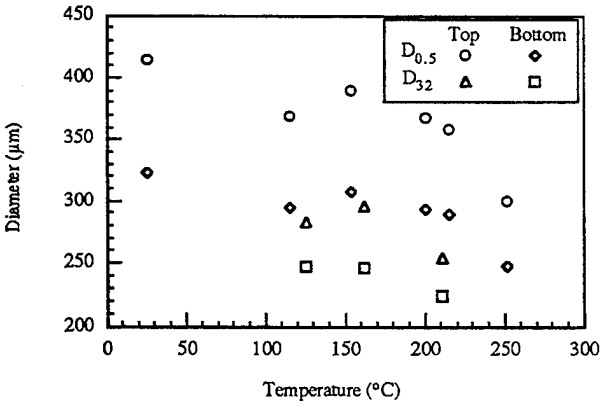

Figure 3 Variation of the representative diameters with temperature for ethanol sprays, D=0.8mm, θ=90°, V=12.5m/s.

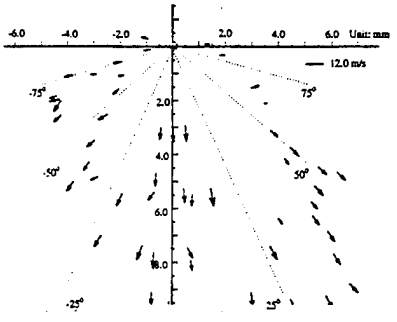

Figure 4 Velocity vector field of dense region ethanol spray. D=0.8mm, θ=90°, V=12.5m/s, T=251°C

MECHANISMS CONTROLLING SOOT FORMATION IN DIFFUSION FLAMES

AFOSR Contract F49620-94-C-0059

Principal Investigators: Meredith B. Colket and Robert J. Hall

United Technologies Research Center
Silver Lane, E. Hartford, CT 06108

SUMMARY/OVERVIEW:

The overall objectives from this work are to (1) refine and update a pyrolytic model which describes PAH formation; (2) modify and validate an opposed jet diffusion flame code which includes soot formation and radiation and then extend model predictions over a range of flame parameters, and (3) with assistance from Prof. M. Smooke, incorporate the soot formation and radiation models into a code for a coflow laminar, diffusion flame. Experiments and modeling on alkylated aromatics will help to minimize discrepancies between known PAH formation rates and those required to explain particle inception rates in flames. Validation (and modification as necessary) of the existing opposed jet flame code with data from ethylene flames will increase its reliability in predicting sooting conditions with other hydrocarbon fuels and inlet conditions.

PAH Formation and Modeling

Phenylacetylene and naphthalene are key intermediates to the formation of PAH and hence to the inception of particles in flames. Unfortunately, there is extremely little data or established chemical kinetic meechanisms describing the pyrolysis of these compounds for comparison to models used in soot formation flame codes. To provide some information on these compounds, we have performed a series of tests on the pyrolysis of phenylacetylene and with mixtures of allene and toluene. The co-pyrolysis of allene and toluene was investigated (see Ref. 1 for details) to provide a facile source of the benzyl and the propargyl radicals. Combination of these radicals (overall) was proposed in Ref. 2 to explain rapid formation of naphthalene during toluene pyrolysis; although definitive information on this postulated reaction could not be obtained in the earlier study of tolune pyrolysis, a rate constant of $6x10^{11}$ cc/mole/sec was estimated. As speculated for the copyrolysis, rapid formation of naphthalene at temperatures much lower than its formation during toluene pyrolysis was observed, as shown in Fig. 1. These results could not be explained by recombination of cyclopentadienyl radicals, which has been proposed as an alternative step to naphthalene formation. The rate constant determined for $C_7H_7+C_3H_3=>C_{10}H_8+2H$ was $5x10^{11}$ exp(-5000cal/mole/RT) cc/mole/sec, which is about six times slower than that estimated in the earlier study. Methylindene appears to be a likely intermediate and indene is probably a byproduct. Detailed chemical kinetic modeling over predicts the formation of biphenyl, until phenyl + biphenyl and analogous reactions were included in the mechanism to describe formation of triphenyl and other large PAHs.

New data has also been obtained on the pyrolysis of phenylacetylene; the results are generally similar to those of Ref. 3. Major products include diphenylethyne (and several isomers of mass 178), benzene, naphthalene, biphenyl, acenaphthylene, fluorene, and phenanthrene. This new, more complete set of data confirm a high phenanthrene/anthracene ratio observed previously (Ref. 1 and 3), and support recently proposed mechanistic routes (Ref. 1) for the formation of these species.

Modeling of Soot Formation in Diffusion Flames

Progress has been made in three areas associated with expanding the soot models described in Refs. 4 and 5. The work includes (1) refinement of the physical and chemical models describing soot formation, (2) development of an arclength continuation method for obtaining solutions of sooting, opposed jet diffusion flames over a wide variation in flow conditions, and (3) addition of the soot formation and radiation models to a coflow, laminar diffusion flame model.

Model refinement

Perhaps the largest uncertainties in present versions of our model are the flame chemistry, and specification of the particle inception and surface growth rates. It is fair to say that we can match any of the spatial distributions determined from opposed jet experiments (by first matching velocity profiles and) using exact or slightly modified literature expressions for inception or surface growth. As an example, comparisons of our model with data obtained on a Tsuji-type burner (by Axelbaum, et al., Ref. 6) is shown in Fig. 2 for flames in which the fuel is diluted with various levels of nitrogen. Full details of particle distributions, sizes, etc. as a function of axial coordinate are also available from the code. This work on selecting appropriate modeling parameters is continuing.

Arclength Continuation

Arclength continuation methods have been incorporated into an opposed jet soot prediction code with complex chemistry, detailed particle transport/kinetics, and radiation. This code greatly reduces the effort required to carry out variations in strain rates with opposed jet programs and can be modified to include variations in pressure and temperature of inlet gas streams, as well. Calculations have been carried out for the strain rate dependence of atmospheric pressure methane-air and ethylene-air counterflow diffusion flames and where possible, comparison to existing data sets have been made. For details, see Ref. 7.

Predicted peak volume fractions for methane and ethylene-air flames are shown in Fig. 3 as a function of a (modified) strain rate . Lower values in the methane flames and the rapid decline are consistent with the known difficulty of stabilizing a low strain rate, sooting methane-air flame, although these methane predictions are believed to be slightly low. The fast in the methane flames is consistent with the fact that methane flames extinguish at a much lower strain rate than do the ethylene flames. Predictions for the ethylene flames are consistent with experimental measurements of the variation in volume fraction strain rates as measured by Vandsburger, et al. (Ref. 8) for a Tsuji-type burner and by Wang, et al. (Ref. 9) in an opposed jet configuration. Because of the different burner types and strain rate definitions, a one-to-one correspondence between the strain rates used in this work and those for the Tsuji data should not be made; instead the trend with varying strain rate is the important feature. By matching velocity profiles and by modifying the inception rate, the spatial distribution and magnitudes of the soot volume fractions as reported recently in Ref. 9 can be almost perfectly reproduced. Also shown in Fig. 3 are predictions utilizing the inception and surface growth expressions as

suggested by Fairweather, et al. (Ref. 10). The general trend (variation in peak volume fraction) is identical to our model, although the magnitudes are much lower. A goal of this effort is to identify a model that explains not just one set of data but is universally applicable to different fuels, inlet temperatures, pressures and for both diffusion and premixed flames.

Perhaps the most surprising feature of these results is that predicted soot volume fractions varied gradually (at least on a log scale) with strain rate and that finite levels of soot were present all the way to flame extinction. Peak concentrations of key growth species are provided in Fig. 4. As can be seen, the concentrations fall much more gradually (at least for ethylene) with increasing strain than does the peak volume fraction and, hence, the changes in these concentrations is not the principal reason for the very rapid fall-off in the soot volume fraction. An examination of particle oxidation effects and of temperature changes suggest that these phenomena while contributing are also not the principle reason for the rapid fall-off in the soot volume fraction. For strain rate variations from 35 sec^{-1} to 1225 sec^{-1} for the ethylene flame, the residence time in the hot section of the flame decreases by a factor of 35. This parameter is likely the largest contributor to the fall-off in soot volume fraction with increasing strain rate.

Coflow model

A previously developed (Ref. 11) coflow, laminar diffusion flame model with full detailed chemistry has been modified to include soot formation and optically thin radiation. The code is in an advanced state of debugging with the aim of comparing predictions to data obtained by Professors R. Santoro (for ethylene) and L. Pfefferle (for methane).

References

1. M. Colket, "Rapid Naphthalene Production from Allene and Toluene," presentation to the Eastern States Section of the Combustion Institute, Oct. 16-18, 1995.
2. M. Colket and D. Seery, Twenty-Fifth Symposium (International) on Combustion, The Combustion Institute, Pittsburgh, p. 883 (1995).
3. K. Guthier, P. Hebgen, K.H. Homann, J. Hofmann, and G. Zimmermann, "Addition and Cyclization Reactions in the Thermal Conversion of Hydrocarbons with Ethyne Structure, II. Analysis of Radicals and Carbenes from Ethynylbenzene, in press, 1995.
4. M. Colket and R. Hall, Proceedings of the International Workshop on Mechanism and Models of Soot Formation (H. Bockhorn, Ed.), Springer-Verlag, Heidelberg, (1994).
5. R. Hall, M. Smooke, and M. Colket, "Predictions of Soot Dynamics in Opposed Jet Diffusion Flames", Combustion Science and Technology Book Series (1995).
6. R. Axelbaum, W. Flower, and C. K. Law, Comb. Sci.Tech., **61**, 51 (1988).
7. M. Smooke, R. Hall, and M. Colket, "Application of Continuation Methods to Soot Formation in Diffusion Flames," Yale University Report, (1996).
8. U. Vandsburger, I. Kennedy, I. Glassman, Twentieth Symposium (International) on Combustion, The Combustion Institute, Pittsburgh, p. 1105, (1984).
9. H. Wang, D. X. Du, C. J. Sung, and C. K. Law, "Experiments and Numerical Simulation on Soot Formation in Opposed-Jet Ethylene Diffusion Flames," Twenty-Sixth Symposium (International) on Combustion, accepted, 1996.
10. M. Fairweather, W. Jones, and R. Lindstedt, Comb. Flame, **89**, 45 (1992).
11. M. Smooke, Y. Xu, R. Zurn, P. Lin, J. Frank, and M. Long, Twenty-Fourth Symposium (International) on Combustion, The Combustion Institute, Pittsburgh, p. 813, (1992).

Formation of 2–Ringed Aromatics

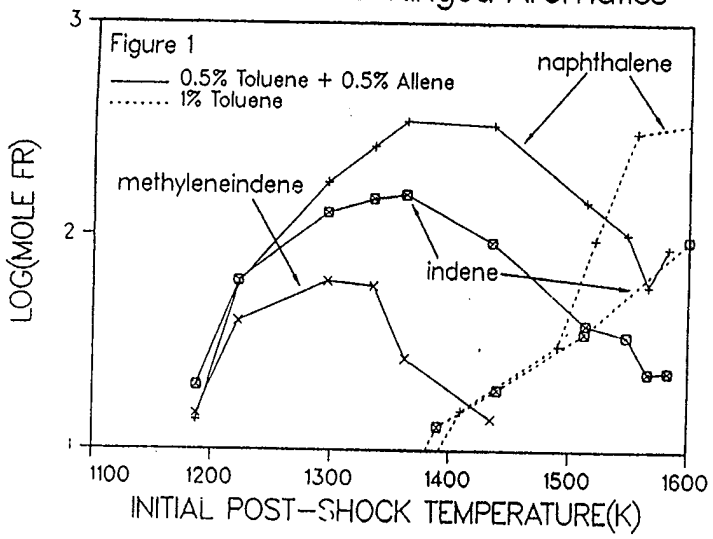

Variation in f_v with N_2 Dilution

Data from Axelbaum, et al

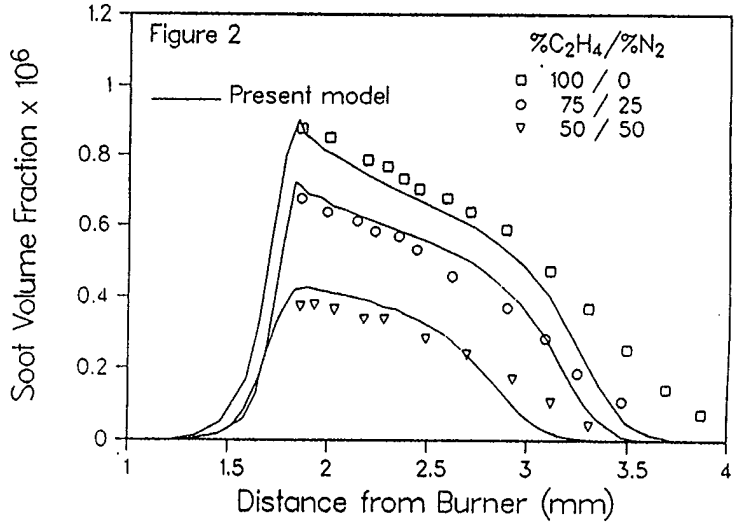

Predicted Peak f_v

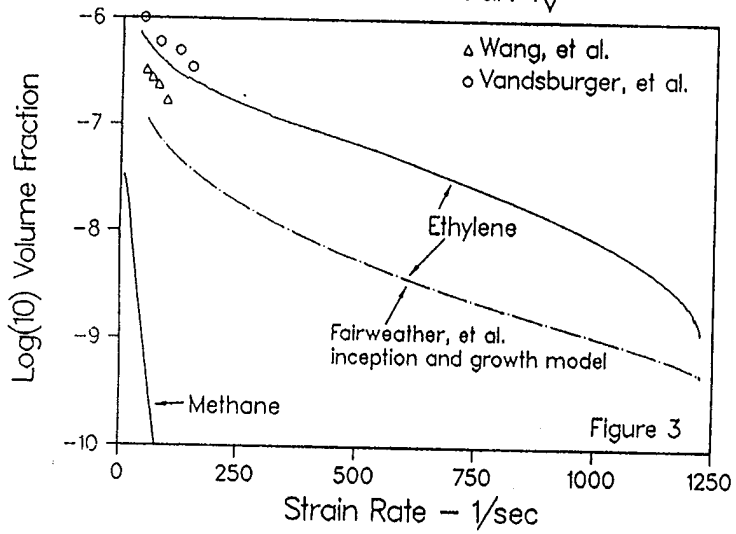

Predicted Peak Mole Fractions of Acetylene and Benzene

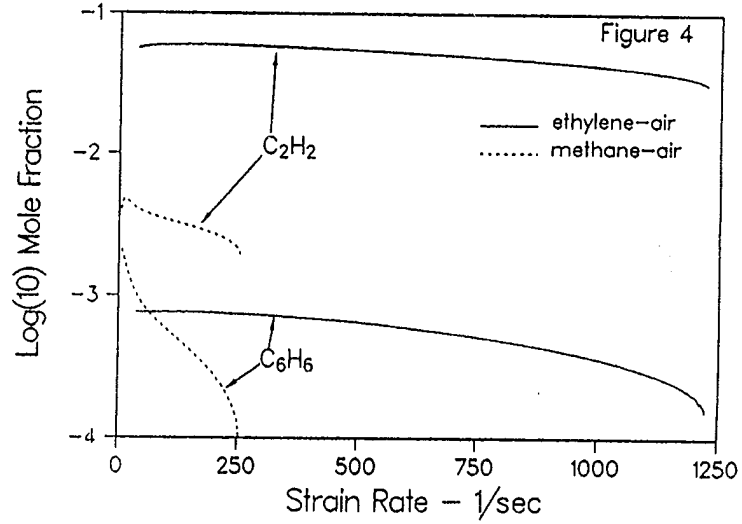

SOOT EVOLUTION AND CONTROL

ARO Grant DAAH04-95-1-0429

R. A. Dobbins

Division of Engineering
Brown University
Providence, RI 02912

SUMMARY/OVERVIEW:
The physical and chemical evolution of soot particles in hydrocarbon flames are studied to gain insight into control of soot formation. Particles are sampled from diffusion flames for subsequent analysis by electron microscopy and by chemical analytical methods. Potential intervention strategies result from the recognition of the role of the liquid-like soot precursor particles that precede the formation of the commonly observed carbonaceous soot aggregates.

TECHNICAL DISCUSSION:
Very small, ca 3 to 12 nm diameter, liquid-like particles in hydrocarbon flames were detected in our laboratory by electron microscopy, and they have also been identified by other groups. These soot precursor particles represent an intermediate step in the formation of the more easily observed carbonaceous soot aggregates. Precursor particles are invariably found low in fuel rich regions of diffusion flames burning methane, acetylene and ethene. The literature suggests these particles are present in premixed flames and in the pyrolysis of hydrocarbons in inert gases. A universality of precursor particles as a predecessor of the normally observed carbonaceous soot is hypothesized. More recently, the progressive conversion of precursor particles to carbonaceous aggregates has been followed by TEM in undiluted and nitrogen-diluted ethene diffusion flames. These observations, in combination with temperature measurements by a modified version of the rapid insertion thermocouple thermometry, lead to data on the chemical reaction rate of the process of carbonization of soot precursor particles.

Tests of the composition of precursor particles have been conducted using laser microprobe mass spectroscopy (LMMS) to determine their chemical makeup. These tests have been conducted on samples from the our laboratory by R. A. Fletcher on the LAMMA-500 instrument located in the Microanalytical Group at the NIST. Initial testing showed the precursor particles sampled low in the flame to contain masses corresponding to the polycyclic aromatic hydrocarbons (PAHs) at 252 u ($C_{20}H_{12}$), 276 u ($C_{22}H_{12}$), and 300 u ($C_{24}H_{12}$). On the other hand, masses high in the flame contained only carbon clusters C_x, $x \leq 25$ and lessor amounts of C_xH and C_xH_2. The use of the laser microprobe method to analyze soot particles initially was described in detail by Mauney et al. [1]. This work defined the capability of the LMMS method as very effective in detecting the

---

1. Mauney, T. et al., J. Total Environ. 36, 215 (1984).
2. Stein, S. and Fahr, A. J., J. Phys. Chem. 89, 3714 (1985).

PAH masses, although not molecular structure, to the very large masses (620 u) that are beyond the capability of the GC and HPLC chromatographic techniques. In an unrelated theoretical study, Stein and Fahr [2] examined the thermodynamic stability of $C_{2n}H_{2m}$ compounds in equilibrium with C_2H_2 and H_2 at 1500 K - conditions that are well approximated in diffusion flames. The values of n and m that yield the most stable class were identified and, within each class, the most stable isomer ("stabilomer") was found. The two dimensional grid 2n vs. 2m of the stabilomer compounds forms the stability valley through which growth of PAHs to large sizes occurs in flames in the presence of C_2H_2. A remarkable outcome is that the products identified by Mauney et al. perfectly correspond to the members of the stabilomer grid in the mass range of 252 u to 620 u. Thus the chemical thermodynamic results of Stein and Fahr were totally supported by the earlier experimental results of Mauney et al. and indicate the growth path for young soot particles. These two studies provide an important background and interpretive basis for the analysis of soot formation in the combustion of hydrocarbon fuels.

The LMMS method, which was selected for the analysis of soot precursor particles because of its ability to obtain information of samples as small as 10^{-12} gm, has been used to follow the development of particles as a function of height in the diffusion flame. This analysis shows that the masses detected within the soot precursor particles correspond to the stabilomer PAH masses as large as 546 u, possibly $C_{44}H_{18}$ which possesses 14 hexagonal rings. The profile of PAHs with increasing height in the diffusion flame is shown in Figure 1. There the count fraction, which is approximately proportional to composition by mole, for species C_xH_y with a common value of x, are plotted for the heights Z=20, 30 and 40 mm above the burner. At Z=20 mm the species with x=20 (e.g., $C_{20}H_{10}$, $C_{20}H_{12}$) display the highest count fraction. The mass distribution broadens with height Z to the larger values of x showing the PAH distribution to increase with Z and hence with time. This result is consistent with concept that the PAH growth occurs along the stabilomer valley defined by Stein and Fahr. The LMMS data also shows that the PAH count as a fraction of the total positive ion count varies from 78% at Z=20, to 42% at Z=30, down to 2.7% at Z=40 mm. Finally, the hydrogen mole fraction X_H decreases from 36% at Z= 20 and 30 mm to 16% at Z=40. Thus the transformation of soot precursor particles to carbonaceous soot aggregates is confirmed to occur between Z=30 and 40 mm by TEM observations and by three attributes that come from the LMMS analysis of particles samples from the diffusion flame.

The literature reveals that the PAHs of masses 152 through 300 u and higher that lie in the stabilomer valley of Stein and Fahr have been found in the carbonaceous particulate product of diverse combustion processes and fuels. These fuels include gaseous hydrocarbons, kerosene, carbon black feedstock, Diesel fuel, kerogen and crude oil. Therefore, it is concluded that a likely universal pathway to the formation of soot is via the PAHs that populate the stabilomer grid. This conclusion explains the often noted observation that the properties of carbons formed in flames are remarkably uniform regardless of the hydrocarbon fuel or device involved in the combustion process.

The process of carbonization is responsible for the conversion of the precursor particles to carbonaceous soot aggregates. We have shown that first order Arrhenius rate constants for the carbonization process can be obtained from observations in a diffusion flames burning ethene diluted with nitrogen. This data is supported by shock tube experiments in which carbons formed by pyrolysis of hydrocarbons highly diluted with argon are observed simultaneously in both transmitted and scattered light. First order Arrhenius reaction kinetics are found applicable, and

the experimental data yield a frequency factor A of $1.78 \times 10^{+6}$ s^{-1} with an activation energy E equal to 113 kJ/mole.

A method of intervening in the formation of soot in flames involves maintaining steady combustion at moderate temperatures to promote oxidation of precursor particles prior to carbonization. This strategy is demonstrated in a laboratory burner by dilution of the fuel with any inert gas to reduce flame temperature. Ignition is accomplished near a stoichiometric fuel-air ratio, and the subsequent addition of inert gas eliminates carbon formation. A blue flame results that is devoid of the incandescent luminosity of carbon particles. A fuel oil burner manufactured by the Viessmann Werke Gmbh of Germany incorporates this technology. Combustion products in this device are recirculated with the air supply to moderate the flame temperature, and efficient mixing is achieved by a turbulent vortex gas motion. Implementation of this method of control in internal combustion (IC) engines requires exhaust gas recirculation in combination with stratification. In the IC engine, fuel components including PAHs are adsorbed at high pressures in the lubrication films and are released at low pressures into the exhaust gas stream. Thus fuel components bypass the combustion process while adding to the volatile organic fraction of particulate emissions. In principle, the bypass organics can be eliminated by the use of a stratified charge in which air and recirculated products are injected in an outer annulus to form a curtain of fuel free gas next to the cylinder walls. This type of design is employed in a spark ignition engine that employs multiple inlet valves with swirl injection to create the desired stratified mixture ratio within the cylinder.

During the coming year, soot samples from a deuterated ethene C_2D_4 flame will be analyzed to confirm the interpretation of the mass identification. Smoke from a Diesel engine will be tested to determine the extent that it differs from laboratory flame particles and to find if bypass fuel components can be differentiated from pyrolytic PAHs. Finally to improve understanding of both composition and analytical techniques, soot from a smoking flame, which can be collected in large milligram quantities, will be analyzed by LMMS and a variety of other methods. The state of the carbonaceous component can be more fully studied by a variety of analytical methods when these larger samples are available.

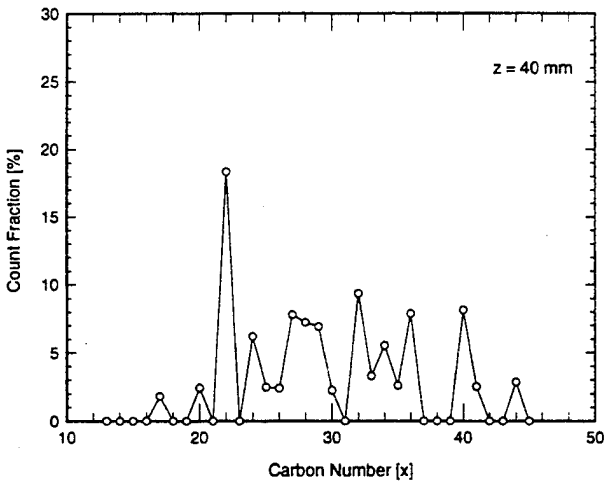

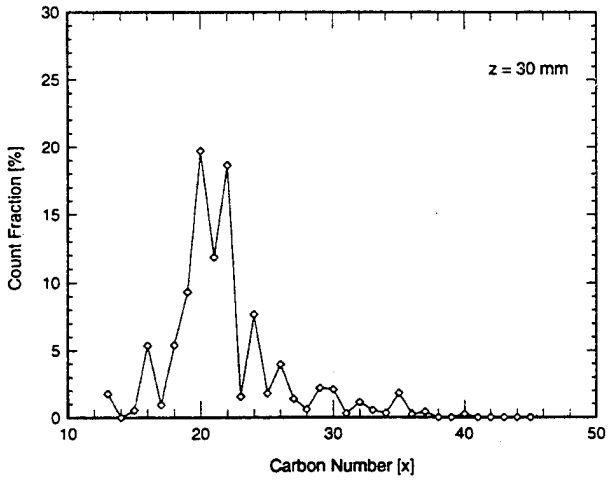

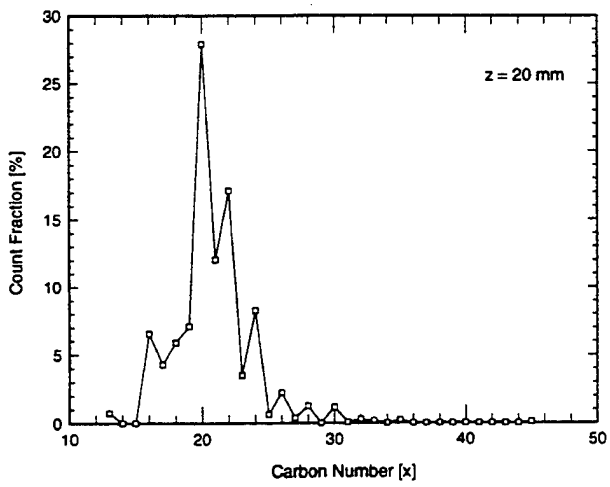

Figure 1. **PAH Count Fraction (%) vs. Carbon Number X in Soot Sampled at Various Heights in the Ethene Diffusion Flame**

MODELING STUDY TO EVALUATE THE IONIC MECHANISM OF SOOT FORMATION

(AFOSR CONTRACT No. F49620-94-C-0014)

Principal Investigator: H. F. Calcote

AeroChem Research Laboratories, Inc.
P. O. Box 12, Princeton NJ 08540

SUMMARY / OVERVIEW

The objective of this program is to examine the possible role of ions in soot nucleation by attempting to model the process of ion growth using assumptions within the range of acceptable values. This has required extending the database of thermochemistry of ions and developing kinetics for ion-molecule reactions and ion-electron recombinations. Since low temperature ion-molecule reactions can proceed on every collision for exoergic reactions, but at high temperatures ion growth reactions become endoergic, the most important part of developing a database is the development of the thermochemistry. In previous work we were unable to obtain a reasonable fit between the experimental result and the computer model unless the temperature was reduced by an unacceptable amount. Ion-molecule growth reactions generally become slower at high temperatures due to entropy effects. Analysis of the cooling of the sampled gas by the metal sampling cone indicates the sampled gas temperature is greatly reduced so that much better agreement is obtained, but at considerable increase in complication of analysis, and with additional questions concerning the accuracy of the fit. Probe cooling of the sampled gas is not a serious problem with neutral species reactions because the reaction rate coefficients are lower. In addition we have added part of the neutral chemiionization mechanism, further complicating the analysis.

THERMOCHEMISTRY

The thermochemical database has been further updated and expanded. In order to estimate values for ions not treated here, and to extend the results to larger ions, the thermochemical values were correlated with the total number of carbon atoms. For this purpose the positive ions were divided into three main classes which we identify as:

Cations, conceived as being produced by removing a hydride ion from a neutral molecule:

$$RH \Rightarrow R^+ + H^-$$

Free Radical Cations, conceived as being produced by removing an electron from a neutral molecule:

$$RH \Rightarrow RH^{+}\bullet + e^-$$

Protonated Molecular Cations, conceived as being produced by adding a proton to a neutral molecule:

$$RH + H^+ \Rightarrow RH_2^+$$

An example of the correlation obtained for the Gibbs Energy of Formation for cations at 2000 K is shown in Fig. 1. The equation fitting this correlation is:

$$\Delta_f G_{2000} = 51.348n + 919.62 \text{ kJ/mol}, \quad R^2 = 0.935$$

where n is the number of carbon atoms in the ion.

For free radical cations, the equation is:

$$\Delta_f G_{2000} = 33.231n + 1130.7 \text{ kJ/mol}, \quad R^2 = 0.923$$

For protonated molecular cations, the equation is:

$$\Delta_f G_{2000} = 48.55n + 956.79 \text{ kJ/mol}, \quad R^2 = 0.949$$

The ions were further divided by structure, which of course gave better correlations. The correlation for the enthalpy of formation at 298 K was very poor, consistent with an earlier observation by others. The specific heats at 2000 K of all the ions at 2000 K were fit by the equation:

$$C_p = 34.03n + 43.74 \text{ J/K} \cdot \text{mol}, \quad R^2 = 0.989$$

COMPARISON OF MODEL WITH EXPERIMENT

In previous versions of the computer model, the complications of including a neutral mechanism was avoided by inputting a set of experimentally measured neutral species profiles and experimentally measured ion profiles for two small ions. The electron concentration profile was then forced to be equal to that of the initial total ions. Neither ion-electron recombination nor the formation of negative ions could be included in the mechanism. This has been corrected by including the chemiionization step in the mechanism. Since experimental profiles for CH* and O are not available, and to avoid encumbering the calculations with a lot of neutral reactions, the profiles for CH* and O were estimated. The CH* profile was estimated from the observation of CH* profiles in other flames. This was done by describing the CH* concentration in terms of three parameters: maximum CH* concentration, distance from the burner at which this concentration occurs, and the width of the concentration profile which was assumed to be parabolic. The O atom profile was calculated from experimental data assuming the equilibrium: $H_2 + O \rightleftarrows OH + H$. The three CH^* parameters were chosen such that the experimental profiles of the two ions, $C_3H_3^+$ and $C_6H_5^+$, previously used to initiate the calculation, were reasonably duplicated.

To produce these ions in the model, the following steps in the ionic mechanism were added and used with experimental profiles of the neutral species involved:

$CH^* + O \rightleftharpoons HCO^+$	$k = 3.3 \times 10^{14}$ mol cm^{-3} s
$HCO^+ + H_2O \rightleftharpoons H_3O^+ + CO$	$k = 19$
$HCO^+ + C_2H_2 \rightleftharpoons C_2H_3^+ + CO$	$k = 8.4$
$HCO^+ + C_3H_2 \rightleftharpoons C_3H_3^+ + CO$	$k = 3.0$
$H_3O^+ + C_3H_2 \rightleftharpoons C_3H_3^+ + H_2O$	$k = 9.0$
$C_3H_3^+ + C_2H_2 \rightleftharpoons C_5H_3^+ + H_2$	$k = 3.0$
$C_3H_3^+ + C_3H_4 \rightleftharpoons C_6H_5^+ + H_2$	$k = 6.6$

Two new techniques were thus used to obtain a reliable calculation which accounts for the observed large concentrations of ions in fuel rich hydrocarbon flames. These two techniques were: (1) correction of the mass spectrometer measurements for sampling probe interference and (2) estimating the profiles of two species, CH* and O atoms (for which experimental data are unavailable) to include the chemiion production.

A fluid mechanical analysis of the flame gases approaching a cooled metal probe shows the incoming gas is cooled for about 34 μs prior to entering the probe sampling orifice; see e.g. Fig. 2 for examples. The sampling cone location is shown and the scale within the influence of the sampling cone is expanded to demonstrate the effect on the profiles. For fast ion-molecule reactions, this rapid change in temperature provides sufficient time for the reaction to proceed to the extent that the sampled ions are different from the ions in the flame. Several types of phenomena are observed, governed largely by the thermochemistry of the reactions. The effect on the equilibrium $C_3H_3^+ \rightleftharpoons H_3C_3^+$ (linear to cyclic) is grossly affected. Only the linear isomer is considered reactive. Some ions react to produce completely different ions, e.g. $C_{12}H_8^+ + H\bullet \rightleftharpoons C_{12}H_9^+$ which, at reduced temperature is driven to the right predominately by a decrease in entropy. In other cases the ion concentration may increase or decrease, e.g. $C_{21}H_{11}^+$ and $C_{19}H_{11}^+$. This cooling of the sampled gas explains why in previous calculations the temperature profile had to be artificially lowered to force agreement between experimental and modeled values.

The results of a calculation incorporating chemiionization and nozzle cooling are presented in Fig. 3 in which maximum experimental and calculated ion concentrations are compared. The maximum CH* (electronically excited CH) concentration assumed for this calculation was 3.0×10^{-6} mol fraction. The ion $C_4H_5^+$, always calculates high by more than two orders of magnitude and is not included in the figure. It is not clear why this large discrepancy is found. The agreement, without $C_4H_5^+$, is excellent and is further support for the ionic mechanism of soot formation.

ACKNOWLEDGMENTS

Participation in this program of Drs. D. G. Keil and R. J. Gill is gratefully acknowledged.

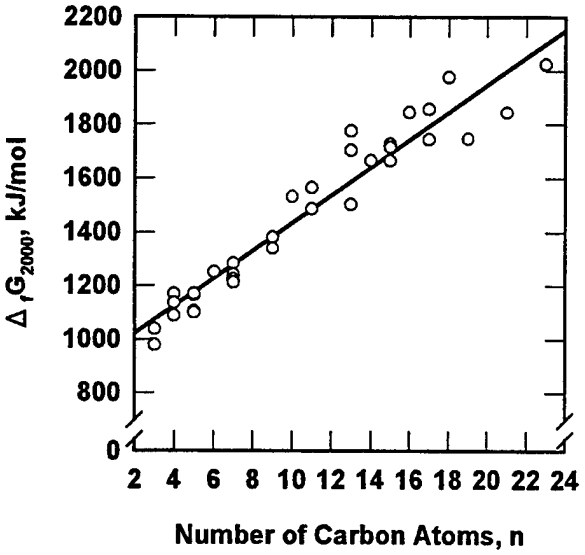

Figure 1 Correlation of Gibbs Energy of Formation with Carbon Number for Cations at 2000K

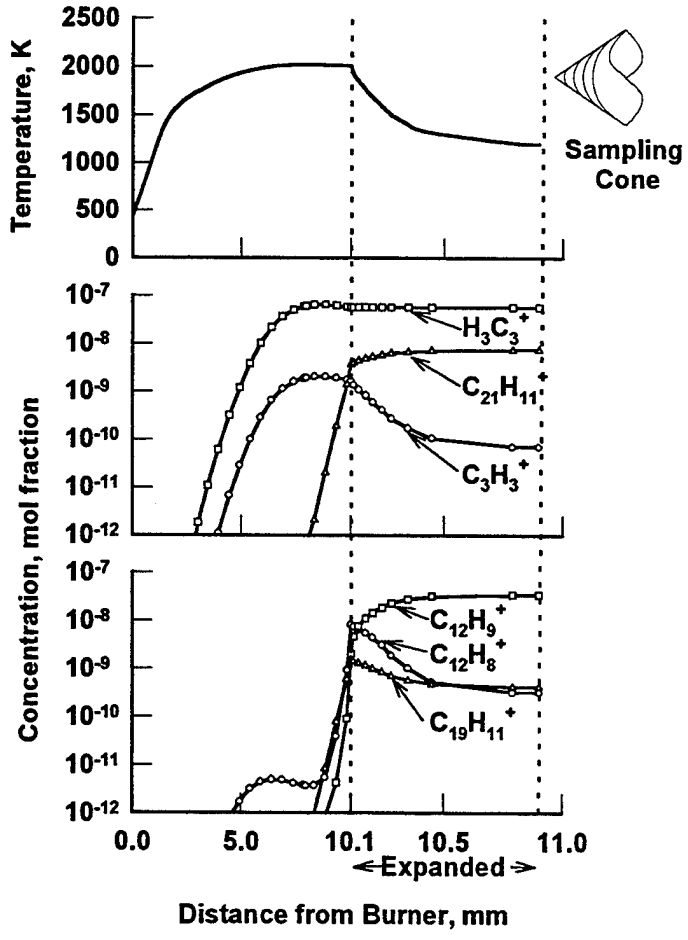

Figure 2 Typical Calculated Profiles Showing Effect of Sampling Cone Acetylene - Oxygen Flame at Φ = 3.0 P = 2.67 kPa and u = 50 cm/s

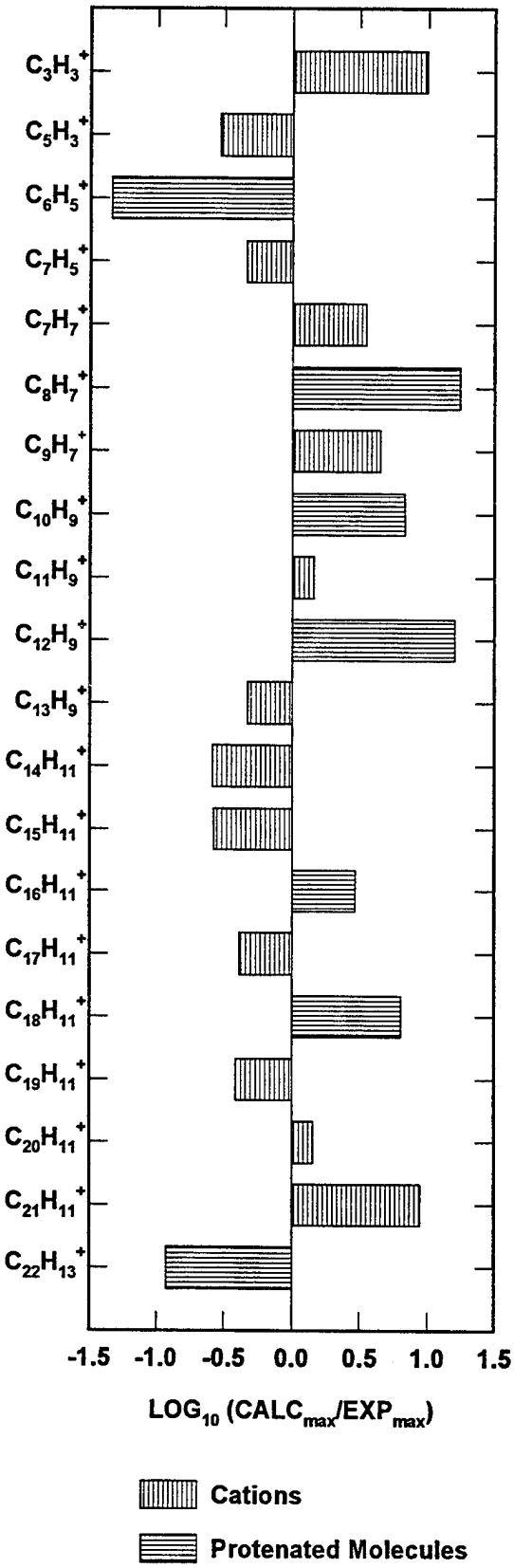

Figure 3 Comparison of Calculated $(CALC)_{maximum}$ and Experimental $(EXP)_{maximum}$ Cation Concentrations

SOOT, TEMPERATURE AND OH MEASUREMENTS IN AN UNSTEADY COUNTER-FLOW DIFFUSION FLAME

(ARO Grant/Contractor No. DAAH04-95-1-0230)

Principle Investigator: William Roberts

Dept. Of Mechanical and Aerospace Engineering
Box 7910
North Carolina State University
Raleigh, NC 27695-7910

SUMMARY/OVERVIEW:

Previous studies have shown that laminar counterflow diffusion flames exposed to steady rates of strain exhibit many of the essential features of turbulent diffusion flamelets. However, all real turbulent flames are subjected to unsteady rates of strain due to the unsteadiness inherent in the flow field. This unsteady strain rate may have a great impact on the fluid mechanic-chemical kinetic interaction and, therefore, may effect the reaction zone temperature and formation of soot. The goal of this project is to measure the effect of unsteady strain on the temperature, OH mole fraction, and the soot formation process using laser based diagnostic techniques.

TECHNICAL DISCUSSION:

A counterflow burner similar to the design of Prof. K. Seshadri was constructed with modification to allow for the placement of two loudspeakers. Figure 1 is a schematic of the CFDF burner used in this study. The upper section supplies the air flow through a central tube which is 2.5 cm in diameter. This air tube is surrounded by a 0.6 cm thick annulus for nitrogen co-flow. The co-flow prevents entrainment of ambient air into the reaction zone and preheating of the air. The air tube is fed from a plenum which is bounded on the top by a 20 cm loudspeaker. The lower section, the fuel side, is the same as the air side except the fuel tube is surrounded by a waterjacket to prevent preheating. This waterjacket is surrounded by an annulus and then a second waterjacket. Product gases are evacuated from the reaction zone by suction through the annulus between the waterjackets and exhausted outside the building.

Five 80 mesh screens separated by 3 mm spacer rings are stacked at exit of both the fuel and air tubes. These screens create a pressure drop which flattens the exit velocity profiles and breaks up any large scales. A signal generator and amplifier are used to send a sine wave to the speakers, which sets up a controlled oscillation in the reactant flow field. Both the amplitude and frequency were varied for this initial study.

Extinction Studies

Flame extinction was measured as a function of speaker frequency, voltage applied to speakers, and initial steady strain rate. A flame was established at a chosen steady strain rate, referred to as the initial strain rate. The speakers were then activated at a chosen frequency and low applied voltage. The voltage (amplitude) was increased until the flame extinguished. This was repeated for all frequencies in the matrix before moving to a different initial strain rate.

The volume of fluid expelled by the speaker is linear with applied voltage. The amplitude of the air velocity oscillation is related to the volume of fluid expelled during a pulse. A steady strain rate is related to the air velocity by:

$$a = \frac{2V}{L} \qquad (1)$$

where L is the separation distance. The amplitude of the oscillations were converted to maximum strain rates by:

$$a_{max} = \frac{2(V_{mean} + V'_{max})}{L} \qquad (2)$$

where V_{mean} is the mean velocity and v'_{max} is the maximum amplitude of the velocity fluctuation at that frequency and applied voltage.

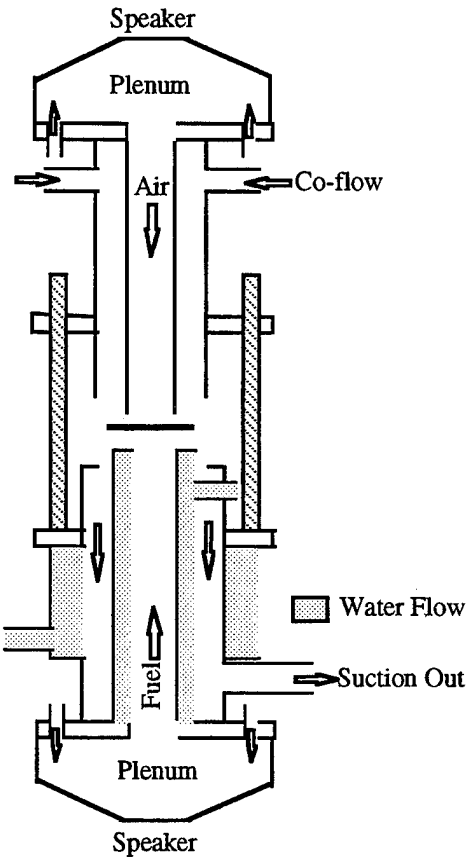

Figure 1. Unsteady Counterflow Diffusion Flame Burner.

The amplitude of the velocity oscillation were measured with a hot film anemometer system at each extinction point in a cold flow experiment. The velocity and speaker oscillation data were collected by a data acquisition system. Measurement of the velocity and calculation of the strain rate in this manner is only an estimate of the true local strain rate experienced by the flame. Studies have shown that velocity measurements with an LDV system are an accurate method of determining the local strain rate in the flame. An LDV system is currently being assembled and will be used to verify the local strain rate in the future.

Results and Discussion

The first step in this study was to verify that the screen combination produced a laminar plug flow velocity profile. A hot film anemometer was used to take traverses across the air tube in a cold flow experiment. The velocity profile is "top hat" over 75% of the tube diameter. No nitrogen co-flow was used for the velocity profile measurements. The reacting experiments are always run

with a velocity matched co-flow, so it is expected that the percentage over which the velocity profile is top hat should increase with the co-flow. The measured turbulent intensities for the profile data does not exceed 2.5% in the jet.

The next step was determining the steady flow extinction strain rate for each fuel. The diluted methane extinguished at 120 s^{-1}. The pure methane flame extinguished at 295 s^{-1}. These results compare well with steady extinction data in the literature. The diluted methane flame was flat and light blue in color over the entire strain rate range. The methane flame was flat and a darker blue over the entire range. Some sooting was seen at very low strain rates for the pure methane flame.

The propane-air flame did not extinguish like the methane-air flames. The steady propane flame in this apparatus becomes less flat at strain rates above 150 s^{-1} and extinguishes in wedges which propagate radially outward from the centerline. The wedges first appear around 310 s^{-1} and grow in annular size and number as strain rate increases. The steady propane flame was extinguished with a combination screens and glass beads near 350 s^{-1}, but this was not repeatable. Other researchers have reported propane extinction strain rates between 300 and 650 s^{-1}. The Reynolds number based on momentum matched jets is the highest for the propane jet, which may explain the difficulty in maintaining a flat flame and achieving global extinction.

The propane results are shown in Figures 2 and 3. Seven initial strain rate were run with frequencies between 10 and 200 Hz. The flame could not be extinguished above 200 Hz within the applied voltage range for any initial strain rate. The data for propane and methane have similar trends. Using this similarity, an estimate of the steady extinction strain rate for propane is approximately 340 s^{-1}. In the low frequency region (10 to 40 Hz), the data for all fuels was linear at low initial strain rates but developed a "bucket" as the initial strain rate was increased. During the study this same frequency range was noted for "flame breakout," where the flame would breakout of the nitrogen curtain near the lip of the suction annulus. For propane this breakout was very severe, but hardly noticeable for diluted methane. At this time it is unclear what is causing the breakout or if it is related to the "bucket" in the data.

Results for pure methane flame are shown in Figure 4. Five initial strain rates were run with frequencies between 10 and 285 Hz. Extinction at frequencies above 200 Hz occurred only for initial strain rates near the steady extinction strain rate. The steady state extinction limit for methane was almost three times that for the diluted methane. Therefore, Figure 4 shows an expanded range of maximum strain rates compared to the diluted methane data. This figure also shows a change in the shape of the curve between 100 and 150 s^{-1}. Extinction does not peak at a low strain rate but does peak at 200 Hz. At initial strain rates of 200 and 250 s^{-1}, the flame began to extinguish in wedges, as described earlier for propane, just before extinguishing completely.

Extinction results are shown in Figure 5 for the diluted methane fuel. For this case, the methane fuel was diluted with nitrogen; methane mole fraction was 0.27. Extinction data was collected for five strain rates between 30 and 115 s^{-1} and frequencies from 10 to 320 Hz. At frequencies above 250 Hz, extinction occurred only at initial strain rates near the steady extinction strain rate, as seen in the pure methane case. The maximum strain rate approaches a strain rate between 130 and 140 s^{-1} for all frequencies as the initial strain rate approaches the steady extinction strain rate. Also, for frequencies between 50 and 100 Hz the maximum strain rate is nearly independent of initial strain rate.

Preliminary planar Laser Induced Incadescence was used to measure the qualitative effect of the unsteadyness on the soot volume fraction. The amount of soot generated drops rapidly with increasing strain rate as expected. Above a strain rate of approximately 100 s^{-1} for the propane-air flame, the signal to noise ratio of the incandescence signal was less than unity. For an initial steady strain rate of 50 s-1, LII images were taken at five instantaneous strain rate by timing the laser and camera system with the speaker oscillation. Significant effects were seen on the volume of soot as a function of whether the strain was increasing or decreasing. This work is currently underway.

Conclusions

The constructed CFDF burner has produced repeatable steady extinction data which compares well with data contained in the literature for diluted methane and methane flames. The velocity profile

exiting the duct can be considered "top hat". A repeatable steady extinction strain rate was not established for the propane/air flame due, we think, to the presence of a mildly turbulent flowfield. Additional measures need to be taken to reduce the turbulence level in the propane jet at strain rates above 150 s^{-1}.

Extinction of the counterflow flame under unsteady flow conditions is a function of initial strain rate, applied speaker voltage, and frequency. As the frequency increases at a given initial strain, the amplitude of the fluctuation must increase in order to strain out the flame. Also at the highest frequencies, the instantaneous maximum strain may exceed the steady strain rate required for extinction. There are regions in the extinction map where the maximum strain rate becomes insensitive to either frequency or initial strain rate.

The strain rate fluctuation in an unsteady flow field has an impact on the soot formation process. The LII images indicate that not only is the oscillation amplitude a factor but also slope of the fluctuation. A different soot structure appears for an increasing strain than for the decreasing strain.

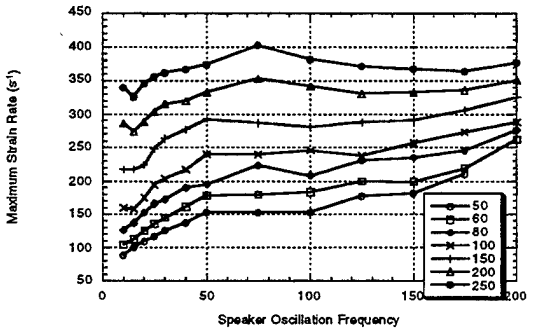

Figure 2. Maximum strain rate required to globally extinguish the flame versus oscillation frequency as a function of initial strain rate for propane-air flame.

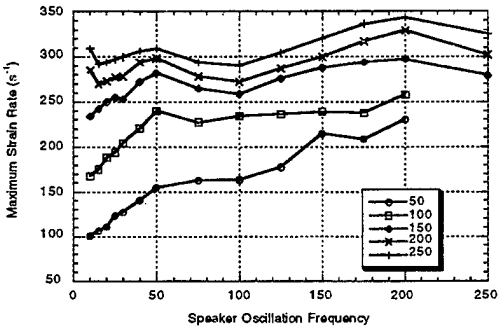

Figure 4. Maximum strain rate versus oscillation frequency as a function of initial strain rate for methane-air flame.

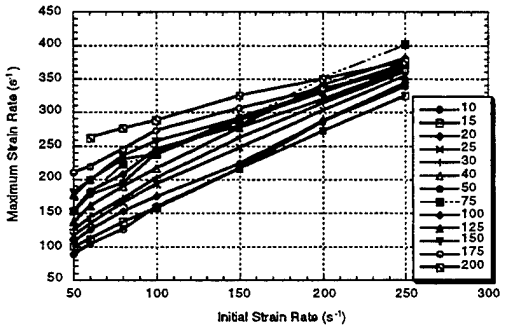

Figure 3. Maximum strain rate versus initial strain rate as a function of oscillation frequency for propane-air.

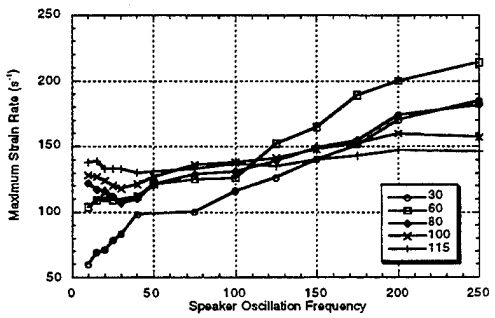

Figure 5. Maximum strain rate versus oscillation frequency as a function of initial strain rate for 27% methane-air flame.

TRANSPORT PHENOMENA AND INTERFACIAL KINETICS IN MULTIPHASE COMBUSTION SYSTEMS

AFOSR Grant No. 94-1-0143

Principal‡ Investigator: Daniel E. Rosner
High Temperature Chemical Reaction Engineering Laboratory
Department of Chemical Engineering, Yale University
New Haven, CT 06520-8286 USA

SUMMARY / OVERVIEW

The performance of ramjets burning slurry fuels (leading to oxide aerosols and deposits), and gas turbine engines in dusty atmospheres depends upon the formation and transport of small particles, often in non-isothermal combustion gas boundary layers (BLs). Even airbreathing engines burning "clean" hydrocarbon fuels can experience *soot* formation/deposition problems (*e.g.*, combustor liner burnout, turbine blade erosion,...). Moreover, particle formation, transport and deposition are important in chemical reactors used to synthesize or process aerospace materials† (turbine coatings, optical waveguides, ceramic precursor powders,...). Accordingly, our research provides chemical propulsion system and aerospace materials engineers with new techniques and quantitative information on important *particle mass* transport mechanisms and rates, and their implications for *deposit* properties. An interactive experimental/theoretical approach is being used to gain an understanding of performance-limiting chemical-, and mass/energy transfer-phenomena at or near interfaces. This includes the development/exploitation of seeded laboratory burners (Fig.1), and new diagnostic/characterization techniques (Figs.5,6). Resulting experimental data (Figs. 2,4,6), together with the predictions of asymptotic theories (Section 2.4), are used to propose/verify simple viewpoints and rational engineering correlations for the future design/optimization of particle-forming air-breathing combustors.

TECHNICAL DISCUSSION / RECENT RESEARCH PROGRESS

Most of our results obtained under Grant AFOSR 94-0143 during 6/95-6/96 can be divided into the subsections below:

2.1. SEEDED LAMINAR COUNTERFLOW DIFFUSION FLAME EXPERIMENTS: FORMATION, COAGULATION, TRANSPORT AND STABILITY OF COMBUSTION-GENERATED PARTICLES

Inorganic particles produced during combustion processes are frequently aggregates of much smaller "primary" spherules, partially sintered due to high temperatures. Consequently, the resulting aggregates can differ in morphology and size according to the flame conditions under which they are generated and 'processed'. Since particle morphology and aggregate transport properties are interrelated, it is important to understand not only aggregate formation but also their *morphological evolution* in flames. We are investigating the morphological evolution of flame-generated aggregates at low particle volume fractions ($O(10^{-1}$ ppm)) in a well-defined/characterized laminar non-premixed combustion environment. Al_2O_3 particles synthesized in a $Al(CH_3)_3$ (TMA)-seeded atmospheric pressure laminar counterflow diffusion flame (CDF; Fig. 1) fueled with $CH_4/O_2/N_2$ are used as the model material/combustion system. Experiments include laser light scattering (LLS) and thermophoretic sampling/Transmission Electron Microscope (TEM) techniques. Aggregate morphology is characterized in terms of spherule ("grain") size, aggregate size (Fig. 2), aggregate shape and fractal structure (Fig. 4). Additionally, the effects of temperature and TMA concentrations on particle sizes and morphology are also investigated systematically and interpreted based on parallel theoretical studies outlined in Section 2.4. LLS signals and typical TEM images clearly illustrated particle/aggregate size and morphology evolution as a result of two competing processes, with coagulation increasing aggregate sizes, and sintering reducing aggregate surface areas. Mean spherule diameters are found to be in the range of 13 to 40 nm, increasing with sampling position (increasing temperature) and with TMA concentration. Mean aggregate sizes reached a maximum near a local temperature of only 1250 K and increased with TMA seed level. The final products are compact spherical particles resulting from complete 'collapse' of the aggregates, apparently as a result of surface diffusion rather than surface energy-driven "viscous

† AFOSR Contractors' Mtg: Airbreathing Combustion/Propulsion-Diagnostics, June 3-6,1996, Virginia Beach VA
‡ For research collaborators consult **REFERENCES**

flow". These results are shown to be compatible with the characteristic times governing each of the participating "unit" rate processes (Fig.3). More comprehensive quantitative predictions are underway for multi-phase laminar CDFs. The experimental and theoretical methods developed and illustrated here will find applications in controlling the synthesis of valuable nano-powders, and facilitate rational extensions into the domain of *turbulent* non-premixed combustors generating desired or inadvertent ultrafine particles.

2.2 IMPLEMENTATION OF THERMOCOUPLE PARTICLE DENSITOMETRY (TPD)

Thermocouple Particle Densitometry (TPD) is a method for measuring absolute and local soot volume fractions, f_v , in flames first suggested by Eisner and Rosner (1985). Based on the laws governing thermocouple response to *thermophoretic soot deposition*, this method has now been successfully implemented in both axisymmetric co-flowing laminar diffusion flames as well as CDFs (McEnally *et.al.*(1996). Since it yields spatially resolved f_v-values directly and can easily measure low soot concentrations, TPD is especially applicable to spatially non-uniform and/or lightly sooting flames. To further evaluate the method, TPD soot volume fractions (ppm) were measured in several laminar non-pre-mixed flames. In methane and ethylene counterflow flames the TPD results agreed to within experimental error (Fig. 6) with laser extinction measurements we performed in the same flames. In axisymmetric methane and ethylene co-flowing flames the shape of TPD f_v profiles also agreed well with published de-convoluted laser extinction measurements in similar flames. However, soot volume fractions inferred from mass deposition were systematically somewhat larger than extinction results in the lower portion of an ethylene co-flowing difffusion flame, and throughout a methane co-flowing flame, possibly due to deposition of visible-light-transparent particles with masses of several thousand *amu* , known to be present in such flames.

2.3 MORPHOLOGY OF FLAME-GENERATED AGGREGATES: 'SELF-AFFINITY' AND 'LACUNARITY'

Based on our investigation of over 3000 electron microscope images of soot aggregates from a variety of laminar and turbulent *hydrocarbon*-fueled flames we have found (Neimark *et.al.*(1996)) that their scaling properties *cannot* be characterized solely using the now-familiar *mass fractal dimension*, D_f. Rather, the *asymmetric* properties of flame-generated soot evidently require the introduction of *longitudinal* ($[(1+H)/2]\cdot D_f$) and *transverse* ($[(1+H)/2H]\cdot D_f$) exponents, where D_f=1.75 and H=0.91. In this sense combustion-generated soot aggregates should be regarded as *self-affine* rather than self-similar. Moreover, widely employed diffusion-limited cluster-cluster aggregation (DLCCA-) models, while undeniably providing a useful first approximation, are unable to accurately describe these aggregate populations not only with respect to $H\neq1$ but also with respect to lacunarity (pre-exponential factor; see Koylu *et.al.*(1995)). We are now investigating the consequences of this statistically significant asymmetry for predicting the essential *transport and radiative properties* of suspended aggregates (Section 2.4).

2.4 THEORY OF TRANSPORT, RESTRUCTURING, AND RADIATIVE TRANSPORT PROPERTIES OF FLAME-GENERATED AGGREGATES

The ability to reliably predict transport properties and morphological stability of *aggregated* flame-generated *particles* (carbonaceous soot, Al_2O_3, SiO_2,...) is important in chemical propulsion and refractory materials fabrication applications. We are developing efficient methods to anticipate coagulation, restructuring, and ultimate deposition rates of suspended populations of such particles in combustion systems, as well as laws needed to interpret laser-based soot diagnostics. In one asymptotic limit large 'fractal' aggregates are treated using a spatially variable, effective porosity pseudo-continuum model (see, *eg.*, Rosner and Tandon (1994) and Tandon and Rosner(1996)). Indeed, the competition between restructuring kinetics and coagulation kinetics determines the observed size of the apparent "primary" particles comprising soot particles, as well as the "collapse" of surface area observed in some high temperature systems (*eg*, see Figs. 2, 3). These studies, together with our methods to predict interactions between aggregates and their surrounding *vapor* environment (interactions which can lead to primary particle growth, or (for carbonaceous soot in the presence of oxidizing species) burn-out) are now being incorporated into our laminar CDF structure modelling. This work will facilitate rational extensions into the uncharted domain of turbulent non-premixed combustors generating ultrafine particles.

2.5 EROSION BEHAVIOR OF CERAMIC OR METAL TARGETS IN HIGH-SPEED ABRASIVE STREAMS; SHAPE EVOLUTION

By capturing with simple formulae the essential features of available *erosion yield* experiments, we have been developing an efficient method to predict local and total surface *erosion rates* for metal or ceramic targets of simple geometry exposed to a 'polydispersed' population of abrasive particles suspended in a high-speed mainstream (Rosner *et.al.* (1995), Kho *et.al.* (1995), Khalil and Rosner(1995)). Our earliest methods/results (*loc. cit.*) were deliberately limited to small relative changes in body shape to allow for arbitrary Stokes numbers. We have now relaxed this assumption for the limiting (worst-) case of rectilinear erodent particle trajectories. We make the assumption that the interface recedes normal to itself at the rate determined by the local particle impaction frequency, angle-of-incidence and velocity (Rosner and Khalil (1996)). The normalized "body" radius $R(\theta, \tau)$ at polar angle θ and dimensionless exposure time τ is found to satisfy an interesting first-order nonlinear PDE. Illustrative results have been obtained comparing the erosion rate behavior of initially circular targets of a *ceramic* and a *metal* by numerically solving this PDE using the "method of lines". Calculated interface positions reveal "nose blunting" for the erosion of *ceramic* targets in a uniform erodent-carrying stream. In contrast, "nose-sharpening" occurs for *metal* targets, with the development of an ogive-shaped feature facing upstream. Our methods are now being used to calculate/correlate the erosion behavior of targets of other important aerodynamic *shapes*, including spheres, cones,.... These methods/results will allow design engineers to anticipate erosion behavior in a variety of particle-laden flow environments, and provide guidance on tolerable particle loadings, required maintainence frequencies, and materials selection.

REFERENCES

Eisner, A.D. and Rosner, D.E.,"Experimental Studies of Soot Particle Thermophoresis in Non-isothermal Combustion Gases Using Thermocouple Response Techniques", *Combustion & Flame* **61**,153-166 (1985)

Farias, T.L., Koylu, U.O., and Carvalho, M.G., "Effects of Polydispersity of Aggregates and Primary Particles on Radiative Properties of Simulated Soot", *J. Quant. Sprectroscop. Radiat. Transfer* **55** (3) 357-371 (1996)

Gomez, A., and Rosner, D.E., "Thermophoretic Effects on Particles in Counterflow Laminar Diffusion Flames", *Combust. Sci. and Tech.* **89**, 335-362 (1993).

Khalil, Y.F., and Rosner, D.E., "Erosion Rate Prediction Technique for Ceramic Surfaces Exposed to High Speed Flows of Abrasive Suspensions", *J. WEAR.*, (in press,1996); also: *Proc. 5th World Congress ChE* (June 1996)

Kho, T. , Rosner, D.E. and Tandon, P., "Simplified Erosion Rate Prediction Technique for Cylindrical Targets in the Crossflow of Abrasive 'Polydispersed' Suspensions", *J. Powder Tech.* (in press, 1996)

Konstandopoulos, A.G. and Rosner, D.E.,"Inertial Effects on Thermophoretic Transport of Small Particles to Walls With Streamwise Curvature---I. Experiment, II. Theory", *Int. J. Heat Mass Transfer* **38** (12)2305-2327 (1995).

Koylu, U., Xing, Y., and Rosner, D.E., "Fractal Morphology Analysis of Combustion-Generated Aggregates Using Angular Light Scattering and Electron Microscope Images", *Langmuir* (ACS) **11** (12) 4848-4854 (1995)

Mackowski, D.W., Tassopoulos, M. and Rosner, D.E., "Effect of Radiative Heat Transfer on the Coagulation Dynamics of Combustion-Generated Particles", *Aerosol Sci. Technol (AAAR)* **20**, 83-99 (1994).

McEnally, C.S., Koylu, U.O., Pfefferle, L.D. and Rosner, D.E., "Soot Volume Fraction and Temperature Measurements in Laminar Non-Premixed Flames Using Thermocouples", *Combustion & Flame* (submitted 1996)

Neimark, A.V., Koylu, U.O. and Rosner, D.E., "Extended Characterization of Combustion-Generated Aggregates: Self-Affinity and Lacunarities", *J. Colloid Interface Sci.* (in press, 1996)

Rosner, D.E., **Transport Processes in Chemically Reacting Flow Systems**, Butterworth-Heinemann (Stoneham MA), 3d Printing (1990) sold out; for 4th printing contact author directly.

Rosner, D.E. and Tandon, P., "Prediction and Correlation of Accessible Area of Large Multi-Particle Aggregates", *AIChE J.* **40** (7) 1167-1182 (1994)

Rosner, D.E. and Tandon, P., "Rational Prediction of Inertially Induced Particle *Deposition* Rates for a Cylindrical Target in a Dust-Laden Stream" *Chem Eng. Sci.* **50** (21) 3409-3431(1995)

Rosner, D.E., Tandon, P. and Labowsky, M.J., "Rapid Estimation of (Metal-)Cylinder *Erosion* Rates in Abrasive Dust-Laden Streams", *AIChE J.* **41** (5)1081-1098 (1995)

Tandon, P., and Rosner, D.E., "Translational Brownian Diffusion Coefficient of Large (Multi-particle) Suspended Aggregates", *Ind Eng Chem-Res* (ACS) **34** 3265-3277(1995)

Tandon, P., and Rosner, D.E., "Sintering Kinetics and Transport Property Evolution of Large Multi-Particle Aggregates", *Chem. Eng. Communic.* (S.K. Friedlander issue), (in press, 1996)

Xing,Y., Koylu,U.O., and Rosner, D.E., "Synthesis and Restructuring of Inorganic Nano-particles Particles in Counterflow Diffusion Flames",*Comb & Flame* (in press,1996);also: Paper #88d *5th World Congress ChE* (6/96)

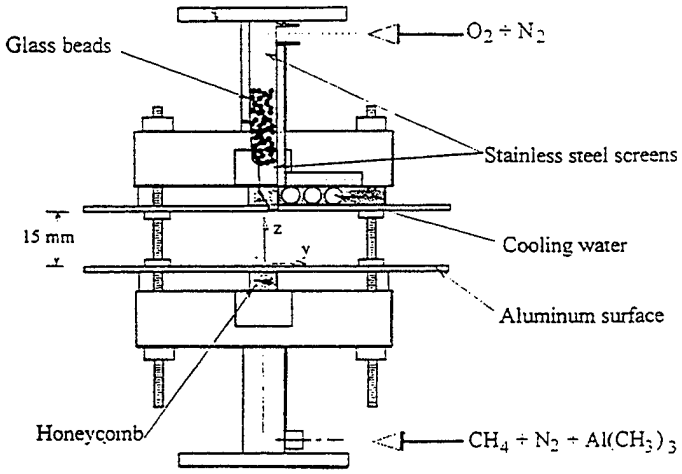

Fig. 1. Schematic of the rectangular counterflow diffusion flame (CDF-) burner assembly (after Xing *et.al.* (1996))

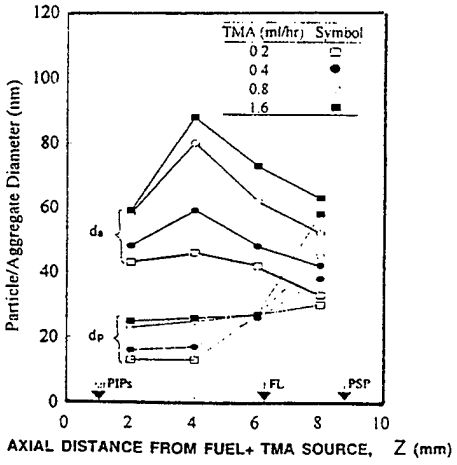

Fig. 2. Mean spherule ("primary" particle) diameter and TEM area-equivalent aggregate diameter as functions of position z in CDF for various TMA seed levels (Xing *et. al.*(1996))

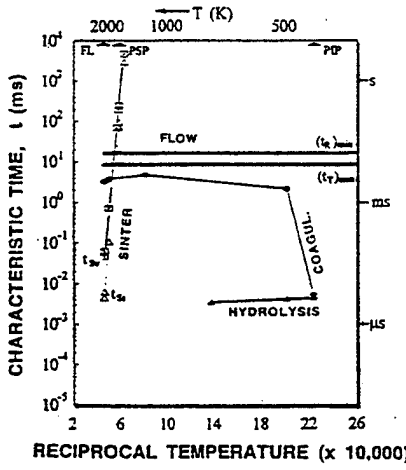

Fig. 3. Characteristic times (log-scale) as a function of $10^4/T_g$; for comparing the relative importance of simultaneous rate processes (after Xing *et.al.* (1996))

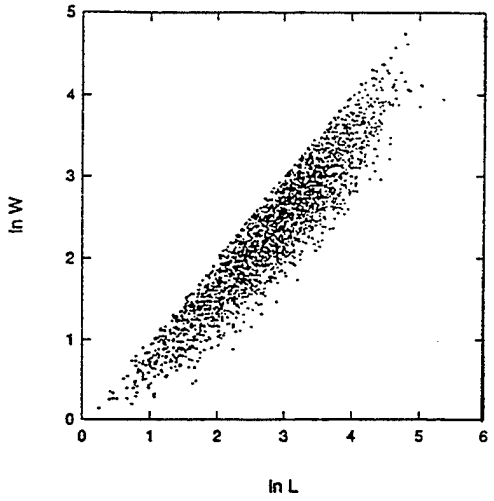

Fig. 4. Aspect-ratio properties of carbonaceous soot thermophoretically sampled from diffusion flames (after Neimark *et.al.* (1996))

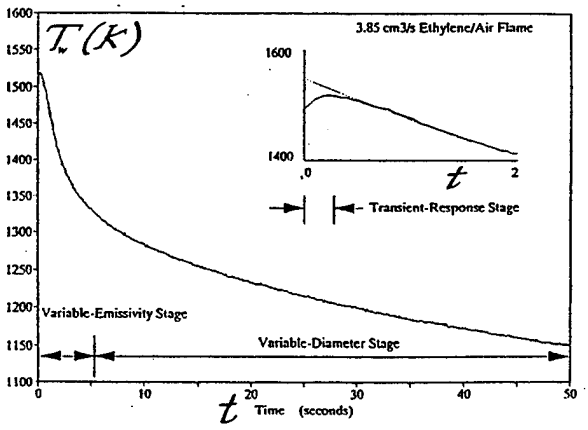

Fig. 5. Typical thermocouple temperature history used to obtain both local soot volume fraction f_v (after McEnally et.al. (1996) and Eisner and Rosner (1985)) and local gas temperature T_g (see inset).

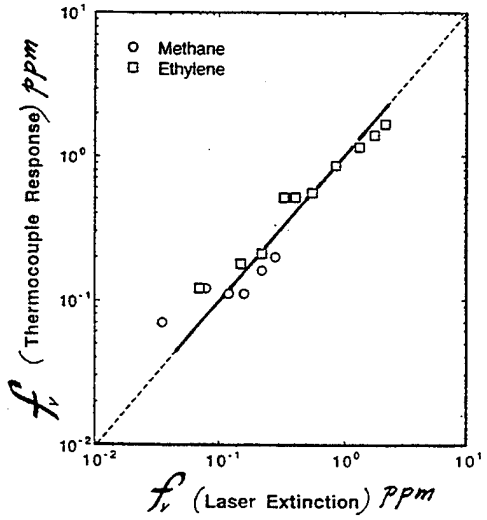

Fig. 6. Plot of f_v measured with TPD *vs.* f_v using laser extinction in the counterflow burner (Fig. 1) (after McEnally *et.al.* (1996))

IGNITION IN CONVECTIVE-DIFFUSIVE SYSTEMS

(ARO Grant No. DAAH04-94-G-0051)

Principal Investigator: Chung K. Law

Princeton University
Princeton, NJ 08544

SUMMARY/OVERVIEW

This program investigates ignition in convective-diffusive media with the goal of better understanding diesel engine ignition. In such non-uniform environments the transport phenomena are tightly coupled to the chemical kinetics and hence can exert a strong influence on the ignition process. These complex interactions are studied using the well-characterized counterflow configuration, in which a cold jet of fuel flows against an opposed jet of hot air, and eventually ignites as the air temperature is gradually raised. During the report period we have studied experimentally, computationally, and analytically the ignition of a variety of fuels. The investigation is basically completed for hydrogen, methane, and hydrogen-doped CO and methane, and has been initiated for butane and iso-butane. Specific issues addressed are thermal versus kinetic feedback in inducing ignition, the existence of ignition kernels and the effects of the convective-diffusive loss of heat and radicals from such kernels, the sensitivity of the ignition temperature on the strain rate and the ambient pressure, the catalytic or dominating role of hydrogen as an ignition additive, and the reduction of detailed reaction mechanisms to skeletal and reduced mechanisms. The extensive experimental data obtained are expected to be of utility in further studies on ignition kinetics.

TECHNICAL DISCUSSIONS

1. Experimental Measurements of H_2-Air Ignition

A variable-pressure counterflow ignition apparatus has been constructed and used to measure nonpremixed hydrogen-air ignition temperatures as a function of pressure (0.1-6.0 atm) and strain rate (50-400 s^{-1}). The experimental data is found to be in good agreement with the results of computational modeling using detailed chemical kinetics and transport properties, thereby validating the concepts and techniques employed. In particular, measured ignition temperatures are seen to exhibit Z-shaped pressure-temperature curves analogous to those observed in the homogeneous H_2-air explosion limits (Fig. 1). In addition, ignition temperatures are found to increase monotonically with increasing strain rate, with high sensitivity in the first and third ignition limits and low sensitivity in the second (Fig. 2).

2. Skeletal and Reduced Chemical Mechanisms for H_2-Air Ignition

Systematic techniques such as flux/sensitivity analyses have been used to identify the dominant kinetic pathways at the hydrogen-air ignition state. We have used this knowledge to distill the original reaction mechanism, which consists of nine species and 19 bi-directional elementary reactions steps, into a skeletal mechanism consisting of the minimum number of elementary steps needed to describe the ignition state. It is found that only seven species and six reaction steps are needed to describe the first and second limits, and nine steps for all three limits

(Fig. 3), with exceptional accuracy throughout an extremely wide range of pressure, temperature, and strain rate. In addition, these skeletal mechanisms have been further condensed to a set of reduced mechanisms composed of non-elementary reaction steps that are derived by exploiting the extremely high reactivity and therefore steady-state nature of radicals. This procedure leads to a 5-species/4-step reduced mechanism that describes the ignition state in all three limits.

3. Kinetic Versus Thermal Feedback in H_2-Air Ignition

The role of heat release in providing thermal feedback at the ignition turning point was computationally studied throughout the pressure range of 0.1-10 atm. Contrary to classical notions based upon one-step overall chemistry, thermal feedback was shown to play essentially no or minimal role in the steady-state solution at the ignition turning point - either in its character or parametric dependence (Fig. 4). In the majority of cases studied, turning point and S-curve behavior were found to exist in the complete absence of heat release, driven solely by kinetic feedback provided by nonlinearities in the coupled chemical kinetics. As a result, the location of the ignition turning point, which depends parametrically upon global variables such as the air temperature, strain rate, pressure, and fuel concentration, was found to be essentially governed by the kinetics of gain versus loss of key radicals in the ignition kernel. One cause of this phenomenon was identified as the extremely small size of the radical pool at the ignition turning point, which necessarily limits the degree of localized heat release and temperature perturbation. The small radical pool was also found to decouple the problem such that, on the lower branch and around the ignition turning point, the temperature and possibly major species profiles may be resolved independently of the complex chemistry involving the minor species. Finally, the smallest skeletal mechanism identified, consisting of six elementary steps, was found to provide sufficient kinetic feedback to induce proper ignition turning point behavior in the complete absence of heat release or thermal feedback. The validity of this mechanism was verified in a separate asymptotic analysis which additionally yielded a simple algebraic expression relating the ignition temperature to the system pressure and strain rate.

4. Computational Study of H_2-Doped CO-Air Ignition

Ignition of H_2-doped CO versus hot air has been studied computationally over a wide range of pressures (0.1-10 atm) and H_2 concentrations (0.003-100% in CO) using detailed mass transport properties and chemical kinetics. The system is found to be readily classified into: (a) a hydrogen-catalyzed regime (from 0.003-7% H_2 in CO), and (b) a hydrogen-dominated regime (from 7-100% H_2 in CO), see Fig. 5. In the former regime, ignition temperatures are found to be extremely sensitive to the concentration of the H_2 dopant; in the latter regime, just the opposite is true. Ignition temperatures in the hydrogen-dominated regime are observed to be extremely close to those found for H_2 in N_2, suggesting that the ignition chemistry is dominated by the kinetics of H_2-O_2 oxidation and that in this region CO, like N_2, acts only as a diluent. However, as the concentration of H_2 is reduced, certain reaction steps such as $O + H_2 \rightarrow H + OH$ and $OH + H_2 \rightarrow H + H_2O$ that are crucial to chain branching become increasingly compromised. This is demonstrated by the fact that at 7% H_2 in N_2 the system is no longer ignitable (or extinguishable) in that it ceases to be a multi-valued response to increasing air temperature. In contrast, H_2 in CO remains ignitable down to extremely small concentrations of H_2 (~0.003%) due to the fact that CO can mimic the H_2 through the reaction $OH + CO \rightarrow H + CO_2$. Similar to the pure hydrogen-air system, H_2-CO-air is found to exhibit Z-shaped curves as a function of pressure, clearly indicating the importance of the underlying H_2-O_2 chemistry.

5. Experimental and Computational Studies of Methane-Air Ignition

The study parallels that for H_2-air ignition, using the full chemical kinetics based on the GRI Mech v1.2 mechanism. As in the situations with hydrogen ignition, a localized ignition kernel of maximum reactivity and heat release is identified. In contrast to the hydrogen case,

however, we have shown that heat release and the thermal feedback are indispensable in the methane-air system, because of the 'slower' characteristic ignition chemistry. The ignition temperature decreased abruptly with increasing fuel concentration, for dilute conditions. However, for methane concentrations in excess of 20-30%, the ignition temperature became insensitive to further increases in the fuel concentration. Ignition temperatures increase with increasing strain rate (Fig. 6), and decrease with increasing system pressure at constant pressure-weighted strain rates (Fig. 7), similar to the homogeneous explosion limits. Over the range of pressures the numerical solution indicated that the homogeneous chemical pathways at ignition do not change significantly. Flux, sensitivity, and the Computational Singular Perturbation (CSP) methods were used to identify the ignition chemistry, and provide several simplified kinetic mechanisms. The results obtained using a skeletal mechanism with 22 species and 64 irreversible reactions were found to agree closely with those obtained using full chemistry.

6. Experimental and Computational Studies of H_2-Doped Methane-Air Ignition

The effect of hydrogen doping on methane ignition is similar to that for the CO system, except that the sensitivity with hydrogen doping in the catalyzed regime is lessened. Of particular interest is the result that both experiments and modeling indicated the existence of a two-staged ignition process as the ignition temperature increases, with the first stage being controlled by radical runaway, while the second stage involving thermal feedback (Fig. 8). Furthermore, methane addition to the H_2/N_2/air system was found to inhibit ignition at low to moderate pressures, while facilitating it at pressures greater than ~5 atm.

MAJOR PUBLICATIONS

[1] "Asymptotic analysis of ignition in nonpremixed counterflowing hydrogen versus heated air," by S.R. Lee and C.K. Law, *Combust. Sci. Technol.* 97, 377-389 (1994).

[2] "The role of kinetic versus thermal feedback in nonpremixed ignition of hydrogen versus heated air," by T.G. Kreutz, M. Nishioka and C.K. Law, *Combust. Flame* 99, 758-766 (1994).

[3] "An experimental study of ignition in nonpremixed counterflowing hydrogen versus heated air," by C.G. Fotache, T.G. Kreutz, D.L. Zhu and C.K. Law, *Combust. Sci. Technol.* 109, 373-394 (1995).

[4] "Ignition in nonpremixed counterflowing hydrogen versus heated air: computational study with detailed chemistry," by T.G. Kreutz and C.K. Law, *Combust. Flame* 104, 157-175 (1996).

[5] "Ignition of counterflowing methane versus heated air under reduced and elevated pressures," by C.G. Fotache, T.G. Kreutz and C.K. Law, *Combust. Flame*, in press.

[6] "Ignition of hydrogen and oxygen in counterflow at high pressures," by B.T. Helenbrook and C.K. Law, *Proceedings of the Twenty-Sixth Symposium (International) on Combustion*, in press.

[7] "Theory of thermal and radical induced ignition of counterflowing hydrogen versus oxygen at high temperatures," by B.T. Helenbrook, H.G. Im and C.K. Law, submitted.

[8] "Ignition in counterflowing CO/H_2 versus heated air," J.Y.D. Trujillo, T.G. Kreutz and C.K. Law, submitted.

[9] "Ignition of hydrogen-enriched methane by heated air," by C.G. Fotache, T.G. Kreutz and C.K. Law, submitted.

[10] "Ignition in nonpremixed counterflowing hydrogen versus heated air: computational study with skeletal and reduced chemistry," by T.G. Kreutz and C.K. Law, submitted.

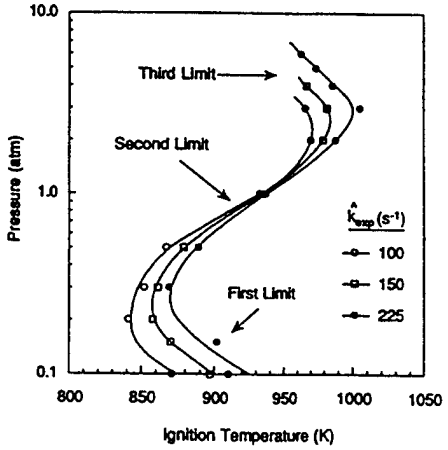

Fig. 1: Ignition temperatures vs. pressure in the H_2/air system.

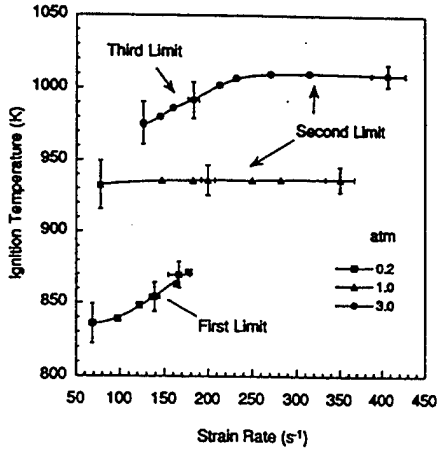

Fig. 2: Ignition temperatures vs. strain rate in the H_2/air system.

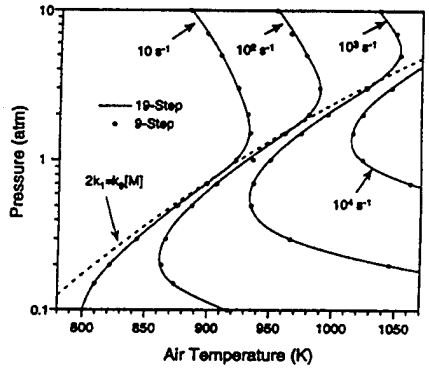

Fig. 3: Comparison between results using full and simplified kinetic mechanisms (H_2/air).

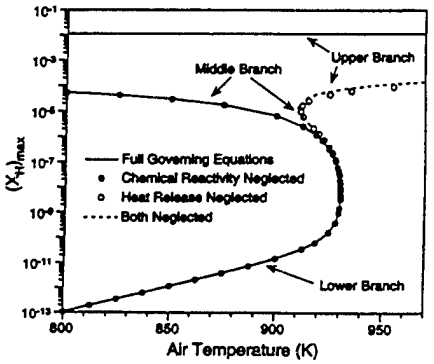

Fig. 4: S-curves calculated using various governing equations approximations (H_2/air).

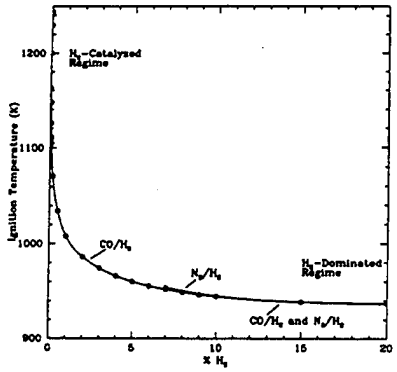

Fig. 5: Effect of H_2 concentration on ignition temperatures in CO/H_2 and N_2/H_2 mixtures.

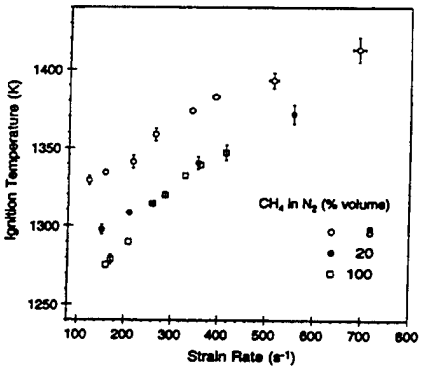

Fig. 6: Ignition temperatures vs. strain rate in the CH_4/N_2/air system.

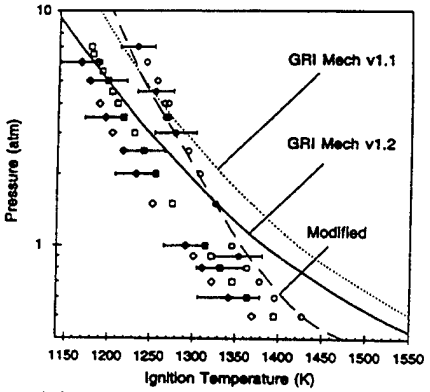

Fig. 7: Ignition temperatures vs. pressure (CH_4/N_2/air).

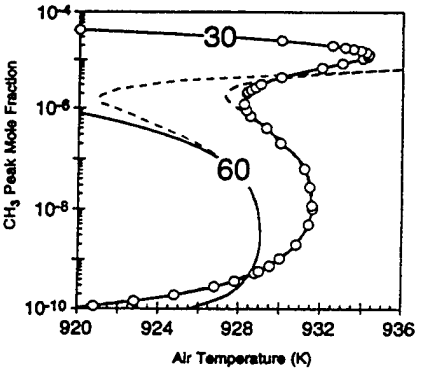

Fig. 8: Double-staged ignitions in the CH_4/H_2/air system.

FLAMELET SURFACE DENSITY AND BURNING RATE INTEGRAL IN PREMIXED FLAMES

ARO Grant # DAAH04-95-1-0109

Principal Investigator: F. C. Gouldin

School of Mechanical and Aerospace Engineering
Cornell University
Ithaca, NY 14853

SUMMARY / OVERVIEW

Our research objective is the development of expressions for mean chemical reaction rates in practical combustion systems. We are studying premixed flames for conditions under which chemical reaction is confined to thin sheets and reaction rates are proportional to the area of these sheets. We plan to measure the area of such sheets by measuring the distribution of surface orientation using multi-sensor thermocouple probes and an average value of the area via conditional flow velocity measurements leading to the determination of the burning rate integral which, in turn, is proportional to the average area. Fully three dimensional flamelet orientation measurements have not been achieved to date, and data for mean flamelet surface area are limited.

TECHNICAL DISCUSSION

Introduction

Premixed turbulent combustion occurs in many practical devices, and for an important range of conditions chemical reaction is confined to thin sheets or interfaces separating reactants from products - the flamelet regime. In this regime the mean flamelet surface density or surface to volume ratio, $\bar{\Sigma}$, is an important quantity that is proportional to the mean chemical reaction rate. A widely used expression for the mean rate of production formation is $\langle w \rangle = \rho_r u_L I_o \bar{\Sigma}$, where ρ_r is the reactant gas density, u_L is the laminar burning velocity of the mixture, and I_o is a correction term to account for the effects of flamelet curvature, strain and transients on the mean flamelet reaction rate per unit surface area.

In previous Cornell work, it has been shown that $\bar{\Sigma} = \langle 1 / | \underline{N} \cdot \underline{n}_y | \rangle n_y$ [1] and, to reasonable approximation; that $n_y = N \langle c \rangle (1 - \langle c \rangle)/l$ [2]. In the first expression $\underline{N}$ is the flamelet surface normal, $\underline{n}_y$ is a unit vector with arbitrary orientation; and n_y is the mean flamelet crossing density on a line parallel to $\underline{n}_y$. In the second expression $\underline{n}_y$ is no longer arbitrary but is locally normal to $\langle c \rangle$ constant surfaces; y is a coordinate parallel to $\underline{n}_y$; n_y is the associated mean crossing density; N is the mean number of flamelet crossings on y across the turbulent flame; and finally l is a measure of the flame brush thickness. A major goal of the current research is the measurement of $\underline{N}$ and N for V- and Bunsen flames.

B_T, the burning rate integral defined as the integral of $\langle w \rangle$ along y across the turbulent flame brush, has been suggested as a well-defined and more appropriate measure of combustion rate than the ill-defined burning velocity [2]. With this definition of B_T and the above expression for $\langle w \rangle$, it follows that

$$B_T / \rho_r u_L = \int I_o \left\langle \frac{1}{| \underline{N} \cdot \underline{n}_y |} \right\rangle N \frac{\langle c \rangle (1 - \langle c \rangle)}{l} dy$$

$$= \langle I_o \langle \frac{1}{| \underline{N} \cdot \underline{n}_y |} \rangle \rangle_N,$$

where the outer angle brackets denote a weighted average along y over the flame brush. A second objective of our research program is the measurement of B_T for a variety of conditions using methods based on integral and control volume analyses.

Flamelet Normal Measurement

As a result of collaborations with Iskender Gökalp and co-workers at CNRS Orléans, France, we have developed a method for measuring $\underline{N}$ in three dimensions [3]. The method involves the determination of flamelet crossing events at 3 or 4 closely spaced points and the measurement of the times required for the finite thickness flamelet to cross the individual observation points, transit times. Using the transit times and the time intervals between flamelet crossings at the different observation points, lag times, it is possible to determine $\underline{N}$ and V_n, the flamelet normal velocity in the laboratory frame.

These point measurements can be made in several different ways including laser induced Rayleigh scattering, compensated thermocouples and ionization probes. Because of their potential for high spatial resolution, we have been working with thermocouples and ionization probes.

Several years ago at Cornell, we developed a new calibration method for determining the response time constant of thermocouples in premixed flames [4]. The method allows one to determine thermocouple time constants for heating in products and cooling in reactants. More recently we completed a series of thermocouple measurements in Bunsen flames and in perturbed laminar flow V-flames undertaken to evaluate the performance of compensated thermocouples under controlled conditions relavent to premixed turbulent flame conditions [5]. Thermocouple voltages are amplified, A/D converted and stored for later computer analyses which include numerical filtering and compensation using a variable time constant. Good results were obtained in the study cited, and it was seen that the keys to success are low noise thermocouple signal amplification, high A/D converter resolution, and appropriate matching of numerical filter cut-offs to experimental conditions.

In the last year we completed a set of experiments using ionization probes intended to evaluate their utility in measurements of $\underline{N}$. The results are not encouraging. Probe response was found to depend on many parameters including the flamelet orientation and velocity with respect to the probe. In several cases it was not possible to detect each flamelet crossing event. As a consequence, we have decided not to pursue further measurements with ionization probes.

For thermocouple measurements, the next step is the development of a multi-sensor probe with several closely spaced thermocouple junctions. Experience with preliminary probe designs indicates there is a potential for interferences between the different sensors. We are now working with a more refined probe design in order to avoid interferences.

Burning Rate Integral Developments

As noted we have suggested that the burning rate integral, B_T, be used as the appropriate measure of the mean combustion rate rather than the burning velocity, u_T, which in general is ill-defined [2]. During the past year we have developed a refined definition for B_T which accounts for complex flame geometries and have extended the idea of burning rates to steady laminar flames [6]. A new way to measure B_T has been demonstrated, and it has been shown that burning velocity measurements, because the quantity is ill-defined, can overstate the effect of turbulence on combustion rates by 100 percent or more.

Consider a general flame and an orthogonal, curvilinear coordinate system with the y coordinate perpendicular to <c> constant surfaces (or c surfaces for laminar flames) and scale factors h_x, h_y, h_z. Then

$$B_T = \int \langle w \rangle \, dy \; / \; h_x^* h_y^* = (\bar{\rho} \tilde{u}_y)^*,$$

where the integral is carried out across the flame [6]. The asterisk denotes values at the point in the flame ($y = y^*$) where the y directed mean mass flux ($\bar{\rho}\tilde{u}_y$) equals B_T. This expression is obtained by consideration of the total combustion rate of the flame and is valid for laminar flames as well as with <w> replaced by w and $(\bar{\rho}\tilde{u}_y)^*$ by $(\rho u_y)^*$. The refinement is the presence of the scale factors which are important for highly convoluted flames, especially laminar flamelets, and the formal linking of the burning rate integral definition to the total combustion rate of the flame.

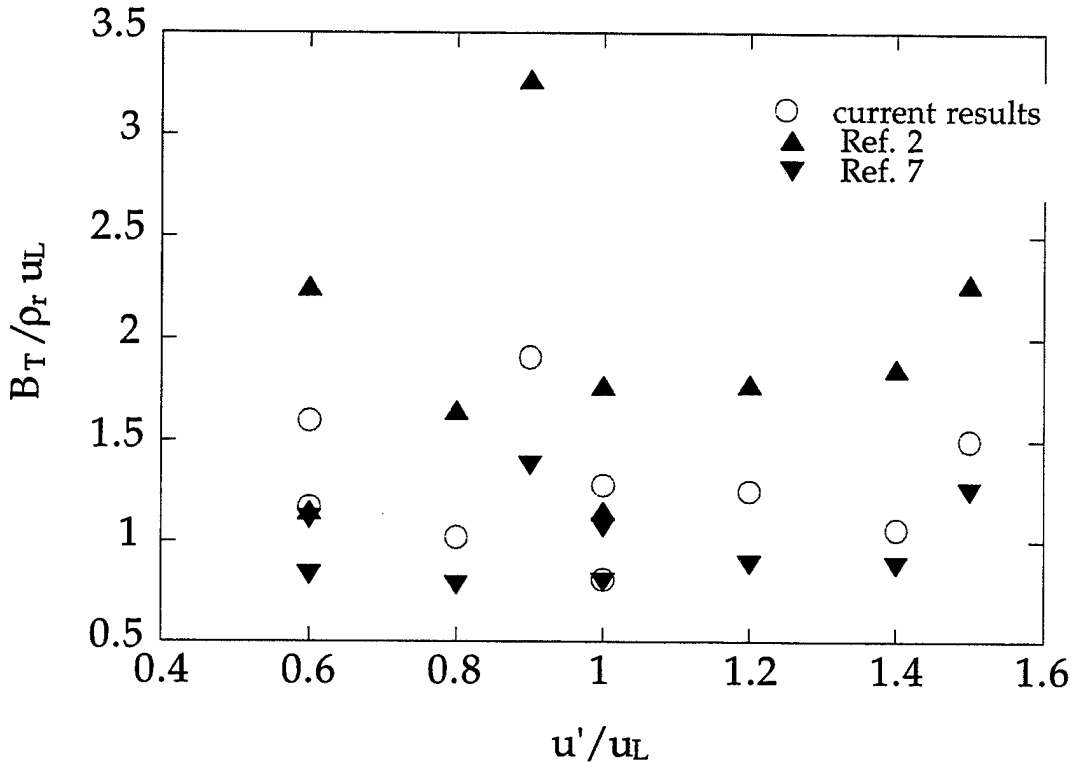

Fig. 3. Plot of burning rate integral results versus turbulent intensity in the reactant flow divided by the laminar burning velocity. For the current results (circles), the reported values are the average for each of 9 turbulent V-flames of values obtained with data at two streamwise locations, 50 and 60 mm from the flame stabilizer rod. The Ref. [2] values (upright triangles) were estimated using reactant conditional velocity data and a control volume analysis; the Ref. [7] (inverted triangles) using a similar control volume analysis and product conditional values. The B_T values are lower than expected based on burning velocity measurements in similar flames.

B_T can be obtained experimentally as follows, using Favre averaging [6].

$$B_T = \left[\int_{-\infty}^{\infty} \bar{\rho}\tilde{u}_y \, h_x h_z (d\tilde{c}/dy)\, dy + \int_{-\infty}^{\infty} \left[\frac{\partial}{\partial x} (h_y h_z \langle \rho u_x'' c'' \rangle) + \frac{\partial}{\partial z} (h_x h_y \langle \rho u_z'' c'' \rangle) \right] dy \right],$$

where as before the asterisk denotes the point $y = y^*$ where $(\bar{\rho}\tilde{u}_y)^* = B_T$. The right hand side of the above can be evaluated provided experimental data for the mean normal mass flux, $\bar{\rho}\tilde{u}_y$, and the two turbulent fluxes are available. We have demonstrated the use of this equation with conditional

velocity data in V-flames. In this case the turbulent fluxes can be neglected, and only the first integral need be evaluated. Results are shown in Figure 1, above.

Future Work

As noted we are developing a thermocouple probe for measuring $\underline{N}$, and this is our primary effort at the present time. A new probe is in the preliminary stages of testing. The major test method for the probe is a laminar V-flame perturbed by a Karman vortex street. In this case the perturbations are two dimensional, and $\underline{N}$ can be measured using laser tomography as well as our sensor. We hope to be in the testing phase in a few months.

In making B_T estimates using conditional velocity data, we have assumed thin flamelets which introduces a systematic error since a certain fraction of velocity measurements are made within the finite thickness flamelet at gas densities between the reactant and product gas densities. The result is that reactant conditional mass fluxes are overestimated, while product conditional fluxes are underestimated. Methods for making corrections to these mass flux estimates are now being developed and will be tested using Miles' data [8]. Once we have tested a method for making such corrections we will return to the laboratory to make a series of B_T measurements based on laser doppler velocimetry.

REFERENCES

1. Gouldin, F.C., *Analysis of Certain Closure Models for Premixed Turbulent Combustion*, in *Physical and Chemical Aspects of Combustion: A Tribute to Irvin Glassman*, R.F. Sawyer and F.L. Dryer, Editors. 1996, Gordon and Breach Science Publishers: Newark, NJ.
2. Gouldin, F.C. and P.C. Miles, *Chemical Closure and Burning Rates in Premixed Turbulent Flames.* Combustion and Flame, 1995. **100**: p. 202 - 210.
3. Ghenaï, C., *et al. Flamelet Spatial and Temporal Dynamics in Turbulent Premixed Flames Based on Two-Point Measurements, presented as poster at* the **25th Symposium (International) on Combustion** *July-August, 1994, Irvine, California.* 1994. Irvine, California.
4. Miles, P.C. and F.C. Gouldin, *Calibration of Fine-Wire Thermocouples for Compensated Temperature Measurements in Premixed Turbulent Flames.* Combustion Science and Technology, 1993. **89**: p. 181 - 199.
5. Tacke, M.M. and F.C. Gouldin, *Evaluation of Compensated Thermocouple Measurements in Premixed Flames*, AIAA 95-0142, presented at the 33nd Aerospace Sciences Meeting, Reno Nevada, January 9-12, 1995.
6. Gouldin, F.C., *Combustion Intensity and Burning Rate of Premixed Flames*, to be presented at the **26th Symposium (International) on Combustion**, Universita Federico II, Naples, Italy, July 28 - August 2, 1996.
7. Gouldin, F.C. and P.C. Miles. *Analysis and experimental estimation of the burning rate in premixed turbulent V-flames,* presented at the *1993 Technical Meeting of the Eastern States Section of the Combustion Institute*. 1993. Princeton University, Princeton NJ.
8. Miles, P.C., *Conditional velocity statistics and time-resolved flamelet statistics in premixed turbulent v-shaped flames*, 1991, Ph.D. thesis *School of Mechanical and Aerospace Engineering*, Cornell University: Ithaca, NY. p. 535.

ADVANCED SUPERCRITICAL FUELS

AFOSR Task # 93WL002

Principal Investigators: Tim Edwards, Jim Gord, Mel Roquemore

USAF Wright Laboratory
WL/POSF Bldg 490
1790 Loop Rd N
Wright Patterson AFB, OH 45433-7103

SUMMARY/OVERVIEW:

Increases in aircraft and engine performance are increasing the heat load being transferred into an aircraft's primary coolant--the fuel. This research is aimed at understanding the limitations of operation of fuel heated to 480 °C (900 °F) and beyond. Important issues are expected to be thermal stability, heat transfer/flow instabilities, and injection/combustion properties. This discussion focuses on thermal stability.

TECHNICAL DISCUSSION

"Thermal stability" refers to the ability of a fuel to absorb heat without the formation of solid deposits or other undesirable reaction products. Current jet fuels are relatively thermally stable up to temperatures of ~170 °C (325 °F). This research is aimed at determining the barriers to the use of a hydrocarbon fuel at 480 °C (900 °F) and beyond. Two distinct types of fuel reactions are involved in thermal stability at these temperatures: thermal-oxidative and pyrolytic reactions. Thermal-oxidative stability has been the subject of a great deal of study for many years, but much remained to be understood about the underlying chemistry and physics of deposition at the beginning of our work [1]. As described in more detail in last year's abstract, advances in diagnostics [2,3] and modeling [4] have been used to improve the understanding of thermal-oxidative deposition and mitigation measures to control it. The mechanism of action of an additive package undergoing field tests at various AF and ANG bases was determined [5]. Counter-intuitive oxygen concentration effects were seen, and studies are continuing to understand this phenomenon [6]. One of the fuel diagnostics developed was used in a totally different application--pressure-sensitive paint [7]. In summary, the understanding of thermal-oxidative deposition is fairly mature, and the methods to control it are known and fairly well understood. Applying this knowledge to aircraft fuel systems is a difficult engineering challenge, however.

In contrast, the pyrolytic deposition (coking) in fuels that occurs at ~400 °C (750 °F) and above is not as well understood [8]. This type of deposition has been studied in detail under petroleum refinery conditions because of its importance to such processes as ethylene production [9,10,11]. A composite of literature mechanisms is presented in Figure 1. This mechanism comes from refinery-type conditions: near-atmospheric pressure, low surface/volume flow

systems, high dilution with steam, and long steady-state periods of operation (months). In contrast, high temperature aircraft fuel systems are characterized by high pressure (~35-70 atm), high surface/volume ratio (e.g., in heat exchangers where mm-scale passages are found), undiluted hydrocarbon flow, and constant changes in flows/temperatures/pressures. Low pressure, low surface/volume ratio, and dilution are thought to minimize deposition in thermal cracking; high (supercritical) pressures have been found to minimize deposition in catalytic cracking [19]. Because of the important differences between aircraft and refinery conditions, we have looked at pyrolytic deposition in more detail in the last year in single-tube heat exchanger tests at fuel temperatures of 550-700 °C (1000-1300 °F) [12,13,14]. It was found that the pyrolytic deposition characteristics for various fuels in flowing tests [12] differed substantially from the characteristics seen in batch reactor tests reported in the literature. Interestingly, multi-component jet fuels showed substantially less pyrolytic deposition than pure compounds or highly processed solvents in these tests. Apparently, some of the thousands of hydrocarbons in typical jet fuels act as hydrogen donors to minimize deposition. In contrast, the processed solvents and pure hydrocarbons produced much less thermal-oxidative deposition.

The filamentous carbon shown in Figure 1 is a particularly pernicious form of coking. Filamentous carbon is catalytically formed, with the catalyst being grains of the metal heat transfer surface which are removed from the surface as the carbon filaments grow [11]. Removal of metal from the thin (sub-mm) heat transfer surfaces on aircraft is an obvious concern. The mechanism and rates of formation of the various types of pyrolytic carbon under aircraft conditions is now a focus of our work. Filamentous carbon has been seen at high pressure in the Princeton flow reactor, where nickel tubes were found to be much more catalytically active than stainless steel [15]. The presence of filamentous carbon was confirmed in larger-scale tests at WL [12]. Tests also confirmed Princeton (and low-pressure literature) results in the activity of various surfaces toward filamentous carbon formation: Ni~Fe>>stainless steel. Inert coatings, such as Silcosteel®, were found to be effective, but only in 1000 Å thicknesses or greater [12]. Ongoing tests with "superalloys" (high Ni or Co alloys from Haynes and Inco) have seen coking behavior similar to stainless steel. A high temperature Re alloy (e.g., see [16]) was also found to be resistant to catalytic carbon formation, consistent with literature predictions [17]. The effect of pyrolysis-suppressing additives [18] was also assessed, with the additives effective at 5% levels in a flow reactor [12]. Work is continuing to find additives that will be effective at suppressing coking at lower concentrations.

[1]. Hazlett, R. N. *Thermal Oxidation Stability of Aviation Turbine Fuels*, ASTM Monograph 1; American Society for Testing and Materials: Philadelphia, 1991.

[2]. Gord, J. R., Buckner, S. W., Weaver, W. L., "Dissolved O_2 Quantitation in Fuel Through Measurement of Dynamically Quenched Fluorescence Lifetimes," 16th International Congress on Instrumentation in Aerospace Simulation Facilities, WPAFB, OH, July 18-21, 1995; IEEE Publication 95CH3482-7, pp. 36.1-36.8.

[3]. Zabarnick, S., Zelesnik, P, M., Grinstead, R. B., "Jet Fuel Deposition and Oxidation: Dilution, Materials and Oxygen Effects," ASME-95-GT-50, presented at 6/95 ASME Turbo Expo, Houston, TX; accepted for publication in Journal of Engineering for Gas Turbines and Power.

[4]. Chin, L. P., Katta, V. R., "Numerical Modeling of Deposition in Fuel Injection Nozzles," AIAA 95-0497, presented at 1/95 AIAA Aerospace Sciences Meeting, Reno, NV.

[5]. Vilimpoc, V., Sarka, B., Weaver, W. L., Gord, J. R., Anderson, S., "Effects of Additives on Particle Size, Mass-Deposition Rate, and Oxygen Concentration in Thermally Stressed Jet Fuel," paper prepared for 6/96 ASME/IGTI Turbo Expo '96, Birmingham, England. For a summary of the additive program, see Heneghan, S. P., Zabarnick, S., Ballal, D. R., "JP-8+100: The Development of High Thermal Stability Jet Fuel," AIAA Paper 96-0403, Jan. 1996.
[6]. Ervin, J. S., Williams, T. F., "Dissolved Oxygen Concentration and Jet Fuel Deposition," Ind. Eng. Chem. Res., Vol. 35, pp. 899-904, 1996.
[7]. Sabroske, K. R., Gord, J. R., "Surface Coatings for Optical Pressure Measurements," 16th International Congress on Instrumentation in Aerospace Simulation Facilities, WPAFB, OH, July 18-21, 1995; IEEE Publication 95CH3482-7, pp. 39.1-39.6.
[8]. Edwards, T., "Recent Research Results in Advanced Fuels," ACS Petroleum Chemistry Division Preprints, Vol. 41(2), pp. 481-487, Mar. 1996.
[9]. Albright, L. F., Marek, J. C., "Mechanistic Model for Formation of Coke in Pyrolysis Units Producing Ethylene," Ind. Eng. Chem. Res., Vol. 27, 755-759, 1988.
[10]. Trimm, D. L., "Fundamental Aspects of the Formation and Gasification of Coke," 203-232 in Pyrolysis, Theory and Industrial Practice, Albright, Crynes, and Corcoran, eds. Marcel Dekker, 1983.
[11]. Baker, R. T., K, Yates, D. J. C., Dumesic, J. A., "Filamentous Carbon Formation over Iron Surfaces" pp. 1-21 in Coke Formation on Metal Surfaces, Albright and Baker, eds., ACS Symp. Ser 202, 1982; Baker, R. T. K., "Catalytic Growth of Carbon Filaments," Carbon, Vol. 27, No. 3, 315-323, 1989.
[12]. Edwards, T. and Atria, J., "Deposition from High Temperature Jet Fuels," ACS Petroleum Chemistry Division Preprints, Vol. 40(4), pp. 649-654, 1995.
[13]. Atria, J. V., Cermignani, W., Schobert, H. H., "Nature of High Temperature Deposits from n-Alkanes in Flow Reactor Tubes," ACS Petroleum Chemistry Division Preprints, Vol. 41(2), pp. 493-497, Mar. 1996.
[14]. Atria, J. V., Edwards, T., "High Temperature Cracking and Deposition Behavior of an n-Alkane Mixture, " ACS Petroleum Chemistry Division Preprints, Vol. 41(2), pp. 498-501, Mar. 1996.
[15]. Stewart, J. F., Brezinsky, K., Glassman, I., "Pyrolytic Formation of Polycyclic Aromatic Hydrocarbons (PAH) and Solids in Supercritical Methylcyclohexane," paper presented at 10/95 Central States Section/Combustion Institute Meeting, Worcester, MA; also, presentations at '94 and '95 AFOSR Contractor's Meetings.
[16]. Schoenman, L., "4000 °F Materials for Low-Thrust Rocket Engines," Journal of Propulsion and Power, Vol. 11(6) pp. 1261-1267, 1995.
[17]. Baker, R. T. K., and Harris, P. S., "The Formation of Filamentous Carbon," Chemistry and Physics of Carbon, P. L. Walker, ed., Vol. 14, 83-165, 1978.
[18]. Coleman, M. M., Selvaraj, L., Sobkowiak, M., Yoon, E., "Potential Stabilizers for Jet Fuels Subjected to Thermal Stress above 400 °C," Energy and Fuels, Vol. 6(5), pp. 535-539, 1992.
[19]. Dardas, Z., Suer, M. G., Ma, Y. H., Moser, W. R., "High-Temperature, High-Pressure In Situ Reaction Monitoring of Heterogeneous Catalytic Processes under Supercritical Conditions by CIR-FTIR," Journal of Catalysis, Vol. 159, pp 204-211 (1996).

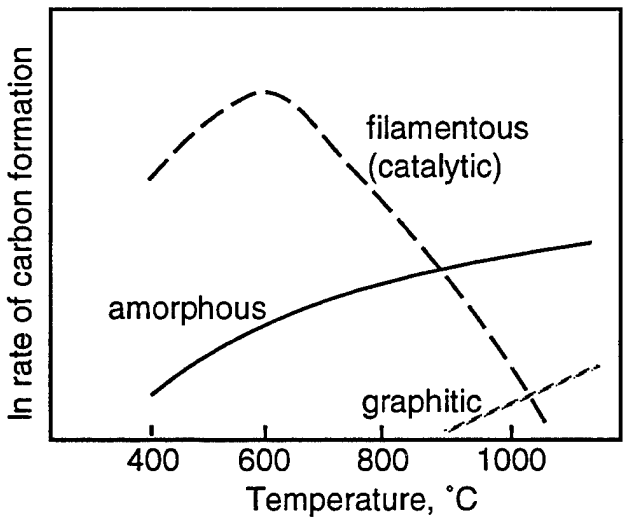

(Baker [11])

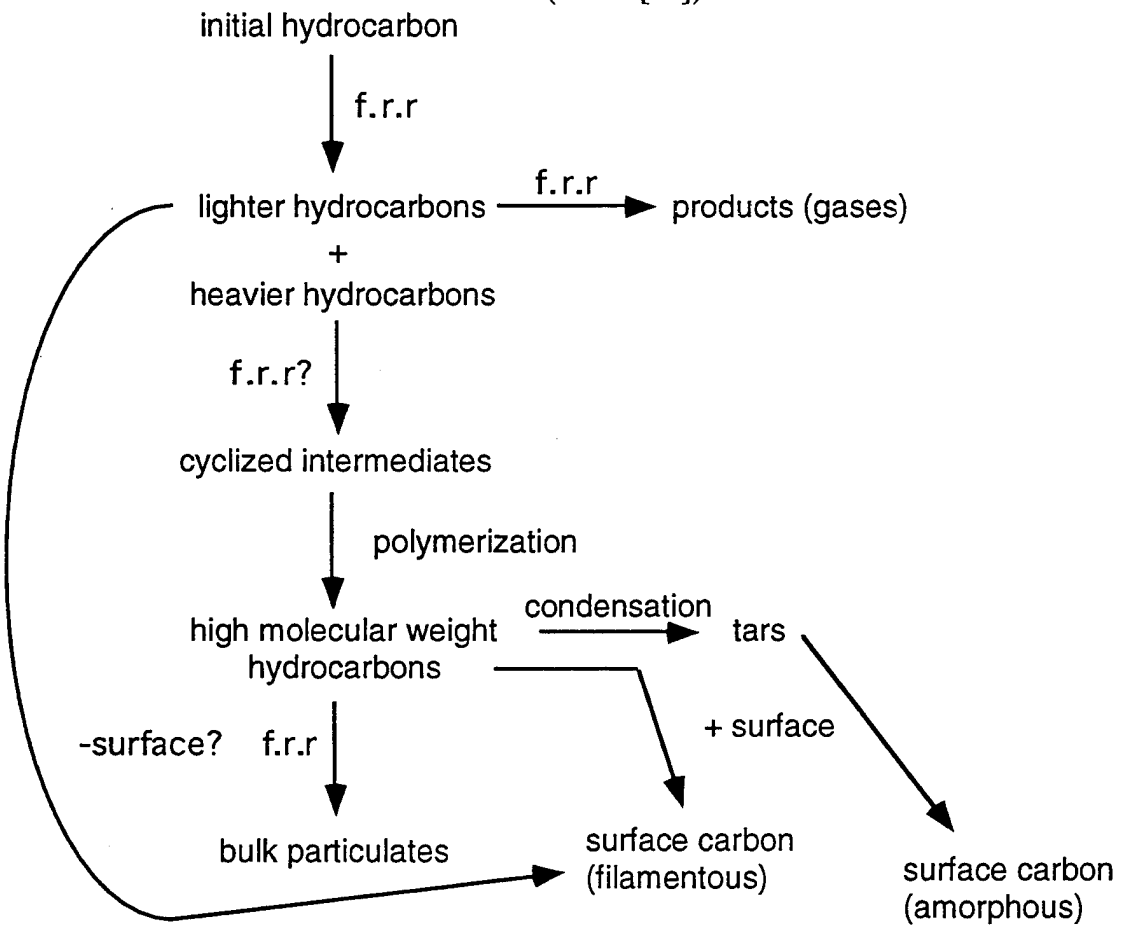

f.r.r = free radical reactions; surface carbon can grow by addition of fluid phase radicals

Figure 1. High temperature coking mechanism--an amalgamation of the views of Trimm (1983), Albright (1988) and Baker (1982) [9-11].

FUELS COMBUSTION RESEARCH
(AFOSR GRANT F49620-95-1-0016)
Principal Investigators: I. Glassman and K. Brezinsky
Department of Mechanical and Aerospace Engineering
Princeton University
Princeton, NJ 08544

Summary

Progress has continued in the investigation of the thermal and combustion characteristics of fuels at conditions of special interest to the Air Force: 1) endothermic fuels subjected to super critical temperatures and pressures 2) mixtures of aromatic and aliphatic hydrocarbons that simulate a thermally cracked jet fuel.

Technical Discussion

1) Supercritical Fuels Degradation

Experimental

A high pressure flow reactor designed to approach the plug-flow idealization has been designed and constructed for the study of supercritical hydrocarbon reactions. A high pressure HPLC pump forces reactants through a capillary tubing coil immersed in a heated-fluidized sand bath. Pressures as high as 15 MPa and temperatures as high as 860 K can be attained. A water-cooled heat exchanger at the entrance and exit of the coil ensure a controlled thermal history and residence time. Experiments were conducted with a residence time on the order of 1 minute in order to simulate a typical residence time of fuel in a next-generation hypersonic aircraft fuel line. Quenched products pass through a stainless-steel frit to filter-out any solids and into a sample collection tube downstream of the reactor. The sample collection tube is removed from the line of flow for separate analysis using GC-FTIR equipment.

In order for the pyrolytic reactions to be studied independently of any auto-oxidative effects, the methylcyclohexane was de-oxygenated by means of a nitrogen sparge for a minimum of 3.75 hours with a nitrogen flow of 2 liters per minute through a maximum of 200 ml of fuel. Based on the results of empirical studies, this sparge time and flow rate reduces the oxygen content to less than 1 part per million. Pressure in the reactor was controlled by means of a dome-loaded back-pressure regulator located downstream of the sample collection tube. Uncertainty in pressure control was +/- 0.2 bar. Temperature was controlled by means of an electronic PID controller with a thermocouple sensing the center of the sand bath. Uncertainty in temperature was +/- 5 Kelvin due to the large size of the sand bath and imperfect fluidization.

Discussion

The effects of temperature on PAH formation in supercritical methylcyclohexane are very pronounced. The results of this study show that methylcyclohexane run through a plug-flow reactor at a reduced pressure of 1.3 and with a residence time of approximately 0.9 minutes will form measurable amounts of PAH, the ostensible precursors to homogeneous solid formation, at temperatures above 820 K. PAH formation increases apparently exponentially at temperatures above 820K -- as expected in situations where Arrhenius kinetics prevail. Solids have been observed to be formed at temperatures slightly above 820 K, supporting the hypothesis that PAH are the precursors to solid formation.

Examination of the condensed and uncondensed products shown in Figures 1 and 2 gives some insight into the types of chemical mechanisms involved in PAH formation. However, possible mechanisms involved in supercritical PAH formation are numerous and these preliminary studies do not provide enough information to discern which reactions dominate. With the ultimate goal of developing a full mechanism for PAH formation in jet fuels, it is useful, however, to describe classes of reactions that are the likely pathways to PAH formation in these experiments.

To summarize these results, PAH formation in supercritical methylcyclohexane at a reduced pressure of 1.3 and temperatures 820 to 844 K is thought to occur through three possible general routes -- although other reaction pathways are likely to exist. First, the molecular structure of some of the products suggests that addition, growth, cyclization and dehydrogenation of aliphatic side chains to form a stable C_6 structure may be one possible mechanism. Second, a Diels-Alder type reaction involving a conjugated diene and a dienophile (both possibly abundant in the flow reactor at the temperatures of reaction) may directly produce a second C_6 structure without going through a radical intermediate. Dehydrogenation of this product may then produce a PAH molecule such as naphthalene. Other authors have noted the importance of the Diels-Alder reaction in supercritical fluids. Third, direct addition of aromatics and aromatic radicals with and without side chains may be another important mechanism in PAH formation.

The effects of pressure on PAH formation in supercritical methylcyclohexane are significant, but not nearly as strong as thermal effects over the range of pressures and temperatures studied. As Figure 3 illustrates, at 784 K, higher pressures result in lower conversion of the reactant, methylcyclohexane to products. Furthermore, there is a shift toward heavier products at higher pressures.

Pressure has two more effects on supercritical methylcyclohexane pyrolysis which should be mentioned. First, an increase in pressure results in an increase in density. Over a reduced pressure range from 0.5 to 2.0 for methylcyclohexane at 784 K, density increases by a factor of 5. At a high density, a molecule can be caged-in by surrounding molecules -- a phenomena commonly associated with chemistry in solution. This cage can have the effect of impeding the opening-up of a cyclical molecule or it can cause molecules to have many rapid encounters with their neighbors rather than the intermittent collisions with a wide variety of partners. In a related work, it has been

postulated that methylcyclopentane, one of the major products of supercritical methylcyclohexane pyrolysis, is produced from such a caging reaction.

Second, the high pressures of this pyrolysis reaction may affect the reaction rates through the following thermodynamic identity:

$$\left(\frac{\partial \ln K}{\partial P}\right)_T = -\frac{\Delta V^{\ddagger}}{RT} \qquad (1)$$

In this equation, $\Delta V^{\ddagger}$ is the volume of activation defined in transition state theory. For a bimolecular reaction, the volume of activation is negative and thus the rate increases with pressure. However, for a unimolecular reaction, the volume of activation is zero or positive and the rate can be expected to remain constant or to decrease with pressure. The decrease in methylcyclohexane conversion to products with increasing pressure can be explained in that the overall reaction, a unimolecular decomposition, has a positive volume of activation, as expected.

Finally, it has been suggested that the structure of the methylcyclohexane molecule makes it particularly prone to PAH and solid formation under the conditions of those estimated for next-generation hypersonic aircraft. That is, it is thought that key steps in the pyrolysis of supercritical methylcyclohexane, the simultaneous production of both stable cyclical C_6 structures and C_1 to C_4 aliphatics and radicals, greatly contribute to the propensity of methylcyclohexane to produce PAH and solids. Potential endothermic fuels which are not prone to produce cyclical C_6 structures, but have comparable abilities to absorb heat may be more suitable for use in these specific aerospace applications.

One alternative endothermic fuel, with an endothermic potential similar to that of methylcyclohexane, is heptane. Preliminary work in our lab has examined the supercritical pyrolysis of n-heptane at a reduced pressure of 1.3 and temperatures up to 830 K. At temperatures above 820 K and with a residence time of less than 1 minute, the products of this reaction were almost entirely uncondensed (gaseous) with, only trace amounts of PAH or solid formation. The major products were C_2 and C_3 aliphatics. This result supports the hypothesis that the ring structure of methylcyclohexane does, in fact, contribute to PAH and solid formation. Thus, n-heptane is less prone to produce PAH and solids than was methylcyclohexane under comparable pyrolytic conditions.

Finally, to further examine the effects of molecular structure on PAH formation, supercritical pyrolysis of toluene and mixtures of 10% heptane and 90% toluene (molar) were conducted under conditions similar to those of the supercritical methylcyclohexane pyrolysis. Toluene alone showed no reaction at temperatures up to 840 K, a reduced pressure of 1.3, and a residence time of approximately 1 minute. This is due to the much higher bond dissociation energies of toluene than of heptane or methylcyclohexane . However, the mixture of toluene and heptane, ran under matching supercritical conditions, showed products that were similar or identical to those seen in methylcyclohexane pyrolysis (Figure 4). Products observed in this study which are identical to those seen in the methylcyclohexane pyrolysis study include: many aromatics with a side chain, indane, indene, and the PAH naphthalene. Furthermore, PAH and solids were observed as products of the pyrolysis of this mixture. This result suggests that the combination of a stabilized C_6 ring structure (from toluene) with aliphatic fragments (from heptane) creates a mixture prone to PAH and solid formation under the conditions of this study. Other proposed endothermic fuels or hydrogen donors with a structure similar to methylcyclohexane may also be particularly prone to PAH and solid formation. Some of the effects of aliphatics on the chemistry of aromatics have been revealed in Part 2 of this program and are discussed in the next section.

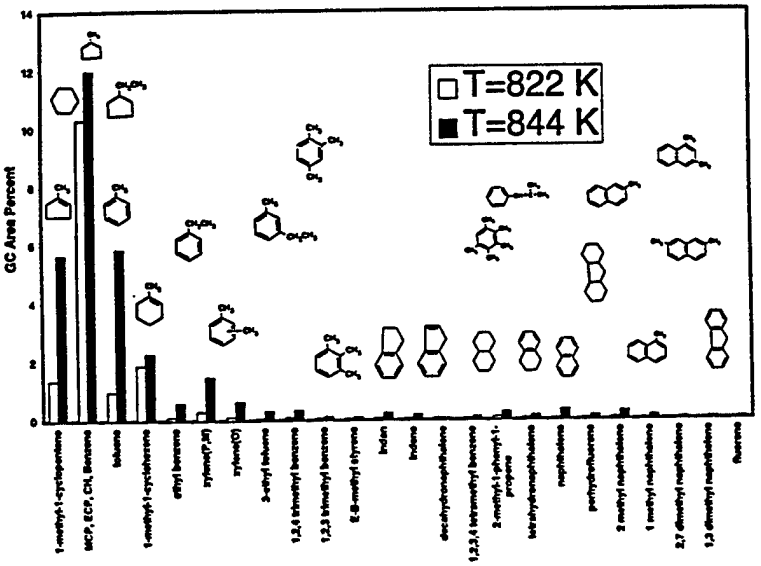

Figure 1: Condensed Products of MCH Pyrolysis

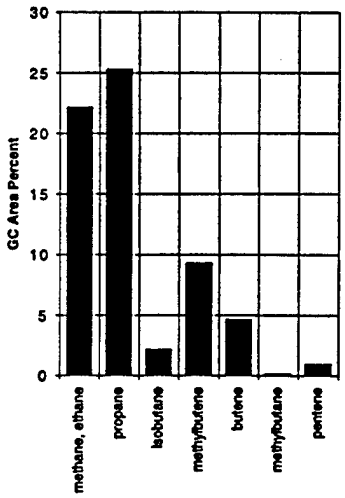

Figure 2: Uncondensed Products of MCH Pyrolysis

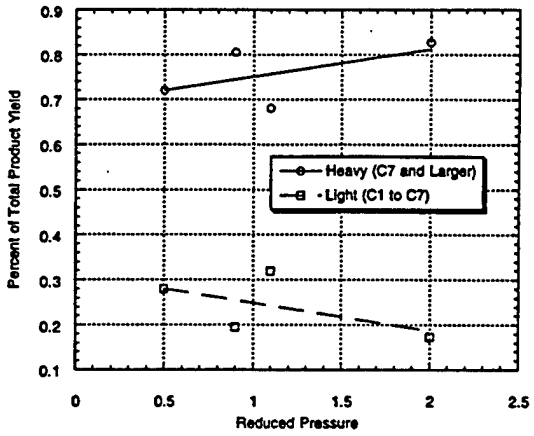

Pigure 3: Effects of Variable Pressure on MCH Pyrolysis

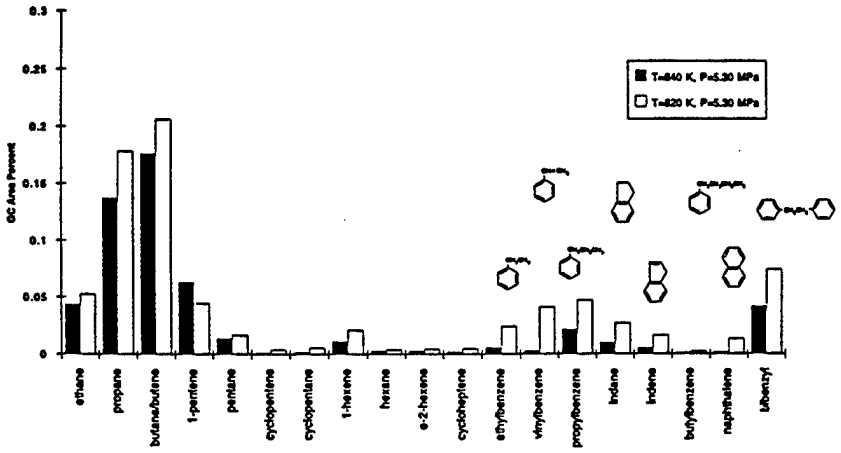

Figure 4: Major Pyrolysis Products from 90% Toluene 10% Heptane Mixture

2) Aromatic-C4 Interaction Chemistry:

Over the past year, the experimental and modeling study of aromatic/aliphatic blends has continued. This examination of the interactive chemistry of blends of C4 aliphatics and monocyclic aromatics has been conducted to better understand the effects of fuel blending on combustion chemistry. Progress has been made in both the experimental and modeling aspects of the study.

Blend oxidation experiments have been compared with oxidation experiments of the associated neat fuels. Experiments that include fuel blend ratios (aromatic to alkane) of 3 to 1 and 1 to 3 were performed at various stoichiometry. Additionally, experimentation has progressed to assure control of initial conditions, improved carbon atom accountability, improved species identification, and repeatability of results. Gas samples were analyzed using gas chromatography. Comparison of chromatograms from any set of three related experiments (i.e., a set could include one chromatogram from a 1500 ppm toluene oxidation, one from a 500 ppm n-butane oxidation, and the third from a 1500 ppm toluene/500 ppm n-butane blend oxidation) indicates that the species produced in the blend oxidation match those found in the oxidation of either neat fuel. Thus far in blend oxidation experiments, no new species were detected, no species that were present for the oxidation of the neat fuels were absent, and the magnitudes of blend intermediates were of the same order as those of both neat fuels. Blending does effect the

decay of fuel components in varying degrees. Compared below are the toluene and n-butane profiles as they occur in both a neat and a 3-to-1 aromatic-to-alkane blend oxidation for various stoichiometry. For these conditions, the presence of n-butane accelerates the toluene decay, while the n-butane decay is slightly inhibited by the toluene. The acceleration of the toluene and the inhibition of the n-butane during the blend oxidation can be explained by the tendency of n-butane to saturate the radical pool while the toluene system is relatively starved for radicals. Other C4 aliphatics less likely to saturate the radical pool to the extent of n-butane (e.g., more tightly bound C4s such as iso-butene and 1,3 butadiene) were substituted. In toluene/iso-butene and toluene/1,3 butadiene experiments, the toluene decay was accelerated, but not to the extent as with n-butane, thereby confirming this radical pool theory. In addition to determining the effect on fuel components, emphasis has been placed on characterizing the effect of blending on all combustion intermediates. Current experiments are being conducted to completely survey the ranges of blend ratios and stoichiometry in order to determine if and when the level of blending affects reactivity beyond the noted effects in radical pool formation.

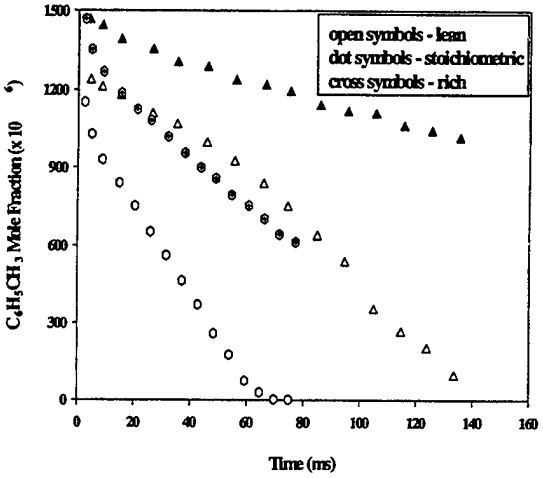

Figure 5. Toluene profiles for experiments with initial toluene of 1500 ppm which demonstrates the effects of 3 to 1 blending at various stoichiometry.

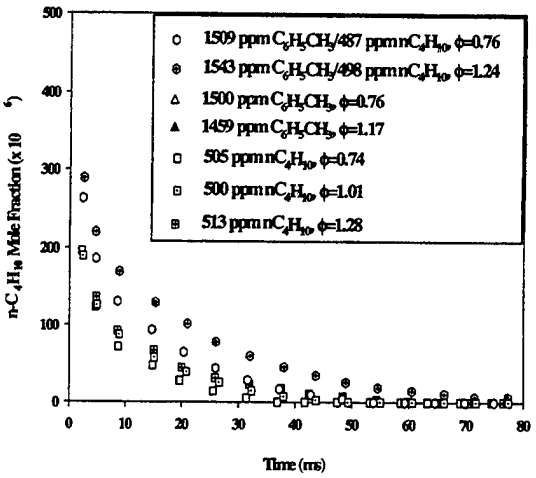

Figure 6. n-Butane profiles for experiments with initial n-butane of 500 ppm which demonstrates the effects of 3 aromatic to 1 alkane blending at various stoichiometry.

A comprehensive aromatic chemical kinetic model has been augmented with detailed C4 and below chemistry. This model is being compared to and adjusted based up flow reactor data. Inclusion of the C4 submechanism has not undermined the original model's ability to predict toluene oxidation at flow reactor conditions. Additionally, the model has demonstrated preliminary success in predicting blend oxidation species. Work continues in the area of model verification and refinement

THEORETICAL AND COMPUTATIONAL STUDIES OF NUCLEATION IN SUPERCRITICAL FUELS

(AFOSR GRANTS F49620-96-1-0169; AASERT F49620-93-1-0054)

Principal Investigator: Pablo G. Debenedetti

Department of Chemical Engineering
Princeton University
Princeton, NJ 08544-5263

SUMMARY/OVERVIEW

In this project we study the influence of fluid-phase non-ideality on the nucleation of pyrolytic products dissolved in supercritical fuels. The complex phase behavior of mixtures composed of non-volatile solutes and a supercritical solvent influences the composition of the solid phases that can form as a result of changes in temperature and pressure along fuel transfer lines. We use thermodynamic and statistical mechanical models of supercritical mixtures to map the regions where precipitation of one or more components of a mixture can occur as a result of cooling, heating, or depressurization. Monte Carlo simulations are used to calculate free energies of nucleation over broad ranges of temperature and pressure. The goal of the research is to improve the basic understanding of how proximity to the critical point influences the thermodynamics and kinetics of deposit formation from supercritical fuels.

TECHNICAL DISCUSSION

A characteristic feature of the phase behavior of non-volatile solutes dissolved in supercritical solvents is retrograde behavior. This is illustrated in Figure 1 (Debenedetti and Kumar, 1988). It can be seen that between 90 and 180 bars, the solubility of acridine in supercritical carbon dioxide decreases with increasing temperature. Retrograde behavior occurs because near the critical point the solvent is highly compressible. Hence in this region the decrease in the solvent's density upon heating is more important than the corresponding increase in the solute's vapor pressure, causing the equilibrium solubility to decrease upon heating (Chimowitz and Pennisi, 1986; Chimowitz et al., 1988). If a mixture is in the retrograde region, the solute will precipitate during heating. A theoretical study was conducted in order to map the retrograde regions of several binary and ternary mixtures composed of polynuclear aromatics in supercritical carbon dioxide. The use of carbon dioxide as the solvent was dictated by the availability of experimental solubility data, which is needed for regressing interaction parameters. Future calculations will be performed using supercritical fuels as solvents.

Figure 2 shows the retrograde regions of phenanthrene, anthracene, and pyrene in supercritical carbon dioxide. Inside the retrograde regions, the solubility of each compound decreases upon heating. The greater a solute's heat of sublimation, the narrower its retrograde region will be.

Figure 3 shows the calculated solid-phase compositions corresponding to isobaric cooling of a saturated mixture of anthracene and pyrene in supercritical carbon dioxide at various pressures. The cooling trajectories and their relationship to the retrograde regions are shown in the inset. The calculation assumes instantaneous precipitation and removal of the solid. The solid-phase composition is cumulative. Note the non-monotonic curve at 120 bar, and the different cumulative compositions that result due to crossing of retrograde boundaries. It can be concluded that the deposition of solids from a supercritical fuel as a result of changes in temperature and pressure will be profoundly influenced by fluid-phase non-idealities. In particular, changes in

temperature and pressure can cause the mixture to enter one or more retrograde regions, whereupon one or more solutes will precipitate upon heating. Furthermore, during adiabatic expansions inside the retrograde region, changes in temperature and pressure have opposite effects: depressurization favors precipitation, but cooling favors dissolution.

The above calculations address the thermodynamic aspects of deposit formation from supercritical fuels. Equally important are the rates of precipitation, and how these are affected by fluid-phase non-ideality. Since the rate of nucleation depends exponentially upon the reversible work of forming a critical-sized nucleus, considerable effort has been expended in calculating this quantity. Approaches range from phenomenological and continuum (i.e., classical nucleation theory) to statistical mechanical, microscopic (i.e., density functional theory). While density functional theory is an important improvement over the classical theory, it requires that the shape of the critical nucleus be assumed. Until recently, no exact method existed for calculating free energy barriers to nucleation. We have developed such a method. The initial results reported here are for crystallization in a supercooled liquid; in future work we plan to apply the technique to calculating free energy barriers to crystallization from supercritical fluids.

The new method consists of a biased Monte Carlo simulation, in which the system under investigation is forced to sample crystalline configurations. Then, the probability of observing the system in a given configuration is related to the free energy cost of forcing the system into the particular configuration,

$$G = - kT \ln P (\xi) + \text{const.}$$

where G is the free energy of the system in a state where the order parameter equals ξ; and $P (\xi)$ is the probability of observing the system in a state such that the order parameter equals ξ. For the crystallization problem being considered here, the order parameter was chosen to be a member of the family of bond-orientational order parameters (Steinhardt et al., 1983). It quantifies the tendency for nearest neighbors of a central molecule to be found along preferred directions, as opposed to the random distribution in a fluid (liquid or gas). The particular bond-orientational order parameter chosen in this work, Q_6, is zero for a fluid, 0.574 for an fcc crystal, and 0.511 for a bcc crystal (van Duijneveldt and Frenkel, 1992). In essence, then, in the course of a simulation the system is forced to sample configurations with high value of the order parameter (i.e., configurations containing crystalline nuclei), and we measure the relative probability of occurrence of a particular value of the bond-orientational order parameter. As the system samples larger values of Q_6, the free energy cost increases. The $G(Q_6)$ relation is non-monotonic. A maximum indicates the formation of a critical nucleus; the corresponding G value is the free energy barrier.

Note that the system is not biased towards any particular crystalline form, since Q_6 is an independent variable. A typical calculation is shown in Figures 4 and 5. The former shows the calculation of the free energy barrier to crystallization (maximum of ΔG vs. Q_6). For this particular example (deeply supercooled Lennard-Jones liquid), the free energy barrier is ca. 25 kT. Another advantage of this method is that it allows the critical nucleus itself to be detected. This is shown in Figure 5. The critical nucleus corresponding to the state point of Figure 4 consists of 240 particles. Note the large deviation from spherical symmetry.

By suitable choice of the order parameter, the new biased Monte Carlo method allows the exact calculation of free energy barriers to nucleation, as well as the determination of the size and shape of the critical nucleus. For example, one can study cavitation in liquids under tension by using density as the order parameter. In future work, we plan to extend the method to mixtures and apply it to nucleation from supercritical fuels. Extension to mixtures is non-trivial: it requires the introduction of semi-permeable membranes in the simulation; the resulting interfaces may require the use of considerably larger systems than the ones we have used so far.

The thermodynamic calculations outlined above will be extended to supercritical fuels. Furthermore, we will include the rate of nucleation into the calculations. This will allow us to investigate the effect of fluid-phase nonidealities on both the driving force (thermodynamics) and rates (kinetics) of deposition from supercritical fuels.

Carnahan, N.F., and K.E. Starling, *J.Chem.Phys., 51,* 635 (1969)
Chimowitz, E.H., and K.J. Pennisi, *AIChEJ., 32,* 1665 (1986)
Chimowitz, E.H., F.D. Kelley, and F.M. Muñoz, *Fluid Phase Equil., 44,* 23 (1988)
Debenedetti, P.G., and S.K. Kumar, *AIChEJ., 34,* 645 (1988)
Steinhardt, P.J., D.R. Nelson, and M. Ronchetti, *Phys. Rev. B, 28,* 784 (1983)
van Duijneveldt, J.S., and D. Frenkel, *J.Chem. Phys., 96,* 4655 (1992)

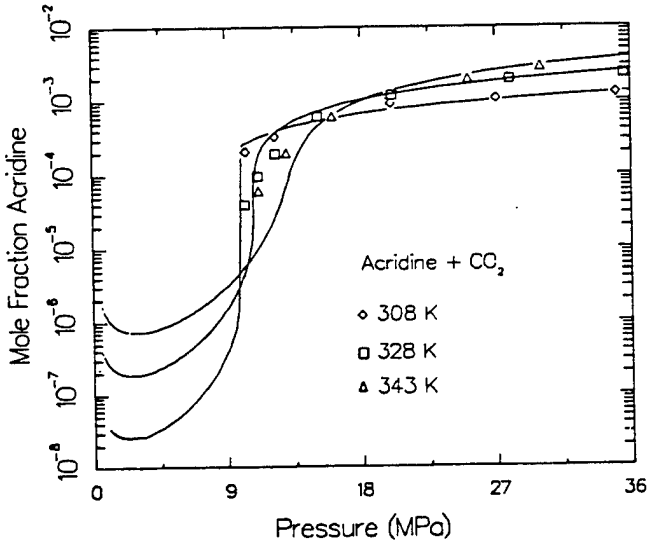

Figure 1: Equilibrium solubility of acridine in supercritical carbon dioxide. Note retrograde behavior between 90 and 180 bar (Debenedetti and Kumar, 1988).

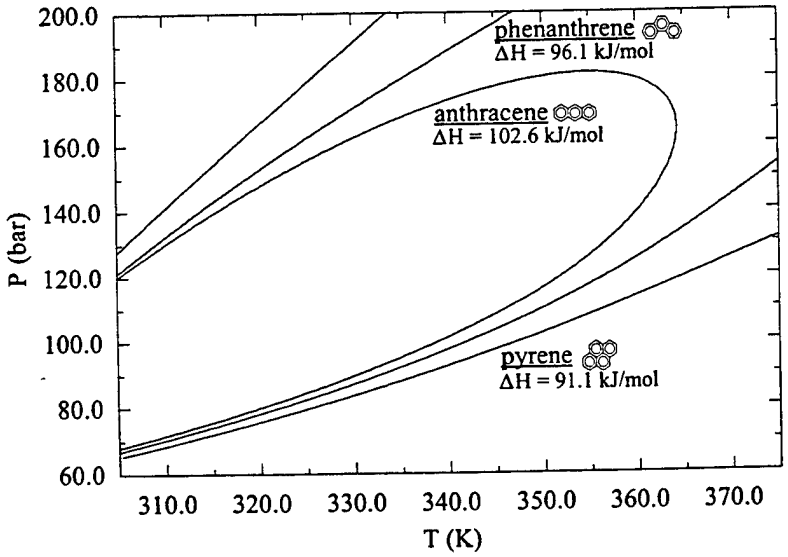

Figure 2: Retrograde regions for anthracene, phenanthrene, and pyrene dissolved in supercritical carbon dioxide. Calculations done with the Carnahan-Starling-van der Waals equation of state (Carnahan and Starling, 1969).

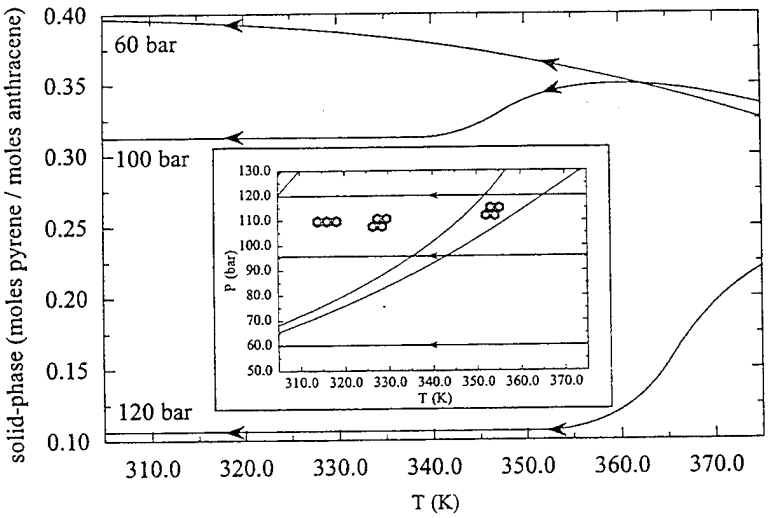

Figure 3: Cumulative solid-phase compositions resulting from the isobaric cooling of a saturated ternary mixture of anthracene and pyrene in supercritical carbon dioxide at three different pressures.

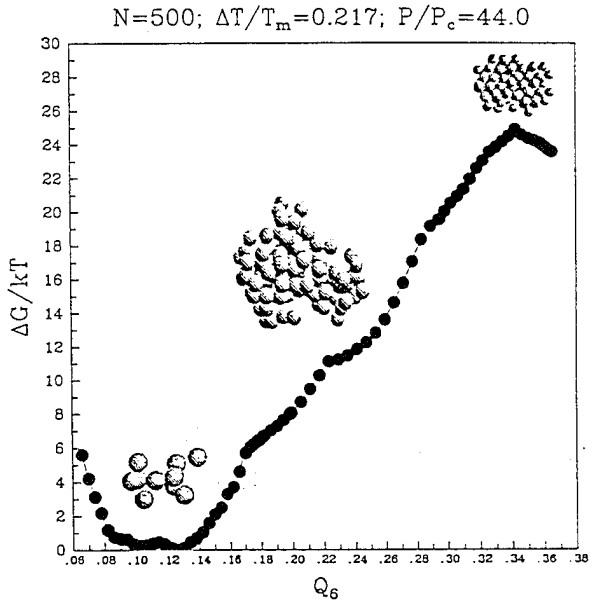

Figure 4: Calculation of free energy barrier to nucleation using novel biased Monte Carlo simulation method. The ordinate gives the free energy cost of creating a crystallite. The abscissa, the bond-orientational order parameter, quantifies the degree of order. The maximum corresponds to the free energy barrier. Also shown on the curve is the growing crystallite. These calculations are for a Lennard-Jones fluid, at an undercooling $(T_m - T)/T_m$ of 22%, and a pressure $P/P_c = 44$ (T_m is the melting temperature, P_c is the critical pressure).

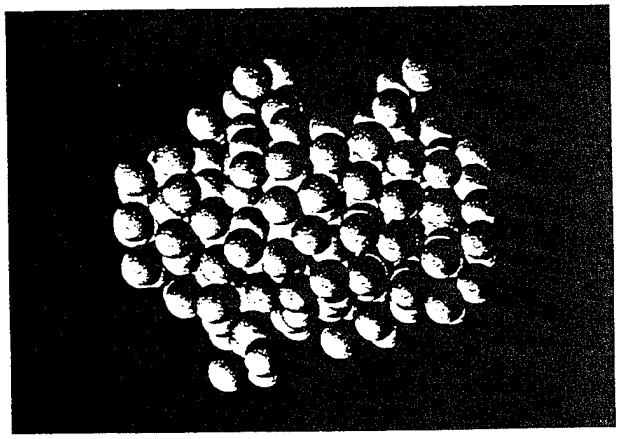

Figure 5: Critical nucleus corresponding to the simulation shown in Figure 4. The critical nucleus contains 240 particles.

HIGH PRESSURE PREIGNITION CHEMISTRY OF HYDROCARBONS AND HYDROCARBON MIXTURES

Contract No's. DAAH04-93-G-0042 and DAAH04-93-G-0145
Reference No's. 30782-EG and 31270-EG-AAS

N.P. Cernansky and D.L. Miller

Department of Mechanical Engineering and Mechanics
Drexel University, Philadelphia, PA 19104

SUMMARY/OVERVIEW

A research program to investigate the high pressure oxidation and ignition characteristics of hydrocarbon fuels has continued, and includes efforts under an associated AASERT Award. The objectives of this program are to develop the kinetic and mechanistic information in the low and intermediate temperature regimes (650-1000 K) and at elevated pressures (up to 20 atm) which will be useful to understand the oxidation of pure hydrocarbons, determine the synergistic and antagonistic effects for binary and ternary mixtures of full boiling range fuel components, and formulate hypotheses on ignition mechanisms. Efforts are directed towards experimental investigation of the oxidation of pure hydrocarbons and hydrocarbon blends using static and flow reactor systems, development of in situ measurement techniques using degenerate four-wave mixing (DFWM), and prediction and validation of mechanisms relevant to preignition chemistry of hydrocarbons and hydrocarbon mixtures.

YEAR ONE

Efforts conducted during the first year of this three year program concentrated on experiments in the static reactor (SR) and pressurized flow reactor (PFR) facilities, development of laser diagnostics, and modeling. Included in the first year were studies of n-pentane oxidation in the SR, which identified the important steps controlling product formation. Results with 1-pentene indicate that long chain alkenes exhibit negative temperature coefficient behavior similar to alkanes. Experimental studies of n-butane, i-butane, and n-pentane oxidation at elevated pressures using the PFR have confirmed that branched chains are less reactive than straight chains and have provided species distribution data for use in modeling. An on-line FTIR was installed and was found to measure significant levels of formic acid, a species difficult to measure by other techniques, from the reaction of n-butane, isobutane, and n-pentane. DFWM development also continued during this period with measurements of OH signals from Bunsen burner flames, slot burner flames, and a low pressure/low concentration discharge chamber. All of these data were used to develop detailed chemical mechanistic information and elucidate the effects of pressure on the mechanisms. A two temperature sensitivity method was adopted to test for the effect of reaction rate changes on negative temperature coefficient (NTC) behavior.

YEARS TWO AND THREE

Static and Pressurized Flow Reactors. Our experimental investigation of n-butane oxidation using the PFR which we initiated in year one was completed. The work consisted of reactivity mapping studies at 5, 8.5 and 12 atm at an equivalence ratio of 0.3, and detailed reaction chemistry studies (i.e., generation of detailed species evolution profiles) at 670, 700 and 715 K for each of the three test pressures. Typical NTC behavior of paraffins was observed. The detailed species measurements indicate a shift in product yields from oxygenates at low temperatures to olefins in the NTC region. This is caused by an exchange of dominance between alkylperoxy (RO_2) and hydroperoxy (HO_2) radical reaction paths. The overall reactivity of the

experiments increases with pressure, but there seems to be a smaller rate dependence on pressure compared to the exponential rate dependence on temperature.

PFR studies with isobutane, 1-butene, trans-2-butene, and mixtures of n-butane with either 1-butene or trans-2-butene were initiated. All experiments involved dilute, lean (ø~0.3) mixtures at 8.5 atm for temperatures ranging from 650 to 850 K. Isobutane was also studied at pressures of 5 and 12 atm. The results of the isobutane oxidation indicate that the rate of excited isobutylperoxy radical (RO_2*) generation is a function of initial fuel concentration, pressure, dilution, equivalence ratio and temperature. Results also indicate that the conversion of RO_2* to stable products is primarily a function of temperature and, to a lesser degree, extent of reaction, and is independent of initial fuel concentration, pressure, dilution, and equivalence ratio. Experiments with neat 1-butene indicate that it does not undergo initiation reactions at temperatures below 850 K. Mixtures of n-butane and 1-butene produce linear product formation trends, suggesting that the radicals which attack 1-butene predominantly interact with the alkane end of the 1-butene. Experiments with trans-2-butene suggest that it is capable of undergoing initiation reactions above 740 K. Mixtures of n-butane and trans-2-butene show significant changes as compared to neat n-butane oxidation, with indications that trans-2-butene oxidation inhibits low temperature reactivity. This is most likely due to trans-2-butene preferentially reacting with the active radical pool, thereby diverting the chemistry into the slower alkene reaction chain. Analysis of these results is ongoing.

Experimental investigation of the oxidation of 1-pentene and a blend of n-pentane and 1-pentene in our static reactor system was completed. Neat 1-pentene experiments were conducted at temperatures spanning the negative temperature coefficient regime (573 to 773 K), at both lean and rich equivalence ratios (0.8 and 1.3), and at pressures in the range 200 to 400 torr. Induction time profiles indicated the presence of an NTC region between 615 and 665 K. Changes in product distribution indicated a transition in the chemistry between the low and intermediate temperatures in the region of the NTC behavior; this was interpreted using a mechanism which describes the main reaction paths and shifts. Studies of a n-pentane / 1-pentene blend indicated that in a mixture the two components reacted intramolecularly through a common pool of small labile radicals such as OH, H and HO_2. At low temperatures, the alkene preferentially reacted with the radicals and diverted the reaction into the slower alkene chain, reducing the reactivity of the alkane. In the region of NTC and just beyond, where the alkane is relatively unreactive, the n-pentane acted as a radical trap for some of the radicals formed in the alkene reaction chain, thereby retarding the activity of the alkene.

As a logical follow-up to our static reactor work with 1-pentene and n-pentane, experimental studies of n-pentane and 1-pentene oxidation utilizing the PFR facility were initiated. These studies were done in the low temperature and NTC regimes (600 to 825 K) and at elevated pressures (4 to 12 atm) under dilute, lean conditions (ø ~ 0.3). Strong NTC behavior was observed with both fuels, and is attributed to the same shifts in radical dominance as occurs with the smaller alkanes. Very high yields of oxygenated hydrocarbons [Figure 1] were observed in the NTC region with both fuels (e.g., propionaldehyde with 1-pentene), primarily as a result of secondary oxidation of C5 alkenes. Also, formaldehyde and carbon monoxide formation exhibited a significant pressure effect, possibly due to enhanced importance of the "Waddington" mechanism with increasing pressure. n-Pentane was consumed faster with increasing pressure, while 1-pentene consumption was unaffected by pressure. These results and general system behavior present a significant challenge to the development of a comprehensive chemical kinetic model. Data analysis and model development work continues.

The effect of nitric oxide (NO) on hydrocarbon oxidation in the low temperature and negative temperature coefficient (NTC) region has been examined. Related engine studies have shown that typical NO concentrations in the end gas can significantly enhance the autoignition of a primary reference fuel blend of octane rating 92. Detailed experiments in a pressurized flow reactor (PFR) with 1-pentene [Figure 2] have shown a similar enhancement of reactivity, particularly at temperatures above 700 K and in the NTC region, while at lower temperatures a significant reduction in reactivity was observed for high concentrations of NO (> 350 ppm). At low temperatures the chain terminating reaction between NO and OH controls the reduction in reactivity with high concentrations of NO, while the observed enhancement of reactivity is due

to NO reacting with hydroperoxy (HO_2) radicals to produce highly reactive hydroxyl (OH) radicals. At any given condition the effect of NO is dependent on the balance between these chain terminating and chain propagating reactions.

Detailed and Reduced Mechanisms. The detailed species evolution profiles generated by our experimental studies are being used in the development and validation of autoignition models incorporating the low temperature and negative temperature coefficient chemistry. The numerical modeling work is being conducted in conjunction with William Pitz and Charles Westbrook at the Lawrence Livermore National Laboratories(LLNL). A pressure dependent kinetic mechanism for propane oxidation has been developed and compared to experimental data from our pressurized flow reactor. The experimental conditions range from 10-15 atm, 650-800 K, and were performed at a residence time of 200 ms for propane-air mixtures at an equivalence ratio of 0.4. Numerical simulations show many of the key reactions involving propylperoxy radicals are in partial equilibrium at 10-15 atm. Major reactions in partial equilibrium include $C_3H_7 + O_2 = C_3H_7O_2$, $C_3H_6OOH = C_3H_6 + HO_2$ and $C_3H_6OOH + O_2 = O_2C_3H_6OOH$. The modeling results show that propyl radical and hydroperoxy-propyl radical reactions with O_2 proceed primarily through thermalized adducts, not chemically activated channels.

A new reduced chemical kinetic model was developed for predicting the preignition oxidation behavior of primary reference fuels at low and intermediate temperatures. It can predict ignition delay, preignition heat release, and the behavior of key chemical species including consumption of the fuel, formation of CO as a major oxidation product, and production of other species classes. The predicted oxidation behavior is in fairly good agreement with experiments. Given the initial success of this model, we set out to explore the breadth of its applicability. Specifically, we are testing the model using neat n-butane and n-butane/isobutane blends under skip fired engine conditions. While this effort is ongoing, it appears that the model will be able to satisfactorily predict the major preignition oxidation behavior at low and intermediate temperatures with appropriate adjustments to the fuel specific rate parameters.

Degenerate Four-Wave Mixing. In our related AASERT work, the development of ultraviolet degenerate four-wave mixing (DFWM) as an in-situ spectroscopic technique has continued. A tilted backward pump beam DFWM geometry has been investigated. Tilting the backward pump beam results in tilting the signal beam below the horizontal plane by an equal angle. This allows for increased signal collection (by replacing the signal-collecting beamsplitter with a mirror) and a significant decrease in scattered background light interference. The resulting order of magnitude [Figure 3] improvement in signal to noise ratio (S/N) has allowed for the detection of the cyanogen (CN) radical in the $B^2\Sigma^+ - X^2\Sigma^+$ band in a H_2 / C_2H_2 / O_2 / N_2 / NO atmospheric-pressure premixed flame. Experiments were also conducted in the flame environment to determine the effect of backward pump tilting angle (θ) on the CN S/N ratio. The strongest signal was obtained when θ was non-zero and as small as experimentally possible (θ = 0.4 for our setup) with a strong falloff at larger angles. There are two effects contributing to this observation. The first is a higher signal intensity for tilted-DFWM due to the use of a high intensity mirror for signal collection. Second, the signal intensity decreases with increasing θ due to a reduction in beam overlap (sampling) volume, with a functional relationship of S proportional to (overlap volume)$^{1/2}$. We have also found that there is an order of magnitude decrease in background noise for tilted-DFWM, with little effect of changing θ on noise detected. The scattered light was found to preferentially scatter in the horizontal plane, hence the lower noise level for the tilted DFWM geometry. We conclude that to achieve the largest possible S/N, the smallest possible tilting angle be chosen to maximize the overlap volume and minimize the background noise level.

In an effort to apply DFWM to further characterize nitrogen chemistry in flames, relative CN concentration profiles have been measured for ten premixed C_3H_8 / N_2 / O_2 / NO atmospheric pressure flat flames at various equivalence ratios [Figure 4]. The laser frequency was tuned to the CN (0,0) vibrational band in the B <- X electronic transition. It was found that the CN concentration profile is strongly dependent on equivalence ratio with a maximum amount produced for an equivalence ratio of 1.73. No CN formation was observed in fuel-lean flame conditions.

CURRENT AND FUTURE WORK

The PFR facility is being upgraded by adding a second stage air heater to allow the reactor to reach reaction temperatures in excess of 1000 K (the current limitation is 850 K). The new heater has been installed and its operation is being verified. Once completed, experimental studies of neo-pentane oxidation will be initiated.

We are also modifying the laser diagnostic laboratory to explore the possibility of infrared detection of polyatomic molecules (CO_2, H_2O, HO_2, etc.). Also, since these optical techniques are invariably developed in simple experiments and configurations, a number of challenges remain in applying them in our research reactors.

FIGURES

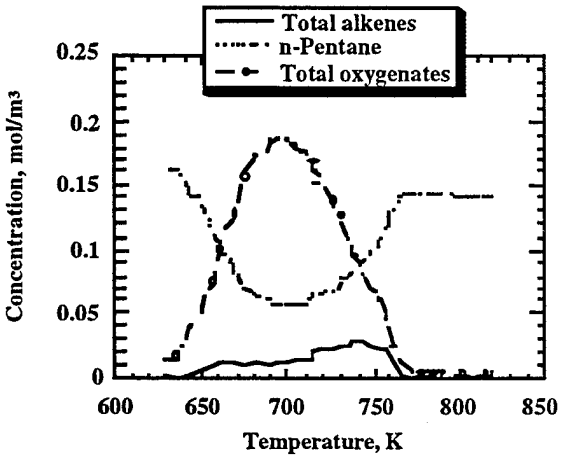

Figure 1. The total alkenes and total oxygenates produced during the oxidation of n-pentane at 12 atm and under dilute, lean (ϕ ~0.3) conditions; relative abundance of oxygenates in the low temperature region and alkenes in the NTC region was observed.

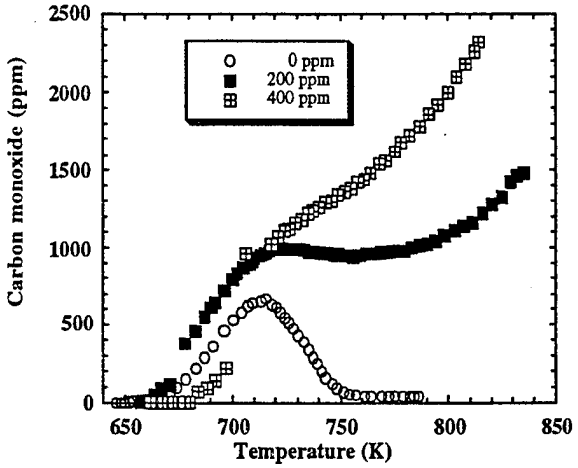

Figure 2. Controlled cool-down PFR experiment showing the effect of NO addition on 1-pentene oxidation at a pressure of 6 atm and an equivalence ratio of 0.4. Using carbon monoxide as an indicator of reactivity, small amounts of NO (200 ppm) increase reactivity at all temperatures, while larger amounts (400 ppm) decrease reactivity below 700 K and increase reactivity above 700 K. NO addition affects overall reactivity by changing the balance of OH chain terminating and propagating reactions.

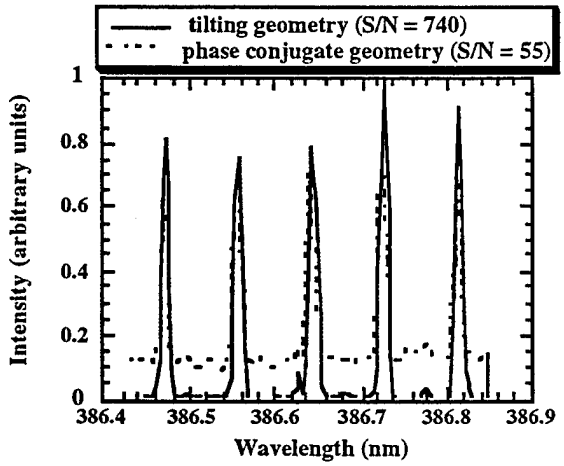

Figure 3. Comparison of signal intensity for tilting geometry and phase conjugate geometry; signal to noise ratio (S/N) has been improved from 55 to 740 using tilting geometry.

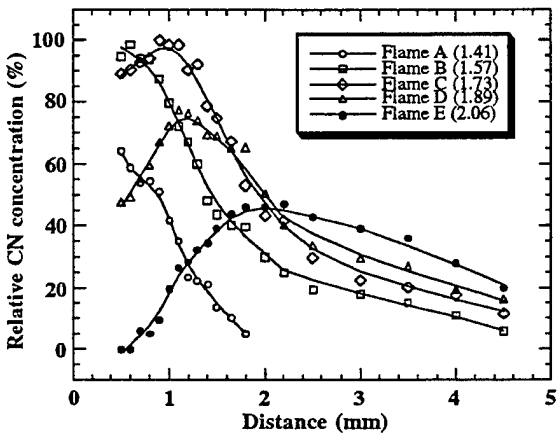

Figure 4. DFWM-measured relative [CN] profiles for five different equivalence ratios for a C_3H_8 / air / O_2 / NO atmospheric pressure flat flame. Measurable CN formation was observed only for fuel-rich flames, with maximum production for ϕ = 1.73.

ADVANCED DIESEL INJECTION STRATEGIES

(ARO DAA L03-92-G-0022)

F. V. Bracco

Department of Mechanical and Aerospace Engineering
Princeton University

SUMMARY

The question being asked is: In Diesel engines, which mixes faster injected liquid or injected gaseous fuel? The question is being addressed experimentally but the measurements are not yet available so that only background and status information can be given at this time.

DISCUSSION

Diesel engine designers have been moving to higher fuel injection pressures for many years. The resulting higher injection velocity of the liquid Diesel fuel brings about faster combustion, which, in turn, can be used either to increase the efficiency or to reduce NO_X emissions (by retarding injection).

It can be argued convincingly that with higher injection pressure, finer sprays are produced and, therefore, that finer sprays vaporize and mix faster than coarse sprays. Thus it would appear that the ultimate Advanced Diesel Injection Strategy is to inject gaseous fuel. But with gaseous injection, the engine does not respond as expected.

Direct injection of natural gas in Diesel engines by several engine companies has yielded the surprising result that combustion time is longer with natural gas than with Diesel fuel (the ignition delay time is not significantly different when appropriate EGR is used). Natural gas also yields unexpectedly high soot emission.

3-D computations of direct injection of gaseous methane and of liquid tetradecane through a multi-hole injector into a Diesel engine were performed (SAE Paper 940895). The study focused on the distribution of fuel/air ratio within the resulting gas and spray jets under typical Diesel conditions prior to ignition. It was computed that for a significant time after the start of injection, the fraction of the vapor fuel which is in flammable mixtures is greater in sprays than in gas jets.

To understand the origin of the difference, computations were made of liquid and gas injections (with the same momentum and mass flow rates) into constant-volume air at Diesel conditions. The computed results indicated that the gas jet remains narrower and penetrates faster than the fine spray that results from liquid injection (see figure), i.e., the initial turbulent mixing is faster for fine sprays than for corresponding gas jets. Such computed results obviously need experimental assessment.

In the experiment, impulsively-started liquid and gas injections into fixed-volume nitrogen are generated and the initial penetration and spreading of the two jets are recorded. The experiment is made difficult by our requirement to match Diesel engine conditions as closely as possible (for poorly understood non-linear processes, extrapolations are unhealthy). Thus the nozzle has a diameter of 133 μm for the liquid and 660 μm for the gas. Injection velocities are about 200 m/s and the field of view of interest is up to 5 cm from the injector. Two injection methods are being developed in parallel: In one, the injected fluid is separated from the chamber gas by a fuse that is

electrically destroyed at injection time; in the other, a pintle is lifted and steady injection pressure is achieved and kept within ± 5% in 0.2 ms. The same nozzle piece is used in both injectors, thus assessing the influence of initiation and upstream conditions on the initial penetration of the jets. The chamber nitrogen is up to 510K and 20 atm. The liquid and gas jets are matched in momentum and mass flow rates and, in a special set of measurements, they will be matched also in density ratios in order to isolate the effect of the phase. All mechanical parts are ready and working. The optical components are not yet satisfactory.

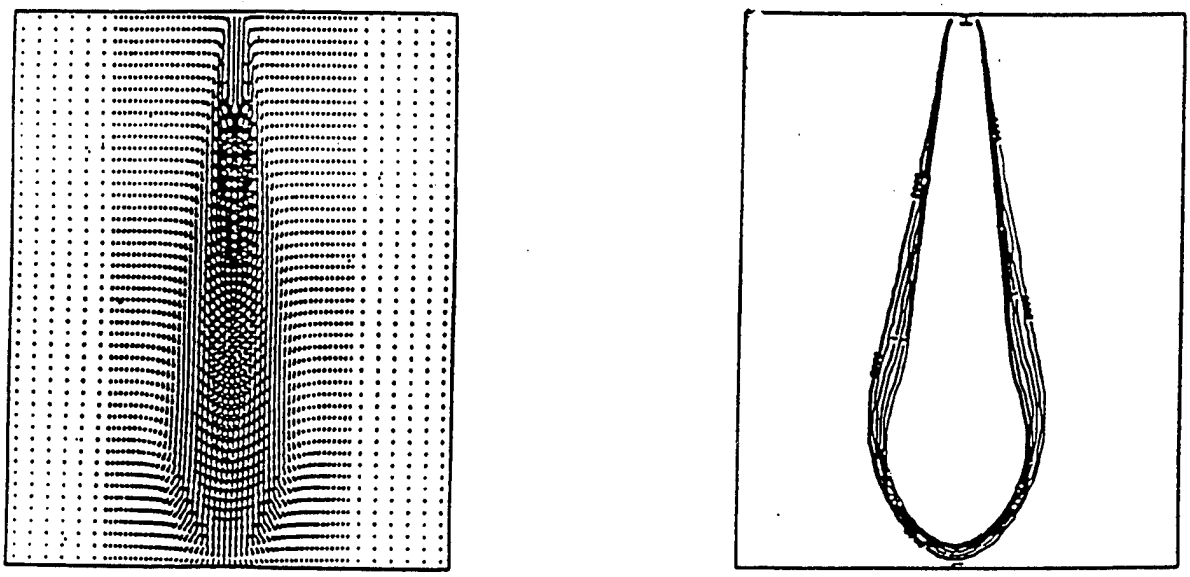

Velocity flowfield and equivalence ratio contour plots for gas injection into a fixed volume, 2ms after the start of injection.

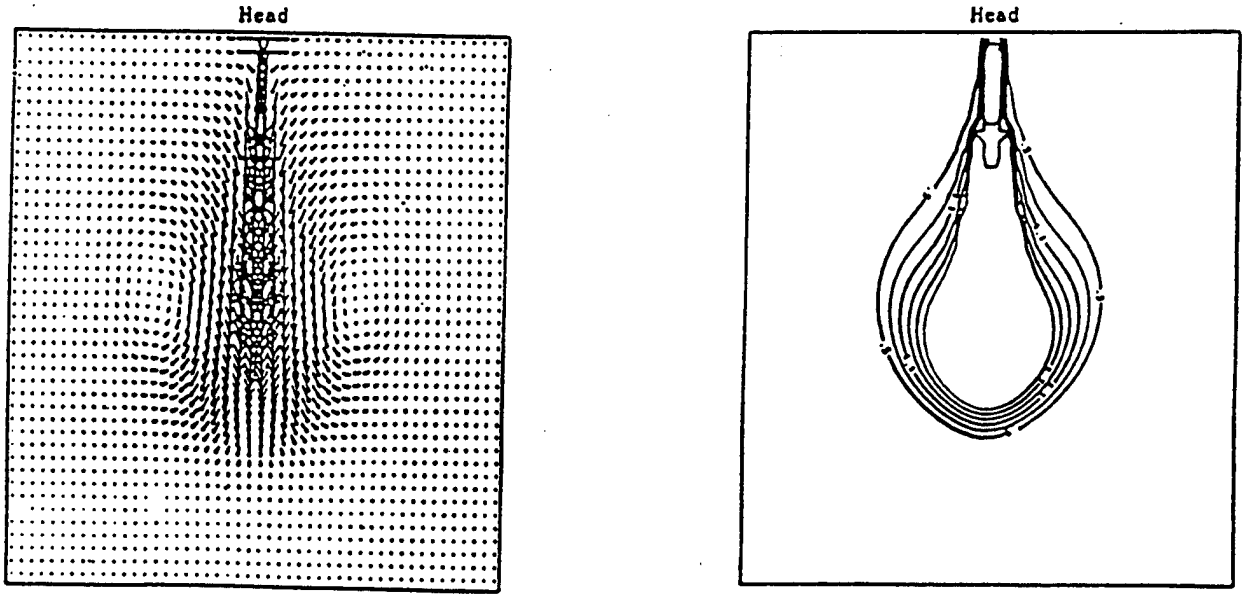

Velocity flowfield and equivalence ratio contour plots for direct injection of liquid into a fixed volume, 2ms after the start of injection.

FUEL INJECTION AND MIXING STUDIES FOR SCRAMJETS AND RAMJETS

AFOSR TASK 2308BW

Pei-Kuan Wu
Taitech, Inc., 3675 Harmeling Dr.
Dayton, OH 45440

Abdollah S. Nejad
Wright Laboratory
Wright-Patterson AFB, OH 45433

SUMMARY

The injection process of supercritical fuels in an initially stagnant environment and the atomization of liquid jets in subsonic crossflows were studied under this task. The study of the supercritical fuel injection was performed to elucidate the effects of the unusual behaviors of thermodynamic and transport properties near the critical point for the applications of endothermic fuels. The atomization of liquid fuels in crossflows was investigated to understand the mechanism of jet disintegration processes. These results are important for the designs of future scramjet and ramjet propulsion systems.

TECHNICAL DISCUSSION

Injection of Supercritical Fuel

Endothermic fuels are being investigated as candidates for regenerative cooling of hypersonic flight vehicles.[1] It has been shown that the thermal cracking (pyrolysis) reaction of endothermic fuels occurs at very high temperatures with a very large endothermic reaction heat. These cracking temperatures are generally much higher than the critical temperature of hydrocarbon fuels, Tc. Therefore, during the takeover stage or a low heat load condition, the fuel will be injected at temperatures between the Tc and the cracking temperature as a supercritical jet. It is well known that thermodynamic and transport properties exhibit unusual behaviors near the critical point.[2] Thus, the objective of the present investigation was to study the fuel injection process with injection temperatures slightly greater Tc and back pressures lower than the critical pressure to simulate the conditions of scramjet/ramjet combustors. Ethylene was selected as the test fluid because its critical temperature (Tc=283K) is near room temperature.

Figure 1 shows that supercritical ethylene jets exhibited an opaque region which, in the most extreme case, persisted for a distance of more than 40 nozzle diameters. This opaque region, which is believed to be caused by fuel condensation, disappears as injection temperature increases. At higher injection temperatures, the supercritical ethylene jets exhibited shock structures similar to those of a highly underexpanded ideal-gas jet. Jet mass flow rates were found to increase as the injection temperature approached the thermodynamic critical value (Fig. 2). For the present test conditions, mass flow rates were about 10% to 25% higher than the mass flow rates calculated with the ideal-gas, isentropic-flow approximation using a specific heat ratio of 1.22. A second ideal-gas isentropic-flow approximation was developed using the specific heat ratio at the injection conditions. The approximation underpredicts the measured values slightly (about 7%) for most conditions, because of the large specific heat ratios near the critical point. This approximation, however, predicts incorrect ratios of nozzle exit to injection choking pressures and temperatures. An isentropic-flow approximation which takes into account the near-

critical-point thermodynamic properties was developed for ethylene, and the resulting predicted mass flow rates agree reasonably well (less than 3% for most of the cases) with the measured values. This approximation produced the same trend of mass flow rates versus reduced temperature, indicating that the increased mass flow rate (at lower reduced temperatures) is caused by the large density increase (characteristic of fluid near its critical point).[2] Thermodynamic path analyses (Fig. 3) revealed that ethylene may pass through a liquid-gas regime at lower injection temperatures. This suggests the possible coexistence of liquid and gas phases at the nozzle exit.

Atomization of Liquid Jets in Crossflows

Liquid jet atomization in an air crossflow has important applications in propulsion systems, including fuel injection in turbojet augmentor sections and ramjet and scramjet combustors.[3,4] The combustion efficiency of these combustors depends closely on the outcome of the jet breakup process. Additionally, current developments in spray simulation techniques require basic understanding of breakup mechanisms to construct more realistic spray atomization models. Therefore, the breakup mechanisms of liquid jets in crossflows have to be analyzed and understood. In order to understand the liquid column disintegration process, phenomenological analyses were employed to highlight the underlying physics and to provide simple correlations without solving exact governing equations, which is beyond the capability of current technology.

In this study, liquid column trajectories were analyzed by balancing liquid acceleration with aerodynamic drag forces in the air stream direction. A schematic plot of the force diagram of a liquid element in a crossflow is shown in Fig. 4. It is assumed that the liquid column can be modeled as a cylindrical fluid element of the diameter of the nozzle exit, d, and of a length, ℓ. The diameter of the fluid element is also assumed to be a constant. These assumptions neglect mass losses due to evaporation and droplet removal along the liquid column. For simplicity, the deformation and flattening of the liquid column are accounted for with an averaged drag coefficient, C_D. It was further assumed that the transverse velocity of the liquid column, v_f, remains constant to the column fracture location and has the same value as the injection velocity, v_j. The x-momentum equation can then be written as:

$$(\rho_f \pi d^2 \ell / 4)(du_f / dt) = 0.5 C_D \rho_g (u_g - u_f)[(u_g - u_f)^2 + (v_g - v_f)^2]^{1/2} \ell d, \qquad (1)$$

where the subscripts f and g denote the properties of liquid and air, respectively. C_D is an average value of the drag coefficients along the entire length of the liquid column and includes the effects of liquid column deformation, flattening, droplet stripping, and disintegration. For the present test conditions, $(v_g - v_f)$ and u_f are neglected. Since the air Mach number is small for the present test conditions, ρ_g can be approximated with the air density in the air free stream, ρ_∞. The trajectory can be obtained by integrating Eq. (1) twice with respect to time and using $y = v_j t$ to yield:

$$y / d = \sqrt{(\pi / C_D)(x / d)\bar{q}}, \qquad (2)$$

where $\bar{q}$ is the liquid/air momentum flux ratio ($=\rho_f v_j^2 / \rho_g u_\infty^2$) and u_∞ is the air velocity in the free stream. The column trajectory follows a parabolic curve as a result of acceleration in the x direction due to aerodynamic forces. Equation (2) was tested with experimental results from conditions of wide ranges of liquid properties and jet injection conditions. An averaged C_D was found to be 1.696. The fit of the correlation with a liquid column is shown in Fig. 5 for a water jet in a Mach 0.2 crossflow. It should be noted that the correlation is developed only for the trajectory of the liquid column.

The column fracture locations were modeled using the time scale for the aerodynamic secondary breakup of a spherical droplet,[5] which can be written as $t_b = 5.0 d_p \sqrt{(\rho_f / \rho_\infty)} / u_\infty$. This approach is plausible since their breakup mechanisms are both due to aerodynamic forces. It

is assumed that the time required for the column to fracture is a fixed portion of the time required for the completion of the breakup process. Since v_j is assumed to be constant up to the column fracture point, the y_b can be obtained by multiplying the breakup time scale, t_b, with the injection velocity, v_j, as:

$$y_b / d = C_y \sqrt{q}, \tag{3}$$

where C_y is a proportionality constant and was found to be 3.44, which was used for the theoretical prediction in Fig. 6. The standard deviation of this mean value is 0.71. The x distance from the nozzle exit to the column fracture point can then be calculated by substituting Eq. (3) into Eq. (2):

$$x_b / d = C_y^2 C_D / \pi = C_x, \tag{4}$$

where C_x is a proportionality constant. Present measurements of x_b/d are plotted in Fig. 7 and exhibit a constant value for C_x of 8.06 ± 1.46. Similar trends were observed by Inamura et al.[6] This phenomenon can be explained by the cancellation of aerodynamic effects on the liquid acceleration and on the column fracture time scale.

The present studies of fuel injection and atomization processes are important for better understanding of the mixing between fuel and air. Future studies will include investigations of the effects of ambient temperature on the supercritical fuel condensation behaviors and of the transport characteristics of the droplets at farther downstream locations.

References

1. Edwards, T., AIAA Paper 93-0807, 1993.
2. Holland, P. M., Eaton, B. E., and Hanley, H. J. M., *J. Phys. Chem. Ref. Data*, Vol. 12, 1983, p. 917.
3. Schetz, J. A. and Padhye, A., *AIAA J.*, Vol. 15, 1977, p.1385.
4. Nejad, A. S. and Schetz, J. A., *AIAA J.*, Vol. 21, 1983, p. 961.
5. Wu, P.-K., Hsiang, L.-P., and Faeth, G. M., *Liquid Rocket Engine Combustion Instability*, ed. V. Yang and W. Anderson, AIAA, Washington, DC, 1995, p. 247.
6. Inamura, T., Nagai, N., Watanabe, T., and Yatsuyanagi, N., Proceedings of 3rd World Conf. Experimental Heat Transfer, Fluid Mechanics and Thermodynamics, Honolulu, HI., 1993.

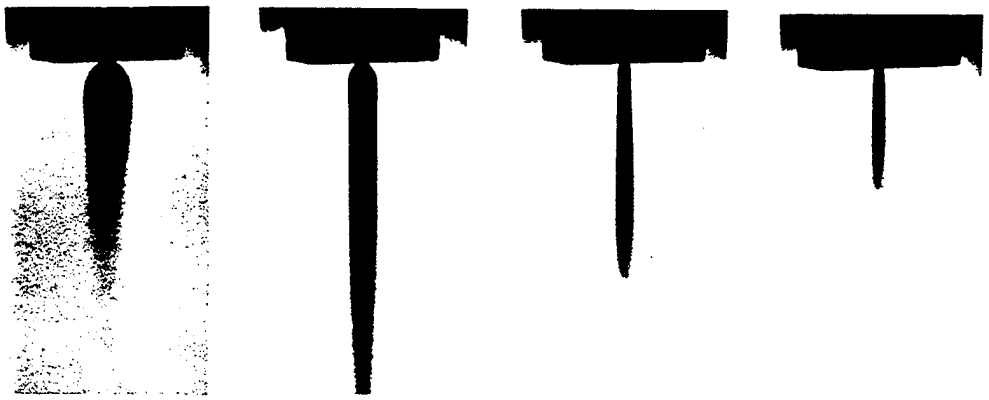

Fig. 1 Shadowgraphs of ethylene jets injected at 293 K into various chamber pressures.

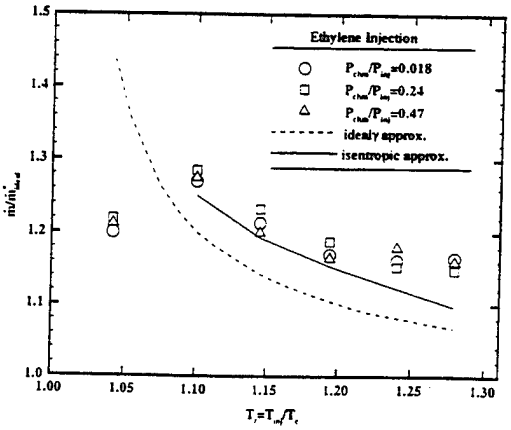

Fig. 2 Measured and calculated mass flow rates of ethylene jets under various injection conditions.

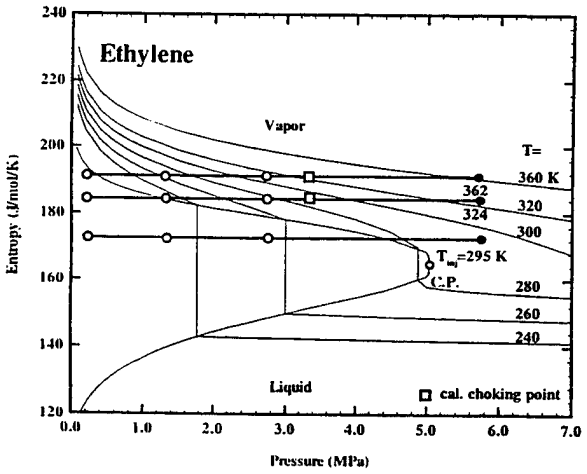

Fig. 3 Thermodynamic paths of injection processes within the nozzle at T_{inj} of 295, 324, and 362 K. C.P. denotes the critical point.

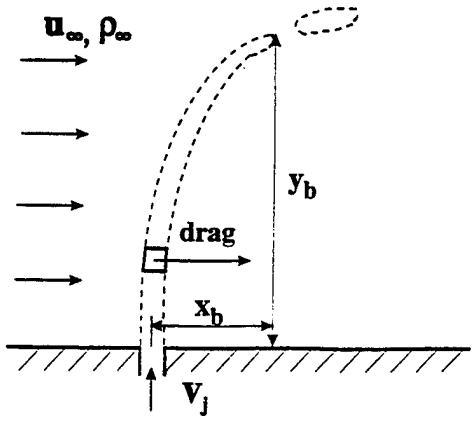

Fig. 4 Sketch of the force diagram for the present phenomenological analysis.

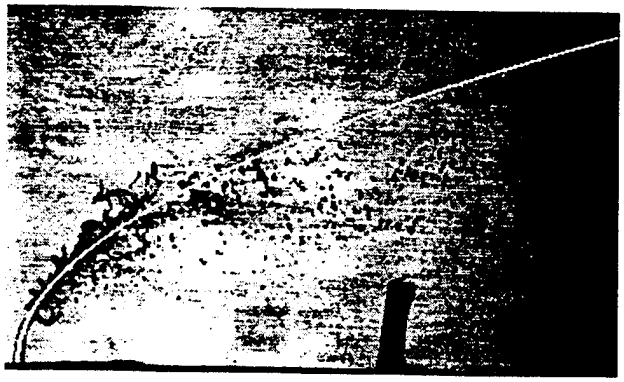

Fig. 5 Fit of correlation on a liquid column.

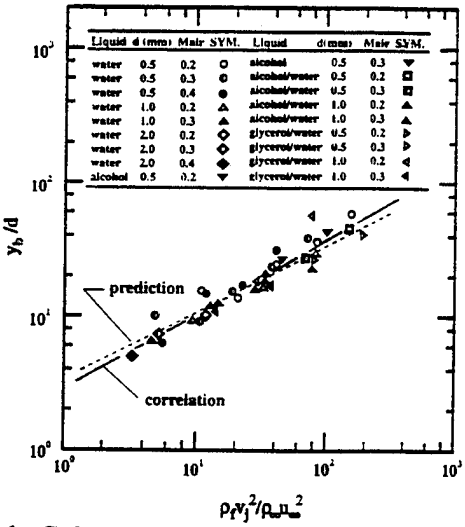

Fig. 6 Column fracture heights (y_b/d) of liquid jets in air crossflows.

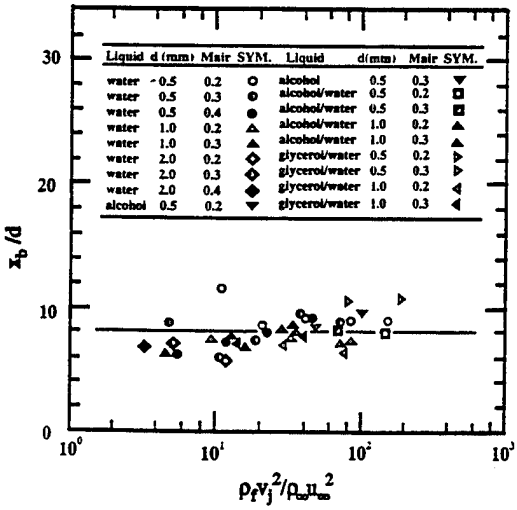

Fig. 7 Column fracture distance (x_b/d) of liquid jets in air crossflows.

8. R.A. Yetter, H. Rabitz, F.L. Dryer, R.C. Brown, and C.E. Kolb, "Kinetics of High-Temperature B/O/H/C Chemistry", Combust. Flame 83, 43 (1991).

9. R.C. Brown, C.E. Kolb, S.Y. Cho, R.A. Yetter, F.L. Dryer, and H. Rabitz, "Kinetic Model for Hydrocarbon-Assisted Particulate Boron Combustion", Int. J. Chem. Kin. 26, 319 (1994).

10. C.T. Stanton, N.L. Garland, and H.H. Nelson, "Temperature Dependence of the Kinetics of the Reaction BO + O_2", J. Phys. Chem. 95, 8741 (1991).

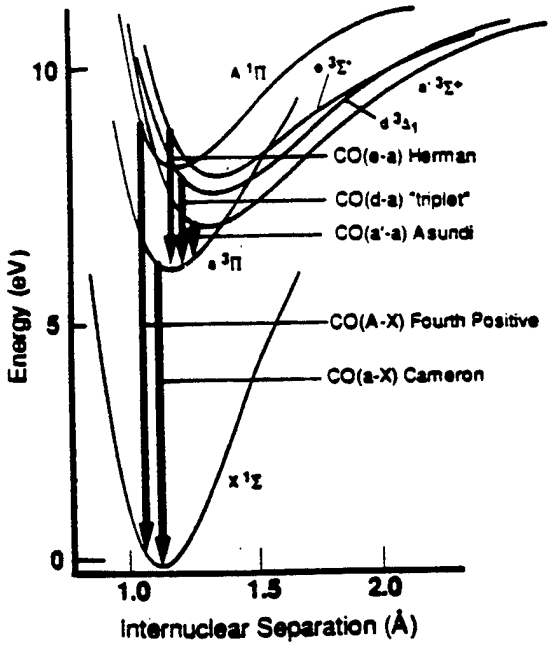

Fig. 1: CO Potential Curves and Transitions. From a presentation by W.L. Dimpfl

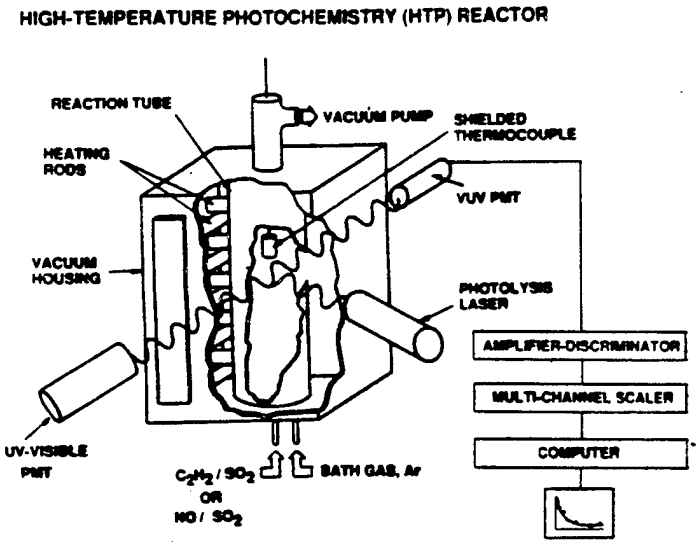

Fig. 2: The HTP reactor, as configured for chemiluminescence observations

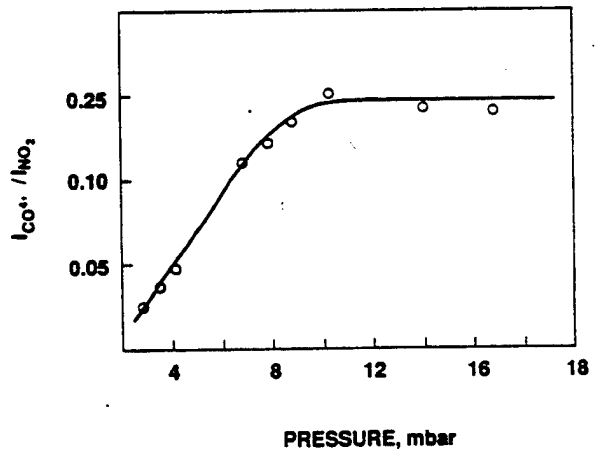

Fig. 3: Pressure dependence of the CO 4+ radiation from the O + C_2H_2 reaction

NONLINEAR DISTORTION AND DISINTEGRATION OF LIQUID SHEETS FOR PRESSURE ATOMIZATION SYSTEM

ARO Grant/Contract No. DAAH-04-96-1-0055

PRINCIPAL INVESTIGATOR:

W.A. Sirignano

Department of Mechanical and Aerospace Engineering
University of California
Irvine, CA 92717

SUMMARY/OVERVIEW:

This is a new program of theoretical and computational research on the nonlinear distortion and disintegration of thin injected liquid sheets. The emphasis will be on the Kelvin-Helmholtz (aerodynamic) instability mechanism in the presence of capillarity for pressure atomization systems. Three-dimensional effects, mean surface curvature effects, and stream divergence will be considered. An analytical technique has been developed that reduces the dimensionality of the governing equations by one: however, the pertinent three-dimensional character will still be described. The research should provide: prediction of ligament and large droplet formation; qualitative information about the formation of smaller droplets; guidance for future experimental research; and the basis for the development of design tools.

AUTHORS

W.A. Sirignano C. Mehring I. Kim

TECHNICAL DISCUSSION

I. Prior Published Work

In a preliminary prior investigation[1], an inviscid, planar unsteady analysis was performed for a thin liquid sheet injected into a gas of zero density. The two-dimensional unsteady inviscid incompressible equations were averaged in the transverse direction across the thin sheet and were placed in a Lagrangian frame of reference. Reduced approximate equations, governing the velocity $\overline{u}$, the thickness $\tilde{y}$, and the displacement $\overline{y}$ were derived for both symmetric (dilational) and "antisymmetric" wave modes.

Symmetric oscillations:

$$\frac{\partial \ln \tilde{y}}{\partial \tau} + \frac{\partial \overline{u}}{\partial z} = 0 \quad ; \quad \overline{y} = 0 \quad ; \quad \frac{\partial^2 \ln \tilde{y}}{\partial \tau^2} + \frac{\sigma}{2\rho}\frac{\partial^2}{\partial z^2}\left(q\frac{\partial^2 \tilde{y}}{\partial z^2}\right) = 0 \qquad (1)$$

where $$q \equiv \left[1 + \tfrac{1}{4}\left(\tfrac{\partial \tilde{y}}{\partial z}\right)^2\right]^{-3/2}$$

"Antisymmetric" oscillations:

$$\frac{\partial \ln \tilde{y}}{\partial \tau} + \frac{\partial \overline{u}}{\partial z} = 0 \quad ; \quad \frac{\partial^2 \overline{y}}{\partial \tau^2} - \frac{2\sigma}{\rho \tilde{y}}\frac{1}{h^3}\frac{\partial^2 \overline{y}}{\partial z^2} = 0 \quad ; \quad \frac{\partial^2 \ln \tilde{y}}{\partial \tau^2} + \frac{\sigma}{2\rho}\frac{\partial^2}{\partial z^2}\left(\frac{1}{h^3}\frac{\partial^2 \tilde{y}}{\partial z^2}\right) = 0 \qquad (2)$$

where $h \equiv \sqrt{1+\left(\frac{\partial \overline{y}}{\partial z}\right)^2}$. In the above nonlinear equations ρ and σ are the density and the surface tension coefficient of the liquid. Analytical solutions for $\tilde{y}(z,\tau)$, $\overline{y}(z,\tau)$ and $\overline{u}(z,\tau)$ were found for the cases of symmetric and "anti-symmetric" steady travelling waves in Lagrangian coordinates. However, in contrast to linear theory, those waves were continuously distorting in Eulerian coordinates.

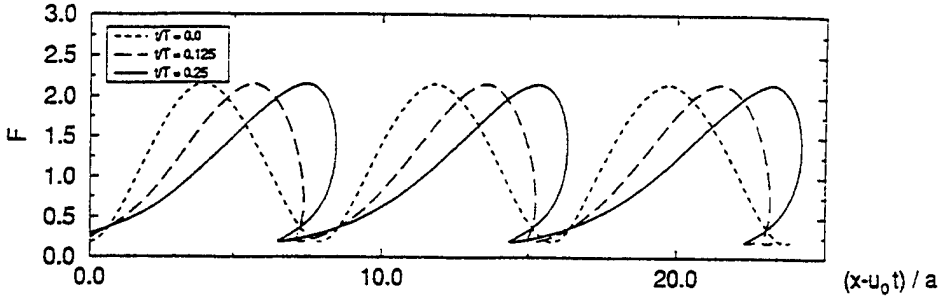

Figure 1: Normalized sheet thickness $F = \tilde{y}/a$, for symmetric disturbed liquid sheet as function of time (a = undisturbed sheet thickness, $T = \lambda/V$ = time period of the travelling wave, u_0 = undisturbed sheet velocity).

For the symmetric wave mode, the injected stream distorts to form branch-like structures so as to resemble a "Christmas tree" as shown by Figure 1. For the "antisymmetric" mode, waves do not remain anti-symmetric beyond first order in amplitude. The waves become thinner in the regions of maximum slope of the mean displacement, implying that the sheet will be torn apart in those regions.

Numerical simulations of Eqns. (1) were also performed to predict the distortion of symmetric oscillating liquid sheets and to investigate the stability and the transition process towards the analytical solution, see Figure 2. The stability of the analytical solution for the case of periodic steady travelling symmetric waves was confirmed as shown in Figure 3. In agreement with perturbation theory, these waves were found to be limit cycle solutions for the symmetric mode. As shown by the numerical results of Figure 4 and as predicted by the theoretical analysis, no limit cycle solution could be identified for sheets with high initial momentum impulse. The same is true for antisymmetric sheet oscillations for general wavelength values, even with low initial momentum impulse.

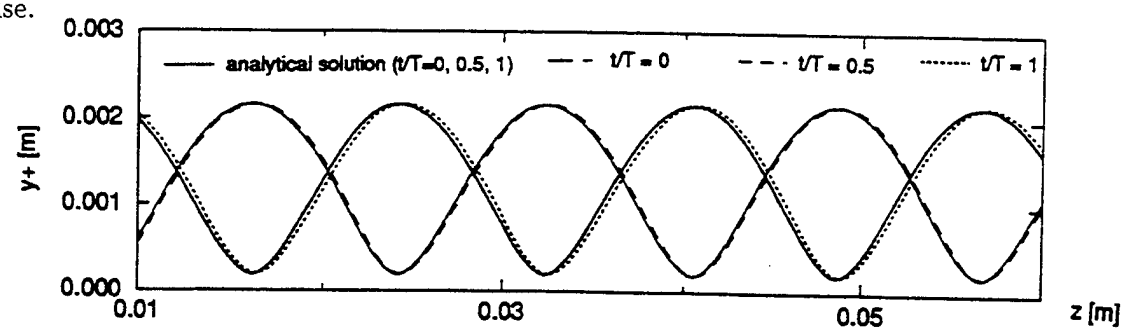

Figure 2: Comparison between analytical[1] and numerical solution for nonlinear periodic travelling (limit cycle) symmetric wave (T= time period of the undisturbed travelling wave).

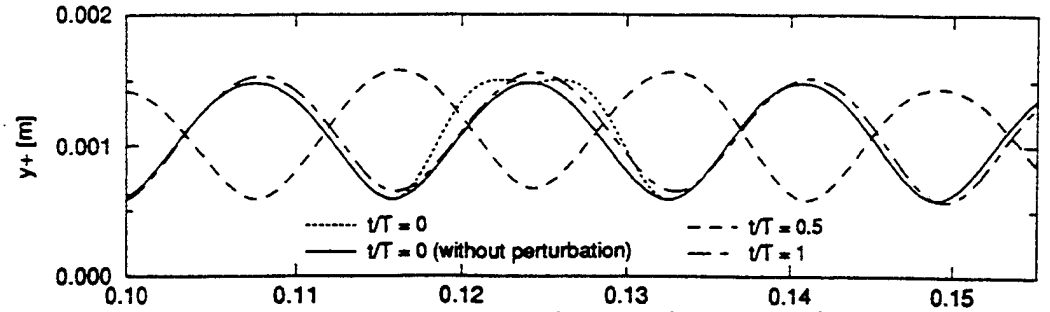

Figure 3: Evolution of locally perturbed limit cycle solution for nonlinear symmetric sheet oscillations (y^+ = upper liquid-void interface).

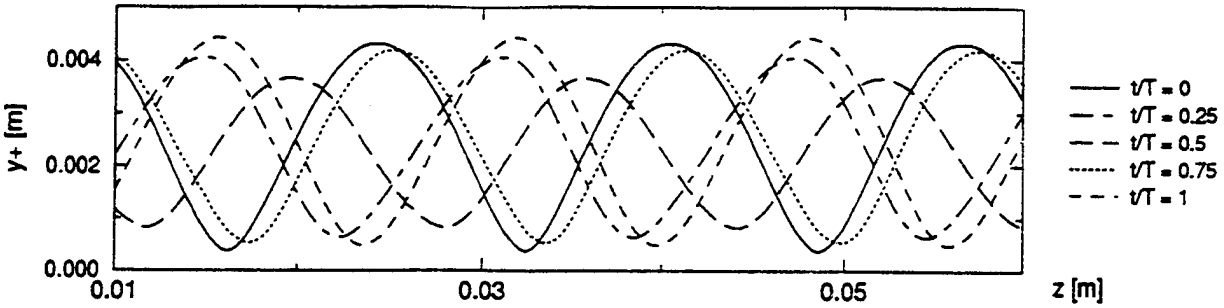

Figure 4: Evolution of a nonlinear symmetric disturbed liquid sheet with high initial momentum impulse (y^+ = upper liquid-void interface).

II. Current Research

The extension of the nonlinear analysis to three-dimensions is a vital factor. Only with a 3-D representation can the break-up into the major ligaments be predicted. Emphasis will be placed upon their liquid sheets; thereby, integration over the thickness of the thin sheet will reduce the dimensionality of the problem by one. The local thickness and the local displacement will still be determined as a function of time. Therefore, the tearing of the sheet and the separation of ligaments will be predicted. The governing equations for the three-dimensional liquid sheet motion are derived as follows. We consider a liquid sheet flowing into the positive x-direction through a gas of negligible density. Assume that the liquid is inviscid, incompressible, and free of gravity force. Then, the continuity and momentum equations are:

$$\frac{\partial u}{\partial x} + \frac{\partial v}{\partial y} + \frac{\partial w}{\partial z} = 0; \qquad \frac{\partial u}{\partial t} + \frac{\partial u^2}{\partial x} + \frac{\partial uv}{\partial y} + \frac{\partial uw}{\partial z} + \frac{1}{\rho}\frac{\partial p}{\partial x} = 0 \tag{3}$$

$$\frac{\partial v}{\partial t} + \frac{\partial uv}{\partial x} + \frac{\partial v^2}{\partial y} + \frac{\partial vw}{\partial z} + \frac{1}{\rho}\frac{\partial p}{\partial y} = 0; \quad \frac{\partial w}{\partial t} + \frac{\partial uw}{\partial x} + \frac{\partial vw}{\partial y} + \frac{\partial w^2}{\partial z} + \frac{1}{\rho}\frac{\partial p}{\partial z} = 0 \tag{4}$$

The upper boundary is given by $z_+(x,y,t)$ while the lower boundary is described as $z_-(x,y,t)$. A surface tension σ exists at the boundaries and affects the force balance at the interfaces. The boundary conditions at the upper and lower surfaces are:

$$w_\pm = \frac{\partial z_\pm}{\partial t} + u_\pm \frac{\partial z_\pm}{\partial x} + v_\pm \frac{\partial z_\pm}{\partial y} \tag{5}$$

$$p_\pm = \sigma\left(\frac{1}{R_{1\pm}} + \frac{1}{R_{2\pm}}\right) = -\sigma\left\{\frac{\partial^2 z_\pm/\partial x^2}{[1+(\partial z_\pm/\partial x)^2]^{3/2}} + \frac{\partial^2 z_\pm/\partial y^2}{[1+(\partial z_\pm/\partial y)^2]^{3/2}}\right\} \tag{6}$$

where $R_{1\pm}$ and $R_{2\pm}$ are the local radii of curvature of the surface in the x and y direction, respectively.

Define the sheet thickness, $\tilde{z}(x,y,t)$, and the displacement of the sheet, $\bar{z}(x,y,t)$, to be

$$\tilde{z}(x,y,t) = z_+ - z_-; \qquad \bar{z}(x,y,t) = (z_+ + z_-)/2 \tag{7}$$

Now for a sheet whose thickness is small compared to the wavelength of a disturbance, we can consider u, v, and p to be nearly constant with variation of z. It is convenient, therefore, to reduce the problem to a two-dimensional, unsteady formulation.

We define average velocities $\bar{u}(x,y,t)$ and $\bar{v}(x,y,t)$, and average pressure $\bar{p}(x,y,t)$ to be

$$\bar{u}(x,y,t) = \frac{1}{\tilde{z}}\int_{z_-}^{z_+} u\,dz; \qquad \bar{v}(x,y,t) = \frac{1}{\tilde{z}}\int_{z_-}^{z_+} v\,dz; \qquad \bar{p}(x,y,t) = \frac{1}{\tilde{z}}\int_{z_-}^{z_+} p\,dz \tag{8}$$

The continuity equation (3) can be integrated term-by-term from z_- to z_+ and incorporated with Equations (5) and (7) to yield

$$\frac{\partial \tilde{z}}{\partial t} + \frac{\partial \tilde{z}\bar{u}}{\partial x} + \frac{\partial \tilde{z}\bar{v}}{\partial y} = 0 \tag{9}$$

where the thickness $\tilde{z}$ plays the role of an artificial density.

Now, we approximate $\bar{u}^2\tilde{z} \approx \int_{z_-}^{z_+} u^2 dz$, $\bar{u}\bar{v}\tilde{z} \approx \int_{z_-}^{z_+} uv dz$, etc. Then the momentum equations (3) and (4) are integrated term-by term and combined with Equations (5) and (9) and with an approximation $\bar{p} = (p_+ + p_-)/2$. The result are

$$\frac{\partial \bar{u}}{\partial t} + \bar{u}\frac{\partial \bar{u}}{\partial x} + \bar{v}\frac{\partial \bar{u}}{\partial y} = \frac{\sigma}{2\rho}\frac{\partial}{\partial x}\left(\frac{1}{h_1^3}\frac{\partial^2 \tilde{z}}{\partial x^2} + \frac{1}{h_2^3}\frac{\partial^2 \tilde{z}}{\partial y^2}\right) \tag{10}$$

$$\frac{\partial \bar{v}}{\partial t} + \bar{u}\frac{\partial \bar{v}}{\partial x} + \bar{v}\frac{\partial \bar{v}}{\partial y} = \frac{\sigma}{2\rho}\frac{\partial}{\partial y}\left(\frac{1}{h_1^3}\frac{\partial^2 \tilde{z}}{\partial x^2} + \frac{1}{h_2^3}\frac{\partial^2 \tilde{z}}{\partial y^2}\right) \tag{11}$$

$$\frac{\partial \bar{w}}{\partial t} + \bar{u}\frac{\partial \bar{w}}{\partial x} + \bar{v}\frac{\partial \bar{w}}{\partial y} = \frac{2\sigma}{\rho\tilde{z}}\left(\frac{1}{h_1^3}\frac{\partial^2 \tilde{z}}{\partial x^2} + \frac{1}{h_2^3}\frac{\partial^2 \tilde{z}}{\partial y^2}\right) \tag{12}$$

The h_1 and h_2 in Equations (10) and (11) are defined for the symmetric mode by

$$h_1 = \sqrt{1 + \frac{1}{4}\left(\frac{\partial \tilde{z}}{\partial x}\right)^2}, \qquad h_2 = \sqrt{1 + \frac{1}{4}\left(\frac{\partial \tilde{z}}{\partial y}\right)^2} \tag{13}$$

For the antisymmetric mode, h_1 and h_2 in Equations (10), (11), and (12) are defined by

$$h_1 = \sqrt{1 + \left(\frac{\partial \tilde{z}}{\partial x}\right)^2}, \qquad h_2 = \sqrt{1 + \left(\frac{\partial \tilde{z}}{\partial y}\right)^2} \tag{14}$$

The two-dimensional, unsteady system of equations (9) through (12) will be solved by finite-difference computations. To facilitate the numerical solution and to allow for the possibility of multivaluedness in the numerical solution procedure, different approaches are investigated: the transformation of the governing equations in a mass coordinate system, and the solution of the governing equations in Eulerian coordinates by using a pseudo method of characteristics.

(1) Sirignano W. A. and Mehring C. (1995). Nonlinear Two-Dimensional Symmetric Travelling Wave Distortion of a Thin Liquid Sheet, Dynamics of Exothermicity, special honorific volume for A. K. Oppenheim, *Combustion Science and Technology* book series (J.Ray Bowen, ed.), Gordon and Breach, in press.

Computational Investigation of Atomization

AFOSR-new contract

Grétar Tryggvason
Department of Mechanical Engineering and Applied Mechanics
The University of Michigan
Ann Arbor, MI 48109-2121

SUMMARY

Computational investigations of atomization are proposed. The main part of the study will focus on the secondary breakup of drops, but the primary breakup of jets will also be examined. The focus is on those aspect of the breakup that are difficult to address experimentally, such as the behavior at high pressures and temperatures.

TECHNICAL DISCUSSION

This is a new contract that will start July 1. We will discuss the proposed work, relevant earlier results, and a few preliminary results.

We will conduct simulations that follow the deformations and breakup of drops for both shock generated disturbances as well as gradual disturbances, fully accounting for inertial and viscous effects for both the drop and the ambient gas as well as surface tension effects. The simulations will help determine where in parameter space the various breakup modes take place, how long breakup takes, and what the resulting drop size distribution is. The effect of heat and mass transfer on the breakup process will be investigated. The goal of the investigation is to provide results that extend and compliment experimental investigations, and taken together with available experimental results, the result will provide a nearly complete picture of the process. We will also start modeling of the three-dimensional breakup of laminar jets due to aerodynamics effects at high pressures.

These computations are made possible by a recently developed numerical technique that has been used already for a number of multifluid problems. The method incorporates an explicit tracking of the drop surface with a finite difference method for the full Navier-Stokes equations for the drop and the ambient gas. Arbitrary differences in density and viscosity are possible, large surface deformations are allowed and surface tension is fully accounted for. For problems with mass and heat transfer, conservation equations for mass and energy are solved also. The technique has been used for two-dimensional, axisymmetric, and fully three-dimensional problems and validated extensively by comparisons with analytical solutions for simple cases, other numerical studies, grid refinement, and experiments. The thrust of the computations proposed here will be on fully three-dimensional situations. Extensions of this investigation will involve other aspect of spray formation such as the disintegration of liquid sheets as well as more complex physics, such as the effect of complex flow fields and eventually combustion.

The following three problems will be examined:

Effect of density on drop breakup. For sprays at high pressures the density ratio is generally much lower than at atmospheric conditions. This results in much stronger interactions between the drops and the ambient fluid, but it is a regime where experiments are difficult. From a computational point of view the opposite is true. While we have simulated flows with density ratios of several hundreds, O(500-1000), the computations are both easier and faster for modest density ratios, O(1-100). Very little is known about drop breakup near the critical point where surface tension vanishes but viscosity is finite. Indeed, there is some controversy over whether the reduction will lead to increased shattering or the breakup will be inhibited. The computations will clarify the exact mechanisms of breakup due to both shock as well as gradual disturbances and extend the deformation/breakup maps generated by experimental investigations to lower density ratios. We will also examine the effect of high Oh, and the viscosity of the ambient gas. At high temperature the gas viscosity is likely to influence the process. In addition to clarifying the boundaries between the various breakup modes, we will provide information about the breakup time and the resulting drop size distribution.

Heat and mass transfer during deformation and breakup. With the realization that breakup takes considerable time and has to be dealt with more are a rate process than an instantaneous change in configuration, heat and mass transfer during break-up become important issue, particularly at high temperatures. Generally, breakup involves substantial stretching of the drop or parts of the drop with a subsequent increase in the surface area/volume ratio. This is likely to increase heat and mass transfer. Even when the drops do not break up, deformation will both change the surface area of the drop and the flow around it and therefore affect the heat and mass transfer. We will examine this effect by direct simulation of both the steady state deformed drop as well as the transient process.

Aerodynamic breakup of jets. Wind induced break-up of jets generally consists of axisymmetric waves that then break-up into filaments and eventually drops. This regime is of key importance to practical applications, but little is understood about the detailed process. The region near the jet surface is generally crowded by drops and filaments and therefore not easily accessible for experimental measurements. The full three-dimensionality of the motion has made theoretical and numerical studies difficult. We intend to address this process by fully three-dimensional computations of only a portion of the jet, where we simulate a small sector, assuming periodicity in the axial and the azimuthal direction. (Initially, some aspects may addressed by neglecting curvature effects.) The simulations will allow us to examine the initial growth of an axisymmetric wave, the subsequent three-dimensional breakup and the eventual formation of drops. Such simulations should give a detailed insight into the breakup process. Particular emphasis will be on estimating the resulting drop size.

We have already examined a number of problems involving both drops and bubbles using the front tracking/finite difference technique, and results for binary collisions of drops and collision of drops with a wall will be shown, along with results for several drops in shear flows. A few preliminary results for the research that will be conducted under this contract will also be shown, including the initial stages of shear breakup of drops—both subject to initial acceleration as well as to steady acceleration—using axisymmetric simulations, along with simulations of the wind generation of surface waves. The relevance of those results to the planned simulations of jet breakup will be discussed. The attached two figures show results from earlier work on binary collision of drops.

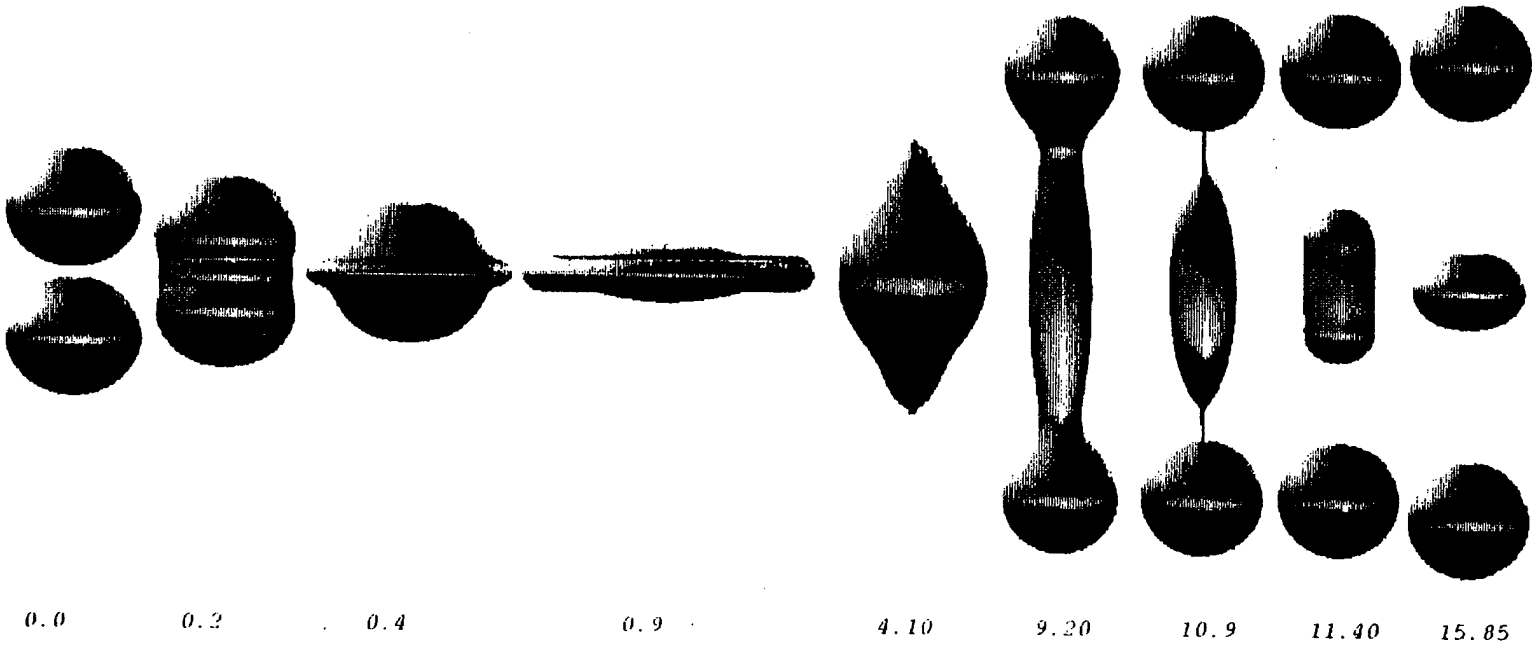

Figure 1. Axisymmetric computation of the head-on collision of two drops. Here, We=115 and Re=185, based on the relative drop velocity just before collision. The drops are allowed to coalesce, but the drops are sufficiently energetic that they break up again after the initial coalescence. For lower Reynolds and Weber numbers the collision results in a permanent coalescence. This behavior is in good agreement with the experiments of Jiang, Umemura, and Law (JFM **234**, 1992), for example.

NUMERICAL SIMULATION

EXPERIMENTS

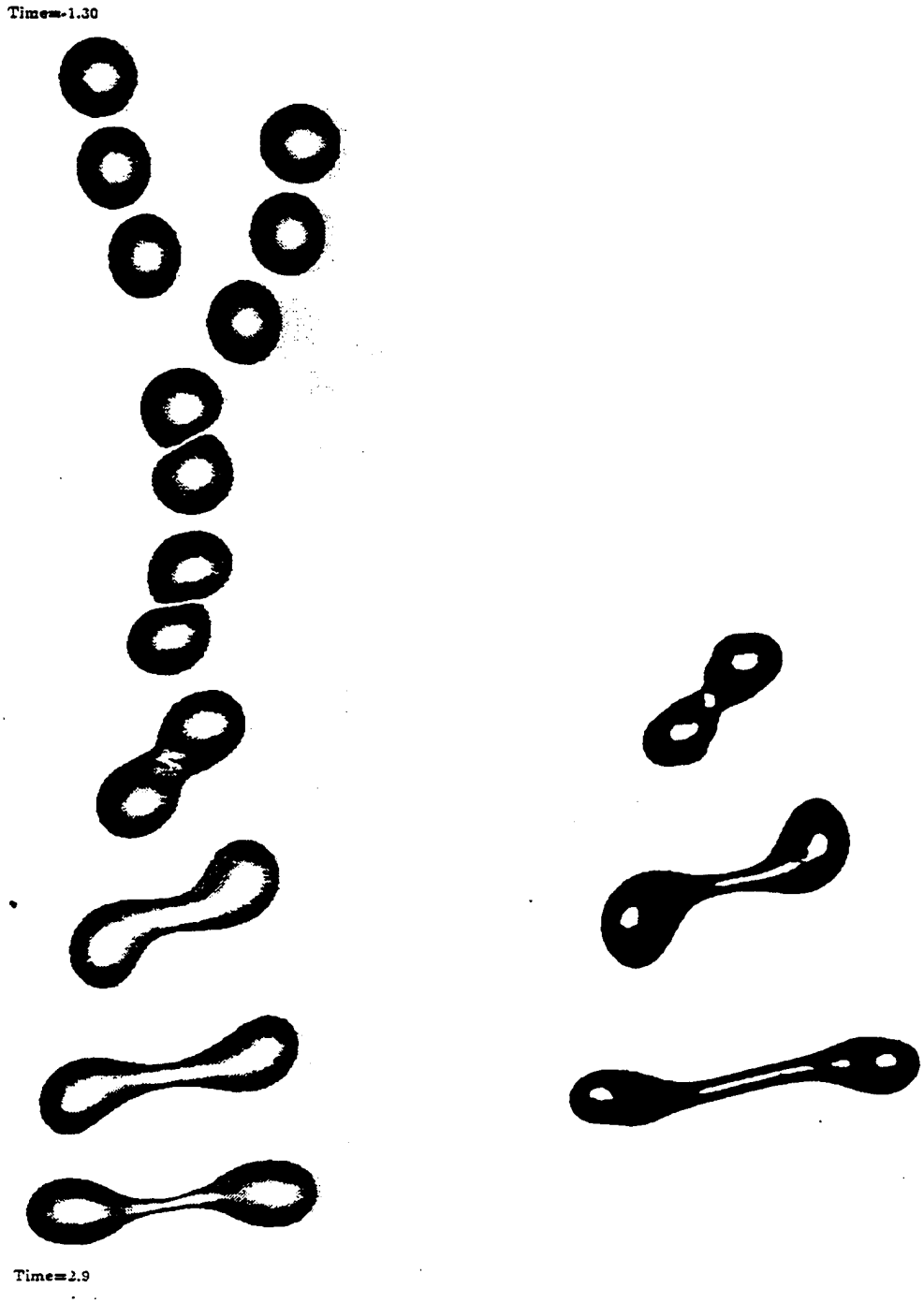

Figure 2. Fully three-dimensional simulation of a "grazing" collision (left column). The drops are initially accelerated towards each other (top frame), coalesce when they collides, but eventually separate again (bottom frame). Here, We=23 and Re=68, based on the relative drop velocity just before collision, and the ratio of the density of the drops to the density of the outer fluid is relatively low (ρ_d/ρ_o =40). Three frames from experiments by Jiang et al (JFM 234, 1992) are shown on the right. The parameters are not the same as in the computations, but the collision mode is the same.

THE EFFECT OF TURBULENCE ON DROPLET DRAG, DISPERSION, VAPORIZATION AND SECONDARY BREAKUP IN DIESEL FUEL SPRAYS

(ARO Grant No. DAAH04-95-I-0116)

Principal Investigator: Domenic A. Santavicca

Mechanical Engineering Department
The Pennsylvania State University
University Park, PA 16802

SUMMARY/OVERVIEW:

Experiments are being conducted to characterize a number of flowfield-droplet interactions which occur in high pressure combustion systems such as Diesel engines and gas turbine combustors. The specific phenomena of interest are i) the behavior of jets and droplets injected into supercritical environments; ii) the effect of turbulence on secondary droplet breakup and iii) droplet vaporization and breakup in unsteady flows. The results of these experiments are intended to provide new information on both the phenomenological and the quantitative nature of these interactions; information which is essential for the development of improved submodels for use in advanced spray calculations.

TECHNICAL DISCUSSION:

As mentioned above, experiments are being conducted for the purpose of studying a number of droplet-flowfield interactions which are important in spray combustion environments, such as those encountered in Diesel engines and gas turbine combustors. These experiments are each briefly described below, followed by a summary of the current status.

The experimental facility for studying the behavior of liquid jets and droplets injected into supercritical environments is illustrated schematically in Figure 1. The test chamber is capable of operation at pressures up to 10.95 MPa (1500 psig) and temperatures up to 350°C, conditions which are above the critical point of many liquid hydrocarbon fuels. Fuel is injected through a hypodermic tube with an inside diameter of 100 microns, thereby producing nominal 100 micron jets or droplets, the latter when a piezoelectric oscillator is used. The diagnostics consist of direct back-lit photography, as illustrated in Figure 1, and two-dimensional Raman imaging, which is specifically intended for visualization of the injected fluid after it has achieved supercritical conditions.

The experimental facility for studying the effect of turbulence on secondary droplet breakup is illustrated in Figure 2. This facility is capable of operating at pressures up to 7.3 MPa (1000 psig) and temperatures up to 325°C with gas velocities as large as 20 m/sec and relative turbulence intensities up to 35%. In this apparatus, the turbulent flow properties are characterized using laser Doppler velocimetry, and the occurrence of secondary droplet breakup is determined from direct back-lit photography.

The experimental facility for studying droplet vaporization and breakup in unsteady flows is illustrated in Figure 3. This system is capable of operating at pressures up to 1 MPa (150 psig) and temperatures up to 300°C with gas velocities up to 40 m/sec. A rotating valve at the exit of the flow tube is used to produce unsteady flows at frequencies up to 1000 Hz. The diagnostics in the experiment are again direct back-lit photography to visualize the occurrence of secondary droplet breakup and two-dimensional exciplex fluorescence to characterize droplet vaporization.

In addition to constructing and making operational the above three facilities, a number of other accomplishments have been made since the inception of this project. This includes conducting a study of subcritical and supercritical n-pentane jet behavior in nitrogen. Figure 4 is a plot of the normalized jet breakup length versus the jet velocity for various cross flow rates at a pressure of 9.13 MPa and a temperature of 200°C. Note that the critical pressure and temperature for n-pentane are 3.37 MPa and 196.6°C. The results which are shown in Figure 4 are consistent with results available in the literature and show no evidence of supercritical phenomena. The results from this study were presented at the JANNAF Combustion Meeting in October, 1995. An exciplex fluorescence scheme has also been developed and optimized to allow visualization of the vapor wake from vaporizing droplets. This scheme is illustrated by the results in Figure 5, which show both the liquid and vapor exciplex fluorescence spectra as well as the interference filters, which are used to selectively view either the liquid droplet or the vapor wake. Results from this study were also presented at the 1995 JANNAF Combustion Meeting.

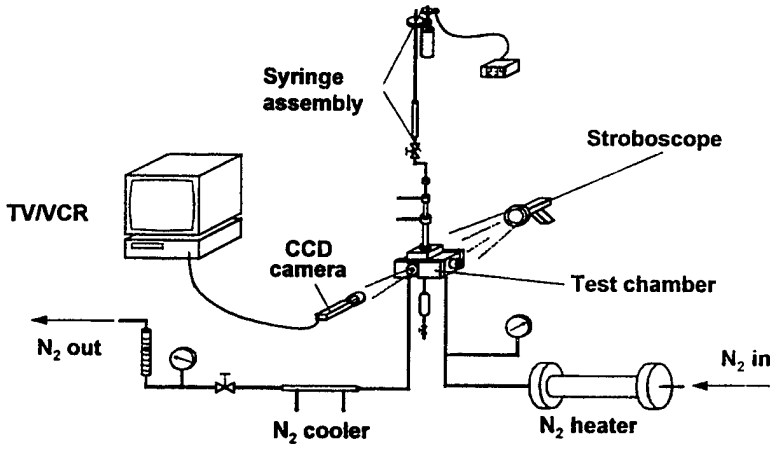

Figure 1. Experimental Setup for Studying the Injection of Liquid Jets and Droplets into Supercritical Environments.

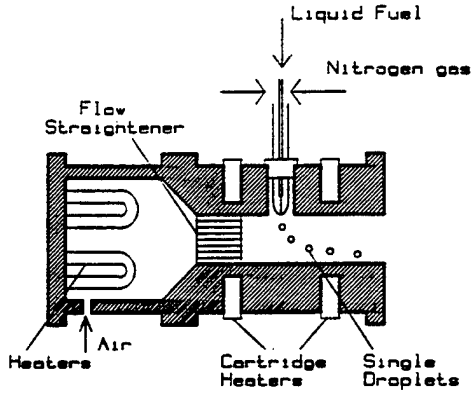

Figure 2. Experimental Setup for Studying the Effect of Turbulence on Secondary Droplet Breakup.

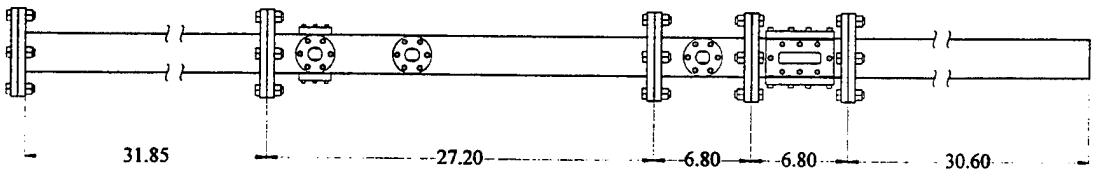

Figure 3. Experimental Setup for Studying Droplet Vaporization and Breakup in Unsteady Flows.

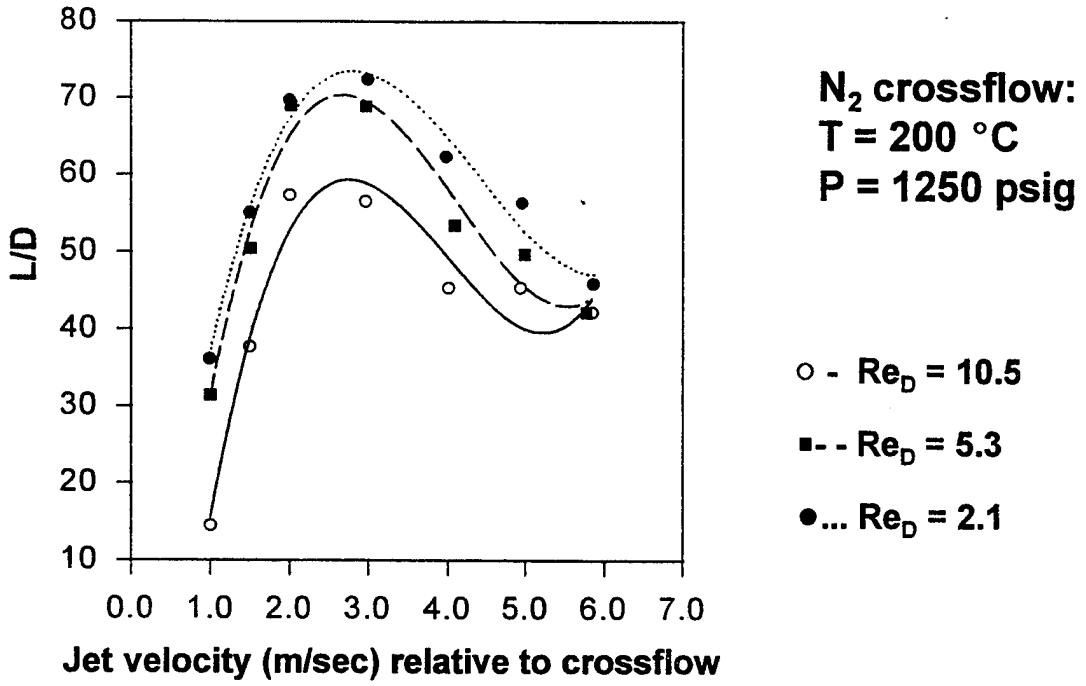

Figure 4. **Normalized Jet Breakup Length versus Jet Velocity for Various Cross Flow Rates. Pressure = 9.13 MPa Temperature = 200°C**

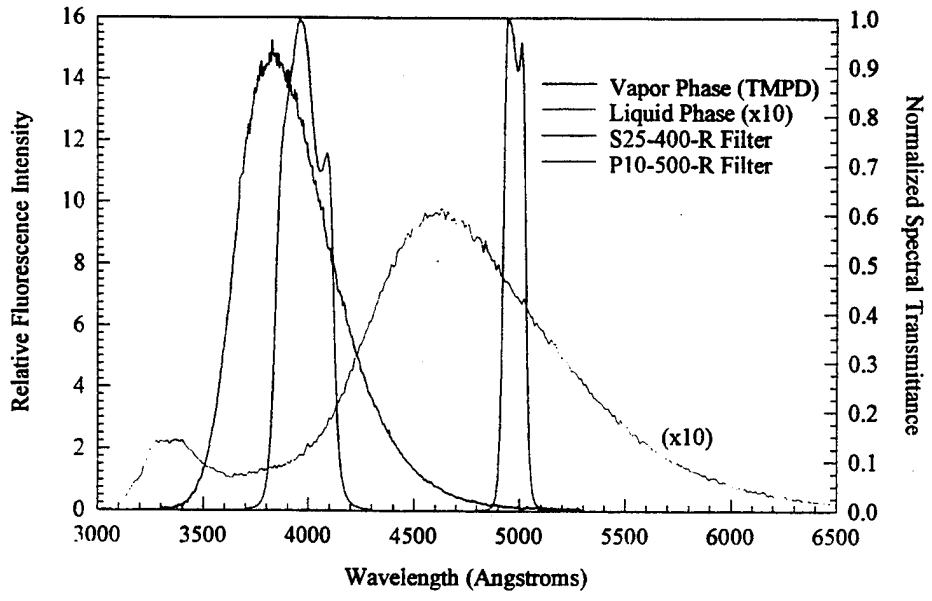

Figure 5. **n-Pentane Liquid and Vapor Exciplex Fluorescence Spectra and Corresponding Detection Filter Spectra.**

SECONDARY BREAKUP AND TURBULENCE INTERACTIONS OF DROPS

(AFOSR Grant No. F49620-95-I-0364)

Principle Investigator: G.M. Faeth

Department of Aerospace Engineering
3000 FXB Building
The University of Michigan
Ann Arbor, Michigan 48109-2118

SUMMARY/OVERVIEW:

Secondary breakup and turbulence interactions of drops are being studied because they are important phenomena of the near-injector (dense) region of sprays. Past work on secondary drop breakup has yielded information about the regimes and outcomes of drop deformation and breakup when effects of liquid viscosity are small; current work is addressing secondary drop breakup as a rate process and effects of liquid viscosity, both of which become important for spray combustion at elevated pressures typical of most practical applications. Measurements are made using multi-pulsed shadowgraphy and holography of drops during breakup caused by shock-wave disturbances; findings have resolved several issues relevant to drop breakup at elevated pressures.

Work on turbulence interactions of drops is concentrating on effects of turbulence generation when relative velocities between the drops and the continuous phase are large because these conditions generally are encountered in practical sprays. Past studies suggest that particle generated turbulence involves a stochastic combination of randomly-arriving drops (particle) wakes and have resolved some features of these moderate Reynolds number wakes in strongly turbulent environments. Current work is emphasizing wake properties in weak turbulence generated by dispersed particle-laden flows, as well as direct measurements of turbulence generation properties at these conditions, in order to systematically develop methods of synthesizing particle wake properties in order to better understand particle-generated turbulence.

TECHNICAL DISCUSSION:

Introduction. Past work has demonstrated the importance of secondary drop breakup and turbulence generation in sprays (Faeth 1990, 1995, 1996; Ruff et al. 1989, 1991, 1992, 1996; Tseng et al. 1992a, b, 1996; P.-K. Wu and coworkers 1991, 1992, 1993, 1995, 1995a, b); therefore, these phenomena are being studied as discussed in the following:

Secondary Drop Breakup. Studies of liquid atomization have shown that drops produced by primary breakup are unstable to secondary breakup (Ruff et al. 1991, 1992; Tseng et al. 1992a, b, 1996; P.-K. Wu and coworkers 1991, 1992, 1993, 1995, 1995a, b); therefore, secondary breakup is being studied during this part of the investigation. Findings during the first phase of the investigation established the need to treat secondary breakup as a rate process. In view of these findings, current work is emphasizing the properties of secondary breakup as a rate process, see Chou et al. (1996) for initial results. The breakup dynamics of individual drops are being observed in a shock tube, currently emphasizing conditions where effects of liquid viscosity are small. Pulsed shadowgraphy and holography are used to observe the properties of the spray field generated by breakup as a function of time.

Measurements are emphasizing shear breakup because this is the most important regime for sprays at high pressures. Initial work improved the definition of the shear breakup regime by measuring the transition to the drop-piercing regime at large Weber numbers, We, and another

transition to a shear-breakup regime having unusually long ligaments at large Ohnesorge numbers, Oh. Based on these findings, present measurements were limited to shear breakup at We in the range 125-375 and Oh less than 0.1. Within this range of conditions, measurements involved flow visualization, parent drop velocities, drop size and velocity distributions produced by secondary breakup, and the rate of removal of mass from the parent drop — all as a function of time after initiation of the velocity disturbance. Phenomenological theories are used to help interpret and correlate the measurements.

The pulsed shadowgraphs of Fig. 1, for We = 250 and Oh = 0.0034, illustrate breakup behavior at several normalized times after the start of breakup, t/t*, where t* is the characteristic drop breakup time (note that breakup is limited to t/t* in the range 1.5-5.5, for reference purposes). Before breakup starts, the drop deforms into a disk-like shape, seen at t/t* = 1, due to the low pressures at its periphery caused by acceleration of gas over the drop surface. The remaining photographs are for various stages of the breakup process: initially, the vortical layer within the parent drop, which causes drops to form, is thin yielding small diameter and relatively short ligaments that divide into small drops; the thickness of the vortical layer increases with time, yielding a corresponding increase of ligament diameters and lengths as well as corresponding drop diameters; finally, as the parent drop becomes small, and the vortical layer increases in size, ligament and parent drop sizes become comparable and breakup stops.

Flow visualization suggests two breakup regimes: (1) a transient regime when the vortical layer is initially growing, and (2) a steady-state regime when the vortical layer becomes comparable to the size of the parent drop. Time-resolved measurements of the Sauter mean diameter, SMD, normalized by the initial parent drop diameter, d_o, support this behavior as illustrated in Fig. 2. These results are plotted as a function of time normalized by the characteristic viscous time of the liquid phase vortical layer, d_o^2 / ν where ν is the liquid kinematic viscosity. As expected, drop sizes during the initial growth period are proportional to the square root of $\nu t / d_o^2$ (which is proportional to the thickness of the vortical layer) while the steady-state period yields drop sizes proportional to the drop diameter.

In contrast to drop sizes, phenomenological analysis suggests that the initial velocities of drops produced by secondary breakup are independent of drop sizes; which agrees with measurements. The time resolved measurements of mean initial drop velocities, u_f, are plotted according to predictions in Fig. 3, where ρ_f / ρ_g is the liquid/gas density ratio, u_p is the parent drop velocity and u_g is the gas velocity. These results show that initial drop velocities are slightly larger than parent drop velocities and that this relationship to the parent drop velocity does not change significantly over the time of breakup. The scatter of the velocities increases with time, however, due to the increasing length of the ligaments whose irregular motion induces corresponding irregularities of drop velocities, see Fig. 1.

Other temporal properties of shear breakup at low Oh — the drop size distribution function, the velocity of the parent drop, drop velocity fluctuations, the rate of production of dispersed liquid, etc. — are reported in Chou et al. (1996). Current work is concentrating on issues relevant to secondary drop breakup at elevated pressures. This work includes resolving the properties of ligaments, as well as addressing effects of large gas/liquid density ratios and Oh on all aspects of secondary drop breakup.

Turbulence Generation. Turbulence generation by drops controls the turbulence properties of dense sprays (Faeth 1990, 1995, 1996; Ruff et al. 1991, 1992). Drop-generated turbulence differs from conventional turbulence because mean velocity distributions in randomly-arriving drop wakes contribute to the velocity field of the turbulence; however, stochastic analysis seems promising for describing this flow (Parthesarathy and Faeth 1990; Mizukami et al. 1992). Past work has developed information about particle wake properties at large turbulence intensities and has demonstrated promising agreement with existing measurements of turbulence generation properties (J.-S. Wu and Faeth 1993, 1994, 1995). Current work is emphasizing particle wake properties in low relative turbulence intensity particle-generated turbulence, as well as turbulence

generation processes at similar conditions, in order to address conditions more representative of practical spray combustion processes.

The main emphasis of current work has been the design, fabrication and assembly of the experimental apparatus. Principle requirements of this facility are provision of particle-generated turbulence at the low relative turbulence intensities characteristic of spray combustion phenomena (less than 2% due to large drop velocities relative to the gas); these requirements have been met using a counterflow wind tunnel consisting of upflowing air with a large contraction ratio to obtain a low turbulence intensity flow, and downflowing particles through a series of dispersing screens to provide controlled levels of particle-generated turbulence. The arrangement is used in two ways: (1) observing the structure of wakes from spheres supported in this flow, similar to J.-S. Wu and Faeth (1993, 1994, 1995); and observing particle-generated turbulence itself, similar to Parthesarathy and Faeth (1990) and Mizukami et al. (1992). In both cases, measurements are made using high spatial resolution laser velocimetry.

Design of the test arrangement and instrumentation has been completed, and fabrication and assembly of these items are currently in progress. Initial measurements will concentrate on particle wake properties at low ambient turbulence intensities, with direct measurements of turbulence generation properties to follow.

REFERENCES

Chou, W.-H., Hsiang, L.-P. and Faeth, G.M. (1996) Int. J. Multiphase Flow, submitted.

Faeth, G.M. (1990) Twenty-Third Symposium (International) on Combustion, The Combustion Institute, Pittsburgh, 1315-1352.

Faeth, G.M. (1995) Proceedings of the Second International Conference on Multiphase Flow (A. Serizawa, T. Fukano and J. Bataille, ed.), Kyoto University, Kyoto, Vol. 1, CO-1 to CO-16.

Faeth, G.M. (1996) Twenty-Sixth Symposium (International) on Combustion, The Combustion Institute, Pittsburgh, in press.

Faeth, G.M., Wu, P.-K., Ruff, G.A. and Hsiang, L.-P. (1996) Ann. Rev. Mult. Flow, in press.

Hsiang, L.-P. and Faeth, G.M. (1992) Int. J. Multiphase Flow, 18, 635-652.

Hsiang, L.-P. and Faeth, G.M. (1993) Int. J. Multiphase Flow, 19, 721-735.

Hsiang, L.-P. and Faeth, G.M. (1995) Int. J. Multiphase Flow, 21, 545-560.

Mizukami, M., Parthasarathy, R.N. and Faeth, G.M. (1992) Int. J. Multiphase Flow, 18, 397-412.

Parthasarathy, R.N. and Faeth, G.M. (1990) J. Fluid Mech., 220, 485-537.

Ruff, G.A., Sagar, A.D. and Faeth, G.M. (1989) AIAA J., 27, 901-908.

Ruff, G.A., Bernal, L.P. and Faeth, G.M. (1991) J. Prop. Power, 7, 221-230

Ruff, G.A., Wu, P.-K., Bernal, L.P. and Faeth, G.M. (1992) J. Prop. Power, 8, 280-289.

Ruff, G.A., and Faeth, G.M. (1996) Prog. Astro. Aero., in press.

Tseng, L.-K., Ruff, G.A. and Faeth, G.M. (1992a) AIAA J., 30, 1537-1544.

Tseng, L.-K., Wu, P.-K. and Faeth, G.M. (1992b) J. Prop. Power, 8, 1157-1166.

Tseng, L.-K., Ruff, G.A., Wu, P.-K. and Faeth, G.M. (1996) Prog. Astro Aero, in press.

Wu, J.-S. and Faeth, G.M. (1993) AIAA J., 31, 1448-1455.

Wu, J.-S. and Faeth, G.M. (1994) AIAA J., 32, 535-541.

Wu, J.-S. and Faeth, G.M. (1995) AIAA J., 33, 171-173.

Wu, P.-K. and Faeth, G.M. (1993) Atom. Sprays, 3, 265-289.

Wu, P.-K. and Faeth, G.M. (1995) Phys. Fluids A, 7, 2915-2917.

Wu, P.-K., Ruff, G.A. and Faeth, G.M. (1991) Atom. Sprays, 1, 421-440.

Wu, P.-K., Tseng, L.-K. and Faeth, G.M. (1992) Atom. Sprays, 2, 295-317.

Wu, P.-K., Miranda, R.F. and Faeth, G.M. (1995a) Atom. Sprays, 5, 175-196.

Wu, P.-K., Hsiang, L.-P. and Faeth, G.M. (1995b) Prog. Astro. Aero., 169, 247-279.

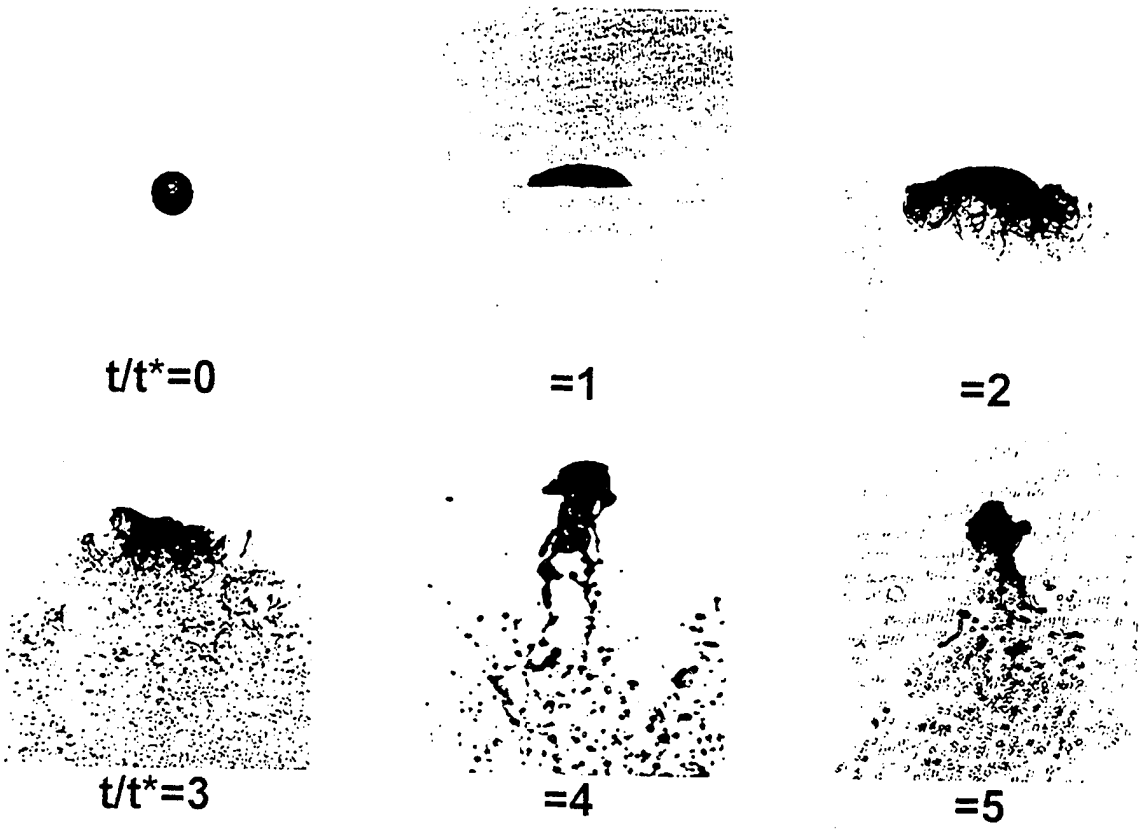

Fig. 1. Pulsed shadowgraphs at various times during shear breakup at low Oh.

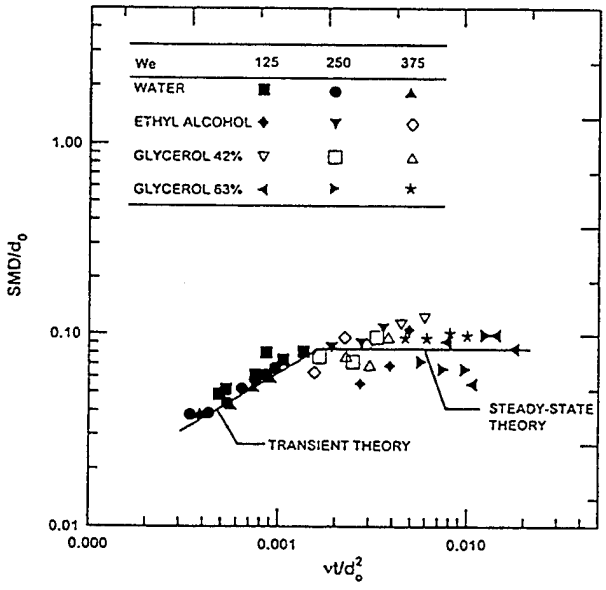

Fig. 2 Evolution of SMD as a function of time during shear breakup at low Oh.

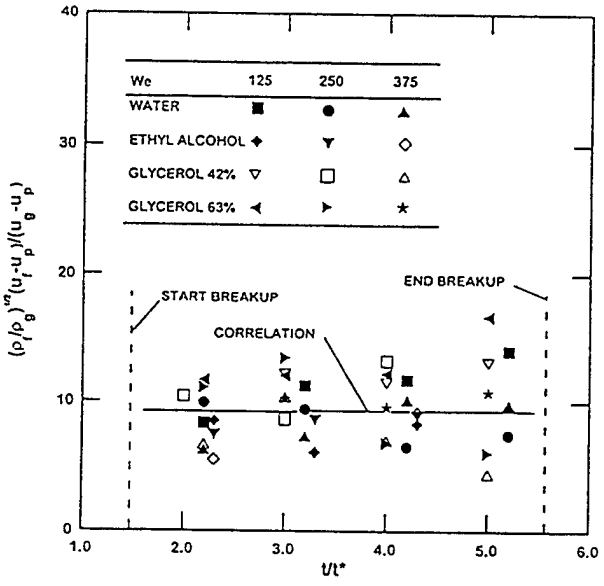

Fig. 3 Evolution of mean streamwise drop velocities as a function of time during shear breakup at low Oh.

THE EVAPORATION OF LIQUID DROPLETS IN HIGHLY TURBULENT GAS STREAMS

ARO Grant No. 34199-EG

Principal Investigator: Richard D. Gould

Dept. of Mechanical and Aerospace Engineering
North Carolina State University
Raleigh, NC 27695-7910

SUMMARY/OVERVIEW

The primary objective of this research program is to gain an increased understanding of the heat/mass transfer process for turbulent flow around single liquid droplets. Useful heat/mass transfer correlations as a function of droplet Reynolds number, Prandtl number, non-dimensional turbulence intensity, and non-dimensional integral and micro length scales (with droplet diameter as normalizing parameter) are the goal of this research. Since correlations usually employed to estimate these transport processes were developed for the case where freestream turbulence effects are small, these new correlations, which consider gas phase turbulence, will allow designers of combustion chambers to more accurately estimate the heat/mass transfer from fuel droplets.

TECHNICAL DISCUSSION

Experimental Setup

Recent experimental efforts include the fabrication and characterization of a low speed, heated vertical wind tunnel facility (Figure 1) capable of producing a well defined turbulent flow field (Yearling and Gould (1995), Yearling (1995)). Varying levels of turbulence intensity (*0.5% to 15%*), mean velocity (*1m/s to 7 m/s*) and turbulent length scales (*2 - 7 mm*) in the test section are possible with this facility. The wind tunnel was used to investigate the effects of turbulent intensity on the evaporation rate of single water, methanol and ethanol liquid droplets. Table 1 gives the parameter ranges for the present experimental study. Figure 2 shows the test section in cross-section and the method of supplying the suspended evaporating droplet with fluid.

The turbulence was produced by fitting the wind tunnel with one of three available turbulence generating grids. The three grids, adopted from the study of Ballal and Lefebvre (1975) were fabricated by drilling an array of circular holes into steel plates. The turbulence intensity and length scales were measured for the present flow conditions and turbulence grid using a single hot wire anemometer (TSI P2 sensor).

By suspending a droplet from a needle tip and positioning it axially along the central core of the test section, the turbulent length scale and turbulence intensity of the gas phase flow incident on the liquid droplet may be selected. Yearling (1995) shows the turbulence intensity decay curves for each grid over a range of test section exit velocities and air flow temperatures. The turbulence intensity decays from approximately *20%* near the grid (not isotropic) to less than *4%* at an axial distances greater than ≈ 25 hole diameters downstream of the grid for all grids.

Beyond a Reynolds number of ~ 300 the drag force caused by the air flow passing over the droplet tended to blow the free liquid droplet off the tip of the syringe needle. To solve this problem Yuen and Chen (1978) and Renksizbulut and Yuen (1983) used porous spheres to model an evaporating liquid droplet. The present study has taken their lead and manufactured a similar *1.587mm* brass ball bearing with a series of *number 80* holes drilled through the ball. A needle can pass through one of the holes allowing evaporative fluid to be deposited into the

center of the porous ball and onto the surface of the ball bearing, thus functioning as a model of a free liquid droplet. The advantages of this method are that the droplet is always spherical in shape and is of a known diameter. The main concern when using a porous sphere is that the recirculation zone inside an actual liquid droplet could be important in the overall energy balance of the liquid droplet. Yuen and Chen (1978) and Renksizbulut and Yuen (1983) investigated this problem and found no experimentally verifiable difference between the evaporation rate of free droplets and the porous sphere model droplets in a laminar air flow. The results of this study agree with this conclusion. In addition, porous spheres of diameters *4.76mm* and *6.35mm* have been manufactured. Unlike the *1.587mm* brass ball bearing these larger porous spheres were made by fusing fine glass frit into a spherical shape.

Table 1. Range of physical parameters and non-dimensional parameters.

Parameter	Range
Suspended droplet diameter	*1 - 2 mm*
Porous sphere diameter	*1.58 - 6.35 mm*
Integral length scale	*2 - 7.0 mm*
Air temperature	*300 - 350 K*

Parameter	Range
Reynolds number, Re_{mod}	*10 - 1000*
Turbulence intensity (grid), *TI*	*0 - 15 %*
Mass transfer number, B_M	*0.002- 0.1*
Taylor microscale	*1 -2 mm*

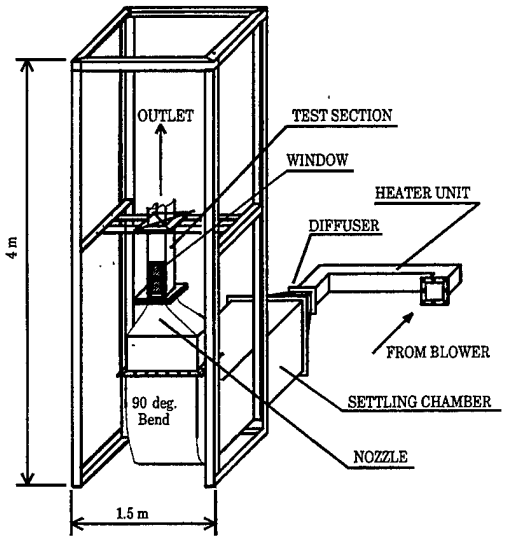

Figure 1. Wind tunnel.

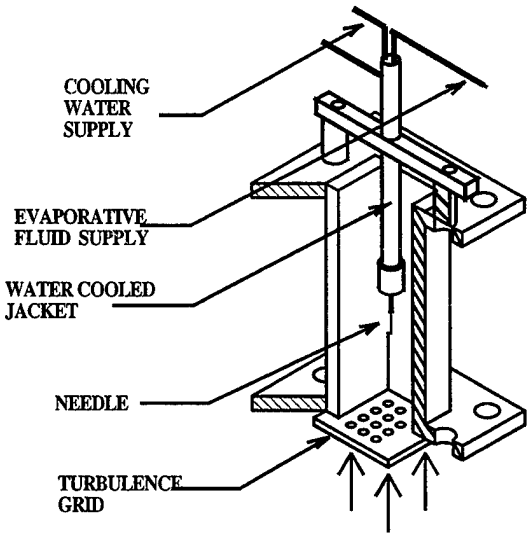

Figure 2. The wind tunnel test-section.

A black and white CCD camera (PULNIX TM545, 510 x 492 pixels) connected to a visual display unit (VDU) were used to observe the suspended droplet or porous sphere. The magnification of the optical system was approximately *20* and the measurement resolution of the droplet diameter was $\pm 2.5 \mu m$ with this system. Quartz windows in the side of the test section allowed optical access. Figure 3 shows the complete experimental setup. A syringe pump delivered a known quantity of evaporative fluid to a suspended droplet. The droplet was monitored via the CCD camera and once the droplet size did not change over a two to five minute time period then steady state heat transfer was assumed. As the evaporative fluid supply rate equals the evaporation rate and by measuring the droplet surface temperature and air temperature an energy balance on the droplet gives the Nusselt number. It must be noted that this method will not work if the droplet cannot be seen due to excessive droplet oscillation or surface vibration.

A steady-state energy balance at the surface of the liquid droplet gives,

$$Q_{conv} = \dot{m} L_{fg} - \left[Q_{rad} + Q_{needle} \right] = A_D h \left(T_\infty - T_{sat} \right) \qquad (1)$$

where the evaporation rate, $\dot{m}$, surface area, A_D, and freestream gas temperature, T_∞, were all measured. All evaporative fluid thermo-physical properties, except for ethanol viscosity, were

estimated using the data tables of pure compounds published by the DIPPD for the AIChE (1984). All air properties and the viscosity for ethanol were evaluated using the CRC handbook by Lide and Kehiaian (1994). Data tables published by Gallant (1968) were used as a check. Further references were also made to Eckert and Drake (1972) and Kuo (1986). For binary mixture thermo-physical properties the highly regarded work of Reid (1977) was consulted.

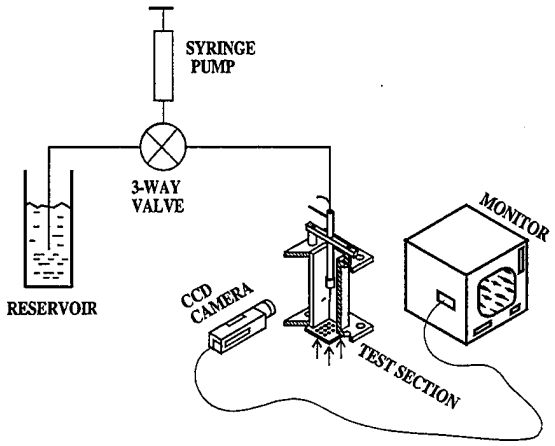

Figure 3. Experimental Setup.

The bracketed term "[ ]" in Equation (1) above represents the total heat energy added to the droplet due to radiation, conduction through the support needle and heat transfer from the evaporative liquid. The heat loss from radiation was approximated by $Q_{rad} = \pi D^2 \sigma \varepsilon \left(T_\infty^4 - T_{sat}^4\right)$ where σ, is the Stefan-Boltzmann constant and the emissivity, ε, was assumed equal to 0.95. To estimate Q_{needle} a simple finite control volume numerical model was used to predict the temperature distribution in the needle and the heat loss. The result of this analysis indicated that all syringe needles should be insulated with a glass tube (*1.47mm* OD, *0.56mm* ID) over approximately two thirds of the *12mm* needle length, thus removing any conductive heat transfer from the hypodermic needle. Q_{needle} was then found from a simple enthalpy difference across the supply needle. The combination of Q_{rad} and Q_{needle} was never greater than *3%* of Q_{conv}. The uncertainty in evaporation rate was *±4%* while the measurement uncertainty for all temperatures was *±0.5°C*. The mean Nusselt number was calculated using

$$Nu_f = \frac{hD}{k_{mix,f}} = \frac{\left(\dot{m} L_{fg} - Q_{rad}\right)}{k_{mix,f} \pi D \left(T_\infty - T_{sat}\right)} \tag{2}$$

where, D, is the droplet diameter and the vapor thermal conductivity, $k_{mix,f}$, is evaluated at the film temperature, $T_f=(T_\infty+T_{sat})/2$. The heat of vaporization, L_{fg}, is evaluated at the surface temperature T_{sat}. The heat transfer coefficient h, as well as the Nusselt number Nu_f, were solved for once all these parameters were determined. The uncertainty in these Nusselt number calculations is *±12%* and is primarily due to the resolution of the droplet diameters measurements.

Results and Discussion

Figure 4 is a plot of mean Nusselt number versus $Re^{1/2}\ Pr^{1/3}$ for suspended liquid water, methanol and ethanol droplets in a laminar air flow. The uncertainty associated with the Nusselt number is *±12%* for all points. Also included in Figure 4 is the highly regarded *laminar flow* heat/mass transfer correlation for droplet evaporation rates from the work of Renksizbulut and Yuen (1983). The Prandtl number is evaluated at the film temperature and film mole fraction, the modified Reynolds number is defined as, $\mathrm{Re}_{\mathrm{mod}} = \rho_\infty DU/\mu_{mix,f}$, where the density, ρ_∞, is evaluated at the free stream temperature and the vapor viscosity, $\mu_{mix,f}$, is evaluated at the film temperature and film mole fraction. The mass transfer Spalding number, B_H, was modified to account for radiation heat transfer effects and $Cp_{mix,f}$ in this equation was evaluated at the film conditions.

Figure 5 shows the evaporation from liquid droplets in turbulent flow, for various turbulence intensity bands. The increased scatter on the left of Figure 5 ($Re^{1/2}Pr^{1/3}<18$) is believed to be due

to flow induced oscillation of the free droplets. This suggests that both droplet oscillation and the turbulent air flow passing over the droplet contribute to the enhancement in the total heat transfer rate. We are presently looking at methods to separate these effects. Note that there is less variation in heat transfer rate on the right side of Figure 5 (porous spheres, $Re^{1/2}Pr^{1/3}>18$) because there is no droplet oscillation when using porous spheres.

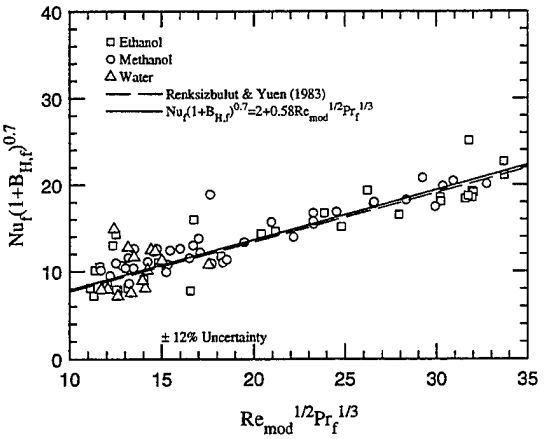

Figure 4. Laminar heat measurements.

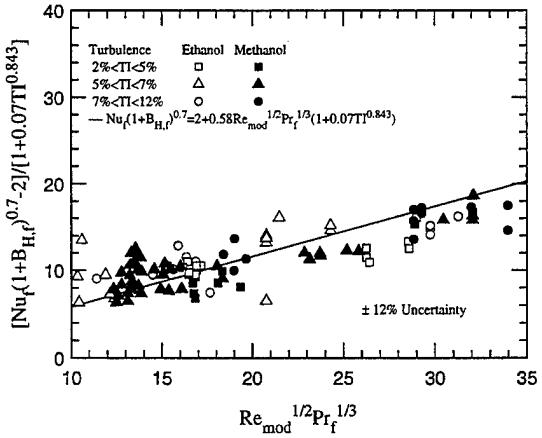

Figure 5. Turbulent measurements.

The resulting generalized laminar/turbulent flow heat transfer correlation is given by,

$$Nu_f\left(1+B_{M,f}\right)^{0.7} = 2+0.58\,\mathrm{Re}_{\mathrm{mod}}^{1/2}\,\mathrm{Pr}_f^{1/3}\left[1+0.07TI^{0.843}\right] \qquad (3)$$

for $50 < Re_M < 1500,\ 0.7 < Pr_{mix,f} < 1.0,\ 0 < B_H < 0.1$ where the turbulence intensity is defined by, $TI = \sqrt{\overline{u^2}}\,/\overline{U} \times 100$.

In conclusion these measurements indicate that mild gas phase turbulence ($\approx$ 5 - *10%*) can increase the heat/mass transfer rates by as much as *30 - 50%* when compared to laminar flow evaporation rates at the same droplet Reynolds number. Therefore, the generalized heat transfer correlation given by Equation (3), which attempts to account for free stream turbulence effects, is an important first step in reducing uncertainties in droplet evaporation in turbulent gas phase flow.

References

AIChE, 1984, "Data Compilation Tables of Properties of Pure Substances," Dept. Chem. Eng. Penn State University.

Ballal, D. R. and Lefebvre, A. H., 1975, "The Structure and Propagation of Turbulent Flames," *Proc. Royal Soc. London A.*, **344**, pp. 217-234.

Eisenklam, P., Arunachalam, S., and Weston, J. A., 1967, "Evaporation rates and drag resistace of burning drops," *Eleventh Symposium (Int.) on Combustion*, p. 715.

Eckert. E.R., Drake, R.M., 1972, "Analysis of Heat and Mass Transfer," McGraw Hill, New York.

Gallant, R.W., 1968, "Physical Properties of Hydrocarbons," Gulf Pub. Co., Houston, Texas.

Kuo. K.K., 1986, "Principles of Combustion," John Wiley & Sons, Inc., pp. 374-383.

Lide, D.R., Kehiaian, H.V., 1994, "CRC Handbook of Thermophysical & Thermochemical Data," CRC Press Inc.

Reid, R.C., Prausnitz, J.M., Sherwood, T.K., 1977, "The Properties of Gases and Liquids, " McGraw Hill, NY.

Renksizbulut, M., and Yuen, M.C., 1983, "Experimental Study of Droplet Evaporation in a High-Temperature Air Stream," *J. of Heat Transfer*, **105**, pp. 384-388.

Paul Yearling, 1995, "Experimental Determination of Convective Heat and Mass Transfer Rates from Single Evaporating Liquid Droplets in a Turbulent Air Flow," PhD Dissertation, North Carolina State University, August.

Yearling, P.R., and Gould, R.D., 1995, "Convective Heat and Mass Transfer from Single Evaporating Water, Methanol and Ethanol Droplets," *1995 ASME IMECE,* HTD-Vol. 321/FED-Vol. 233, pp. 33-38.

Yuen, M.C., and Chen, L.W., 1978, "Heat Transfer Measurements of Evaporating Liquid Droplets," *Int. J. of Heat and Mass Transfer*, **21**, pp. 537-542.

PARTICLE DISPERSION IN A TURBULENT SHEAR FLOW

AFOSR Grant F49620-95-1-0276

Annual Report: 8/1/1995 - 7/31/1996

Principal Investigators: Ian M. Kennedy and W. Kollmann

Department of Mechanical and Aeronautical Engineering

University of California, Davis CA 95616

SUMMARY

The project consists of an experimental and a numerical component. The experimental research is concerned with obtaining reliable, Lagrangian measurements of particle dispersion and vaporization in turbulent jets and sprays. The major effort in the experimental component of the project during this reporting period was directed towards redesigning the experimental rig to accommodate a much higher spray loading than was achieved in earlier efforts. A new spray injection system has been developed to overcome problems with the impact of the spray on walls. Loadings of about 50be obtained with the new system. An imaging spectrograph is being installed to measure droplet lasing from the fluorescent dye with a view to measuring droplet diameters and vaporization rates.

The numerical component of the project is aimed at the simulation of the jet under conditions that match the experimental conditions so that droplet dispersion and vaporization rates can be compared and correlations of drag and mass transfer evaluated. Our specific goals for the present year of the project were the development of a LES method for the particles and the improvement of the solution method for the Eulerian frame fluid motion. Both aspects of the simulation procedure should allow significantly higher mass loading for the spray computations.

TECHNICAL DISCUSSION: EXPERIMENTS

The original design of the experimental rig used two ultrasonic atomizers to produce a fine spray. The spray was directed through a duct and eventually out a nozzle along with the flow of air. The design attempted to prevent the impact of spray droplets on the wall by using porous walls through which air was bled. This method was able to yield a spray mass loading of only around 7% maximum. Dripping off walls became severe beyond this mass loading. Therefore, an entirely new approach has been adopted to produce the spray.

A series of miniature air blast atomizers have been installed within the nozzle in a straight section near the exit as shown in Fig. 1. Each atomizer consists of two tubes, one a 22 gauge and the second a 25 gauge needle. The tube through which air flows is directed in the main flow direction and the fuel tube is at a 30 degree angle to the air tube. When the liquid exits the tube, it is immediately met by air from the adjacent air tube and is atomized instantly. The flow leaving the 0.5 inch nozzle exit contains only air and droplets. At this point primary atomization is finished.

Due to the presence of the atomizers in the air flow, some uniformity of the exit flow of the spray has been sacrificed but we are now able to reach much higher mass loadings of liquid in the spray, around 50%. This loading is achieved without dripping from the nozzle. As

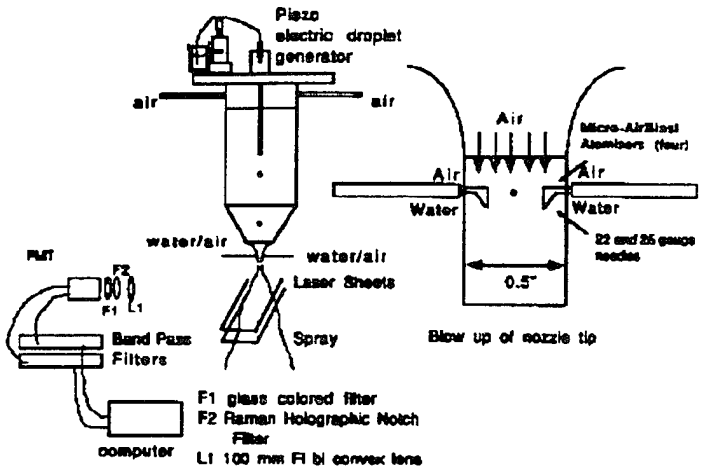

Figure 1: Schematic of system and diagnostic for dispersion measurements in a spray.

before, a water droplet doped with Rhodamine 6G is formed by the piezo drop generator and introduced into the spray. In addition, other advantages gained in injecting the spray near the exit of the jet, are that the air flow within the duct can be properly conditioned and since there are no droplets in the upper sections of the duct, there is no problem with making sure the "tagged" droplet is on the centerline of the jet. A pulsed photograph of the spray can be seen in Fig. 2. Because of the much higher spray mass loading that we are now able to achieve, the photomultiplier tube that was used for position detection has been moved off axis to the side of the jet. It was subject to excessive wetting when it remained in its axial viewing location. Also, because of the higher loading the signal to noise ratio is decreased due to the increase in Mie scattering from the spray. In the past, a holographic notch filter has been used inconjunction with a colored glass filter in order to filter out the Mie scattering. Now, this is not enough. To improve the signal to noise ratio, electronic band pass filters have been added to remove any information associated with the random arrival of non-tagged spray droplets.

In addition to hardware modifications and improvements in the dispersion measurement system, preparations for the implimentation of a droplet lasing system are in progess. There are a number of challenges in performing this measurement within a turbulent, heated spray. The first, is having an imaging system capable of imaging a relatively large area onto the entrance slit of an imaging spectragraph while meeting depth of field and light intensity requirements. This was not necessary in previous work because the position of the droplets in question was always known. At this time an imaging system consisting of 5 cylindrical lenses, has been designed and is being tested.

TECHNICAL DISCUSSION: THEORY and COMPUTATION

The computation of the turbulent flow field is based on the notion of simulating the large eddies and modelling the effect of the small and unresolved eddies on the large and resolved ones as described in the contract proposal. The work on the LES model for the continuous phase has been concluded and the LES idea has been extended to the particles. Particles in a spherical subdomain $\mathcal{D}^i(t)$ of the flow field with constant radius R are defined as an entity, that is governed by dynamic equations for position and velocity similar to an individual particle, but these equations contains additional terms representing the effect of particle

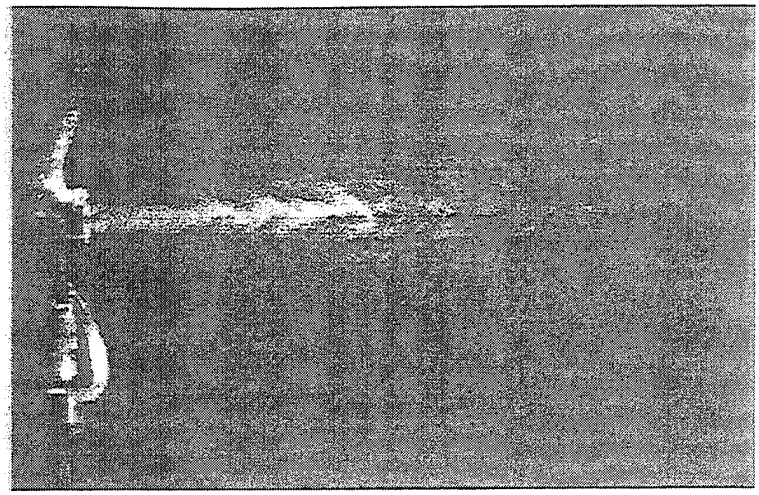

Figure 2: Mie scattered light image of the first 14 diameters of the spray at a mass loading of approximately 25 percent and a Re=30,000.

motion inside the subdomain and the particles leaving and entering the subdomain. The evolution of $\mathcal{D}^i(t)$ is determined by its centre location $\underline{\hat{X}}^i(t)$, the particle centroid location $\underline{X}^i(t)$, $\underline{Y}(t) = \underline{\hat{X}}^i(t) - \underline{X}^i(t)$ and the number of particles in the subset $N^i(t)$, since particles may leave and enter the subdomain $\mathcal{D}^i(t)$. The distance $\underline{Y}(t)$ between $\underline{\hat{X}}^i(t)$ and $\underline{X}^i(t)$ represents the unresolved part of the subset position and a closure model is given by

$$\underline{Y} = \underline{\hat{X}}^i - \underline{X}^i = c_X R\Big(1 - \frac{1}{N^i(\underline{\hat{X}}^i(t), t)}\Big) \int_0^t dt' \int_0^{t'} dt'' \underline{w}(t'')$$

where $\underline{w}(t)$ is a vector-valued white noise process and c_X is a constant. The velocity of a subset $\mathcal{D}^i(t)$ changes with time according to

$$\frac{d\underline{\hat{v}}^i}{dt} = \underline{P}^i + \underline{Q}^i + \underline{S}^i + \frac{d^2\underline{Y}}{dt^2}$$

The forces acting on a subset are: $\underline{P}^i(t)$ is the particle force based on the centroid properties, $\underline{Q}^i(t)$ the difference between the average acceleration and $\underline{P}^i(t)$ requiring a closure model. The third contribution is due to the motion of particles through the subset boundary and the motion of particles inside the subset, given to first order by

$$\underline{S}^i = \frac{2}{N^i}\Big\{\frac{\triangle N^+}{\triangle t}(\underline{v}^i - \underline{v}^{i+}) - \frac{\triangle N^-}{\triangle t}(\underline{v}^i - \underline{v}^{i-})\Big\}$$

$$+\frac{d}{dt}\Big\{\frac{1}{N^i}\frac{\triangle N^+}{\triangle t}\Big\}(\underline{X}^i - \underline{X}^{i+}) - \frac{d}{dt}\Big\{\frac{1}{N^i}\frac{\triangle N^-}{\triangle t}\Big\}(\underline{X}^i - \underline{X}^{i-})$$

where $\triangle N^{\pm}$, $\underline{X}^{i\pm}$, $\underline{v}^{i\pm}$ are the number, position and velocity of particles entering/leaving the subset. Closure models have been developed based on integrated white-noise processes, which can be simulated using stochastic differential equations of the Ornstein-Uhlenbeck type.

The second major effort during the last year was devoted to the improvement of the numerical solution method for the fluid phase equations. The radial direction is treated

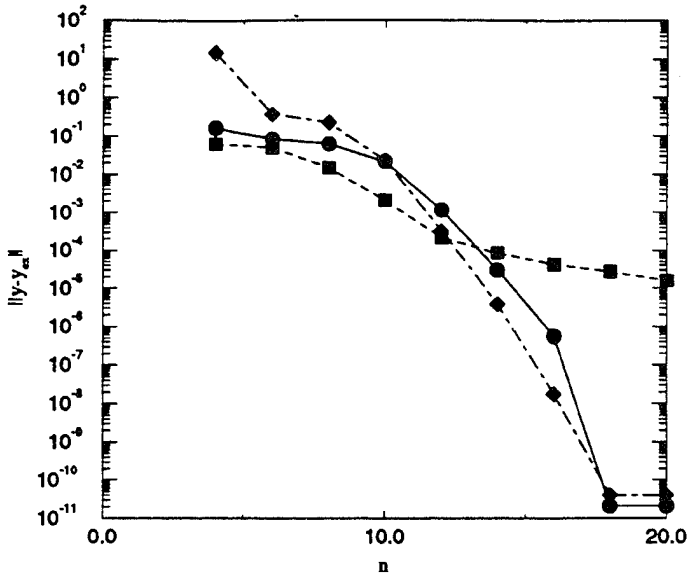

Figure 3: L_2 error norms for $\chi_n^{(\alpha,\beta)}(\eta)$ (circles), $\phi_n^{(\alpha,\beta)}(\eta)$ (squares) and $\psi_n^{(\alpha,\beta)}(\eta)$ (diamonds) using Gauss-Jacobi quadrature

using a mapping of the unbounded interval $[0,\infty]$ onto $[0,1]$ and a spectral method based on Jacobi polynomials is introduced. The mapping removes the problem of prescribing unknown conditions at the outer edge of a finite radial domain, thus allowing proper treatment of the entrainment fluxes. The spectral method for the radial direction must be adapted to the conditions at the coordinate axis $r = 0$. The cylindrical coordinate system introduces metric coefficients to mass and momentum balances, that become singular as the axis $r = 0$ is approached. This necessitates careful analysis of the behaviour of all circumferential Fourier modes as $r \to 0$. This analysis shows that three types of variation near $r = 0$ occur:

(i) Zero value and nonzero radial derivative;

(ii) Nonzero value and zero radial derivative;

(iii) Zero value and zero radial derivative.

It follows then that three sets of expansion/test functions are required for the radial direction.

The spectral method for the radial direction was tested extensively using a seond order ode containing the viscous terms of the momentum balances. It is seen in Fig.3 that better than exponential accuracy $||y_n - y_{ex}|| = O(\exp(-n))$ is obtained for the first twelve modes for each of the three sets of expansion functions. The Jacobi parameters were $\alpha = 0$, $\beta = 1$ for $\phi_n^{(\alpha,\beta)}(\eta)$ $(m = 0)$ and $\psi_n^{(\alpha,\beta)}(\eta)$ $(m > 1)$, and $\alpha = 0$, $\beta = 1$ for $\chi_n^{(\alpha,\beta)}(\eta)$ $(m = 1)$. The second kind of expansion functions $\phi_n^{(\alpha,\beta)}(\eta)$ applicable to $m = 0$ shows for higher modes slower than exponential convergence due to the fact that the boundary value at $\eta = 1$ is not fixed. The integration was done using the Gauss-Jacobi quadrature with $5m/3$ collocation points (using the 2/3 rule to avoid aliasing errors), where $m = M+1$ is the number of Jacobi polynomials in the set of expansion functions, $n = -1$ being the additional (transzendental) function not orthogonal to any other expansion function. The performance of all three sets of expansion functions is satisfactory. Currently the Poisson solver is adapted to the spectral method for the radial direction.

APPLICATION OF PARALLEL PROCESSING TO THE INVESTIGATION OF SUPERCRITICAL DROPLET EVAPORATION AND COMBUSTION USING MOLECULAR DYNAMICS

AFOSR Grant No. F49620-94-1-0133

M. M. Micci and L. N. Long

Dept. of Aerospace Engineering
The Pennsylvania State University
University Park, PA 16802

SUMMARY/OVERVIEW:

The evaporation and combustion of LOX or fuel droplets in the combustion chambers of current or future liquid propellant rocket or gas turbine engines occurs under supercritical pressures and temperatures, however little is known about droplet phenomena above the critical point. Molecular dynamics (MD) is being used to model the supercritical evaporation and combustion of three-dimensional submicron oxygen and argon droplets without any a priori geometrical constraints as well as to obtain quantitative information on the transport coefficients and effects of surface tension. The extensive computational workload is handled by developing algorithms to take advantage of parallel processing. The computed subcritical evaporation rates obtained by observing the droplet regression agrees with those predicted by Knudsen aerosol theory. Under subcritical conditions the droplets remain spherical while evaporating but under supercritical conditions the droplet disintegrated in a cloud-like, possibly fractal, manner with no spherical symmetry and a disappearance of surface tension.

TECHNICAL DISCUSSION:

Lox Evaporation. The evaporation of liquid oxygen (LOX) droplets under both subcritical and supercritical conditions is being modeled via molecular dynamics (MD). Oxygen molecules can be modeled by treating each atom in the molecule as a separate Lennard-Jones site (site-site). The equations of motion, which now contain angular dependencies, are solved by solving the equations of motion for each atomic site subject to a constraint which is the fixed bond length. This is referred to as constraint dynamics. The constraint results in a force which is added to the potential force. Constraint dynamics is computationally simpler for small molecules and was chosen for implementation in this study. Figure 1 shows a small test liquid oxygen droplet in equilibrium with its vapor. Future work will include vibrational energy storage, dissociation and reaction with hydrogen.

Evaporation Scaling. The scaling of the computations for the submicron droplets to micron size droplets is being investigated by examining the evaporation behavior of argon droplets under both subcritical[1] and supercritical conditions for initial droplet sizes which range over an order of magnitude. For the subcritical simulations, the d^2 versus time law was obtained. For the supercritical simulations, both a 5,500 and a 27,000 atom drop reached the same surface area regression rate after an initial heat-up period. Perhaps more significant is the result that the surface tension disappeared after the same time interval for the differently sized drops. The fractal dimension of the droplet surface is being measured as a function of droplet size under both subcritical and supercritical conditions.

Surface Tension. Since there is no standardized method for numerically calculating the surface tension in a system not in equilibrium, the computation is based on the molecular interpretation presented by Tabor[2].

> "The free surface energy of a liquid lends itself to a very simple molecular interpretation. Molecules in the bulk are subjected to attraction by surrounding molecules; the field is symmetrical and has no net effect. At the surface, however, the surface molecules are pulled in towards the bulk of the liquid. Apart from a few vapour molecules these is no attraction in the opposite direction. Consequently if we wish to increase the area we have to pull molecules up to the surface from the bulk against this one-sided attraction. This accounts for the surface energy."

In the code, the force components on each atom are summed for all atoms in each linked-list cell. Along with the summing of the force components, the total number of contributing atoms to this sum is recorded (for each cell). If requested, this sum can be continued over several time steps to provide time averaging of this data. After the requested time period is complete, the force components are averaged by dividing the sums by the number of contributions. This now gives the average force vector on each atom in the cell. Within bulk regions, these values approach zero, but on the droplet surface, the one sided forces are readily apparent. The data is represented on contour plots by computing the magnitude of these cell based force vectors (Figures 2 and 3). Figure 2 shows density, temperature and surface tension contours for a 5500 atom argon drop evaporating under subcritical conditions (P=3 MPa, T=300 K) while Figure 3 shows an argon drop of the same initial size evaporating under supercritical conditions (P=7.5 MPa, T=200 K). The high force values at the surfaces are revealed as a bright ring. The images are smoothed by adjusting the average force magnitude for each cell as an additional average of its value and a weighted contribution from the surrounding 26 cells. Typically a weighing value of 10% to 20% yields a good image. The density contours show that under subcritical conditions the droplet retains its spherical symmetry but under supercritical conditions the droplet quickly loses its spherical symmetry and disintegrates in a cloud-like, possibly fractal, manner.

Boundary Conditions. New boundary conditions as discussed by Allen and Tildesley[3] were implemented this year. The simulation of a spherical shape in a cubic boundary causes the environment to have an increased evaporation contribution at the points of the sphere closest to the sides of the cube. At these points, the density of the environment will be greater since the image of the evaporation process is much closer than at any other point on the droplet. Also, the heated boundaries are closer to these points imbalancing the energy profile of the environment. There is a computational overhead problem as well. The ratio of image lengths (the distance between the droplet center and the farthest image droplet divided by the minimum image distance) is 1.73. A value of 1.0 is optimal. Anything more means the environment consists of wasted simulation volumes and therefore wasted computations.

To resolve these problems, the most spherical shaped periodic boundary is desired. This shape is the truncated octahedron. It has 14 sides and an image ratio of just 1.29. While it is not a perfect representation of a sphere, it comes much closer than the cube. The coding is not very complicated, but referenced codes add additional computations in the force loop. The coding used for our investigation avoids this overhead by using a unique linked-list based structure.

Transport Coefficients. The transport coefficients that are of interest include self-diffusion, shear viscosity, and thermal conductivity. The coefficients are computed using Green-Kubo formulas[4] in which a correlation function is integrated over time. A time autocorrelation function measures the relation between the values of some dynamic quantity at two different times.

$$C(t) = \lim_{\tau\to\infty} \frac{1}{\tau} \int_0^{\tau} A(t_o)\ A(t_o+t)\ dt_o \tag{1}$$

For the self-diffusion, the Green-Kubo formula contains the velocity autocorrelation function,

$$D=\frac{1}{3N}\int_0^{\infty}\sum_{i=1}^{N} \langle v_i v_i(t) \rangle\, dt \tag{2}$$

For the shear viscosity the integration is over the non-diagonal terms of the stress tensor,

$$\eta_s=\frac{1}{Vk_BT}\int_0^{\infty} \langle J_p^{xy} J_p^{xy}(t)\rangle\, dt \qquad \text{where} \quad J_P=m\sum_{i=1}^{N} v_i v_i=\frac{1}{2}\sum_{i\neq j}^{N}\sum r_{ij}\nabla\phi(r_{ij}) \tag{3,4}$$

The thermal conductivity involves the heat current.

$$\lambda=\frac{1}{Vk_BT^2}\int_0^{\infty} \langle J_q^x J_q^x(t)\rangle\, dt \quad \text{where} \quad J_q=\frac{m}{2}\sum_{i=1}^{N} v_i^2 v_i-\frac{1}{2}\sum_{i\neq j}^{N}\sum [r_{ij}\nabla\phi(r_{ij})-\phi(r_{ij})i]v_i \tag{5,6}$$

The functions are computed during the simulation. The velocity autocorrelation is computed outside the force subroutine, while the other components of the other autocorrelation functions are calculated within it. Once the functions have been obtained, standard numerical techniques are used to obtain the transport coefficients. The statistical precision of the self-diffusion coefficient is improved by averaging over all the particles in the system. The viscosity and thermal conductivity values are improved by averaging over all the six terms from the stress tensor, and the three terms of the heat current, respectively. Table 1 compares the transport coefficients of liquid argon at its triple point (T=86.4 K, P=0.09 MPa) obtained via molecular dynamics versus experimentally obtained values from the literature.

Table 1

	Self-Diffusion D (cm^2s^{-1})	**Shear Viscosity η_s (Pas)**	**Thermal Conduct. λ ($Jm^{-1}s^{-1}K^{-1}$)**
Experiment[5,6]	1.60×10^{-5}	2.83×10^{-4}	132.7×10^{-4}
MD	1.69×10^{-5}	2.91×10^{-4}	152.8×10^{-4}

REFERENCES

1. Long, L.N., Micci, M.M. and Wong, B.C., "Molecular Dynamics Simulations of Droplet Evaporation," to be published in *Computer Physics Communications*.
2. Tabor, D., *Gases, Liquid, Solids: and Other States of Matter*, Cambridge University Press, New York, NY, 1991.
3. Allen, M.P. and Tildesley, D.J., *Computer Simulation of Liquids*, Clarendon Press, Oxford, 1987.
4. Hohersel, C. and Vogelsang, R., "Thermal Transport Coefficient for One- and Two-Component Liquids From Time Correlation Formations Computed by Molecular Dynamics," *Computer Physics Reports*, Vol. 8, 1988, pp. 1-69.
5. Hanley, H.J.M. and Cohen, E.G.D., "Analysis of Transport Coefficients for Simple Dense Fluids: The Diffusion and Bulk Viscosity Coefficients," *Physica* 83A, 1976, pp. 215-232.
6. Hanley, H.J.M., McCarty, R.D. and Haynes, W.M., "The Viscosity and Thermal Conductivity Coefficients for Dense Gaseous and Liquid Argon, Krypton, Xenon, Nitrogen, and Oxygen," *Journal of Physical Chemistry Ref. Data*, Vol. 3, No. 4, 1974, pp. 979-1018.

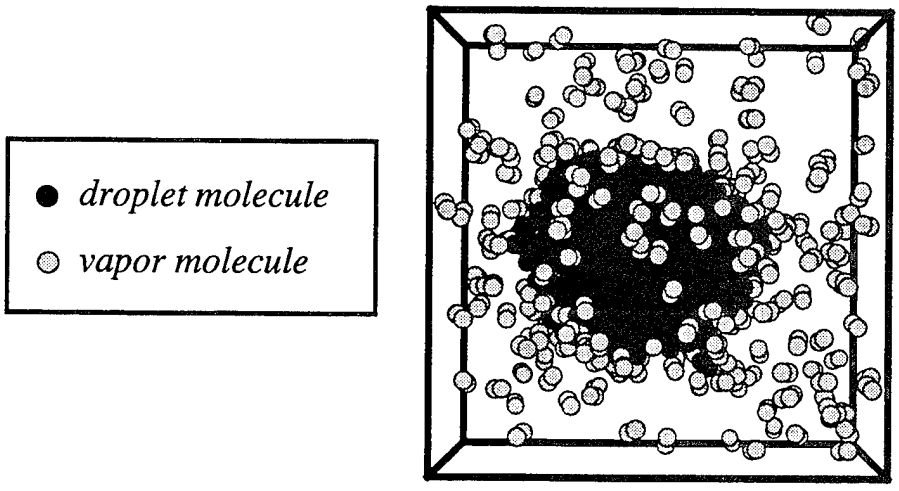

Fig. 1 Liquid oxygen droplet in equilibrium with its vapor in a system of 424 molecules at 110 K and $1.2 \cdot 10^{28}$ moleules/m^3. Each oxygen atom is modeled separately subject to a force constraint to maintain the bond length.

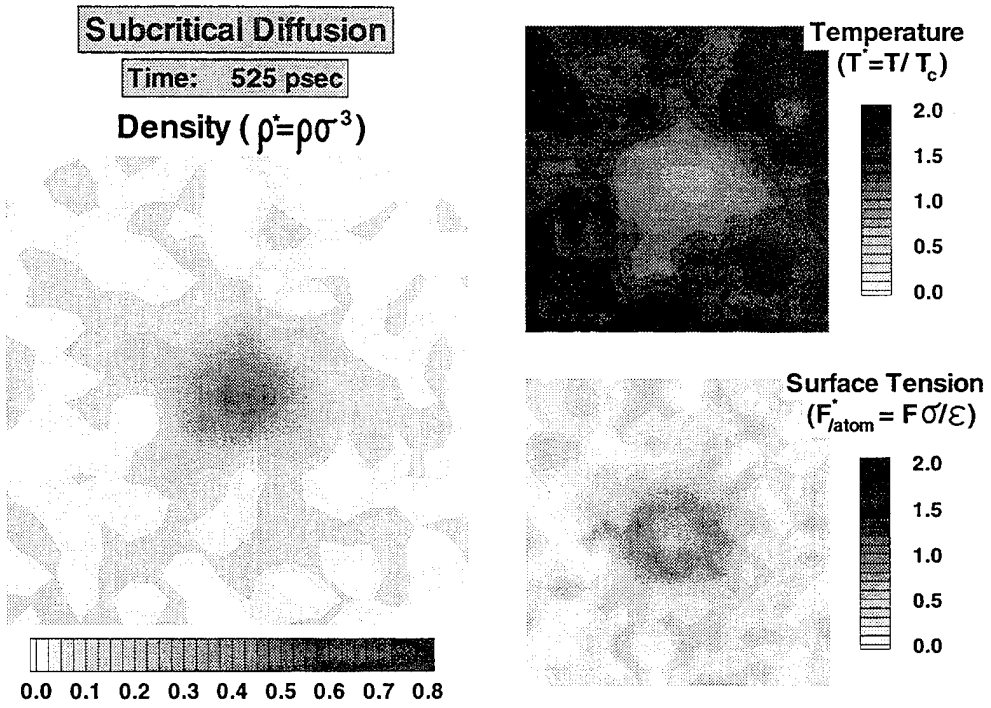

Figure 2. Argon droplet evaporating under subcritical conditions (P=3 MPa, T=300 K).

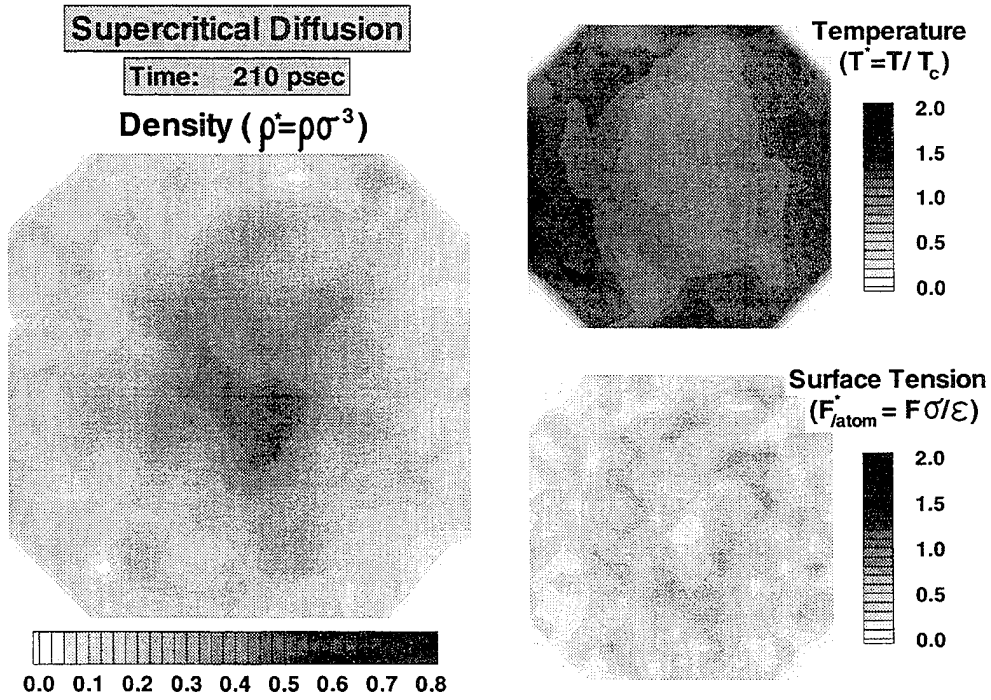

Figure 3. Argon droplet evaporating under supercritical conditions (P=7.5 MPa, T=200 K).

FLUORESCENT DIAGNOSTICS AND FUNDAMENTAL DROPLET PROCESSES

ARO Grant DAAH04-94-G-0020

Principal Investigator: Lynn A. Melton
Co-Principal Investigator: Michael Winter*

Department of Chemistry
University of Texas at Dallas
Richardson, TX 75083-0688

SUMMARY/OVERVIEW:

In this presentation, the extension of Droplet Slicing Imaging (DSI) techniques to (1) the imaging of the transient temperature field in a heating droplet and (2) the imaging of droplets as they pass through the flame front of a diffusion flame will be discussed. In (1), decane droplets fall into quiescent hot nitrogen; very little evaporation occurs during the initial transient heating. In (2), droplets are ejected from an aerodynamic droplet generator along the core of the diffusion flame, an environment which provides changing shear velocities and a high temperature zone, and droplet evaporation is expected to be significant. The DSI studies of flow patterns within the droplets will provide significant information about heat and mass transfer processes for droplets in combustion environments.

TECHNICAL DISCUSSION:

At UT-Dallas (UTD), the transient temperature field within a droplet, which has been injected as a cold droplet into high temperature nitrogen, has been imaged using combined droplet slicing imaging (DSI)/exciplex fluorescence thermometry (EFT) techniques. This work builds on a succession of prior work: exciplex fluorescence thermometry (UTRC and UTD), droplet thermometry (UTD), droplet slicing imaging (UTRC), and restoration of DSI images (UTD). A room temperature decane droplet, which has been doped with the PYPYP EFT system, falls into hot (400-500 C) nitrogen. It is intercepted by a DSI laser sheet, and the resulting fluorescence is made to form two images on a CCD camera, which images are filtered to isolate two distinct wavelength regions. Restoration of both images, pixel-by-pixel ratioing of the two images, and conversion of the ratios using laboratory calibrations yields a temperature image. The images may be taken as a function of the distance the droplet has fallen since entering the high temperature region. Preliminary images seem to show that hot surface liquid is carried by internal circulation into the core of the droplet.

AT UTD, strongly fluorescent liquid phase systems have been identified for which (1) the total fluorescence is virtually independent of oxygen concentration and temperature and (2) the change in the band shape with temperature can be used to measure the liquid phase temperature. These systems are relatively involatile and are recommended only for applications such as imaging of the temperature field on a cylinder wall.

The material presented in the remainder of this abstract arises from work carried out at United Technologies Research Center (UTRC).

*United Technologies Research Center, East Hartford, CT 06108

Program Objectives

The purpose of the droplet slicing experiments is to investigate the shear-induced, internal motion of single fuel droplets and characterize the mass and thermal transport effects. The program utilizes 2-D images of laser-induced fluorescence from equatorial planes in the droplets to measure flow and temperature patterns. The slicing experiments have been performed in cold-flow, inert conditions and extended to a combustion environment with the further extension to a high pressure regime. Differences in the data from the various regimes will be evaluated and compared to model predictions.

Analytical Model of Droplet Shear

An analytical model of the aerodynamic droplet generator was developed to help design an unambiguous experiment to elucidate shear-induced internal circulation by providing flow conditions that result in shear reversal during the droplet trajectory. Shear reversal was observed in the fluorescent images from the cold flow experiments and its effect on the internal motion of the droplet was studied. This behavior may only result if the droplet velocity which is initially less than the gas velocity, exceeds the gas velocity to allow reversal of flow patterns. Comparison with data from a high temperature environment is desired as well as data from the high pressure regime to more closely simulate conditions within a gas turbine combustor.

The droplet trajectory is calculated from the balance of forces on the drop. The droplet is accelerated by the drag force from the jet flow while gravity acts to decelerate the drop in this configuration. The flow from an axisymmetric jet is composed of a potential core which has a constant velocity that persists for approximately 5-10 orifice diameters downstream. This core region is followed by the axisymmetric decay region where the velocity decays as $(y/a)^{-1}$, 'a' being the orifice diameter.

$$\frac{d}{dt}\left(\frac{dy}{dt}\right) = \frac{A_{drop} \cdot C_D}{m_{drop}} \cdot \frac{\rho_M}{2} \cdot \left[u(y) - \frac{dy}{dt}\right]^2 - \frac{\rho_d \cdot g \cdot V_d}{m_{drop}}$$

C_D is the drag coefficient, a function of Reynolds number and A_{drop} and m_{drop}, are the area and mass of the decane droplet. V_d is the volume of the drop, ρ_d and ρ_M are the densities of decane and methane and, g is the acceleration of gravity. The jet flow velocity is a function of distance from the orifice and is modeled by the function u(y). The nozzle orifice of the droplet generator is 1 mm. The differential equation is solved for the position and velocity of the drop as a function of height above the nozzle orifice.

Cold Flow comparison. The analytical model was used to predict the injection of fuel droplets downward into air. This configuration prevailed in many of the earlier fluorescence experiments and their results provide data to validate the model of droplet injection. In particular, it was mentioned in earlier reports that shear reversal was observed during previous experiments. The decane drops exhibited shear reversal approximately 36 droplet diameters downstream of the nozzle throat. This experiment utilized a jet of air to strip and accelerate the drop. The model was set up to simulate these conditions and the results of the comparison are shown in Fig. 1. The model predicts shear reversal at 37 droplet diameters, in excellent agreement with the experiment. No shear reversal is predicted when the drop is injected upwards under the same flow conditions. Simulating flame conditions by including temperature and buoyancy effects results in marginal shear reversal for a 1 atmosphere flame.

Prediction for high pressure flames. Increasing the pressure has a beneficial effect on the shear velocity; the relative velocities of the drop and methane flow are predicted to reverse 10 cm above the nozzle for a 5 atm flame as shown in Fig. 2. This analysis provides the design of an unambiguous experiment to elucidate shear-induced internal circulation by providing flow conditions that result in shear reversal during the droplet trajectory. The model predicts a clearly defined region of shear reversal in flame environments at elevated pressure. This outcome is beneficial to the ultimate goal of the investigation, i.e., droplet studies above the critical conditions of the decane fuel.

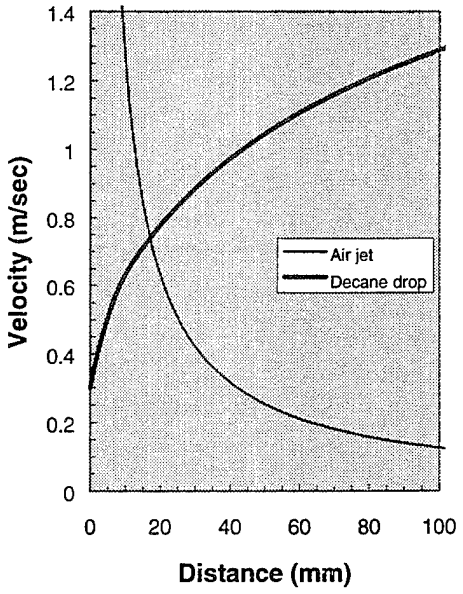

Figure 1. Analytical model prediction for decane droplet injection with an air jet downward into 1 atmosphere air. Shear reversal is predicted at 37 droplet diameters from the orifice.

High Pressure Burner. The aerodynamic droplet generator has been incorporated into the design of a jet diffusion flame burner. The major design parameters are shown in Figure 3. The burner is made of quartz and mounted in a high pressure vessel capable of sustaining flames to 20 atmospheres. The decane is fed to a tapered quartz tube where a droplet is extruded and held by surface tension. The gas fuel (methane) is flowed into the droplet region under pressure and strips the drop, accelerating it through the 1 mm orifice. The methane is saturated with acetone by bubbling the gas through an acetone bath. A provision for nitrogen diluent to control sooting and flame height is also incorporated. The burner has a novel design feature, swirl control tubes, to control the droplet spin induced by the injection process. The spin may be created by the effects of nonuniform throat conditions or, slight misalignment of the droplet delivery tube within the orifice.

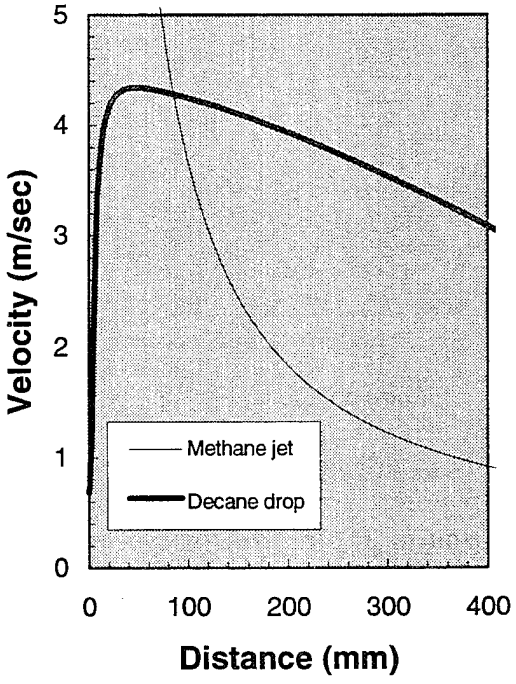

Figure 2. Decane droplet injection with a methane jet upwards into a 5 atmosphere adiabatic flame environment.

Droplets were successfully injected into the fuel flow of the methane/air diffusion flame mounted in the high pressure combustion vessel. They traveled through the flame core where they experienced a rapid temperature rise in their environment. The nozzle was positioned to eject the droplets upward because the flame behavior is optimized in that configuration. Figure 4 is a picture of the flame/injector apparatus in open

air and shows a single (burning) droplet exiting from the post flame gases after being injected through the fuel flow nozzle. Efforts were made to characterize the gaseous flows in an attempt to match the aerodynamic variables (such as Reynolds and Weber number) between the cold flow and combustion regimes.

The flame has been operated to 4.5 atmospheres and fluorescence measurements of shear reversal are in progress..

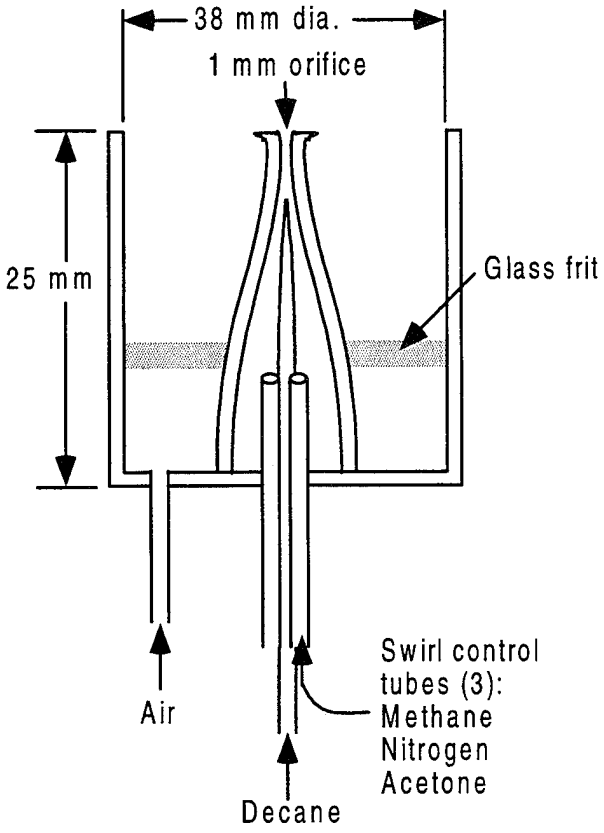

Figure 3. Quartz burner for aerodynamic droplet injection into the diffusion flame environment.

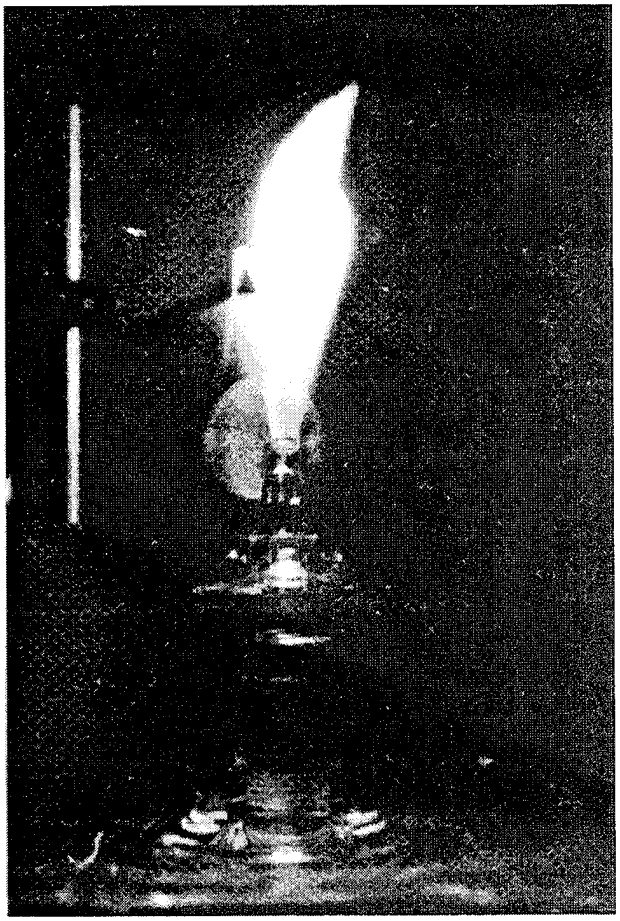

Figure 4. Diffusion flame burner with an aerodynamic droplet generator incorporated in the central fuel jet.

Intelligent Turbine Engines

(ARO Grant No. DAAH04-96-1-0008)

Principal Investigator: Dr. Ben T. Zinn, David S. Lewis Jr. Chair and Regents' Professor

Georgia Institute of Technology
School of Aerospace Engineering
Atlanta, GA 30332-0150

Summary/Overview

This new program investigates fundamental and practical issues that hinder development of intelligent control systems for improving the performance of turbine engines. It includes research on transient and off-design system performance models, component-specific and integrated control strategies, and robust sensors and actuators, in an approach that closely couples experiments, computations and theory. The initial focus is on control of compressors and combustors. Combustor efforts include pulsed fuel injection for control of combustion instabilities, and enhanced fuel/air mixing with small-scale actuators for control of parameters such as pattern factor and emissions. Control of compressor performance focuses on suppression of stall and surge using adaptive temporal filtering and hybrid fuzzy logic/model-based controllers to identify precursors and provide appropriate feedback. Development of advanced theory for control of complex, nonlinear systems, and investigation of enabling technologies, such as miniaturized sensors and actuators, and parallelized, neural network integrated circuitry are also included.

Authors

M. G. Allen, M. A. Brooke (School of Electrical and Computer Engineering); A. Glezer (School of Mechanical Engineering); W. M. Haddad, J. Jagoda, O. G. McGee, S. Menon, Y. Neumeier, J.V.R. Prasad, L. N. Sankar, J. M. Seitzman, B. T. Zinn (School of Aerospace Engineering)

Technical Discussion

For continued improvement of turbine engine (TE) performance, the use of advanced systems for active control of transient events and control of off-design operation offers great potential. For example, compressor flow constraints intended to avoid transient phenomena, such as rotating stall and surge, lower overall TE efficiency. Failure to control these transient events can also lead to catastrophic engine failure. Thus, active control schemes that can delay or eliminate the onset of these phenomena will increase the range of stable operation, improve fuel efficiency and reduce "wear" on engine components. Similarly, transient combustor events, such as flame out and instabilities, result in rapid loss of power and potential engine damage. Controlled management of fuel injection and mixing processes would minimize the likelihood of these detrimental combustor events, as well as provide the ability to reduce NO_x, CO, unburned hydrocarbons, soot and other undesirable emissions. Intelligent turbine engine systems can also improve poor off-design performance and improve fuel efficiency.

Our approach to development of an intelligent control system hinges on advances in four broad categories. First, we are stressing improvements in the basic understanding of specific transient engine phenomena. Second, accurate engineering tools, including computer models, that incorporate these improvements in the knowledge base are being developed. Third,

appropriate enabling technologies are being refined in order to develop control system components, i.e., sensors, actuators and controllers, that are specifically designed to be effective for turbine engine control. Fourth, these improvements are being combined to develop practical control strategies for specific engine components, e.g., compressors and combustors, as well as integrated strategies that account for component interactions.

Substantial improvements in physical understanding and the development of engineering tools are being carried out through a combination of state-of-the-art numerical tools and advanced diagnostic measurement techniques that can provide physical insight into the transient and off-design performance of turbine engine components. Numerical models based on existing computational fluid dynamics and large eddy simulation (LES) tools are being adapted to predict the transient behavior of a typical TE compressor and combustor. For example, a two-dimensional compressor cascade model, which includes unsteady and viscous effects, has already been developed and successfully used to model the compressor performance map for the Georgia Tech Aerospace Compressor facility. For modeling of unsteady liquid fuel-air mixing and other combustion processes, LES tools are being modified to include two-phase flow, i.e. gas and liquid fuel, to account for the fuel droplet stream breakup and vaporization processes. The multi-phase flow models are being based on those used in the ALLSPD3D code. Robust initial and boundary conditions are also being developed for ALLSPD3D so that it can be used to provide baseline and preliminary design data for development of our combustor control system. While the addition of multi-phase flow to the LES codes is currently underway, gas phase LES tools have already been used to study the use of microjet actuators for control of mixing in the combustor (see below for details). Figure 1 shows a comparison between experimental measurements of the turbulent power spectrum in the far-field of a jet, with and without controlled forcing. The LES simulations are able to predict the ability of the actuators to enhance the small-scale turbulence in the jet, which should lead to improved small-scale mixing.

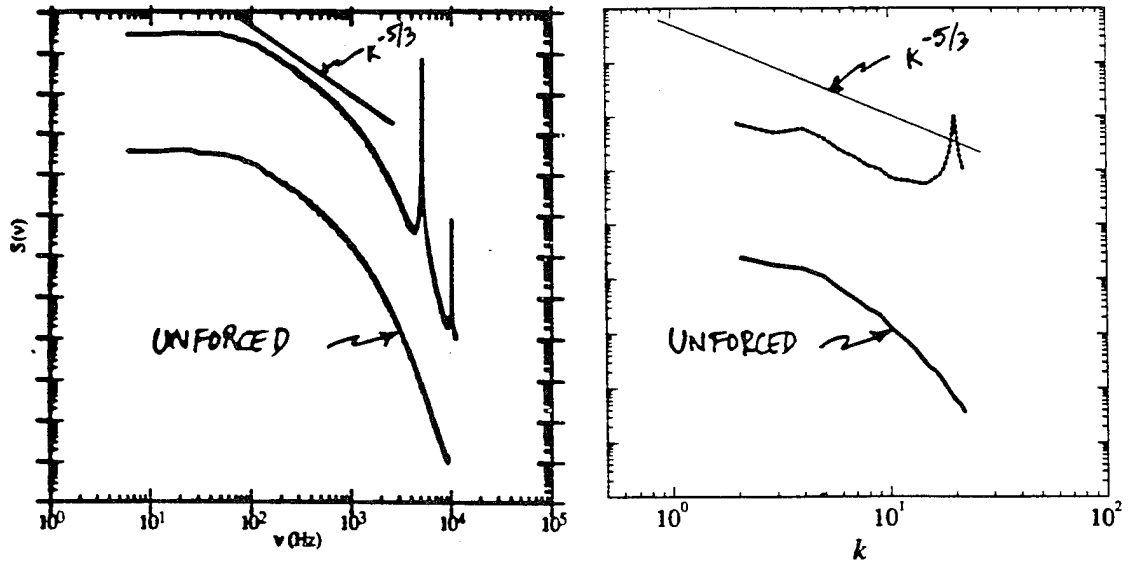

Figure 1. Comparison of (left) experimental measurements of the turbulence spectrum in the far-field of a jet with and without forcing at the jet exit using a zero-mass-flux microjet, and (right) LES prediction; note the LES plot has an expanded horizontal scale.

Validation of the transient codes is part of a complementary experimental effort. For the compressor models, pressure data acquired at various facilities, including a low-speed centrifugal compressor facility at NASA Lewis, are being used for code validation. For the combustor models, the computational results will be compared to measurements obtained with advanced optical diagnostic techniques, such as PDA, PIV and PLIF, in conjunction with traditional techniques. The advances in physical insight provided by the computational tools and experiments will be used determine engine parameters that provide the most effective control of

specific performance issues, and the combination of computational tools and experiments will provide a test bed for evaluation of engine control strategies.

The development of effective control systems requires methods for identification of necessary sensor and actuator technologies, as well as techniques that result in improved utilization of current and future sensors and actuators. For example, the computational tools described above are being designed to allow determination of a minimal set of sensors required to diagnose critical TE states and indicate optimal placement of sensors within the engine. While the use of current sensor and actuator technologies are planned, new technologies are also under development. For potential cost and manufacturing considerations, arrays of microjet actuators and pressure sensors may be implemented using rapidly evolving microelectromechanical systems (MEMS) technologies. The goal of the current MEMS development is investigation of the appropriateness of this technology for application to intelligent gas turbine engines, and development of devices that can be used in future engine designs. Probably the most severe requirement for MEMS devices in this application is operation at high temperatures, since many of the materials commonly used in MEMS fabrication will not withstand the full range of engine temperatures. We are investigating the use of high temperature materials such as silicon carbide and refractory metals, and examining approaches that minimize the need for active electrical circuitry, with its attendant restrictions on higher temperature operation. One promising actuator technology that may be implementable using MEMS is the zero-mass flux microjet for enhanced small-scale mixing. The traditional approach to control of mixing at the small scales has been indirect and relied on manipulation of global 2D and 3D instability modes of the base flow upstream of the mixing transition, with the objective of controlling mixing through the modification of the ensuing vortical structures. Because this depends on the classical turbulent cascade to transfer control influence down to the molecular mixing scales, small scale mixing in fully turbulent flows is only weakly coupled to the control input. For control of combustor mixing (and thus local stoichiometry and temperature), we are using a strategy that is based on concurrent manipulation of both the small- and large-scale dynamical processes by direct couplings between large- and small-scale motions in the flow. The data shown in Fig. 1 shows the ability of small-scale forcing in the shear layer at the jet exit to enhance the small-scale (high frequency) content in the far-field of the jet flow.

Since development of intelligent turbine engines involves control of a variety of components and issues, model- and rule-based control strategies are being developed, each suited to specific conditions. A promising and novel rule-based strategy utilizes a fast digital transformer to identify the time varying amplitudes, frequencies, and phases of the dominant modes of a measured signal, which can then be input to a rule-based controller. Without *apriori* information, this real-time observer has successfully identified the dominant, but time varying, instability mode(s), e.g., frequency and phase, of a combustor. Damping of the combustor instabilities is accomplished by pulsed fuel injection out-of-phase with the dominant instability mode(s). This same concept may be applicable to control of coupled combustor/engine behavior. Recently, the observer has also been used for real-time identification of rotating stall in a compressor. The intent is to identify a characteristic of the pressure signature that heralds incipient stall. As shown in Fig. 2, the observer is able to track the leading drop in dominant mode frequency that is associated with the onset of stall (large pressure fluctuations in Fig. 2). Moreover, time reconstruction of the observed mode shows that the observer follows the rotating stall without significant attenuation or phase shift. Again, this was accomplished without providing any *apriori* knowledge of the stall frequency spectrum to the observer. Thus this technique would be capable of dealing with evolution of the compressor characteristics.

For model-based control of turbine engines, which can often be characterized as highly nonlinear systems, advances in appropriate control theory are also required. For compressor control, the three-state Moore-Greitzer model for post-stall and surge transients in axial compression systems has been generalized to a multi-mode model, wherein a finite by arbitrary sum of harmonic functions was used to represent the disturbance potential at the compressor inlet. Using the time-varying coefficients of the relative perturbation velocity potential along

with the pressure rise and the mean flow as state variables, an affine nonlinear state space model has been developed. For combustor control design and evaluation, analysis and synthesis of combustion feedback systems with robust stability and performance is an important issue. In order to address the problem of fixed-architecture robust controller synthesis for combustion instabilities, parameter-dependent Lyapunov function methods have been developed to capture real parameter uncertainty. This framework has been used to design robust, reduced-order controllers for a combustor possessing four modes with a collocated sensor (microphone)/actuator (speaker) pair. Damping system uncertainty was assumed in the second mode. The results of the robust reduced-order controller is illustrated in Fig. 3, and compared to standard full- and reduced-order linear-quadratic Gaussian (LQG) controllers.

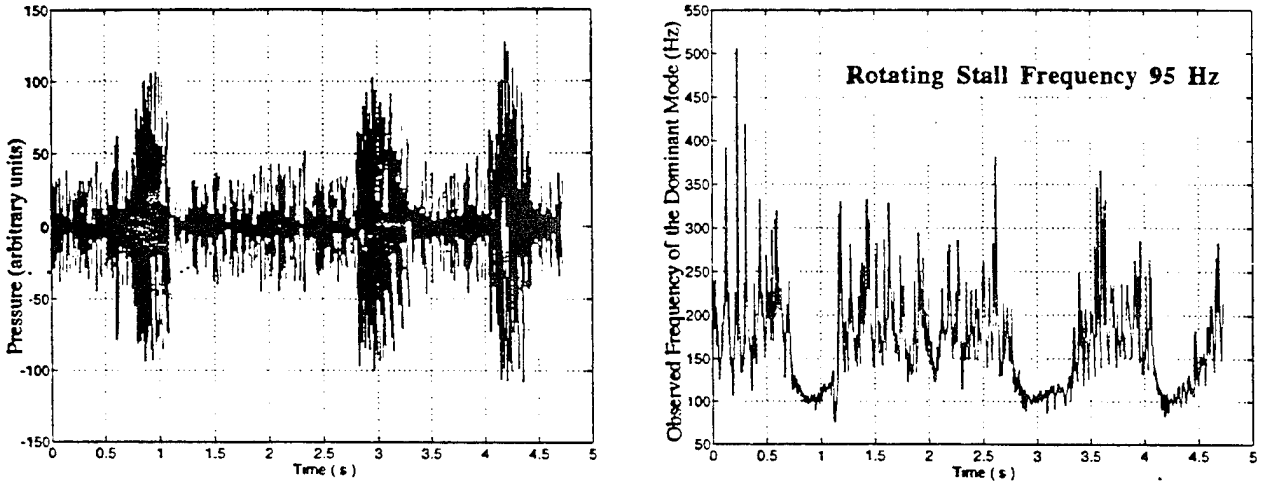

Figure 2. Real-time identification of rotating stall in the Georgia Tech axial compressor facility: (left) pressure from a single sensor and (right) frequency of the dominant mode determined by the real-time observer.

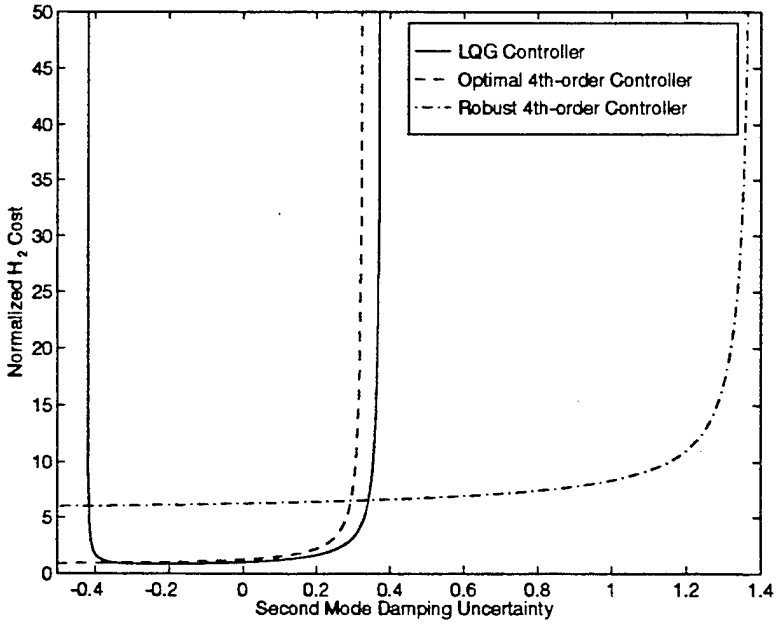

Figure 3. Response of various controllers for increasing damping uncertainty illustrating the nonconservatism of the robust reduced-order controller in comparison to the standard full- and reduced-order LQG controllers.

A MULTIDISCIPLINARY RESEARCH PROPOSAL FOR MEMS-BASED SMART GAS TURBINE ENGINES

ARO Contract #DAAH04-95-10097

Principal Investigators: Mehran Mehregany, Wen H. Ko, Steven L. Garverick, Francis L. Merat, and Stephen M. Phillips

Authors: M. Mehregany, W. Ko, S. Garverick, F. Merat, S. Phillips, and R. De Anna*

Microfabrication Laboratory
Department of Electrical Engineering & Applied Physics
Case Western Reserve University
Cleveland, Ohio 44106

SUMMARY/OVERVIEW

Our objective is to investigate sensor/actuator arrays for distributed measurement and actuation to monitor and improve the performance of gas turbine engines. Array architectures require integration of sensors/actuators with electronic circuitry for multiplexing and interfacing. The large volume of data resulting from sensor arrays requires signal processing for real-time data compression, providing feedback to control the actuator arrays. Array architectures require intelligent control to accommodate individual device failure and exploit the multiplicity of the elements in the arrays. Finally, gas-turbine applications require high-temperature capabilities.

TECHNICAL DISCUSSION

The smart-engine concept leverages microelectromechanical system (MEMS) as an enabling technology for providing efficient, high-performance systems which have inherent simplicity and reliability. Although our focus is a gas turbine engine, the results of our research in general apply to intelligent control of systems by using integrated and distributed sensor/actuator arrays. Below, an overview of progress in various aspects of our research is presented.

Sensor and Actuator Arrays

One area of our device development, in collaboration with Parker Hannifin Corporation, Cleveland, Ohio, has been the development of microfabricated silicon fuel atomizers [1]. These devices are intended for use as nozzles in pressure-swirl atomizers for gas-turbine combustors. The concept is a low-cost alternative to the conventional and metallic devices. The silicon atomizers have radial dimensions of a few millimeters, while their thicknesses are ~400 μm. The channels and the spin chamber are etched to a depth of ~275 μm from the front side of the wafer, while the outlet hole is etched from the back side of the wafer. Spray tests have shown that the micromachined devices meet or exceeded the performance of the conventional metallic devices when droplet size and spray angle are measured versus pressure ratio. The silicon atomizer does suffer erosion degradation compared to the metallic counterpart. To address this issue, we have used our silicon carbide (SiC) deposition technology (see below) to deposit a 1.5 μm-thick coating of SiC on the silicon atomizers. Prior to this experiment, conformal coverage of non-planar structures with SiC had not been attempted, in particular with step heights as high as 275 μm. Excellent conformality was achieved with the SiC coating. The SiC-coated atomizers are currently being erosion tested.

* with Vehicle Propulsion Directorate, Army Research Laboratory, NASA-Lewis, Cleveland, Ohio

Another area of our device work, in collaboration with Advanced MicroMachines Incorporated (AMMi), Cleveland, Ohio, addresses heat flux measurements. A heat flux sensor array for measuring heat transfer phenomenon in turbomachinery is being developed by AMMi with AFOSR support [2]. This sensor array also serves as a vehicle for developing a flexible substrate technology for use on curved surfaces. An array of heat flux sensors is contained in a flexible surface that is sized to conform over a turbine blade or other test article. Accurate calibration of the heat flux sensors is difficult but critical to the employment of the devices in actual tests. We are developing techniques and models for calibration of these heat flux sensors which are intended for high-frequency measurements. We also plan to use this technology as a platform for sensor arrays which must be mounted on curved surfaces.

Another area of our device work addresses the development a surface ice detection sensor. A resonant-diaphragm mounted as a parallel-plate capacitor is used to detect surface ice. Accumulation of water and formation of ice on the diaphragm affect the resonant frequency differently, allowing for the detection of ice formation. The sensor is fabricated with bulk micromachining of silicon and has a 7 μm-thick diaphragm with lateral dimensions of 1 to 3 mm. In the first generation of devices fabricated, we were not able to achieve resonance due to the relative diaphragm thickness and high level of residual stress in the diaphragm material. However, the diaphragms do deflect with applied voltage when there is no ice and remain fixed when covered with ice. Alongside a diaphragm lies a thin-film resistor which can also be used to detect ice if operated as a hot-wire probe. The thin-film resistor's temperature is a function of both the applied power dissipated in the resistor and its heat loss through convection and conduction. Thus, the thin-film resistor can also be used to measure fluid velocity or used to melt ice after detection. These and other novel ice-detection techniques are being investigated.

Another area of our device work studies the use of a multiplicity of coarse sensors calibrated with a precision sensor to improve the measurement accuracy when using the coarse sensor array. This effort is to take advantage of the fact that microfabricated sensor arrays allow design and signal-processing techniques which are not practical with conventional sensors. We are testing an array of temperature sensors in a temperature-controlled water bath. One precision sensor and ten coarse sensors are generating data for a neural network which will be used for accurate temperature measurements when the precision sensor is removed. (This experiment is also being duplicated with accelerometers.) The neural network will also compensate for individual sensor failures and anomalies to ensure successful operation even under adverse conditions. The neural network will be used on a test structure instrumented with arrays of accelerometers. Various impact forces will be applied and the accelerometer signals processed and analyzed to determine the location and magnitude of the impact.

While our current device development is based on silicon, we are developing the technology infrastructure for silicon carbide (SiC) MEMS to enable high-temperature (e.g., eventually up to 650°C) operation. While semiconductor silicon is well-known for its electronic properties, it is also an excellent mechanical material (e.g., modulus ~190 GPa) for MEMS applications. However, silicon electronics are generally limited to operations below ~200°C, and silicon's excellent mechanical properties start to diminish over ~400°C. With SiC, diodes and more complex electronics have been shown to operate up to ~600°C, while the excellent mechanical properties of SiC are maintained to much higher temperatures [3].

We are developing epitaxial growth of 3C-SiC films on four-inch-diameter (100) silicon wafers using atmospheric-pressure chemical vapor deposition. In connection with bulk micromachining of the silicon substrate, these films are used for high-temperature pressure sensor development using a piezoresistive readout scheme. Mechanical properties of the 3C-SiC films are being studied. A square diaphragm of the film, fabricated by bulk micromachining of the substrate, is pressurized and the deflection versus pressure data is used to determine Young's Modulus (392 GPa) and residual stress (380 MPa).

We have also deposited polycrystalline SiC on polysilicon, which is used as a sacrificial layer to enable surface micromachining of SiC micromechanical devices [4]. In the this case, the SiC film is patterned to form the device structure of interest, after which the polysilicon sacrificial layer is etched away in KOH. Deposited SiC films have a surface roughness of about 150Å, thus they must be polished subsequent to deposition before further processing can be performed. Starting with an unpolished SiC film, we have been able to reduce the surface roughness to near 33Å after polishing. SiC lateral resonant electrostatic actuators have been fabricated using the described surface micromachining technique.

Integration with Electronics

In regards to electronics, progress has been made in three areas during the first year of the program: design methodology, sensor array interfacing, and capacitive sensing. The establishment of a structured design methodology for integrated micromechanical and electronic systems will reduce design time and improve the probability of first-time success, and will be particularly important in the latter years of this program when the designs will be very complex. An important circuit function will be the acquisition of data from sensor arrays, and our goal is to minimize circuit area and power while achieving the best possible noise performance. Micromechanical sensors often output their signals in the form of varying capacitances. The acquisition of data from these types of sensors has been specifically addressed in the array study, and an interface circuit has been designed to support the development of new sensors.

The integrated design methodology has been adapted from our prior work, and expanded to meet the needs of this program. Designs are constructed with the help of a library of predefined cells and entered graphically into a data base. In this year, key "level one" subcircuits, such as op amps and memory cells, have been gathered to form the foundation of the reusable cell library. The database is used to drive a system simulation. Closed-loop micromechanical/analog/digital systems, including the Delta modulator described below, have been successfully simulated using a commercial version of SPICE. Micromechanical devices and electronic circuits are laid out on separate abstract layers, which simplifies the integration of the work from various engineering disciplines, and the actual photomasks are generated by software. Layout rules and photomask generators have been updated from a prior 3 μm NMOS process to a 2 μm CMOS which is presently being developed.

Noise limitations in the sensing of signals from arrays of capacitive sensors having substantial interconnect resistance has been a focus of the work this year. In performing this study, four basic amplifier options have been identified and studied: single-ended, differential, split bootstrap, and split differential. Guidelines for optimizing the tradeoff between noise, power, and circuit area have been derived. A test chip is being designed to test these theories. The test chip will include test circuits for all the options studied, as well as an optimized low-noise interface to an array of integrated capacitors. Our goal is 25 aF resolution at a 1 MHz total sampling rate using a flexible architecture that would permit the trading of array size for sampling speed. For example, an array of 128 sensors could be sampled at a rate of 8 kHz per sensor. A multiplexing scheme has been devised that requires only one amplifier transistor per sensor, and it is only biased when addressed, so power consumed in the array will be minimized.

A Delta modulator is being developed to support the development of capacitive sensors, specifically the ice sensor. The Delta modulator employs a previously developed low-noise, charge-integrating amplifier IC, and provides a digital output proportional to the rate of capacitance change, as well as an analog output proportional to capacitance. The design has been simulated, constructed, and tested. The circuit was functional, but performance was limited due to problems with the amplifier IC. The design of the amplifier IC has been adjusted and new chips are being fabricated. A minimum detectable charge 0.5 fC, e.g. 1 V driving 0.5 fF, and a dynamic range of 60 dB is expected.

Signal Processing and Control

We have developed a neural-net based sensor processing system which can: (i) correct for sensor noise, drift, and failure; and (ii) estimate system parameters. We use an autoassociative memory using a random vector enhanced phasor neural network. This approach uses redundant sensor information to provide corrected sensor outputs. A second neural network combines the sensor information to estimate the required system control parameters. This two-step neural net approach avoids the use of complex analytical models and has several advantages which are important to MEMS based sensor arrays:

1. it dramatically reduces the effects of individual sensor noise;
2. it accommodates sensor-to-sensor variation in arrays by treating the variation as noise;
3. it performs data compression upon the output of an array of sensors; and
4. it should be capable of multi-sensor fusion (not yet confirmed).

We have tested this system on an array of optical sensors, and are in the process of simulating performance for the thermal sensor array described above.

We are investigating techniques for incorporating sensor/actuator arrays into feedback control systems. This task has been divided into four components. The first is the choice of control structure. The second is the development of a design methodology which accommodates the chosen structure. The third component is to find techniques to provide the required fault tolerance, and the fourth is the determination of appropriate sensor and actuator locations. As far as controls structure is concerned, the traditional approach to this control problem would be to consider the system being controlled to be a multiple-input, multiple-output, highly-coupled dynamical system. Although this approach allows the full use of all of the sensor information and complete freedom in the use of the actuators, it poses some significant difficulties. The primary difficulty is in the management of information flow. The traditional technique requires full interconnection in the control system since each actuator has the potential to receive information form each sensor. This becomes impractical for more than a few tens of array elements. A related issue is that of communication bottlenecks which would result if a bus architecture is used instead of individual interconnects. Finally, although there are techniques for designing and implementing multiple-input multiple-output controllers, these would be computationally intractable for large arrays. To avoid these problems we have investigated a distributed control strategy. This controller has a series of local, high performance controllers augmented by a global, low performance controller. The local controllers are single-input, single-output, high-bandwidth controllers readily designed by traditional tools. Since these local controllers cannot accommodate the cross channel coupling, they will not provide the overall system performance. This will instead by handled by the global controller which will only require low bandwidth information. The choice of control structure has been verified through testing on a small (ten channels) simulated thermal control system. Preliminary results have provided proof of concept for this structure. Since this is not an established design technique, design tools are currently being developed. Supplementing this approach will be the investigation of incorporating fault tolerance into the control structure. Finally, the problem of sensor and actuator location is being investigated.

REFERENCES

[1] A. Singh, et al., "Micromachined Silicon Fuel Atomizers for Gas Turbine Engines," in *Proc. of IEEE Micro Electro Mechanical Systems Workshop*, San Diego, CA, Feb. 1996.

[2] M. Mehregany, et al., "Microelectromechanical Systems for Aerodynamics Applications," *AIAA 96-0421, 34th Aerospace Sciences Meeting*, Reno, NV, Jan. 1996.

[3] G. Krotz, et al., "Silicon Carbide as a Mechanical Material," in *Technical Digest, The 8th Int. Conf. on Solid State Sensors and Actuators*, Stockholm, Sweden, June 1995.

[4] A. Fleischman, et al., "Polycrystalline SiC for Surface Micromachining," in *Proc. of IEEE Micro Electro Mechanical Systems Workshop*, San Diego, CA, Feb. 1996.

ENGINE RESEARCH CENTER: ADVANCED DIESEL ENGINE RESEARCH

ARO contract DAAHL03-92-0122
ARO grant DAAH04-94-G-0328

Principal Investigators: Mike Corradini, Pat Farrell, Dave Foster, Jaal Ghandhi, Jay Martin, Rolf Reitz, Chris Rutland, Emeritus Professors: Gary Borman and Phil Myers

Engine Research Center
1500 Engineering Drive
Madison, WI 53706

OVERVIEW:

The Engine Research Center at the University of Wisconsin - Madison is the U.S. Army's Center of Excellence for Advanced Propulsion. It is a cooperative effort which has the objectives of providing knowledge and research tools for solution of long range problems of special interest important to mobility needs and identifying new technologies important to mobility and studying those technologies in a research environment. This effort is primarily conducted through the education of graduate student researchers. The current focus of research efforts are the fundamental phenomena associated with increasing power density and air utilization of combustion propulsion systems.

TECHNICAL DISCUSSION

The Engine Research Center at the University of Wisconsin - Madison is a multi-investigator cooperative effort doing research in the fundamental aspects of advanced propulsion systems addressing unique needs of the Army. The research effort is a parallel development of experimental investigations on state of the art engines using advanced diagnostics and sophisticated 3-D model development. This effort currently includes approximately 60 graduate students working on MS and Ph.D. degrees.

The presentation will be in three parts. A very brief introduction to the Engine Research Center followed by highlights of two specific research projects. The first an experimental effort to pursue further understanding of the effect of surface temperature on flame quenching distance and heat transfer rates and second a computational effort using direct numerical simulation to investigate the interaction between combustion and boundary layer turbulence.

Single-Surface Flame Quenching Distance Dependence on Wall Temperature, Quenching Geometry, and Turbulence

The effect of wall temperature on single-surface flame quenching distance was characterized for atmospheric, premixed methane-air flames. The study includes a comparison of the wall temperature dependent, single-surface flame quenching distance for laminar and turbulent flames. The laminar flame-wall interaction was studied for flames that were configured at angles near 0° and 45° relative to a temperature-controlled surface. For each flame quenching configuration, the flame quenching distance was chosen as the location from the surface for which a constant value of C_2 concentration occurred; spatially resolved measurements of C_2 concentration were obtained with the technique of laser-induced fluorescence. The results indicated that the single-surface flame quenching distance, for each flame configuration, decreased with increasing wall temperature. For the laminar flames, Raman-based gas temperature measurements indicated that the near-wall temperature gradient was reduced when the wall temperature was increased. The wall heat flux was estimated from the measured near-wall temperature profile and gas thermal conductivity. These results indicated that the wall heat flux decreased for the laminar sidewall flame and increased for the laminar stagnation flame for increasing wall temperature from 250 °C to 600 °C.

Figure 1 shows the measured sidewall flame quenching distances as a function of wall temperature for both a laminar and turbulent sidewall flame. The quench distance was assessed using 50% of Fo, where Fo is the maximum fluorescence intensity.

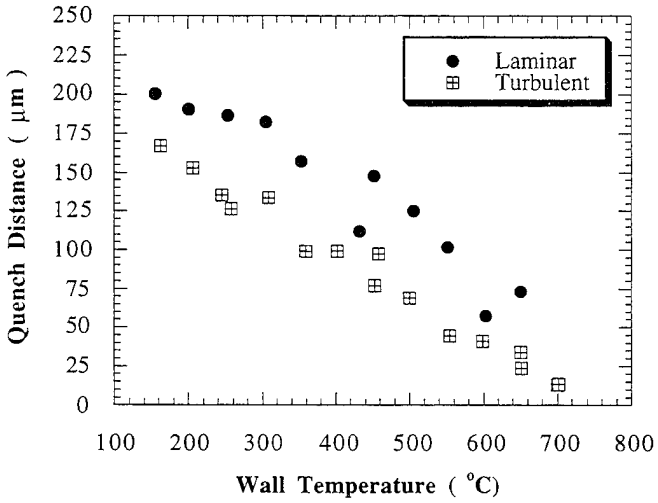

Figure 1: Comparison of laminar and turbulent sidewall (maximum near-wall C2, 50% F_o) quenching distance.

Figure 2 gives the measured temperature profiles as a function of distance from the wall for a laminar sidewall flame with two different wall temperatures.

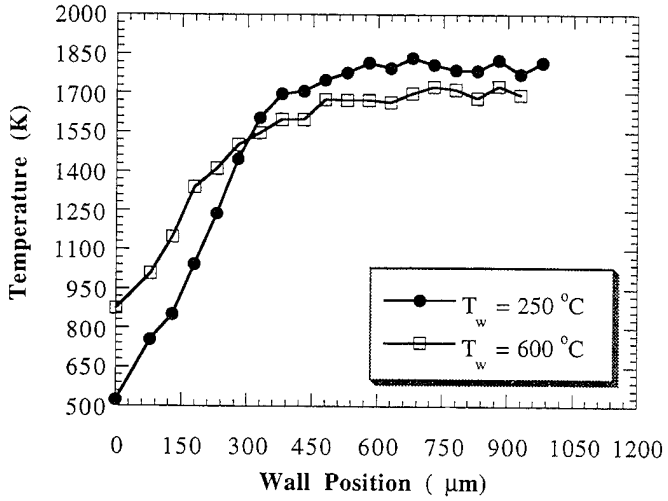

Figure 2: Gas temperature as a function of wall position; laminar sidewall flame.

DNS of Flames in Turbulent Channel Flow

Emissions regulations are currently driving substantial efforts to use CFD modeling to study and design IC engines. A pacing item in these calculations is the accuracy of the turbulent combustion models. The unresolved issues pertaining to combustion modeling can be broadly grouped into two categories: how turbulence affects species transport and reaction kinetics and how combustion heat release alters turbulent transport. In both of these areas, direct numerical simulations (DNS) are providing important insights.

Currently, DNS is being used to study premixed flames in turbulent channel flow. The two main goals of the work are: (i) to understand how combustion alters the turbulent boundary layer structure to guide new modeling efforts, and (ii) to describe basic mechanisms controlling increased heat transfer from turbulent flames to the wall. The flow configuration is sketched in Fig. 3. Note that it uses a simple, 'numerical' flame holder consisting of specified temperature cells but no recirculation zone. The flames are represented by single step premixed reactions. The turbulent inflow is obtained from an unsteady non-reacting, turbulent channel flow calculation. Turbulence statistics are determined by averaging in time and in the span wise (z) direction.

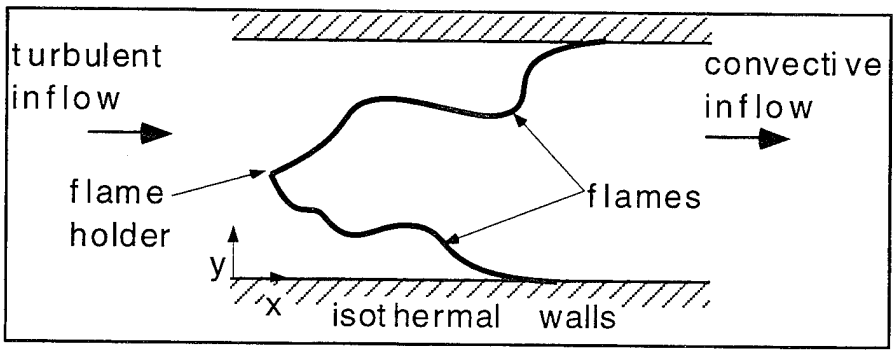

Figure 3: Schematic of DNS channel flow calculations.

To help determine how combustion affects the turbulent boundary layer, the turbulent kinetic energy budget was evaluated at several downstream locations. Figure 4 shows the major terms in the budget as a function of the wall normal coordinate. The main sources of turbulence generation are the pressure terms (pressure dilatation and pressure transport) and the main sink is dissipation. While the role of dissipation is expected, the pressure terms are not normally important in turbulent boundary layers. Their increase role in reacting flows is due to heat release from the flame that results in increased correlation of fluctuating pressure and velocity terms.

An even more significant result in Fig. 4 is the change in sign of what is normally called the production term. This term is the interaction of the Reynolds stresses with the mean velocity gradient and is the primary source of turbulence generation in a non-reacting boundary layer. The presence of the flame completely changes the character of this term so that it becomes a turbulence sink in the region of the flame. This effect has been traced to mean dilatation effects in the flame zone and will probably require incorporation into turbulent wall models at some future date.

Experimental results generally show that turbulence enhances wall heat transfer from a flame. This effect has been found in the current DNS calculations where turbulence causes the instantaneous heat flux can be up to 40% higher. The mechanisms associated with this effect are being investigated using unsteady flow visualization. The collapse and generation of the boundary layer streaks appear to be a primary cause for the enhanced heat flux. The streaks are streamwise vortex structures. As these structures oscillate in the flow they periodically break apart and collapse, and then reform downstream. As the streaks collapse against the wall, they bring more reactants into the flame and increase the local reaction rates. This results in higher heat flux in these regions.

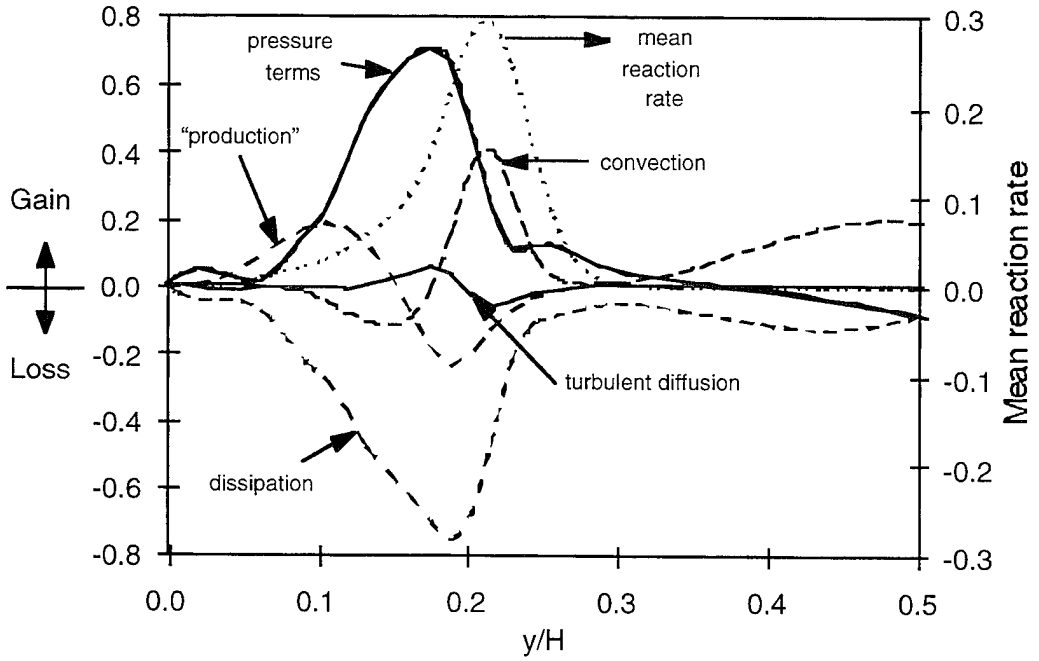

Figure 4: Major terms in the turbulent kinetic energy budget plotted as a function of distance from the wall (y). Terms are plotted with their sign to indicate whether they increase or decrease turbulent kinetic energy. Downstream location is 1.5 H from the flame holder where H is the channel half width. The mean reaction rate indicates the mean flame position which has not reached the wall at this downstream location.

ENGINEERING MODEL DEVELOPMENT FOR DIESEL PERFORMANCE AND EMISSIONS

ARO Contract No. DAAH04-94-G-0236

A.M. Mellor and K.P. Duffy, Vanderbilt University

R.J. Tabaczynski, Ford Motor Co.

S.L. Plee, Motorola, Inc.

OVERVIEW:

The specific aim of the research is to develop a characteristic time model (CTM) for diesel engine emissions. In the model, expressions describing the spatial and temporal fuel/air mixing and kinetic aspects of the combustion process are sought which, when combined in the appropriate manner, correlate the soot and NOx emissions from direct injection diesel engines. Experimental work on a high speed direct injection diesel is ongoing at Ford Motor Co. to acquire additional data for CTM model validation. Collaborative efforts are underway at both Ford and the University of Wisconsin-Madison to use CFD to model the engine intake and compression stroke air and fuel motion. Present and future efforts include utilizing the above information to better understand the diesel fuel/air mixing and combustion process and implementing it into the CTM.

DISCUSSION

The stoichiometric adiabatic flame temperature has been used in past studies by Plee et al. (1981) to correlate the effects of oxygen, nitrogen and exhaust gas recirculation (EGR) addition on NOx and soot emissions from several diesel engines under carefully controlled operating conditions. Similar activation energies for NOx formation were found for different operating conditions for several different engines suggesting the NOx chemistry could be correlated with a single characteristic stoichiometric flame temperature. One aspect of this research is an attempt to extend the Plee et al. methodology to more modern engines and determine if similar results can be obtained. A technique is established to calculate the EGR-influenced stoichiometric adiabatic flame temperature and use it in NOx emissions correlations. Parametric studies were performed to determine the sensitivity of the computed activation temperature to changes in selected variables including definition of EGR rate (mass or volumetric) and the pressure and temperature for flame temperature calculation evaluated at motoring versus firing TDC conditions. With appropriate parameters selected, the activation temperature for the new data is lower than the previously obtained value by a factor of approximately two-thirds. The reason for the dissimilar value is postulated to be primarily due to fundamental differences between the fuel injection systems and the resulting effect of increased premixed burn fraction on the NOx emissions. Further details of this work are found in Duffy et al. (1996).

Turbulent mixing during diffusion flame combustion is dominated by the characteristics of the fuel injection system for large, low speed, quiescent chamber diesels and by the air motion for smaller high speed diesels incorporating squish/swirl. However, most engines are of the type in which both of these processes play a role in the turbulent mixing, and the challenge is to evaluate the relative contributions of both. Concerning soot emissions, the method of their reduction involves minimizing the formation process by decreasing the mixing (residence) time the fuel spends in the formation region and maximizing the oxidation process by increasing the mixing (residence) time the soot particles spend in the oxidation regions.

By analogy with gas turbine studies (Derr and Mellor, 1990), mixing expressions relevant to the gas-phase stoichiometric contours may determine the NO_x and soot formation. Mixing times and zones for soot oxidation must be determined to complete the model. The task at hand is therefore to identify relevant mixing times and relate these to engine design and operating conditions and then formulate emissions expressions using these mixing times in combination with kinetic times.

As a point of departure, the model of Dodds (1976) was examined in which the overall net soot emission is obtained by multiplying the amount formed by the oxidation efficiency to yield:

$$\text{EIsoot} \propto (\tau_m / \tau_{sf})\,(\tau_{so} / \tau_{sl,so}) \qquad (1)$$

where the EI stands for an emissions index given in units of g soot/kg fuel. The τ s are characteristic times describing either mixing (fluid mechanics) or chemical kinetics. τ_m is the controlling mixing time associated with the soot formation process. $\tau_{sl,so}$ is the time a fluid element spends in the lean oxidative shear layer and τ_{sf} and τ_{so} are kinetic times associated with soot formation and oxidation, respectively. A similar expression was postulated for NOx emissions:

$$\text{EINOx} \propto (\tau_{sl,no} / \tau_{no,\,form})\,(\tau_{no,\,decomp.} / \tau_{sl,no\text{-}decomp.}) \qquad (2)$$

Yu and Shahed (1981) noted that for a well optimized DI diesel engine, the NOx/soot tradeoff at a constant equivalence ratio was fairly independent of engine speed, fuel rate, injection timing, and EGR rate. Furthermore, they suggest NOx formation and soot oxidation may be spatially and temporally similar. Experimental evidence of this idea is also presented by Kosaka et al. (1995). Using this assumption and the above equations, an attempt is made to explain the NOx/soot tradeoff curves for various data as follows.

Theoretical NOx/soot tradeoff curves are sketched in Fig. 1a. An equation of the form y = m/x + b or NOx = m/SOOT + b is used to fit the data. Low values of the constant m indicate NOx/soot tradeoff curves which fall closer to the origin. The data are more amenable to analysis when cast in a straight line form by plotting NOx versus 1/SOOT as indicated in Fig. 1b. NOx/soot tradeoff curves which fall closer to the origin have a lower slope when plotted in this manner. In general, a series of NOx/soot curves produce a fan of straight lines emanating roughly from the origin. In the present analysis, an attempt is made to explain the slope differences with various characteristic fluid mechanic and chemical kinetic times.

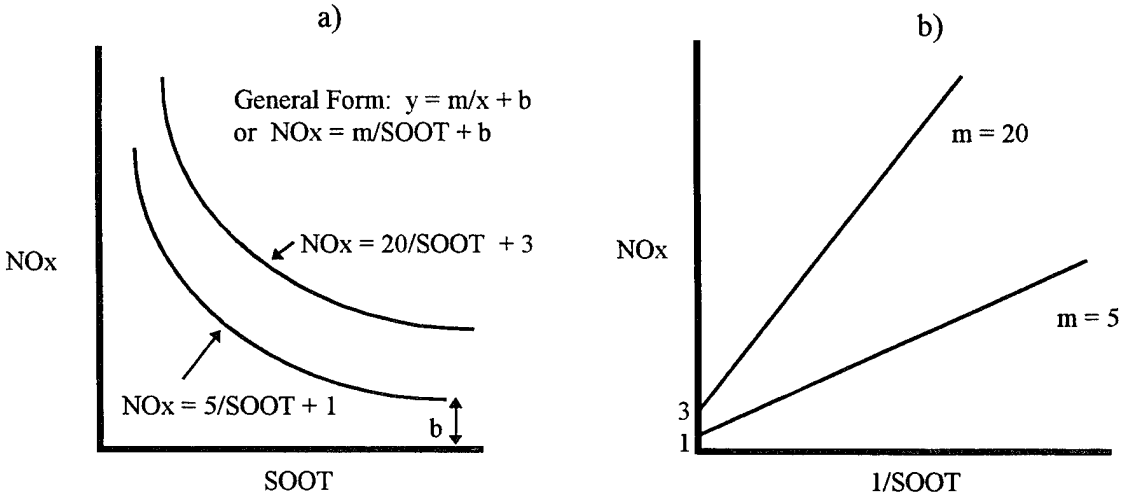

Fig.1 - a) Theoretical NOx/soot tradeoff curve model; b) plotted for straight line variation

Combining the kinetic times in equations 1 and 2 as net values, $\tau_{net,soot}$ and $\tau_{net,no}$, and by the previous argument concerning the equivalence of the mixing times for NOx formation ($\tau_{sl,no}$) and soot oxidation ($\tau_{sl,so}$), the following expression is obtained:

$$EINOx \propto \frac{\tau_{net,soot}\tau_{fi}}{EIsoot \cdot \tau_{net,no}\tau_{sl,no-decomp}} \quad (3)$$

Comparing this form to that of Fig. 1, the differences in slope are attributed to the magnitudes of the various characteristic soot and NOx mixing and kinetic times. Evaluation of these terms was sought as a possible method to collapse the data onto a single line, thus explaining the various NOx/soot tradeoffs.

When the model of Fig. 1 is applied to actual data from two different engines, a straight line fan pattern results as hypothesized (see Fig. 2). The Set B data are from a small HSDI diesel with a high pressure common rail fuel injection system. The CAT data are from experiments conducted on a medium size DI diesel by Tow (1994). Both sets encompass a range of speeds, loads, injection pressures and injection timings. Note the slopes of the CAT datum sets are substantially lower (by a factor of approximately 70) than the Set B values. For the model equation 3 to prove successful it must be able to account for these differences in slope.

As a first step the net kinetic characteristic times were evaluated using global Arrhenius expressions with the stoichiometric flame temperatures evaluated at the peak firing cylinder conditions for each datum point. The overall activation energies for soot and NOx emissions as determined by Plee et al. (1981) were used. Because the data examined did not consist of diluent variations such as N_2 or EGR addition which are known to affect the kinetic aspects of combustion, the difference in slopes could not be explained by the kinetic expressions alone. Additional temperature definitions such as the estimated end of combustion temperature were evaluated as well but could not collapse the data to a single line. Numerous characteristic mixing times which are a function of engine speed, injection pressure, fuel delivery, etc. (see Duffy and Mellor, 1995) were also evaluated. However, these attempts were also unable to explain the differences in slope among the datum sets.

The major factor unaccounted for in the above analyses is the different injection timings of the respective curves. The CAT timings span a range of -14 to +3 degrees (TDC=0) whereas the Set B timings are more retarded and encompass a larger range of -40 to -7 degrees. Since the global characteristic time equations are evaluated at a representative crank angle location (TDC or maximum pressure), they cannot adequately capture the important temporal aspects of the diesel combustion and emissions processes. Furthermore, mixing phenomena such as impingement and swirl lead to combustion and emissions formation/oxidation which vary spatially and temporally. Therefore, a new framework for implementing the characteristic time model equations is being investigated which allows for evaluation of the these aspects of the fuel/air mixing and kinetics.

The present version of MERLIN, the phenomenological diesel cycle simulation code used at Ford, includes a common set of expressions for the time rate of change of the mass of soot formed and oxidized (attributed to Hiroyasu and Kadota, 1976). These equations include terms such as cylinder pressure, mass of unburned fuel vapor, and Arrhenius terms which require a crank angle resolved (temporal) computation. In addition, empirical model constants are required to match the computed and measured emissions levels. The constants are typically adjusted both when operating conditions and engine geometry change.

Temporal and spatial fuel spray development and interaction with the air flow field are computed and thus allows a framework for implementing characteristic time model equations. For example, a soot emissions expression of the form:

$$soot_{NET} = \left.\frac{dSoot}{dt}\right|_{FORM} \times \tau_{sl,sf} - \left.\frac{dSoot}{dt}\right|_{OXID.} \times \tau_{sl,so} \quad (4)$$

may be defined where the formation and oxidation rate terms are Arrhenius expressions using appropriate activation energies, and the τ s describe the turbulent mixing in the formation (spray) region and oxidation region (stoichiometric contour). Cast in this form, the characteristic mixing times may describe the physics behind the previously empirical adjustments of the pre-exponential factors. Potential expressions for the characteristic mixing times are presently being investigated.

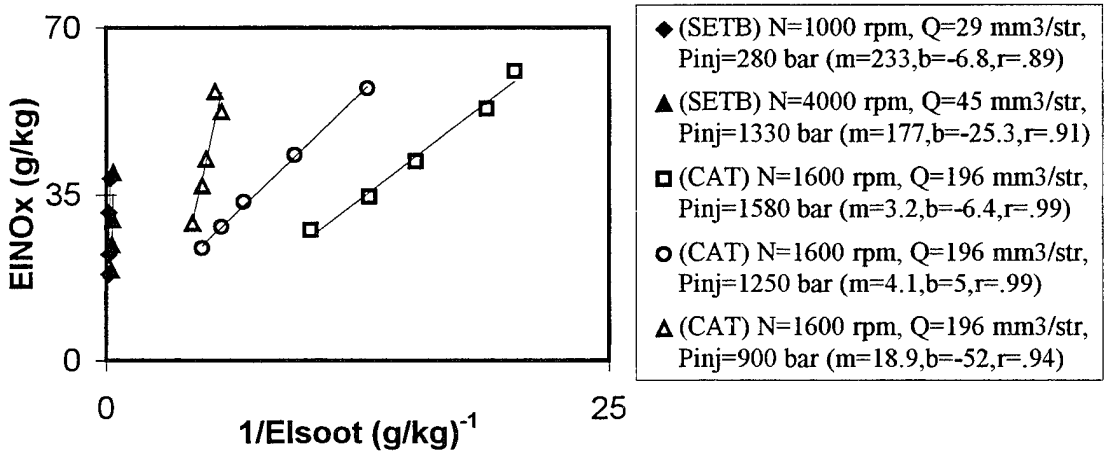

Fig. 2 - EINOx versus 1/EISoot for data from two different engines

REFERENCES

Derr, W.S. and Mellor, A.M. (1990), "Recent developments," Design of Modern Turbine Combustors, Academic Press, London, pp. 474-544.

Dodds, W.J. (1976), "Experimental study of carbon particulate formation in a model turbine combustor," MS Thesis, Purdue University.

Duffy, K.P. and Mellor, A.M. (1995), "Characteristic time model for diesel particulate emissions," Interim Technical Report, US Army Research Office.

Duffy, K.P., Nicols, J.T, Mellor, A.M. and Plee, S.L. (1996), "Flame temperature correlations for effects of EGR in high speed direct injection diesel engines," Proceedings of the 1996 Technical Meeting of the Central States Section of the Combustion Institute.

Hiroyasu, H. and Kadota, T. (1976), "Models for combustion and formation of nitric oxide and soot in direct injection diesel engines," SAE Paper 760129.

Kosaka, H., Nishigaki, T, Kamimoto, T. and Harada, S. (1995), "A study on soot formation and oxidation in an unsteady spray flame via laser induced incandescence and scattering techniques," SAE Paper 952451.

Plee, S.L., Ahmad, T. and Myers, J.P., (1981), "Flame temperature correlation for the effects of exhaust gas recirculation on diesel particulate and NOx emissions," SAE Paper 811195.

Tow, T. (1993), "The effect of multiple pulse injection, injection rate, and injection pressure on particulate and NOx emissions from a DI diesel engine," MS Thesis, University of Wisconsin.

Yu, R. and Shahed, S. (1981), "Effects of injection timing and exhaust gas recirculation on emissions from a DI diesel engine," SAE Paper 811234.

ANALYSIS OF ADVANCED DIRECT-INJECTION DIESEL ENGINE DEVELOPMENT STRATEGIES

(ARO Contract No. DAAH04-95-1-0430)

Principal Investigator: K. T. Rhee

Rutgers, The State University of New Jersey
Mechanical and Aerospace Engineering Department
Brett and Bowser Roads
Piscataway, NJ 08855-0909

SUMMARY/OVERVIEW:

In-cylinder reactions are studied from a direct-injecton Diesel engine with optical access by using the Rutgers High-speed Spectral Infrared Imaging System when the engine is incorporated with some advanced engine strategies. Measurements are made in order to help achieve a high power-density Diesel engine with low soot-emission. The main events being studied include: preflame reactions; flame propagations; formation of combustion products (water vapor and soot); and temperature distribution. To date, some new findings were obtained on effects of high-pressure fuel injection, fuel formulation, and additives.

TECHNICAL DISCUSSION:

In recent years, some significant progress has been made in two main areas: (1) the Rutgers High-speed Spectral IR Imaging System has been further improved and (2) a new spectral analysis method is being developed for achieving quantitative imaging, i.e., the three-band-method.

The Rutgers System, which was made operational about two years ago, produces images with better quality than ever offering greater opportunities for not only maximizing information out of the raw data but also analyzing the effects of various engine and fuel variables, as mentioned above.

Retgarding the three-band method, the basic idea is to solve three simultaneous equations in order to determine three unknowns, i.e., distributions of temperature, water vapor and soot (κL). The governing equation for this method is an extension of Beer's law. They include an emissivity term which is defined in terms of spectral intensity (at individual pixels) measured by the Rutgers System and Plank's equation, and extinction coefficients which are calculated by using experimental values tabulated in NASA Handbook of Infrared Radiation. Due to the complexity of the problem, the solutions for the simultaneous equations require a new iteration method.

These research methods (being developed in collaboration with other sponsors) are also employed for investigation of SI engine combustion processes.

Briefly, the basic idea of the Rutgers System shown below is to capture four geometrically (pixel-to-pixel) identical images in respective spectral bands at successive instants of time. Note that sine they were not commercially available items indicated in outlined font were all newly designed and fabricated at Rutgers Internal Combustion Engines Laboratory.

The following page includes: a spectral diagram generated by using our data-based spectrometric program which facilitates discussion of spectral imaging, and representation of three new spectrometric methods being developed under the present ARO sponsorship in order to process the raw data obtained by the Rutgers System.

Displayed in the last page are: a set of two spectral IR images obtained of in-cylinder reactions in an SI engine which reveal some new information (e.g. preflame reactions and reactions around liquid fuel layers) which is difficult to find by the conventional methods; four-color instantaneous successive images obtained from a reacting spray plume in a DI-CI engine equipped with an electronic-controlled high-pressure fuel injection system; and some of results achieved by the Rutgers three-band method.

(A)

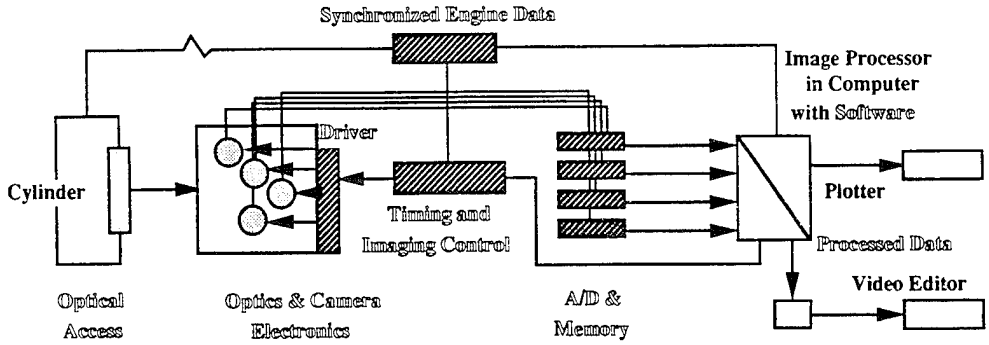

(B)

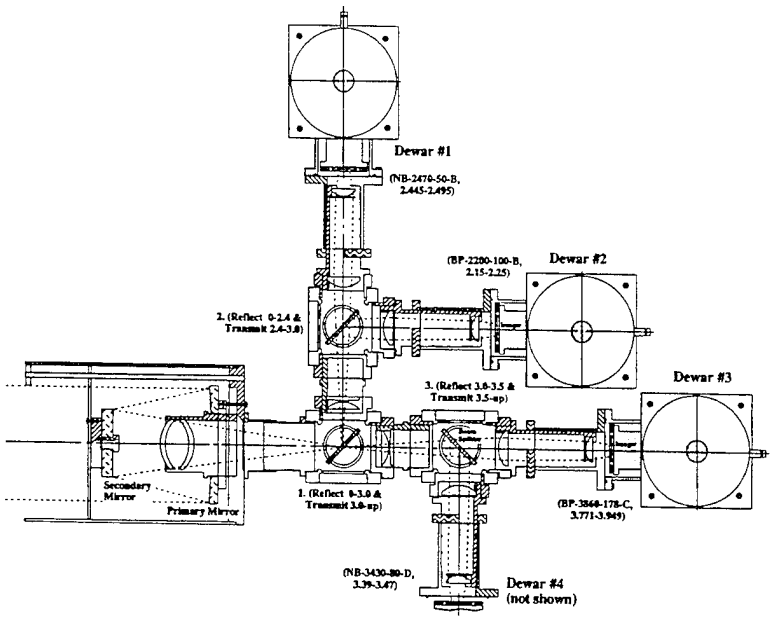

Schematics of Rutgers System or SIS: (A) Total System and (B) Optics and Cameras.

(A)

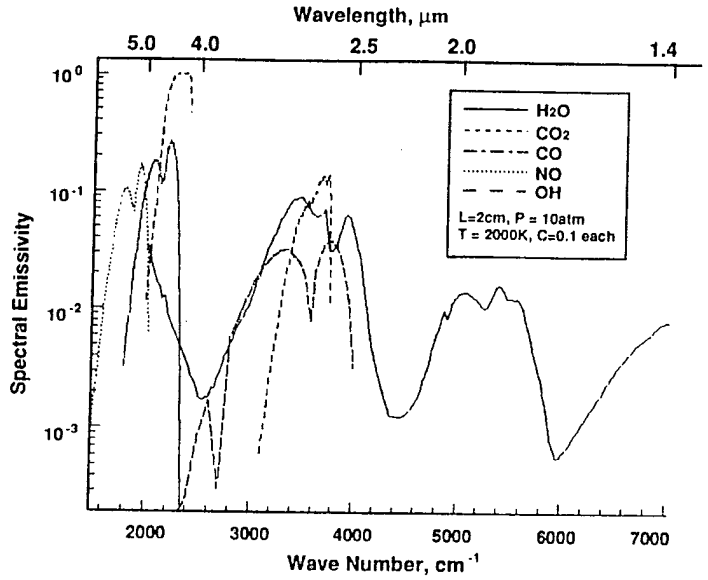

(C)

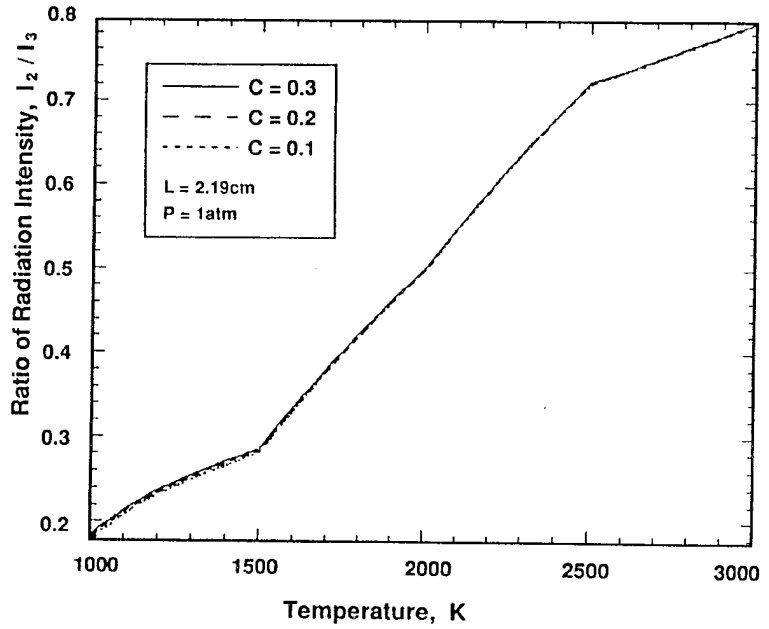

(B)

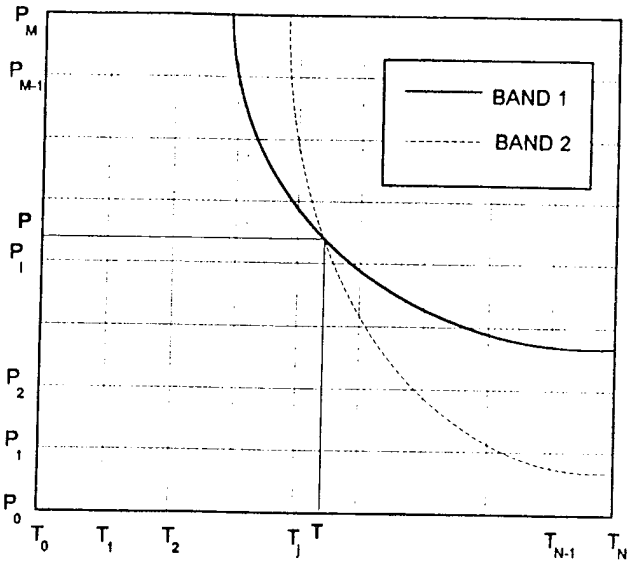

(D)

Rutgers
Three-Band Method

Basic Idea: Three (3) Relationships from Rutgers' SIS to find three (3) Unknowns: Soot; Water Vapor; and Temperature

Governing Equations:

From Beer's Law, $\varepsilon_{\lambda T} = 1 - \exp(-\chi_{\lambda S} - \chi_{\lambda H})$, and $\chi_{\lambda S} = \kappa L / \lambda^{\alpha}$,

We obtain, $\kappa L = -\lambda^{\alpha} \ln(1 - \varepsilon_{\lambda T}) - \lambda^{\alpha} \chi_{\lambda H}$

where, λ = 2.47, 3.43 (or 2.2), and 3.8μm;

$\chi_{\lambda S}$ and $\chi_{\lambda H}$ are determined using SLG Model and NASA IR Handbook; and

$\varepsilon_{\lambda T}$ is expressed in terms of measurements and Plank's equation.

(A) Spectrodiagram; (B) Dual-band Method; (C) Band Ratio Method; (D) Three-band Method.

(A)

(B)

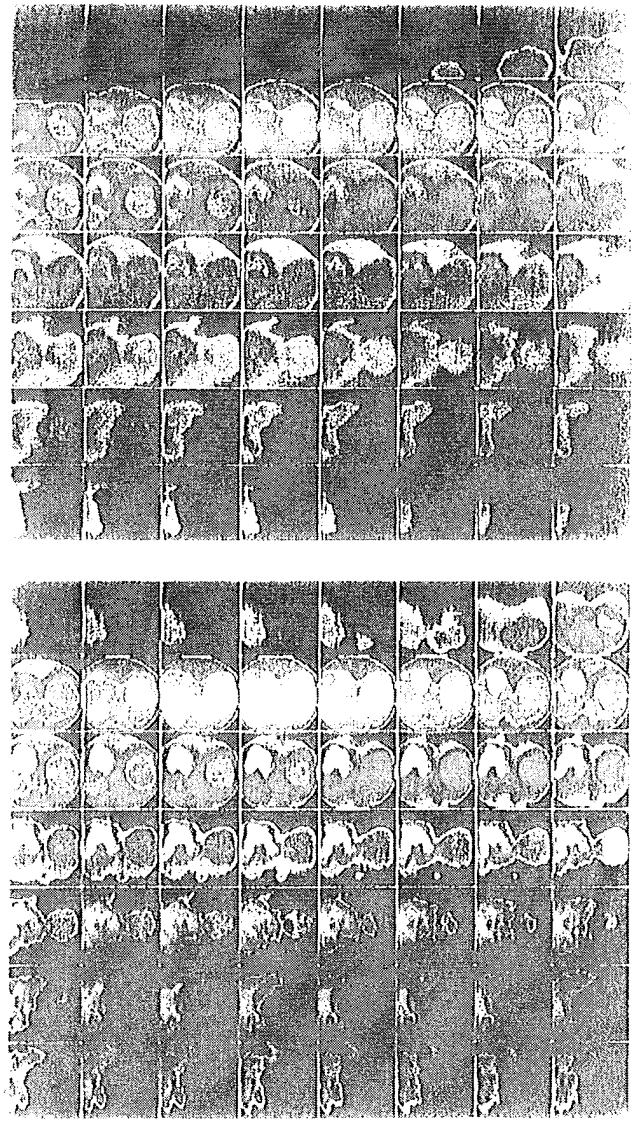

High-speed Spectral IR Images of In-cylinder Events in a Gasoline-operated SI engine under Relatively Warm Condition: (A) 2.47mm and (B) 3.43mm.

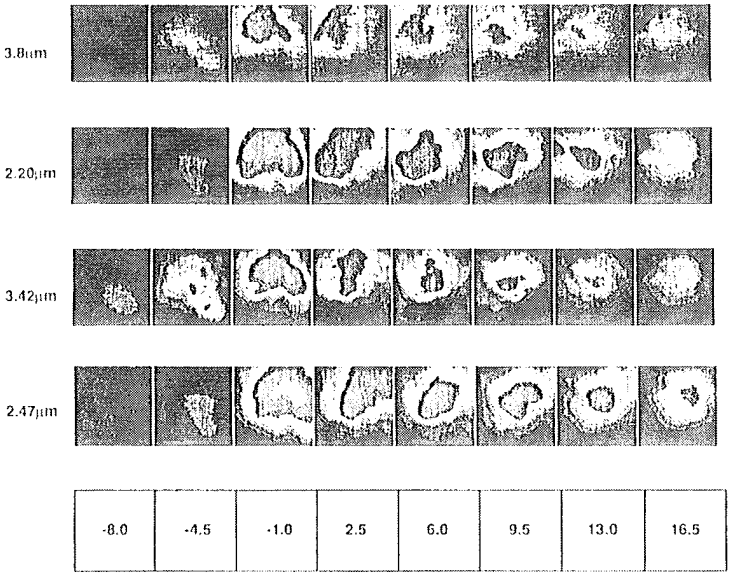

Injection at -9.0 bTDC
Spray Directed from low right corner to upper left end

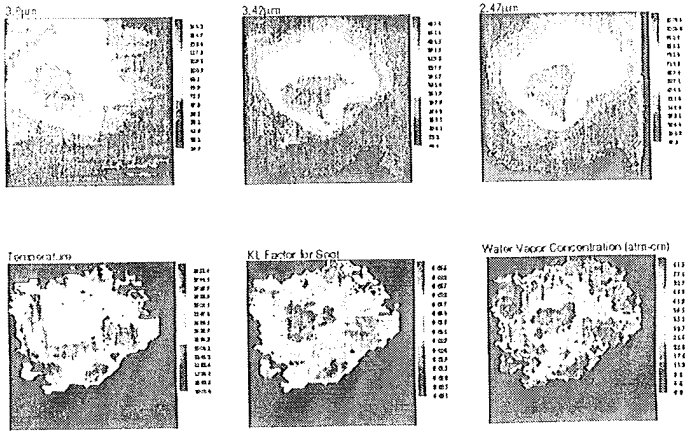

Determination of Soot and Water Vapor Formation and Temperature Distribution by Three-band Method. Spectral Plume Images Obtained at 9.5ATDC were used.

ADVANCED DIAGNOSTICS FOR REACTING FLOWS

AFOSR 95-1-0041

Principal Investigator: Ronald K. Hanson

High Temperature Gasdynamics Laboratory
Mechanical Engineering Department
Stanford University, Stanford, CA

SUMMARY/OVERVIEW

This research is aimed at establishing laser-based absorption and fluorescence techniques for nonintrusive measurements in combustion gases and plasmas, with emphasis on high speed, high temperature, and high pressure flowfields.

TECHNICAL DISCUSSION

Primary activities are highlighted below. Related publications are cited at the end.

Diagnostics for Combustion Sensing/Control

Over the past few years we have made significant progress in the development of multiplexed diode-laser sensors. A multiplexed sensor system, composed of multiple diode laser sources, enables monitoring of absorption at several wavelengths, thereby allowing simultaneous determination of multiple gasdynamic parameters and/or species concentrations. These measurements can be made remotely and at multiple measurement locations through use of fiberoptics. Figure 1 illustrates possible applications to a gas turbine engine. Accomplishments have included air mass flux sensing in a supersonic stream by O_2 aborption, measurement of momentum flux (thrust) in a high-speed combustion flow via H_2O detection, and simultaneous monitoring of H_2O, O_2 (or CH_4), and temperature in a benchtop combustor.

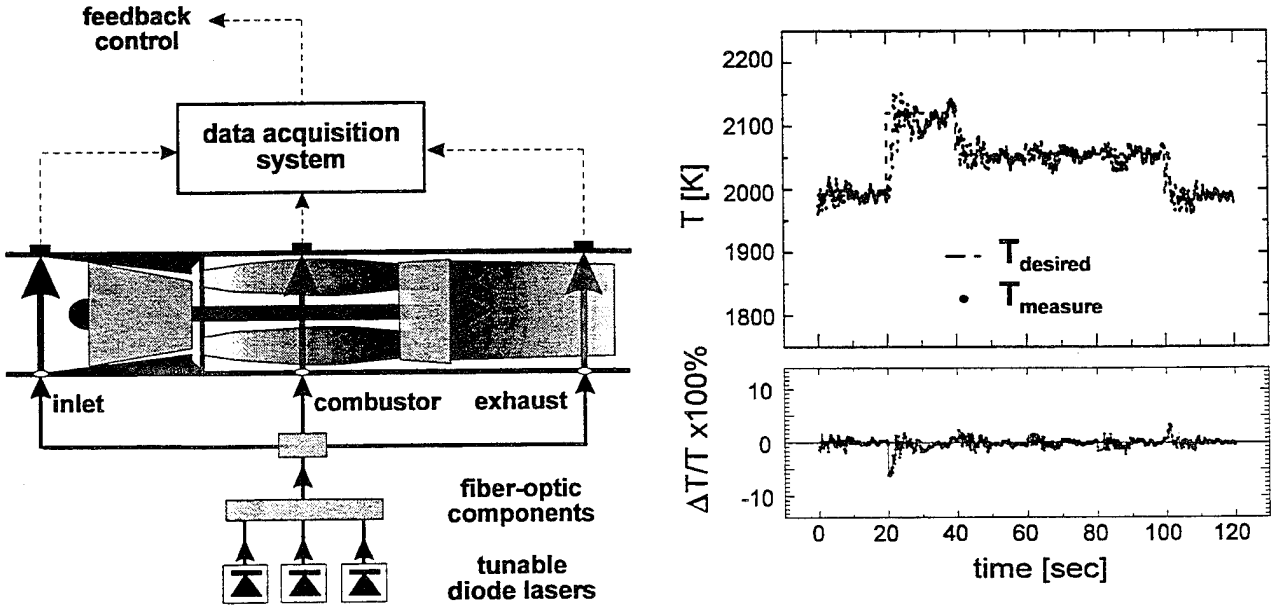

Fig. 1 Left panel: Proposed sensor system for a gas turbine combustor; Right panel: Comparison of measured and set-point temperatures with control system in operation.

In the past year we focussed on sensing temperature for use in fast-response, closed-loop combustion control. The experiments were conducted using a Hencken burner, operating on methane and air at atmospheric pressure. Temperature was sensed along a line in the post-combustion zone from the ratio of absorption at two wavelengths (1.34 and 1.39 microns) in combination vibrational bands of H_2O. The intensity data was processed by computer to yield the measured temperature, and this temperature was compared with the set-point temperature to calculate a correction to the fuel flow which would recover the desired temperature. The time required for the measurement and data processing to produce the correction signal was less than 2 milliseconds. An example result, showing the ability to maintain a programmed temperature sequence, is shown in Fig. 1. The residual difference in temperature (righthand panel) is typically less than 2%.

Diode laser absorption sensors have high potential for application in ground- and flight-based systems. Work is in progress to monitor additional species including methane, hydrazine, nitric oxide, carbon monoxide and NO_2.

Diagnostics for High-Pressure Gases

Progress has been made on two projects to develop high-pressure laser diagnostics. The first program, an extension of work conducted for NASA-Lewis, is aimed at PLIF measurements of NO and O_2 in the post-flame region of a high-pressure, lean-burning combustor. The problem to be resolved is that the spectra of NO and O_2 are highly overlapped in the spectral region (near 225 nm) best suited for measuring low levels of NO, a problem seriously exacerbated by collision broadening of the NO and O_2 spectral features at the pressures of interest (10-50 atm) and the fact that the concentrations of NO (10-100 ppm) are much smaller than the O_2 concentrations (10%). We have assembled a computer code incorporating the latest information on line positions, strengths and shapes (including pressure shifts), and have used this code to simulate absorption and fluorescence spectra for a variety of excitation and detection strategies. One attractive approach involves detection of the PLIF signal in two (or three) spectral channels following excitation at a single wavelength. Our simulations indicate that this approach can allow simultaneous monitoring of NO, O_2 and temperature. Experiments are planned to verify these simulations.

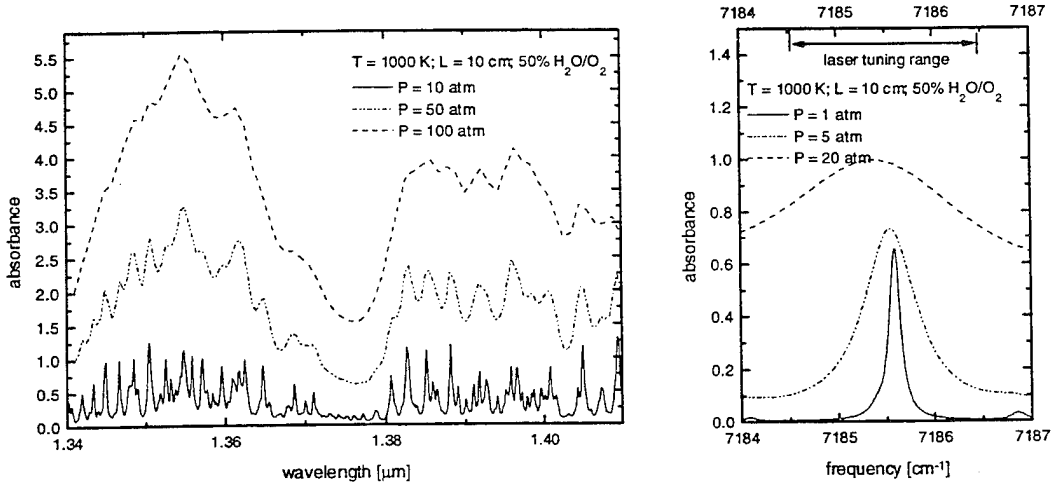

Fig. 2. Calculated absorbance [$\ln(I/I_0)$] for combination bands of H_2O at various pressures.

The second diagnostic activity is aimed at monitoring H_2O and temperature at high pressures using diode laser absorption. Example calculations of H_2O spectra for representative conditions of interest are shown in Fig. 2. The lefthand panel indicates the influence of pressure over a broad spectral region encompassing the combination bands used in our past measurements of H_2O; the righthand panel shows the effects of pressure over a narrower spectral region encompassing a single prominent feature. Note that at pressures above 1 atm there are no longer any gaps in absorption between features. This invalidates our past strategy of wavelength tuning to establish the reference (non-absorbed) laser intensity. For high pressures we propose to use a strategy

which utilizes multiplexed diode laser sources. In this approach, multiple excitation wavelengths will be used, and these will be selected from computer simulations of the type shown in Fig. 2. As an example, two wavelengths will be selected to infer temperature (from the ratio of absorption) and one non-absorbed wavelength will be selected as a means of tracking changes in the reference intensities. Current work is aimed at developing and validating spectroscopic models of H_2O through experiments in heated static cells and a shock tube to produce a range of temperatures and pressures.

Plasma Diagnostics

Work continued on development of a diagnostic technique for xenon plasmas based on spectrally resolved laser-induced fluorescence of electronically excited states. Studies were conducted in a low pressure discharge of xenon and, quite recently, in an ion thruster. The initial low-pressure-discharge experiments involved probing two 6s-6p transitions: one at 823 nm involving a metastable lower state, resulting in a lineshape dominated by Doppler broadening; and a second transition at 828 nm dominated by resonance broadening. Use of a tunable diode laser source enabled spectrally-resolved recording of the lineshapes for these transitions, and these lineshapes were used to infer both temperature (from the 823 nm transition) and pressure (from the 828 nm transition). It was necessary to account for the complex nature of the lines resulting from multiple isotopes and complex hyperfine splitting. This diagnostic approach, combining lines with Doppler and resonance broadening, has good potential for nonintrusive measurements of kinetic temperature and pressure in low pressure plasmas.

The second and most recent experiment is being conducted in the plasma thruster recently fabricated by Prof. Cappelli's research group (under AFOSR support). Measurements involve excitation of neutral xenon, using the 823 nm transition, in the exit plane of the thruster. The data acquired enable determination of the xenon temperature (from the shape of the line) and velocity (from the Doppler shift), which provide critical information on the energy transfer which occurs between neutral and ionized xenon in the acceleration process. Future experiments in this collaboration with Prof. Cappelli's group will involve LIF measurements of ionized xenon, from which we hope to measure both exit velocity and ion temperature.

Frequency-doubled Diode Laser Diagnostic

The wavelength availability of diode lasers has been limited to specific spectral windows in the overall range 650 nm to 1.6 microns. Fortunately, a number of groups are working to extend the range and to improve availability at intermediate wavelengths. We have collaborated with the Applied Physics Department at Stanford to access a prototype laser system which yields tunable output at 394.5 nm from frequency-doubling of a high power diode laser operating near 790 nm. This new laser source enables detection of several species which could not be accessed by previous diode laser systems. Figure 3 (lefthand panel) provides a room temperature absorption spectrum of NO_2, from which it is clear that there is a large potential gain in sensitivity using detection at 395 nm rather than, say, 670 nm, which is the shortest wavelength at which we have been able to obtain sustained, single-mode output using commercially available tunable diode lasers. We conducted a study of the absorption spectra of NO_2, using both laser sources, as a function of temperature and pressure. A summary of the results is shown in the righthand panel of Fig. 3. Note that the absorption coefficient at 394.5 nm ranges from about 30 to 50 times that at 670 nm, enabling detection of ppm levels of NO_2 over pathlengths of 10 cm.

PLIF of Acetone for Temperature Imaging

Acetone has proved to be an attractive tracer species for application of PLIF, largely because the method is both simple to implement and yields large signal intensities. However, most experience with acetone has been limited to moderate temperatures, near room temperature. Other investigators have raised questions about temperature and pressure dependencies of acetone PLIF, and this led us to initiate research aimed at characterizing these effects and, subsequently, at

exploiting our findings to develop a new scheme for imaging temperature. During the past year we completed experiments in which the absorption coefficient, fluorescence yield, and fluorescence spectrum have been characterized over a range of excitation wavelengths (from 248 nm to 320 nm) and as a function of temperature. These data have been used to predict and optimize the performance of a dual-excitation-wavelength, dual-camera scheme for PLIF thermometry. Work is currently in progress to validate and demonstrate this PLIF diagnostic which has high potential as a relatively simple yet powerful method for accurate temperature imaging,

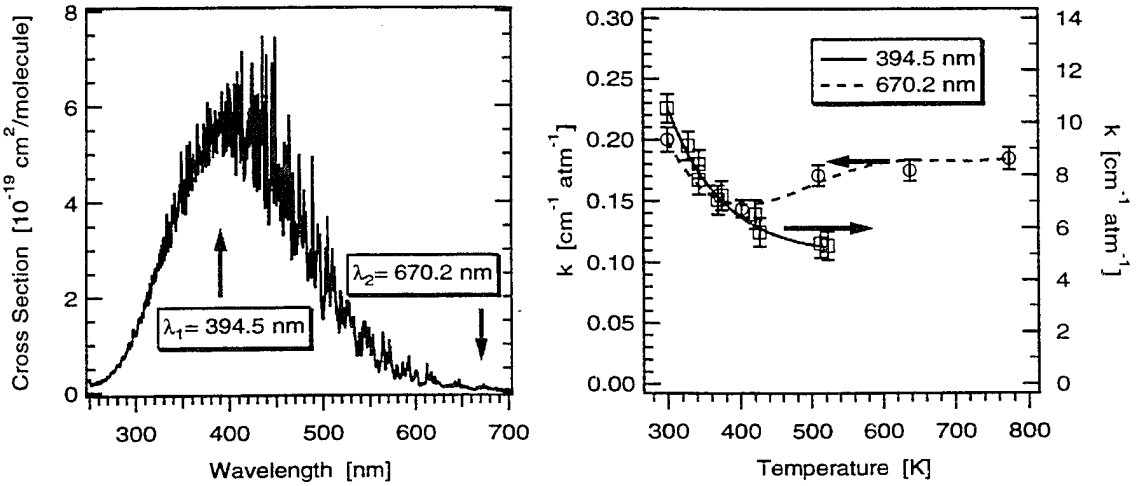

Fig. 3. Left panel: Room temperature absorption spectra of NO_2. Right panel: Absorption coefficients as function of temperature.

PUBLICATIONS/PRESENTATIONS

R. M. Mihalcea, D. S. Baer and R. K. Hanson, "NO_2 Measurements Using Diode-Laser Absorption Spectroscopy, paper AIAA-96-0173 at the 34th Aerospace Sciences Meeting/Aerodynamic Measurement Technology, Reno, Jan. 1996.

C. Morris, M. Kamel and R. K. Hanson, "NO PLIF Imaging of Supersonic Reactive Flows Around Projectiles in an Expansion Tube," paper AIAA-96-0855 at the 34th Aerospace Sciences Meeting, Reno, Jan. 1996.

J. L. Palmer and R. K. Hanson, 'Temperature Imaging in a Supersonic Free Jet of Combustion Gases using Two-Line OH Fluorescence," App. Optics **35**, 405-499 (1996).

F. Grisch, M. Thurber and R. K. Hanson, "Temperature Measurement by Acetone LIF with Dual-Wavelength Excitation," WSS/CI paper 95F-192, Stanford, CA, Oct. 30-31, 1995.

R. J. Cedolin, R. K. Hanson and M. A. Cappelli, "Laser-Induced Fluorescence Measurements of Resonance Broadening in Xenon," Phys. Rev. A, in press.

V. Nagali, S.-I. Chou, D. S. Baer and R. K. Hanson, "Tunable Diode Laser Absorption Measurements of Combustion Products at Elevated Pressures," 19th AIAA Advanced Measurement and Ground Testing Conf., New Orleans, June 17-20, 1996.

E. R. Furlong, D. S. Baer and R. K. Hanson, "Combustion Control and Monitoring using a Multiplexed Diode-Laser Sensor System," 26th Combustion Symposium, July 1996.

TITLE: RESONANT HOLOGRAPHIC INTERFEROMETRY: AN INNOVATIVE COMBUSTION DIAGNOSTICS

Contract No. DAAL03-92-C-0019

Principal Investigator: Peter A. DeBarber

MetroLaser, Inc.
18006 Skypark Circle, Suite 108
Irvine, CA 92714

SUMMARY/OVERVIEW:

During the past three years, MetroLaser embarked on theoretical and experimental efforts to develop new optical diagnostics applied to combustion research. Our particular program with the ARO focused on the development of an entirely new diagnostic technology called Resonant Holographic Interferometry (RHI). RHI has shown the potential to circumvent certain problems plaguing more conventional approaches namely, quenching, absorption, and high background luminosity. Since most chemical species of importance in combustion exhibit absorptions in the visible, ultraviolet (UV), or near infrared (IR) wavelength regions, our development efforts explored RHI applications in each of these areas.

TECHNICAL DISCUSSION

RHI is a laser-based diagnostic which combines the three-dimensional imaging capability of holography, the phase sensitive detection of interferometry, and the species specificity of resonance spectroscopy to form a powerful, versatile diagnostic package. RHI provides researchers a method of obtaining nonintrusive measurements in environments that are characterized by a high degree of scattering, luminosity, and/or optical density. This is accomplished by recording two simultaneous holograms at two different laser wavelengths: one tuned near an absorption line, and the other tuned off this feature. Upon reconstruction, the resulting interference fringes correspond uniquely to the density of the species under interrogation because phase contributions from background species, thermal and pressure instabilities, and optical aberrations are automatically subtracted out.

The ability to distinguish individual species is important for many diagnostics applied to combustion environments. Conventional holographic interferometry measures the total non-resonant phase contributions from all species present, which are inseparable from each other as well as the temperature and pressure gradients present. However, with RHI, the observation of minor combustion species in the presence of major background species and large temperature and pressure gradients is possible because of the large variation in the index-of-refraction near an absorption resonance. Thus, by utilizing the resonant refraction with the background subtraction inherent to holographic interferometry, RHI becomes a valuable species-specific combustion diagnostic.

Visible

We began our examination of RHI applications in the visible spectral region. For this study we probed three different environments. In increasing order of complexity, we made RHI measurements of I_2 in a heated sample cell, Na in a seeded methane - air flame, and C_2 in an arcjet torch reactor.

In an effort to produce quantitative RHI results, an experiment was set up utilizing a wedge-shaped static test cell. Iodine was placed in the test cell which was then inserted into a tube furnace to provide precise control of the vapor pressure, and thus the amount of I_2 in the gas phase. For constant volume conditions, the vapor pressure is directly proportional to the temperature of the cell and therefore, a precise amount of I_2 may be introduced into the object path of the RHI instrument. The wedge shape of the test cell provided a known pathlength variation over the field-of-view.

In Figure 1 we show the qualitative results for the I_2 experiment. The results are not quantitative due to poor reproducibility. The difficulty resulted from multiple longitudinal mode effects caused by dye laser cavity

instability. The multi-mode behavior adversely affected laser linewidth, and hence our ability to consistently generate data sets with consistent fringe shifts. Subsequent experiments in the UV and near IR spectral regions used a more stable dye laser, and therefore, the dye laser cavity instabilities were less of a problem.

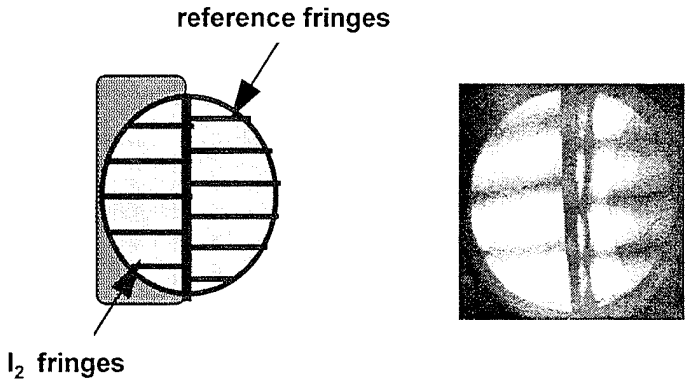

Figure 1. RHI interferogram of I_2 in a static test cell.

The first successful combustion RHI experiments were carried out in the flame of a CH_4-air diffusion burner. This experiment was designed to unequivocally demonstrate the RHI effect. High quality, Na RHI interferograms were recorded in this flame environment. Demonstrations of the RHI technique in a Na-seeded and unseeded CH_4-air flame are presented below. Figure 2 illustrates the geometry of the flame, imaged area, and flowfield seeding method.

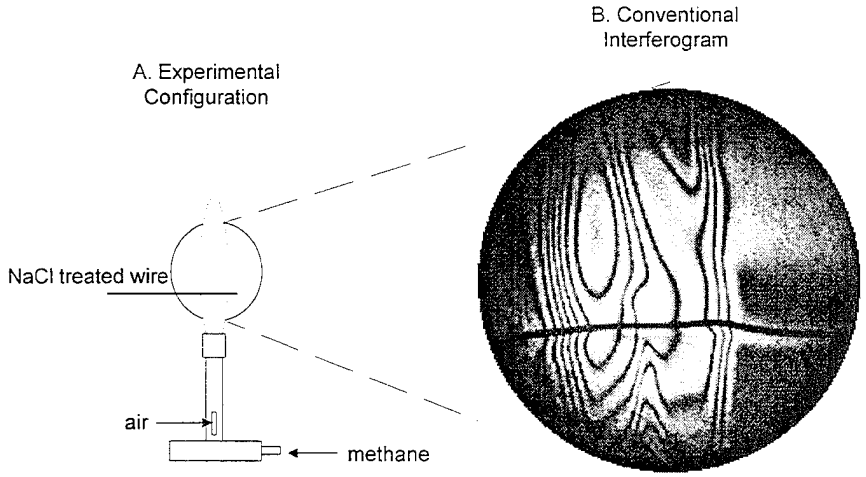

Figure 2. (a) Experimental configuration. (b) Conventional holographic interferogram.

In the configuration shown in Figure 2a, a CH_4-air burner was seeded with Na by introduction of a pre-treated wire approximately one third of the way into the flame. This configuration generates both seeded and unseeded flame regions which are recorded in a single image. The wire had been pre-treated by immersion in saltwater. Na^+ ions from the treated wire entered the hot combustion gases through vaporization and ablation and were rapidly neutralized by free electrons in the flame, resulting in the formation of Na atoms. The strongest Na atomic line D_2 (j=3/2) was used for probing at approximately 589.015 nm. An intense yellow-orange emission was clearly visible by eye in the Na-seeded portion of the flame above the screen. In the unseeded portion of the flame below the wire, the only emission visible by eye was blue.

Figure 2b shows a reconstruction of a conventional holographic interferogram. In this case, a single laser beam (tuned to 588.972 nm, a wavelength which is well off the D-line resonance) was used to double expose the holographic plate at two instances in time. The first exposure was taken with the flame on. The second exposure was taken with the flame off. The resultant fringe pattern shows the combined effects of variations in bulk density, temperature, and pressure associated with all the species present in the flame.

In contrast to this conventional hologram, Figure 3a shows a single exposure holographic interferogram with the flame on, taken with two simultaneous laser pulses of the same wavelength (both tuned off resonance to 588.972 nm). This demonstrates that phase variations due to temporal fluctuations and bulk density gradients are completely subtracted out in the holographic reconstruction process.

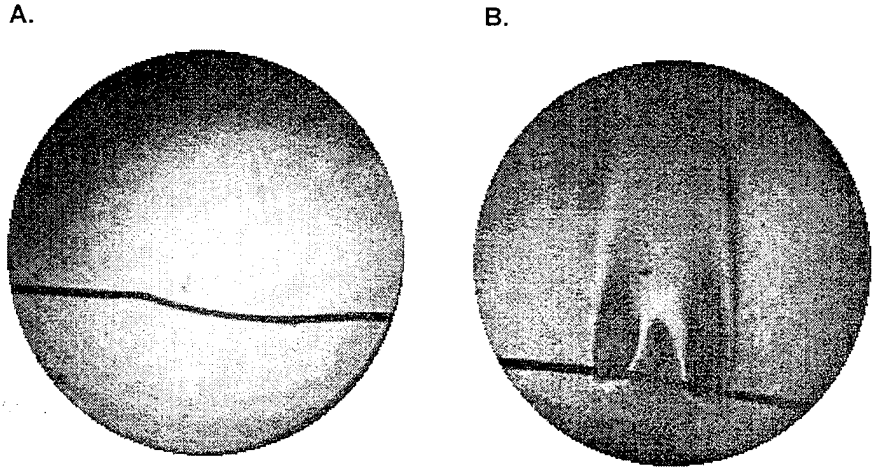

Figure 3. (a) Two-wavelength off-resonance interferogram of flame demonstrating total background subtraction inherent to holographic reconstruction. (b) RHI interferogram of Na seeded into a CH_4-air diffusion burner flame.

Figure 3b is a RHI interferogram of the Na target species in the flame. The two lasers were tuned symmetrically to either side of the Na D_2 line (589.009 nm and 589.021 nm). The fringes are due solely to the Na variation in the flame. In the lower part of the flame below the wire and upstream of the Na seeding, there are no fringes present due to the absence of Na and the complete subtraction of the background refractive index variations. Because of the high concentration of Na atoms in the seeded portion of the hot inner cone of the flame, regions of total absorption are evident. These results provide information regarding both the minimum detectable concentration for a given path length and molecular species, and the range of concentration values that can be detected in a single hologram.

Attempts at obtaining RHI interferograms of diatomic carbon in an arcjet torch were unsuccessful. An arcjet torch running on a 10 to 20 torr mixture of Ar, H_2, and CH_4, was probed by the RHI instrument. The RHI lasers were tuned in the vicinity of the bandhead near 516 nm. Our goal was to resolve the spatial distribution of C_2 in the high temperature plasma. Initial estimates of the C_2 number density in the plasma indicated that RHI would have the necessary sensitivity for its detection; however, since no RHI fringe shifts were detected, we were not able to verify these predictions. We concluded that the low pressure arcjet environment does not have appreciable C_2 number densities for detection by single-pass RHI methods.

Ultraviolet (UV)

Since many important combustion species exhibit absorptions in the UV spectral region, we reconfigured the RHI breadboard for examinations at these shorter wavelengths. We chose the hydroxyl radical as the target species for the UV investigations for several reasons. Hydroxyl is an important combustion intermediate that is often used for thermometry, it is useful for marking the reaction zone, and its spectroscopy is well known. The environment we chose was the methane - air diffusion flame produced from a laboratory slot burner.

RHI interferograms were recorded for species naturally occurring in flames. Figure 4 shows a reconstructed interferogram of OH radicals in a CH_4-air diffusion flame. For this work, the RHI lasers were tuned in the vicinity of the bandhead near 308 nm. The single dark fringe visible in Figure 4 uniquely corresponds to the location of OH in the post flame gases and is an indicator of OH number densities on the order of 10^{15} cm^{-3}. This result agrees well with our theoretical estimates and observations reported by others.

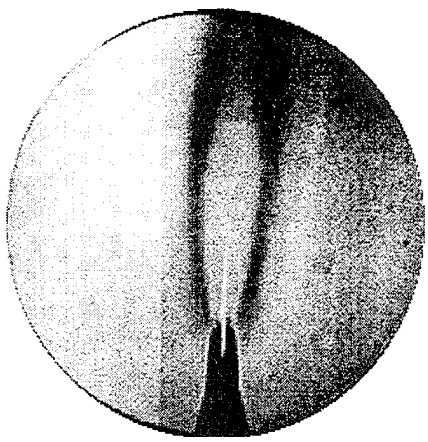

Figure 4. RHI interferogram of OH in methane-air diffusion flame.

Near Infrared (near IR)

One of the primary attractions for examining RHI applications in the near IR spectral region is the potential use of inexpensive, compact laser diodes. In order to examine RHI applications in the near IR spectral region, we substantially modified the RHI holocamera to accommodate photorefractive recording media. Several important benefits are gained by using photorefractives for the RHI holographic recording medium. Photorefractives allow real-time writing, reading, and erasing capability. The ability to collect and process the data in real-time facilitates experimental alignment. Photorefractives are also less susceptible to fogging from incoherent background radiation.

For our RHI examination in the near IR, we doped fuel (methanol) with potassium (KCl). The potassium was used to mark the flame front boundary of the combusting fuel droplet. Demonstration RHI experiments using novel photorefractive materials were performed. New photorefractive crystals make it possible to not only generate RHI interferograms in the near IR spectral region, but to generate them at video framing rates (30 Hz). As one example of this work, Figure 5 shows a single frame of an RHI interferogram of a KCl-seeded methanol droplet undergoing combustion. The droplet was suspended on the end of a fine wire and ignited. The RHI lasers were tuned near 766 nm. When potassium ions are released from the methanol, they become neutralized by free electrons in the flame front reaction zone. The neutral potassium atoms are a clear marker for the flame front. The fringes due to potassium in the flame were traced manually and digitized. The integrated number density is calculated and displayed to the right of the image.

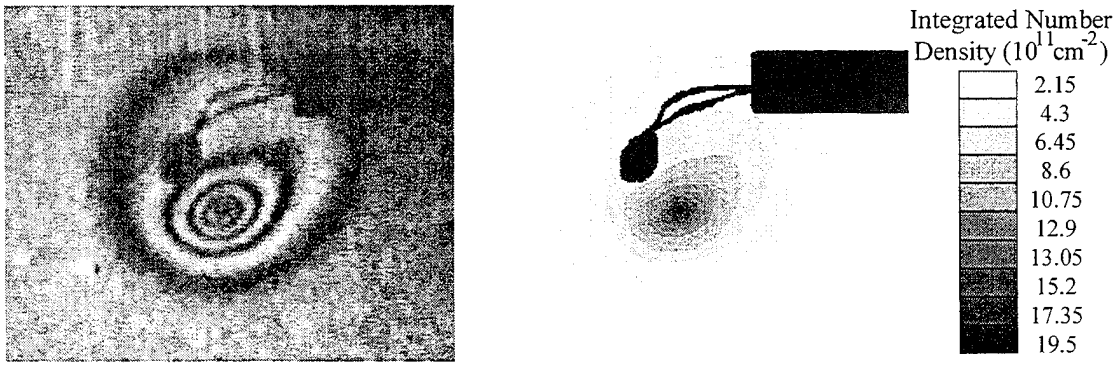

Figure 5. Real-time RHI of potassium seeded combusting 1 mm methanol drop.

NONLINEAR SPECTROSCOPY OF MULTICOMPONENT DROPLETS

(AFOSR Grant No. 94-1-0135)

Co-Principal Investigator: Richard K. Chang

Yale University
Department of Applied Physics and Center for Laser Diagnostics
New Haven, Connecticut 06520-8284

SUMMARY/OVERVIEW

One of the key objectives of this research is to extract from the nonlinear optical spectra, information pertaining to the species in a multicomponent fuel droplet, evaporation rate of closely spaced flowing droplets, droplet shape deformations, and droplet temperature. In the past, we have demonstrated that nonintrusive in-situ optical diagnostics techniques have the potential to determine the chemical species, physical properties (size and shape), and temperature of multicomponent liquid droplets in a spray combustion. During the past two years, we have been developing a technique which might be used to deduce the droplet temperature based on the wavelength shift of lasing droplets as their temperature is changed. The three main research results during the past year are: (1) the observation of temperature-dependent wavelength shifts of the dye lasing spectra with a thermochromic additive;[1] (2) the inability to use photon resident time measurement (cavity-ring-down time) to directly measure the absorption coefficient of a thermochromic absorber; and (3) the demonstration that enhanced signal of stimulated Raman scattering (SRS) of minority species can be achieved by externally seeding the droplet at the Raman-shifted wavelength.

TECHNICAL DISCUSSION

The spherical liquid-air interface of a droplet, with radius **a** much larger than the wavelength, acts as an optical cavity. The normal modes of a dielectric sphere are referred to as morphology-dependent resonances (MDRs), which occur at discrete size parameters $x_{n,\ell} = 2\pi\mathbf{a}/\lambda_{n,\ell}$, where $(\lambda_{n,\ell})$'s are discrete wavelengths, which depends on the droplet radius **a**, index of refraction of the liquid, and on the droplet shape. The index n designates the MDR mode number, which is equal to 1/2 of the number of intensity maxima around the equatorial plane. The index ℓ designates the MDR radial mode order, which is the number of angle-averaged intensity maxima along the radial direction. For a perfect sphere, a MDR at $x_{n,\ell}$ is (2n + 1) degenerate, i.e., the frequency of this MDR is independent of the azimuthal mode number m, which can assume values $\pm n, \pm(n - 1),...., 0$.

Temperature determination

We have observed that the lasing spectrum of droplets shifts toward the blue as the absorption loss within the droplet increases, e.g. by increasing the concentration of a *temperature-independent* black dye (Nigrosin).[2] The lasing threshold is achieved when the round-trip loss is just overcome by the total round-trip gain, which increases toward the blue. Similar blue shift is observed when a *temperature-dependent* absorber (thermochromic absorber, such as $CoCl_2 \cdot 6H_2O$ salt)[1] is added to the droplet. By calibrating the absorption coefficient of the thermochromic absorber as a function of temperature and by measuring the lasing spectrum at room temperature, we are now able to deduce the droplet temperature (far above and slightly below room temperature) from the wavelength shifts of the lasing spectrum.[1]

During the past year we have attempted, but failed, to determine directly the *temperature-dependent* absorption by a time decay technique, known as "cavity ring down".[3] This technique is known to be highly sensitive to small amounts of absorption within the high-Q factor cavity.[3,4] Because our droplets act as high-Q factor cavities ($Q \approx 10^6$ -10^8), we attempted to deduce directly the thermochromic absorber loss by measuring the decay time of the dye-lasing photons resident in the droplet (τ_{photon}). The absorption coefficient $\alpha = [m(\omega)/c\tau_{photon}]$, where $c/m(\omega)$ is the speed of light in the liquid and $m(\omega)$ is the index of refraction of the liquid. The total loss of photons within the droplet cavity is the summation of all the loss processes and can be expressed as an effective absorption coefficient at the dye-laser wavelength in the following manner:

$$\alpha_{total} = \alpha_{leakage} + \alpha_{abs}(\lambda,T) + \alpha_{abs}(\lambda) + \alpha_{NL}$$

where $\alpha_{leakage}$ is the leakage loss out of the droplet, $\alpha_{abs}(\lambda,T)$ is the absorption coefficient of the thermochromic absorber at the dye-lasing wavelength, $\alpha_{abs}(\lambda)$ is the absorption coefficient of the lasing dye itself, and α_{NL} is the loss of lasing photon associated with nonlinear processes, such as conversion of the dye-lasing photons to stimulated Raman scattering photons. This depletion of the dye-lasing photons become significant when the lasing intensity within the droplet is high. We have found that it is difficult to limit the dye-lasing intensity such that $\alpha_{NL} << \alpha_{abs}(\lambda,T)$. In other words, the τ_{photon} is limited by unavoidable photon loss to nonlinear conversion rather than by the desirable photon loss associated with the thermochromic absorber. We will continue to find ways to measure the droplet temperature by an all-optical technique, be it through lasing wavelength shifts or changes in τ_{photon}.

Species determination

Stimulated Raman scattering (SRS) is amplified spontaneous Raman scattering, where the amplification is provided by the four-wave mixing process involving the Raman gain. The Raman gain is proportional to the species concentration Raman scattering cross section, and because the SRS intensity is exponentially proportional to the Raman gain, the SRS intensity is very much larger (some e^{30} times) than the spontaneous Raman intensity. The frequency shift of the SRS from the input pump laser frequency is identical to that of the spontaneous Raman scattering, i. e., the frequency shift is equal to molecular vibrational frequency. Thus, the SRS has the potential of detecting the presence (or absence) of a particular species in a multicomponent fuel droplet. Generally, in an optical cell (without feedback mirrors), SRS is observed from only the highest gain vibrational mode of the species with the highest concentration. Our objective is to increase the SRS intensity from minor species in a multicomponent fuel droplet. In our last report, we have shown that the SRS of the majority species is more efficient in pumping the SRS of the minority species than the input laser.[5]

We have succeeded in enhancing the SRS signal from a Raman mode (with a weak gain) by externally seeding light at the Raman-shifted frequency of the weaker gain Raman mode. Without seeding, the SRS builds from spontaneous Raman photons that are generated at the beginning of the laser-material interaction. Should the injected radiation be greater than the spontaneous Raman scattering, the SRS builds from a larger initial number of photons and, hence, may achieve a larger final intensity. Two implementation make the external seeding technique viable. First, by using a spectrally broadband seed beam ($\approx$ 2 nm wide), we were able to spectrally discriminate the elastically scattered seed light from the narrow linewidth SRS, which occurs only on MDR's because at these wavelengths the droplet provides the optical feedback to the SRS. Second, by incorporating an analyzer in front of the detector that is crossed to the linear polarization of the seed beam, we prevent detector saturation. The elastic scattering by the droplet preserves the polarization of the input beam. Hence, the crossed analyzer can block a large fraction of the intense elastically scattered radiation.

Figure 1 illustrates the polarization geometry of the pump, incident seed, elastically scattered seed, and the generated SRS. The seed radiation (at the Raman-shifted wavelength) is horizontally polarized ($\theta = 90°$) and the analyzer is usually vertically polarized ($\theta = 0°$), which blocks out most of the intense elastically scattered radiation. The pump radiation (at the second harmonic of the Nd:YAG laser) can be set at any θ relative to the vertical.

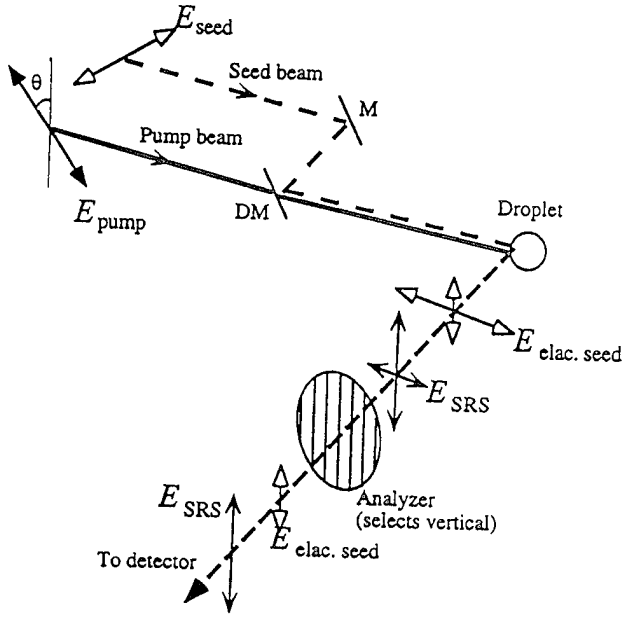

Figure 1. Experimental arrangement for external seeding of SRS. The polarization geometry of the pump, incident seed, elastically scattered seed, and the generated SRS is shown.

Figure 2 shows that by tuning the seed radiation to ≈ 632 nm, the SRS of the weaker gain Raman mode of methanol (at 2944 cm^{-1}), can be made stronger than the SRS of the stronger gain Raman of methanol (at 2835 cm^{-1}). The SRS and the elastically scattering of the seed can be readily distinguished, because the bandwidth of the seed is purposely selected to be much wider than that of the SRS, which acquires the MDR linewidth as the MDR is providing the optical feedback for the SRS. Note that with seeding at the weaker Raman gain mode, the seeded SRS of the weaker gain mode can be made stronger than the SRS of the stronger gain mode. Whereas, without seeding, the SRS of the weaker gain mode is smaller than that of the stronger gain mode.

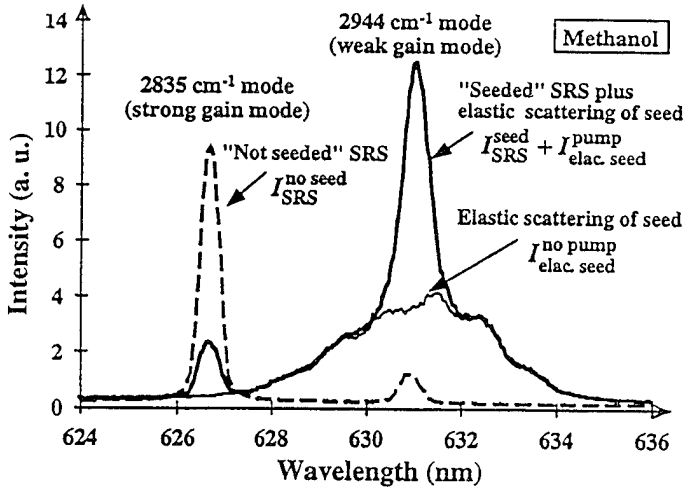

Figure 2. The detected spectra with following conditions: (1) with no pump, only the elastic scattering of the seed is detected; (2) with no seed, only the SRS is detected; and (3) with seed and pump both on, the seeded SRS plus the elastic scattering of the seed are detected. Outside the seed bandwidth, the SRS of the stronger gain mode actually diminishes when the seed beam is on in order to enhance the weaker gain mode.

We demonstrate that external seeding of a minority species (3% acetone in water) is feasible. Without seeding at the acetone Raman mode (2925 cm^{-1}), only the SRS of O-H stretching mode of water is detected (3200 and 3400 cm^{-1} bands) [see Fig. 3]. The SRS of 3% acetone is not detected. However, with seeding at the acetone Raman mode, the SRS is definitely observable in Fig. 3. The inset in Fig. 3, shows the SRS with and without seed on a magnified intensity scale.

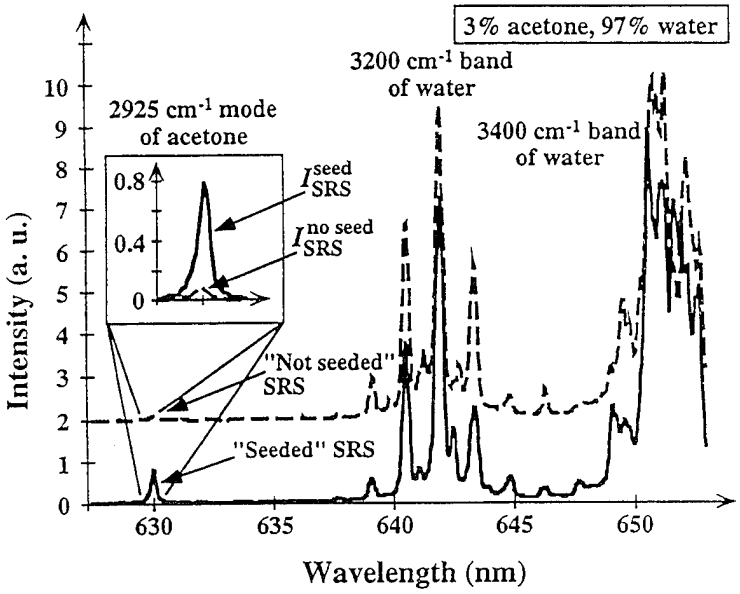

Figure 3. The SRS spectra with and without seed beam tune that is to the 3% acetone Raman mode at 2925 cm^{-1}. The elastically scattered spectrum has been subtracted from the seeded SRS spectra.

REFERENCES

1. Md. Mohiuddin Mazumder, Gang Chen, Peter J. Kindlmann, R. K. Chang, and James B. Gillespie, "Temperature-Dependent Wavelength Shifts of Dye Lasing in Microdroplets with a Thermochromic Additive," Opt. Lett. 20, 1668 (1995).

2. Md. Mohiuddin Mazumder, Gang Chen, Richard K. Chang, James B. Gillespie, "Wavelength Shifts of Dye Lasing in Microdroplets: Effect of Absorption Change" Opt. Lett. 20, 287 (1995).

3. Anthony O'Keefe and David A. G. Deacon, "Cavity ring-down optical spectrometer for absorption measurements using pulsed laser sources," Rev. Sci. Instrum., vol 59, 2544-2551 (1988).

4. D. Romanini and K. K. Lehmann, "Ring-down cavity absorption spectroscopy of the very weak HCN overtone bands with six, seven,and eight stretching quanta," J. Chem. Phys. vol. 99, 6287-6301 (1993).

5. Md. Mohiuddin Mazumder, Karl Schaschek, Richard K. Chang and James B. Gillespie, "Efficient Pumping of Minority Species Simulated Raman Scattering (SRS) by Majority Species SRS in a Microdroplet of a Binary Mixture," Chem. Phys. Lett., 239, 361 (1995).

NONLINEAR DIAGNOSTICS FOR COMBUSTION AND PLASMA PROCESSES

(AFOSR Contract F49620-94-C-0027)

Principal Investigators: David L. Huestis, Gregory W. Faris, and Jay B. Jeffries

SRI International
Molecular Physics Laboratory
Menlo Park, California 94025

SUMMARY/OVERVIEW

Task 1: UV and VUV Generation and Detection Techniques

We are developing techniques to extend laser-based diagnostics into the vacuum ultraviolet (vuv) region for the detection of ground state atomic ions, planar imaging of light atoms, and other applications. To increase the power from our vuv source, we are investigating the use of phase-matched gas mixtures. With this approach, we have produced energies of 1 μJ near Lyman α (121.6 nm). We expect to increase this energy by an order of magnitude in the near future.

Task 2: Laser-Excited Amplified Spontaneous Emission (ASE)

Two-photon-excited ASE of atomic hydrogen and oxygen was studied in low-pressure flames and the afterglow of microwave discharges with atom number densities near 1×10^{15} cm^{-3}. Near threshold ASE was well described by a coupled rate model and atom density was obtained by direct measurements of ASE gain. The ASE experiences higher gain with increased excited state population, which can be accomplished by increased energy in the excitation laser pulses or by increased atom number density. With increased laser pulse energy, model predictions require a complex description of the spatial distribution of the laser pulse fluence and energy dependent lineshape. A dc-arcjet was constructed and the hydrogen dissociation determined by calorimetry. Atomic hydrogen concentrations in excess of 1×10^{16} cm^{-3} were attained in the plume of this plasma. ASE measurements in this large atomic density are underway.

TECHNICAL DISCUSSION

Task 1: UV and VUV Generation and Detection Techniques (G. W. Faris)

We are investigating approaches to two interesting problems in laser-based diagnostics; the detection of ground state atomic ions and the single-photon detection of light ions. Both of these detection problems require high power vacuum ultraviolet radiation. Two-photon excited fluorescence using vuv radiation can provide quantitative detection of ground state atomic ion populations for studying plasma propulsion, highly-ionized flows, and other applications. Single photon vuv excitation of light atoms can allow very sensitive detection or planar imaging in arc jets or hot rarefied flows.

We use two-photon-resonant difference frequency mixing to produce high-power widely-tunable vuv radiation.[1] The output of a tunable ArF excimer laser at frequency ν_{ArF} is mixed with the fundamental or frequency-doubled output from a Nd:YAG-pumped dye laser at frequency ν_{dye} to produce radiation at frequency $\nu_{vuv} = 2 \times \nu_{ArF} - \nu_{dye}$. Enhanced efficiency is provided by tuning the ArF laser onto resonance with two-photon transitions in the mixing gas (krypton or hydrogen). By tuning the dye laser frequency, the vuv wavelength can be varied

from 110 to 180 nm. Energies of up to 65 μJ have been measured at 133 nm. The feasibility of ground state atomic ion detection has been demonstrated through two-photon-excited fluorescence detection of atomic neon using 133 nm light.[2] Practical ground state atomic ion detection will require higher powers, however.

To improve the power from our vuv source, we have been investigating the use of phase-matched mixtures of gases. For nonlinear frequency conversion processes such as that in our vuv source, the dispersion for different wavelengths leads to different phase propagation velocities for the pump (input) and generated waves. If these phases do not propagate in conjunction (i.e., there is phase mismatch), then the nonlinear conversion process is not optimally efficient. By reducing the phase mismatch (phasematching), we can significantly improve the vuv power from our source. Of the various techniques for phasematching,[3] the most useful in the vuv region is the use of gas mixtures. This uses the anomalous dispersion (decreasing refractive index with increasing photon energy) that gases can exhibit above allowed ground state transition frequencies.

We are examining phasematching in the region of Lyman α (121.6 nm), the shortest wavelength we have generated to date. This wavelength may be used for planar imaging or other diagnostics of ground state hydrogen atoms. Krypton gas exhibits negative dispersion in this region.

The vuv power generated near Lyman α by mixing in hydrogen without phasematching is shown as a function of wavelength in Figure 1. This figure shows there is production of hydrogen atoms during the mixing process. The hydrogen atoms lead to absorption near Lyman α, and asymmetrical vuv generation on either side of Lyman α due to the dispersion contribution of the hydrogen atoms. Preliminary experiments with phasematching produced vuv radiation that was visible by eye on a white card, and measured energies of 1 μJ near Lyman α. These measurements were limited by poor transmission of the lens we are using to separated the vuv from the pump beams. With better optics we expect to improve the energy by one order of magnitude. We have two options to eliminating the high loss directly at Lyman α from hydrogen atom production. One is to use a looser focus combined with better conversion from phasematching. The second is to use a resonance in krypton rather than hydrogen. Conversion in krypton without phasematching is much less efficient than hydrogen. However, krypton has a larger phase mismatch than hydrogen, and good conversion in krypton may be possible using phasematching.

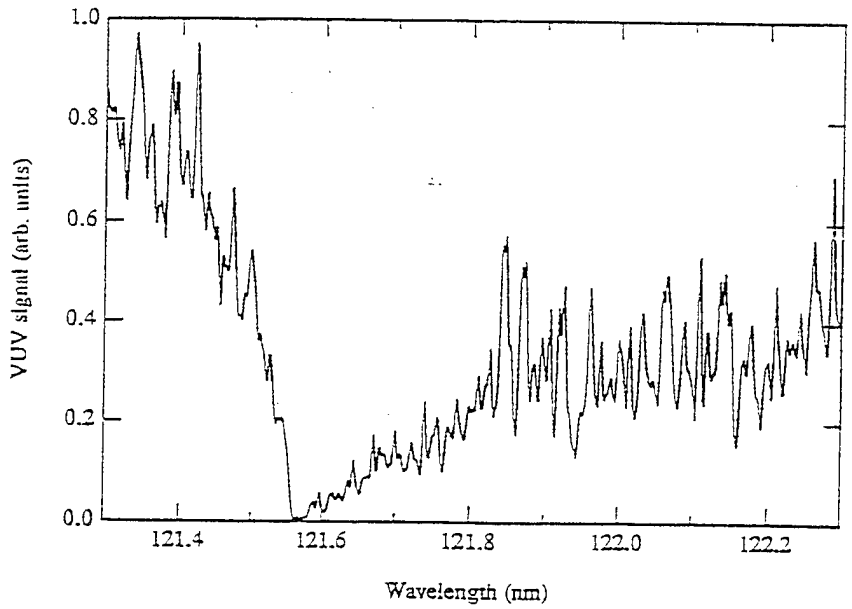

Fig.1. Tunable vuv generation in the Lyman-a region using 20 Torr of hydrogen.

Task 2: Laser-Excited Amplified Spontaneous Emission (ASE) (J. B. Jeffries)

Two-photon-excited ASE was observed from atomic hydrogen in low-pressure hydrogen oxygen flames. The 3S and 3D states of atomic hydrogen were excited near 205 nm by two-photon absorption from the ground state. Laser-induced fluorescence at Balmer α near 656 nm was simultaneously detected. In the flame, there is no significant thermal population in the 2P state which is the lower level of the Balmer α transition. Therefore, as soon as the excitation laser moves any significant population to the excited state, a population inversion is created and spontaneous emission forward and backward along the excitation laser path will experience gain. Balmer α ASE is observed in all the flames studied, with the largest signals observed in a rich H_2/O_2 flame. This 7.2 Torr flame has the largest H atom concentration and a relatively low, 1200 K gas temperature.

The dynamics of the atomic population and ASE photon fields were described with a set of coupled rate equations. The volume is defined by the confocal range of the incident pump beam and the diameter of the beam at its waist. This volume acts as a mirrorless cavity for the amplification of spontaneous emission. The model couples the population in the ground state, excited state, intermediate state, and the ions produced by 2+1 REMPI. To predict the spatial dependence of the ASE beam, the focused pump laser is assumed to be Gaussian. Exploiting the cylindrical symmetry, the gain region is divided into a set of concentric shells of thickness Δr. The populations in each of the radial shells are then calculated as a function of time. The model predicts that the ground state is rapidly depleted in the center of the excitation beam, even with modest 100 μJ, 10 ns laser pulses focused with a 10 cm lens. After only 2-4 ns, the center of the focal volume is converted to ions with nearly a 100% efficiency as shown in Figure 2. Thus, the time integrated gain is largest in a ring around the center of the focal volume. The ASE spatial profile predicted from this excited state distribution is also a ring about the excitation beam. as shown in Figure 3. Tests of this model require use of lower excitation pulse energy; to maintain useful signal to background, we must perform these tests on a higher density of atoms.

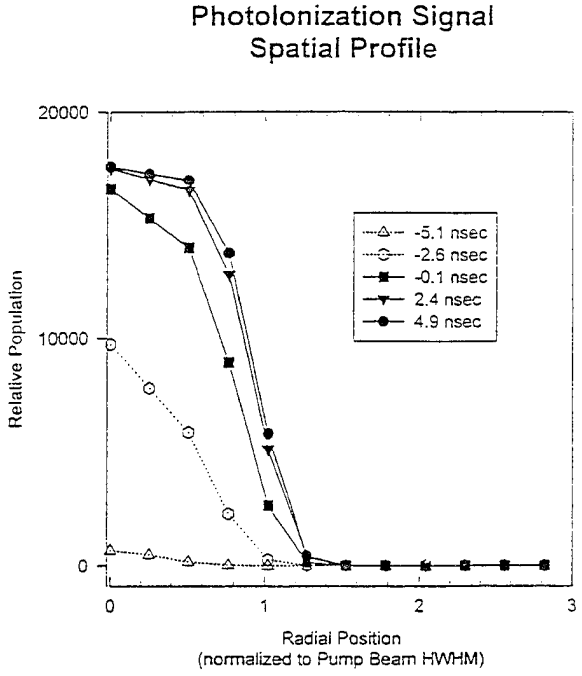

Fig. 2 The predicted population of photo-ionized H atoms for a series of times with respect to the peak of the excitation laser pulse.

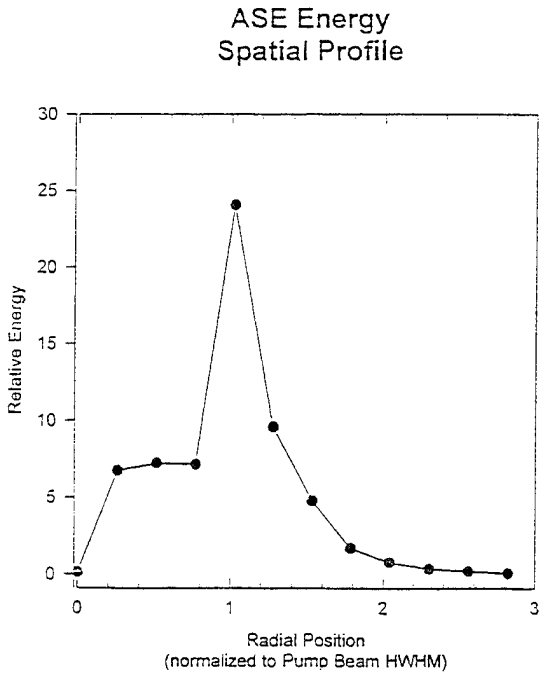

Fig. 3 The time integrated ASE energy as a function of radial position.

An atom density well above 1×10^{16} cm^{-3} can be produced in the plume of a dc-arcjet thruster. A dc-arcjet plume has been used in our laboratories to grow CVD diamond film and study the chemistry of diamond film deposition. Atomic hydrogen concentration is measured in this reactor by calorimetry. The input electrical energy is distributed into gas heating, ionization, dissociation, directed velocity, and the heating of the converging/diverging nozzle. Langmuir probe measurements of the ion density and electron temperature show that only a tiny fraction of the input energy is partitioned into ionization. Laser-induced fluorescence measurements to determine the gas temperature and velocity measurements are underway. Because there are no visible shock structures in the plume even when it strikes the substrate, the gas velocity is assumed subsonic which indicates nearly 50% of the feedstock hydrogen is dissociated producing a hydrogen atom density well above 1×10^{16} cm^{-3} in good agreement with work at Phillips Laboratory[4] on arcjet thrusters.

The arcjet plume is an ideal test bed for atomic hydrogen ASE; large ASE signals were observed at Phillips laboratory with modest excitation laser fluence.[4] The plume is nearly uniform temperature, density, and velocity, with a well defined diameter. The plume size and shape were measured previously with beam deflection tomography. Accurate velocity measurements combined with calorimetry will determine the atomic hydrogen concentration. Simultaneous measurements of LIF and ASE will provide quantitative tests of the ASE model.

REFERENCES

1. G. W. Faris and M. J. Dyer, in *Short Wavelength Coherent Radiation: Generation and Applications,* Philip H. Bucksbaum and Natale M. Ceglio, Eds. (Optical Society of America, Washington, DC, 1991).
2. G. W. Faris and M. J. Dyer, Opt. Lett. **18**, 382 (1993).
3. J. F. Reintjes, *Nonlinear Optical Parametric Processes in Liquids and Gases*, (Academic Press, New York, 1984) pp. 49-58.
4. J. A. Pobst, Ingrid, J. Wysong, and R. A. Spores, "Laser-Induced Fluorescence of Ground State Hydrogen Atoms in an Arcjet Plume," 24th Electric Propulsion Conference, Moscow, Russia, September, 1995.

RAPID CONCENTRATION MEASUREMENTS BY PICOSECOND TIME-RESOLVED LASER-INDUCED FLUORESCENCE

AFOSR Grant Number F49620-95-1-0218

Principal Investigators: Galen B. King and Normand M. Laurendeau

Flame Diagnostics Laboratory
School of Mechanical Engineering
Purdue University
West Lafayette, IN 47907-1288

SUMMARY/OVERVIEW

This research is concerned with the development of a laser-based diagnostic technique, called picosecond time-resolved laser-induced fluorescence (PITLIF). The PITLIF instrument employs a mode-locked Ti:Sapphire laser system which has the power and repetition rate (80 Mhz) needed to rapidly obtain probability density functions (PDFs) and power spectral densities (PSDs). During the past year, time-series measurements of CH concentrations have been made in laminar and turbulent non-premixed CH_4/Air flames. Both PDFs and PSDs were obtained from the CH fluorescence signals. The PSDs are, to our knowledge, the first measured for a naturally occurring radical in either a laminar or turbulent flame.

TECHNICAL DISCUSSION

Quantitative measurements of radical concentrations in flames are required to understand many important interactions between fluid mixing and chemical reaction[1]. Advances in laser-based techniques have enabled nonperturbing quantitative measurements of such species concentrations. In particular, laser-induced fluorescence (LIF) possesses the spatial and temporal resolution necessary to monitor radical concentrations in reacting flows. The present work focuses on the application of a new diagnostic technique, picosecond time-resolved laser-induced fluorescence (PITLIF), to the measurement of the number density of CH radicals in both laminar and turbulent non-premixed flames. These measurements represent the first time-series (to our knowledge) of the fluorescence signal of a naturally-occurring minor species in a turbulent flame.

The PITLIF technique permits direct measurement of both the integrated fluorescence signal and the quenching environment. Measurement of the quenching rate coefficient allows quantitative number densities to be found from corrected concentration measurements. Time-series measurements of minor species are possible due to the picosecond, mode-locked laser source used in the technique. Previous work has demonstrated the ability to measure both the quenching rate coefficient and the integrated fluorescence signal for a naturally-occurring minor

[1] M. C. Drake and R. W. Pitz. *Experiments in Fluids* **3**, 283 (1985).

species (OH)[2] and for a seeded substance (sodium)[3] in laminar flames. Here, we report on further development of the low-bandwidth aspects of the PITLIF instrument.

A schematic diagram of the experimental apparatus is shown in Fig. 1. The laser source is a Spectra-Physics Tsunami™ mode-locked laser which is pumped by a multi-mode argon-ion laser. The laser system delivers a series of mode-locked pulses of 1.5 ps FWHM at a repetition rate of 80 MHz. The output of the Tsunami™ is frequency-doubled with a CSK Supertripler using an angle-tuned LBO crystal. The spectral width of the beam after being frequency-doubled is estimated to be 10 cm^{-1} (0.7 nm). The wavelength (430 nm) and spectral width of the laser exiting the doubling crystal allows simultaneous excitation of a number of transitions within the (0,0) band of the A^2 - X^2 system of CH. Spectrally-narrower pulses and excitation of a single transition would be desirable for quantitative spectroscopic studies and can be obtained with the current system, but with lower average laser energy. This lower energy may be counteracted by a better overlap between the laser and absorption line shapes when using a spectrally-narrower pulse. This alternative strategy will be pursued in future work utilizing the PITLIF technique.

A concentric-tube burner was utilized for creating both the non-premixed laminar and turbulent flames. Methane was supplied through a central tube (5.5 mm inner diameter). A stabilizing co-flow air stream was supplied to an outer tube (23.6 mm inner diameter) concentric to the central fuel tube. The air stream passed through glass beads and a honeycomb flow straightener and was used only in the laminar flame study to dampen out any flame fluctuations due to the movement of surrounding room air. The Reynolds number (based on the average velocity at the exit of the fuel tube) was 180 and 4800 in the laminar and turbulent flames, respectively. The turbulent flame remained attached to the central fuel tube.

Fluorescence emission was collected perpendicular to the beam axis (see Fig. 1) and focused onto the entrance slit of a 0.25-m monochromator. The output of the monochromator was centered at 480 nm which corresponds to the (0,1) band of the A^2 - X^2 system of CH. The width of the exit slit of the monochromator was 4.2 mm, resulting in the detection of fluorescence in a 16-nm region about 480 nm. The probe volume (as defined by the entrance slit of the monochromator and the beam diameter) in the flame was 500 μm high, 100 μm wide, and 60 μm deep; the resulting laser irradiance was 4.4×10^6 mW/cm^2 (assuming an average measured laser power of 125 mW at the probe volume location after losses through the apertures, optics and optical chopper). The PMT mounted at the exit slit is a Hamamatsu H5321 which has a risetime of 0.70 ns and a transit time spread of 0.16 ns.

To demonstrate the temporal resolution of the current PITLIF system, time-series measurements of CH were made in both a laminar and a turbulent CH_4 non-premixed sooting flame. Radial profiles of the mean CH signal at two different axial locations are shown for the laminar flame in Fig. 2. Since CH is only present in high-temperature regions of the flame, the displayed trends are to be expected. At the lower axial position, CH is present only at positions near the flame front and drops off very rapidly on either side of this location. No CH is found in the cold, fuel-rich central core of the non-premixed flame. At the higher axial location in the flame, the CH follows the shift in the flame front location (due to flame narrowing) and some CH is found in the central region of the flame. Some self-absorption (and scattering due to soot) of

---

[2] T. A. Reichardt, M. S. Klassen, G. B. King, and N. M. Laurendeau. *Applied Optics* **35**, 2125 (1996).

[3] M. S. Klassen, B. D. Thompson, T. A. Reichardt, G. B. King, and N. M. Laurendeau. *Combustion Science and Technology* **97**, 391 (1994).

the fluorescence emanating from positive radial locations is evident owing to a greater path length between the probe volume and the detection system.

Figure 3 shows similar profiles of the mean CH signal across the radius of the turbulent non-premixed CH_4 flame for three different axial stations. Many of the overall trends in CH location found in the laminar flame are also evident in the turbulent flame. At the lowest axial station (x/D = 5), the highest CH signal is found near the flame-front, though the trailing edge towards the fuel-rich core is much longer than that found in the laminar flame. At the higher axial positions, the location of maximum CH signal again follows the location of the mean flame front as the flame narrows.

PDFs demonstrating the distribution of CH signal levels are shown in Fig. 4 for both the laminar (x/D = 5.3) and the turbulent (x/D = 5) flames. These time-series measurements were taken at the radial location with the highest mean CH fluorescence signal at the given axial station (i.e. r = 2 mm for the laminar flame and r = 8 mm for the turbulent flame). The difference in the range of CH signals encountered in the flames is quite apparent; the PDF generated using data from the turbulent flame is much wider, as would be expected, owing to turbulent mixing effects.

The most unique aspects of the PITLIF technique are its ability to make quenching corrections by direct measurement of the excited-state lifetime and its ability to follow transient events by making time-series measurements. Measurements of the CH quenching rate coefficients are not demonstrated in this report, but as mentioned previously, such lifetime measurements have been made previously for OH in a flame by using the PITLIF technique. Time-series measurements provide a complete description of the turbulent processes, as higher-order statistics (e.g., kurtosis and skewness) can be computed. Furthermore, a better understanding of energy exchange between scales can be gained through spectral analysis of the time-series[4]. This feature is generally presented as a power spectral density (PSD).

Figure 5 demonstrates the frequency bandwidth of the present system by showing PSDs generated from time-series measurements in both the laminar (x/D = 5.3) and turbulent flames (x/D = 5). The PSDs were generated from data taken at the same axial and radial positions as presented in Fig. 4. The differences between the two frequency spectra are quite apparent. The spectrum from the laminar flame is quite flat, indicating that little redistribution of energy occurs between the different scales of the flow. The spike at 20 Hz corresponds to the large scale pulsation frequency of this flame. The spike at 1000 Hz is the aliased signal of the modulation or reference frequency used for phase-sensitive detection. The relatively flat spectrum for the laminar flame also demonstrates that the detection system has the bandwidth necessary to accurately capture energy contributions at frequencies up to at least 1500 Hz (set by the sampling frequency). Much larger bandwidths (up to 50 kHz) are available with the current system. The spectrum from the turbulent flame shows the classic energy transfer found in turbulent flows. For locally isotropic turbulent flow at high Re number, the spectrum of turbulent scalar fluctuations is expected to display a -5/3 power-law region[5]. As shown in Fig. 5, the spectrum clearly does not follow this trend, though not unexpectedly, due to the relatively low Re number of the flame. The relatively flat noise floor evident in the spectrum from the turbulent flame also shows that an adequate data sampling rate was used to resolve the necessary spectral information.

---

[4] H. Tennekes and J. L. Lumley. A First Course in Turbulence, MIT Press, Cambridge, MA, 248 (1972).

[5] D. R. Dowling and P. E. Dimotakis. *Journal of Fluid Mechanics* **218**, 109 (1990).

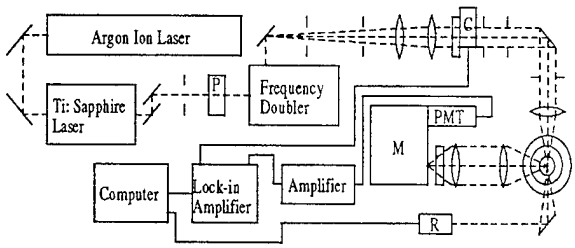

Figure 1. Experimental setup used for the time-series measurements of CH. P is a polarization rotator, C a chopper, M the 0.25 m monochromator, and R a radiometer.

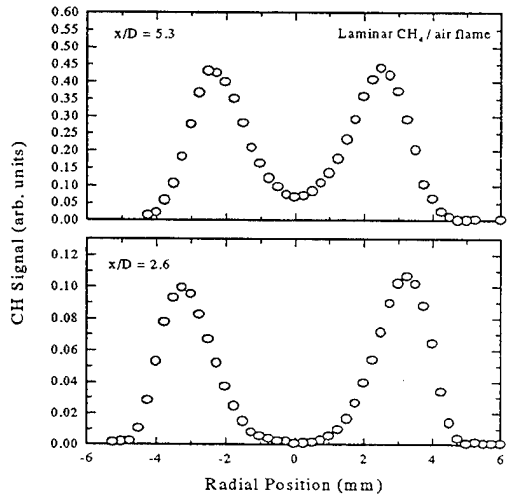

Figure 2. Mean CH signal measured in a laminar CH_4/Air non-premixed flame. The mean values are based on ~100,000 data points.

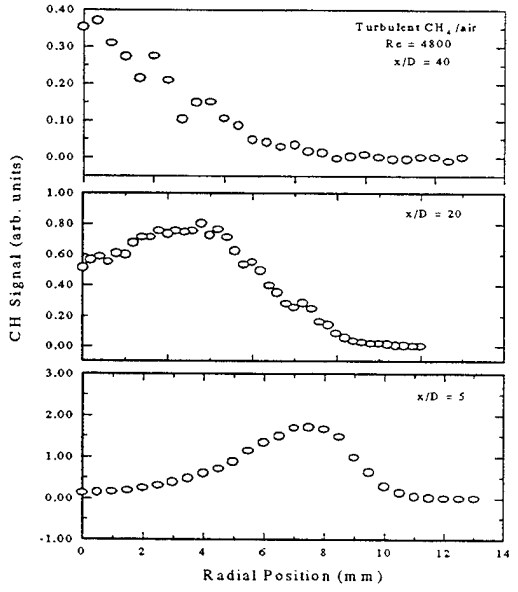

Figure 3. Mean CH signal measured in a turbulent CH_4/Air flame. The mean values are based on ~100,000 data points.

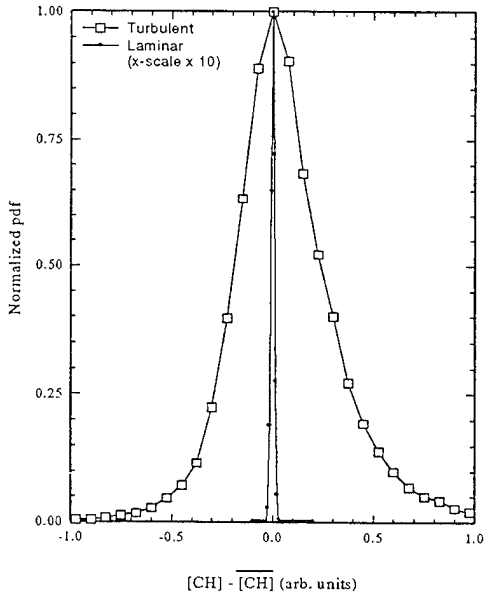

Figure 4. Probability density functions for the turbulent and laminar CH_4/Air flames. The measurements were made at the radial location corresponding to the peak mean CH signal (x/D = 5, turbulent; x/D = 5.3, laminar)

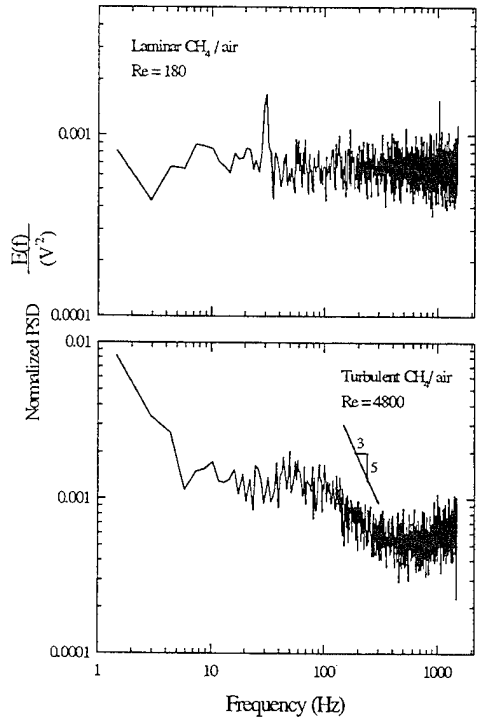

Figure 5. Power spectra for the laminar and turbulent CH_4/Air flames. The measurement locations are the same as those indicated in Fig. 4.

ABSTRACTS OF WORK UNITS NOT PRESENTED

RESEARCH ON SUPERSONIC REACTING FLOWS

AFOSR Grant No. F49620-94-1-0152

Principal Investigators: C.T. Bowman, R.K. Hanson, M.G. Mungal and W.C. Reynolds

Department of Mechanical Engineering
Stanford University
Stanford, CA 94305-3032

SUMMARY/OVERVIEW:

A major technological challenge in achieving sustained hypersonic flight is the development of advanced air-breathing propulsion systems in which combustion takes place in supersonic flow. Combustion in supersonic flow is fundamentally different from combustion in the subsonic flow regime employed in existing air-breathing propulsion systems. The current understanding of fundamental aspects of supersonic combustion is inadequate to support the development of these advanced propulsion systems. Recent advances in diagnostics capabilities and significant improvements in our abilities to compute complex flows offer new opportunities to obtain needed fundamental understanding of flow physics and chemistry interactions in compressible reacting flows. To achieve this understanding, a combined experimental and computational investigation of supersonic flows is in progress. The primary elements of the investigation are mixing and combustion studies, refinement of previously-developed laser-based diagnostics for application in the experiments, and analysis and simulation. Specific accomplishments during the past year are summarized below.

TECHNICAL DISCUSSION:

Experiments on Supersonic Mixing and Combustion

Previous experiments performed in our supersonic combustion tunnel investigated the effects of compressibility upon turbulent mixing and combustion. A primary conclusion of the non-reacting studies was that compressibility induces a change in large-scale, turbulent structure from 2D to 3D associated with a reduction in mixing layer growth rate (Clemens & Mungal 1995). Reacting studies showed that compressibility affects the entrainment ratio, which in turn alters the overall stoichiometry and combustion process (Miller *et al.*, 1996). Our current work is aimed at *quantitatively* measuring the impact of compressibility on scalar mixing, in particular the mixing efficiency and mixed mean concentration (Island *et al.*, 1996). Additionally, techniques for mixing enhancement are being evaluated on the basis of growth rates, mixing efficiency, and pressure loss.

Scalar mixing visualizations and measurements were made for compressible, planar mixing layers having convective Mach numbers, M_c, of 0.25, 0.39, and 0.63. To investigate Reynolds number effects, the measurements were taken at three streamwise locations for each compressibility. The passive scalar visualizations were obtained using planar laser-induced fluorescence (PLIF) of nitric oxide diluted with nitrogen. The largely unquenched fluorescence provides high quality (SNR = 18) visualizations of the instantaneous structure of the mixing layer. The quantitative measurements were made with a cold chemistry PLIF technique (Clemens & Paul, 1993). The technique employs fluorescence quenching to provide a resolution-independent measure of fluid unmixedness from which the mixing efficiency and mixed fluid composition can be derived.

As seen in Figure 1a, the fraction of mixed fluid in the layer was measured as 0.50, 0.54, 0.59 for convective Mach numbers of 0.25, 0.39, and 0.63, respectively. The trend of slightly increased mixing efficiency with M_c appears, however, more likely due to Reynolds number effects, as indicated by the increase in mixing efficiency with Re shown in Figure 1b for all M_c. We conclude that mixing efficiency is essentially independent of compressibility over the range investigated.

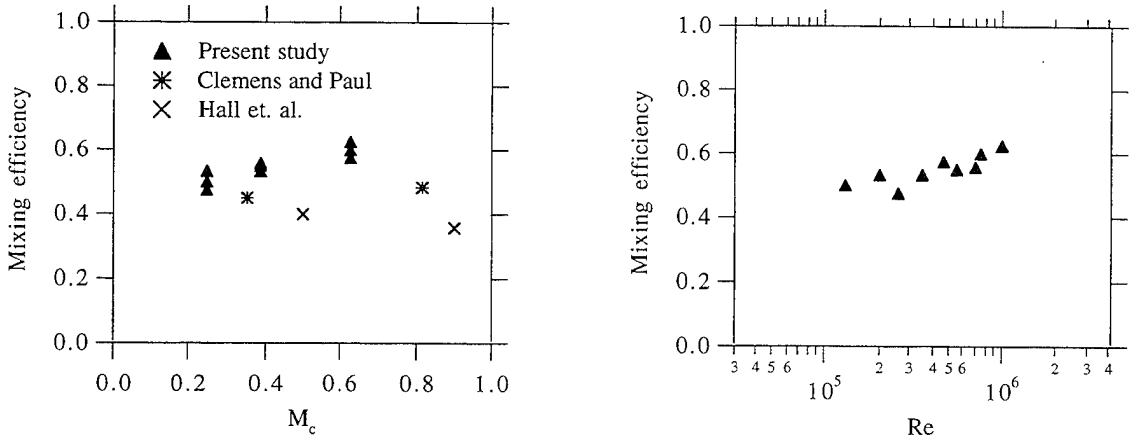

Figure 1: Mixing efficiency vs. (a) compressibility and (b) Reynolds number.

The mixed-fluid composition, shown in Figure 2a, exhibits a similar profile at each M_c but is shifted towards lower composition with increasing compressibility. To separate the effects of density ratio and compressibility, the mean value of all profiles, the mean mixed-fluid composition, is plotted against density ratio in Figure 2b. The observed shift towards lower concentration is slightly greater than that predicted by density ratio effects alone (incompressible data), implying a possible (but small) compressibility effect.

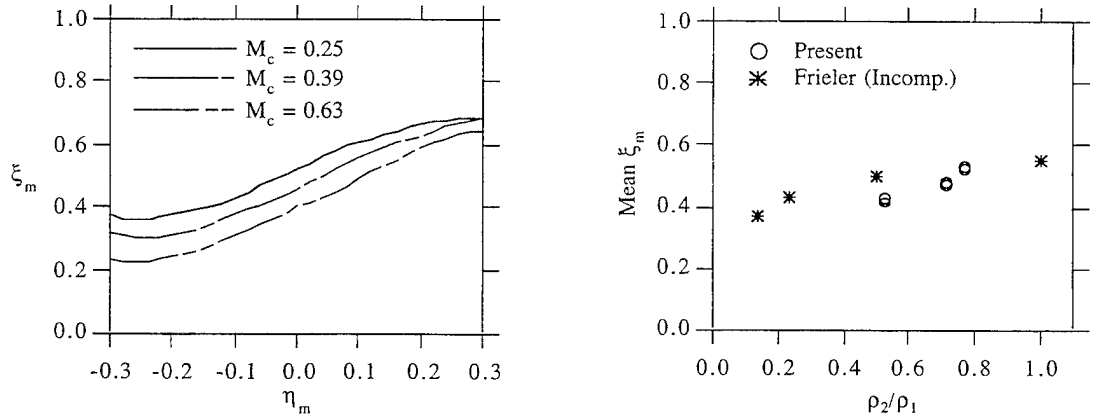

Figure 2: (a) Mixed-fluid high-speed mixture fraction vs. normalized transverse distance. (b) Mean mixed-fluid composition vs. density ratio.

In an effort to improve compressible mixing, several mixing enhancement strategies have been evaluated at M_c= 0.63 and M_c= 0.79. In contrast to previous work that has mostly focused on relatively large disturbances, such as vortex generators, tabs, or strong shock waves, our emphasis is on boundary layer perturbations which have a minimal pressure-loss penalty. The effects of size, shape, number, thickness, and relative position of disturbances located on the supersonic side of the splitter tip were investigated. Using planar laser Mie scattering visualizations of mixed fluid, we found that 3D disturbances as short as 5% of δ_{99} introduced significant streamwise structure which may affect the mixing efficiency of these layers; the impact on mixing efficiency is currently being evaluated with the cold chemistry PLIF technique. The 3D disturbances are also effective in increasing the thickness of the mixing layer, δ_{vis}, although the increase, as well as the pressure loss, scales with the height of the disturbance. Note, however, that equivalent pressure losses by other methods, such as 2D perturbations, resulted in no appreciable increase in δ_{vis}. The thickening occurs in the near-field region of the mixing layer after which the growth rate relaxes to its natural spreading angle. Analysis of quantitative cold chemistry PLIF measurements of the most promising geometries is currently underway.

PLIF Thermometry in Shock Tunnel Flows

Previous two-line rotational temperature measurements with PLIF have been performed in our laboratory in a variety of shock tube-generated flowfields, including a model SCRAMJET flow with PLIF of NO (McMillin *et al.*, 1993) and shock-induced H_2-air combustion with PLIF of OH (Seitzman et al., 1994). Currently the focus is on application of similar techniques in high-speed flows with even more extreme temperature and pressure variations (Palmer and Hanson, 1995, Palmer *et al.*, 1996); these developments are needed for future experiments which are planned for high M_c. The primary goal is the implementation of PLIF imaging for measurements of the rotational temperature of NO in a highly-underexpanded free jet flowfield created in a small-scale, reflection-type shock tunnel. During each run of the shock tunnel, an isolated rovibronic transition in the $A\ ^2\Sigma^+ \leftarrow X\ ^2\Pi$ (0, 0) band of NO at ~226 nm is excited with a frequency-doubled dye laser pulse formed into a thin sheet and directed perpendicularly through the axis of the jet. The red-shifted components of the resulting fluorescence at 90° with respect to the laser are imaged onto an intensified, charge-coupled device array. Transitions originating from four different rotational states (K'') are used; and the temperature field may be inferred from any two individual images acquired with excitation of transitions from different states. However, in the inviscid core of the jet (*i.e.*, the primary portion of the flowfield imaged here), the fluorescence signal is undetectable in the low-temperature, low-density regions for images obtained with high-K'' lines; and the temperature sensitivity in the high-temperature regions is poor for pairs of images from low-K'' excitation (*i.e.*, small lower-state energy separation). Consequently, no single image pair yields an adequate evaluation of the temperature field throughout the free jet expansion. By combining images from the four rovibronic lines excited, the mean temperature may be inferred accurately over its entire range (*i.e.*, ~100–3100 K). Although single-shot fluorescence images (*i.e.*, signals acquired with single laser pulses) are used, the temperature measurements are not temporally-resolved because the images are acquired during separate shock tunnel runs. As the flow is laminar and reproducible, temporal resolution is not required, except insofar as the fluorescence image must be captured during its brief, quasi-steady period, which makes necessary the use of a single-shot imaging technique. Results of the PLIF imaging experiments, including single-shot and frame-averaged temperature fields derived from four-line combinations, are displayed in Fig. 3, along with the results of a numerical simulation of the flow performed by the method of characteristics (MOC). Excellent agreement is achieved between the measured and predicted temperature fields.

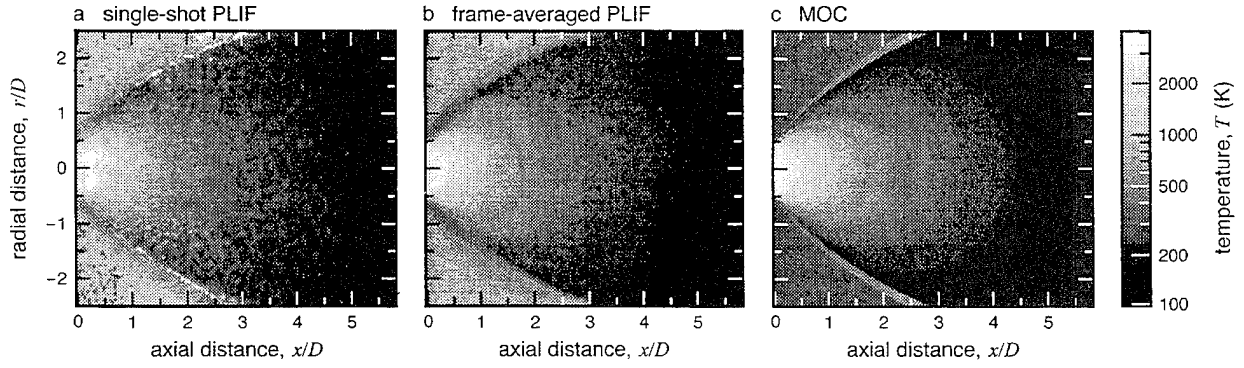

Figure 3: (a) Single-shot and (b) frame-averaged temperature fields inferred from PLIF images obtained by pumping the $Q_1(5)$, $Q_2(7)$, $Q_1(18)$, and $Q_1(28)$ transitions of the $A\ ^2\Sigma^+ \leftarrow X\ ^2\Pi$ (0, 0) band of NO at ~226 nm. Also shown is the temperature field predicted by the MOC (c).

Stability Analysis and Numerical Simulation

The computational portion of our project is in the final stages of an effort to detail the structure of the compressible reacting mixing layer throughout its parameter space. A linear stability technique has been used to gain a broad understanding of how the effects of compressibility, heat release and the density, equivalence and velocity ratios influence the amplification, speed and structure of different

stability modes. The purpose of this work was to provide an initial base of information to be used for guiding both future experimental and computational investigations.

The stability results were found to be most insightful when placed in the form of regime charts that detail the type of structure that is expected to dominate across a chosen parameter space. An example of this is shown in Figure 4a, a regime chart in the compressibility and density ratio plane. This structure map has proven particularly useful in the planning stages of the shock driven supersonic mixing layer experiment. More detailed information can also be supplied to guide the experiment; Figures 4b-c detail the normalized eigenfunction energy distribution ($\hat{u}_i \hat{u}_i^*$) of the three different modes plotted against both the layer thickness (b) and $\overline{u}$ velocity (c) for the conditions $M_c = 3.7$ and $\rho_1/\rho_2 = 1.2$, a proposed experimental measurement position. These plots clearly demonstrate the compact nature of the fast and slow outer modes relative to the wide distribution of the central mode, a fact that has important consequences for the mixing efficiency at these conditions where the slow mode is expected to dominate the flow structure. The next stage in this work is to improve the quality of the stability predictions through the use of a parabolized analysis that will account for non-parallel and weakly non-linear flow effects.

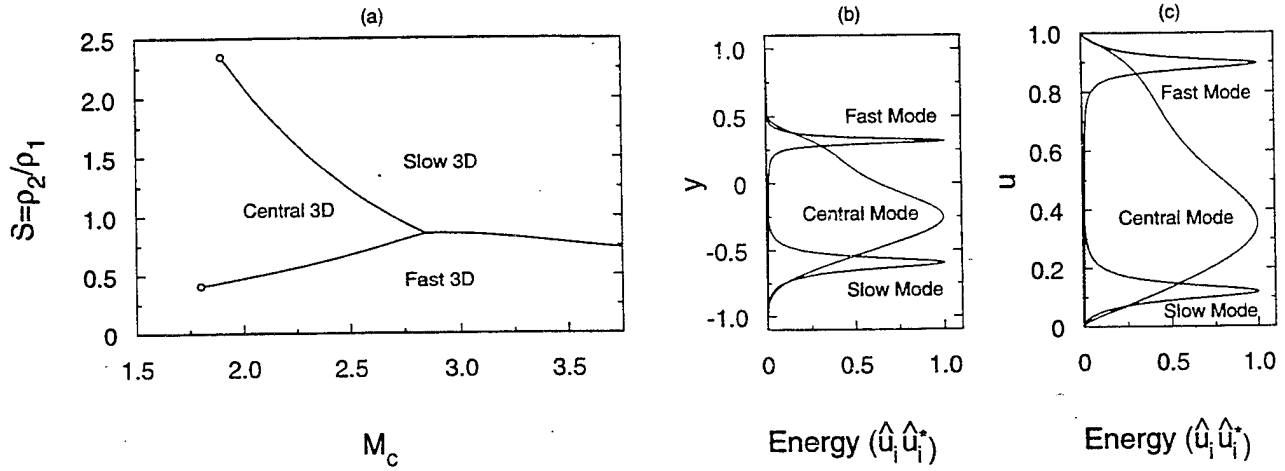

Figure 4: (a) Dominant structure regime chart for the compressibility and density ratio plane. Eigenfunction energy profile ($\hat{u}i\,\hat{u}i = \hat{u}\,\hat{u} + \hat{v}\,\hat{v} + \hat{w}\,\hat{w}$) for the flow conditions $M_c = 3.7$ and $\rho_1/\rho_2 = 1.2$ plotted against (b) y position and (c) mean velocity in the streamwise direction.

References

1. N. T. Clemens and P. H. Paul (1993), "Scalar measurements in compressible axisymmetric mixing layers", AIAA 93-0220, 31st AIAA Aerospace Sciences Meeting, Reno, NV.
2. N. T. Clemens and M. G. Mungal (1995), "Large-scale structure and entrainment in the supersonic mixing layer", *J. Fluid Mech.*, 284, 171-216.
3. T. C. Island, W. D. Urban and M. G. Mungal (1996), "Quantitative scalar measurements in compressible mixing layers", AIAA-96-0685, 34th Aerospace Sciences Meeting, Reno, NV.
4. B. K. McMillin, J. L. Palmer and R. K. Hanson (1993), "Temporally resolved, two-line fluorescence imaging of NO temperature in a transverse jet in a supersonic crossflow", *Appld. Opt.*, 32 (6), 7532-7545.
5. M. F. Miller, C. T. Bowman, and M. G. Mungal (1996) "An experimental investigation of the effect of compressibility on a turbulent reacting mixing layer", submitted to *J. Fluid Mech.*
6. J. L. Palmer and R. K. Hanson (1996) "Temperature imaging in a supersonic free jet of combustion gases using two-line OH fluorescence," *Appld. Opt.*, 35(3), 485–499.
7. J. L. Palmer, B. K. McMillin, and R.K. Hanson (1996) "Multi-line fluorescence imaging of the rotational temperature field in a shock-tunnel free jet," *Appld. Phys. B*, in press.
8. J. M. Seitzman and R. K. Hanson (1994), "Application of quantitative two-line OH planar laser-induced fluorescence for temporally resolved planar thermometry in reacting flows", *Appld. Opt.*, 33 (18), 4000-4012.

TURBULENCE–CHEMISTRY MODELS IN HIGHLY STRAINED NON–PREMIXED FLAMES

AFOSR Contract F49620–94–C–0020

Sanjay M. Correa and Iris Z. Hu
General Electric Corporate Research and Development Center
Schenectady, New York, 12301

SUMMARY: OBJECTIVES AND PRIOR RESULTS

The practical objective of turbulent combustion modeling is to increase engineering productivity and hence the rate of technological innovation, by contributing to design codes for the prediction of flame stability, flow/temperature fields and emissions from air–breathing combustors. The specific objective of this research program is to develop and assess models for turbulence–chemistry interactions in highly strained flames.

Prior results include:
(i) PDF/CFD An "elliptic" 2D axisymmetric CFD code was combined with the joint velocity–composition pdf model. A 2–variable partial equilibrium scheme was used for CO/H_2–air chemistry [1]. A 4–step 5–variable scheme was used for CH_4–air chemistry [2]. In each case, the calculations compared favorably with Raman data (mixture fraction, major species, and temperature). Hence this approach is being used in design codes. However, the work also indicated inadequacies in the physical and chemical sub–models.
(ii) PaSR To address some of the latter inadequacies in greater detail, the Partially Stirred Reactor (PaSR) model was developed. We have used the PaSR to study premixed CO/H_2 flames with full or partial equilibrium chemistry [3]; CH_4 flames with full and 25–step or 4–step reduced chemistry schemes [4]; alternate methods for computational "parallelization" of particle–tracking algorithms [4]; comparison of the Curl, modified Curl and IEM mixing models in the context of full chemistry [5]; the effect of the level of initial unmixedness on autoignition delay time (including comparison with premixed data in the baseline case of zero initial unmixedness) [6]; and to test a global three–variable chemistry scheme for kerosene [7].

PROGRESS MADE OVER THE PAST YEAR

A Model for Non–Premixed Flames Based on a PSR Microstructure and Full Kinetic Schemes

Given the complexity of the phenomena and fuels of interest, full rather than reduced chemistry schemes will probably be required. In principle, the laminar flamelet model (LFM) is available [8]. In the context of intensely turbulent combustion, the LFM breaks down because the reaction zone is not thin and the fluctuation of mixture fraction in the reaction zone is not small [9]. Here, an alternative to the LFM is developed.

The turbulent mixing–scale structure of the flame is assumed to be in the "distributed reaction zone" regime. Assuming that fluctuations in the mixture fraction ξ and the scalar dissipation rate χ are statistically independent, their joint pdf $P(\chi,\xi)$ is separable, i.e., $P(\chi,\xi)=P_1(\chi)P_2(\xi)$.

The assumed shape PDF approach is adopted. Following [10], the pdf of scalar dissipation $P_1(\chi)$ is taken to be log normal with a mean related to the local turbulence kinetic energy k, the local dissipation rate ε, and the local mean scalar variance, $\overline{g}$, viz., $\overline{\chi}=C_{g2}\,(\varepsilon/k)\,\overline{g}$, where C_{g2} is a constant in the $k-\varepsilon-g$ model.

The residence time "τ" in the mixing scales is related to the dissipation by $\tau = C\,\overline{g}/\chi$, where C is a constant (C=10) in the model. The pdf of residence time in the mixing scales is therefore $P(\tau)= \chi^2 P_1(\chi)/(C\overline{g})$. Note that in contrast to Magnussen et al. [11], who ascribed a single residence time $(\nu/\varepsilon)^{1/2}$ to the mixing scales, here we consider a distribution of the residence times and relate it to the pdf of the scalar dissipation.

Following the standard k−ε−g model, $P_2(\xi)$ is assumed to be a beta function

$$P_2(\xi) = [\xi^{a-1}\ (1-\xi)^{b-1}] \ / \int_0^1 \xi^{a-1}\ (1-\xi)^{b-1}\ d\xi$$

where "a" and "b" are related to the local mean and variance of the fluctuations in the mixture fraction,

$$a \equiv \bar{\xi}\ \left(\frac{\bar{\xi}(1-\bar{\xi})}{g} - 1 \right) \qquad \text{and} \qquad b \equiv (1-\bar{\xi})\ \left(\frac{\bar{\xi}(1-\bar{\xi})}{g} - 1 \right)$$

Finally, the mean of a thermochemical quantity $\bar{\phi}_k$ ("k" represents the species mass fractions, density, and temperature) at a point in in the turbulent reacting gas is obtained by convolution with the pdf at that point

$$\bar{\phi}_k = \int_0^\infty \int_0^1 \phi_k(\xi,\tau)\ P(\xi,\tau)\ d\xi\ d\tau$$

where $\phi_k(\xi,\tau)$ describes the dependence of ϕ_k on mixture fraction and PSR residence time.

Calculations have been compared with Raman data from three turbulent bluff−body stabilized flames [12]: (i) a non−premixed $CO/H_2/N_2$−air flame, (ii) a non−premixed CH_4/H_2−air flame, and (iii) a premixed CH_4−air flame, with very encouraging results. Here we can review only the first set of these comparisons.

The bluff−body stabilized non−premixed $CO/H_2/N_2$−air flame is shown in Fig. 1. The fuel is a mixture comprised of 27.5%CO/32.3%H_2/40.2%N_2 and air, at a pressure of one atmosphere and an inlet temperature of 300K. The cylindrical axisymmetric bluff body has an outer diameter of 38.1 mm with an axial jet of diameter "d" of 3.18 mm located in the center. It is well known that parts of such flowfields − notably, the annular shear layer shed off the bluff body − can be dominated by unsteady effects. Hence, care was taken to operate in a velocity (jet and coflow) regime where the flame was steady. The cold jet Reynolds number was 12,000, based on the jet diameter and jet exit velocity of 80 m/s. The coflow air velocity is 6.5 m/s. The downstream surface of the bluff body was coated with a thermal barrier material to reduce heat loss. The flame was stabilized by the recirculation zone provided by the bluff body.

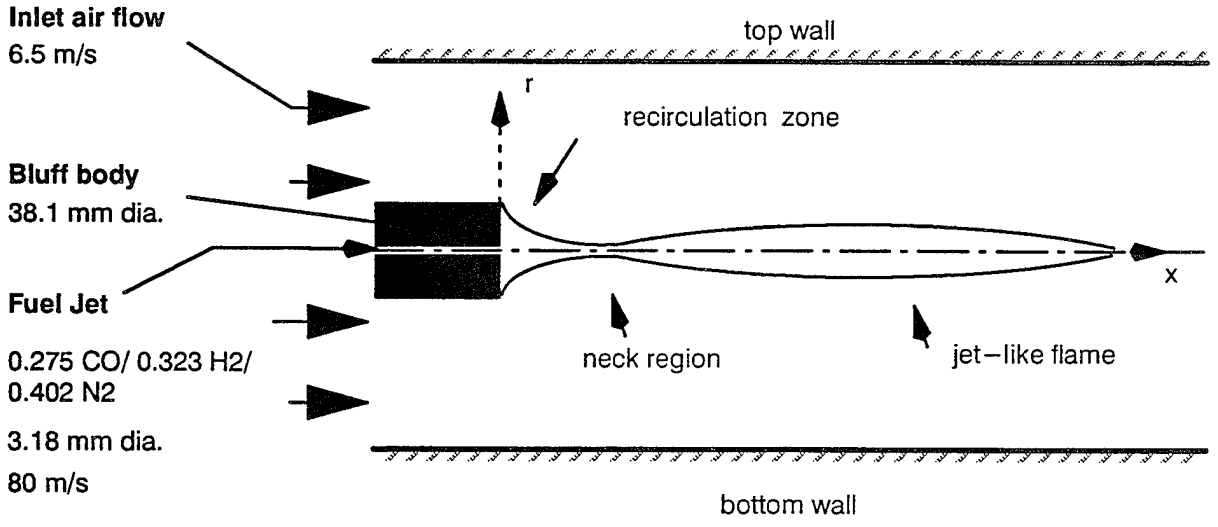

Figure 1. Schematic of the Bluff−Body Stabilized Non−Premixed $CO/H_2/N_2$−Air Flame.

Calculated quantities are compared with Raman data at two axial locations (x/d=10, x/d=20), which are in the highly turbulent part of the flame. Calculated radial profiles of the mean temperature (Fig. 2), the mean mass fraction of CO (Fig. 3), and the mean mass fraction of H_2O (Fig. 4) compare very well with the data, at both locations. The results show the annular shear–layer nature of the flame and the (kinetically–limited) cool fuel–rich nature of the jet core at x/d=10. The profiles become more uniform by x/d=20, as the centerline region starts to burn.

In the other two flames as well, the calculated fields of mean temperature and major species are similar to the data, with quantitative agreement to within 200K or better on mean temperature and to within a factor of two or better even on highly non–equilibrium quantities such as CO in the core of a non–premixed CH_4–air flame or CO and NO in a lean premixed CH_4–air flame.

Based on assessment in three quite different flames, the PSR–microstructure model appears to be adequate for calculating the mean fields, at least, of turbulent flames. Work in progress will assess the accuracy of the calculation of fluctuating quantities.

Kinetic Schemes for Complex Fuels

Since aeropropulsion gas–turbine engines burn fuels such as kerosene, (i) appropriate (full or reduced) kinetic schemes are needed and (ii) combustion models must be able to accomodate the schemes. Ref. 7 describes prior work on a simple three–variable reduced scheme, which has been applied in the context of the 3D CFD/particle–tracking PDF transport approach to a gas–turbine combustor [13].

In the event that full schemes are needed, the PSR–microstructure model described above is capable of including full chemical schemes at the very modest computational cost of *a priori* PSR calculations for the look–up tables in mixture fraction and residence time, followed by k–ε–g flowfield calculations.

REFERENCES

1. Correa, S.M. and Pope, S.B., Twenty–Fourth Symposium (International) on Combustion, The Combustion Institute, Pittsburgh, PA, pp. 279–285, 1992.
2. Correa, S.M., Gulati, A., and Pope, S.B., Twenty–Fifth Symposium (International) on Combustion, The Combustion Institute, Pittsburgh, PA, pp. 1167–1173, 1994.
3. Correa, S.M., *Comb. and Flame,* 93, pp. 41–60, 1993.
4. Correa, S.M. and Braaten, M.E., *Comb. and Flame,* 94, pp. 469–486, 1993.
5. Correa, S.M., *Comb. and Flame,* 103, pp. 194–206, 1995.
6. Correa, S.M. and Dean, A.J., Twenty–Fifth Symposium (International) on Combustion, The Combustion Institute, Pittsburgh, PA, pp. 1293–1299, 1994.
7. Correa, S.M., *J. Prop. Power,* Vol. 11, No. 3, pp. 448–455, May–June, 1995.
8. Peters, N., Twenty–First Symposium (International) on Combustion, The Combustion Institute, Pittsburgh, PA, pp. 1231–1250, 1988.
9. Bilger, R.W., Twenty–Second Symposium (International) on Combustion, The Combustion Institute, Pittsburgh, PA, pp. 475–488, 1988.
10. Liew, S.K., Bray, K.N.C., and Moss, J.B., *Comb. and Flame* 56, pp. 199–213, 1984.
11. Magnussen, B.F., Hjertager, B.H., Olsen, J.G., and Bhaduri, D., Seventeenth Symposium (International) on Combustion, The Combustion Institute, Pittsburgh, PA, pp. 1383–1393, 1979.
12. Hu, I.Z. and Correa, S.M.,"Calculations of Turbulent Flames Using a PSR Microstructural Library," Twenty–Sixth Symposium (International) on Combustion, Naples, Italy, July 28 – August 2, 1996.
13. Tolpadi, A.K., Hu, I.Z., Correa, S.M., and Burrus, D.L.,"Coupled Lagrangian Monte Carlo PDF–CFD Computation of Gas–Turbine Combustor Flow Fields with Finite–Rate Chemistry," 41st ASME Turbo Expo, Birmingham, UK, June 10–13, 1996.

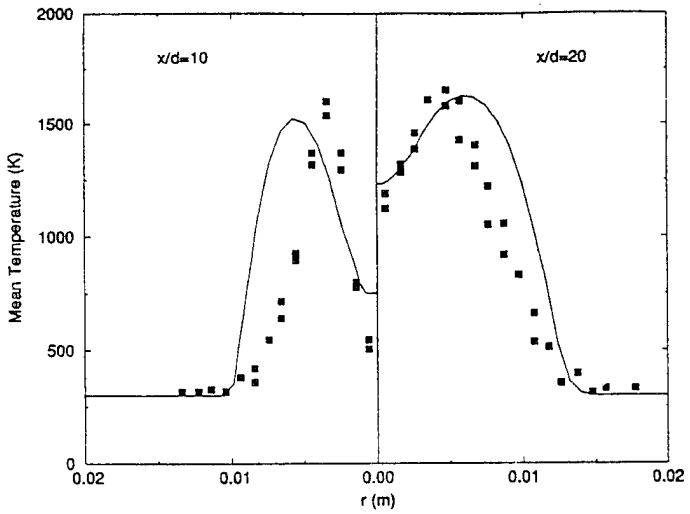

Figure 2. Comparison of calculated mean temperature profiles with Raman data at two axial locations.

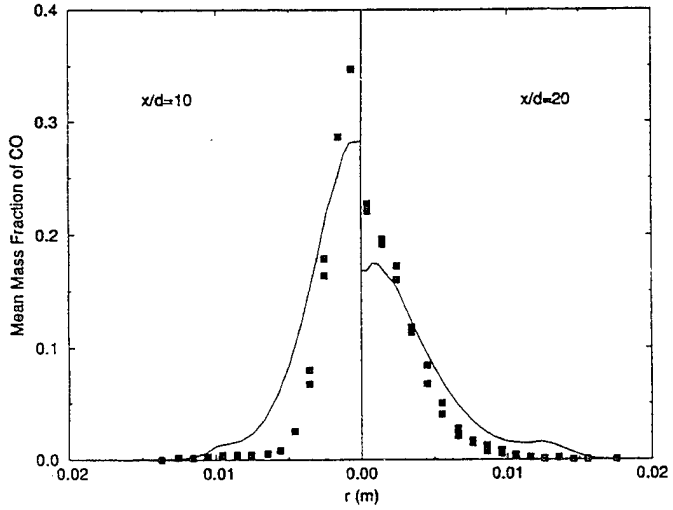

Figure 3. Comparison of calculated mean CO profiles with Raman data at two axial locations.

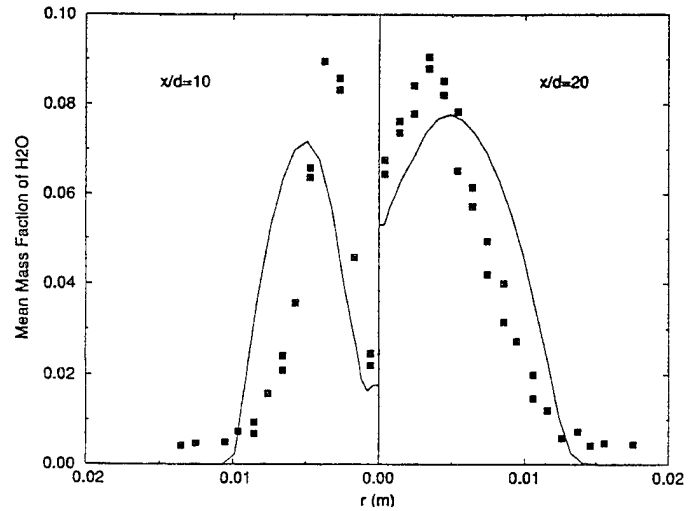

Figure 4. Comparison of calculated mean H_2O profiles with Raman data at two axial locations.

HIGH RESOLUTION MEASUREMENTS OF SUPERSONIC MIXING AND COMBUSTION IN COFLOWING TURBULENT JETS

AFOSR Grant No. F49620-95-1-0115

Werner J.A. Dahm and James F. Driscoll

Gas Dynamics Laboratories
Department of Aerospace Engineering
The University of Michigan
Ann Arbor, MI 48109-2118

Summary/Overview

Supersonic mixing and combustion in coflowing turbulent jets are being investigated and compared with results from compressible mixing layers to identify generic features of supersonic turbulent reacting shear flows. Experiments are used to investigate mixing and combustion in a turbulent fuel jet issuing into a supersonic ($M_\bullet = 2.2$) coflowing air stream with stagnation temperatures as high as 600 K. Results are compared with supersonic turbulent mixing layers under investigation elsewhere to discern changes in large-scale and small-scale structure due to compressibility, and identify consequent effects on mixing and combustion properties. Such comparisons with results from compressible mixing layer studies allow identification of compressibility effects that are common to supersonic combustion in turbulent shear flows from those that are specific to the mixing layer only.

Technical Discussion

Early experiments have been conducted in the supersonic coflowing turbulent jet facility shown in Figure 1 to obtain insights into basic effects of compressibility in jets, and assess their effects on mixing and combustion. These have included nonreacting flows (see Figures 2 and 3) as well as reacting flows (see Figure 3). These studies have shown significant effects of compressibility. The facility is currently being outfitted with a two-dimensional nozzle and jet injector, to allow schlieren imaging of large scale structure. The nozzle and injector designs have been completed and are currently being fabricated. A fast pulsed schlieren system is being retrofitted to allow such imaging studies. The two-dimensional flow follows outer flow scaling laws characterizing the large scale structures that are conceptually similar to those for the present axisymmetric case (see Figure 4). These scaling laws have been documented by Bradbury & Riley (1967) and Everitt & Robins (1978), and will allow for assessment of compressibility effects on the two-dimensional flow.

The parameter that scales compressibility effects in the turbulent shear layer, namely the convective Mach number, does not appear to play the same role in the coflowing jet. At a minimum, the convective Mach number (if its definition is simply interpreted for the jet) would vary with downstream distance, thus rendering compressibility effects that change with position. More importantly, the classical separatrix arguments that lead to the convective Mach number in the shear layers (see Figure 5), do not apply to the coflowing jet (as well as to a wide range of other turbulent shear flows as well). This opens up basic issues as to the proper parameter to scale compressibility effects on most turbulent shear flows. It would appear on this basis that the turbulent shear layer may be only partly representative of most shear flows, and that conclusions drawn from it regarding compressibility effects may not be universal.

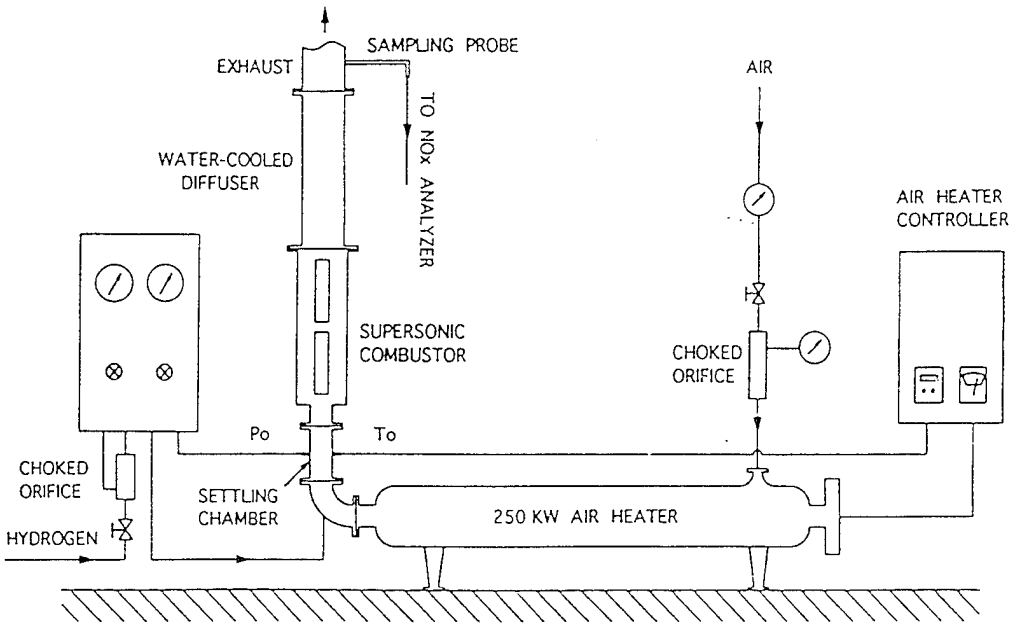

Figure 1. Schematic of the Michigan supersonic turbulent combustion facility, showing major components. Facility has a test section designed for Mach 2.2 airflow at stagnation temperatures up to 600 K and nominal test section pressures of 6.4 atm. Test section is 55 cm long and nominally 5.77 × 4.06 cm in cross section. A 250 kW electric air heater, with length of 5.3 m, is capable of heating up to 1.0 kg/sec of air flow to emperatures as high as 1100K.

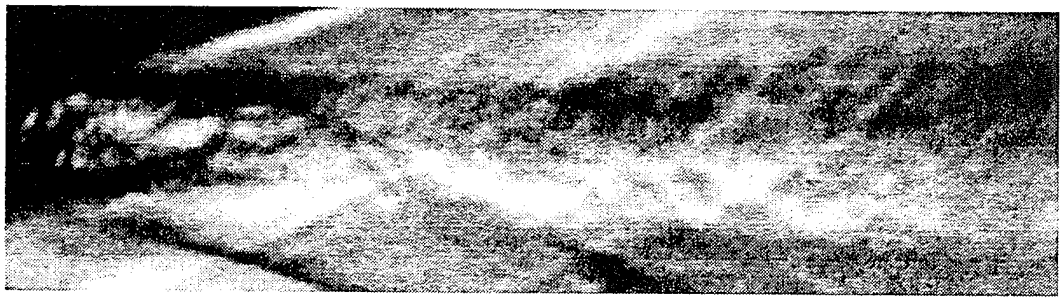

Figure 2. Schlieren image of the nonreacting supersonic axisymmetric turbulent propane jet issuing into a M = 2.2 coflowing air stream. Note the mixing region that is formed, and its growth rate with downstream distance $\delta(x)$. The corresponding two-dimensional flow will show much slower propane concentration decay. Convective Mach number in such a flow decreases with x. As noted in Figure 5, the case for convective Mach number based on separatrix arguments fails in this type of flow.

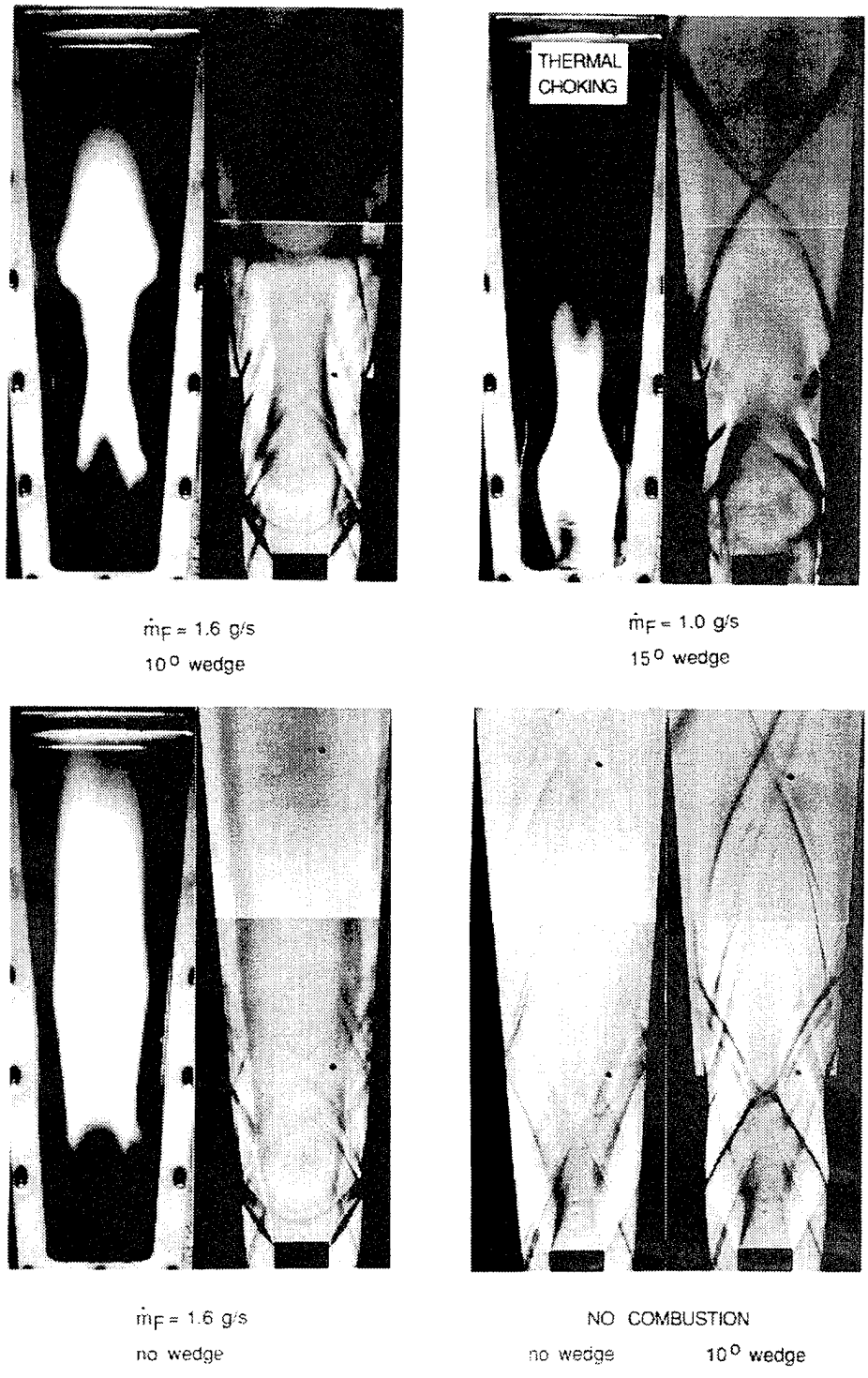

Figure 3. Direct and schlieren photographs of supersonic jet-like flames with and without interacting shock waves. Hydrogen mass flowrate is varied from 0.4 to 1.4 g/s. Shock waves generated by wedges on the sidewalls interact with the flow to produce significant effects on the reacting flows. Window height is 30.5 cm (12 in.), and distances in the schlieren images are 20% larger than in the direct images.

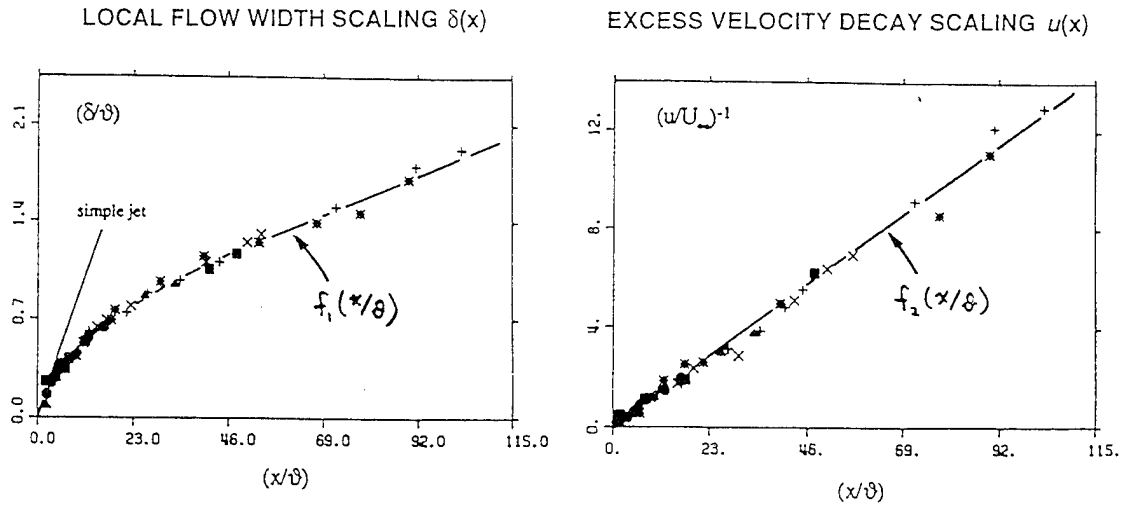

Figure 4. The outer flow scaling laws for the flow width $(\delta/\vartheta) \sim f_1(x/\vartheta)$ and centerline velocity decay $(u/U_\infty)^{-1} \sim f_2(x/\vartheta)$ for the incompressible limit of axisymmetric coflowing turbulent jets as given by Maczynski (1962) and verified experimentally by Biringen (1975), Reichardt (1965), Bradbury & Riley (1967), Everitt & Robins (1978), and more recently over a wide range of (x/ϑ) by Nickels & Perry (1996).

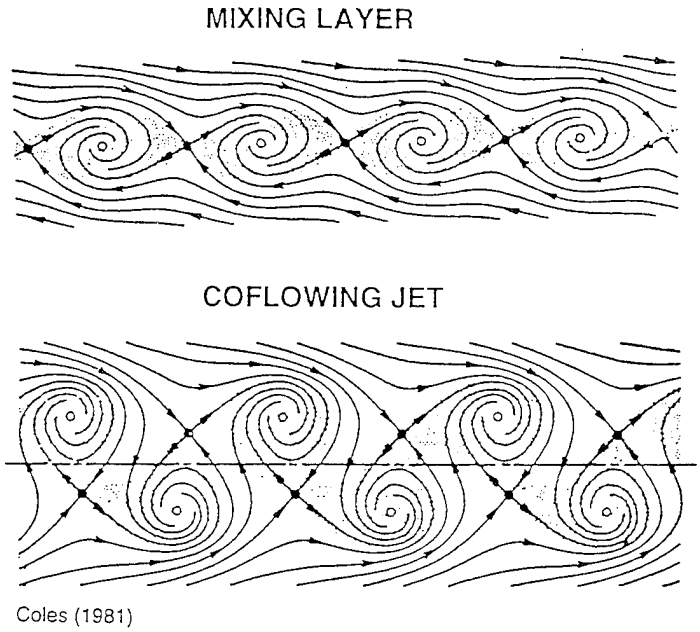

Figure 5. Comparison of separatrix topologies for the shear layers and the coflowing jet. In the former, arguments based on matching total pressures at the local stagnation points lead naturally to the convective Mach number as a controlling parameter. However, in the jet, similar separatrix arguments fail, since both streamlines originate from the same stream. Moreover, even if the definitin of the convective Mach number is extended to the jet, it must, at a minimum, vary with downstream distance x, unlike in the shear layer.

CHEMICAL REACTIONS in TURBULENT MIXING FLOWS

AFOSR Grant F49620–94–1–0353

P. E. Dimotakis and A. Leonard

Graduate Aeronautical Laboratories
California Institute of Technology, Pasadena, CA 91125

Summary/Overview

The purpose of this research is fundamental investigations of mixing, chemical reaction, and combustion processes; in turbulent, subsonic, and supersonic free-shear flows. The program is comprised of an experimental effort; an analytical, modeling, and computational effort; and a diagnostics and data-acquisition development effort, as dictated by the specific needs of the experimental effort. The computational studies are focused on fundamental issues pertaining to the numerical simulation of compressible flows with strong fronts, in both chemically-reacting and nonreacting flows. Parts of this effort are cosponsored by AFOSR URI Grant No. F49620–93–1–0338.

Technical discussion

Chemically-reacting runs in the Supersonic Shear Layer (S^3L) Facility were resumed in June 1995. These runs, along with further preliminaries in November 1995, resulted in upgrades and modifications to the facility-control software and the facility test section. After these modifications, a new series of runs, beginning in late December 1995, are producing archival data on Reynolds number and Mach number effects in high-speed shear-layer mixing. The new data are bridging the gap in Reynolds number between the previous subsonic-flow regime and the previous, chemically-reacting, supersonic-flow data.[1–3] A set of experiments is also in progress, at the same conditions, to provide an independent experimental assessment of differential-diffusion effects.

As part of a continuing effort to understand the behavior of compressible, turbulent, mixing-layer flows, we have investigated a moderate-compressibility ($M_c \approx 0.5$) in a bi-subsonic ($M_1, M_2 < 1$) flow, shown in Fig. 1. A downstream-traveling, turbulent-structure-generated (oblique) pressure wave system is observed in the bottom (low-speed) freestream. These waves are the signature of supersonic disturbances in

an all-subsonic flow. An upstream-traveling normal (vertical) wave system is also evident in this schlieren realization, characteristic of a downstream-to-upstream feedback mechanism in the flow. Additionally, the growth rate of this mixing layer is substantially reduced with respect to that of the incompressible mixing layer with the same density and velocity ratios. Significantly, the large-scale, quasi-two-dimensional structures commonly associated with incompressible mixing-layer flows are also evident in this visualization. A preliminary report of this work was made in the November 1995 APS/DFD meeting.[4]

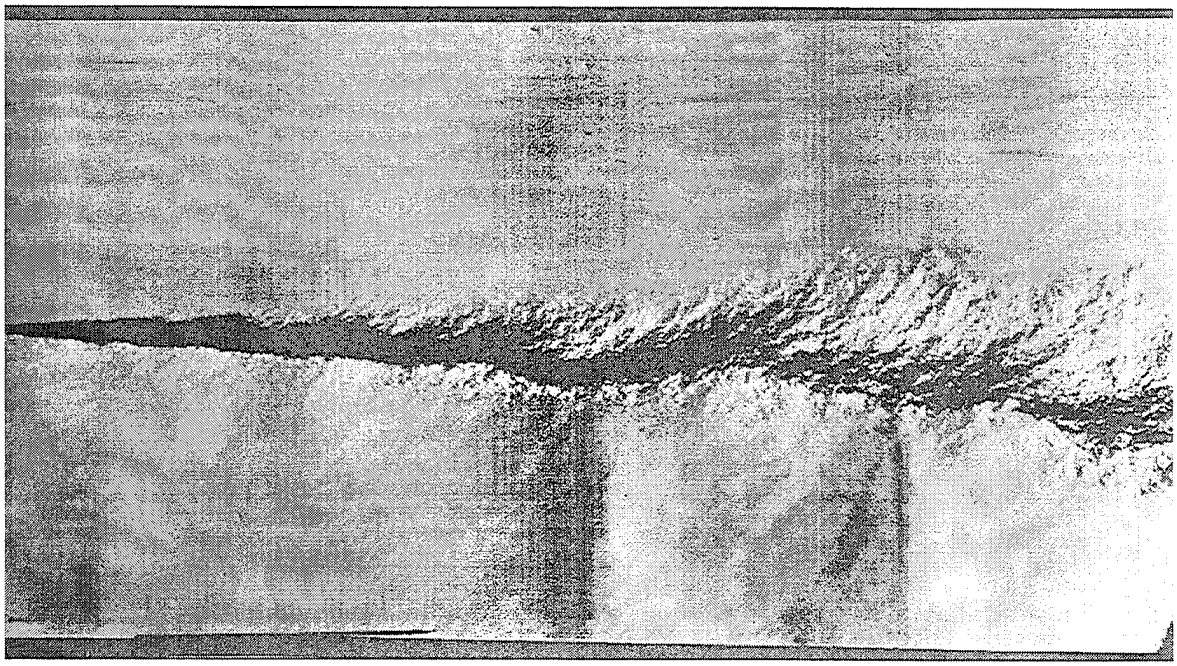

FIG. 1 Schlieren (vertical cutoff) photograph of $M_1 = 0.9\,[\mathrm{He}]$, $M_2 = 0.6\,[\mathrm{C_2H_4/N_2}]$ (nominal nozzle-exit conditions) mixing-layer flow.

We have obtained a new set of high signal-to-noise ratio digital image slices in high-speed mixing layers, in the $\mathrm{S^3L}$ Facility, from low-compressibility ($M_c = 0.15$) to high-compressibility ($M_c = 0.95$) conditions, using a newly-developed, thinned, back-illuminated $1,024^2$ pixel CCD-array with a quantum efficiency close to 75% at 532 nm, fabricated by Scientific Imaging Technologies, Inc. (SITe), and installed in a Princeton Instruments camera system. Our data indicate a progressive dependence of the flow structure and wave interactions on increases in the convective Mach number.

The structure of the scalar field in the turbulent mixing of liquid-phase turbulent jets has been analyzed in the Reynolds number range, $4.5 \times 10^3 \leq Re \leq 18 \times 10^3$. Specifically, 2-D, spatial images of the jet-fluid concentration, measured in the far field ($z/d = 275$) using laser-induced techniques, have been analyzed in terms of both scalar-field and scalar-isosurface measures. Re effects are found for the scalar field as well as for the geometry of the scalar isosurfaces, with the latter also exhibiting scalar-threshold effects.[5] The behavior of such surfaces is important in hydrocarbon combustion, for example, which proceeds on the unsteady, stoichiometric surface, *i.e.*, the instantaneous surface on which the jet-fluid concentration is at the stoichiometric-mixture ratio. The Re behavior we have found is consistent with a previously-documented mixing transition, observed in several turbulent flows, at $Re \approx 10^4$ (*e.g.* Ref. 6). The geometry of the isosurfaces has been quantified in terms of scale-dependent-fractal (SDF) geometry, *i.e.*, the scale-dependent extension of the original (power-law) fractal (PLF) ideas, and found to have a SDF dimension that increases smoothly with scale.[5] This SDF geometry has also been connected to the distribution of scales, for complex geometries in general, and has been used to compute the distribution of the sizes of the largest regions in the jet far field that are not visited by the isosurfaces. Further analysis of the isosurfaces, in terms of area-perimeter measures of individual (island/lake) contours, indicates a lognormal distribution of size and a power-law distribution of shape complexity, with values of the latter that increase with size.[7]

We report on further developments of the Image Correlation Velocimetry (ICV) method.[8] The robusteness of ICV solutions has been partially quantified using images degraded with intentionally-added random noise. Modifications involving a B-spline representation of the velocity field allow better handling of complex, curved bounding surfaces of the flow field. A test case application of ICV investigating unsteady (ramp-start) flow over a NACA-0012 airfoil shows the ability of the method to determine the large-scale characteristics of the flow including shed vortices, while simultaneously capturing the development of the boundary layer and separation along the airfoil surface.[9]

As part of our computational effort, we have completed a numerical investigation of unsteady, one-dimensional detonation waves, using our new, unsplit algorithm developed last year. This algorithm is the first effort to integrate all the terms of the governing equations in a single, fully-coupled and nonlinear, step. The numerical tests performed on detonation problems clearly demonstrate the accuracy and robustness of the new scheme. The limiting behavior of detonations at the Chapman-Jougouet point was also investigated. Recently published results, ob-

tained with conventional numerical schemes, predict quenching of the detonation front. Our results, however, suggest a very unstable and chaotic behavior.[10]

This algorithm has been generalized to multidimensional, chemically-reacting flows, and we implemented this algorithm in a FORTRAN code. The implementation was performed in a modular way, so that the code is able to run under the AMRITA environment, developed by Dr. James Quirk, that performs Adaptive Mesh Refinement of the computational domain. Currently, numerical simulations are in progress on two-dimensional, unsteady detonations.

References

[1] Hall, J. L., *An Experimental Investigation of Structure, Mixing and Combustion in Compressible Turbulent Shear Layers*, Ph.D. thesis, California Institute of Technology (1991).

[2] Hall, J. L., Dimotakis, P. E., and Rosemann, H., "Some measurements of molecular mixing in compressible turbulent mixing layers," *AIAA 22nd Fluid Dynamics, Plasma Dynamics and Lasers Conference*, Paper 91–1719 (1991).

[3] Dimotakis, P. E., "Turbulent Free Shear Layer Mixing and Combustion," *High Speed Flight Propulsion Systems*, in *Progress in Astronautics and Aeronautics* **137**, Ch. 5, 265–340 (1991).

[4] Slessor, M. D., and Dimotakis, P. E., "Some new compressible mixing-layer experiments," *Bull. Am. Phys. Soc.* **40**(12), 1975 (1995).

[5] Catrakis, H. J., and Dimotakis, P. E., "Mixing in turbulent jets: scalar measures and isosurface geometry," *J. Fluid Mech.* , to appear (1996).

[6] Dimotakis, P. E., "Some issues on turbulent mixing and turbulence," GALCIT Report FM93–1a (1993).

[7] Catrakis, H. J., and Dimotakis, P. E., "Perimeter and area of isoscalar contours," *Bull. Am. Phys. Soc.* **40**(12), 1936 (1995).

[8] Tokumaru, P. T., and Dimotakis, P. E., "Image Correlation Velocimetry," *Exps. in Fluids* **19**(1), 1–15 (1995).

[9] Gornowicz, G. G., and Dimotakis, P. E., "Continuous-field image correlation velocimetry," *Bull. Am. Phys. Soc.* **40**(12), 2000 (1995).

[10] Papalexandris, M. V., Leonard, A., and Dimotakis, P. E., "Unsplit Schemes for Hyperbolic Conservatin Laws with Source terms in One Space Dimension," California Institute of Technology, GALCIT Report FM96–1 (1996).

STUDIES ON HIGH PRESSURE AND UNSTEADY FLAME PHENOMENA

(AFOSR Grant No. F49620-95-1-0092)

Principal Investigator: Chung K. Law

Princeton University
Princeton, NJ 08544

SUMMARY/OVERVIEW

The objective of the present program is to study the structure and response of steady and unsteady laminar premixed and nonpremixed flames in reduced and elevated pressure environments through (a) non-intrusive experimentation, (b) computational simulation using detailed flame and kinetic codes, and (c) asymptotic analysis with reduced kinetic mechanisms. During the reporting period progress has been made in the following projects: (1) An analytical computational, and experimental study of unsteady diffusion flames. (2) An experimental study of the effects of pressure on the extinction of counterflow nonpremixed hydrogen-air flames. (3) A further experimental and computational study on the effect of thermophoresis on the seeding particles in LDV measurements of flames.

TECHNICAL DISCUSSIONS

1. Studies on Unsteady Diffusion Flames

The effect of unsteadiness of the environment on the flame behavior is of particular relevance to the modeling of turbulent flames through the concept of laminar flamelets. These flamelets are subject to fluctuating flows with various intensities of straining, and it is reasonable to expect that the flame would respond differently in an oscillating strained flow field than in a steady strained flow field.

Regarding contributions during the reporting period, we first note that the phenomenon of flame extinction under an imposed oscillatory strain rate has not been experimentally studied in a systematic manner. For instance, for the limited experimental studies conducted previously, effects of frequency and amplitude of the perturbations were not separately identified. We have therefore designed and conducted our experiments in such a manner that the separate influences of frequency and amplitude were identified. The investigation was also conducted over a substantially extended range in frequency and amplitude than previous experiments. A speaker-driven counterflow apparatus was used to investigate the effects of sinusoidal velocity perturbation on the extinction response of diffusion flames of nitrogen-diluted methane versus air. The speaker signal was synchronized with the LDV measurement interval through a system consisting of an optical chopper, a phase delay unit, a lock-in amplifier for producing a phase-locked sine wave, and an amplifier for the speakers. In order to quantify the oscillation properties (mean and amplitude) at the extinction condition as a function of position throughout the flow field, various "phase-resolved" methods were developed that could measure the entire cycle of the oscillation of the flow velocity, from which the maximum and minimum strain rates could be determined.

Computationally, the phenomena of interest were simulated with detailed descriptions of chemistry and transport. Moreover, we note that previous theoretical studies have been mainly concerned with the effect of frequency variation on the flame response, with the amplitude of perturbation mostly restricted to small values. Since large amplitude oscillation do exist in practical flames, and since the extinction of a fairly strong flame requires the imposition of substantial perturbation, we have computationally studied the influence of such large amplitude perturbations

on flame extinction, and consequently demonstrated their strong coupling with the perturbation frequency. Studies of large amplitude perturbations are particularly suitable for computational simulation in that they are not always readily amenable to analysis.

For the experimental quantification of the flow field under oscillation, we have found that, over the course of one cycle, the fluctuation of the local strain rate is nearly sinusoidal with the flow perturbation. For low frequency, small amplitude oscillations, the instantaneous oscillating velocity profile was found to be similar in appearance to the unperturbed steady-state profile, as shown in Fig. 1. However, with increases in either frequency or amplitude, noticeable lag develops between the imposition of the perturbation at the nozzle and the response of the flow further downstream, as shown in Fig. 2. Thus the use of the potential flow solution for the outer, hydrodynamic velocity field could be inadequate in that the flow might not respond instantaneously to the imposed velocity oscillation.

For flame extinction, we have computationally shown in Fig. 3 that at low frequencies, extinction behaves quasi-steadily in that the (maximum) extinction strain rate is mostly independent of the mean strain rate, and is only slightly larger than the steady-state extinction strain rate. As the frequency increases, increasingly larger amplitudes are needed to extinguish an initially strongly burning flame. However, if the flame is initially already close to extinction, then the extinction strain rates are again close to the steady-state value even for high frequency situations. Experimentally, we have verified the computational results of quasi-steadiness for low frequency oscillations as well as for near-extinction flames subjected to high frequency oscillations, as shown in Fig. 4. The above results are reported in Publication No. 1.

An analytical study was also conducted for the response of counterflow premixed flames subject to oscillating strain rates. Results suggest the possibility of a wide spectrum of unsteady flame characteristics depending on the mixture Lewis number, and that extinction can be delayed when the strain rate oscillates about the static extinction point. Thus the laminar flamelet regime of turbulent combustion may be broader than predicted by steady analysis. This work is reported in Publication No. 2.

2. Experimental Investigation of the Effects of Pressure on Flame Extinction

In our computational study on the effects of pressure and dilution on the extinction of counterflow nonpremixed hydrogen-air flames reported last year, the variation of the density-weighted strain rate with pressure for a diluted hydrogen mixture was found to initially increase rapidly with pressure, indicating the increase in the burning intensity, then decrease at some pressure (say 7 atm), and eventually increase again. Consequently, for a given density-weighted strain rate, increasing pressure from a low value will bring the system from a state of extinction, to burning, to extinction again, and to burning again. This nonmonotonic pressure dependence is due to the competition between chain branching and termination reactions as observed for the well-known homogeneous hydrogen-oxygen explosion limits.

It is of fundamental importance to experimentally scrutinize the above computational results. Furthermore, since previous experimental extinction data were mostly based on global parameters, there exists considerable uncertainty in comparing these data with results from computational studies based on local strain rates. Therefore, it is essential to obtain well-defined, benchmark experimental data on hydrogen-air flame extinction based on local measurements. Comparisons of these experimental data with results obtained from computational simulations utilizing detailed chemistry and transport properties are then appropriate and meaningful.

Preliminary experimental results of extinction strain rate and density-weighted extinction strain rate as a function of pressure are shown in Figs. 5 and 6, respectively, for 12 and 13% hydrogen-nitrogen mixtures impinging onto an air stream. The density is chosen as the exit air density. It is seen that while the extinction strain rate monotonically decreases with increasing pressure, the density-weighted extinction strain rate indeed exhibits a nonmonotonic behavior. The final increase was not observed because of the present experimental limitation. The above result

nevertheless partially substantiates the nonmonotonic response of the density-weighted extinction strain rate to pressure variations.

3. Further Studies on Effects of Thermophoresis on LDV Seeding Particles in Flames

In a previous study of ours reported last year, we demonstrated experimentally and computationally for laminar premixed flames that the thermophoretic force acting on the seeding particles in LDV measurements of flow velocities can be substantial in the flame region characterized by large temperature gradients. If uncorrected, such a biasing can cause erroneous interpretation of the dynamic as well as the scalar flame structure. We have now extended the study to diffusion flames in which the directions of the thermophoretic force and convection are parallel to each on one side of the flame but anti-parallel on the other. The resulting LDV-measured velocity structure is therefore very rich. The velocity profile becomes more peculiar as the flame is located closer to the stagnation surface. When the flame is coincident with the stagnation surface, a humpless velocity profile and a wider particle-free zone are observed. The study again emphasizes the importance of thermophoresis and the need to account of it in the study of flame structures, both laminar and turbulent. This work is reported in Publication No. 3.

4. A Continuation Method in Generating S-Curves with Detailed Chemistry

The intrinsically-nonlinear nature of combustion phenomena is best demonstrated by the occurrence of the S-shaped ignition-extinction response curves. Computationally such curves are very difficult to be generated. especially if complex chemistry is to be included, because of the presence of infinite gradients at the turning points. In this study we proposed a new numerical technique which is shown to be very efficient in generating such curves. The work is reported in Publication No 4.

5. Review Activities

Two review articles were prepared. In the first (Publication No. 5), the role of chain mechanisms in some fundamental combustion phenomena are discussed. The emphasis is on the intrinsic coupling between chain mechanism and transport processes in order to successfully explain some well-known combustion phenomena.

The second (Publication No. 6) reviews recent advances in the description of the dynamics and geometry of surfaces of premixed flames under the influence of stretch, as manifested by the aerodynamic straining, flame curvature, and flame/flow unsteadiness. Discussions are conducted at both the aerodynamic, flame-sheet scale and the transport-affected, reaction-sheet scale.

MAJOR PUBLICATIONS (April, 1995 – March, 1996)

1. "Extinction of counterflow diffusion flames under velocity oscillations," by J.S. Kistler, C.J. Sung, T. G. Kreutz, C.K. Law and M. Nishioka, *Twenty-Sixth Symposium (International) on Combustion* , in press.
2. "Counterflow diffusion flames with unsteady strain rates," by H.G. Im, J.K. Bechtold and C.K. Law, *Combustion Science and Technology*, Vol. 106, pp. 345-361 (1995).
3. "Further studies on effects of thermophoresis on seeding particles in measurements of strained flames," by C.J. Sung, J.S. Kistler, M. Nishioka and C.K. Law, *Combustion and Flame*, Vol. 105, pp. 189-201 (1996).
4. "A flame controlling continuation method for generating S-curve responses with detailed chemistry," by M. Nishioka, C.K. Law and T. Takeno, *Combustion and Flame*, Vol. 104, pp. 328-342 (1996).
5. "The role of chain mechanisms in some fundamental combustion phenomena," by C.K. Law, *Physical and Chemical Aspects of Combustion*, in press.
6. "On the aerodynamics of flame surfaces," by C.K. Law, C.J. Sung and C.J. Sun, Annual Review of Heat Transfer, Vol. VIII, in press.

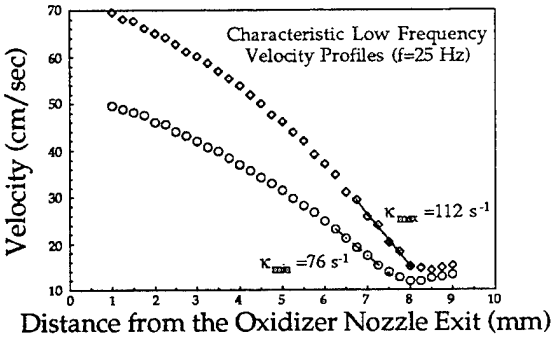

Figure 1

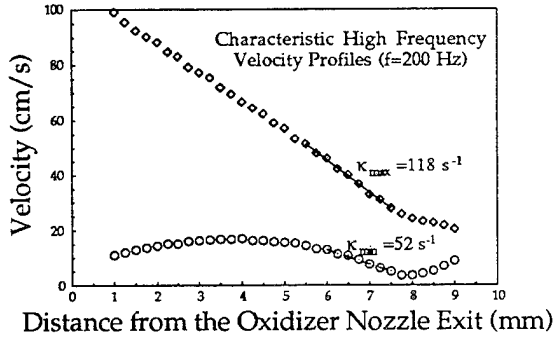

Figure 2

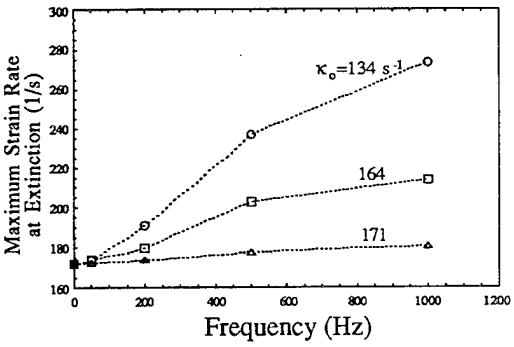

Figure 3

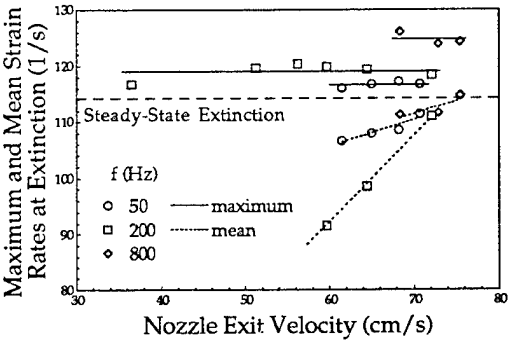

Figure 4

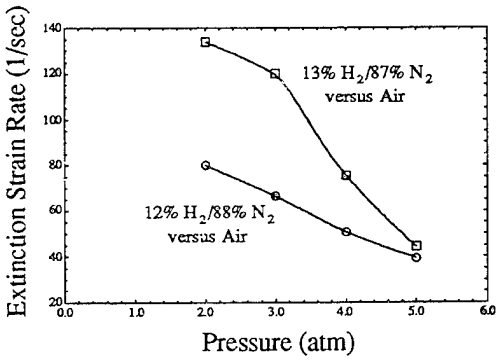

Figure 5

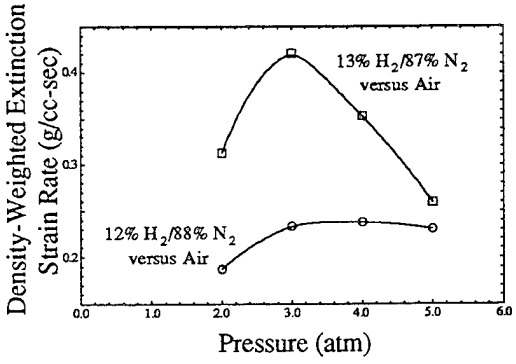

Figure 6

TWO- AND THREE-DIMENSIONAL MEASUREMENTS IN FLAMES

AFOSR Grant No. 94-1-0135
Co-Principal Investigator: Marshall B. Long

Yale University
Department of Mechanical Engineering and Center for Laser Diagnostics
New Haven, Connecticut 06520-8284

SUMMARY/OVERVIEW

Laser-based imaging techniques are being developed and applied to the study of turbulent reacting flows. These techniques incorporate a variety of light scattering mechanisms to allow the measurement of the spatial distributions of quantities such as temperature, species concentration, velocity, and mixture fraction. The data provided by these measurements can afford a better understanding of the interaction of turbulence and chemistry in turbulent flames and thus aid in the modeling of this interaction. During the past year, a new set of experiments in highly turbulent premixed flames was initiated in which temperature, progress variable, and OH mass fraction are measured simultaneously.[1] In addition, we have continued to analyze and present the results from our mixture fraction imaging experiments in nonpremixed flames.[2-5]

TECHNICAL DISCUSSION

A new set of experiments in highly turbulent premixed flames was initiated within the past year. There is currently a need for quantitative, three-dimensional measurements in premixed flames to assess the applicability of flamelet modeling approaches as well as to advance other modeling techniques such as conditional moment closure (CMC) methods. To be of most use to modelers, the scalar data must be of sufficient quality to allow calculation of three-dimensional gradients (and thus scalar dissipation).

The current experiment involves the simultaneous measurement of Rayleigh scattering from two parallel laser sheets, as well as OH fluorescence from a third laser sheet located between the other two (see Fig. 1). The laser illumination sheets for the Rayleigh measurements (beam energies of 250 and 325 mJ, 10 ns nominal pulse duration) are provided by two separate frequency doubled Nd:YAG lasers. The laser pulses were separated temporally by 0.8 μs. The Rayleigh signals were collected by a single camera lens, separated into parts by a 50/50 pellicle beam splitter, and each part was focused with a separate camera lens onto an image intensifier. The intensifiers were optically coupled to two cooled CCD detectors. Cross talk between the Rayleigh signals from the two different sheets was eliminated by gating one intensifier to correspond to the first laser pulse and the second intensifier coincident with the second. The 200 ns gate times used on the intensifiers were sufficiently small to eliminate luminosity from the recorded signals. Since the accuracy of the cross-sheet component of the gradient is critically dependent on accurate measurement of the separation between sheets, a portion of the laser beams was split off and focused onto a

separate unintensified CCD detector. The image from this detector gives a shot-to-shot monitor of the sheet spacing (typically 200 μm) as well as the beam intensity profile.

The OH fluorescence required a third uv laser beam at 283.2 nm (1.6 mJ/pulse) corresponding to the $Q_1(7)$ transition of the OH $A^2\Sigma$-$X^2\Pi$ (1,0) system. The uv beam was introduced just above the Nd:YAG beams at an angle such that all sheets overlapped in the imaged region. The OH fluorescence was isolated by an interference filter (313 nm peak transmission, 12 nm FWHM) and imaged onto another intensified CCD detector with a pair of fused silica lenses. A portion of the uv beam was split off and passed through the post-flame zone of a laminar premixed flame. The OH fluorescence from this reference burner was separated with a second interference filter and focused onto a photomultiplier. The resulting signal served as a monitor of the energy of the uv beam and was used to ensure that the wavelength did not drift from the center of the fluorescence transition. The combination of the Rayleigh and OH fluorescence signals in the experiment allowed determination of temperature, progress variable, scalar dissipation, and hydroxyl mass fraction within the imaged region. Spatial resolution within the sheet was < 100 μm.

The premixed flame investigated consisted of a 38 mm diameter Bunsen burner with an annular pilot, which was able to stabilize turbulent flames over a wide range of equivalence ratios ($\Phi_{min} < 0.6$). Turbulence was generated by a plate in the approach flow in which 4 mm holes were drilled at 10 mm spacing. Figure 2 shows images obtained from two different laser shots. Each set of images consists of two Rayleigh images (from sheets separated by ~200 μm) and an OH image from a third uv sheet between the two Rayleigh sheets. For the images shown, the flame had an equivalence ratio, $\Phi = 0.60$. The imaged region covers an area of 17 x 5 mm^2, located 30 mm downstream from the burner exit (see inset in Fig. 1).

Preliminary analysis of the results shows several unusual features. The gradients of the temperature and OH mass fraction at the flame front are substantially lower than predicted by theory. Increasing the turbulence and decreasing the equivalence ratio below stoichiometric further reduces the gradients. In the most turbulent flames, there is substantial OH present at temperatures below 1000K. In addition, there appears to be a correlation between flame front curvature, low gradients, and OH at low temperature. An abstract has been submitted for a work-in-progress poster session at the 26th International Symposium on Combustion in Naples, Italy[1] and further analysis of the data is planned.

A second focus area during the current funding period has been to continue our work on mixture fraction imaging in turbulent nonpremixed flames. The mixture fraction and its gradient are important parameters in the modeling of turbulent nonpremixed flames, and the experimental determination of mixture fraction over a wide field is essential for testing these models. Since 1992, we have been collaborating with Dr. Sten Stårner and Prof. Robert Bilger at the University of Sydney to develop and apply a two-scalar approach to mixture fraction imaging. The method assumes unity Lewis number and a simplified one-step reaction between fuel and oxidizer. It has been shown that the measurement of fuel concentration and Rayleigh scattering is sufficient to determine the mixture fraction.

One of the systems that is amenable to study using mixture fraction imaging is the classical lifted flame of a turbulent methane jet. Of particular interest is the nature of the stabilization mechanism at the base of the lifted flame, which is neither that of simple diffusion flamelets or of a simple premixed stoichiometric flame front. The flame base propagates into a classical turbulent jet where the fuel mass fraction is a conserved scalar whose structure is well known. There is in such a jet a continuous, distorted contour of stoichiometric mixture, surrounded on each side by a layer of varying thickness, containing all the flammable mixture. It is along this contour that the flame must necessarily propagate, at a

rate which varies locally with the mixture fraction gradient, as well as other parameters such as fluid dynamic strain and curvature.

A series of experiments was performed in a lifted methane flame in which the mixture fraction and temperature were imaged in the region of flame stabilization. The methane fuel jet issued from a nozzle of diameter 6.1 mm into a filtered, vertical, coflowing 0.1 m/s air stream, at Reynolds number Re = 3,000. The lift-off height was approximately 10 cm. The mixture fraction was measured using a novel intra-cavity technique, in which the laser sheet was formed within the laser cavity of a flashlamp-pumped dye laser. This configuration resulted in a sheet energy of roughly five times that of a more conventional setup. The scattered Raman and Rayleigh light were detected with two intensified CCD cameras located on opposite sides of the laser sheet. The images obtained were then transferred to a computer for storage and processing. Once in the computer, the two images were scaled, rotated and cropped to allow comparison on a pixel-by-pixel basis. After this matching, each pixel corresponded to a volume of 0.06 x 0.06 x 0.56 mm^3, with the largest value being the sheet thickness. In order to further increase the signal/noise ratio in the Raman data, some degree of smoothing is desirable. Because the Raman and Rayleigh images are highly correlated in the regions where the Raman signal is non-zero, the Rayleigh image can be used to optimize the smoothing of the Raman image. By performing smoothing of the Raman image along constant intensity contours derived from the Rayleigh image, we have shown that it is possible to increase the signal/noise by a factor of 10, while retaining the gradient information.[3]

Analysis of mixture fraction and temperature images showed features at the flame base that were intermediate between premixed and diffusion flame structure. Strong mixture fraction gradients indicated that the flame propagation rate into the unburnt mixture may be several times that of the premixed flame speed into a homogeneous fuel mix. Results of the study have been accepted for publication in Combustion and Flame.[4]

REFERENCES

1. S.H. Stårner, R.W. Bilger, D.F. Marran, and M.B. Long, "Simultaneous High Resolution Measurements of Temperature, Progress Variable and OH Mass Fraction in a Highly Turbulent Premixed Flame," Abstract submitted for poster session at the 26th Symposium (International) on Combustion, Naples, Italy (1996).
2. J.H. Frank, K.M. Lyons, and M.B. Long, "Simultaneous Scalar/Velocity Field Measurements in Turbulent Gas-Phase Flows," *Combust. Flame* (in press).
3. S.H. Stårner, R.W. Bilger, and M.B. Long, "A Method for Contour-Aligned Smoothing of Joint 2D Scalar Images in Turbulent Flames," *Combust. Sci. Tech.* **107**, 195 (1995).
4. S.H. Stårner, R.W. Bilger, J.H. Frank, D.F. Marran, and M.B. Long, "Mixture Fraction Imaging in a Lifted Methane Jet Flame," *Combust. Flame* (in press).
5. S.H. Stårner, R.W. Bilger, J.H. Frank, D.F. Marran, and M.B. Long, "Measurements of Mixture Fraction and Scalar Dissipation in a Turbulent Hydrogen Diffusion Flame," paper presented at the 15th International Colloquium on the Dynamics of Explosions and Reactive Systems, University of Colorado, Boulder, CO, July 30 - August 4 (1995).

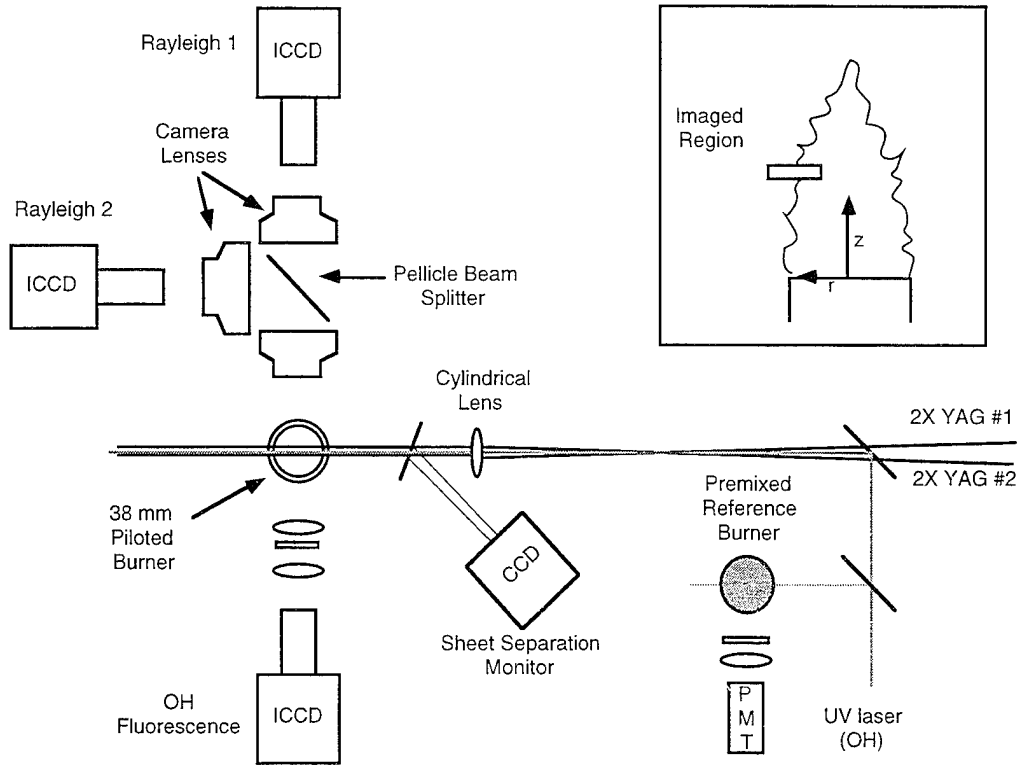

Figure 1. The experimental configuration used for the simultaneous measurement of Rayleigh scattering from two parallel laser sheets, as well as OH fluorescence from a third laser sheet located between the other two.

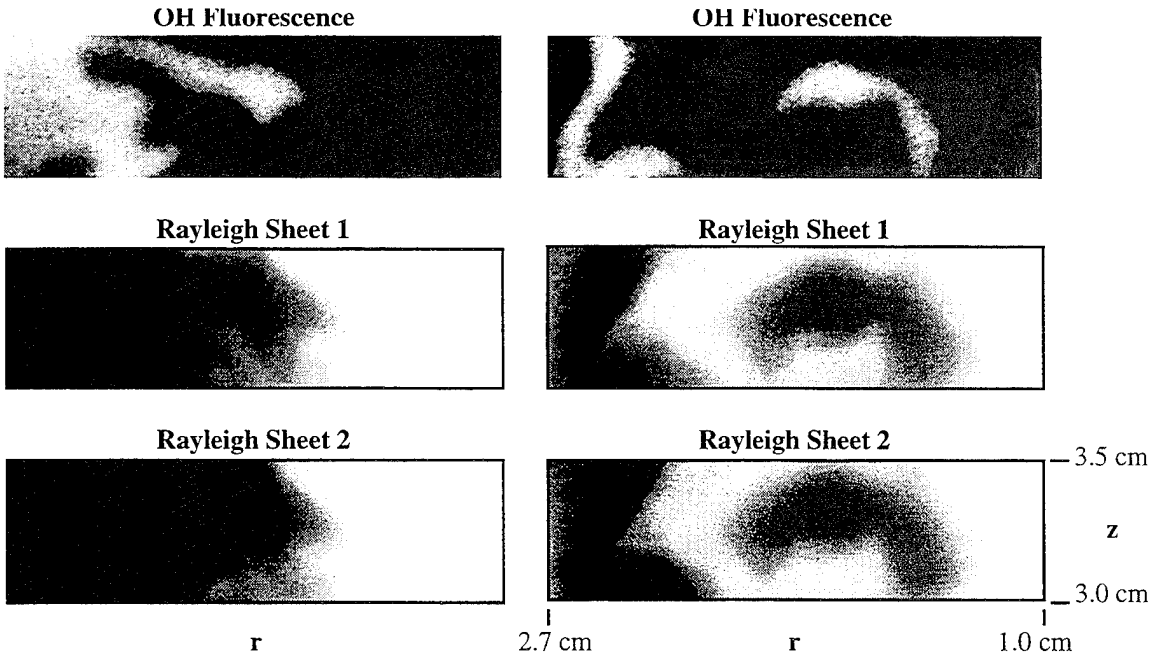

Figure 2. Experimental results obtained from a turbulent premixed flame using the experimental configuration shown in Fig. 1. The Rayleigh images are used to determine the temperature, progress variable, and scalar dissipation; the OH fluorescence (along with the Rayleigh images) gives the OH mass fraction. The equivalence ratio for these shots was $\Phi = 0.6$.

MODELLING MIXING AND REACTION IN TURBULENT COMBUSTION

AFOSR Grant F-49620-94-1-0098

Principal Investigator: S. B. Pope
Mechanical & Aerospace Engineering
Cornell University
Ithaca, NY 14853

SUMMARY

The overall objective of the research project is to develop, test and demonstrate a combined methodology for modelling turbulent combustion. The method is based on the solution—by a particle/Monte Carlo method—of a modelled transport equation for the joint probability density function (PDF) of velocity, turbulence frequency, and thermochemical composition. Progress on different aspects of the work are described in the following sections. Of particular note is the demonstration of the capabilities of the EMST mixing model in application to piloted jet diffusion flames.

RAPID PRESSURE MODELLING

In simple laboratory jet flames, the $k - \varepsilon$ turbulence model may provide an adequate representation of the turbulence. But it is widely appreciated that for the complex flow fields encountered in engineering applications such an eddy viscosity approach is inadequate. Higher levels of closure are required, such as a Reynolds stress model or a velocity-PDF model.

In the higher-level models, a primary quantity to be modelled is the effect of the fluctuating pressure gradient. In the PDF context we have developed a model for pressure fluctuations that is exact in the limit of rapid distortions (Pope & Van Slooten 1995, Van Slooten & Pope 1995). This model has now been extended to the "slow" pressure also, and has been tested for homogeneous turbulence (see Fig. 1). It is soon to be implemented and tested for inhomogeneous such as swirling jets.

EMST MIXING MODEL

In PDF methods, a "mixing model" is required to account for the effects of molecular diffusion. It has been realized for some time (Norris & Pope 1990) that standard models (e.g. IEM and Curl's model) are not in accord with the principle that mixing occurs locally in composition space. This deficiency leads to qualitatively incorrect model behavior in some important test problems.

The EMST mixing model—which is based on Euclidean Minimum Spanning Trees—has been developed to overcome this difficulty. The development of this model has not been simple, and considerable testing and development of variants has been required. A final version has now been established which performs well on a broad range of test problems. The model and its performance are described by Subramaniam & Pope (1996).

To test and demonstrate the capabilities of the model, it has been applied to a piloted jet diffusion flame (Masri, Subramaniam and Pope 1996). In this test case the chemistry is fast so that the composition is everywhere close to equilibrium. Figure 2 shows scatter plots of reaction progress variable b and mixture fraction ξ according to the EMST and IEM mixing models. The correct, equilibrium, behavior corresponds to all points lying on the upper two sides of the triangle that is evident in the Figure. Clearly in the EMST model calculations, nearly all of the samples do lie on these lines: but, because of the non-local mixing it involves, the IEM model incorrectly yields a significant fraction of partially burnt fluid.

MODEL FOR TURBULENCE FREQUENCY

In modelling approaches to turbulent flows, a crucial ingredient is the equation that determines the scale of the turbulence. In the current PDF model, the turbulence frequency ω determines the scales. A simple stochastic model has been developed for ω following a fluid particle. This is simpler than the lognormal model of Pope and Chen (1990), and has advantages in regions of turbulent/non-turbulent intermittent flows. This model is described in Jayesh & Pope (1995). It has been used to make calculations of a step-swirl combustor by Anand, Hsu and Pope (1996).

REFERENCES

M.S. Anand, A.T. Hsu and S.B. Pope (1996) "PDF calculations for swirl combustors," AAIA Paper 96–0522.

Jayesh and S.B. Pope (1995) "Stochastic model for turbulent frequency," Cornell Report FDA 95–05.

A.R. Masri, S. Subramaniam and S.B. Pope (1996) "A mixing model to improve PDF simulation of turbulent diffusion flames," Twenty-Sixth Symp. (Int'l) on Combust., (to be published).

A.T. Norris and S.B. Pope (1990) "Turbulent mixing model based on ordered pairing," Combustion and Flame **83**, 27-42.

S.B. Pope and Y.L. Chen (1990) "The velocity-dissipation pdf model for turbulent flows," Physics of Fluids A. **2**, 1437-1449.

S.B. Pope and P. Van Slooten (1995) "Exact PDF model for rapid distortion of homogeneous turbulence." Bull. Amer. Phys. Soc., **40**, 1999.

S. Subramaniam and S.B. Pope (1996) "Model for turbulent mixing based on Euclidean minimum spanning trees," (in preparation).

P. Van Slooten and S.B. Pope (1995) "Velocity-wavenumber PDF model for turbulent flows," Bull. Amer. Phys. Soc., **40**, 1999.

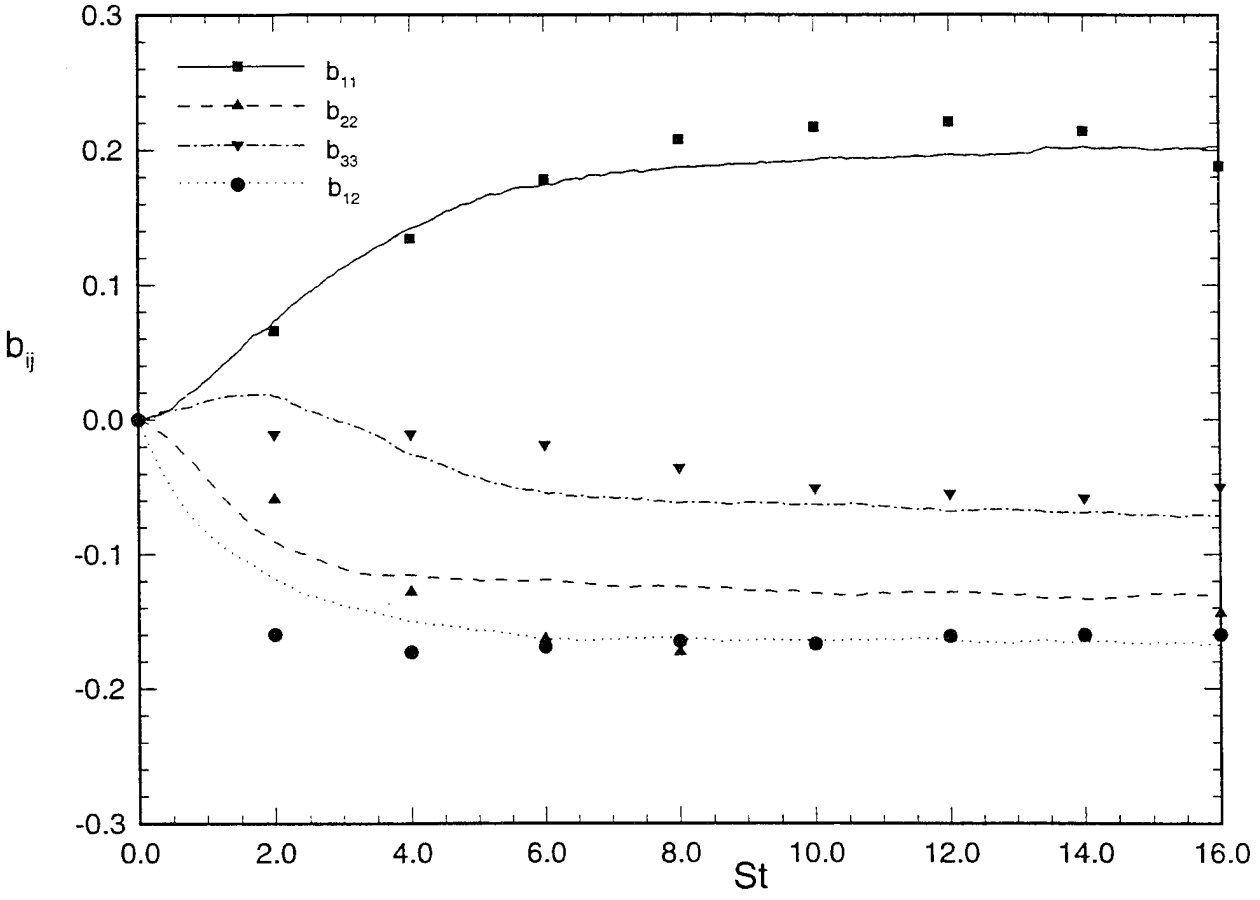

Figure 1: Velocity-wavenumber joint PDF model applied to homogeneous shear flow. Reynolds-stress anisotropies ($b_{ij} \equiv \langle u_i u_j \rangle / \langle u_\ell u_\ell \rangle - \frac{1}{3}\delta_{ij}$) as a function of the total shear ($S\,t$). Comparison with DNS (symbols) of Rogers (1986).

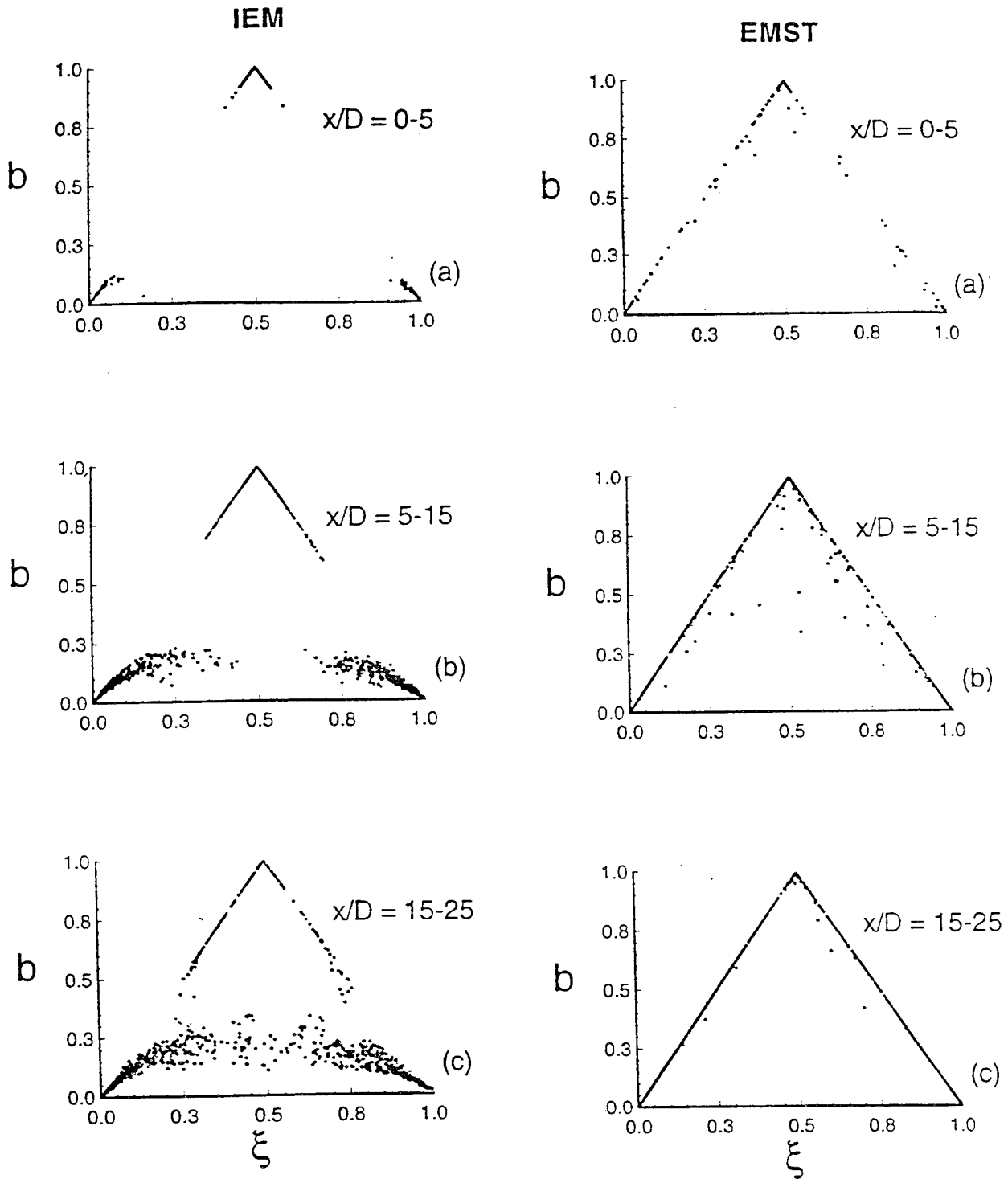

Figure 2: Scatter plots of reaction progress variable b against mixture fraction ξ in a piloted jet diffusion flame according to IEM and EMST mixing models. Each plot covers an axial range of x/D, where D is the jet diameter. The known correct result is for all points to lie on the two upper sides of the triangle. (From Masri et al. 1996.)

AFOSR SPONSORED RESEARCH IN AIRBREATHING COMBUSTION

PROGRAM MANAGER: JULIAN M. TISHKOFF

AFOSR/NA
110 Duncan Avenue, Suite B115
BOLLING AFB DC 20332-0001

SUMMARY/OVERVIEW: The Air Force Office of Scientific Research (AFOSR) program in airbreathing combustion currently is focused on six areas of study: supersonic combustion, turbulent combustion, soot, sprays, kinetics, and supercritical fuel behavior. An assessment of major research needs in each of these areas is presented.

TECHNICAL DISCUSSION

AFOSR is the single manager for Air Force basic research, including efforts based on external proposals and in-house work at Air Force laboratories. Airbreathing combustion is assigned to the AFOSR Directorate of Aerospace and Materials Sciences along with programs in rocket and space propulsion, propulsion diagnostics, fluid and solid mechanics, and structural materials.

Interests of the AFOSR airbreathing combustion subarea are given in the SUMMARY section above. Many achievements can be cited for these interests, yet imposing fundamental research challenges remain. The objective of the program is publications in the refereed scientific literature describing significant new understanding of multiphase turbulent reacting flow. Incremental improvements to existing scientific approaches, hardware development, and computer codes fall outside the scope of this objective. In recent years two major emphases have defined the main thrusts of this research activity: issues affecting the future utilization of hydrocarbon fuels and supersonic combustion to support hypersonic airbreathing propulsion technology.

Decisions on support for research proposals are based on scientific opportunities and technology needs. Proposals are submitted for panel review. Therefore, researchers interested in submitting proposals should contact Dr. Tishkoff for information on time constraints associated with proposal evaluations.

Future airbreathing propulsion systems will require fuels to absorb substantial thermal energy, raising fuel temperatures to supercritical thermodynamic conditions. Understanding and controlling fuel properties at these conditions will be crucial for avoiding thermal degradation and for optimizing subsequent processes within the combustor. Environmental concerns and the availability of petroleum supplies also will

contribute to future propulsion system design and operational needs. Novel gas turbine design methodology affecting both high performance and reduced harmful emissions was chosen to be the Air Force representative subject area in the Department of Defense Focused Research Initiative, which couples university, industry, and Government laboratory research beginning in 1995.

Designing propulsion systems that will offer reliability, maintainability and long service life represents a new motivation for propulsion research. Future budgets likely will dictate the acquisition of reduced quantities of new operational aerospace vehicles, with a corresponding increase in requirements for durability. Research topics such as soot and supercritical fuel behavior will be relevant to these new service constraints.

Beginning in fiscal year 1996 AFOSR funded an initiative addressing integrated scramjet combustor design for hypersonic propulsion. A specific research objective related to combustion will explore the sensitivity and stability of supersonic combustion to transient behavior. A primary focus of future research activities for supersonic combustion will be an examination of the utilization of hydrocarbon fuels.

Because of the termination of the Propulsion Diagnostics Subarea after fiscal year 1996, research on diagnostics relevant to airbreathing combustion will be considered for support in this subarea.

The purpose of this abstract has been to communicate AFOSR perceptions of research trends to the university and industrial research communities. However, communication from those communities back to AFOSR also is desirable and essential for creating new research opportunities. Therefore, all proposals and inquiries for fundamental research are encouraged even if the content does not fall within the areas of emphasis described herein. Comments and criticisms of current AFOSR programs also are welcome.

AFOSR SPONSORED RESEARCH IN PROPULSION DIAGNOSTICS

PROGRAM MANAGER: JULIAN M. TISHKOFF

AFOSR/NA
110 Duncan Avenue, Suite B115
BOLLING AFB DC 20332-0001

SUMMARY/OVERVIEW: After 1996 there will be no funding for new work units (contracts or grants) in this subarea. Ongoing work units will continue to receive support to their completion. Proposals for new research in diagnostics related to airbreathing combustion should be referred to that subarea through Dr. Tishkoff, while research on diagnostics for rocket and space propulsion should be discussed with Dr. Birkan.

COMPRESSIBLE TURBULENT REACTING FLOWS

(AFOSR Grant No. F49620-96-1-0106)

Principal Investigators: F.A. Williams, P.A. Libby and S. Sarkar

Department of Applied Mechanics and Engineering Sciences
University of California San Diego, La Jolla, CA 92093-0411

SUMMARY/OVERVIEW

The objective of this research was to advance fundamental understanding of reacting flows that are relevant to Air Force needs in high-speed airbreathing propulsion. Specific areas investigated were direct numerical simulation of compressible turbulent combustion, theory and modeling of compressible turbulent combustion, high-speed turbulent Couette flows with combustion, and combustion in turbulent counterflowing streams. The approaches involved computation, theoretical modeling and small-scale experimentation. Solutions to problems in the areas addressed should ultimately increase predictive capabilities of flows in combustion chambers, including supersonic combustion, thereby reducing needs for extensive trial and error in engine upgrades. The results could help to improve abilities to design propulsion systems that employ high-speed turbulent combustion.

TECHNICAL DISCUSSION

This is a new project that began March 15, 1996. However, some of the research from a previous grant is relevant to the present research. This previous work, which is just appearing in the literature, is referenced and discussed first. Future plans are then presented.

In the area of simulation, evolution of diffusion flames with large heat release in compressible homogeneous turbulence was addressed [1]. Simulations of hydrogen-oxygen diffusion flames at high turbulent Mach number have been performed to estimate the effect of large heat release on decaying isotropic turbulence. It was shown that even at high Mach numbers the effect of large density gradients on the volume-averaged statistics of turbulence was minimal for the case of partially premixed reactants in decaying isotropic turbulence.

Results from reacting and nonreacting cases are compared in Figs. 1-2. The reacting case involved combustion between hydrogen (diluted with nitrogen) and oxygen with a large heat release parameter, $Ce = Q / C_v T_{o_2} = 12$ and a large Damkohler number. The reactants were initially in a partially premixed condition. The turbulent Mach number $M_t = 0.4$, Reynolds number $Re_\lambda = 45$ and initial velocity fluctuations were identical between the reacting and nonreacting cases. A 96^3 spatial grid was used. As shown in Fig. 1, the effect of heat release on the evolution of volume-averaged turbulent kinetic energy was insignificant in spite of the large density changes present in the reacting case. The evolution of turbulent dissipation rate was also relatively unaffected by combustion.

An examination of the budget for enstrophy $\overline{\omega_i^2}$ (see Fig. 2) showed that the vortex stretching and dissipation terms dominate the enstrophy balance and appear to be changed little by

combustion. Although the baroclinic and dilatational terms were an order of magnitude larger than in the corresponding nonreacting case, their magnitudes remained much smaller than the vortex stretching and dissipation terms. Therefore, the overall effect of heat release on the vorticity and turbulent dissipation rate was relatively small. The pressure-dilatation correlation for the combusting cases was shown to be much larger and to exhibit temporal oscillations on a fast time scale. However, when integrated over time, the rapid component had a negligible contribution to the decay of turbulent kinetic energy. Comparison with DNS of zero-heat-release, passive-scalar flows at different Mach numbers have clearly shown the inhibition of scalar mixing by large heat release. Finally, it was also shown that fluctuations in mixture fraction and scalar dissipation were uncorrelated but not necessarily statistically independent and that the assumption of the equality of conditional and volume average of scalar dissipation rate was a poor approximation.

Studies were completed of counterflow hydrogen-air flames [2]. The structure, extinction and ignition of counterflow hydrogen heated-air systems were investigated for pressures and temperatures of interest in high-speed aerospace applications. A critical assessment of the recent literature was made to determine a chemical-kinetic scheme applicable for the aforementioned conditions of interest. Numerical integrations were performed for various strain rates using a continuation code which handled the singularities in the Jacobian matrix at critical strain-rate parameters. The numerical results with the detailed chemical scheme were compared with results obtained from a four-, three-, and two-step reduced chemical-kinetic scheme. Although good agreements for extinction and ignition strain rates were obtained, the two-step mechanism provided rather poor predictions of minor-species concentrations. Thermal diffusion was found to play an important role in diluted flames at high oxidizer temperatures and low fuel temperatures but to be relatively inconsequential at high fuel temperatures or in pure hydrogen-air systems. Suggestions were offered for the use of reduced chemical schemes in applications.

Turbulent reacting counterflows have relevance to combustion in nonuniform turbulent flows. Although laminar counterflows have been studied extensively, there have been only a few experiments, and one purely theoretical study [3] on the turbulent counterpart of these problems. In that work non-premixed turbulent flames in opposed air and methane streams were analyzed on the basis of the $\tilde{k}-\tilde{\varepsilon}$ theory under conditions of chemical equilibrium. The methane-air system was chosen to permit comparison with existing experimental data. It was found that the thickness of the experimentally observed flames was so large as to prelude application of the current thin-flame analyses. Accordingly, the usual thin-flame approach was avoided, and solutions for the entire flow from the exit plane of one jet to that of the other were obtained. Difficulties were encountered in comparing theory and experiment as a consequence of the flow conditions and the instrumentation used to collect the data. Nevertheless it was considered worthwhile to attempt this comparison; indeed some aerothermochemical quantities were satisfactorily predicted. The influences of several aerothermochemical quantities on the character of these flames have been examined.

Since Couette flows capture some important aspects of wall interactions in more complex configurations, the present contract will address high-speed turbulent Couette flows without and with combustion. The Reynolds-stress theory with low Reynolds number corrections will be applied first; comparison will be made with DNS results obtained elsewhere. An analysis of the low-speed, laminar counterpart of this problem has been published [4]. The flow arising from the injection of reactants through a lower porous wall and from the withdrawal of products through an upper wall which is moving in its plane at arbitrary but steady speed was analyzed. In addition to parameters characterizing the reactants and products a Reynolds number and Mach number identified the flow. The analysis was simplified by assuming that the rate of injection of reactants and the deviation of the Lewis number of the gas from unity were small and that the activation temperature was large. The latter assumption led to a description of chemical kinetic behavior in

terms of activation-energy asymptotics. Despite the resultant simplifications the parameter space characterizing these flows was found to be large. Representative solutions were given to expose the effect of variations in the Reynolds, Mach and Damköhler numbers.

Plans for new work are to complete the study of the evolution of diffusion flames with large heat release in compressible isotropic turbulence. Then, nonpremixed turbulent combustion with uniform mean shear will be calculated. Finally, turbulent combustion in spatially evolving jets will be approached. In this sequence of studies, successively more complicated situations arise, and three-dimensional simulations of the last problem with significant heat release and Taylor-scale Reynolds numbers above 50 are challenging. Associated numerical issues that will be addressed in the last problem include the specification of inflow-outflow boundary conditions, the development of stable, high-order discretization in the presence of large density and temperature gradients, and optimal spatial grid distribution.

Modeling of the flows defined above also presents challenges. It is intended to apply Reynolds-stress methods to the flow with uniform mean shear, complementing earlier such investigations of the constant-density counterpart of this problem. It is anticipated that modeling revisions, particularly for pressure-rate-of-strain effects, will be needed when compressibility is important, if the modeling is to agree with the direct numerical simulation. Approaches to improvement will employ conserved scalars with presumed probability-density functions. Also to be addressed theoretically are the spatially evolving compressible mixing layers and jets, with anisentropic effects considered to explain observed convective Mach numbers.

Further studies of Couette flows, as mentioned above, are continuing, as are additional investigations of turbulent counterflows based on a Reynolds stress formulation. This combination of analytical and numerical studies is intended to advance understanding of compressible turbulent reacting flows.

REFERENCES

[1] G. Balakrishnan, S. Sarkar and F.A. Williams, "Direct Numerical Simulation of Diffusion Flames with large Heat Release in Compressible Homogeneous Turbulence", AIAA Preprint No. 95-2375, 31st AIAA/ASME/SAE/ASEE Joint Propulsion Conference, San Diego, CA, July 1995.

[2] G. Balakrishan, M.D. Smooke and F.A. Williams, "A Numerical Investigation of Extinction and Ignition Limits in Laminar Nonpremixed Counterflowing Hydrogen-Air Streams for Both Elementary and Reduced Chemistry", Combustion and Flame, Vol. 102, pp. 329-340, August, 1995.

[3] F.A. Maury and P.A. Libby, "Nonpremixed Flames in Stagnating Turbulence. Part I. The k-ε Theory with Equilibrium Chemistry for the Methane-Air System", Combustion and Flame, Vol. 102, pp. 341-356, August, 1995.

[4] K.N.C. Bray, M. Champion and P.A. Libby, "Premixed Combustion in Laminar Couette Flow", Combustion and Flame, Vol. 104, pp. 241-259, February, 1996.

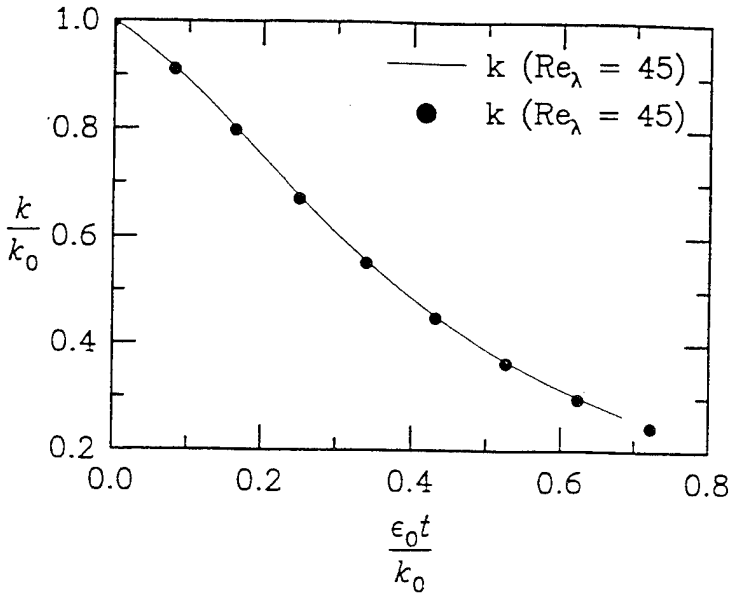

Figure 1: The evolution of normalized turbulent kinetic energy, K/K_0, as a function of eddy-turnover time, $\epsilon_0 t/K_0$, in reacting (solid line) and nonreacting (symbols) isotropic turbulence. The reacting case involves non-premixed combustion with heat release parameter, $Ce = Q/C_v T_{O_2} = 12$.

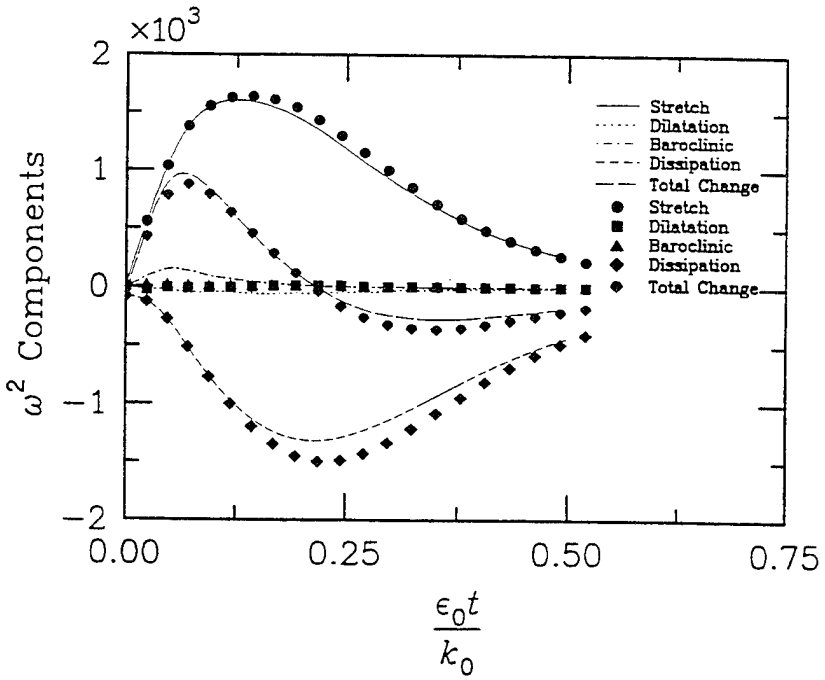

Figure 2: The evolution of all components of the enstrophy evolution equation for the reacting (solid line) and nonreacting (symbols) cases of Fig. 1.

SPACE AND ROCKET PROPULSION - GRANTEES AND CONTRACTORS

Prof. Merrill BECKSTEAD
Dept. of Chemical Engg.
Brigham Young University
Provo UT 84602
(801) 378-6239
(801) 378-7799
mwb@caedm.byu.edu

Dr Iain Boyd
Cornell University
Sibley School of Mechanical &
Aerospace Engg,216 Upson H
Ithaca NY 14853-7501
(607)255-4563
FAX: 255-1222

Dr Melvyn Branch
Center for Combustion Rsch
Mechanical Engineering Dept.
University of Colorado
Boulder CO 80309-0427
(303)492-7427
(303)492-2149
branch@spot.colorado.edu

Prof. Thomas B. Brill
Department of Chemistry
University of Delaware
Newark DE 19716
(302)831-6079
(302)831-6335
brill@brahms.udel.edu

Dr G.W.(Bill) Butler
Rocket Research Company
11441 Willows Rd
P.O. Box 97009
Redmond WA 98073-9709
(206)885-5000
FAX: (206)882-5804

Dr Mark Cappelli
Stanford University
Mechanical Engineering Dept.
Stanford CA 94305-3032
(415)725-2020
Fax 723-1748

Dr Edgar Choueiri
Department of Mechanical And
Aerospace Engineering
Princeton University
Princeton NJ 08544-5263
(609)258-5220
FAX:(609) 258-6109

Dr F E C Culick
Engrg and Appl Sci Dept
California Institute of
Technology
Pasadena CA 91125
(818)395-4783
(818)449-2677
culick@intruder.caltech.edu

Prof. Nathaniel J. Fisch
Princeton University Plasma
Physics Laboratory
PO Box 451
Princeton NJ 08543
(609)243-2643
(609)243-2662

Dr Arthur Fontijn
Chemical & Environmental
Engineering Department
Rensselaer Polytechnic Inst.
Troy NY 12180-3590
(518)276-6508
FAX: 276-4030
fontia@rpi.edu

Dr Alec D. Gallimore
The University of Michigan
Dept. of Aerospace Engineering
1320 Beal Avenue
Ann Arbor MI 48109-2118
(313)764-8224
(313)764-0578
rasta@umich.edu

Dr David Hastings
Department of Aeronautics
and Astronautics
Massachusetts Inst of Tech
Cambridge MA 02139
(617)253-0906
FAX: (617)258-7566
hastings@mit.edu

Prof. Stephen D. Heister
Purdue University
372 Grissom Hall
Aero&Astro
West Lafayette IN 47907
(317)494-5126
(317)494-0307
heister@ecn.purdue.edu

Dr David Kassoy
Associate Vice-Chancellor
Graduate School, B-26
University of Colorado
Boulder CO 80309-0026
(303)492-2991
(303)492-5777

Dr Dennis Keefer
University of Tennessee
Space Institute
Tullahoma TN 37388
(615)455-0631
FAX: (615)454-2271

Dr Herman Krier
Department of Mech&Ind Engg
104 Mechanical Engineering Bld
University of Illinois at UC
Urbana IL 61801
(217)333-0529
FAX (217)244-6907
hkrier@ux1.cso.uiuc.edu

Dr C K Law
Department of Mechanical and
Aerospace Engineering
Princeton University
Princeton NJ 08544-5263
(609)258-5271
(609)258-6233
cklaw@princeton.edu

Dr Deborah A. Levin
Institute for Defense Analysis
1801 N. Beauregard Street
Alexandria VA 22311-1772
(703) 578-2868
(703) 578-2877
dlevin@ida.org.

Dr Manuel Martinez-Sanchez
Aeronautics and Astronautics
Massachusetts Inst of Tech
Building 37-401
Cambridge MA 02139
(617)253-5613
(617)258-5143

Dr Michael Micci
233 Hammond Building
Pennsylvania State University
University Park Pa 16802
(814)863-0043
FAX: 865-3389
micci@psu.edu

Dr Dimos Poulikakos
Univ of Illinois at Chicago
Dept. of Mech. Engg.
842 West Taylor Str.
Chicago IL 60607-7022
(312)996-5239
FAX: 413-0447

Dr J W Rich
Department of Mechanical Engg
206 West 18th Ave
The Ohio State University
Columbus OH 43210
(614)292-6309
(614)292-3163

Prof. Robert J. Santoro
Propulsion Engineering Rsc.Ctr
The Pennsylvania State Univ.
110 Research Bldg East-Bigler
University Park PA 16802
(814)863-6289
(814)865-3389
bill@uther.psu.edu

Dr V V Subramaniam
Department of Mechanical Engg
206 West 18th Avenue
The Ohio State University
Columbus OH 43210
(614)292-6096
(614)292-3163
subramaniam.1@osu.edu

Dr Bagher M. Tabibi
Department of Physics
Hampton VA 23668
(804)727-5277
(804)728-6910

Dr Peter Turchi
Aero/Astro Engineering
328 CAE Building
Ohio State University
Columbus OH 43210
(614)292-2990

Prof. Forman A. Williams
University of CA, San Diego
Center for Energy and Comb.Res
9500 Gilman Drive
La Jolla CA 92093-0411
(619)534-4285
(619)534-5354
faw@ames.ucsd.edu

Dr Vigor Yang
Department of Mechanical
Engineering
Pennsylvania State University
University Park PA 16802
(814)863-1502
FAX 865-3389
vigor@aurthur.psu.edu

Prof. Ben T. Zinn
School of Aerospace Engineerin
Georgia Institute of Technolog
Atlanta GA 30332
(404)894-3033/3032
(404)894-2760
ben.zinn@aerospace.gatech.edu

SPACE AND ROCKET PROPULSION - INVITEES

Dr William Bailey
AFIT/ENP
Wright-Patterson AFB OH 45433-6583
(513)255-4498

Dr Robert Barker
AFOSR/NE
Bolling AFB
DC 20332-6448
(202)767-5011

Dr Joseph Baum
SAIC
1710 Goodridge Drive
P.O. Box 1303,
McLean VA 22102
(703)827-4952

Dr Roger Becker
KL-462
Research Institute
University of Dayton
Dayton OH 45469
(513)229-3938

Dr Michael Berman
AFOSR/NC
Bolling AFB
DC 20332-6448
(202)767-4963

Dr Oscar Biblarz
Department of Aeronautics
Naval Post Graduate School
Monterey CA 93943-5100
(408)646-2972

Dr S Binkley
Combustion Research Facility
Sandia National Laboratories
Livermore CA 94551-0969

Dr Robert Beddini
Univ of Illinois
AAE Department
104 South Mathews Avenue
Urbana IL 61801-2997
(217)333-4239

Dr Fred Blomshield
Code 3892,Propulsion
Research Branch
Naval Weapons Center
China Lake CA 93555
(619)939-3650

Dr John Brandenburg
Mission Research Corporation
8560 Cinderbed Road
Suite 700
Newington VA 22122
(703)339-6500

Dr Rodney Burton
Dept. of Aero. And Astro. Engg
University Of Illinois-UC
101 Transportation Building
Urbana IL 61801-2997
(217)333-2651

Dr George Caledonia
Physical Sciences Inc
20 New England Business Center
Andover MA 01810
(617)475-9030

Dr David Campbell
OLAC PL/DYC
Stop 24
Edwards AFB CA 93523-5000

Dr Robert Carrol
Pratt & Whitney
P.O. Box 109600
West Palm Beach FL 33410-9600
(407)796-2889

Dr Leonard Caveny
OSD/SDIO/IST
Pentagon
Washington DC 20301-7100
(703)604-0133

Dr Yunus Ali Cengel
University of Nevada-Reno
Dept of Mechanical Engg
Reno NV 89557-0030

Dr May Chan
Naval Weapons Center
China Lake CA 93555-6001
(619)939-7519

Dr C I Chang
AFOSR/NA
Bolling AFB DC 20332-6448
(202)767-4987

Dr Franklin Chang-Diaz
Lyndon B Johnson Space Center
Code CB
Houston TX 77058
(713)483-2714

Dr Malcolm Chase
Center for Chemical Physics
National Inst of Stds & Tech
Building 222, Room A158
Gaithersburg MD 20899
(301)975-2526

Dr Fan-Bill Cheung
Penn State University
208 Mechanical Engineering
University Park PA 16802
(814)863-4281

Dr Peck Cho
Dept. of Mechanical Engg.
College of Engineering
Michigan Technological Univ.
Houghton MI 49931

Dr Won-Ho Choe
214 Nuclear Engineering Lab
University of Illinois
103 South Goodwin Avenue
Urbana IL 61801
(217)333-2821

Dr Chan K Choi
Purdue University
School of Nuclear Engrg
West Lafayette IN 47907
(317)494-6789

Dr George Clark
Aerojet Tactical Systems
PO Box 13400
Building 0525
Sacramento CA 95813
(916)988-6919

Dr William Clark
Naval Weapons Center
Code 3895
China Lake CA 93555-6001

Dr Ronald Cohen
The Aerospace Corporation
PO Box 92957
Mail Stop M5-754
Los Angeles CA 90009
310 336-5946

Dr Norman Cohen
Aerospace Corporation
PO Box 92957
M/S 747
Los Angeles CA 90045
(213)648-7427

Dr Norman Cohen
Professional Services
141 Channing St
Redlands CA 92373
(714)792-8807

Dr Robert Corley
OLAC PL/RK
Stop 24
5 Pollux Dr
Edwards AFB CA 93524-7048
(805)275-5353

Ms. Victoria H. Cox
EOARDC
Edison House
223/231 Old Marylebone Road
London, NW1 5TH NY England
071-514-4437

Dr George Cox
United Technologies
Pratt-Whitney
P.O. Box 109600
West Palm Beach FL 33410-9600
(407)796-2887

Dr F E C Culick
Engrg and Appl Sci Dept
California Institute of
Technology
Pasadena CA 91125
(818)356-4470

Dr John Daily
University of Colorado
Engineering Center ME 1-13
Campus Box 427
Boulder CO 80309-0427
(303)492-7110

Dr B R Daniel
School of Aerospace Rngrg
Georgia Institute of
Technology
Atlanta GA 30332

Mr S T Demetriades
STD Research Corp
P.O. Box C
Arcadia CA 91006
(818)357-2311

Dr Gregory Dobbs
United Technologies Res. Ctr.
MS 129-90 Silver Lane
East Hartford CT 06108
(203)727-7145

Dr Joel Dubow
Materials Science
Univ of Utah
2008B Mechanical Engrg Bldg
Salt Lake City UT 84112
(801)581-8388

Dr John Eisch
Department of Chemistry
State University of New York
Binghamton NY 13901
(607)798-3994

Dr William Escher
NASA Headquarters
Code RP
Washington DC 20546
(202)453-9111

Dr James Fang
Rockwell/Rocketdyne Division
6633 Canoga Park
Canoga Park CA 91303
(818)718-3728

Dr John Fischer
Code 3853
Naval Weapons Center
China Lake CA 93555-6001
(619)939-1641

Dr Gary Flandro
School of Aerospace Engg.
Georgia Institute of Tech.
Atlanta GA 30332-0420
(404)853-9160

Dr Arthur Fontijn
Chemical & Environmental
Engineering Department
Rensselaer Polytechnic Inst.
Troy NY 12180-3590
(518)276-6508

Dr R A Frederick
Sverdrup Technology, Inc
Mail Stop 900
Arnold AFB TN 37389-9998
(615)454-3130

Dr Sheilah Fultz
Naval Weapons Center
China Lake CA 93555-6001
(619)939-7521

Dr Robert Ghirardelli
U.S. Army Research Office
P.O. Box 12211
Research Triangle Pk NC 27709-2211
(919)549-0641

Dr David Golden
SRI International
333 Ravenswood Avenue
Menlo Park CA 94025-3696
(415)859-0811

Dr William Graham
Morton Thiokol, Inc
Huntsville Division
Huntsville AL 35807-7501
(205)882-8397

Dr Alten Grandt
Department of Aeronautics
and Astronautics
Purdue University
West Lafayette IN 47907

Dr Ashwani K Gupta
Director, Combustion Lab.
The University of Maryland
Dept. of Mechanical Engrg.
College Park MD 20742
(301)454-8865

Mr Eugene Haberman
OLAC PL/MK
Stop 24
Edwards AFB CA 93523-5000
(805)275-5420

Dr V E Haloulakos
Advanced Propulsion
McDonnell Douglas
5301 Bolsa Avenue
Huntington Beach CA 92647
(714)896-3456

Dr Elmer Hansen
Department of Mechanical
Engineering
University of Florida
Gainesville FL 32611
(904)392-0802

Dr Kenneth Harstad
Jet Propulsion Laboratory
4800 Oak Grove Drive
Pasadena CA 91109

Dr David Hastings
Department of Aeronautics
and Astronautics
Massachusetts Inst of Tech
Cambridge MA 02139

Ms Sharon Hasty
John Hopkins Univ/APL
CPIA
John Hopkins Road
Laurel MD 20707
(301)992-7306

Dr Donald Hautman
United Technologies Res. Ctr.
Silver Lane
East Hartford CT 06108
(203)727-7424

Dr Helmut Hellwig
Deputy Assistant Secretary
SAF/AQR
1919 S. Eads St., Suite 100
Arlington VA 22202-3053
703 602-9301

Dr Rich Hollins
Naval Weapons Center
China Lake CA 93555-6001
(619)939-1650

Dr H R Jacobs
Mechanical Engg Bldg, 208
Penn State University
University Park PA 16802
(814)863-2519

Dr J I Jagoda
Aerospace Engineering Dept
Georgia Institute of
Technology
Atlanta GA 30329
(404)894-3060

Dr Donald Jassowski
Aerojet Technical Systems Co
PO Box 13222
Sacramento CA 95813
(916)355-2849

Dr Robert Jensen
Rockwell/Rocketdyne Division
6633 Canoga Ave
Canoga Park CA 91303
(818)718-3730

Dr M W Johnson
Head of Neutron Inst. Division
Rutherford Appleton Laboratory
Science Department
Chilton, Didcot, Oxon UK OX11 OQX
0235-21900

Dr Walter Jones
AFOSR/NA
Bolling AFB
DC 20332-6448
(202)767-0470

Dr Abraham Kadish
Earth and Space Sciences Div.
Atmospheric Sciences Group
Mail Stop D466, LANL
Los Alamos NM 87545

Dr Jordin Kare
Building 197, Room 1020
Lawrence Livermore Nat'l Lab
P O Box 808
Livermore CA 94550
(415)423-8300

Dr David Kassoy
Dept of Mechanical Engineering
University of Colorado at
Boulder, Campus Box 427
Boulder CO 80309
(303)492-2991

Dr Myron Kaufman
Department of Chemistry
Emory University
Atlanta GA 30322
(404)727-6619

Dr Dennis Keefer
University of Tennessee
Space Institute
Tullahoma TN 37388
(615)455-0631

Dr Arnold A Kelly
Department of Mechanical and
Aerospace Engineering
Princeton University
Princeton NJ 08544-5263
(206)452-5221

Dr Philip Kessel
OLAC PL/LSCF
Edwards AFB CA 93523-5000

Dr Sue Kim
California State University
6000 J Street
Sacramento CA 95819
(916)454-6712

Dr David King
Mail Stop 125-224
Jet Propulsion Laboratory
4800 Oak Grove Drive
Pasadena CA 91103
(818)354-3315

Mr Mark Kleim
NASA Lewis Research Center
21000 Brookpark Rd
MS 510-219
Cleveland OH 44135

Dr Herman Krier
Dept of Mechanical and
Industrial Engineering
University of Illinois
Urbana IL 61801
(217)333-0529

Prof M Kristiansen
P.W. Horn Professor
Dept of Electrical Engg,MS3102
Texas Tech University
Lubbock TX 79409-4439
(806)792-3007

Dr Warren Krueger
167 Alvana Street, NW16-160
Massachusetts Institute of
Technology
Cambridge MA 02139
(617)253-0236

Dr Paul Kuentzmann
Office National D'Etudes et de
rechersches Aerospatiales
29,Ave. de la Division Leclerc
Chatillon-sous-Bagneux France

Dr Kenneth Kuo
Penn State University
208 Mechanical Engineering
University Park PA 16802
(814)863-6741

Dr C K Law
Department of Mechanical and
Aerospace Engineering
Princeton University
Princeton NJ 08544-5263
(609)258-5271

Dr Joel Lebowitz
Rutgers-The State University
Department of Mathematics
Hill Center-Busch Campus
New Brunswick NJ 08903
(201)932-3117

Mr Edward Lee
Special Projects Leader
P.O. Box 808,L-368
LLNL-University of California
Livermore CA 94550
(415)422-1316

Dr Ja H Lee
NASA Langley Research Center
M/S493
Hampton VA 23665
(804)864-4332

Dr Guy Lengelle'
Office National D'Etudes et de
Recherches Aerospatiales
29,Ave de la Division Lecherc
BP 72 - 92322, Chatillon,CEDEX France

Mr Jay Levine
Phillips Lab, OLAC PL/RKFA
10 E Saturn Blvd
Edwards AFB CA 93524-7660
(805)275-5366

Dr P Y Liang
Advanced Combustion Devices
Rocketdyne Div, Rockwell Int.
6633 Canoga Avenue
Canoga Park CA 91303

Dr George Lo
Lockheed Palo Alto Research
Laboratory
3251 Hanover St, 8204-93-50
Palo Alto CA 94304
(415)424-2514

Dr David Mann
Army Research Office
P.O. Box 12211
Research Triangle Pk NC 27709-2211
(919)549-4249

Prof Alan Marchand
Dept of Chemistry
North Texas State Univ
NTSU Station, Box 13767
Denton TX 76203-5068
(817)565-3823

Dr Stephen Margolis
Combustion Research Facility
Sandia National Laboratories
Livermore CA 94551-0969

Dr Manuel Martinez-Sanchez
Aeronautics and Astronautics
Massachusetts Inst of Tech
Building 37-401
Cambridge MA 02139
(617)253-5613

Dr Peter Mattern
Combustion Sciences
Sandia National Laboratories
Livermore CA 94551-0969

Dr Jyotirmoy Mazumder
Department of Mechanical and
Industrial Engineering
University of Illinois
Urbana IL 61801
(217)333-1964

Dr John McVey
Rasor Associates, Inc
253 Humboldt Court
Sunnyvale CA 94086
(408)734-1622

Dr Franklin Mead
OLAC PL/LKVE
Edwards AFB CA 93523-5000
(805)275-5540

Dr Carl Melius
Sandia National Laboratories
Livermore CA 94551-0969
(415)294-2650

Dr Charles Merkle
205 ME
Pennsylvania State University
University Park PA 16802
(814)863-1501

Dr Claude Merrill
OLAC PL/MKPL
Stop 24
Edwards AFB CA 93523-5000
(805)275-5169

Dr Michael Micci
233 Hammond Building
Pennsylvania State University
University Park Pa 16802
(814)863-0043

Dr George Miley
University of Illinois
103 South Goodwin Avenue
214 Nuclear Engineering Lab
Urbana IL 61801
(217)333-3772

Dr Richard Miller
Office of Naval Research
Mechanics Division, Code 432
800 North Quincy Street
Arlington VA 22217-5000
(202)696-4403

Dr Charles Mitchell
Dept. of Mechanical Engineerin
Colorado State University
Fort Collins CO 80523
(303)491-6654

Dr Philip Muntz
Dept. of Aerospace Engineering
University of Southern
California
Los Angeles CA 90089

Dr S N B Murthy
Dept of Mechanical Engineering
Purdue University
West Lafayette IN 47907
(317)494-1509

Dr Jeffery Muss
Aerojet Techsystems
P.O. Box 13222
Sacramento CA 95813
(916)355-3663

Dr Subhash Narang
Chemistry Laboratory
SRI International
333 Ravenswood Avenue
Menlo Park CA 94025-3696

Dr Vittorio Nardi
Stevens Institute of
Technology
Castile Point Station
Hoboken NJ 07030
(201)420-5938

Dr Thong Nguyen
Aerojet Techsystems
P.O. Box 13222
Sacramento CA 95813
(916)355-3664

Dr Jim Nichols
OLAC PL/RKLB
Edwards AFB CA 93523-5000
(805)275-5249

Dr Arnold Nielsen
Naval Weapons Center
China Lake CA 93555-6001
(619)939-1614

Mr Randy Nishiyama
R/E/WPS
US Dept of Commerce
NOAA, 325 Broadway
Boulder CO 80303-3328

Mrs Karen Olson
OLAC PL/RKLB
Edwards AFB CA 93524-7048
(805)275-5393

Dr Douglas Olson
AeroChem Research Laboratories
Inc.
P. O. Box 12
Princeton NJ 08542
(609)921-7070

Ms Dorothy Pecker
The John Hopkins Univ/APL
John Hopkins Rd
Laurel MD 20707

Dr Don Penn
OLAC PL/RKLB
Edwards AFB CA 93523-5000
(805)275-5316

Dr Jerry Pieper
Aerojet Techsystems
P.O. Box 13222
Sacramento CA 95813
(916)355-3087

Dr Robert Poeschel
Plasma Physics Department
Hughes Research Laboratories
3011 Malibu Canyon Road
Malibu CA 90265
(213)317-5443

Dr Dimos Poulikakos
University of Illinois
(Chicago Circle)
Dept. of Mechanical Engg.
Chicago IL 60680
(312)996-5239

Dr Edward Price
School of Aerospace Engrg
Georgia Institute of
Technology
Atlanta GA 30332-0420
(404)894-3063

Dr Richard Priem
Priem Consultants
13533 Mohawk Trail
Cleveland OH 44130
(216)845-1083

Dr Lawrence Quinn
OLAC PL/DYC
Edwards AFB CA 93523-5000
(805)275-5353

Dr Frederick Reardon
Cal State U.-Sacramento
Dept of Mechanical Engineering
6000 J Street
Sacramento CA 95616
(916)278-6727

Dr Russell Reed
Naval Weapons Center
China Lake CA 93555-6001
(619)939-7296

Dr Robert Rhein
Research Chemist
Code 3244
Naval Weapons Center
China Lake CA 93555-6001
(619)939-7392

Dr J W Rich
Department of Mechanical
Engineering
The Ohio State University
Columbus OH 43212-1194
(614)292-6309

Dr Stephen Rodgers
OLAC PL/LKLR
Stop 24
Edwards AFB CA 93523-5000
(805)275-5416

Mr Wayne Roe
OLAC PL/XRX
Stop 24
Edwards AFB CA 93523-5000
(805)275-5206

Dr David Rosen
Physical Sciences Inc.
Dascomb Research Park
Andover MA 01810
(617)475-9030

Dr Thomas Rosfjord
United Technologies Res.Ctr.
Silver Lane
East Hartford CT 06108
(203)727-7418

Dr David Ross
Director,Physical Organic Chem
SRI International
333 Ravenswood Avenue
Menlo Park CA 94025-3696
(415)859-2430

Dr J Reece Roth
Dept of Elec and Comp Engrg
316 Ferris Hall
The University of Tennessee
Knoxville TN 37996-2100
(615)974-4446

Dr Gabriel Roy
ONR Code 1132P
800 North Quincy Street
Arlington VA 22217
(202)696-4405

Dr Kevin Rudolph
Martin Marietta Corporation
Mail Stop S8071
PO Box 179
Denver CO 80201
(303)977-3681

Dr Michael Salkind
President
Ohio Aerospace Institute
2001 Aerospace Parkway
Brookpark OH 44142
(216)891-2100

Dr Robert Santoro
Penn State University
Mechanical Engineering Dept
208 Mechanical Engineering
University Park PA 16801
(814)863-1285

Dr Keith Schofield
Quantum Institute
University of California,
Santa Barbara
Santa Barbara CA 93106

Dr Herbert Schrade
Institut Fur Raumfahrtantriabe
Universitat Stuttgart
Pfaffenwaldring 31
D-7000 Stuttgart GE
7116-852-383

Dr Gary Sega
Aerospace Corp
P.O. Box 92957
MS/747
Los Angeles CA 90004
(213)648-6501

Dr Isaac F Silvera
Harvard University
Department of Physics
Cambridge MA 02138
(617)495-9075

Dr William Sirignano
College of Engineering
University of California
Irvine CA 92717
(714)856-6002

Dr Ronald Spores
OLAC PL/RKAS
4 Draco Drive
Edwards AFB CA 93524-7190
(805)275-5528

Dr V V Subramaniam
Department of Mechanical
Engineering
The Ohio State University
Columbus OH 43212-1194
(614)292-6096

Dr Douglas Talley
Phillips Laboratory
OLAC PL/RKFA
10 E. Saturn Blvd.
Edwards AFB CA 93524-7660
(805)275-6174

Mr Robert L Talley
Viritay Technologoies, Inc
4845 Millersport Highway
East Amherst NY 14051
(716)689-0177

Dr James Tien
Case Western Reserve
University
Glennan Building, Room 415
Cleveland OH 44106
(216)368-4581

Dr Julian Tishkoff
AFOSR/NA
Bolling AFB DC 20332-6448
(202)767-0465

Prof William Trogler
Department of Chemistry
University of California, San
Diego
La Jolla CA 92093-0310
(619)452-6175

Dr Wing Tsang
National Institute of Standard
and Technology
Chemical Kinetics Division
Gaithersburg MD 20899
(301)975-3507

Dr Peter Turchi
Aero/Astro Engineering
328 CAE Building
Ohio State University
Columbus OH 43210
(614)292-2691

Mr Gary Vogt
OLAC PL/DYCR
Stop 24
Edwards AFB CA 93523-5000
(805)275-5258

Dr Robert Vondra
PO Box 596
Wrightwood CA 92397
(619)249-3451

Dr Francois Vuillot
Office National D'Etudes et de
resherches Aerospatiales
29,Ave de la Division Lecherc
Chatillon-sous-Bagneux France

Dr R H Woodrow Waesche
SAIC
1710 Goodridge Drive
McLean
VA 22102
(703)448-6489

Dr Richard Walker
Aerojet Techsystems
P.O. Box 13222
Sacramento CA 95813
(916)355-2694

Dr David Weaver
Phillips Laboratory
OLAC PL/RKFA
10 E. Saturn Blvd.
Edwards AFB CA 93524-7660
(805)275-5657

Dr Forman A Williams
Center for Energy and
Combustion Research, 0411
University of California
La Jolla CA 92093-0411
(619)534-5492

Dr W S Williamson
Plasma Physics Department
Hughes Research Laboratories
3011 Malibu Canyon Road
Malibu CA 90265
(213)317-5443

Dr D O Woolery
Rocketdyne
6633 Canoga Avenue
Canoga Park CA 91304

Dr Ted Yang
Massachusetts Institute of
Technology
167 Albany Street
Cambridge MA 02139
(617)253-8453

Dr Vigor Yang
Department of Mechanical
Engineering
Pennsylvania State University
University Park PA 16802
(814)863-1502

Dr Thomas York
AERO/ASTRO Engineering
328 CAE Building
Ohio State University
Columbus OH 43210
(614)292-2691

Dr Ben Zinn
School of Aerospace Engrg
Georgia Institute of
Technology
Atlanta GA 30332
(404)894-3033

AIRBREATHING COMBUSTION INVITEES

Dr. M. S. Anand
Allison Engine Company
P.O. Box 420
Speed Code T-14
Indianapolis IN 46206-0420
(317)230-2828
FAX:230-3691
iemsa@agt.gmeds.com

Dr Griffin Anderson
NASA Langley Research Center
M/S 168
Hampton VA 23665
(804)864-3772

Dr K Annamalai
Mechanical Engineering Dept
Texas A&M University
College Station TX 77843-3123

Dr Kurt Annen
Aerodyne Research, Inc.
45 Manning Road
Manning Park Research Center
Billerica MA 01821-3976
(508)663-9500
FAX:663-4918
kannen@aerodyne.com

Dr William Bachalo
Aerometrics, Inc.
755 North Mary Avenue
Sunnyvale CA 94086
(408)738-6688
FAX:738-6871

Dr S L Baughcum
Boeing Company
P O Box 3999, MS 87-08
Seattle WA 98124
(206)965-0426
FAX:234-4543

Dr Howard Baum
National Institute of
Standards and Technology
Center for Fire Research
Gaithersburg MD 20899
(301)975-6668

Dr John Bdzil
Los Alamos National Laboratory
Los Alamos NM 87545

Dr. Bruce Beaver
Department of Chemistry
Duquesne University
Mellon Hall
Pittsburgh PA 15282-1503
(412)434-6340
FAX:434-5683

Mr. Steve Beckel
Pratt and Whitney
M/S 715-83
P.O. Box 109600
West Palm Beach FL 33410-9600

Dr Edward Beiting
Aerophysics Lab, Prop & Env Sc
The Aerospace Corporation
P O Box 92957, M5/754
Los Angeles CA 90009-2957
(310)336-7035

Dr Josette Bellan
Applied Technologies Section
Jet Propulsion Laboratory
4800 Oak Grove Drive
Pasadena CA 91109
(818)354-6959

Dr Michael Berman
AFOSR/NC
110 Duncan Avenue, Suite B115
Bolling AFB DC 20332-0001
(202)767-4963
DSN 297-4963

Dr Kevin Bowcutt
North American Aircraft Div.
Rockwell International Corp.
P.O. Box 3644
Seal Beach CA 90740-7644

Dr C T Bowman
Department of Mechanical
Engineering
Stanford University
Stanford CA 94305-3032
(415)723-1745
FAX:723-1748
bowman@navier.stanford.edu

Dr Frediano V. Bracco
Department of Mechanical and
Aerospace Engineering
Princeton University
Princeton NJ 08544-5263

Dr K N C Bray
University of Cambridge
Department of Engineering
Trumpington Street
Cambridge CB2 1PZ, England UK
0223 332744
0223 337733
FAX0223 332662

Dr Robert Breidenthal
Department of Aeronautics and
Astronautics
University of Washington, FS10
Seattle WA 98195
(206)685-1098

Dr Kenneth Brezinsky
Department of Mechanical and
Aerospace Engineering
Princeton University
Princeton NJ 08544-5263
(609)258-5225
FAX:258-5963
kenb@cougarxp.princeton.edu

Dr Garry Brown
Department of Mechanical and
Aerospace Engineering
Princeton University
Princeton NJ 08544-5263
(609)258-6083

Dr R C Brown
Aerodyne Research, Inc.
45 Manning Road
Manning Park Research Center
Billerica MA 01821-3976
(508)663-9500
FAX:663-4918

Dr John D Buckmaster
Department of Aerospace
Engineering
University of Illinois
Urbana IL 61801

Dr Dennis Bushnell
NASA Langley Research Center
Mail Stop 168
Hampton VA 23665
(804)864-4546

Dr Ron Butler
WL/POSF
Building 490
1790 Loop Road, N
Wright-Patterson AFB OH 45433-7103

Dr T D Butler
Group T-3
Los Alamos National Laboratory
Los Alamos NM 87545
(505)667-4156

Dr H F Calcote
AeroChem Research Laboratories
Inc.
P. O. Box 12
Princeton NJ 08542
(609)921-7070
FAX:(908)329-8292
hfc@aerochem.com

Mr. Donald Campbell
NASA Lewis Research Center
21000 Brookpark Road
Mail Stop 3-2
Cleveland OH 44135
(216)433-2929
(216)433-5266

Dr Graham V Candler
Department of Aerospace
Engineering & Mechanics
University of Minnesota
Minneapolis MN 55455

Dr Brian Cantwell
Department of
Mechanical Engineering
Stanford University
Stanford CA 94305-3032
(415)723-4825

Dr. Nicholas Cernansky
Department of Mechanical Engrg
Drexel University
32nd and Chestnut Streets
Philadelphia PA 19104-2884

Dr Richard Chang
Applied Physics Department
P. O. Box 208284
Yale University
New Haven CT 06520-8284
(203)432-4272
FAX: 432-4274
RK_CHANG@RAMAN.ENG.YALE.EDU

Dr Chine I Chang
AFOSR/NA
110 Duncan Avenue, Suite B115
Bolling AFB DC 20332-0001
(202)767-4987
DSN 297-4987
FAX:767-4988
chang@afosr.af.mil

Dr Tryfon Charalampopoulos
Mechanical Engineering Dept.
Louisiana State University
Baton Rouge LA 70803
(504)388-5792
(504)388-5799
FAX:388-5894

Dr Lea D Chen
Mechanical Engineering Dept
University of Iowa
Iowa City IA 52242
(319)335-5674
FAX:335-5669
ldchen@icaen.uiowa.edu

Dr Wai K Cheng
Department of Mechanical
Engineering
MIT
Cambridge MA 02139
(617)253-4531

Dr Robert Childs
Nielsen Engineering and
Research, Inc.
510 Clyde Avenue
Mountain View CA 94043-2287
(415)968-9457

Dr S Y Cho
Department of Mechanical and
Aerospace Engineering
Princeton University
Princeton NJ 08544-5263

Dr M-S Chou
Building R1, Room 1044
TRW Space and Technology Group
One Space Park
Redondo Beach CA 90278
(310)812-0469
FAX:812-7589

Mr R.W. Claus
NASA Lewis Research Center
21000 Brookpark Road
Cleveland OH 44135-3127
(216)433-5869

Dr M B Colket
United Technologies Research
Center
411 Silver Lane
East Hartford CT 06108
(860)727-7481
(860)658-9502
FAX:727-2151
colket%vfs2@utrcgw.utc.com

Dr S M Correa
GE Research Center
K1-ES210
P. O. Box 8
Schenectady NY 12301
(518)387-5853
FAX:387-7258
correa@crd.ge.com

Dr David Crosley
Molecular Physics Department
SRI International
333 Ravenswood Avenue
Menlo Park CA 94025-3696
(415)326-6200

Dr Clayton Crowe
Department of Mechanical
Engineering
Washington State University
Pullman WA 99164-2920
(509)335-3214

Dr E T Curran
WL/PO
Building 18
1921 Sixth Street, Suite 5
Wright-Patterson AFB OH 45433-7650
(513)255-2520
DSN 785-2520
FAX:476-4657

Dr Eli Dabora
Mechanical Engineering Dept
University of Connecticut
Box U-139 ME
Storrs CT 06268
(203)486-2415
(203)486-2189

Dr Werner Dahm
Department of Aerospace
Engineering
The University of Michigan
Ann Arbor MI 48109-2118
(313)764-4318
(313)761-2026
FAX:763-0578
wdahm@engin.umich.edu

Dr John Daily
Center for Combustion Research
Mechanical Engineering Dept
University of Colorado
Boulder CO 80309
(303)492-7151

Dr Ron Davis
Chemical Science and Techn Lab
Building 221, Room B312
National Inst of Stds & Tech
Gaithersburg MD 20899

Dr. Peter A. DeBarber
MetroLaser
18006 Skypark Circle #108
Irvine CA 92714-6428

Dr Pablo G Debenedetti
Department of Chemical Engineering
Princeton University
Princeton NJ 08544-5263
(609)258-5480
PDEBENE@pucc.princeton.edu

Dr George Deiwert
NASA Ames Research Center
MS 230-2
Moffett Field CA 94035
(415)604-6198

Dr R W Dibble
Department of Mechanical Eng
6159 Etcheverry Hall
University of California
Berkeley CA 94720
(415)642-4901
FAX:642-6163
rdibble@firebug.me.berkeley.edu

Dr Paul Dimotakis
California Institute of Tech
1201 East California Blvd.
MC 301-46
Pasadena CA 91125
(818)395-4456
(818)395-4447
dimotakis@caltech.edu

Dr. Richard A. Dobbins
Department of Engineering
Brown University
Providence RI 02912

Dr Gregory Dobbs
United Technologies Research Center - Mail Stop 90
Silver Lane
East Hartford CT 06108
(203)727-7145

Mr Lee Dodge
Southwest Research Institute
P O Drawer 28510
San Antonio TX 78284
(512)684-5111
Ext 3251

Dr Michael Drake
Physical Chemistry Department
General Motors Research Labs
Twelve Mile and Mound Roads
Warren MI 48090-9055

Dr. James F. Driscoll
Department of Aerospace Engrg
3004 FXB Building
University of Michigan
Ann Arbor MI 49109-2118
(313)939-0101
james_driscoll@um.cc.umich.edu

Dr. J. Philip Drummond
NASA Langley Research Center
Mail Stop 197
Hampton VA 23681-0001
(804)864-2298
FAX:864-7923
j.p.drummond@larc.nasa.gov

Dr Frederick Dryer
Department of Mechanical and Aerospace Engineering
Princeton University
Princeton NJ 08544-5263
(609)258-5206

Dr C Dutton
Department of Mechanical and
Industrial Engineering
University of Illinois
Urbana IL 61801

Dr Harry Dwyer
Department of Mechanical
Engineering
University of California
Davis CA 95616

Dr A C Eckbreth
United Technologies Research
Center
411 Silver Lane
East Hartford CT 06108
(860)727-7269

Dr A C Eckbreth
United Technologies Research
Center
Silver Lane
East Hartford CT 06108
(203)727-7269

Dr. Charles A. Eckert
Department of Chemical Engrg
Georgia Institute of
Technology
Atlanta GA 30332-0100
(404)853-9344
FAX:894-6956

Dr Raymond Edelman
WC 70
Rocketdyne
6633 Canoga Avenue
Canoga Park CA 91304
(805)371-7196

Dr J T Edwards
WL/POSF
Building 490
1790 Loop Road, N
Wright-Patterson AFB OH 45433-7103
(513)255-3524
DSN 785-3524
FAX:255-1125

Dr. Fokion N. Egolfopoulos
Department of Mechanical Engrg
University of Southern Calif
Olin Hall 400B
Los Angeles CA 90089-1453
(213)740-0480
egolfopo@alnitak.usc.edu

Ms Charlotte Eigel
WL/POSF
Building 490
1790 Loop Road, N
Wright-Patterson AFB OH 45433-7103
(513)255-5106
DSN 785-5106

Dr Said Elghobashi
Department of Mechanical
Engineering
University of California
Irvine CA 92717
(714)856-6002

Dr Phillip Emmerman
Harry Diamond Laboratories
Attn. SLCHD-ST-RD
2800 Powder Mill Road
Adelphi MD 20783-1197
(301)394-3000

Dr K C Ernst
Pratt and Whitney Aircraft
Group
Government Products Division
West Palm Beach FL 33402

Dr G M Faeth
Department of Aerospace
Engineering
University of Michigan
Ann Arbor MI 48109-2118
(313)764-7202
FAX:763-0578
gmfaeth@um.cc.umich.edu

Dr. Daniel Fant
South Carolina Energy Research
and Development Center
386-2 College Avenue
Clemson SC 29634-5180
(864)656-2267
FAX:656-1429

Dr Gregory Faris
SRI International
333 Ravenswood Avenue
Menlo Park CA 94025-3493
(415)859-4131
FAX:859-6196
faris@mplvax.sri.com

Dr Francis Fendell
TRW Space and Technology Group
Building R1, Room 1022
One Space Park
Redondo Beach CA 90278
(213)812-0327

Dr Richard Field
U. S. Army Armament R&D Center
DRSMC-LCA-G(D)
Building 382-S
Dover NJ 07801
(201)724-5844
(201)724-5682

Dr. David E. Foster
Engine research Center
University of Wisconsin
Madison WI 53706

Dr Michael Frenklach
Department of Mechanical
Engineering
University of California
Berkeley CA 94720-1740
(510)643-1676
FAX:642-6163
myf@euler.berkeley.edu

Mr Jack Fultz
WL/POPR
Wright-Patterson AFB OH 45433-6563
(513)255-2175
DSN 785-2175

Dr Bish Ganguly
WL/POOC-3
Wright-Patterson AFB OH 45433-6563
(513)255-2923
DSN 785-2923
FAX:476-4095

Dr Alon Gany
Faculty of Aerospace Engrg
Technion-Israel Institute of
Technology
32000 Haifa, ISRAEL
972-4-8292554
FAX:972-4-8230956
gany@aerodyne.technion.ac.il

Dr Alan Garscadden
WL/CA
Building 45
2130 Eighth Street, Suite 1
Wright-Patterson AFB OH 45433-7542
(513)255-9400
DSN 785-9400
FAX:785-6641

Dr Alan Garscadden
WL/CA
Building 45
2130 Eighth Street, Suite 1
Wright-Patterson AFB OH 45433-7542
(513)255-9400
DSN 785-9400
FAX:785-6641

Dr Ahmed Ghoniem
Department of Mechanical Engineering
MIT
Cambridge MA 02139
(617)253-2295
FAX:253-5981
ghoniem@mit.edu

Mr R Giffen
General Electric Company
Aircraft Engine Group
Neumann Way
Cincinnati OH 45215

Dr P Givi
Department of Mechanical and Aerospace Engineering
State University of New York
Buffalo NY 14260

Dr Irvin Glassman
Department of Mechanical and Aerospace Engineering
Princeton University
Princeton NJ 08544-5263
(609)258-5199
(813)442-1118
FAX:258-5963
glassman@pucc.edu

Dr A D Gosman
Department of Mechanical Engrg
Imperial College of Science and Technology
London WS7 2BX UK

Dr Larry Goss
Research Applications Division
Systems Research Labs, Inc.
2800 Indian Ripple Road
Dayton OH 45440-3696
(513)252-2706

Dr. Richard D. Gould
Department of Mechanical and Aerospace Engineering
North Carolina State Univ
Raleigh NC 27607

Dr Frederick Gouldin
Department of Mechanical and Aerospace Engineering
Cornell University
Ithaca NY 14853-1301
(607)255-5280

Dr Frederick Gouldin
Department of Mechanical and Aerospace Engineering
Cornell University
Ithaca NY 14853-1301
(607)255-5280

Dr F Grinstein
Laboratory for Computational Physics & Fluid Dynamics
Naval Research Laboratory
Washington DC 20375-5344

Dr Ephraim Gutmark
Mechanical Engineering Dept
2508 CEBA
Louisiana State University
Baton Rouge LA 70803
(504)388-5899
(504)388-5792
FAX:388-5924
gutmark@me.lsu.edu

Dr. Mark A. Hagenmaier
WL/POPS
Building 18
1950 Fifth Street, Suite 10
Wright-Patterson AFB OH 45433-7251
(513)255-5210
DSN 785-5210
FAX:476-4659
hagenma@possum.appl.wpafb.af.mil

Dr. Robert B. Hall
SAF/AQT
1919 South Eads Street
Suite 100
Arlington VA 22202-3053
(703)746-8914
DSN 286-8914
(703)746-8918
hall@aqpo.hq.af.mil

Dr Ronald Hanson
Department of Mechanical Engineering
Stanford University
Stanford CA 94305-3032
(415)723-1745
FAX:723-1748
rhanson@cdr.stanford.edu

Dr Stephen Harris
Physical Chemistry Department
General Motors Research Labs
30500 Mound Road
Warren MI 48090-9055
(313)986-1305

Dr D L Hartley
Sandia National Laboratories
MS0735
Albuquerque NM 87185-5800

Dr Simon Henbest
Airframes & Engines Division
Aero & Maritime Research Lab
P O 4331
Melbourne, Victoria AUSTRALIA 3001
(03)647 7585
FAX:646 6771
henbests@aedmel.arl.dsto.gov.au

Dr Cecil F. Hess
MetroLaser
18006 Skypark Circle
Suite 108
Irvine CA 92714-6428
(714)553-0688
FAX:553-0495

Dr L Hesselink
Department of Aeronautics and Astronautics
Stanford University
Stanford CA 94305-3032
(415)723-3466

Dr E D Hirleman
Department of Mechanical and Aerospace Engineering
Arizona State University
Tempe AZ 85287
(602)965-3895
FAX:965-1384

Mr Norman Hirsch
WL/POPR
Wright-Patterson AFB OH 45433-6563
(513)255-2175
DSN 785-2175

Dr David Hofeldt
125 Mechanical Engineering
111 Church Street, S E
University of Minnesota
Minneapolis MN 55455
(612)625-2045

Mr Robert Holland
United Technologies Chemical Systems Division
P O Box 49028
San Jose CA 95161-9028
(408)224-7656

Dr Hans G Hornung
Graduate Aeronautical Labs
California Institute of Technology
Pasadena CA 91125
(818)395-4551

Dr David Huestis
SRI International
333 Ravenswood Avenue
Menlo Park CA 94025-3493
(415)859-3464
(415)325-4568
FAX:859-6196
huestis@mp1vax.sri.com

Dr Lawrence Hunter
Applied Physics Laboratory
Johns Hopkins University
Johns Hopkins Road
Laurel MD 20707-6099
(301)953-5000
Ext. 7406

Dr M Y Hussain
ICASE, Mail Stop 132C
NASA Langley Research Center
Hampton VA 23665
(804)864-2175

Dr A K M F Hussain
Mechanical Engineering Dept
4800 Calhoun Road
University of Houston
Houston TX 77204-4792
(713)743-4545
FAX:743-4503
mece1w@jetson.uh.edu

Dr Essam A Ibrahim
Department of Mechanical
Engineering
Tuskegee University
Tuskegee AL 36088
(205)727-8974
FAX:727-8090
emeei@acd.tusk.edu

Dr Thomas Ishii
Department of Electrical
Engineering
Marquette University
Milwaukee WI 53233
(414)288-6998
FAX:288-7082

Dr T A Jackson
WL/POSF
Building 490
1790 Loop Road, N
Wright-Patterson AFB OH 45433-7103
(513)255-6462
DSN 785-6462
FAX:255-1125

Dr Jay Jeffries
SRI International
333 Ravenswood Avenue
Menlo Park CA 94025-3493
(415)859-6341
(415)473-1553
FAX:473-6196
jeffries@mp1vax.sri.com

Mr. Jeff Jensen
Kaiser-Marquardt
16555 Staycoy Street
Van Nuys CA 91406

Mr Gordon Jensen
United Technologies Chemical
Systems Division
P O Box 49028
San Jose CA 95161-9028
(408)365-5552

Mr. Craig Johnston
Lockheed Advanced Dev. Company
Lockheed-Martin Corporation
1011 Lockheed Way
Palmdale CA 93599-7212

Dr Sheridan Johnston
Combustion Sciences
Sandia National Laboratories
Livermore CA 94551-0969
(510)294-2138

Dr K Kailasanath
Code 6410, LCP&FD
US Naval Research Laboratory
4555 Overlook Avenue, SW
Washington DC 20375-5344
(202)767-2402
FAX:767-4798
KAILASANATH@lcp.nrl.navy.mil

Dr Ann Karagozian
Mechanical, Aerospace and
Nuclear Engineering Department
University of California, LA
Los Angeles CA 90024
(213)825-5653

Dr Laurence R Keefe
Nielsen Engineering and
Research, Inc.
510 Clyde Avenue
Mountain View CA 94043-2287
(415)968-9457
FAX:968-1410

Dr Arnold Kelly
Department of Mechanical and
Aerospace Engineering
Princeton University
Princeton NJ 08544-5263
(609)258-5221

Dr John Kelly
Altex Technologies Corporation
650 Nuttman Road
Suite 114
Santa Clara CA 95054
(408)980-8610

Dr Lawrence A Kennedy
Department of Mechanical
Engineering
The Ohio State University
Columbus OH 43210-1107
(614)292-5782

Dr Ian Kennedy
Mechanical & Aero Engrg
University of California,
Davis
Davis CA 95616-5294
(916)752-2796
FAX:752-4158
IMKENNEDY@ucdavis.edu

Dr James Kezerle
Gas Research Institute
8600 West Bryn Mawr Avenue
Chicago IL 60631
(312)399-8331

Dr G B King
Department of Mechanical
Engineering
Purdue University
West Lafayette IN 47907
(317)494-6518
kinggb@mn.purdue.edu

Dr Merrill K King
NASA Headquarters
Code SNB
300 E Street, SW
Washington DC 20546
(202)358-0818

Dr William H Kirchhoff
Division of Chemical Sciences
Office of Basic Energy Science
Department of Energy
Washington DC 20585
(301)903-5820
william.kirchhoff%er@mailgw.er.doe.gov

Dr. David E. Klett
Department of Mechanical Engrg
North Carolina A&T State Univ
1601 East Market Street
Greensboro NC 27401-3209

Dr Charles Kolb
Aerodyne Research, Inc.
45 Manning Road
Manning Park Research Center
Billerica MA 01821-3976
(508)663-9500
FAX:663-4918

Dr Wolfgang Kollmann
Mechanical & Aerospace Engrg
University of California,
Davis
Davis CA 95616-5295
(916)752-4152
FAX:752-4158
wkollmann@ucdavis.edu

Dr George Kosaly
Mechanical Engineering Dept
University of Washington
Box 352600
Seattle WA 98195-2600
(206)543-6933
FAX:685-8047
kosaly@u.washington.edu

Mr David Kruczynski
Attn SLCBR-IBA
Interior Ballistics Division
Army Research Laboratory
Aberdeen Proving Gnd MD 21005-5066
(410)278-6202
DSN 298-6202

Dr Kenneth Kuo
Department of Mechanical
Engineering
Pennsylvania State University
University Park PA 16802
(814)865-6741
FAX:863-3203

Dr Samuel C Lambert
WL/CA-M
101 West Eglin Boulevard
Suite 101
Eglin AFB FL 32542-6810
(904)882-3002
DSN 872-3002
FAX:882-8689

Dr Marshall Lapp
High Temperature Interfaces
Division
Sandia National Laboratories
Livermore CA 94551-0969
(510)294-2435

Dr John Larue
Department of Mechanical
Engineering
University of California
Irvine CA 92717

Dr A Laufer
Office of Energy Research
U. S. Department of Energy
1000 Independence Avenue, N.W.
Washington DC 20585
(202)903-5820
allan.laufer%er@mailgw.er.doe.gov

Dr Normand Laurendeau
Department of Mechanical
Engineering
Purdue University
West Lafayette IN 47907
(317)494-2713

Dr Moshe Lavid
ML Energia, Inc.
P. O. Box 1468
Princeton NJ 08540
(609)799-7970

Dr C K Law
Department of Mechanical and
Aerospace Engineering
Princeton University
Princeton NJ 08544-5263
(609)258-5271
FAX:258-6233
cklaw@pucc.princeton.edu

Dr C C Lee
Environmental Protection
Agency
Cincinnati OH 45268
(513)569-7520

Dr Spiro Lekoudis
Office of Naval Research
Mechanics Division, Code 432
800 North Quincy Street
Arlington VA 22217-5000
(703)696-4406

Dr Anthony Leonard
Graduate Aeronautical Labs
California Institute of
Technology
Pasadena CA 91125
(818)395-4465

Dr Chiping Li
Naval Research Laboratory
Code 6910, CCP&FD
Washington DC 20375-5344
(202)767-3254
FAX:767-4078
LI@lcp.nrl.navy.mil

Dr Paul Libby
Department of AMES 0310
9500 Gilman Drive
University of California
La Jolla CA 92093-0310
(619)534-3168
FAX:534-4543
libby@ames.ucsd.edu

Dr Wilbert Lick
Department of Mechanical and
Environmental Engineering
University of California
Santa Barbara CA 93106

Dr Hans Liepmann
Graduate Aeronautical Labs
California Institute of
Technology
Pasadena CA 91125
(818)395-4535

Dr. Milt Linevsky
National Science Foundation
4201 Wilson Boulevard
Arlington VA 22230
(703)306-1371
FAX:306-0319
mlinevsk@nsf.gov

Dr. Charles L. Liotta
Department of Chemical Engrg
Georgia Institute of
Technology
Atlanta GA 30332-0100
(404)853-9344
FAX:894-6956

Dr Marshall Long
Department of Mechanical
Engineering
Yale University
New Haven CT 06520
(203)432-4229

Dr Lyle N Long
Department of Aerospace Engrg
233 Hammond Building
Pennsylvania State University
University Park PA 16802
(814)865-1172
lnl@psu.edu

Dr Marshall Long
Department of Mechanical
Engineering
Yale University
New Haven CT 06520
(203)432-4229

Dr F E Lytle
Department of Chemistry
Purdue University
West Lafayette IN 47907
(317)494-5261

Dr Bruce MacDonald
Research Applications Division
Systems Research Labs, Inc.
2800 Indian Ripple Road
Dayton OH 45440-3696
(513)252-2706

Dr Andrej Macek
National Institute of
Standards and Technology
Physics Building, B-312
Gaithersburg MD 20899
(301)975-2610

Dr Edward Mahefkey
WL/POOC-5
Wright-Patterson AFB OH 45433-6563
(513)255-6241
DSN 785-6241

Mr Nick Makris
SA-ALC/SFT
Kelly AFB TX 78241-5000
AV945-8212
FAX:945-9964

Dr David Mann
U. S. Army Research Office
Engineering Sciences Division
P. O. Box 12211
Research Triangle Pk NC 27709-2211
(919)549-4249
DSN 832-4249
FAX:549-4310
david@aro-emh1.army.mil

Dr Nagi Mansour
Computational Fluid Mechanics
Branch, RFT 202A-1
NASA Ames Research Center
Moffett Field CA 94035
(415)604-6420

Dr Frank Marble
Engrg. and Appl. Sci. Dept.
California Institute of
Technology
Pasadena CA 91125
(818)395-4784

Dr John Marek
NASA Lewis Research Center
21000 Brookpark Road
Cleveland OH 44135-3127

Dr Bruce Masson
PL/LIDD
3550 Aberdeen Avenue, SE
Building 401
Kirtland AFB NM 87117-5776
(505)844-0208
DSN 244-0208

Dr James McDonald
Code 6110
Naval Research Laboratory
Chemistry Division
Washington DC 20375-5342
(202)767-3340
DSN 297-3340

Dr D K McLaughlin
233 Hammond Building
Pennsylvania State University
University Park PA 16802
(814)865-2569

Dr James McMichael
AFOSR/NA
110 Duncan Avenue, Suite B115
Bolling AFB DC 20332-0001
(202)767-4936
DSN 297-4936
FAX:767-4988
mcmichael@afosr.af.mil

Dr. Mehran Mehregany
Department of Electrical Engrg
Case Western Reserve Univ
University Circle
Cleveland OH 44106-4931

Dr A M Mellor
Mechanical Engineering Dept
Box 1592, Station B
Vanderbilt University
Nashville TN 37235-1592
(615)343-6214
FAX:343-6687

Dr R Metcalfe
Department of Mechanical
Engineering
University of Houston
Houston TX 77004
(713)749-2439

Dr Andrzej Miziolek
Ignition and Combustion Branch
Interior Ballistics Division
Army Research Laboratory
Aberdeen Proving Gnd MD 21005-5066
(410)278-6157
FAX:278-6094

Dr P J Morris
233-L Hammond Building
Pennsylvania State University
University Park PA 16802
(814)863-0157

Dr Constantine M Megaridis
University of Illinois-Chicago
Mechanical Engineering Dept
842 West Taylor Street
Chicago IL 60607-7022
(312)996-3436
(312)996-5317
FAX: 413-0447
cmm@dino.me.uic.edu

Dr A M Mellor
Department of Engineering
Vanderbilt University
Nashville TN 37203
(615)343-6214

Dr Lynn Melton
Programs in Chemistry
University of Texas, Dallas
P. O. Box 830688
Richardson TX 75083-0688
(214)883-2913
(214)680-2163
FAX:883-2925
melton@utdallas.edu

Dr Michael M Micci
Department of Aerospace Engrg
233 Hammond Building
Pennsylvania State University
University Park PA 16802
(814)863-0043
(814)692-8751
FAX:865-7092
micci@psu.edu

Dr Parviz Moin
Center for Turbulence Research
Stanford University
Stanford CA 94305-3032
(415)725-2081

Dr Edward Mularz
Attn: AMSRL-VP-C
NASA Lewis Res. Ctr., MS 77-12
21000 Brookpark Road
Cleveland OH 44135-3191
(216)433-5850
FAX:433-3720
Edward.Mularz@lerc.nasa.gov

Dr M G Mungal
Department of Mechanical
Engineering
Stanford University
Stanford CA 94305-3032
(415)725-2019
(408)257-6702
FAX:723-1748
mungal@leland.stanford.edu

Dr Phillip E Muntz
Department of Aerospace Engrg
Univ of Southern California
854 West 36th Place, RRB 101
Los Angeles CA 90089-1191
(213)740-5366

Dr Arje Nachman
AFOSR/NM
110 Duncan Avenue, Suite B115
Bolling AFB DC 20332-0001
(202)767-5028
DSN 297-5028
nachman@afosr.af.mil

Dr Abdollah Nejad
WL/POPT
Building 18
1950 Fifth Street, Suite 10
Wright-Patterson AFB OH 45433-7251
(513)255-9991
DSN 785-9991
FAX:255-1759
nejadas@possum.appl.wpafb.af.mil

Dr Herbert Nelson
Code 6110, Chemistry Division
Naval Research Laboratory
4555 Overlook Avenue, SW
Washington DC 20375-5342
(202)767-3686

Dr David Nixon
NWING, Inc.
883 North Shoreline Boulevard
Suite B200
Mountain View CA 94043
(415)254-0202
FAX961-9286

Dr G B Northam
NASA Langley Research Center
MS 168
Hampton VA 23665-5225
(804)864-6248

Dr A K Oppenheim
Department of Mechanical
Engineering
University of California
Berkeley CA 94720
(415)642-0211

Dr Elaine Oran
LCP&FD, Code 6404
US Naval Research Laboratory
4555 Overlook Avenue, SW
Washington DC 20375-5344
(202)767-2960
FAX:767-4798
ORAN@lcp.nrl.navy.mil

Dr Simon Ostrach
Case Western Reserve Univ
Department of Mechanical and
Aerospace Engineering
Cleveland OH 44106

Dr T E Parker
Engineering Division
Colorado School of Mines
Golden CO 80401-1887
(303)273-3657
FAX:273-3602
tparker@mines.colorado.edu

Dr Timothy Parr
Naval Air Warfare Center
Weapons Division
C02392
China Lake CA 93555-6001
(619)939-3367
FAX:939-6569
t.parr@genie.geis.com

Dr S S Penner
Center for Energy and
Combustion Research, 0411
University of California
La Jolla CA 92093-0411
(619)534-4284

Dr Richard Peterson
Department of Mechanical
Engineering
Oregon State University
Corvallis OR 97331-6001
(503)754-2567

Dr Lisa Pfefferle
Department of Chemical
Engineering
Yale University
New Haven CT 06520-8286
(203)432-2222
FAX:432-7232
pfefferle@htcre.eng.yale.edu

Dr Emil Pfender
Department of Mechanical Engrg
125 Mechanical Engineering
The University of Minnesota
Minneapolis MN 55455

Dr W M Pitts
National Institute of
Standards and Technology
Center for Fire Research
Gaithersburg MD 20899
(301)975-6486

Dr Robert Pitz
Department of Mechanical and
Materials Engineering
Vanderbilt University
Nashville TN 37235
(615)322-0209
FAX:343-8730
pitzrw@ctrvan.vanderbilt.edu

Dr S B Pope
Department of Mechanical and
Aerospace Engineering
Cornell University
Ithaca NY 14853-1301
(607)255-4314
FAX;255-1222
pope@pdf.tn.cornell.edu

Dr C L Proctor II
Department of Mechanical
Engineering
University of Florida
Gainesville FL 32611
(904)392-7555

Dr Herschel Rabitz
Department of Chemistry
Princeton University
Princeton NJ 08544-1009
(609)258-3917
FAX:258-6746

Dr S R Ray
National Institute of
Standards and Technology
Center for Chemical Engrg
Gaithersburg MD 20899

Dr. Mohan K. Razdan
Allison Engine Company
P.O. Box 420
Speed Code T-14
Indianapolis IN 46206-0420
(317)230-6404
FAX:230-3691
iemkr@agt.gmeds.com

Mr. Robert Reed
Sverdrup Technology, Inc.
AEDC
1099 Avenue C
Arnold AFB TN 37389-9013
(615)454-4648
DSN 340-4648
(615)454-6317

Dr R G Rehm
National Institute of
Standards and Technology
Center for Fire Research
Gaithersburg MD 20899
(301)975-2704

Dr Rolf D Reitz
Mechanical Engineering Dept
University of Wisconsin
1500 Johnson Drive
Madison WI 53706
(608)262-0145
FAX:262-6717

Dr M Renksizbulut
Department of Mechanical
Engineering
University of Waterloo
Waterloo, Ontario CN N2L 3G1
(519)885-1211
Ext 3977

Dr Eli Reshotko
Case Western Reserve Univ
Department of Mechanical and
Aerospace Engineering
Cleveland OH 44106
(216)368-6447
FAX:368-6445
exr3@po.cwru.edu

Dr David Reuss
Fluid Mechanics Department
General Motors Research Labs
30500 Mound Road
Warren MI 48090-9055
(313)986-0029

Dr William Reynolds
Department of Mechanical
Engineering
Stanford University
Stanford CA 94305-3032
(415)723-3840

Dr. Kyung T. Rhee
Department of Mechanical and
Aerospace Engineering
Rutgers University
Piscataway NJ 08854

Dr James Riley
Mechanical Engineering Dept
University of Washington
Seattle WA 98195
(206)543-5347

Dr. William L. Roberts
Department of Mechanical and
Aerospace Engineering
North Carolina State Univ
Raleigh NC 27607

Dr Michael Roco
National Science Foundation
Chemical and Thermal Syst Div
4201 Wilson Boulevard
Arlington VA 22230
mroco@nsf.gov

Mr. Gerald A. Roffe
GASL
77 Raynor Avenue
Ronkonkoma NY 11779

Dr Won B Roh
Department of Engrg Physics
Air Force Institute of
Teechnology
Wright-Patterson AFB OH 45433-6583

Dr U S Rohatgi
Department of Nuclear Energy
Brookhaven National Laboratory
Upton NY 11973
(516)282-2475

Dr Glenn Rolader
Science Applications
International Corporation
1247-B N Eglin Parkway
Shalimar FL 32579
DSN 872-0391
(904)882-0391

Dr W M Roquemore
WL/POSC
Building 490
1790 Loop Road, N
Wright-Patterson AFB OH 45433-7103
(513)255-6813
DSN 785-6813
FAX:255-1125
melr@snake.appl.wpafb.af.mil

Dr Anatol Roshko
Graduate Aeronautical Labs
California Institute of
Technology
Pasadena CA 91125
(818)395-4484

Dr Daniel Rosner
Department of Chemical
Engineering
Yale University
New Haven CT 06520-8286
(203)432-4391
FAX:432-7232
rosner@htcre.eng.yale.edu

Dr John Ross
Department of Chemistry
Stanford University
Stanford CA 94305-3032
(415)723-9203

Dr Gabriel Roy
Office of Naval Research
Mechanics Division, Code 1132
800 North Quincy Street
Arlington VA 22217-5000
(703)696-4406
FAX:696-0934
roy@ocnr-hq.navy.mil

Mr Kurt Sacksteder
NASA Lewis Research Center
MS 500-217
21000 Brookpark Road
Cleveland OH 44135
(216)433-2857

Dr Leonidas Sakell
AFOSR/NA
110 Duncan Avenue, Suite B115
Bolling AFB DC 20332-0001
(202)767-4935
DSN 297-4935
FAX:767-4988
sakell@afosr.af.mil

Dr Mohammad Samimy
Ohio State University
Mechanical Engineering Dept
206 West 18th Street
Columbus OH 43210-1107
(614)422-6988
(614)848-9439
FAX:292-3163
msamimy@magnus.acs.ohio-state.edu

Dr G S Samuelsen
Department of Mechanical
Engineering
University of California
Irvine CA 92717
(714)856-5468

Dr Billy Sanders
University of California
Davis CA 95616

Dr Joseph Sangiovanni
United Technologies Research
Center
Silver Lane
East Hartford CT 06108
(203)727-7328

Dr Lakshmi Sankar
School of Aerospace Engrg
Georgia Institute of
Technology
Atlanta GA 30332
(404)894-3014

Dr Domenic Santavicca
Department of Mechanical
Engineering
Pennsylvania State University
University Park PA 16802
(814)863-1863

Dr Domenic Santavicca
Department of Mechanical
Engineering
Pennsylvania State University
University Park PA 16802
(814)863-1863

Dr R J Santoro
Department of Mechanical
Engineering
Pennsylvania State University
University Park PA 16802-2320
(814)863-1285
FAX:865-3389
rjs@ec1.psu.edu

Dr Satanu Sarkar
Department of Applied Mech
and Engr Science, MC 0411
University of California
La Jolla CA 92093-0411
(619)534-8243
FAX: 534-7078
sarkar@ames.ucsd.edu

Mr William Scallion
NASA Langley Research Center
Mail Stop 408
Hampton VA 23665
(804)864-5235

Dr Klaus Schadow
Naval Air Warfare Center
Code 3892
China Lake CA 93555-6001
(619)939-6532
DSN 437-6532
FAX:939-6569

Dr John Schaefer
Energy and Environmental Div.
Acurex Corporation
555 Clyde Ave., P. O. Box 7555
Mountain View CA 94039

Dr W H Schofield
Aeronautical Research Labs
506 Lorimer St, Fishermen's Bn
Box 4331, P O
Melbourne, Victoria AUSTRALIA 3001

Maj Scott Schreck
AFOSR/NM
110 Duncan Avenue, Suite B115
Bolling AFB DC 20332-0001
(202)767-5028
DSN 297-5028
schreck@afosr.af.mil

Mr. Lee Scuderi
McDonnell Douglas Aerospace
P.O. Box 516
St. Louis MO 63166-0516

Dr D J Seery
United Technologies Research
Center
Silver Lane
East Hartford CT 06108

Dr Hratch Semerjian
National Institute of
Standards and Technology
Chem Sci & Tech Laboratory
Gaithersburg MD 20899
(301)975-3145
FAX:975-3845
HRATCH@micf.nist.gov

Dr Robert V. Serauskas
Gas Research Institute
8600 West Bryn Mawr Avenue
Chicago IL 60631
(312)399-8208
FAX:864-2774
rserausk@gri.org

Dr K Seshadri
Center for Energy and
Combustion Research, 0411
University of California
La Jolla CA 92093-0411
(619)534-4876

Dr G S Settles
309 Mechanical Engrg Building
Pennsylvania State University
University Park PA 16802
(814)863-1504

Dr Robert Shaw
Division of Chemical and
Biological Sciences
U S Army Research Office
Research Triangle Park NC 27709-2211
(919)549-0641

Dr. Adam Siebenhaar
Aerojet Propulsion Division
P.O. Box 13222
Sacramento CA 95813-6000

Mr David Siegel
Chief of Naval Research,
804 BCT1
800 North Quincy Street
Arlington VA 22217-5660
(703)696-4771
FAX:696-4274

Dr William Sirignano
Department of Mechanical and
Aerospace Engineering
University of California
Irvine CA 92717-3975
(714)824-3700
FAX:824-3773
sirignan@uci.edu

Dr William Sirignano
Department of Mechanical and
Aerospace Engineering
University of California
Irvine CA 92717-3975
(714)824-3700
FAX:824-3773
sirignan@uci.edu

Dr Gregory Smith
Department of Chem Kinetics
SRI International
333 Ravenswood Avenue
Menlo Park CA 94025-3493
(415)859-3496

Mr. Davey Smith
Northrop Grumman Corporation
B-2 Division Dayton Office
2850 Presidential Dr., Ste 100
Fairborn OH 45324

Dr Alan Stanton
Southwest Sciences, Inc.
1570 Pacheco Street
Suite E-11
Santa Fe NM 87501
(505)984-1322

Dr F Dee Stevenson
Office of Basic Energy Science
U. S. Department of Energy
1000 Independence Avenue, N W
Washington DC 20585

Dr David Stewart
Department of Theoretical and
Applied Mechanics
University of Illinois
Urbana IL 61801

Dr Anthony Strawa
NASA Ames Research Center
MS 230-2
Moffett Field CA 94035
(415)604-3437

Dr Robert M. Stubbs
Mail Stop 5-11
NASA Lewis Research Center
21000 Brookpark Road
Cleveland OH 44135-3127
(216)433-6303
FAX:433-5802
rstubbs@lerc.nasa.gov

Dr F D Stull
WL/POPS
Wright-Patterson AFB OH 45433-6563
(513)255-5210
DSN 785-5210

Dr Geoffrey J Sturgess
ISSI
3845 Woodhurst Court
Dayton OH 45430
(513)252-2706

Dr B Sturtevant
Engrg and Appl Sci Dept
California Institute of
Technology
Pasadena CA 91125

Dr G Sullins
Applied Physics Laboratory
Johns Hopkins University
Johns Hopkins Road
Laurel MD 20707-6099
(301)953-5000

Dr Larry Talbot
Department of Mechanical
Engineering
University of California
Berkeley CA 94720
(415)642-6780

Dr. Douglas Talley
OLAC PL/RKFA
9 Antares Road
Edwards AFB CA 93524-7660
(805)275-6174
DSN 525-6174

Dr. Richard Tankin
Mechanical Engineering Dept
Northwestern University
Evanston IL 60208-3111
(708)491-3532
FAX:491-3915

Dr Julian Tishkoff
AFOSR/NA
110 Duncan Avenue, Suite B115
Bolling AFB DC 20332-0001
(202)767-0465
DSN 297-0465
FAX:767-4988
tishkoff@afosr.af.mil

Dr T Y Toong
Department of Mechanical Engineering
MIT
Cambridge MA 02139
(617)253-3358

Dr Michael Trenary
Department of Chemistry
The University of Illinois
Chicago IL 60680

Dr James Trolinger
MetroLaser
18006 Skypark Circle
Suite 108
Irvine CA 92714-6428
(714)553-0688
FAX:553-0495
jtrolinger@vmsa.oac.uci.edu

Dr Timothy Troutt
Department of Mechanical Engineering
Washington State University
Pullman WA 99164-2920

Dr. Gretar Tryggvason
Dept of Mech Engrg & Appl Mech
2350 Hayward, Room 2250
The University of Michigan
Ann Arbor MI 48109-2125
(313)763-1049
FAX:764-4256
gretar@umich.edu

Dr Allen Twarowski
Rockwell International Sci Ctr
1049 Camino dos Rios
P O Box 1085
Thousand Oaks CA 91360
(805)373-4576
FAX:373-4775
ajtwarow@scimail.remnet.rockwell.com

Dr C J Ultee
United Technologies Research Center
Silver Lane
East Hartford CT 06108

Dr A D Vakili
University of Tennessee
Space Institute
Tullahoma TN 37388

Dr John Vanderhoff
Ballistic Research Laboratory
DRSMC-BLI(A)
Aberdeen Proving Ground MD 21005
(410)278-6642

Dr S P Vanka
Department of Mechanical and Industrial Engrg
University of Illinois
Urbana IL 61801

Dr James Verdieck
Rockwell International
Rocketdyne Div, M/S FA26
6633 Canoga Avenue
Canoga Park CA 91303
(818)700-4709

Dr Juan A. Vitali
WL/FIVCO (Stop 37)
139 Barnes Drive, Suite 2
Tyndall AFB FL 32403-5323
(904)283-9708
DSN 523-9708
FAX:283-9707
75023.56@compuserve.com

Dr P J Waltrup
Applied Physics Laboratory
Johns Hopkins University
Johns Hopkins Road
Laurel MD 20707-6099
(301)953-5000
Ext. 5626

Dr Joe Wanders
AL/EQS
139 Barnes Drive
Tyndall AFB FL 32403-5319
(904)283-6026
DSN 523-6026

Dr Charles Westbrook
Lawrence Livermore National
Laboratories
P. O. Box 808
Livermore CA 94550

Dr. Phillip R. Westmoreland
Department of Chemical
Engineering
University of Massachusetts
Amherst MA 01003
(413)545-1750
(413)545-2507
(413)545-1647
westm@ecs.umass.edu

Dr James Whitelaw
Department of Mechanical Engrg
Imperial College of Science
and Technology
London SW7 2BX UK

Dr Forman Williams
Center for Energy and
Combustion Research, 0310
University of California
La Jolla CA 92093-0310
(619)534-5492
(619)534-4285
FAX: 534-5354
faw@ames.ucsd.edu

Dr Michael Winter
United Technologies Research
Center
411 Silver Lane, MS/90
East Hartford CT 06108
(860)727-7805
(860)397-1420
FAX:727-7911
mw@utrc.utc.com

Mr Steve Wirick
WL/AAWW-3
Wright-Patterson AFB OH 45433-6543
(513)255-4174
DSN 785-4174
FAX:476-4642

Dr Bernard T Wolfson
Wolfson Associates
International
4797 Lake Valencia Blvd West
Palm Harbor FL 33563
(813)786-3007

Dr Joda Wormhoudt
Aerodyne Research, Inc.
45 Manning Road
Manning Park Research Center
Billerica MA 01821-3976
(508)663-9500
FAX:663-4918

Dr J M Wu
University of Tennessee
Space Institute
Tullahoma TN 37388

Dr Richard Yetter
Department of Mechanical and
Aerospace Engineering
Princeton University
Princeton NJ 08544-5263
(609)258-2947
FAX:258-1939
rich@dante.princeton.edu

Dr Pui-kuen Yeung
School of Aerospace Engrg
Georgia Institute of
Technology
Atlanta GA 30332-0150
(404)894-9341
FAX:894-2760
yeung@peach.gatech.edu

Dr Shaye Yungster
Institute for Computational
Mechanics in Propulsion
NASA Lewis Research Ctr
Cleveland OH 44135
(216)433-6680

Dr Michael Zachariah
National Institute of
Standards and Technology
Center for Chemical Engrg
Gaithersburg MD 20899
(301)975-2063

Mr Fred Zarlingo
Code 3246
Naval Air Warfare Center
China Lake CA 93555-6001
(619)939-7395
DSN 437-7395

Dr. Ben T. Zinn
School of Aerospace Engrg
Georgia Institute of
Technology
Atlanta GA 30332-0150
(404)894-3033
FAX:894-2760
ben.zinn@aerospace.gatech.edu

Dr E E Zukoski
Engrg. and Appl. Sci. Dept.
California Institute of
Technology
Pasadena CA 91125
(818)395-4785